JPL PUBLICATION 85-61

Advanced Moisture and Temperature Sounder (AMTS) Baseline V Study Report

Nathan L. Evans, Jr.
Valerie G. Wright

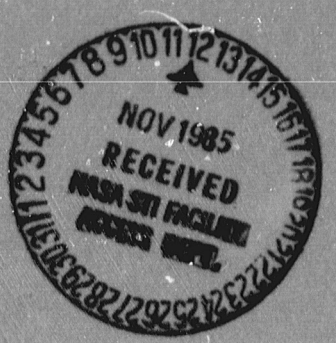

September 15, 1985

NASA
National Aeronautics and Space Administration

Jet Propulsion Laboratory
California Institute of Technology
Pasadena, California

JPL PUBLICATION 85-61

Advanced Moisture and Temperature Sounder (AMTS) Baseline V Study Report

Nathan L. Evans, Jr.
Valerie G. Wright

September 15, 1985

National Aeronautics and
Space Administration

Jet Propulsion Laboratory
California Institute of Technology
Pasadena, California

The research described in this publication was carried out by the Jet Propulsion Laboratory, California Institute of Technology, under a contract with the National Aeronautics and Space Administration.

FOREWORD

The primary responsibility of the authors was to explore instrumentation aspects of an advanced passive IR atmospheric sounder system. This exploration started with establishment of goal instrument performance requirements based upon the science investigators' study results; it ended with identification of residual issues which could be considered as a basis for sounder system optimization. We were able to treat thermal noise limited performance aspects with considerable rigor. Beyond this, we concentrated upon identifying other possible sources of error which could affect system performance. In a number of cases we have raised issues which we would have liked to explore in greater depth. We have tried to present the material at a level of detail which would be most useful to system and instrument design engineers. We trust that the more general reader will bear with us.

This study was performed in support of and with the support of the science investigators: Dr. M. T. Chahine, Dr. H. H. Aumann, Dr. J. Susskind and Dr. L. D. Kaplan. Support at the science interface was provided by Robert Haskins. Engineering support was provided by Don Langford, Frank Murphy, Greg Goodson, and Ron Salazar during the early years when we were finding our way. Additional support was provided by a number of our colleagues within the JPL and from industry.

Nathan L. Evans, Jr.
Instrument Study Manager

ABSTRACT

An Advanced Moisture and Temperature Sounder (AMTS) passive infrared atmospheric sounding system is described. Instrument requirements are developed. Parametric and scaling equations for a grating spectrometer instrument approach are developed which define detector noise limited performance in terms of instrument, orbit, and spatial coverage parameters. Instrument design criteria are developed and a baseline instrument design is presented. Error sources are identified and corresponding system error component values are estimated. Within narrow limits, the highest level of performance achievable with a stand-alone infrared sounder using current state-of-the-art technology is established. Additional trade-offs necessary to establish a reasonably optimal system design in terms of performance, cost, and risk are identified.

TABLE OF CONTENTS

LIST OF TABLES

LIST OF FIGURES

Appendix Figures

GLOSSARY

ΔT	delta temperature
AC	alternating current
ADC	analog to digital converter
AMSU	Advanced Microwave Sounder Unit
AMTS	Advanced Moisture and Temperature Sounder
AR	antireflective
ATMOS	Atmospheric Trace Molecule Spectroscopy
BRDF	bidirectional reflectance distribution function
C/C	center of curvature
CCW	counterclockwise
CH	channel
CsBr	cesium bromide
CsI	cesium iodide
CW	clockwise
D^*_{BLIP}	D* (background limited performance)
DC	direct current
DFT	discrete Fourier transform
EMI	electromagnetic interference
EOS	Earth Observation System
FFT	fast Fourier transform
FIFO	first in first out
F/NO	F-number
FTS	Fourier transform spectrometer
GFDL	Geophysical Fluid Dynamics Laboratory
GLAS	Goddard Laboratory for Atmospheric Sciences
GR	generation-recombination
GSE	ground support equipment
GSFC	Goddard Space Flight Center
HgCdTe	mercury cadmium telluride
HIRS	High Resolution Infrared Radiation Sounder
IFOV	instantaneous field of view
IMC	image motion compensation
InSb	indium antimonide
IR	infrared
JFET	junction field effect transistor
JPL	Jet Propulsion Laboratory
KBr	potassium bromide
LEO	low earth orbiter
LOHARP	Lockheed Orbital Heat Rate Program
LPE	liquid phase epitaxy
MBE	molecular beam epitaxy
MLI	multilayer insulation
MSU	Multiwave Sounder Unit
NASA	National Aeronautics and Space Administration
NCAR	National Center for Atmospheric Research
NEAT	noise equivalent delta temperature
NEN	noise equivalent radiance
NEN_ν	spectral noise equivalent radiance
NIMS	Near-Infrared Mapping Spectrometer (Galileo)
NOAA	National Oceanographic and Atmospheric Administration
OA	operational amplifier
OD	outer diameter
PC	photoconductive
P.E.	Perkin-Elmer
pixel	picture element
PP	peak to peak
preamp	preamplifier
PV	photovoltaic
R2	a grating having a blaze angle = $\tan^{-1} 2$
RC	resistance-capacitance product
RMS	root mean square
ROM	rough order of magnitude
RPM	revolutions per minute
RSS	root sum square
SAA	South Atlantic Anomaly
S/C	spacecraft
SNR	signal to noise ratio
SST	skin surface temperature
TBD	to be determined
TIA	transimpedance amplifier
TIROS	Television Infrared Observation Satellite
TOSCA	Temperature of Ocean Surface for Cloudy Atmospheres sounder
TR	transfer ratio
U.S.	United States
VTPR	Vertical Temperature Profile Radiometer

EXECUTIVE SUMMARY

INTRODUCTION

This report summarizes the results of a study covering the past eight years. It presents performance requirements and study results for an all-IR Advanced Moisture and Temperature Sounder (AMTS) using a Low Earth Orbiter (LEO) instrument. A number of AMTS implementation options using both grating spectrometers and Fourier transform spectrometers have been considered. Results of the design study indicate that a multichannel grating spectrometer is the most promising approach for the LEO instrument.

High performance passive IR atmospheric sounder systems require high spectral resolution and high radiometric precision. It was necessary during the coarse of this study to develop a number of new concepts and analytic tools to deal with this level of precision. The objective of this report is to document the options and constraints which govern design of a passive sounding system and to identify, within a relatively narrow range, system performance limits within the current state of the art. Specific report objectives are to:

- Present a consistent set of study results for a defined baseline AMTS system and instrument approach (Baseline V).
- Identify significant residual problem areas and areas of uncertainty with the Baseline V configuration. Indicate approaches for resolving uncertainties and options for resolving problem areas.
- Present a set of rules, including parametric and scaling equations, which allow first order performance of a wide range of system and instrument configurations to be quickly scaled from the Baseline V results.
- Present new, or unfamiliar, technology needed for understanding and further development of advanced atmospheric sounders, particularly technology applicable to a general class of high precision IR instruments.

AMTS SYSTEM DESCRIPTION AND INSTRUMENT REQUIREMENTS

Atmospheric temperature profiles from current satellite sounders fall short of the requirements for numerical prediction models mainly because of insufficient vertical resolution and because of cloud contamination effects. For the AMTS, a carefully chosen set of 28 narrow bandwidth channels from the 3.7 to 16.5 μm band will provide temperature sounding channels with narrow weighting functions along with complementary channels to account for the effects of surface emissivity and reflectivity, clouds, and reflected solar flux. Narrow bandpasses are required to avoid contamination by ozone and water vapor lines and to achieve maximum linear independence of the information content of the sounding channels. Based upon suitable

brightness temperature measurements from above the atmosphere this IR sounding system, using a physical method of profile retrieval, can provide global data on:

- Temperature profiles derived in the presence of up to three layers of broken clouds
- The fractional cover and height of multiple cloud layers
- Relative humidity profiles, and total precipitable water vapor
- Total ozone burden of the atmosphere
- Land surface temperatures
- Sea surface temperatures
- Air-sea temperature differences

Instrument requirements are for:

- Relatively high spectral resolution
- Relatively high spatial resolution
- High radiometric precision
- Good radiometric stability

Systematic radiometric errors, including atmospheric transmissivity effects, can be reduced by in-orbit system tuning using radiosonde data as a reference standard.

System performance has been verified through system simulations, including a set of NASA/NOAA blind tests. The physical profile retrieval method has also been verified using operational sounder data.

Goal instrument requirements for a Baseline V AMTS system were defined based upon system simulation results. In general, a worst case interpretation of possible system drivers on instrument requirements was assumed in order to best establish limits of instrument capabilities and instrument constraints.

INSTRUMENT DESCRIPTION

Design tools necessary for defining instrument design criteria were developed. Single footprint detector noise limited NEN parametric and scaling equations were developed in terms of instrument design parameters for generalized grating spectrometer optical configurations. Relative detector noise limited single footprint and composite footprint NEN parametric and scaling equations were developed in terms of earth coverage parameters (assuming crosstrack pushbroom spatial scan), spatial resolution parameters, and the number of pixel elements in the crosstrack pushbroom scan array. Detector performance parametric equations were developed which show D*

dependency upon instrument optical design parameters; upon detector photon background, temperature, and bias voltage; upon detector material and design parameters; and upon preamplifier parameters. A scalar grating efficiency model was developed which can be used for high dispersion echelle gratings. A performance quality criterion was developed for multiblaze gratings, and an approach for developing a scalar efficiency model for multiblaze gratings was outlined. Computer models for evaluating figures of merit for a number of optical chopper/noise filter configurations were developed. These models include 1/f noise effects. Slit function considerations, including effects of spatially distributed noncoherent area sources and of foreoptics aberrations, were developed. Earth coverage characteristics for a number of sun synchronous low earth orbits were examined. For ±45 degrees cross-track scan and using a single satellite, only orbits close to the 833 km altitude TIROS orbit provide full earth coverage once in each 24 hour period. For this orbit, gaps left near the equator between ascending orbits are covered by the descending orbits about 12 hours later. The 705 km orbit proposed for the EOS would provide full earth coverage once in each 36 hour period. A 1350 km orbit represents the minimum altitude for full earth coverage twice in each 24 hour period. For this orbit, coverage would be contiguous between successive orbits. Two satellites in properly synchronized orbits could provide full earth coverage twice in each 24 hour period for orbit altitudes between ~700 and 1350 km.

Using these design tools, optical design criteria and functional requirements were specified. Functional requirements for instrument electronics and radiative coolers were developed. A conceptual optical design was developed for a Baseline V instrument. This design was based upon a high dispersion echelle grating optimized for maximum efficiency rather than for minimum polarization sensitivity. This instrument uses a 16 element linear inlet slit array scanned crosstrack in a pushbroom mode. The image plane assembly contains 16 detectors per spectral channel for a total of 448 signal channel detectors. Provisions for in-orbit radiometric calibration and spectral monitoring were included. Conceptual design of the instrument electronics was completed through the detail block diagram level. A conceptual design was developed for the instrument optical assembly package. Radiative coolers, designed for a TIROS orbit, are an integral part of this package design.

BASELINE V ERROR ANALYSIS

Baseline V instrument error sources were identified and, for all error sources considered significant, nontunable error values were estimated in terms of equivalent radiometric NEΔT. Instrument systematic radiometric error component values were also estimated. Significant uncertainties in the data base or method of analysis were identified. System tuning error sources, including error sources in addition to instrument sources, were identified. Error component values for noninstrument sources were not estimated.

SYSTEM PERFORMANCE SUMMARY

Estimated Baseline V performance was compared with the goal instrument requirements and with estimated AMTS instrument performance used for the NASA/NOAA tests. Baseline V detector noise limited performance

effectively satisfies the goal instrument requirements, and betters the performance used for the NASA/NOAA tests. Other sources of error, specifically spatial crosstalk effects and scene polarization effects, predominate when the instrument views sunlit clouds to a degree that could make the uncorrected Baseline V performance unacceptable. It is shown that spatial crosstalk errors could be removed through image processing of the measured scene radiometric values. Instrument scene polarization sensitivity could be effectively eliminated by using higher grating orders in conjunction with a multiblaze grating. Alternatively, both spatial crosstalk and scene polarization effects could be effectively eliminated by using only night-side soundings. Operationally, this would require two satellites in low earth orbit or one satellite in a higher orbit to obtain full night-side earth coverage in each 24 hour period.

Study results lead to high confidence that an all-IR sounder using a grating spectrometer instrument aproach is technically feasible. The only significant physical uncertainties concern slit function wing response crosstalk effects and, possibly, multiblaze grating efficiency and buildability. Relatively simple approaches are outlined for resolving these uncertainties.

This study was focused upon establishing instrument feasibility and performance limits for a state-of-the-art instrument. Prior to building an instrument using the Baseline V concept another pass should be made at optimizing the instrument design, including instrument cost as a consideration.

ADVANCED SYSTEM DESIGN CONSIDERATIONS

Some system trade-off considerations associated with each instrument requirement specified for Baseline V are identified. Corresponding data needs in terms of unanswered system performance and instrument performance questions are also identified. These trade-off considerations are targeted at advanced system designs beyond Baseline V.

IR instrument options and constraints are reasonably well understood. It is now possible to seriously explore advanced sounder system aspects beyond hardware design. The sounder system design selected can have an impact on system performance, instrument complexity, the satellite vehicle, ground processing software, and system development costs and risks. Whatever the instrument approach, this study illustrates the importance of identifying all sources of system error and of understanding their impact upon overall system performance as a basis for committing to major hardware or software development. A high precision atmospheric sounder system design which considers only instrument detector/preamp noise limited performance to the exclusion of other sources of error will almost certainly result in disappointing sounder system performance. The results of this study strongly suggest that the overriding requirement for the next generation atmospheric sounder will remain high precision radiometry, and that the basic physics of the problem will dictate a relatively complex instrument.

STUDY SUMMARY AND CONCLUSIONS

The ultimate objective of this study was to develop an advanced infrared atmospheric sounder system which could meet the requirements of the numerical weather prediction models of the 1990s. In the course of this study, an Advanced Moisture and Temperature Sounder (AMTS) design approach was developed which establishes the highest level of performance achievable with a stand-alone infrared sounder with current state-of-the-art technology.

While an AMTS is technically feasible and would achieve superior performance compared to current operational sounders, compared to this current generation of sounders it is a large and complex instrument. The design concepts and parametric equations developed in this report could be used in an effort to explore a middleground between the higher performance and complexity of a state-of-the-art AMTS and the lower performance and complexity of current sounders.

SECTION 1

1.0 INTRODUCTION

1.1 Scope

This report presents performance requirements and study results for an all-IR system using a Low Earth Orbiter (LEO) Baseline V grating spectrometer instrument approach for an Advanced Moisture and Temperature Sounder (AMTS). (Microwave instrumentation considerations are beyond the scope of this report.)

1.2 Study Objective and Approach

The objective of this AMTS system study was to carry a detailed conceptual design of an AMTS system to the point where instrument hardware performance, performance options, and their relationships to end user requirements and ground data processing requirements are well understood. To this end, goal instrument performance requirements were established based upon preliminary AMTS system simulation results. In general, for the purpose of the instrument feasibility study, a "worst case" interpretation of possible system drivers on instrument requirements was assumed in order to best establish limits of both instrument capabilities and instrument constraints. "Baseline" instrument conceptual designs were established and tested for performance capability and buildability. Where a design failed a test for performance or feasibility, the baseline was modified and retested.

A conceptual design for a LEO operational instrument was used for this study. The performance of experimental instruments--for use on the space shuttle or a space platform, for example--could be quickly scaled from the performance calculated for the baseline operational instrument using a set of parametric and scaling equations. Modification of the operational instrument approach for experimental purposes would not be difficult, and would maximize hardware design inheritance from an experiment.

1.3 Study Status

A number of AMTS implementation options using both grating spectrometers and FTS spectrometers have been considered. Results of the design study indicate that the multichannel grating spectrometer is the most promising approach for a LEO IR instrument. The FTS approach has been studied in some depth, both in-house by JPL and by Perkin-Elmer under contract to JPL. An interferometer study report was prepared by Perkin-Elmer (Ref 1-1). A JPL summary analysis of this study report is presented in Appendix A.

The study program is at the point where IR instrument options and constraints are reasonably well understood. It is now possible to seriously explore AMTS system aspects beyond hardware design. The AMTS system design selected from the possible options can have an impact on system performance, instrument complexity, the satellite vehicle, ground processing software, and system development costs and risks.

1.4 Report Objectives

The AMTS study has been conducted over a period of approximately 8 years at a relatively low level of funding. This has allowed a number of iterations of the AMTS design approach and has resulted in development of some expertise. High performance passive IR atmospheric sounding systems require high spectral resolution and high radiometric precision in the sounding instrument. It was necessary during the course of this study to develop a number of new concepts and analytic tools to deal with this level of precision.

The objective of this report is to document the options and constraints which govern design of a passive infrared atmospheric sounding system and to identify, within a relatively narrow range, system performance limits within the current state-of-the-art. Specific report objectives are to:

- Present a consistent set of study results for a defined baseline AMTS system and instrument approach (Baseline V).
- Identify significant residual problem areas and areas of uncertainty with the Baseline V configuration. Indicate approaches for resolving uncertainties and options for resolving problem areas.
- Present a set of rules, including parametric and scaling equations, which allow first order performance of a wide range of system and instrument configurations to be quickly scaled from the Baseline V results.
- Present new, or unfamiliar, technology needed for understanding and further development of the AMTS—particularly technology applicable to a general class of high precision IR instruments.

1.5 Report Organization

The AMTS system description and goal instrument performance requirements are presented in Section 2. Instrument optical design criteria and the Baseline V grating spectrometer conceptual design are presented in Section 3. Identification and analysis of instrument error sources which impact AMTS system performance are presented in Section 4. Instrument and system performance is summarized in Section 5. Section 5 also identifies risk areas and uncertainties associated with the Baseline V approach. Some advanced system design considerations (beyond Baseline V) are identified in Section 6. Study summary and conclusions are presented in Section 7.

In the sense that instrument performance options and constraints form the basis for the conclusions and recommendations presented, Sections 3 and 4 document a significant part of the study, particularly since a number of error sources applicable to the AMTS grating spectrometer are also applicable to other passive IR sounding systems and to other instrument approaches.

REFERENCES - SECTION 1

1-1 "Feasibility of a Fourier Transform Spectrometer for the Advanced Moisture and Temperature Sounder," Report No. 15407, Perkin-Elmer Electro-Optical Division, January 29, 1982.

SECTION 2

2.0 AMTS SYSTEM DESCRIPTION AND INSTRUMENT REQUIREMENTS

This section describes the AMTS system and presents goal requirements for the AMTS instrument. These requirements are not necessarily final instrument requirements. Their purpose is to define a consistent set of interim baseline requirements for development and evaluation of a baseline instrument conceptual design. The purpose of this instrument design, in turn, is to provide further insight into the capabilities and limitations of an AMTS system, specifically in those areas where overall system design is affected by instrument capabilities, options, and constraints.

2.1 AMTS System Description

2.1.1 Requirements for Improved Atmospheric Sounding

Atmospheric temperature profiles are the most important meteorological parameter for numerical weather prediction currently derived from satellites. During the past 20 years considerable progress has been made in passive infrared remote sensing of vertical temperature profiles and different techniques have been developed to recover profiles globally with an rms accuracy of ≈2.25 K (Ref 2-1, 2-2). This accuracy, however, falls short of the requirements for numerical prediction models mainly because of insufficient vertical resolution and cloud contamination effects. Furthermore, the need for improved sounding is accentuated by the fact that, during the past decade, models have evolved far more rapidly than the capabilities of satellite-borne temperature sounders to supply accurate data (Ref 2-2). For example, the various numerical circulation models developed at GLAS, NOAA, GFDL, and NCAR have eight layers or more below 100 mbar. The current generation of sounders is capable of sounding the troposphere at only three or four levels.

The limitation in vertical resolution is caused mainly by the broadness of contribution functions of current instruments. When the contribution functions are broad, emitted energy reaching the satellite in each channel will have components originating from a thick layer of the atmosphere, thereby making reconstruction of fine-scale vertical details practically impossible. Because of this, as well as difficulties in eliminating cloud contamination effects, surface emissivity effects, and contamination by O_3, H_2O and other minor constituents, the rms errors in the retrieved temperature profiles remain high. Progress in these areas is essential for improving the utilization of satellite data.

2.1.2 Components of the Upwelling Radiance

The clear column radiance, $\bar{I}(\upsilon,\theta)$, at frequency υ and zenith angle θ can be expressed in terms of four main components:

$$\bar{I}(\upsilon,\theta) = I_s(\upsilon,\theta) + I_a(\upsilon,\theta) + I_d(\upsilon,\theta) + I_h(\upsilon,\theta) \qquad (2.1)$$

where

$\bar{I}(\upsilon, \theta)$ = clear-column radiance reconstructed from $\tilde{I}(\upsilon, \theta)$ according to Eq 2.2

$I_s(\upsilon, \theta)$ = surface emission

$I_a(\upsilon, \theta)$ = atmospheric emission

$I_d(\upsilon, \theta)$ = reflected thermal downward-flux

$I_h(\upsilon, \theta)$ = reflected solar flux

It is very difficult to predict when an observed field of view is cloud free, no matter how small the field of view. The clear column radiance, however, can be determined with an accuracy of ±1% from observations in two different spectral bands obtained over adjacent fields of view according to a method used by Chahine (Ref 2-3, 2-4, 2-5, 2-6, 2-7). According to this method $\bar{I}(\nu, \theta)$ is expressed as

$$\bar{I}(\upsilon, \theta) = \tilde{I}_1(\upsilon, \theta) + \eta_1[\tilde{I}_1(\upsilon, \theta) - \tilde{I}_2(\upsilon, \theta)] + \eta_2[\tilde{I}_1(\upsilon, \theta) - \tilde{I}_3(\upsilon, \theta)] + \ldots \quad (2.2)$$

where η_1 and η_2 are parameters independent of frequency and $\tilde{I}_1(\upsilon, \theta)$, $\tilde{I}_2(\upsilon, \theta)$ and $\tilde{I}_3(\upsilon, \theta)$ are the observed radiance values in three fields of view having different amounts of clouds. The method does not require any field of view to be cloud free.

The radiance due to surface emission, $I_s(\upsilon, \theta)$, is expressed as

$$I_s(\upsilon, \theta) = \varepsilon_s(\upsilon, \theta)\ B(\upsilon, T_s)\ \tau(\upsilon, \theta, p_s) \quad (2.3)$$

where $\varepsilon_s(\upsilon, \theta)$ is the surface emissivity, and $\tau(\upsilon, \theta, p_s)$ is the atmospheric spectral transmittance between the surface and the instrument. The Planck function, $B(\upsilon, T_s)$, is given by

$$B(\upsilon, T) = a\upsilon^3/(e^{b\upsilon/T} - 1) \quad (2.4)$$

The radiance due to atmospheric emission, $I_a(\upsilon, \theta)$, is expressed as

$$I_a(\upsilon, \theta) = \int_{p_s}^{0} B[\upsilon, T(p)] \frac{\partial \tau(\upsilon, \theta, p)}{\partial \ln p}\, d \ln p \quad (2.5)$$

where $T(p)$ is the vertical atmospheric temperature profile as a function of pressure.

For an optically thin isotropic atmosphere, radiance due to reflected thermal downward flux, $I_d(\upsilon,\theta)$, is expressed as

$$I_d(\upsilon,\theta) = \rho_s(\upsilon,\theta)\ I_a(\upsilon)\ \tau(\upsilon,\theta,p) \tag{2.6}$$

with $I_a(\upsilon) = 2I_a(\upsilon,0)$. For a Lambertian surface

$$\rho_s(\upsilon,\theta) = 1 - \epsilon_s(\upsilon,\theta) \tag{2.7}$$

The radiance due to reflection of solar flux, $I_h(\upsilon,\theta)$, is expressed as

$$I_h(\upsilon,\theta) = H_h(\upsilon)\cos\theta_h\ \tau(\upsilon,\theta_h,p_s)\ \hat{\rho}_s(\upsilon,\ \tau(\upsilon,\theta,p_s) \tag{2.8}$$

where $H_h(\upsilon) = 2.16 \times 10^{-5}\pi\ B(\upsilon,T_h)$, θ_h is the direction of the sunbeam, $T_h = 5600$ K, and $\hat{\rho}_s$ is the bidirectional surface reflectance.

In order to solve Eq 2.1 for accurate retrieval of atmospheric temperature profiles, $T(p)$, a set of temperature sounding channels with narrow weighting functions, $\partial\tau/(\partial \ln p)$, is needed In addition, a complementary set of channels is needed to account for the effects of surface emissivity, ϵ_s; reflectivity, $\hat{\rho}_s$; and clouds, η; and account for the reflected solar flux during daytime observations (Ref 2-6). Sounding frequencies with narrow bandpasses are required in order to avoid contamination by ozone and water vapor lines and to achieve maximum linear independence of the information content of the sounding channels. Similar considerations apply to the selection of a set of channels for retrieving water vapor profiles.

2.1.3 Sounding Frequencies

2.1.3.1 Spectral Channels

The spectral range from 3 to 17 μm was investigated in order to choose an optimum set of sounding frequencies to satisfy the criteria discussed in Para 2.1.2. The resulting channel set, shown in Table 2-1, includes:

- 4.3 μm CO_2 band channels to determine the temperature profile in the lower troposphere, and a compatible number of channels from the 15 μm CO_2 band to determine the rest of the temperature profile (Ref 2-8).
- Three long-wave channels from the 15 μm CO_2 band to correct for the effects of clouds and haze (Ref 2-4).
- Three narrow bandpass channels from the 3.7 μm region to account for sea-surface emissivity and reflectivity and to retrieve sea-surface temperature (Ref 2-9, 2-10).
- 6.3 μm to 11 μm water vapor channels for water vapor profiles.

2.1.3.2 Vertical Resolution of Temperature Profiles

Table 2-2 shows that the R-branch of the 4.3 μm CO_2 band between 2383 and 2390 cm^{-1} is the best choice for selection of temperature sounding channels. In this branch advantage is taken of the temperature dependence of the high-J lines. This dependence acts to enhance the pressure effect in the troposphere where the temperature decreases with height, and also makes use of the strong dependence of the Planck function on changes in temperature. These two properties combine to make the contribution functions of the AMTS 4.3 μm tropospheric channels narrower by a factor of two than those of present infrared or microwave sounders. For sounding the upper atmosphere a corresponding set of narrow-band channels was selected from the 15 μm CO_2 band as shown in Table 2-1. The contribution functions of the complete set of temperature sounding channels are shown in Fig 2-1. The extent to which the set of channels is affected by H_2O and O_3 lines is summarized in Table 2-3.

2.1.3.3 Cloud Filtering Capability

The set of channels given in Table 2-1 results in a substantial improvement in retrieving clear-column profiles accurately even in the presence of multiple cloud layers (Ref 2-1). This is achieved by an AMTS design which insures that all channels observe the same field of view (i.e., the same clouds) at the same time, and by properly selecting three 15 μm "cloud-filtering" channels which are optimally sensitive to low, middle, and high clouds respectively. Further, a data analysis method is employed which does not require any field of view to be cloud free. This method has been verified with the VTPR (Ref 2-11) and HIRS data.

2.1.3.4 Determination of Surface Effects

To account for surface reflectivity and emissivity and to retrieve accurate skin surface temperature of both land and oceans (Ref 2-6) a set of three "super window" channels was chosen from the 3.7 μm region. The 3.7 μm region offers two distinct advantages in terms of sensitivity and ability to observe the surface with minimum interference by the atmosphere (Ref 2-9, 2-10). First, because of the exponential dependence of $B(\upsilon,T_s)$ on υ and T_s, the sensitivity of $B(\upsilon,T_s)$ to changes in T_s decreases with decreasing frequency until it becomes linear in the microwave region. Figure 2-2 shows that in order to derive T_s with an accuracy of 1 K it is necessary to determine $B(\upsilon,T_s)$ with an accuracy of ~4% for the 3.7 μm channels, and ~1.5% for the 11 μm channels. (For microwave frequencies, $B(\upsilon,T_s)$ would have to be determined with an accuracy of ~0.3%.) Second, attainment of a 4% accuracy in $B(\upsilon,T_s)$ is possible in certain parts of the 3.7 μm region because in these "transparent" parts the surface emission term is nearly equal to the clear-column radiance $\bar{I}(\upsilon,\theta)$. In fact, if nighttime observations in a humid tropical atmosphere are simulated and all effects corresponding to ε, τ and $I_a(\upsilon,\theta)$ are neglected, brightness temperature values, T_b, are obtained where

$$B(\upsilon,T_b) = \bar{I}(\upsilon,\theta)$$

Table 2-1 AMTS narrow bandpass channels (Baseline V)

Band	Channel	Wave-length	Spectral Fre-quency	Half-Power Band-width	Equivalent Scene Blackbody Temperature Above Atmosphere			Main Channel Function
No.	No.	$\lambda(\mu m)$	$\upsilon(cm^{-1})$	$\Delta\upsilon(cm^{-1})$	T_{min} (K)	T_{std} (K)	T_{max} (K)	
1	1	16.476	606.95	0.50	230	263.83	286	Cloud filtering
	2	16.046	623.20	0.50	229	260.15	283	
	3	15.929	627.80	0.50	218	236.51	260	
	4	15.765	634.30	0.50	211	226.46	256	Temperature profile upper atmosphere
	5	15.466	646.60	0.50	202	219.66	248	
	6	15.282	654.35	0.50	195	219.68	255	
	7	15.025	665.55	0.50	197	222.69	266	
	8	14.996	666.85	0.50	194	223.38	279	
	9	14.967	668.15	0.50	198	254.00	300	
	10	14.938	669.45	0.50	199	233.04	285	
2	11	11.429	875.00	0.75	231	285.00	327	H_2O/SST
	12	9.608	1040.80	1.00	198	256.26	290	Ozone
	13	8.120	1231.60	1.00	231	285.40	327	H_2O/SST
	14	6.060	1650.10	1.30	220	239.30	261	H_2O profile
	15	5.881	1700.30	1.30	216	219.50	255	
3	16	5.437	1839.40	1.50	232	259.32	282	H_2O profile
	17	5.403	1850.90	1.50	233	266.90	289	
	18	5.181	1930.10	1.50	232	280.28	315	
4	19	4.195	2384.00	2.00	214	229.56	274	Temperature profile lower atmosphere
	20	4.191	2386.10	2.00	222	240.97	299	
	21	4.187	2388.20	2.00	229	254.69	313	
	22	4.184	2390.20	2.00	231	265.88	321	
	23	4.180	2392.35	2.00	232	273.30	325	
	24	4.176	2394.50	2.00	232	276.20	326	
	25	4.125	2424.00	2.50	232	281.38	331	Air-surface ΔT
	26	3.992	2505.00	2.50	232	285.22	342	Skin surface temperature (SST)
	27	3.822	2616.50	2.50	232	286.57	354	
	28	3.723	2686.00	2.50	232	286.53	364	

Table 2-2 Comparison of the half-widths of contribution functions

Band	$\Delta\upsilon/\upsilon$	Half-Width In Scale Heights	Remarks
14.5 μm	10^{-2}	2.4	VTPR/HIRS
15 μm	10^{-3}	1.6	AMTS
15 μm	10^{-4}	1.4	Wings of lines
60 GHz	10^{-3}	1.3	AMSU
15 μm	10^{-2}	1.6	VTPR
60 GHz	10^{-3}	1.5	MSU/AMSU
4.46 μm	10^{-2}	1.3	HIRS
4.18 μm	10^{-3}	0.69	AMTS
4.18 μm	10^{-4}	0.60	Wings of lines

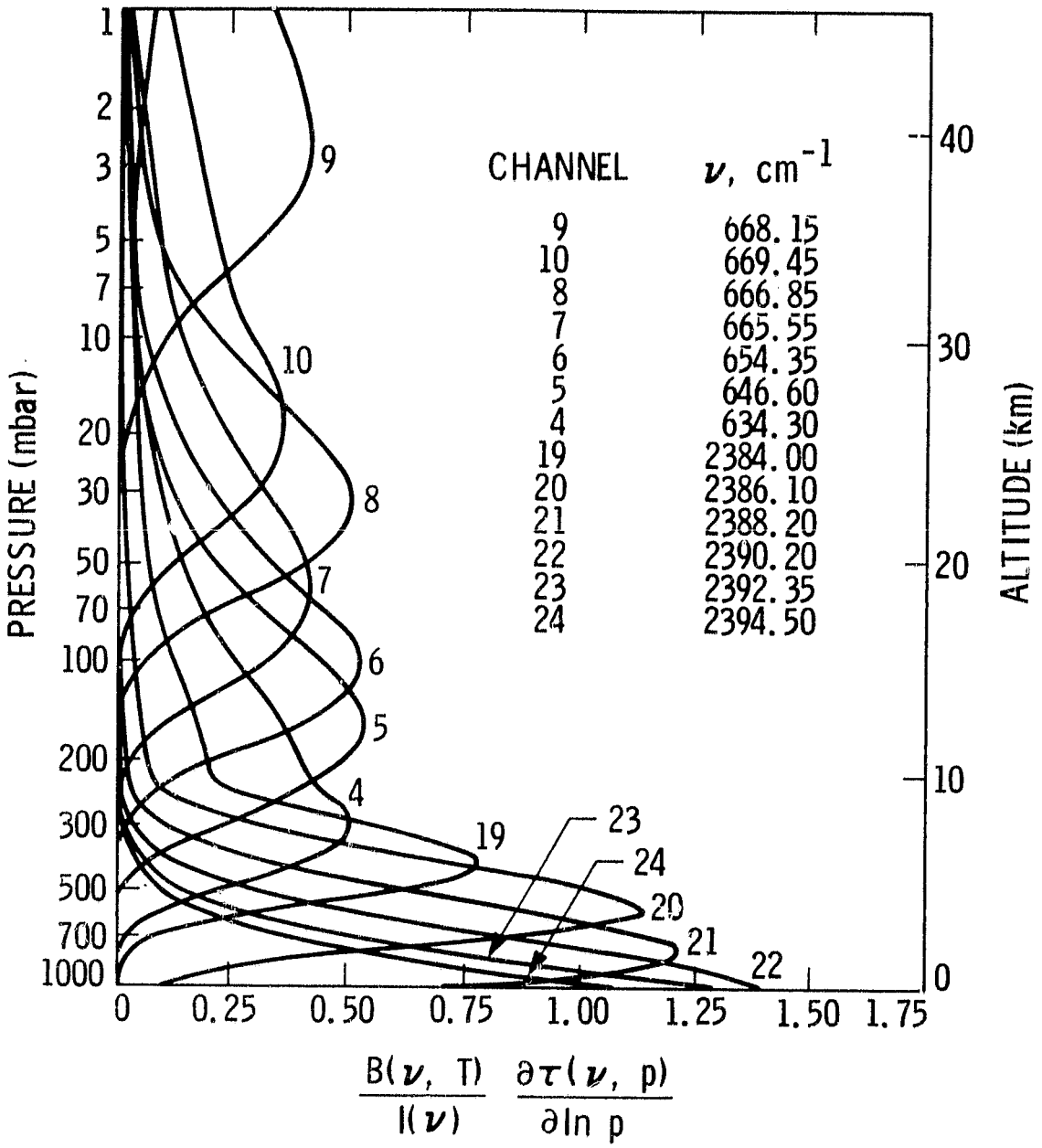

Figure 2-1 Contribution function of the AMTS temperature sounding channels at nadir for the U.S. Standard Atmosphere

Table 2-3 Contamination effects of O_3 and H_2O on the observed brightness temperature

AMTS($\Delta\upsilon/\upsilon = 0.1\%$)				
Channel υ (cm^{-1})	ΔT O_3 (K)	ΔT^1 H_2O (K)	ΔT^1 $O_3 + H_2O$ (K)	Peak Sensitivity (mbar)
668.15	0.01	0	0.01	3
669.45	0.10	0	0.10	20
666.85	0.37	0	0.37	30
665.55	0.19	0	0.19	70
654.35	0.1	0	0.1	90
646.60	0.1	0	0.1	180
634.30	0	-0.06	0.06	270
2384.00	0	0	0	350
2386.10	0	-0.01	-0.01	500
2388.20	0	-0.01	-0.01	650
2390.20	0	-0.01	-0.01	850
2392.40	0	-0.03	-0.03	Surface
2394.50	0	-0.09	-0.09	Surface

[1]Effects of H_2O continuum are not included.

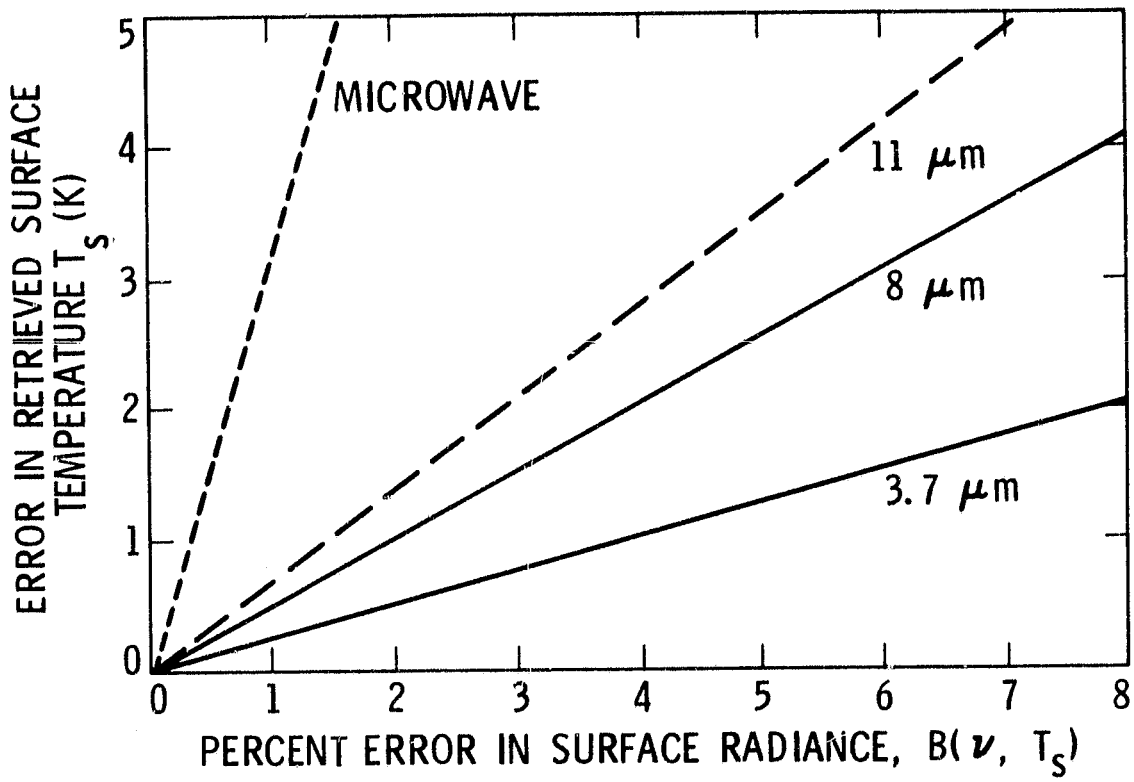

Figure 2-2 Skin-surface temperature sensitivity to noise for the case of T_s = 300 K

These values differ only slightly from that of the exact sea-surface temperature, T_s. Table 2-4 shows, for example, that the resulting difference between T_s and T_b is less than 1 K for narrow bandpass channels located around 2686 cm^{-1} and 2616 cm^{-1}.

2.1.3.5 Determination of Atmospheric Humidity

Passive infrared soundings are not sensitive to changes in the concentration of water vapor near the surface. This is due in part to the fact that a change in the concentration near the surface decreases the surface term, I_s, and increases the atmospheric term, I_a, in Eq 2.1. The net result is a very small change in the upwelling radiance. This problem is addressed with the use of the 1930.1 cm^{-1} channel. Figure 2-3 shows that at 1930.1 cm^{-1} the surface term is much smaller than the contributions from the lower atmosphere, resulting in improved sensitivity to changes in water vapor content near the surface. The other channels shown in Fig 2-3 indicate that the narrow-band water vapor channels can sound in the upper regions of the troposphere at pressure levels near the tropopause.

2.1.4 Capabilities of the Sounding System

The properties and advantages of narrow bandpass channels go far beyond just offering improved spectral purity by reducing channel contamination by water vapor lines and other minor atmospheric constituents and achieving the necessary frequency separation between channels. Essentially, they provide the basic concept for a new integrated atmospheric/surface sounder. Specifically, by treating the surface and cloud corrections as an integral part of the temperature sounding, an rms accuracy in $T(p)$ of about 1.5 K (Ref 2-1) can be achieved. The reverse is also true. In fact, accurate determination of atmospheric temperature is essential for accurate determination of surface temperature.

The availability of measurements obtained simultaneously in different parts of the spectrum will allow the effects of variability in surface emissivity, surface reflectivity and atmospheric thermal, radiative and compositional structures to be accounted for. The set of channels in Table 2-1 also provides the necessary data for determining the quality of the results.

With a field of view of 10 x 10 km, simulations have shown that this sounder can provide global data on:

- Temperature profiles derived in the presence of up to three layers of broken clouds with an absolute accuracy of 1.5 K using 8 sounding frequencies below 100 mbar (Ref 2-1).
- Relative humidity profiles using up to 6 sounding frequencies between the surface and 200 mbar, and the total precipitable water vapor.

Table 2-4 Differences between sea-surface temperature and brightness temperature[1]

Frequency υ (cm^{-1})	Bandwidth $\Delta\upsilon$ (cm^{-1})	Dry Atmosphere[2]		Water Lines[2]		Water Lines and Continuum[2]	
		τ_s	(T_s-T_b) (K)	τ_s	(T_s-T_b) (K)	τ_s	(T_s-T_b) (K)
2686.00	2.5	0.99	0.1	0.93	0.6	0.92	0.7
2616.50	2.5	0.98	0.2	0.97	0.3	0.96	0.4
2505.00	2.5	0.89	1.5	0.88	1.6	0.87	1.7
2424.00	2.5	0.66	5.4	0.65	5.4	0.65	5.5
1231.60	1.0	0.99	0.35	0.84	1.7	0.52-	4.6

[1]Nighttime Tropical Atmosphere with 5.3 g/cm^2 of H_2O; T_s = 300.0 K, ε_s = 1.0.

[2]T_s is sea-surface temperature, T_b is brightness temperature, and τ_s is atmospheric transmittance.

- Sea-surface temperature with an absolute accuracy of 1 K and a relative accuracy of 0.5 K (Ref 2-1).
- Air-sea temperature difference with a relative accuracy of ±1 K.
- Surface temperature of land with an absolute accuracy of 1.5 K (Ref 2-1).
- The fractional cover and height of multiple cloud layers (as seen from above) with an absolute accuracy of 0.05 and 0.25 km respectively (Ref 2-12).
- Total ozone burden of the atmosphere.

2.1.5 Functional Components of the AMTS System

A functional diagram of the AMTS system is shown in Fig 2-4. Major system elements are the measurement subsystem and the meteorological subsystem, supported by satellite tracking data and meteorological surface truth data. Spectral channel radiances at the instrument aperture are detected by the instrument and, along with housekeeping data, are transmitted to the ground via the satellite data link. The instrument data in conjunction with satellite tracking data is calibrated and reduced to channel radiances, channel spectral characteristics, and footprint spatial locations and supplied to the meteorological subsystem. Profile retrievals are accomplished in the meteorological subsystem, and selected profile sets are compared with surface truth data. The system is "tuned" to remove the effects of long-term systematic errors by adjusting atmospheric transmission factors.

2.1.6 System Tuning

For simplicity in presenting the argument, it is assumed that only upwelling thermal atmospheric radiance is present. The instrument radiometric balance can then be described as

$$\int_{\upsilon_1}^{\upsilon_2} ff(\upsilon - \upsilon_o)\, B(T_{BB}, \upsilon)\, d\upsilon = \int_{\upsilon_1}^{\upsilon_2} \left[ff(\upsilon - \upsilon_o) \int_{p_s}^{o} B(T_p, \upsilon) \frac{\partial \tau(\upsilon, p)}{\partial \ln p}\, d \ln p \right] d\upsilon, \quad (2.9)$$

where:

- υ_1 and υ_2 represent the lower and upper cutoff frequencies of the instrument filter function
- $ff(\upsilon - \upsilon_o)$ represents the instrument filter function with respect to a normalizing frequency, υ_o

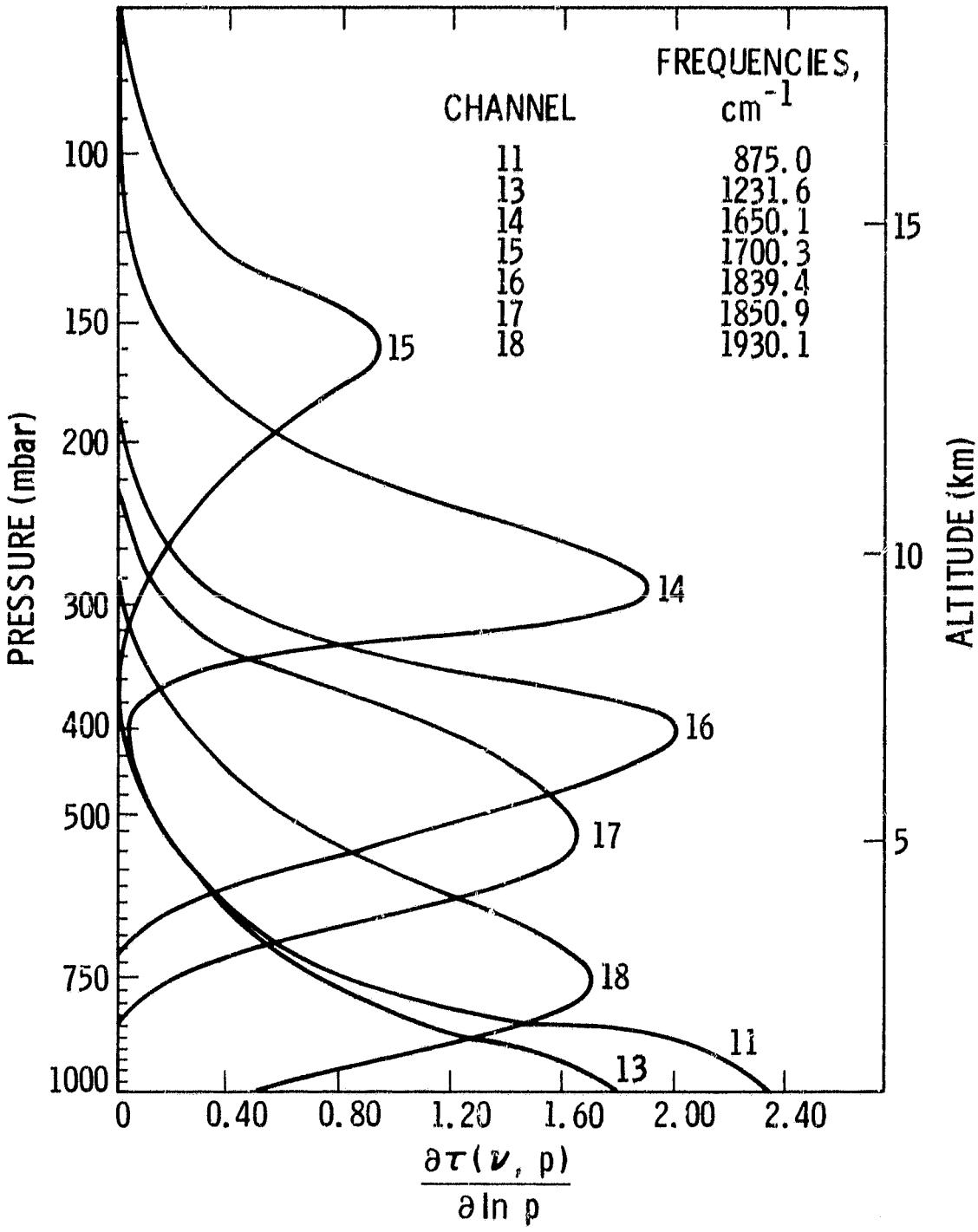

Figure 2-3 Weighting function for the AMTS water vapor channels at nadir for the U.S. Standard Atmosphere

$B(T_{BB}, \upsilon)$ represents the Planck function in terms of an equivalent calibration blackbody temperature, T_{BB}. (This is the instrument estimate of brightness temperature.)

$B(T_p, \upsilon)$ represents the Planck function in terms of atmospheric temperature, T_p, at pressure, p

$\frac{\partial \tau(\upsilon,p)}{\partial \ln p}$ represents the atmospheric weighting function in terms of atmospheric transmissivity, τ

p_s is pressure at the earth's surface

If $ff(\upsilon - \upsilon_o)$, T_{BB}, and $\partial\tau(\upsilon,p)/\partial \ln p$ were known, then T_p could be determined. This would be the ideal AMTS condition.

If $ff(\upsilon - \upsilon_o)$, T_{BB}, and T_p are known, then the weighting function can be "fine tuned" by adjusting values of τ to bring the equation into balance and, in effect, to calibrate the AMTS system.

In the actual AMTS system, uncertainties will exist in $ff(\upsilon - \upsilon_o)$, T_{BB}, and $\partial\tau(\upsilon,p)/\partial \ln p$. For a sufficiently large statistical set of profiles from radiosonde data, and to the extent that $\partial\tau(\upsilon,p)/\partial \ln p$ can be defined as a function of T_p, water vapor, and other atmospheric constituents, τ values can be adjusted to compensate for systematic spectral and radiometric system uncertainties. In effect, the satellite sounding system is tuned using the mean radiosonde values as a standard (Ref 2-13).

2.1.7 Spatial Coverage Grid Considerations

Cloud filtering requires two or more individual fields of view having different amounts of clouds (Eq 2.2 and Para 2.1.3.3). These fields of view can consist of individual footprints or of composite footprints. Individual footprints having relatively high spatial resolution are needed to exploit the nonhomogeneous pattern of cloud fields. Composite footprints are formed by grouping the individual footprints within a given grid area into two or more groups according to degree of cloudiness. The radiance for all individual footprints within a group is averaged to obtain the radiance of the composite footprint. The random noise of the composite footprint is equal to the random noise of the individual footprint divided by $\sqrt{N}$, where N is the number of individual footprints within the composite footprint (Ref 2-14).

An example of composite footprints used for the NASA/NOAA tests (Para 2.2.2) is shown in Fig 2-5. Four composite footprints were formed for each 6 x 6 individual footprint element grid. Note that the individual footprint elements forming a composite footprint are not necessarily spatially contiguous. For these tests, composite footprints 1, 2 and 4 were used with a three field of view algorithm for profile retrievals. Infrared clear column brightness temperatures were reconstructed by making the assumption that conditions in all three composite footprints were identical except for percentage cloud cover (Ref 2-13).

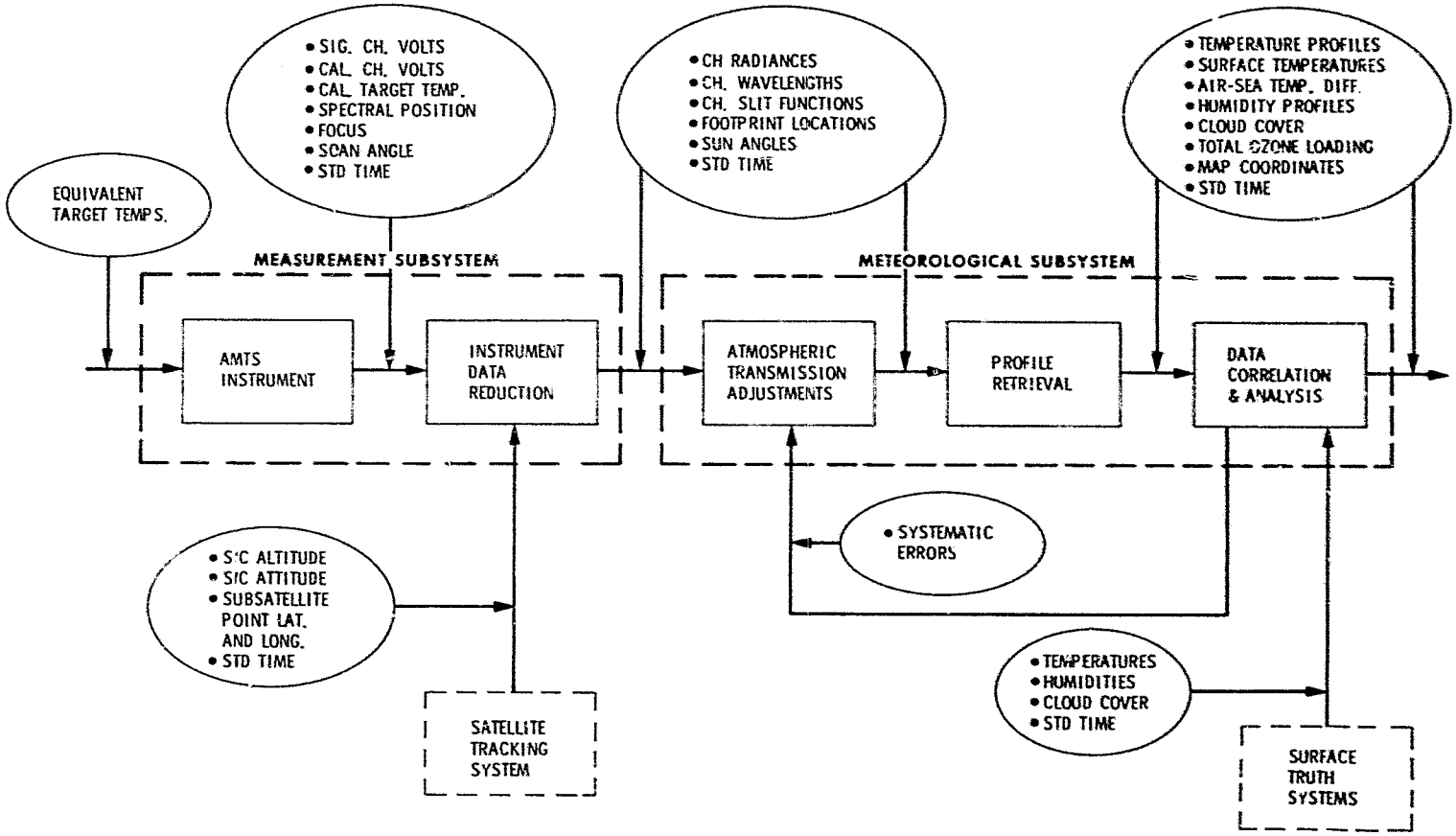

Figure 2-4 AMTS system diagram

2.2 AMTS System Analysis and Simulation

Summary results of selected AMTS system simulation tests are presented. These results are used as guidelines for establishing AMTS Baseline V instrument goal requirements (Para 2.3). They also serve as guidelines for estimating Baseline V system performance based upon instrument error estimates (Section 5).

2.2.1 Simulated AMTS System Performance

RMS temperature error of the recovered profile as a function of instrument Noise Equivalent Delta Temperature (NEΔT) is shown in Fig 2-6 in the absence of clouds and in Fig 2-7 in the presence of clouds. NEΔT values are for all error sources, including residual systematic errors remaining after system tuning. NEΔT values used for simulation were the same for all channels and were assumed to have a Gaussian distribution.

2.2.2 NASA/NOAA AMTS/HIRS Comparison Tests

Summary AMTS system performance from the NASA/NOAA simulation tests (Ref 2-1) are listed in Table 2-5 for clear column profile retrievals and in Table 2-6 for cloudy profile retrievals. Vertical distribution of clear column RMS retrieval error is plotted in Fig 2-8. The AMTS channel set used for this test and the Noise Equivalent Radiance values (NEN) per 10 km footprint are listed in Table 2-7.

For the clear column tests four 10 x 10 km footprints were combined to form one 20 km footprint. NEN for the composite footprint was taken as

$$NEN_{20} = \frac{NEN_{10}}{\sqrt{4}}$$

NEN values for the clear column tests were derived from Table 2-7. For selected altitudes and seasons, NEN values from Table 2-7 were doubled to test the system sensitivity to noise.

For the cloudy tests, a three footprint algorithm was used. Four composite footprints, each consisting of nine individual 10 km footprints, were obtained from a 6 x 6 element grid (Para 2.1.7). The least cloudy, next least cloudy, and most cloudy composite footprints were used for profile retrievals. Cloudy tests used NEN values from Table 2-7. Noise levels per composite footprint were taken as

$$NEN_{COMP} = \frac{NEN_{10}}{\sqrt{9}}$$

The clear column tests used only IR channel data. Microwave data was used for the cloudy tests to aid determination of cloud coefficients.

1	1	4	4	2	2
1	3	4	2	2	3
2	3	3	4	3	3
2	3	4	4	4	3
2	2	3	4	4	1
1	2	1	1	1	1

1 - LEAST CLOUDY COMPOSITE FOOTPRINT ELEMENTS

2 - MORE CLOUDY THAN COMPOSITE FOOTPRINT ELEMENTS No. 1

3 - MORE CLOUDY THAN COMPOSITE FOOTPRINT ELEMENTS No. 2

4 - MOST CLOUDY COMPOSITE FOOTPRINT ELEMENTS

- THREE FIELD-OF-VIEW ALGORITHM USED COMPOSITE FOOTPRINT ELEMENTS 1, 2, AND 4
- NEN PER COMPOSITE FOOTPRINT = NEN PER 10x10 km IFOV/$\sqrt{9}$
  (FOR RANDOM ERRORS UNCORRELATED BETWEEN IFOV)

Figure 2-5 Composite footprint example used for AMTS retrievals for NASA/NOAA tests

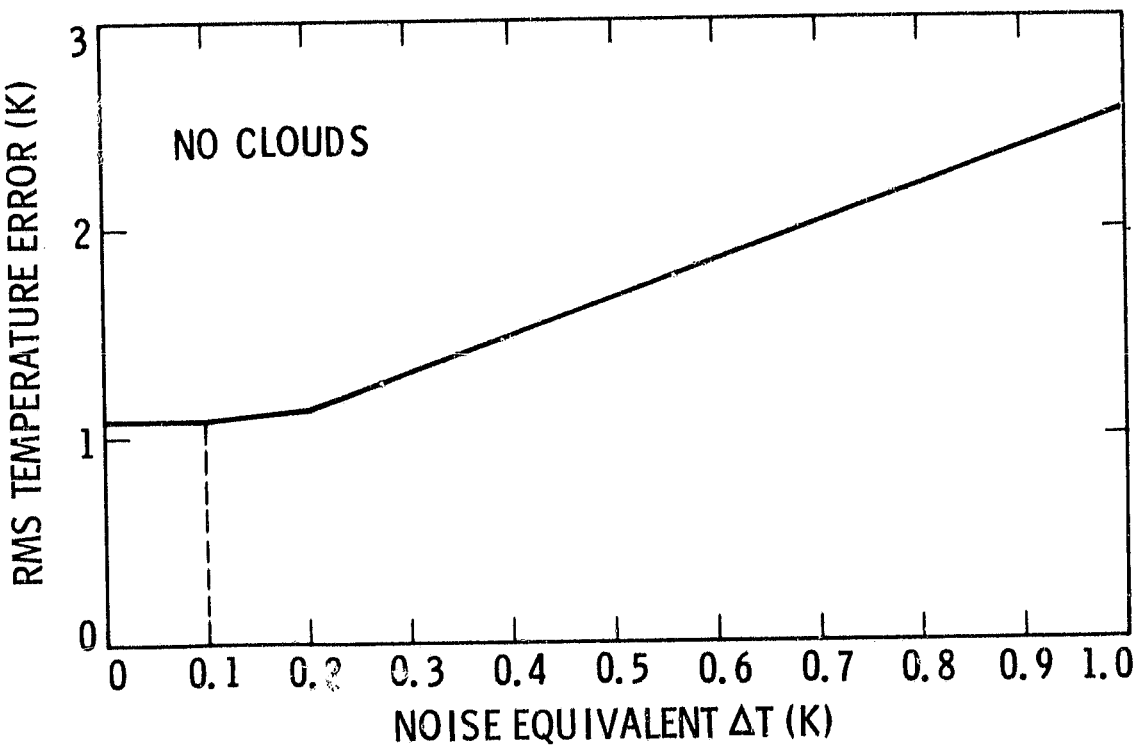

Figure 2-6 AMTS clear column performance as a function of system noise

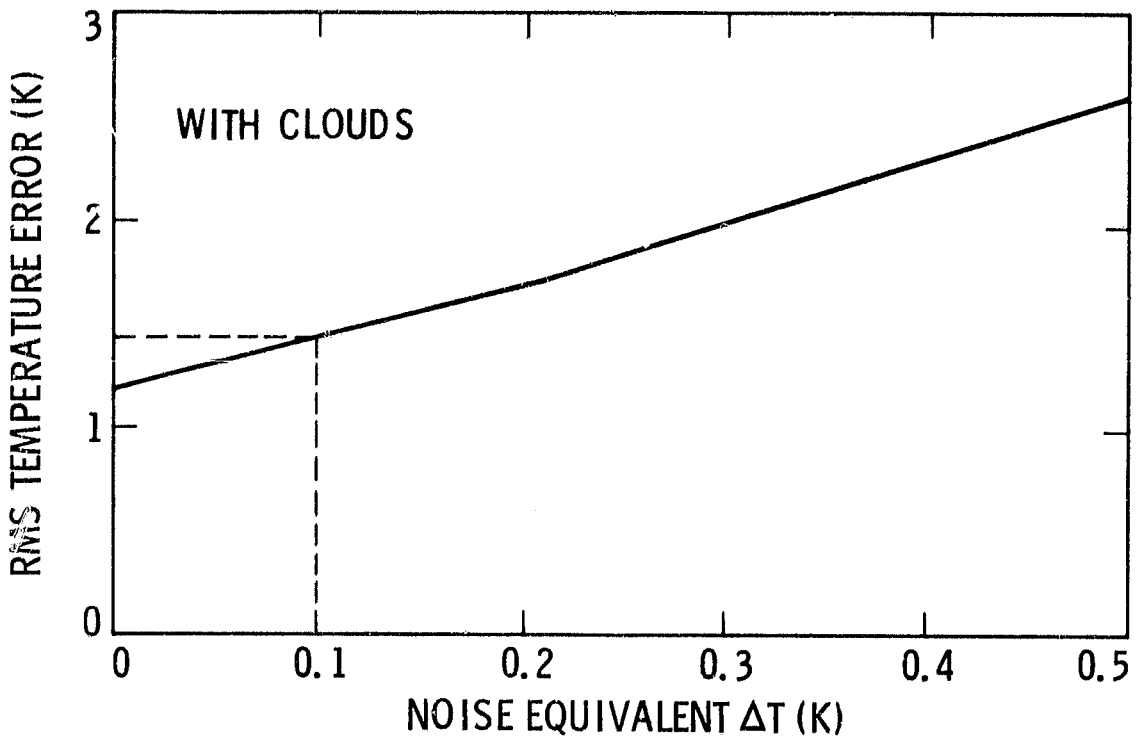

Figure 2-7 AMTS performance with clouds as a function of system noise

Table 2-5 Summary RMS temperature errors for clear column profiles (from NASA/NOAA tests -- AMTS/physical)

Pressure Height (mbar)	No. Layers	No. Profiles	Data Set		Temperature Error (K)	
			Month	Latitude	Normal Noise	"Doubled" Noise
1000-100	18	192	Jan	30S-30N	1.18	
			Jan	30N-60N	1.72	1.96
100-16	4	192	Jan	30S-30N	1.85	
			Jan	30N-60N	1.94	2.14
			Jan	(mean)	1.70	2.05
1000-100	18	192	Jun	30S-30N	1.16	
			Jun	30N-60N	1.43	
100-16	4	192	Jun	30S-30N	1.36	
			Jun	30N-60N	0.98	
			Jun	(mean)	1.25	
			Jan/Jun	(mean)	1.49	

Table 2-6 Summary RMS temperature errors for cloudy profiles (from NASA/NOAA tests -- AMTS/physical)

Pressure Height (mbar)	No. Layers	Temperature Error (K)				
		Clear Column	Percent Clouds			
			61-74	75-84	85-91	61-91
No. Profiles--->		96	13	14	13	40
1000-464	7	1.21	0.92	1.01	1.19	1.04
464-190	6	2.07	2.40	1.94	1.79	2.05
190-16	9	1.82	1.84	1.94	1.70	1.83
(1000-16 mean)		1.74	1.83	1.69	1.58	1.70

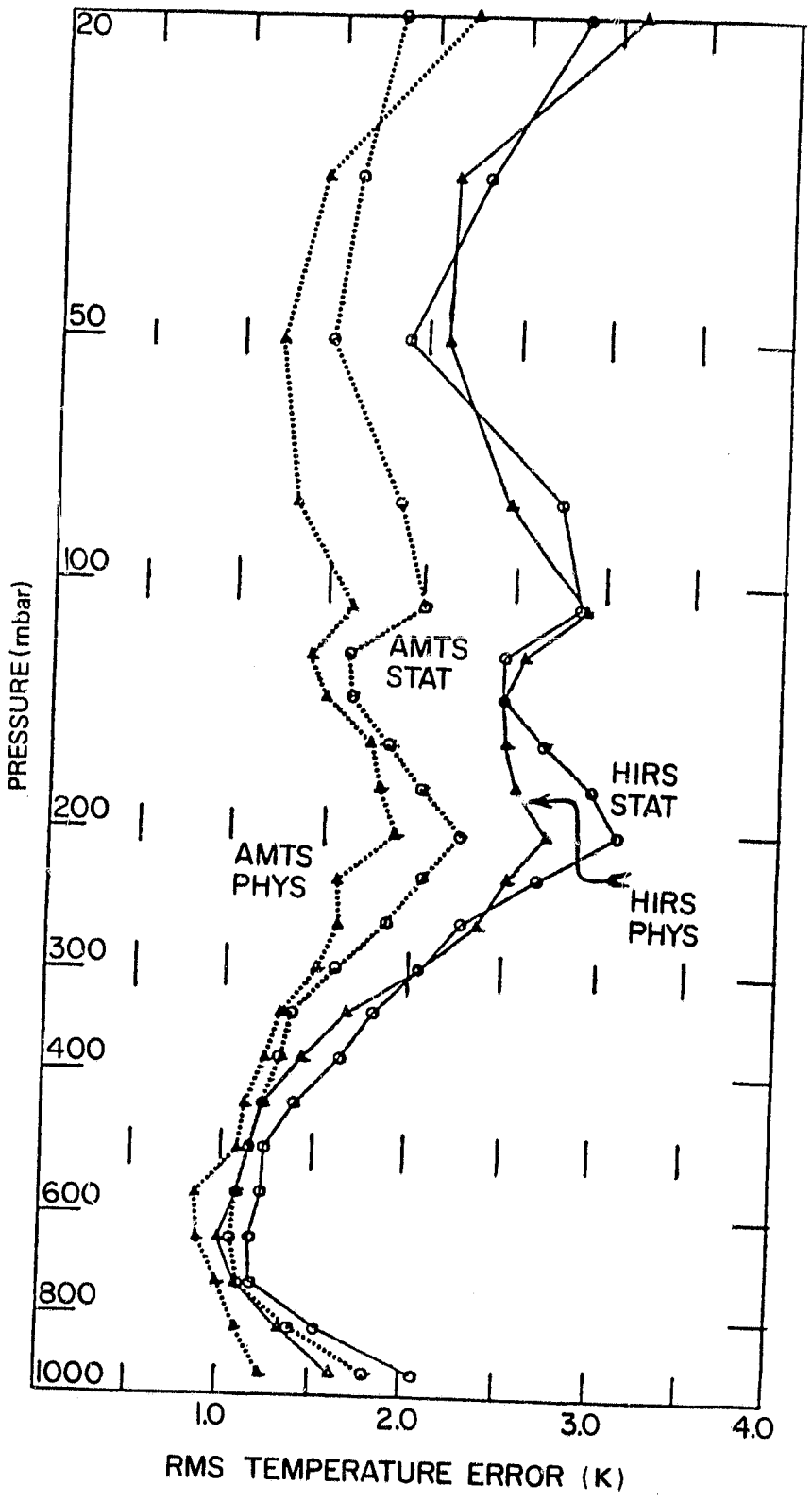

Figure 2-8 Vertical distribution of clear column RMS retrieval error averaged over all latitudes and both seasons. Values are plotted at the mean log P for each layer. (From NASA/NOAA tests.)

Table 2-7 AMTS NEN values used for NASA/NOAA tests

Band No.	Channel No.	Channel Wavelength $\lambda(\mu m)$	Spectral Frequency $\upsilon(cm^{-1})$	Spectral Resolution $\Delta\upsilon(cm^{-1})$	Noise Equivalent Radiance For 10 x 10 km Footprint $\left(\frac{W}{cm^2\ Sr\ cm^{-1}}\right)$	NEΔT 1σ (K) T_{min}	NEΔT 1σ (K) T_{std}	NEΔT 1σ (K) T_{max}	Mean/Std. Dev.
1	1	16.476	606.95	0.50	51.2×10^{-9}	.495	.389	.346	.462/.125
	2	16.046	623.20	0.50	50.4	.492	.388	.340	
	3	15.929	627.80	0.50	49.8	.541	.455	.383	
	4	15.765	634.30	0.50	49.3	.580	.494	.388	
	5	15.466	646.60	0.50	50.1	.666	.540	.417	
	6	15.282	654.35	0.50	44.4	.658	.481	.350	
	7	15.025	665.55	0.50	44.1	.644	.465	.321	
	8	14.996	666.85	0.50	44.0	.674	.461	.295	
	9	14.967	668.15	0.50	44.4	.641	.352	.265	
	10	14.938	669.45	0.50	44.0×10^{-9}	.627	.418	.284	
2	11	8.313	1203.00	1.00	2009.0×10^{-12}	.054	.020	.012	.028/.020
	12	8.118	1231.80	1.00	1834.0×10^{-12}	.053	.019	.011	
3	13	5.649	1770.30	1.50	462.0×10^{-12}	.141	.064	.033	.043/.037
	14	5.526	1809.50	1.50	291.0	.069	.024	.014	
	15	5.437	1839.40	1.50	219.0	.054	.020	.011	
	16	5.422	1844.50	1.50	201.0	.124	.059	.027	
	17	5.403	1850.90	1.50	194.0	.048	.015	.008	
	18	5.292	1889.57	1.50	147.0	.076	.032	.014	
	19	5.181	1930.10	1.50	135.0×10^{-12}	.048	.009	.004	
4	20	4.195	2384.00	2.00	56.4×10^{-12}	.421	.165	.021	.085/.108
	21	4.191	2386.10	2.00	71.9	.329	.115	.011	
	22	4.187	2388.20	2.00	58.6	.180	.049	.006	
	23	4.184	2390.20	2.00	67.2	.186	.035	.006	
	24	4.180	2392.35	2.00	59.7	.158	.023	.004	
	25	4.176	2394.50	2.00	62.4	.167	.022	.005	
	26	4.125	2424.00	2.50	38.8	.119	.013	.003	
	27	3.992	2505.00	2.50	24.6	.109	.009	.002	
	28	3.723	2686.00	2.50	19.7×10^{-12}	.203	.013	.001	

Atmospheric transmissivity coefficients were based upon GLAS codes. These coefficients were blind modified to derive test radiances, resulting in systematic errors of about 1 to 2 percent in test radiance values. Using the resulting test radiances GLAS "tuned" the system using given clear column reference profiles. This correction was of the form:

$$T_O' = T_O + (A\,T_O + B) \qquad (2.10)$$

where

T_O' is the corrected brightness temperature

T_O is the measured brightness temperature

A and B are channel dependent matrices

2.3 AMTS Instrument Requirements (Baseline V)

Baseline goal performance requirements for an AMTS instrument are summarized in Table 2-8. Items 1 through 3 are assumed Baseline V system requirements. Items 4 through 12 are essential for the AMTS method of atmospheric profile retrieval. Channel frequencies, channel bandwidths, and equivalent scene temperatures are listed in Table 2-9. Spectral radiance values corresponding to equivalent scene temperature are also listed in Table 2-9, along with NEN_U and SNR corresponding to NEΔT values of 0.1 K and 0.5 K. In general, a "worst case" interpretation of possible system drivers on instrument requirements has been assumed in order to best establish limits of instrument capabilities and instrument constraints.

2.3.1 In-Orbit Lifetime

The instrument should be capable of operating for five years without servicing.

2.3.2 Orbit

A sun synchronous orbit no later than 8:30 a.m. or no earlier than 3:30 p.m. is needed to allow use of radiative coolers. The TIROS altitude of 833 km is assumed for the baseline study.

2.3.3 Spatial Coverage

One hundred percent earth coverage is required each 24 hours. Practically, this means that the instrument must scan across track ±45 degrees with respect to nadir. Nominal size of the individual nadir footprint is 10 x 10 km. Footprints shall be essentially contiguous at nadir along the subsatellite point ground track. They shall also be contiguous along the scan vector across the subsatellite point ground track. One profile retrieval is required for each 100 x 100 km grid element over the surface of the earth. Each grid element will include about 100 individual footprints near nadir and 27 near the end of scan. For a three footprint profile retrieval algorithm each composite footprint could contain about 33 individual footprints near nadir and 9 near the end of scan.

Table 2-8 AMTS instrument goal requirements (Baseline V)

Parameter	Value
1) In orbit lifetime	5 years
2) Orbit	
Type	Sun synchronous
Time	8:30 a.m. or 3:30 p.m.
Altitude	833 km
3) Spatial coverage	
Scan coverage	100% Earth coverage each 24 hours
Individual nadir footprint size	10 x 10 km (nominal)
Earth coverage grid size	100 x 100 km (nominal)
Minimum number composite footprints per grid element	3
Minimum number individual footprints per composite	9
4) Spectral IR channels	28 (Table 2-9)
5) Equivalent scene temperature	(Table 2-9)
6) Spectral resolution - $\upsilon/\Delta\upsilon$	≈1200 (Table 2-9)
7) Absolute channel frequency tolerance (1σ)	7.5×10^{-5} of ch. freq.
8) Knowledge of channel frequency (1σ)	1.5×10^{-5} of ch. freq.
9) Knowledge of channel intensity vs frequency response (1σ)	0.15% of area
10) "Nontunable" radiometric error (1σ) (per composite footprint)	0.1 NEΔT
11) "Tunable" radiometric error (1σ)	1.0 K ΔT
12) Correlated relative radiometric error	(subset of 10 above)

Table 2-9 Radiometric values as a function of equivalent target temperature and noise equivalent ΔT

Band No.	CH No.	CH Wavelength λ (μm)	Spectral Frequency υ (cm^{-1})	CH Bandwidth $\Delta\upsilon_{1/2}$ (cm^{-1})	Equivalent Target Temperature T_{min} (K)	T_{std} (K)	T_{max} (K)	FOR T_{min} Nυ/W ($\frac{W}{cm^2 \cdot Sr \cdot cm^{-1}}$)	NEΔT = .1K NENυ/W ($\frac{W}{cm^2 \cdot Sr \cdot cm^{-1}}$)	SNR	NEΔT = .5K NENυ/W ($\frac{W}{cm^2 \cdot Sr \cdot cm^{-1}}$)	SNR	FOR T_{std} Nυ/W ($\frac{W}{cm^2 \cdot Sr \cdot cm^{-1}}$)	NEΔT = .1K NENυ/W ($\frac{W}{cm^2 \cdot Sr \cdot cm^{-1}}$)	SNR	NEΔT = .5K NENυ/W ($\frac{W}{cm^2 \cdot Sr \cdot cm^{-1}}$)	SNR	FOR T_{max} Nυ/W ($\frac{W}{cm^2 \cdot Sr \cdot cm^{-1}}$)	NEΔT = .1K NENυ/W ($\frac{W}{cm^2 \cdot Sr \cdot cm^{-1}}$)	SNR	NEΔT = .5K NENυ/W ($\frac{W}{cm^2 \cdot Sr \cdot cm^{-1}}$)	SNR
	1	16.476	606.95	0.50	230	263.83	286	6.11×10^{-6}	1.03×10^{-8}	592	5.17×10^{-8}	118	1.01×10^{-5}	1.31×10^{-8}	768	6.58×10^{-8}	153	1.32×10^{-5}	1.48×10^{-8}	892	7.40×10^{-8}	178
	2	16.046	623.20	0.50	229	260.15	283	5.86×10^{-6}	1.02×10^{-8}	573	5.12×10^{-8}	114	9.48×10^{-5}	1.30×10^{-8}	731	6.50×10^{-8}	146	1.27×10^{-5}	1.48×10^{-8}	855	7.41×10^{-8}	171
	3	15.929	627.80	0.50	218	236.51	260	4.75×10^{-6}	9.18×10^{-9}	518	4.60×10^{-8}	103	6.61×10^{-5}	1.09×10^{-8}	605	5.47×10^{-8}	121	9.42×10^{-6}	1.30×10^{-8}	725	6.51×10^{-8}	145
	4	15.765	634.30	0.50	211	226.46	256	4.08×10^{-6}	8.47×10^{-9}	481	4.24×10^{-8}	96	5.50×10^{-5}	9.97×10^{-9}	552	4.99×10^{-8}	110	8.85×10^{-6}	1.27×10^{-8}	698	6.35×10^{-8}	139
1	5	15.466	646.60	0.50	202	219.66	248	3.25×10^{-6}	7.49×10^{-9}	434	3.76×10^{-8}	87	4.73×10^{-5}	9.26×10^{-9}	511	4.64×10^{-8}	102	7.74×10^{-6}	1.20×10^{-8}	645	6.01×10^{-8}	129
	6	15.282	654.35	0.50	195	219.68	255	2.69×10^{-6}	6.72×10^{-9}	400	3.37×10^{-8}	80	4.66×10^{-5}	9.22×10^{-9}	505	4.62×10^{-8}	101	8.53×10^{-6}	1.27×10^{-8}	673	6.34×10^{-8}	134
	7	15.025	665.55	0.50	197	228.69	266	2.74×10^{-6}	6.82×10^{-9}	402	3.42×10^{-8}	82	4.83×10^{-5}	9.46×10^{-9}	511	4.74×10^{-8}	102	9.86×10^{-6}	1.37×10^{-8}	718	6.87×10^{-8}	143
	8	14.996	666.85	0.50	194	223.38	279	2.53×10^{-6}	6.50×10^{-9}	389	3.26×10^{-8}	78	4.88×10^{-5}	9.52×10^{-9}	513	4.47×10^{-8}	102	1.17×10^{-5}	1.49×10^{-8}	785	7.47×10^{-8}	157
	9	14.967	668.15	0.50	198	254.00	300	2.79×10^{-6}	6.90×10^{-9}	404	3.46×10^{-8}	81	8.26×10^{-5}	1.26×10^{-8}	656	6.31×10^{-8}	131	1.50×10^{-5}	1.67×10^{-8}	998	8.37×10^{-8}	179
	10	14.938	669.45	0.50	199	233.04	285	2.85×10^{-6}	6.99×10^{-9}	408	3.50×10^{-8}	81	5.82×10^{-5}	1.05×10^{-8}	555	5.26×10^{-8}	111	1.26×10^{-5}	1.55×10^{-8}	814	7.74×10^{-8}	163
	11	11.429	875.00	0.75	231	285.00	327	3.44×10^{-6}	8.16×10^{-9}	422	4.09×10^{-8}	84	9.74×10^{-5}	1.53×10^{-8}	637	7.66×10^{-8}	127	1.73×10^{-5}	2.09×10^{-8}	831	1.05×10^{-7}	166
	12	9.608	1040.80	1.00	198	256.26	290	6.97×10^{-7}	2.67×10^{-9}	261	1.32×10^{-8}	52	3.90×10^{-5}	8.93×10^{-9}	437	4.48×10^{-8}	87	7.72×10^{-6}	1.38×10^{-8}	558	6.93×10^{-8}	111
2	13	8.120	1231.60	1.00	231	285.40	327	1.04×10^{-6}	3.45×10^{-9}	301	1.73×10^{-8}	60	4.48×10^{-5}	9.78×10^{-9}	458	4.90×10^{-8}	91	9.90×10^{-6}	1.65×10^{-8}	600	8.26×10^{-8}	120
	14	6.060	1650.10	1.30	220	239.30	261	1.10×10^{-7}	5.41×10^{-10}	203	2.73×10^{-9}	40	2.63×10^{-7}	1.09×10^{-9}	241	5.49×10^{-9}	48	6.00×10^{-7}	2.09×10^{-9}	287	1.05×10^{-7}	57
	15	5.881	1700.30	1.30	216	229.50	255	7.06×10^{-8}	3.71×10^{-10}	190	1.87×10^{-9}	38	1.37×10^{-7}	6.40×10^{-10}	215	3.22×10^{-9}	43	3.99×10^{-7}	1.50×10^{-9}	265	7.56×10^{-9}	53
	16	5.437	1839.40	1.50	232	259.32	282	8.24×10^{-8}	4.06×10^{-10}	203	2.05×10^{-9}	40	2.74×10^{-7}	1.08×10^{-9}	254	5.43×10^{-9}	50	6.23×10^{-7}	2.07×10^{-9}	300	1.04×10^{-8}	60
3	17	5.403	1850.90	1.50	233	266.90	289	8.21×10^{-8}	4.04×10^{-10}	203	2.30×10^{-9}	40	3.51×10^{-7}	1.31×10^{-9}	267	6.60×10^{-9}	53	7.52×10^{-7}	2.40×10^{-9}	313	1.21×10^{-8}	62
	18	5.181	1930.10	1.50	232	280.28	315	5.22×10^{-8}	2.80×10^{-10}	193	1.41×10^{-9}	38	4.27×10^{-7}	1.51×10^{-9}	282	7.59×10^{-9}	56	1.27×10^{-6}	3.56×10^{-9}	357	1.79×10^{-8}	71
	19	4.195	2384.00	2.00	214	229.56	274	1.77×10^{-9}	1.33×10^{-11}	133	6.72×10^{-11}	26	5.23×10^{-9}	3.41×10^{-11}	153	1.73×10^{-10}	30	5.90×10^{-8}	2.70×10^{-10}	218	1.36×10^{-9}	43
	20	4.191	2385.10	2.00	222	240.97	299	3.11×10^{-9}	2.17×10^{-11}	143	1.10×10^{-10}	28	1.05×10^{-8}	6.23×10^{-11}	169	3.15×10^{-10}	33	1.67×10^{-7}	6.42×10^{-10}	260	3.23×10^{-9}	52
	21	4.187	2388.20	2.00	229	254.69	313	4.94×10^{-9}	3.24×10^{-11}	152	1.64×10^{-10}	30	2.24×10^{-8}	1.19×10^{-10}	188	6.01×10^{-10}	37	2.77×10^{-7}	9.73×10^{-10}	285	4.89×10^{-9}	57
	22	4.184	2390.20	2.00	231	265.88	321	5.57×10^{-9}	3.60×10^{-11}	155	1.82×10^{-10}	31	3.93×10^{-8}	1.91×10^{-10}	205	9.65×10^{-10}	41	3.62×10^{-7}	1.21×10^{-9}	299	6.08×10^{-9}	60
4	23	4.180	2392.35	2.00	232	273.30	325	5.87×10^{-9}	3.77×10^{-11}	156	1.90×10^{-10}	31	5.53×10^{-8}	2.55×10^{-10}	217	1.29×10^{-9}	43	4.10×10^{-7}	1.34×10^{-9}	306	6.72×10^{-9}	62
	24	4.176	2394.50	2.00	232	276.20	326	5.81×10^{-9}	3.73×10^{-11}	156	1.89×10^{-10}	31	6.26×10^{-8}	2.83×10^{-10}	221	1.43×10^{-9}	44	4.21×10^{-7}	1.37×10^{-9}	308	6.86×10^{-9}	61
	25	4.125	2424.00	2.50	232	281.38	331	5.02×10^{-9}	3.26×10^{-11}	154	1.65×10^{-10}	30	7.02×10^{-8}	3.10×10^{-10}	227	1.59×10^{-9}	45	4.50×10^{-7}	1.44×10^{-9}	314	7.21×10^{-9}	62
	26	3.992	2505.00	2.50	232	285.22	342	3.35×10^{-9}	2.25×10^{-11}	149	1.14×10^{-10}	29	6.09×10^{-8}	2.70×10^{-10}	225	1.36×10^{-9}	45	4.96×10^{-7}	1.53×10^{-9}	324	7.69×10^{-9}	64
	27	3.821	2616.50	2.50	232	286.57	354	1.91×10^{-9}	1.34×10^{-11}	143	6.80×10^{-11}	28	4.21×10^{-8}	1.93×10^{-10}	218	9.73×10^{-10}	43	5.14×10^{-7}	1.54×10^{-9}	332	7.76×10^{-9}	66
	28	3.723	2686.00	2.50	232	286.53	364	1.35×10^{-9}	9.69×10^{-12}	139	4.91×10^{-11}	27	3.20×10^{-8}	1.51×10^{-10}	212	7.62×10^{-10}	42	5.65×10^{-7}	1.65×10^{-9}	342	8.29×10^{-9}	68

2.3.4 Spectral IR Channels

The AMTS channel frequency set is listed in Table 2-9 (as well as in Table 2-1). Nominal channel wavelengths are listed for information.

2.3.5 Equivalent Scene Temperature

Minimum, maximum and U.S. Standard Atmosphere equivalent temperatures listed in Table 2-9 represent the temperatures of a blackbody source, located above the atmosphere, which would result in the same spectral irradiance at the input to the instrument as that received from the actual meteorological target. The maximum equivalent temperatures include solar reflection from clouds and the earth's surface.

2.3.6 Channel Bandwidth

Nominal half-power bandwidths are listed in Table 2-9. The (3σ) half-power bandwidth limits shall be within ±10% of these nominal values. The rolloff characteristics of the instrument line function, including response in the wings of the line function, shall be compatible with satisfying the radiometric requirements of Para 2.3.10 and 2.3.12. If a spatial array is used, the instrument line functions for all footprint elements within the spatial array for any spectral channel must have the same relative amplitude vs frequency response to the extent that the system can be tuned in orbit for each channel (rather than for each footprint array element for each channel).

2.3.7 Absolute Channel Frequency Tolerance

The (1σ) absolute accuracy within which each channel center frequency shall be set to the channel wavenumber specified in Table 2-9 is 7.5×10^{-5} parts of the channel wavenumber. Channel center frequency is defined as the wavenumber centered between the half-power wavenumbers.

2.3.8 Knowledge of Channel Frequency

The (1σ) absolute accuracy within which each channel center wavenumber shall be known in orbit shall be 1.5×10^{-5} parts of the channel wavenumber specified in Table 2-9.

2.3.9 Knowledge of Channel Intensity vs Frequency Response

The (1σ) relative channel intensity vs frequency response shall be known in orbit to within 0.15% of the area under the curve.

2.3.10 "Nontunable" Radiometric Error

The RMS (1σ) value of the radiometric error from all sources which is not subject to reduction through in-orbit system tuning shall not exceed 0.1 K NEΔT for the composite footprint. Any variation in systematic radiometric error within any 30 day interval shall be considered to be a nontunable error. (Note that not all nontunable errors are random on a footprint-to-footprint basis; consequently, not all individual footprint radiometric errors are reduced in the composite footprint.)

2.3.11 "Tunable" Radiometric Error

Tunable (1σ) radiometric errors shall not exceed 1 K ΔT. Tunable radiometric errors are systematic errors which are linear as a function of input signal level and which are subject to reduction through in-orbit system tuning. (Note that tunable errors include systematic spectral radiometric error due to incomplete knowledge of channel frequency and of channel intensity vs frequency response.)

2.3.12 Correlated Relative Radiometric Errors

The nontunable, correlated, relative radiometric error component between spectral channels for the composite footprint is a subset of the nontunable radiometric error of Para 2.3.10. For cloud filtering purposes, the differential error between composite footprints is a function of this correlated relative radiometric error (Para 2.1.7). This error includes the effects of lack of footprint spatial registration for all channels. It also includes the effects of differential footprint radiometric weighting between channels, such as could be caused by scene dependent spatial crosstalk and scene dependent polarization error, for example.

REFERENCES - SECTION 2

2-1 Phillips, N.A., [results of comparative simulation studies on AMTS and HIRS conducted by NASA and NOAA] (to be published).

2-2 Bengtsson, L., M. Kanamitsu, P. Kallberg, and S. Uppala, Bull. Am. Meteorol. Soc., 63, 29 (1982).

2-3 Chahine, M.T., J. Atmos. Sci., 31, 233 (1974).

2-4 Chahine, M.T., J. Atmos. Sci., 34, 744 (1977).

2-5 Chahine, M.T., J. Atmos. Sci., 32, 1946 (1975).

2-6 Chahine, M.T., in "Inversion Methods in Atmospheric Remote Sounding" (A. Deepak, ed.), p. 67 Academic Press, New York (1977).

2-7 Smith, W.L., Mon. Wea. Rev. 96, 387 (1968).

2-8 Kaplan, L.D., M.T. Chahine, J. Susskind, and J.E. Searl, Applied Optics, 16, 322 (1977).

2-9 Chahine, M.T., in "Remote Sensing of Oceans and Atmospheres" (A. Deepak, ed.), p. 411 Academic Press, New York (1980).

2-10 Chahine, M.T., H.H. Aumann, and F.W. Taylor, J. Atmos. Sci. 34, 758 (1977).

2-11 Susskind, J., J. Rosenfield, D. Reuter, and M.T. Chahine "The GLAS physical inversion method for analysis of HIRS-2/MSU sounding data," NASA Technical Memorandum 84936 (1982).

2-12 Chahine, M.T., J. Atmos. Sci. 39, 159 (1982).

2-13 Susskind, J., J. Rosenfield, and D. Reuter, Journal of Geophysical Research, Volume 88, No. C13, Pages 8550-8568, October 20, 1983.

2-14 Susskind, J., J. Rosenfield, and D. Reuter, Journal of Geophysical Research, Vol. 89, No. D3, Pages 4677-4697, June 20, 1984.

SECTION 3

3.0 INSTRUMENT DESCRIPTION (BASELINE V)

This section describes the conceptual design of a "Baseline V" multichannel grating spectrometer in accordance with goal AMTS baseline instrument requirements as specified in Para 2.3. A numerical evaluation of this baseline instrument performance is presented in Section 4.

3.1 Optical Design

In this major paragraph, optical design criteria are developed. A baseline optical design is presented in accordance with these optical design criteria. It is shown that the performance capability of this baseline in conjunction with a set of parametric and scaling equations consitutes a general first order solution for the limits of AMTS detector noise limited performance obtainable using a grating spectrometer instrument approach.

3.1.1 Optical Design Criteria and Scaling Factors

Detector noise limited NEN parametric and scaling equations are developed for a generalized grating spectrometer optical configuration. (In Para 3.1.3 it is shown that this general configuration is optimum in terms of minimum NEN.) Overall system design parametric and scaling equations are developed which specify overall system NEN performance in terms of the degrees of freedom in:

- Earth Coverage
  - Altitude
  - Crosstrack scan width
- Spatial Resolution
  - Pixel size
  - Composite footprint size and earth coverage grid size
- Instrument Parameters
  - Instrument scale
  - Number of elements in the crosstrack pushbroom array
  - Grating optimization criteria

Additional optical design criteria affecting other than detector limited aspects of radiometric performance and affecting spectral performance are developed. AMTS optical design criteria are summarized.

3.1.1.1 NEN Parametric and Scaling Equations

The general equation for detector limited Noise Equivalent Radiance (NEN) per individual footprint (pixel element) of an infrared grating spectrometer using a chopper and viewing an extended source is

$$NEN_p = \frac{\sqrt{A_d}}{A\Omega} \cdot \frac{1}{E_g} \cdot \frac{1}{\tau} \cdot \frac{\sqrt{\Delta F}}{F_c} \cdot \frac{1}{D^*} \qquad (3.1)$$

Noise equivalent spectral radiance is

$$NEN_\upsilon = \frac{NEN}{\Delta\upsilon} \qquad (3.2)$$

where

A_d = detector area

$A\Omega$ = area/solid angle product of the instrument

D^* = detector/preamp detectivity within the photon background and thermal environment of the instrument

E_g = relative grating efficiency

F_c = chopper factor ≤ 1 (If the beam is not chopped, $F_c = 1$)

ΔF = electrical noise bandwidth of the signal channel

τ = optical transmissivity of the instrument

A generalized grating spectrometer configuration is shown in Fig 3-1. For the case of a rectangular inlet slit, a rectangular detector following a field lens—whose principle plane is coincident with the image plane of the instrument—and a hemispheric immersion lens, where the exit slit width is equal to or greater than the image of the inlet slit width, and where the grating mask is a system pupil, the first term of Eq 3.1 can be written in terms of parameters to the right of the inlet slit (Appendix B):

$$\frac{\sqrt{A_d}}{A\Omega} = \frac{\sqrt{G_{H\alpha}\, G_{w\alpha}}}{A_{g\alpha}} \cdot \frac{F_s}{\Delta\upsilon \left| \frac{d\alpha}{d\upsilon} \right|} \qquad (3.3)$$

$$\cdot \sqrt{\frac{\cos\beta}{\cos\alpha} + \frac{\cos\alpha}{\cos\beta}\left(F_s \frac{S_{w\alpha}}{S_{h\alpha}}\right)^2} \cdot \frac{F/NO}{n} \cdot F_d$$

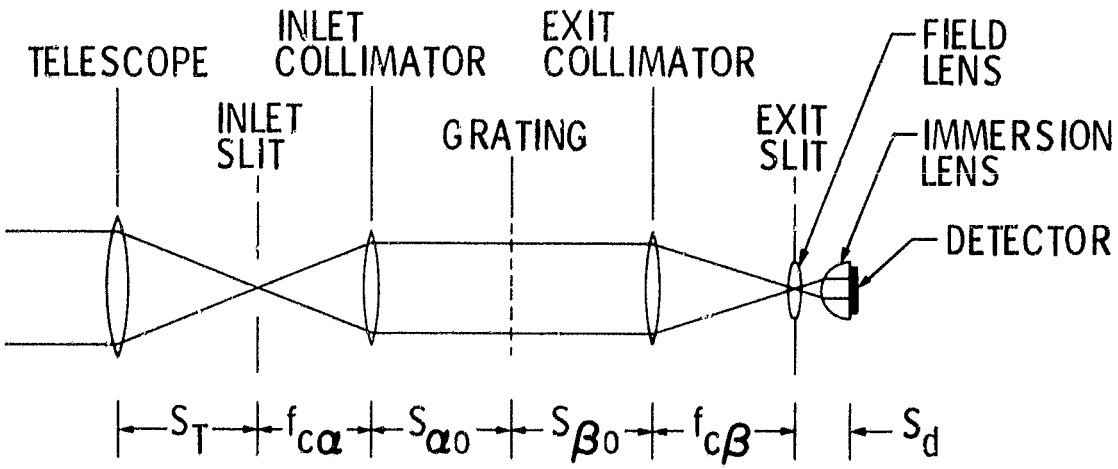

Figure 3-1 Generalized grating spectrometer configuration

where

$$\left|\frac{d\alpha}{d\upsilon}\right| = \frac{1}{\upsilon}\,\frac{\sin\alpha + \sin\beta}{\cos\alpha} \tag{3.4}$$

is the grating spectral dispersion with respect to the incident angle;

$$S_{w\alpha} = f_{c\alpha}\,\Delta\upsilon_o\left|\frac{d\alpha}{d\upsilon}\right| \tag{3.5}$$

is the inlet slit width;

$$F_s = \frac{S_{w\beta i}}{S_{w\alpha}} = \frac{\Delta\upsilon}{\Delta\upsilon_o} \geq 1 \tag{3.6}$$

is a slit factor (and excess bandwidth ratio);

$$F_d = \frac{1}{\frac{f_d}{f_{c\beta}^2}\,(s_{\beta o} - f_{c\beta}) + 1} \approx 1 \tag{3.7}$$

is a detector size factor, and

α = grating incident angle

β = grating diffraction angle

υ = channel frequency (expressed as a wavenumber)

$\Delta\upsilon$ = channel half-power bandwidth

$\Delta\upsilon_o$ = channel bandwidth for which F_s would be unity

$A_{g\alpha}$ = projected area of grating with respect to α

$f_{c\alpha}$ = inlet collimator focal length

$f_{c\beta}$ = exit collimator focal length

f_d = field lens focal length

F/NO = F/NO of the field lens

$G_{H\alpha}$ = maximum projected grating height with respect to α

$G_{w\alpha}$ = maximum projected grating width with respect to α

$S_{h\alpha}$ = inlet slit height

$S_{w\beta i}$ = width of exit slit image at inlet slit plane

$s_{\beta o}$ = distance from grating to exit collimator

n = refractive index of hemispheric detector immersion lens

In Fig 3-1, $s_{\beta o}$ would practically lie between the limits of $s_{\beta o} = 0$ and $s_{\beta o} = 2f_{c\beta}$. Assuming that $f_{c\beta} > 100 f_d$, Eq 3.7 shows that F_d would lie between the limits of 1 ± 0.01. Setting $F_d = 1$, and expressing the grating dispersion (Eq 3.4) in terms of wavenumber and grating angles, Eq 3.3 can be written in terms of the projected grating aperture:

$$\frac{\sqrt{A_d}}{A\Omega} = \frac{\sqrt{G_{H\alpha}\, G_{w\alpha}}}{A_{g\alpha}} \cdot \frac{\cos\alpha}{\sin\alpha + \sin\beta} \sqrt{\frac{\cos\beta}{\cos\alpha} + \frac{\cos\alpha}{\cos\beta}\left(F_s \frac{S_{w\alpha}}{S_{h\alpha}}\right)^2} \cdot \frac{F/NO}{n} \cdot \frac{\upsilon}{\Delta\upsilon_o} \tag{3.8}$$

In terms of grating size measured on the surface of the grating, Eq 3.3 can be written:

$$\frac{\sqrt{A_d}}{A\Omega} = \frac{\sqrt{H_g\, L_g}}{A_g} \cdot \frac{1}{\sin\alpha + \sin\beta} \sqrt{\frac{\cos\alpha}{\cos\theta}\left[\frac{\cos\beta}{\cos\alpha} + \frac{\cos\alpha}{\cos\beta}\left(F_s \frac{S_{w\alpha}}{S_{h\alpha}}\right)^2\right]} \cdot \frac{F/NO}{n} \cdot \frac{\upsilon}{\Delta\upsilon_o} \tag{3.9}$$

where

H_g = maximum grating height (parallel to grating grooves)

L_g = maximum grating length (perpendicular to grating grooves)

A_g = effective area of the grating

θ = grating out-of-plane angle

Equation 3.8 is convenient for comparing configurations having the same or similar instrument apertures, while Eq 3.9 is convenient for configurations having the same or similar grating sizes. From Eq 3.1 and 3.8, NEN per pixel can be written:

$$NEN_p = \frac{\sqrt{G_{H\alpha}\, G_{w\alpha}}}{A_{g\alpha}} \cdot \frac{\cos\alpha}{\sin\alpha + \sin\beta} \sqrt{\frac{\cos\beta}{\cos\alpha} + \frac{\cos\alpha}{\cos\beta}\left(F_s \frac{S_{w\alpha}}{S_{h\alpha}}\right)^2} \cdot \frac{1}{E_g} \cdot \frac{F/NO}{n} \cdot \frac{1}{\tau} \cdot \frac{\sqrt{\Delta F}}{F_c} \cdot \frac{1}{D^*} \cdot \frac{\upsilon}{\Delta\upsilon_o} \qquad (3.10)$$

Relative grating efficiency in a well made grating is a function of grating orders and angles; i.e.,

$$E_g = f(m, \alpha, \beta, \theta, \phi, \overline{\phi}) \qquad (3.11)$$

where

m = grating order

ϕ = blaze angle

$\overline{\phi}$ = antiblaze angle

Electrical noise bandwidth

$$\Delta F \propto \frac{1}{T_d} = f(R_{NADIR}, S_{ANGLE}, A_{p(NADIR)}, N_{ARRAY}, N_{CAL}, T_{SLEW}) \qquad (3.12)$$

where

R_{NADIR} = altitude

S_{ANGLE} = maximum crosstrack half scan angle with respect to nadir

$A_{p(NADIR)}$ = the contiguous rectangular nadir area (pixel) sampled by an individual footprint

N_{ARRAY} = number of elements in the crosstrack pushbroom array

N_{CAL} = number of calibration target dwells per crosstrack line scan

T_{SLEW} = spatial scan total slew time per crosstrack line scan interval

T_d = dwell time per pixel per spatial channel (shutter open plus shutter closed time)

Equation 3.10 is a primary parametric and scaling equation useful for optimizing instrument design to minimize NEN.

The first term of Eq 3.10 represents an instrument aperture factor. The optimum aperture configuration is a rectangular grating without obscurations. For a given grating configuration, NEN is inversely proportional to the linear scale of the instrument.

The second term represents a grating angle factor. It is a function of grating angles, somewhat modified by the slit factor and inlet slit aspect ratio. For at least one channel, normally $F_s = 1$. The inlet slit aspect ratio, $S_{w\alpha}/S_{h\alpha}$, may approach 1. In general, the grating angle factor decreases as grating spectral dispersion increases. The third term represents a grating efficiency factor. Equation 3.11 indicates that relative grating efficiency is a function of grating orders and grating angles. In a very general way, grating efficiency can be considered to decrease as grating orders and spectral dispersion increase. Consequently, both the grating angle factor and the grating efficiency factor are primary drivers on the optimum grating configuration. Selection of the grating configuration--orders and angles--for a given channel set is a logical and necessary starting point for AMTS instrument design. Grating specification considerations are treated in greater detail in Para 3.1.1.2.

The fourth term is the optical convergence factor. It shows that in terms of optical convergence NEN is only a function of the F/NO of the field lens and of the index of refraction of the hemispheric immersion lens. NEN is independent of the F/NO of the grating collimators and foreoptics.

The fifth term is the optical transmissivity factor, not including the relative efficiency of the grating.

The sixth term, $\sqrt{\Delta F}/F_C$, represents a figure of merit for an optical chopper/signal processor system. It involves the electrical noise bandwidth of the system. Equation 3.12 shows that noise bandwidth is inversely proportional to pixel dwell time in the instrument. Noise bandwidth and optical chopping considerations are treated in greater detail in Para 3.1.1.3.1.

The seventh term represents the detectivity factor. An ideal detector would operate background noise limited (D^*_{BLIP}) and would have insignificant 1/f noise. The degree to which a detector is background noise limited is a function of the type and material used for the detector and of the degree to which temperature, instrument background, and optical convergence have been controlled within the instrument to achieve this result.

The 1/f noise is a function of detector type and material, and of the processing used in detector manufacture. Detector D* considerations are treated in greater detail in Para 3.1.1.3.1 and 3.1.1.4.

The eighth term represents the spectral resolution for which F_s would be unity. Normally, this would be the spectral resolution of the highest resolution channel in the instrument. For channels having lower spectral resolution, the excess bandwidth ratio $F_s = \Delta\upsilon/\Delta\upsilon_o > 1$. Thus, decreasing the maximum spectral resolution will decrease NEN, but decreasing the spectral resolution for any channel below this maximum established by the limit channel will degrade NEN performance of the lower resolution channel (Para 3.1.1.2; Fig 3-9).

There are compelling reasons for including the field lens and the immersion lens in the generalized spectrometer configuration of Fig 3-1:

- The field lens:
  - Places the detector in a pupil plane, minimizing radiometric errors due to varying responsivity over the area of the detector.
  - Controls wide angle background flux on cooled detectors. Only flux within the focused ray bundle falls upon the detector from ahead of the exit slit.
  - Makes NEN independent of the F/NO of the optical system ahead of the exit slit.
  - Has an inherent NEN advantage over a configuration with detectors on the image plane (Para 3.1.3).
- The hemispheric immersion lens reduces the linear size of the detector by a factor of 1/n, resulting in:
  - A reduction in NEN by a factor of $\approx 1/n$ for temperature noise limited detectors.
  - A reduction in bias power dissipated in PC detectors and their bias resistors by a factor of $1/n^2$ (for a given bias potential).
  - A reduction in susceptibility to nuclear radiation effects by a factor of $1/n^2$.

Parametric Eq 3.1 and 3.10 are useful for defining optical design criteria and for scaling instrument performance. In using these equations, however, the following limitations and conditions should be considered:

- $S_{w\alpha}/S_{h\alpha}$ is the inlet slit (and IFOV) aspect ratio. Equation 3.5 shows that in Eq 3.3, 3.8, 3.9, and 3.10 $S_{w\alpha}$ is not an independent parameter.

- Equations 3.3, 3.8, 3.9, and 3.10 are valid only for values of $F_s \geq 1$. For values of $F_s < 1$ channel bandwidth, $\Delta\upsilon$, would be controlled by the inlet slit width rather than by the exit slit width, and the effective $A\Omega$ for the instrument would be controlled by the exit slit width rather than by the inlet slit width.

- In a realizable configuration, the field lens shown in Fig 3.1 would probably be located behind the exit slit. This means the field lens diameter would be slightly larger than the diagonal of the exit slit and the value of $\sqrt{A_d}/A\Omega$ would be larger than the value calculated by Eq 3.8 and 3.9. Consequently, final values of NEN calculated using Eq 3.1 should use actual instrument design values for determination of $\sqrt{A_d}/A\Omega$.

- In Eq 3.10 the diameter of the field lens is taken equal to the diagonal of the exit slit. From Eq 3.10 the ratio of NEN (where $F_s > 1$) to NEN_o (where $F_s = 1$), where D is the diagonal of the exit slit, is

$$\frac{NEN}{NEN_o} = \frac{F/NO}{(F/NO)_o} \cdot \sqrt{\frac{1 + \left(F_s \frac{S_{w\alpha}}{S_{h\alpha}} \frac{\cos\alpha}{\cos\beta}\right)^2}{1 + \left(\frac{S_{w\alpha}}{S_{h\alpha}} \frac{\cos\alpha}{\cos\beta}\right)^2}} = \frac{F/NO}{(F/NO)_o} \cdot \frac{D}{D_o} \qquad (3.13)$$

If the F/NO is held constant as a function of channel bandwidth, $NEN/NEN_o = D/D_o$. If the field lens focal length is held constant, however, $F/NO/(F/NO)_o = D_o/D$, and for a given focal length excess channel bandwidth has no effect on NEN. This point is significant where it is advantageous to use the same focal length lenses for a number of channels. It does not change the fact that increasing the focal length of the lens for any channel above the minimum practical value will result in degradation of channel NEN performance.

- D* is not always independent of detector area. In the limit, the following apply:

  - To the extent that the detector is Johnson and/or GR noise limited, D* and A_d are essentially independent parameters. For this condition, minimum NEN corresponds to maximum optical convergence; i.e., the optical convergence factor, (F/NO)/n, should be minimized. (PC HgCdTe detectors tend to fall into this category.)

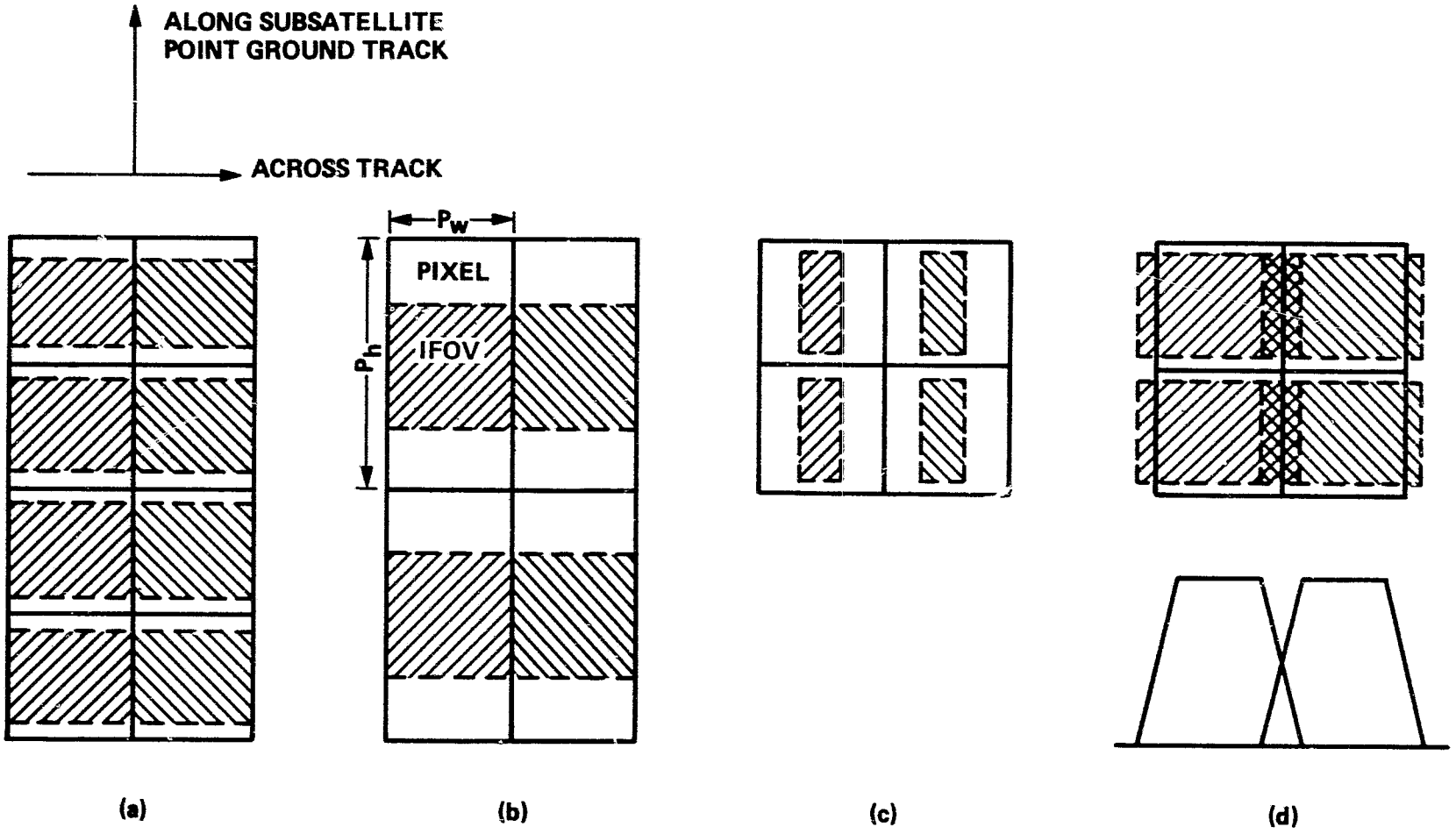

Figure 3-2 Examples of near nadir spatial sampling configurations

- To the extent that the detector is background noise limited by background flux which is contained within the focused optical ray bundle, $\sqrt{A_d}/D^*$ is a constant, since D* is inversely proportional to the square root of background flux density. For this condition, minimizing the optical convergence factor, (F/NO)/n, has no effect upon NEN. (PV detectors tend to fall into this category; HgCdTe detectors more so than InSb detectors.)

- To the extent that the detector is background noise limited by unfocused flux which originates within the detector dewar, minimum NEN corresponds to minimum field lens F/NO. Detector immersion has no effect upon NEN. (For a dewar temperature near that of liquid nitrogen, none of the detectors under consideration for baseline V tend to fall into this category.)

These effects do not affect the validity of the NEN parametric and scaling equations. Final values for instrument NEN, however, must be calculated using D* values corresponding to detector temperature and background flux density values to be encountered within the instrument environment. In addition, overall instrument D* values can be significantly affected by detector/preamplifier circuit design. These D* considerations are treated in greater detail in Para 3.1.1.4.

Equation 3.12 states that electrical noise bandwidth is inversely proportional to pixel (individual footprint) dwell time, and that dwell time can be defined in terms of spatial coverage and instrument parameters. Examples of spatial sampling configurations near nadir are illustrated in Fig 3-2. Pixels are defined as contiguous areas sampled by the individual footprints, and are represented by the solid grid lines in Fig 3-2. Individual footprints are represented by the individual shaded area. Figure 3-2a pictures two crosstrack footprint dwell intervals for an instrument using a four-element linear array in a step-and-stare crosstrack scan mode. Pixel elements in this example are square. The along track gaps between the individual footprint IFOV used to sample each pixel represent an inability to achieve a 100 percent area fill factor within the array. Figure 3-2b represents a two-element array used in a step-and-stare mode. Square IFOV are used to sample pixel elements which are twice as high (along track) as they are wide (across track). This represents a very poor fill factor between elements within the array. Figure 3-2c represents a two-element array used in a step-and-stare mode. IFOV elements, almost twice as high as they are wide, are used to sample square pixels. This represents a good fill factor between elements within the array, but the area fill factor for the total area scanned is less than that of (b). Figure 3-2d represents the basic configuration of (c) used in a constant angular velocity crosstrack scan mode. There is some spatial weighting and spatial overlap of the pixel areas. Total area fill factor is good, and crosstrack slew time within the line scan is effectively eliminated.

A multichannel grating spectrometer, in which a separate exit slit is used for each spectral channel, enjoys a multiplex advantage at least equal to the square root of the number of channels over a monochromator-type instrument using a scanning grating. For the grating spectrometer, neglecting spatial scan slew time and radiometric calibration target dwell times, maximum dwell time

$$T_{d(MAX)} = \frac{T_{LINE}}{N_{LINE}} \tag{3.14}$$

The spatial slew and calibration dwell time amortization factor is represented by

$$\frac{T_d}{T_{d(MAX)}} = \frac{N_{LINE}}{T_{LINE}} \cdot \frac{T_{LINE} - T_{SLEW}}{N_{LINE} + N_{CAL}}$$

$$= \frac{1 - \frac{T_{SLEW}}{T_{LINE}}}{1 + \frac{N_{CAL}}{N_{LINE}}} \tag{3.15}$$

and actual dwell time

$$T_d = \frac{T_{LINE}}{N_{LINE}} \cdot \frac{1 - \frac{T_{SLEW}}{T_{LINE}}}{1 + \frac{N_{CAL}}{N_{LINE}}} \tag{3.16}$$

where

N_{LINE} = number of pixel elements in the crosstrack line scan for each element in the array

T_{LINE} = repeat crosstrack line scan time for the array

Since

$$N_{LINE} = \frac{2\, S_{ANGLE}\, R_{NADIR}}{P_w} \tag{3.17}$$

and

$$T_{LINE} = \frac{N_{ARRAY}\, P_h}{V_g} \tag{3.18}$$

where

P_h = length of nadir pixel element along the subsatellite point ground track

P_w = length of nadir pixel element along the crosstrack scan direction

V_g = subsatellite point ground velocity [$V_g = f(R_{NADIR})$]

actual dwell time

$$T_d = \frac{N_{ARRAY}\, A_{p(NADIR)}}{2\, S_{ANGLE}\, (V_g\, R_{NADIR})} \cdot \frac{1 - \dfrac{V_g\, T_{SLEW}}{P_h\, N_{ARRAY}}}{1 + \dfrac{P_w\, N_{CAL}}{2\, S_{ANGLE}\, R_{NADIR}}} \qquad (3.19)$$

and, from Eq 3.10 and 3.12,

$$NEN_p \propto \sqrt{\frac{1}{A_{p(NADIR)}} \cdot \frac{2\, S_{ANGLE}\, (V_g\, R_{NADIR})}{N_{ARRAY}}} \cdot \sqrt{\frac{1 + \dfrac{P_w\, N_{CAL}}{2\, S_{ANGLE}\, R_{NADIR}}}{1 - \dfrac{V_g\, T_{SLEW}}{P_h\, N_{ARRAY}}}} \qquad (3.20)$$

NEN for the composite footprints used for atmospheric profile retrievals

$$NEN_{COMP} = \frac{NEN_p}{\sqrt{N_{COMP}}} \qquad (3.21)$$

or

$$NEN_{COMP} \propto \sqrt{\frac{A_p}{A_{p(NADIR)}} \cdot \frac{1}{A_{COMP}} \cdot \frac{2\, S_{ANGLE}\, (V_g\, R_{NADIR})}{N_{ARRAY}}} \cdot \sqrt{\frac{1 + \dfrac{P_w\, N_{CAL}}{2\, S_{ANGLE}\, R_{NADIR}}}{1 - \dfrac{V_g\, T_{SLEW}}{P_h\, N_{ARRAY}}}} \qquad (3.22)$$

where

N_{COMP} = number of individual pixels within each composite footprint

A_{COMP} = area of composite footprint

$A_p/A_{p(NADIR)}$ = ratio of contiguous pixel area at a given scan angle to nadir pixel area

The second terms in Eq 3.19, 3.20 and 3.22 represent radiometric calibration and slew time amortization factors. If calibration and slew times are neglected, these factors become unity. These equations are valid for any rectangular nadir pixel configuration sampled by a rectangular instrument IFOV.

Two AMTS requirements are major factors in the choice of individual footprint size: 1) NEN requirements are for the composite footprint rather than for an individual footprint, and 2) high spatial resolution for the individual footprint allows exploitation of the granularity of the cloud field when building composite footprints for cloud filtering during atmospheric profile retrieval. Equation 3.20 shows that NEN for the individual pixel element

$$NEN_p \propto \sqrt{\frac{1}{A_{p(NADIR)}}}$$

is independent of the pixel location in the crosstrack line scan. Equation 3.22 shows that NEN for the composite footprint

$$NEN_{COMP} \propto \sqrt{\frac{A_p}{A_{p(NADIR)}} \cdot \frac{1}{A_{COMP}}}$$

is dependent upon the composite footprint location in the crosstalk line scan. The individual pixel area is a function of location with respect to nadir, as represented by the term $A_p/A_{p(NADIR)}$, while the area of the composite footprint, A_{COMP}, on average is independent of location. To the first approximation, NEN_{COMP} is independent of the size of the individual nadir pixel; coupling exists only because the calibration and slew time amortization factor is smaller for a larger nadir pixel area.

Equation 3.19 is the design and scaling equation for footprint dwell time. Equations 3.20 and 3.22 are NEN scaling equations for the individual and composite footprints respectively. The noise bandwidth factor, $\sqrt{\Delta F}/F_c$, used in calculating NEN from Eq 3.1 must be determined in accordance with the considerations of Para 3.1.1.3.1 using dwell time values calculated from Eq 3.19. Scaling of NEN performance for a given system design configuration can be accomplished using the instrument equation, 3.10, and the spatial resolution and spatial coverage equations, 3.20 and 3.22. First order system NEN scaling factors, neglecting calibration and slew time amortization, are summarized in Table 3-1. At the detail design level, however, calibration and slew time effects must be considered. Examples of representative calibration and slew time effects are shown in:

- Fig 3-3 vs (square) pixel size and number of array elements
- Fig 3-4 vs (square) pixel size and altitude
- Fig 3-5 vs (square) pixel size and maximum crosstrack scan angle

The following data is plotted in each figure:

- Dwell time (a)
- Calibration and slew time factor (b)
- Relative NEN per pixel (c)
- Relative NEN per composite footprint (d)

The following constants and reference parameter values are used for these examples:

- V_g = f(altitude) (see Fig 3-6)
- $A_p/A_{p(NADIR)}$ (see Fig 3-7)
- N_{CAL} 2
- Number of Array Elements (Ref) 16
- T_{SLEW} (Ref) 7.179 sec

Table 3-1 First order system NEN scaling factors[1]

Parameter	Factor
a) Instrument scale	$NEN \propto \frac{1}{\text{linear scale}}$
b) Altitude	$NEN_{(MIN)} \propto \sqrt{7.69\ R_{NADIR} - 1.33 \times 10^{-3}\ R^2_{NADIR}}$
c) Maximum crosstrack half scan angle	$NEN_{(MIN)} \propto \sqrt{S_{ANGLE}}$
d) Number of elements in linear pushbroom array	$NEN_{(MIN)} \propto \frac{1}{\sqrt{N_{ARRAY}}}$
e) Nadir pixel size	$NEN_{P(MIN)} \propto \frac{1}{\sqrt{A_{p(NADIR)}}}$
f) Composite footprint area	$NEN_{COMP(MIN)} \propto \frac{1}{\sqrt{A_{COMP}}}$

[1]Factors (b) through (f) neglect calibration and spatial slew time effects. For scaling over other than small ranges, calibration and slew time amortization factors should be considered. Factors (e) and (f) are (first order) independent of each other.

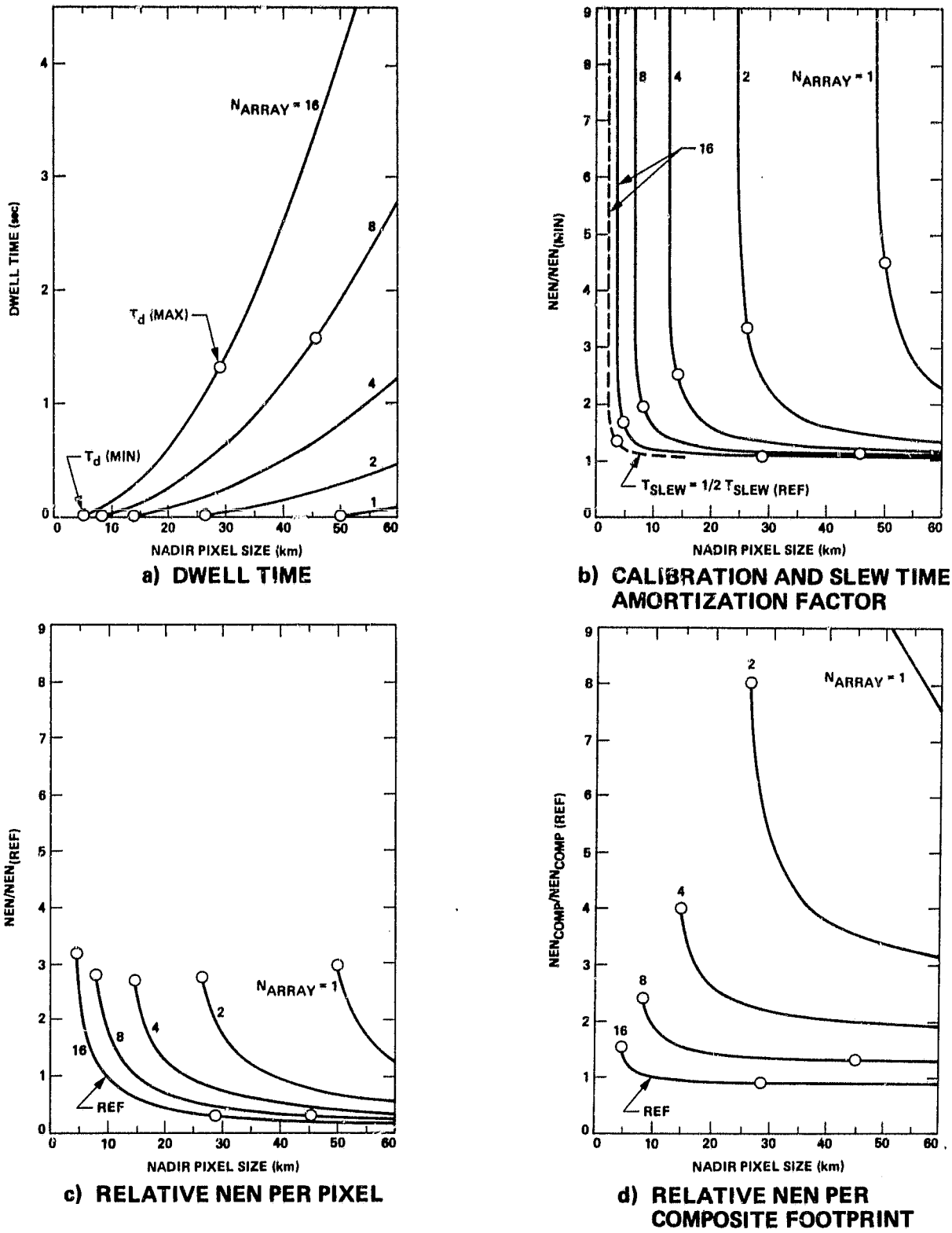

Figure 3-3 Calibration and slew time effects vs (square) pixel size and number of array elements

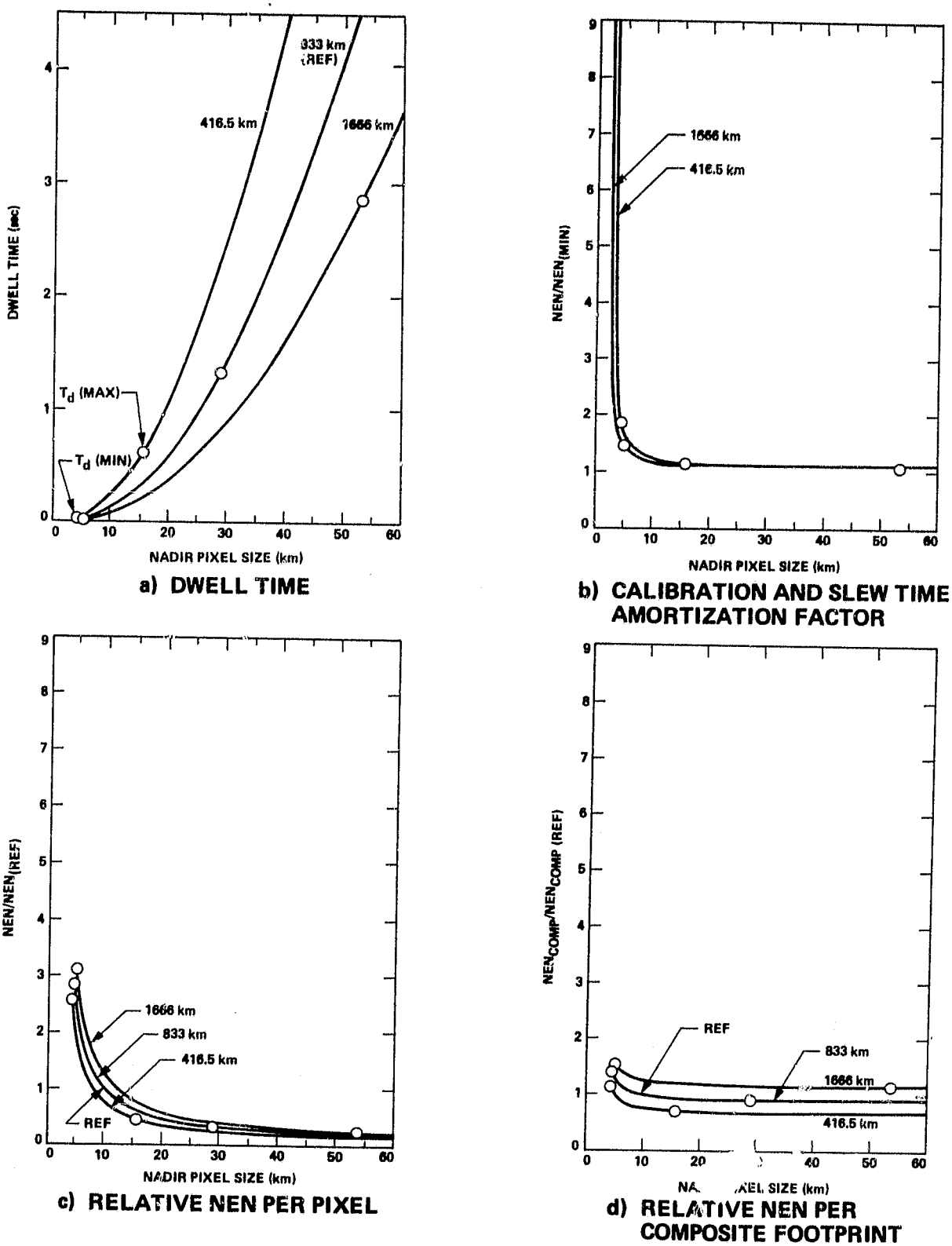

Figure 3-4 Calibration and slew time effects vs (square) pixel size and altitude

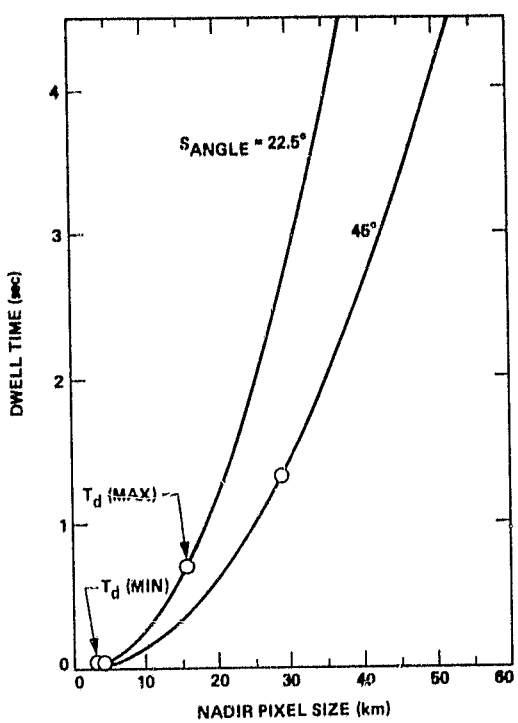

a) DWELL TIME

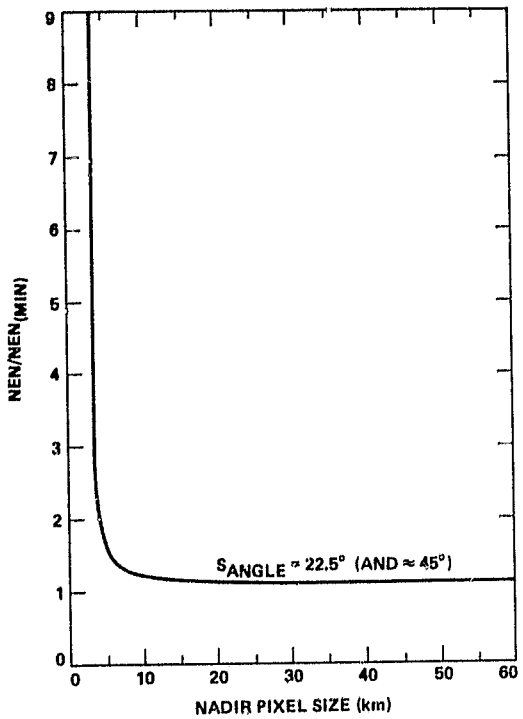

b) CALIBRATION AND SLEW TIME AMORTIZATION FACTOR

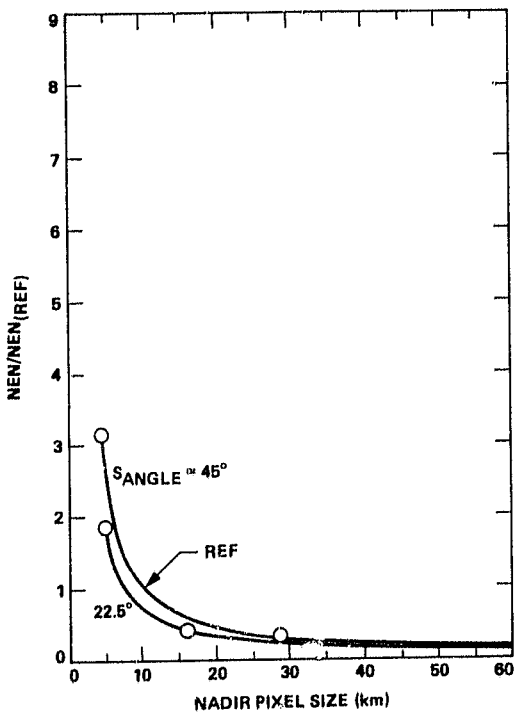

c) RELATIVE NEN PER PIXEL

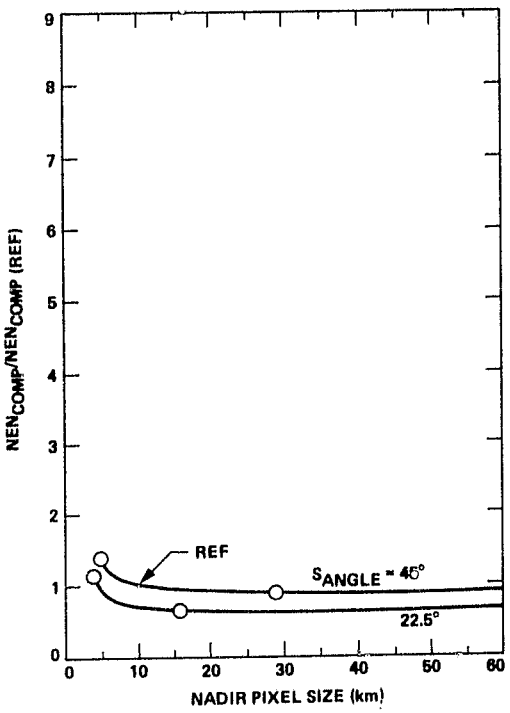

d) RELATIVE NEN PER COMPOSITE FOOTPRINT

Figure 3-5 Calibration and slew time effects vs (square) pixel size and maximum crosstrack scan angle

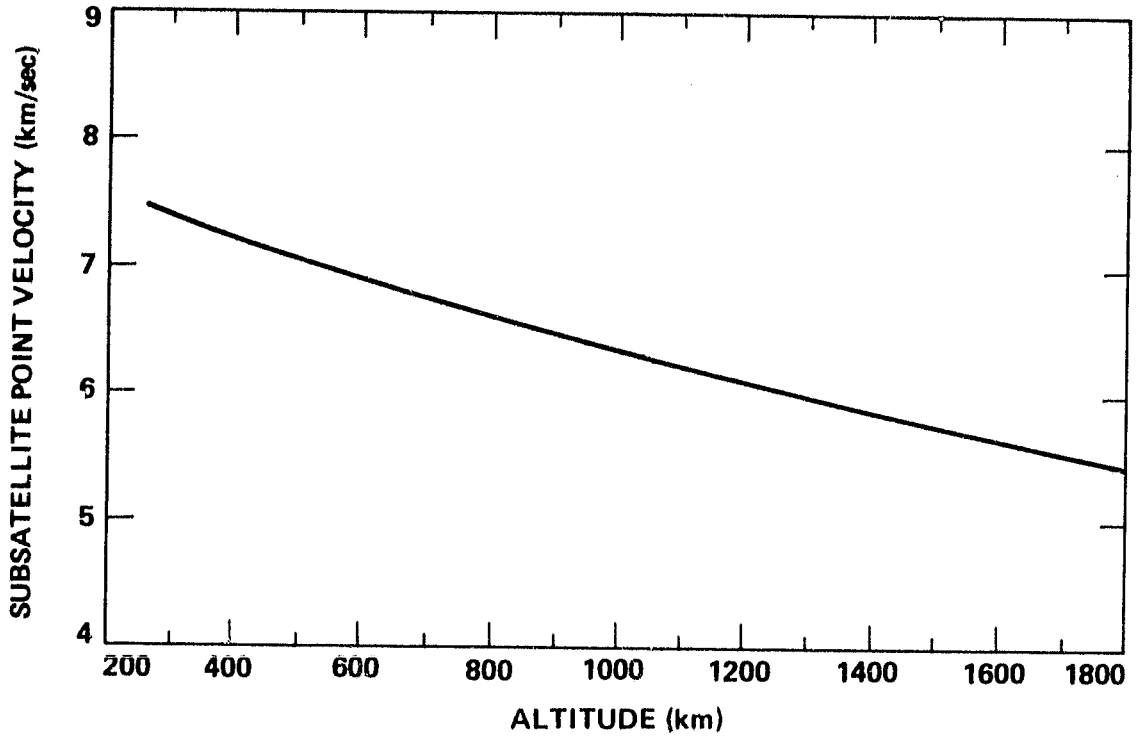

Figure 3-6 Subsatellite point velocity (V_g) vs altitude

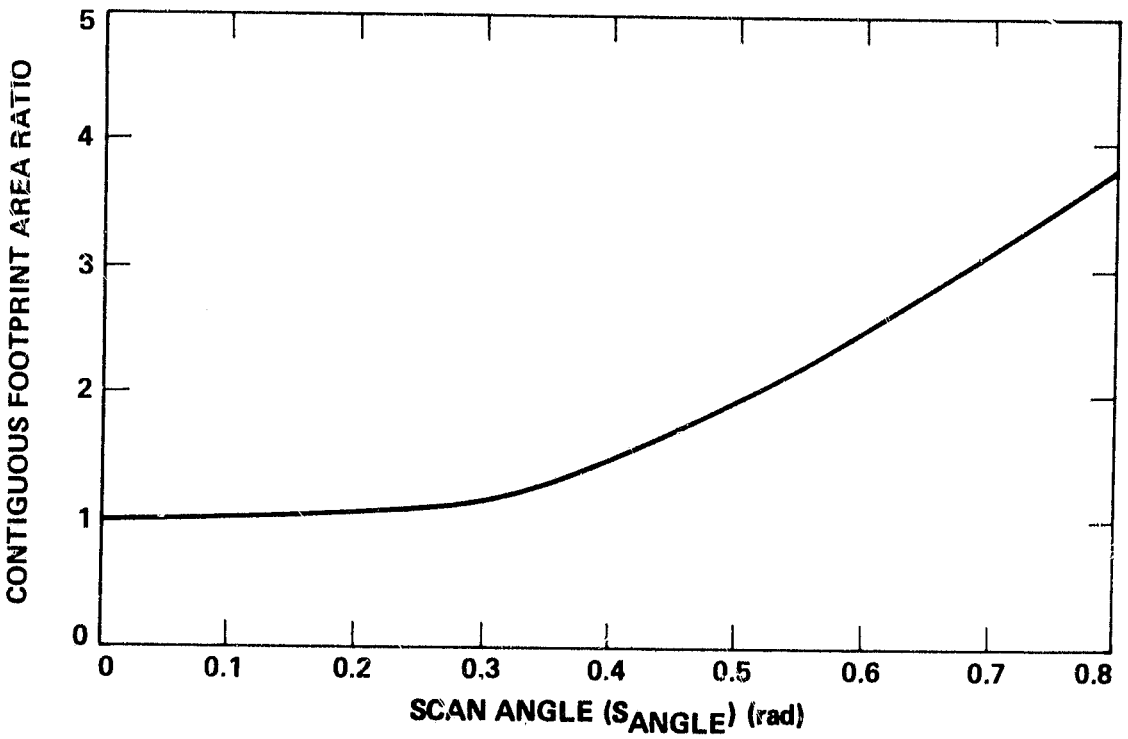

Figure 3-7 Pixel area ratio vs crosstrack half-scan angle

- Altitude (Ref) 833 km
- NADIR pixel size (Ref) 10 x 10 km
- Maximum crosstrack scan angle (Ref) ± 44.71°

Except where otherwise stated in the figures, reference values apply.

Each curve in Fig 3-3, 3-4, and 3-5 is marked correspondingly to minimum and maximum dwell time limits. T_d minimum was set equal to approximately 15 msec and T_d maximum was selected to limit pixel area smear due to subsatellite point velocity to 30 percent. In general, the amortization factor rather than minium dwell time tends to place a limit on the minimum pixel size. In each figure the relative NEN per composite footprint (d) is of prime importance to the AMTS. The goal is to select as small a pixel size as possible without encountering an excessive amortization factor penalty in order to enhance cloud filtering capability of the system. Figure 3-3b shows the effect upon the amortization factor of reducing the reference slew time by a factor of 2. (To achieve this degree of slew time reduction would require heroic measures if, indeed, it were possible.) The relative change in composite footprint performance as a function of altitude or as a function of maximum crosstrack scan coverage is primarily the result of covering more or less of the earth's surface per unit time. From the system design point of view, earth coverage per unit time is the important parameter here. Earth coverage considerations are treated in more detail in Para 3.1.1.6. It is important to realize that for a given instrument $\sqrt{A_d}/A\Omega$, altitude, maximum crosstrack scan angle, and number of elements in the linear footprint array, NEN per rectangular pixel area is a function of the contiguous pixel dimensions; it is independent of the dimensions of the rectangular IFOV with which the pixel is sampled. For the composite footprint, NEN is a function of the composite pixel area and of the crosstrack scan angle. Above a minimum individual pixel size — which is a function of the number of elements in the footprint array — NEN per composite pixel is practically independent of individual pixel size. There is no way to escape these parametric relationships through creative sampling.

In summary, the parametric and scaling equations developed this paragraph show that the only significant degrees of freedom in optical design and earth coverage parameters affecting the achievable limit in detector noise limited radiometric NEN performance are:

- In system design
  - Channel spectral resolution
  - Nadir pixel size and aspect ratio
  - Composite footprint size
  - Altitude

- crosstalk scan width

- In instrument design

  - Use of a multichannel grating spectrometer vs a scanning monochromator

  - Number of footprint elements within a linear array

  - Along track fill factor within a linear array

  - Grating size and form factor (instrument scale)

  - Grating angles

  - Detector field lens F/NO

  - Detector immersion lens index of refraction

  - Detector quality (D* and 1/f noise knee)

A baseline instrument designed to satisfy a particular set of system design parameters and optimized for minimum NEN in accordance with the instrument design equation 3.10, in conjunction with the scaling equations, 3.10, 3.20, and 3.22, constitutes a general first order solution for detector noise limited NEN performance achievable with any set of earth coverage and spatial resolution requirements as a function of instrument scale and the number of elements in the footprint array.

3.1.1.2 Grating Considerations

The grating angle factor, represented by the second term in Eq 3.10, is defined as

$$F_g = \frac{\cos \alpha}{\sin \alpha + \sin \beta} \sqrt{\frac{\cos \beta}{\cos \alpha} + \frac{\cos \alpha}{\cos \beta}\left(F_s \frac{S_{w\alpha}}{S_{h\alpha}}\right)^2} \qquad (3.23)$$

The grating angle factor is plotted in Fig 3-8 for the special case where the slit factor, F_s, and the slit aspect ratio, $S_{w\alpha}/S_{h\alpha}$, are both unity. The angle factor is shown for an R1, an R2, and an R3 grating, for both a near-Littrow and an off-Littrow configuration. The range of interest for the AMTS corresponds to υ/υ_o values of approximately 0.96 to 1.08. The relative grating angle factor is plotted in Fig 3-9 as a function of the product of the slit factor and inlet slit aspect ratio for the R2 grating used off-Littrow.

Figure 3-8 shows that the grating angle factor improves (decreases) as grating angles are increased. For a given grating R-value the off-Littrow performance is superior to near-Littrow performance. The near-

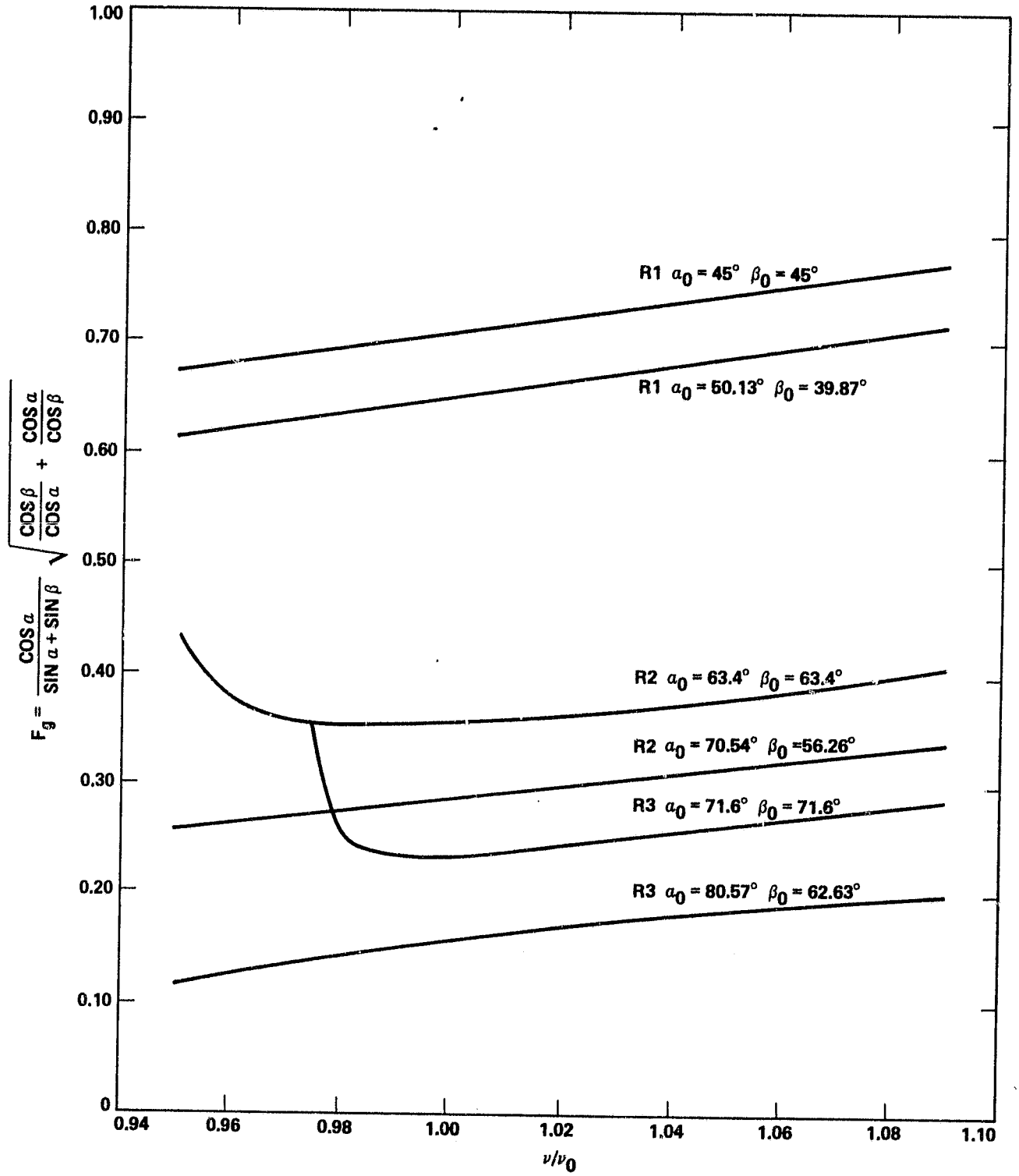

Figure 3-8 Grating angle factor vs relative frequency vs grating angles

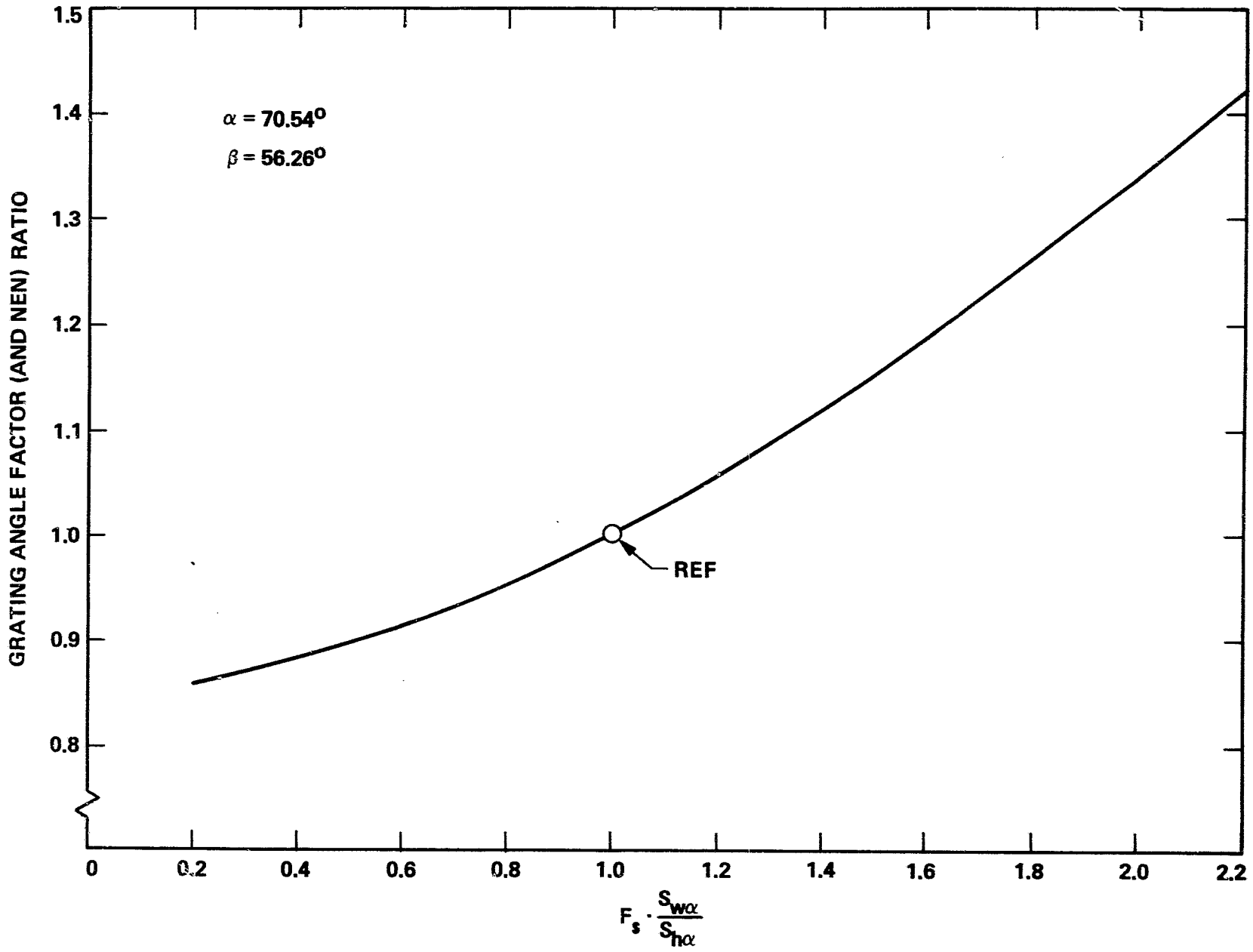

Figure 3-9 Relative grating angle factor (and NEN) as a function of the slit factor and inlet slit aspect ratio for an R2 grating used off Littrow (for F_S values > 1)

Littrow performance of the R2 grating degrades for υ/υ_o values of less than unity where the diffraction angle, β, approaches 90 degrees. The R3 grating is not useable for the AMTS in the near-Littrow configuration, since the diffraction angle reaches 90 degrees within the range of υ/υ_o values of interest. Figure 3-9 shows that the effects of excess channel bandwidth, F_s, and of inlet slit aspect ratio can be significant. The worst case value of F_s for the Baseline V channel set ($F_s = 1.53$ for Channel 25), for example, would result in an NEN degradation of 17 percent. An along track spatial fill factor of 70 percent in a square nadir pixel ($S_{w\alpha}/S_{h\alpha} = 1.43$), would result in an NEN degradation of 13 percent. Both parameters together ($F_s \cdot S_{w\alpha}/S_{h\alpha} = 2.19$) would result in an NEN degradation of 42 percent.

Equation 3.11 states that relative grating efficiency — in the scalar domain — can be expressed in terms of grating orders and angles; i.e.:

$$E_g = f(m, \alpha, \beta, \theta, \phi, \bar{\phi})$$

A dual-vector scalar efficiency model (Ref 3-1) developed as a part of this study effort is presented in Appendix C. Grating angles are defined in Fig 3-10. The out-of-plane angle, θ, is not shown in this figure. The effective illuminated facet width, b_α, is defined in Fig 3-10. Calculated relative grating efficiency as a function of relative frequency for the 3rd through the 48th orders is plotted in Fig 3-11 for an R1 and an R2 grating in both near-Littrow and off-Littrow configurations, and for an R3 grating in the off-Littrow configuration. Blaze and antiblaze angles were adjusted to give approximately equal efficiencies at the ends of the frequency range of interest for the 3rd and 12th orders. The frequency bandwidth of the grating efficiency decreases as the grating order increases. The bandwidth is wider for the larger R-number gratings, and for the off-Littrow configurations. The characteristics of the R3 grating, however, are so erratic that it is of no practical use for the AMTS.

Equation 3.10 shows that NEN is proportional to the ratio of the grating angle factor to relative grating efficiency. The problem in instrument design is to choose grating angles and orders which will optimize overall system performance for a given channel set. F_g/E_g ratios averaged over the frequency range of interest to the AMTS are listed vs grating configurations and grating orders in Table 3-2. This table, in conjunction with the efficiency bandwidth characteristic details of Fig 3-11, indicate that the R2 grating used off-Littrow in the 3rd through the 12th — or possibly 15th—orders is near the preferred configuration for the AMTS in terms of minimizing NEN.

Calculated values for the grating angle factor are accurate and precise. As shown in Appendix C, however, the dual vector grating model predicts correct numerical values for relative grating efficiency only within the scalar domain; i.e., within the region where the grating exhibits no significant polarization sensitivity. The model does provide an insight into the physics of grating performance, even for orders below the scalar region. A general rule of thumb is that scalar performance occurs for orders for which the relative illuminated facet width with respect to wavelength (b_α/λ) is equal to or greater than 6:1. Measured relative

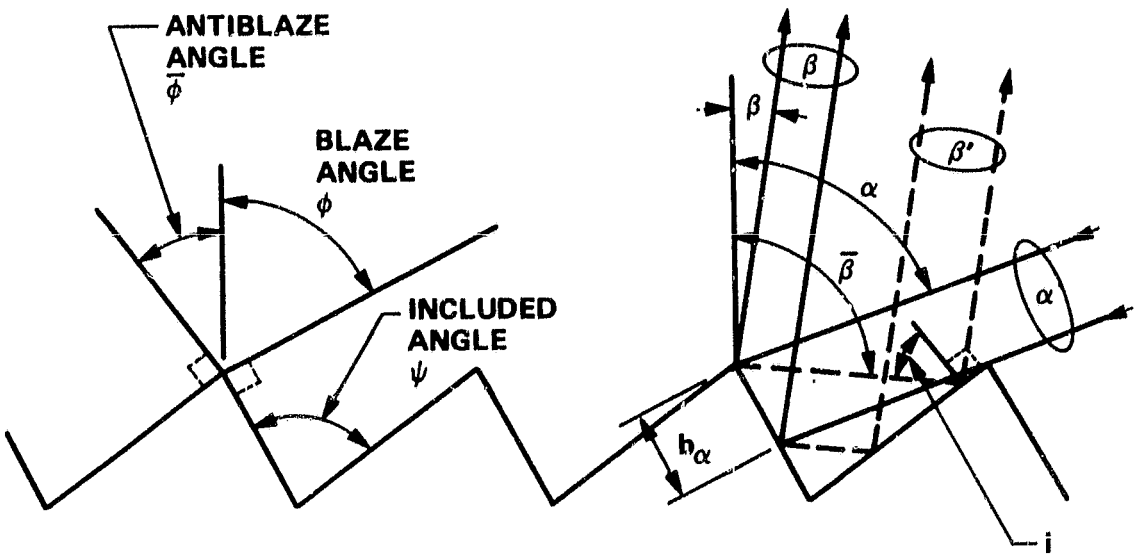

$$\overline{\beta} = 180^{o} - 2\overline{\phi} - \beta$$
$$i = 180^{o} - \overline{\phi} - \beta$$
$$\psi = 180^{o} - \overline{\phi} - \phi$$

Figure 3-10 Grating angles

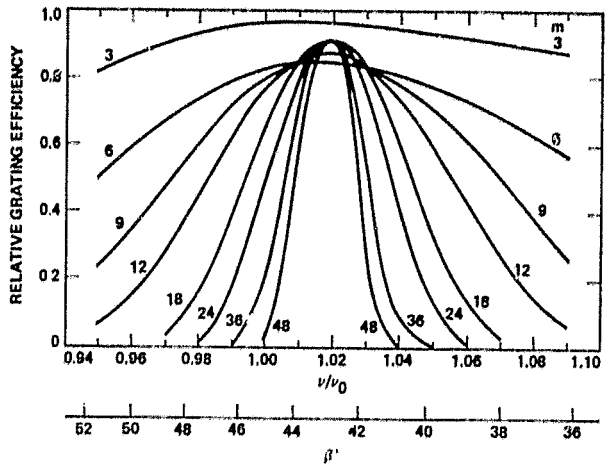

a) R1 NEAR LITTROW

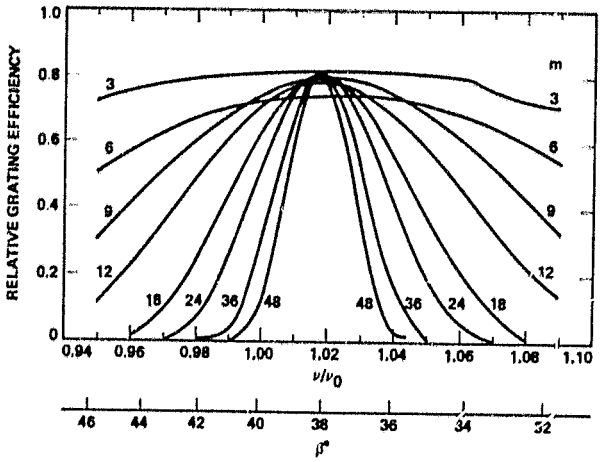

b) R1 OFF LITTROW

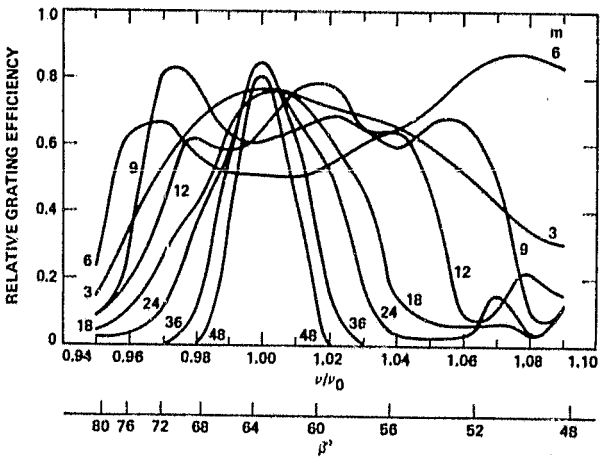

c) R2 NEAR LITTROW

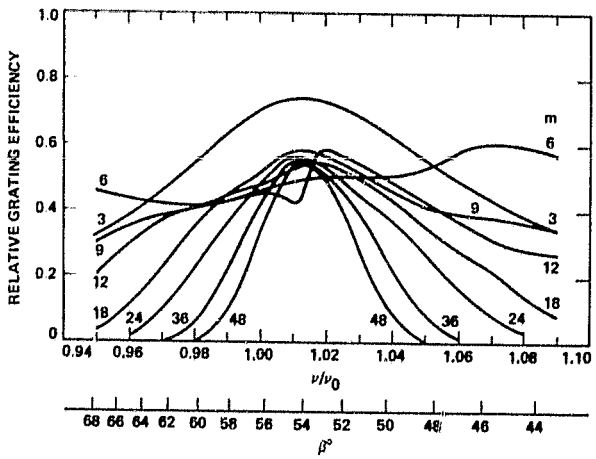

d) R2 OFF LITTROW

GRATING ANGLES

FIG.	α_0^b	θ^c	ϕ^c	$\bar{\delta}^c$
a)	45	5.35	44	55
b)	50.13	0	44.1	56
c)	63.4	5.35	63.4	29
d)	70.54	0	62.2	38
e)	80.57	0	72.6	14.9

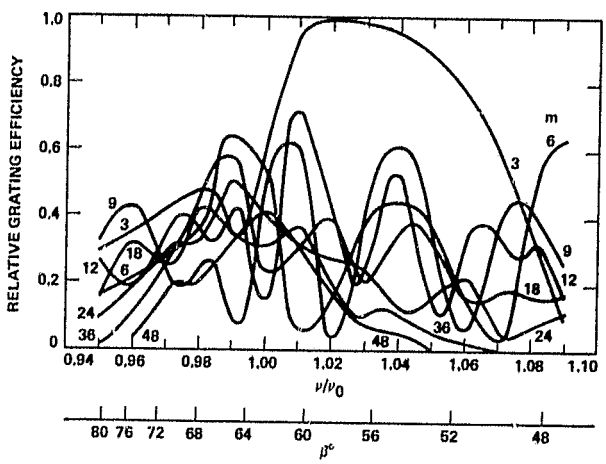

e) R3 OFF LITTROW

Figure 3-11 Calculated relative grating efficiency vs grating order and diffraction angle as a function of relative frequency

Table 3-2 Ratio of average grating angle factor to average grating efficiency[1] vs grating order for near-Littrow and off-Littrow configurations

		F_g/E_g				
		R1		R2		R3
Grating Order	$\alpha_o°$ ⟶	45	50.13	63.4	70.54	80.57
	$\beta_o°$ ⟶	45	39.87	63.4	56.26	62.63
3		0.78	0.84	0.62	0.52	0.24
6		0.96	0.97	0.57	0.59	0.52
9		1.11	1.03	0.62	0.62	0.49
12		1.33	1.23	0.77	0.69	0.48
18		1.90	1.73	1.09	0.82	0.55
24		2.48	2.27	1.33	1.04	0.66
27		2.76	2.52	1.46	1.18	0.76
36		3.59	3.26	1.77	1.52	0.91
48		4.69	4.28	2.54	1.96	1.17

[1]Averaged over relative frequency range, υ/υ_o, of 0.96 to 1.08.

grating efficiency for P-plane (E vector parallel to grooves) and S-plane (E vector normal to grooves) radiation for an R2 grating used in a monochromator configuration is shown in Fig 3-12. For this particular grating configuration, it would appear that grating polarization sensitivity would be quite small by the 18th order, where b/λ would be 5.6:1. In comparing calculated grating efficiency from Fig 3-11 with the measured efficiency of Fig 3-12 it must be remembered that the calculated efficiency is for a grating in a spectrometer configuration (fixed incident angle; detection at multiple diffraction angles) and the measured efficiency is for a grating in a monochromator configuration (fixed angular spacing between incident and diffraction angles; variable grating angle). In addition, in terms of bandwidth and polarization sensitivity, relative values of b/λ must be considered. Mean values of b/λ corresponding to the calculated grating efficiencies of Fig 3-11 are listed in Table 3-3. Values of b/λ corresponding to the nominal blaze wavelength for the measured efficiencies of Fig 3-12 are shown in Fig 3-12.

For grating orders below the scalar domain, the following general observations can be made with respect to relative grating efficiency:

- As grating orders increase, efficiency characteristics vs wavelength become quite regular. Grating anomalies appear to be very much reduced.

- As grating orders decrease below the scalar region polarization sensitivity increases.

- The separation in terms of wavelength of the P-plane and S-plane frequency response for orders below the scalar region results in a reduction in peak efficiency and a broadening of the overall frequency response for random polarization with respect to frequency response calculated using the scalar model.

- By adjusting blaze and antiblaze angles, it is generally possible to simultaneously adjust the relative efficiencies at selected band edges for one relatively low order and one relatively high order. The blaze angle primarily affects relative frequency response in the higher orders; the antiblaze angle primarily affects frequency response in the lower orders. In the scalar region, peak efficiency can be a relatively strong function of the antiblaze angle, while the skirt response is a relatively weak function of the antiblaze angle.

- Peak efficiencies are higher for Littrow configurations, but relative bandwidths are broader for off-Littrow configurations. If the required bandwidth is wide enough, the off-Littrow configuration may provide greater absolute efficiency near the band edges.

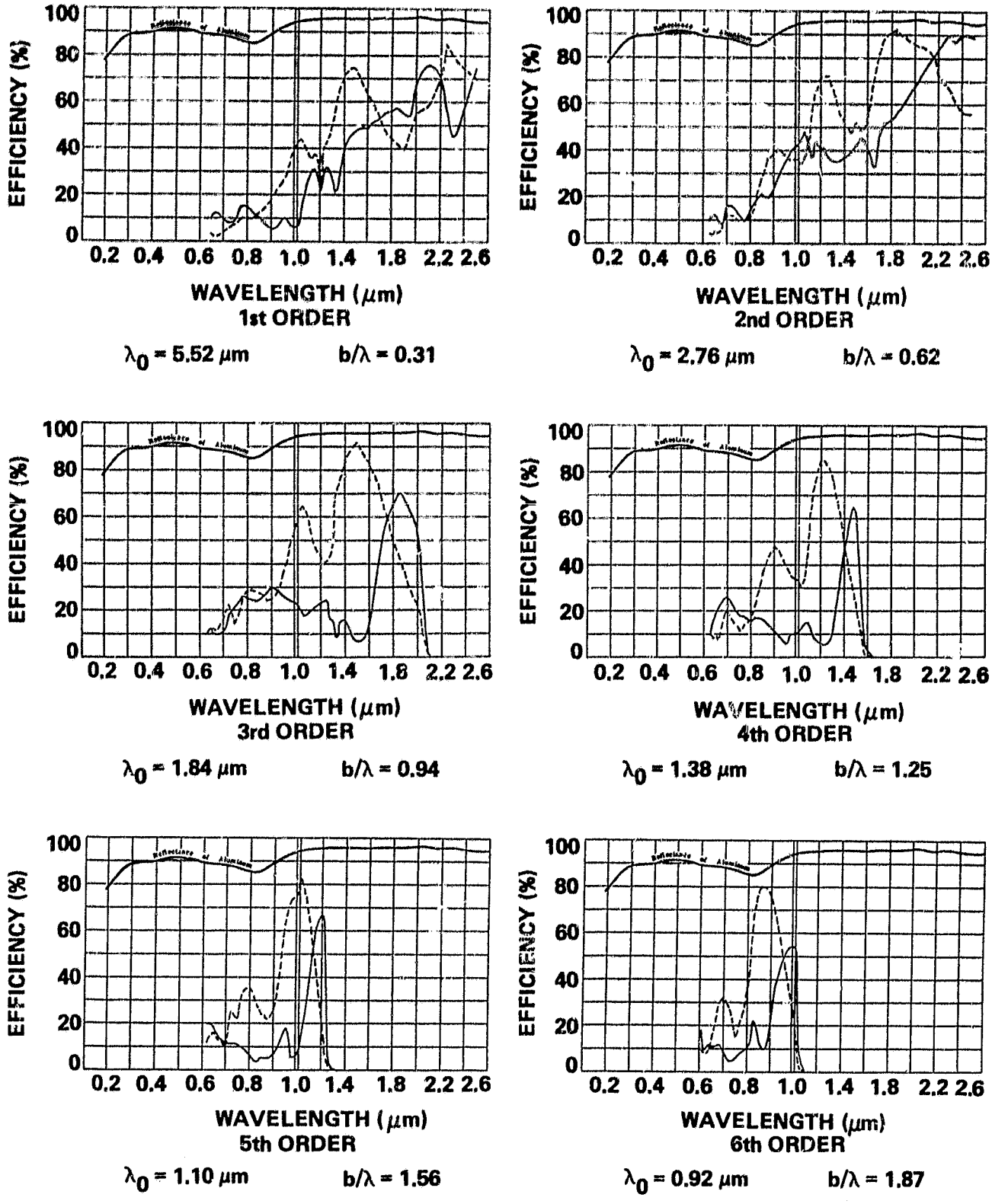

Figure 3-12 Measured relative efficiency for P-plane (dashed lines) and S-plane (solid lines) for an R2 echelle grating used near Littrow ($\beta - \alpha = 7.5°$) in a monochromator configuration (grating pitch = 316 g/mm, $\phi \approx 61.5°$)

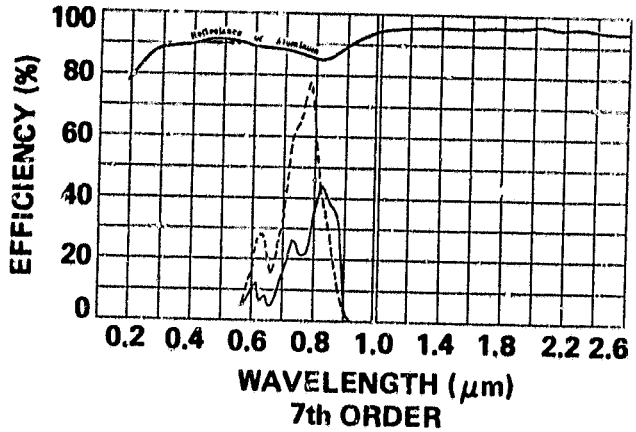

$\lambda_0 = 0.74\ \mu m$ $b/\lambda = 2.3$

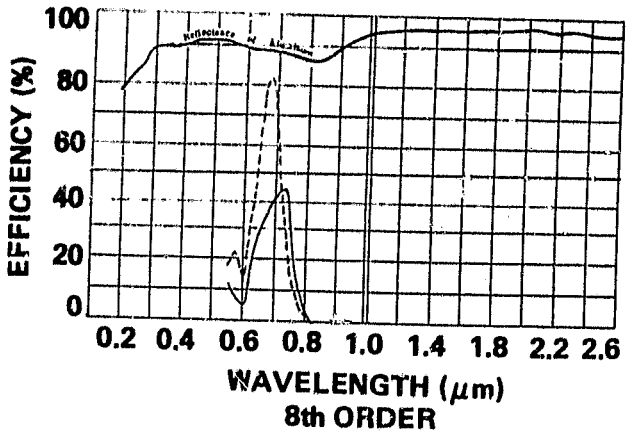

$\lambda_0 = 0.69\ \mu m$ $b/\lambda = 2.49$

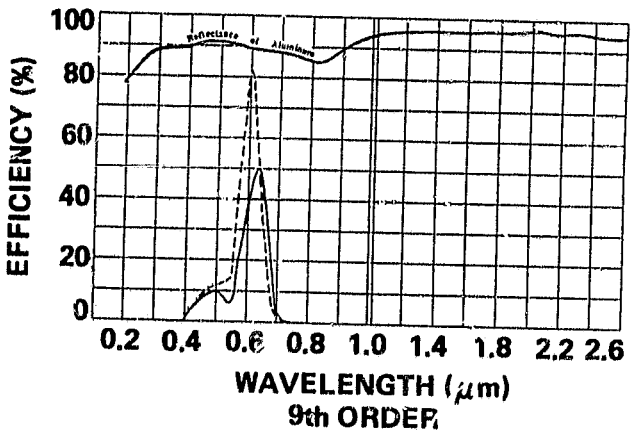

$\lambda_0 = 0.61\ \mu m$ $b/\lambda = 2.82$

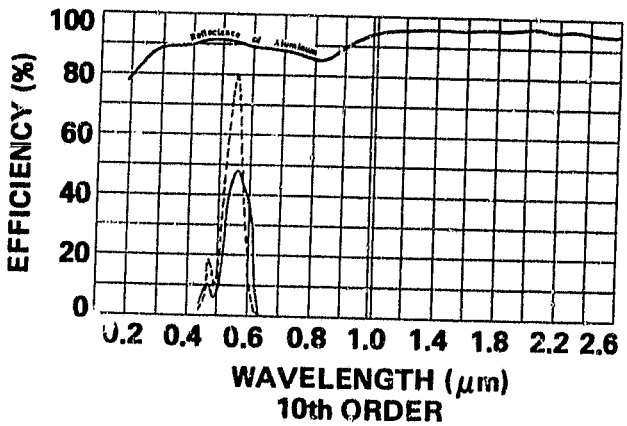

$\lambda_0 = 0.55\ \mu m$ $b/\lambda = 3.13$

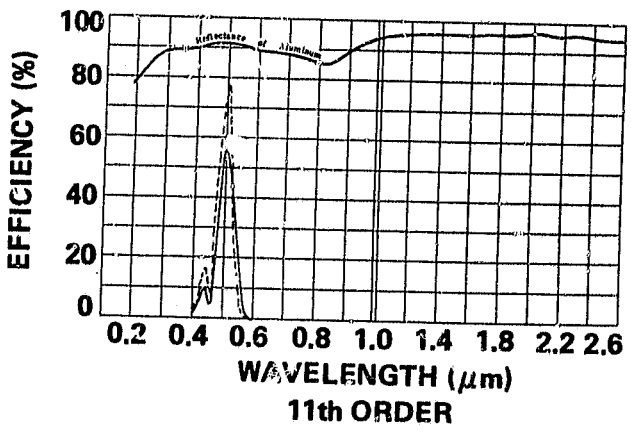

$\lambda_0 = 0.50\ \mu m$ $b/\lambda = 3.44$

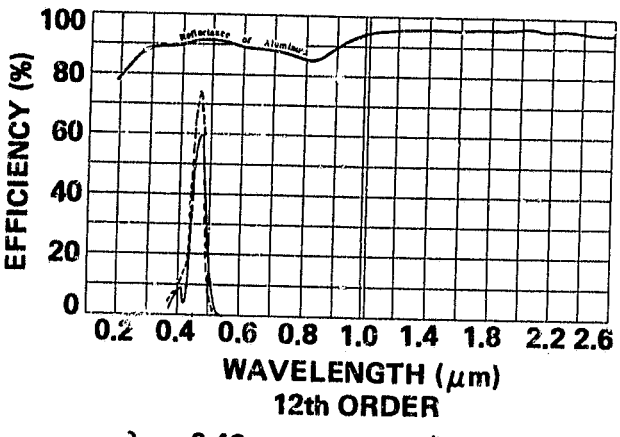

$\lambda_0 = 0.46\ \mu m$ $b/\lambda = 3.74$

Figure 3-12 (continued)

For first order design there is some validity in using the scalar grating model with reduced peak efficiencies for the lower nonscalar orders. In order to specify optimum grating angles for a hardware design for the echelle grating, however, it would be necessary to build and test sample gratings under the proposed angular conditions of use. In effect, a grating design for use under nonscalar conditions would have to be arrived at through a cut-and-try procedure using insights derived from the scalar model to guide the effort.

While considerable progress has been made in France and in Australia during the last few years in modeling grating efficiency outside the scalar domain, it is reported that these models are inadequate for steep echelle gratings.

Figure 3-11 shows that an echelle grating optimized for minimum NEN must be used in relatively low orders if the spectral channel set results in diffraction angles which extend over a relatively large angular range. Figure 3-12 indicates that such gratings will exhibit considerable polarization sensitivity. A blazed grating could be used in higher orders in the scalar domain to effectively eliminate polarization sensitivity if the bandwidth in the higher orders could be widened. Conceptually, this could be accomplished by using multiple blaze angles for the grating.

To be successful, the amplitude fields from each blazed section of a multiblazed grating must effectively be in-phase at the desired diffraction angles. For example, for out-of-phase angles of 10 degrees the resultant field amplitude degradation for equal amplitude fields is approximately 1 percent; for 25 degrees, 5 percent; for 45 degrees, 15 percent; and of course, for 180 degrees, 100 percent. Neglecting reflections from the antiblaze facets, the phase centers for each grating groove can be taken at the center of the illuminated width of the blaze facets, as illustrated in Fig 3-13. The phase difference (in radians) between two blazed sections having the same groove pitch is

$$\Delta P' = \frac{2\pi}{\lambda} \left[w'(\sin \alpha + \sin \beta) + h(\cos \alpha + \cos \beta) \right] \qquad (3.24)$$

or, in terms of grating orders and angles, and with the blaze ruling error offsets expressed as ratios with respect to the grating pitch,

$$\Delta P' = 2\pi m \left(\frac{w'}{a} + \frac{h}{a} \cdot \frac{\cos \alpha + \cos \beta}{\sin \alpha + \sin \beta} \right) \qquad (3.25)$$

where

h = height of phase center offset between blazed sections normal to grating surface

Table 3-3 Illuminated facet width to wavelength ratio (b/λ) vs grating orders and angles

		b/λ				
		R1		R2		R3
Grating Order	$\alpha_o°$ → 45 $\beta_o°$ → 45	50.13 39.87	63.4 63.4	70.54 56.26	80.57 62.63
3		1.5	1.4	0.75	0.57	0.26
6		3.0	2.8	1.5	1.1	0.53
9		4.5	4.1	2.3	1.7	0.79
12		6.0	5.5	3.0	2.3	1.1
18		9.0	8.2	4.5	3.4	1.6
24		12.0	11.0	6.0	4.6	2.1
27		13.6	12.4	6.8	5.1	2.4
36		18.1	16.5	9.1	6.8	3.2
48		24.1	22.0	12.1	9.1	4.2

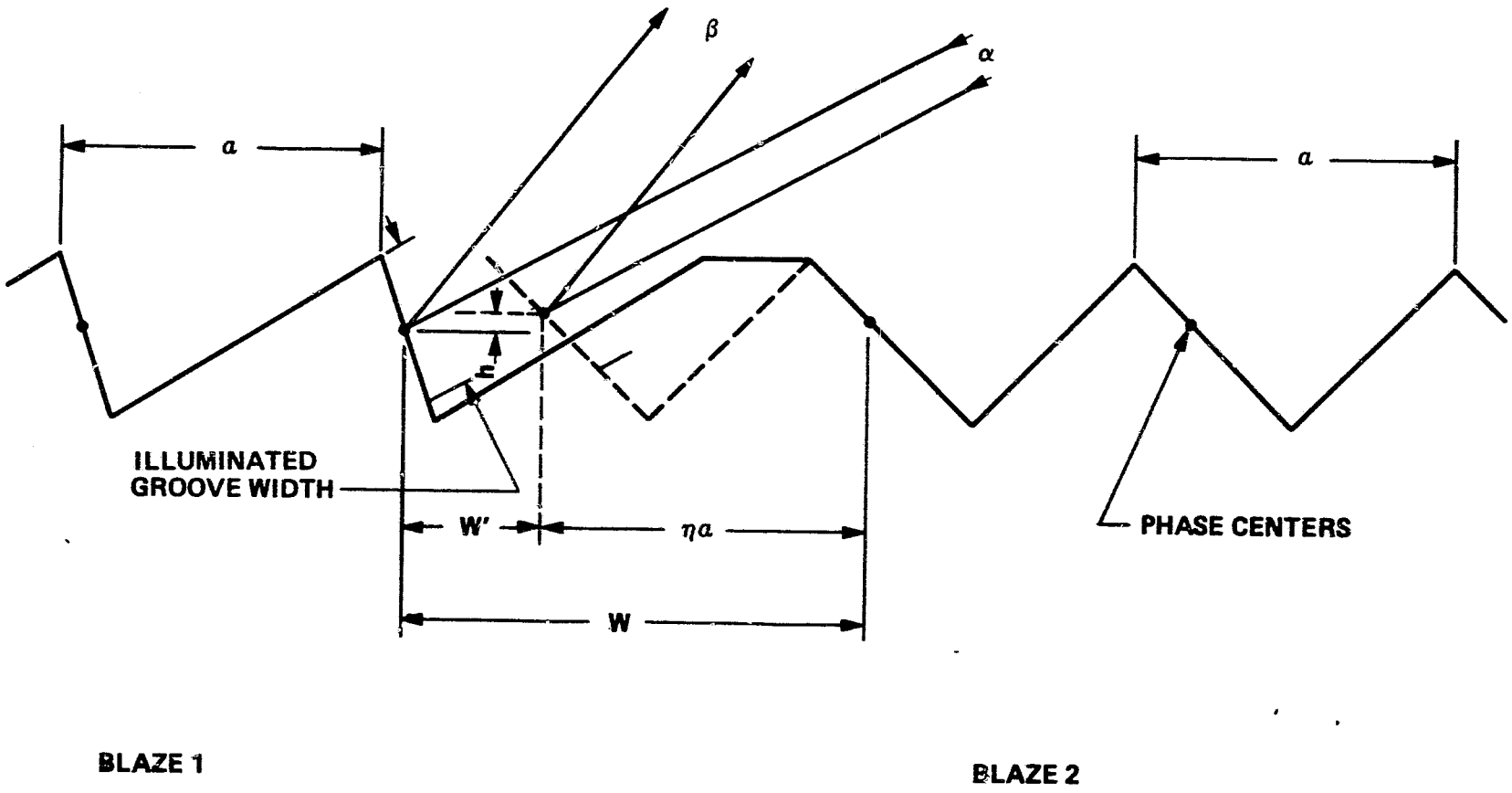

Figure 3-13 Multiple blazed grating parameter definitions

w = distance between phase centers between any two selected grooves, one in each of the two blaze sections

$w' = w - na$, where n is an integer and $w < a$

For a fixed incident angle and for all diffraction angles less than or equal to the incident angle, fields from the different blaze sections would be in-phase if the ruling offset errors, w' and h, were both zero. Equation 3.24 shows that $\Delta P'$ is a funtion of λ, α, β, w', and h, and that it is inversely porportional to λ. It is independent of grating order. (In Eq 3.25 m/a is a constant for a given wavelength.) In the AMTS channel set, for example, the shortest wavelength channel, Channel 28, has a wavelength of 3.723 μm. Assuming an incident angle of 71 degrees and a diffraction angle of 57 degrees, for a maximum phase error of 25 degrees it would be necessary to hold w' to less than 0.15 μm if h were zero, or to hold h to less than 0.30 μm if w' were zero.

In point of fact, reflection of the diffracted wave from the blaze facet by the antiblaze facet will affect the phase shift between blaze sections for echelle gratings. In the limit, it would be possible to rule a perfect multiblazed echelle grating for only one order for a given set of grating angles. In addition, widening grating bandwidth by using multiblazed gratings would significantly decrease the peak efficiency available from the grating. In order to examine these effects in detail, it would be necessary to expand the dual-vector grating efficiency model of Appendix C to include a set of dual vectors for each blaze section and the effects of effective phase offset errors between them.

The above arguments for multiblazed gratings are valid in collimated optical space at infinity. The degree to which a particular optical configuration or the quality of the optics might affect this argument has not been determined.

It would appear that ruling a good multiblazed grating is not a trivial task. For the AMTS, this would result in tight alignment tolerances for the phase centers in a very coarse grating. At the same time, such an approach should not be rejected out-of-hand if the task requires it. Such a grating would tend to fall into the scalar domain where the math model for grating performance would yield good numeric values.

3.1.1.3 Optical Chopping Considerations

3.1.1.3.1 NEN Effects

Equation 3.1 can be used to calculate NEN for a radiometer using an optical chopper. A figure of merit for an optical chopper/signal processor configuration is $\sqrt{\Delta F}/F_C$. If the optical beam is not chopped, the chopper factor, F_C, is unity.

In Eq 3.1 and 3.10 D* is assumed to be invariant within the electrical passband of the system. As illustrated in Fig 3-14, total detector/preamp noise consists of the sum of 1/f noise and noise that is

essentially constant as a function of frequency. If the 1/f noise is significant, D* can be a function of the amplitude vs. absolute frequency response of the system noise passband. This difficulty can be avoided in Eq 3.1 and 3.10 if D* is specified in terms of the frequency invariant noise component (i.e., D* is evaluated at a frequency well beyond the 1/f noise knee, F_K) and an equivalent noise bandwidth is used which accounts for the relative 1/f noise integrated over the passband of the noise filter.

Equivalent noise bandwidths and figures of merit from computer modeling are listed in Table 3-4 for four chopper/noise filter configurations for three values of the 1/f noise frequency knee using computer simulation models developed in Appendix D. In the numeric examples of Table 3-4, the total footprint dwell time, $T_d = 0.12$ sec, is the same for all configurations, but the shutter open time per footprint, T_s, varies. For chopped waveforms an ideal square wave chopper is assumed.

Configuration (a) - No optical chopper is used in this configuration. Detector output is integrated over the full footprint dwell interval.

Configuration (b) - An optical chopper is used with one cycle per footprint dwell. The light interval per cycle is twice the length of the dark interval. The sum of the integrated detector outputs for the dark intervals on either side of the light interval is subtracted from the integrated detector output for the light interval.

Configuration (c) - A square wave optical chopper is used, with one cycle per footprint dwell. The integrated detector output for the dark interval is subtracted from the integrated detector output for the light interval.

Configuration (d) - A square wave optical chopper is used, with multiple cycles per footprint dwell. The sum of the integrated detector outputs for the dark intervals is subtracted from the sum of the integrated detector outputs for the light intervals.

For Configuration (a), noise was integrated over a bandwidth of 0.02 to 200 Hz. For Configurations (b) and (c), integration was from 0.05 to 200 Hz. For Configuration (d), integration was from 0.5 Hz to 400 Hz for 6, 12, and 24 cycles per footprint dwell and 0.5 Hz to 600 Hz for 48 cycles per footprint dwell. The decrease in effective noise bandwidth as the number of cycles per footprint dwell increases for Configurations (c) and (d) is believed to be the result of limiting the high frequency cutoff point.

In the absence of significant 1/f noise in the detector and preamp, optical chopping could be avoided ($F_c = 1$). In the limit, for the integrated detector output, $\Delta F \approx 1/(4T_d)$. If significant 1/f noise is present, then the best strategy could be to use an optical chopper with the chopping frequency well above the 1/f noise frequency knee. For a square wave

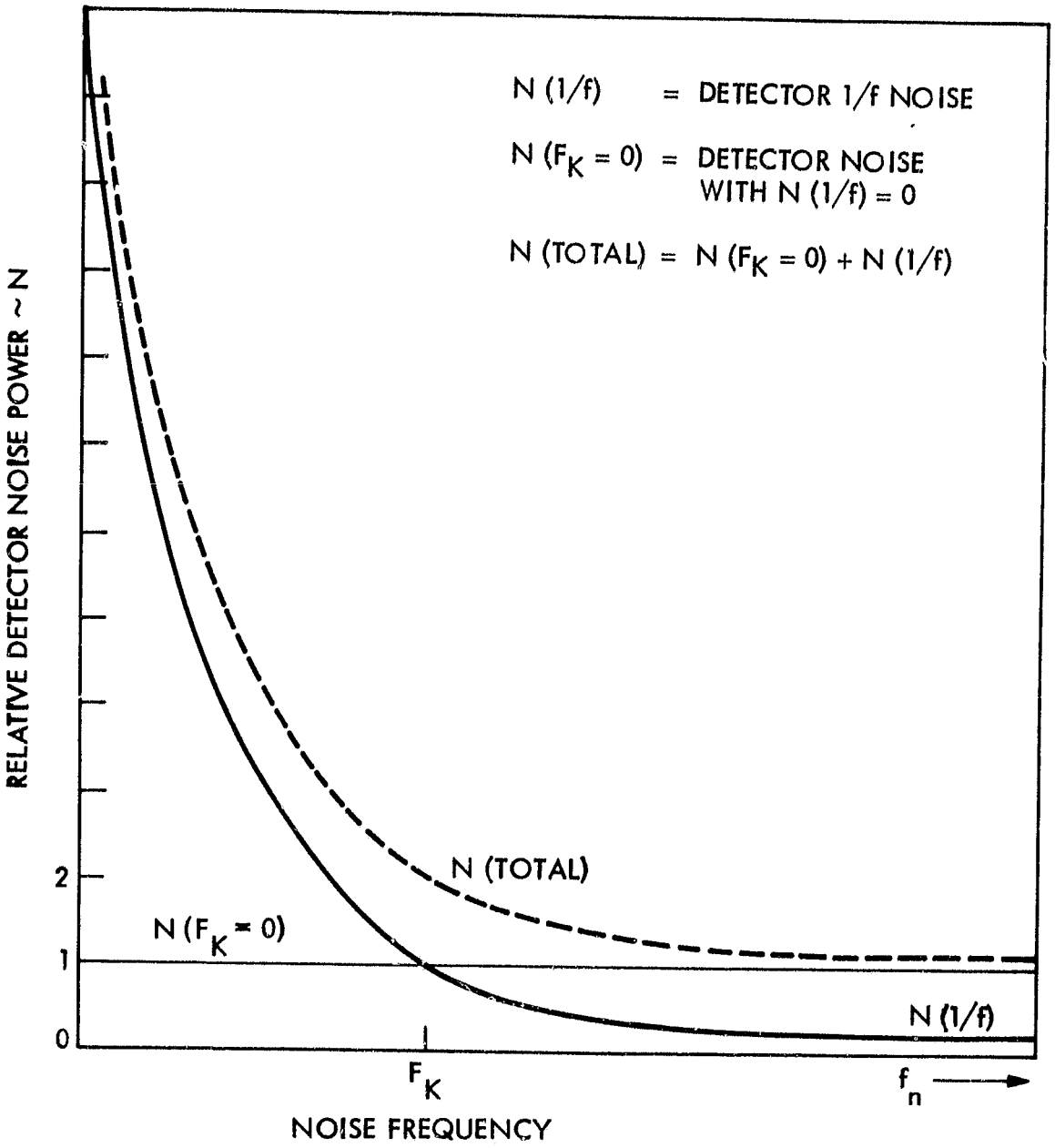

Figure 3-14 Relative detector noise power vs noise frequency

chopper and synchronous demodulation, $F_c = 0.5$ and in the limit $\Delta F \approx 1/T_d$. If no 1/f noise were present, there would be a factor of 4 NEN advantage in using an unchopped rather than a chopped system. The computer simulation models developed in Appendix D offer a means of evaluating the effects of 1/f noise and low pass filters upon system noise bandwidth.

To minimize NEN (i.e., to minimize $\sqrt{\Delta F}/F_c$):

- If detector 1/f noise frequency knee is low, use a simple integrator without optical chopping (Configuration (a)).
- If detector 1/f noise frequency knee is high, use an optical chopper at a frequency considerably higher than that of the 1/f knee (Configuration (d)).
- Use a low pass filter to limit the high frequency noise bandwidth ahead of the channel integrator.

3.1.1.3.2 Spatial and Spectral Weighting Effects

An optical chopper placed close to and ahead of a field stop — generally the inlet slit — can result in spatial weighting of the footprint and spectral weighting of the instrument slit function response.

Optical chopper blades which cover and uncover the inlet slit from the same side -- like a tuning fork chopper — will result in spatial weighting of the footprint. This is due to the fact that the instrument does not view every point in the footprint for the same amount of time . A chopper blade which covers and uncovers the inlet slit while moving in the same direction — like a chopper wheel — will not result in spatial weighting, since the instrument views every point in the footprint for the same amount of time.

For every point source in object space, chopper blades which move side to side across the ray bundle ahead of the inlet slit result in a time varying weighting of the effective length of the grating illuminated by the point source. This will result in a spectral weighting of the slit function response. The principle effect of this weighting will be to increase the wing response of the slit function. To the extent that spectral weighting occurs in AMTS, it should be the same for all footprint elements within an array. If the chopper blades move up and down along the slit length, however, the effective length of the grating is not affected and spectral weighting will not occur.

Spatial footprint weighting can be avoided by using a chopper wheel. Spectral weighting of the slit funtion response can be minimized by using a large diameter chopper wheel with its axis placed to the side of the slit array and operated close to the inlet slit jaws. This configuration will result in some differential spectral weighting of the footprints within the array.

Table 3-4 Comparison of noise bandwidth and figure of merit for typical chopper/integrator configurations as a function of 1/f noise frequency knee

T_d = 0.12 sec			$F_K = 0$, b = 1		$F_K = 1$, b = 1		$F_K = 100$, b = 1	
			ΔF (Hz)	$\sqrt{\Delta F}/F_c$	ΔF (Hz)	$\sqrt{\Delta F}/F_c$	ΔF (Hz)	$\sqrt{\Delta F}/F_c$
(a) +	$T_s = 0.12$ sec $F_c = 1.0$		2.06	1.44	5.48	2.34	343.1	18.5
(b) + − −	$T_s = 0.08$ $F_c = 0.67$		6.08	3.68	6.86	3.91	83.7	13.7
(c) + −	$T_s = 0.06$ $F_c = 0.5$		8.14	5.71	9.51	6.17	145.4	24.1
(d) + − + −	$T_s = 0.06$ $F_c = 0.5$	C=6	7.93	5.63	8.10	5.69	24.8	9.96
		C=12	7.52	5.48	7.60	5.51	15.3	7.82
		C=24	6.77	5.20	6.81	5.22	10.4	6.45
		C=48	6.76	5.20	6.78	5.21	8.51	5.83

T_d = total time per footprint dwell

T_s = shutter open time per footprint dwell

C = number of cycles in T_s

F_c = chopper factor

1/f noise $\propto \left(\frac{F_K}{f_n}\right)^b$, when F_K is expressed in Hz

3.1.1.4 Detector Considerations

Math models for calculation of D* for PC HgCdTe, PV HgCdTe, and PV InSb detectors are contained in Appendix F. In general, D* is not completely independent of the optical configuration of the instrument, as represented by the term $\sqrt{A_d}/A\Omega$ of Eq 3.1. In this paragraph detector parametric equations are presented which show D* dependency upon optical design parameters for the instrument configuration of Fig 3-1; upon photon background, temperature, and detector bias voltage; upon preamplifier parameters; and upon detector material and design parameters. The method for calculating background for the basic instrument configuration of Fig 3-1 is also presented.

The following symbols and expressions are used in the parametric equations presented in this paragraph:

A_{un} = unimmersed detector area (cm^2)

$A_1 = 10/[1 + F_c R_F C_F - (R_F/(R_d A_o))(1 + F_c R_d C_d)]$

A_d = area of detector (cm^2)

$A_{g\alpha}$ = area of grating with respect to α (cm^2)

A_o = open loop gain of preamp

α = grating incident angle (rad)

$A\Omega_\alpha$ = area-solid-angle product with respect to inlet slit ($cm^2 \cdot sr$)

$A\Omega_\beta$ = area-solid-angle product with respect to exit slit ($cm^2 \cdot sr$)

$A\Omega_{DET}$ = area-solid-angle product with respect to the detector ($cm^2 \cdot sr$)

A_z = transimpedance of preamp (Ω)

$$B_{InSb} = \frac{q^2 B_3{}^2 (B_2 NA\sqrt{B_1} + B_1 ND\sqrt{B_2})}{K_b \sqrt{B_1 B_2 \tau_c}\, ND \cdot NA} \qquad (K^{-5/2} \cdot \Omega^{-1} \cdot cm^{-2})$$

$$B_{HgCdTe} = \frac{q^2 B_4{}^2 (B_2 NA\sqrt{B_1} + B_1 ND\sqrt{B_2})}{K_b \sqrt{B_1 B_2 \tau_c}\, ND \cdot NA} \qquad (K^{-5/2} \cdot \Omega^{-1} \cdot cm^{-2})$$

$B_1 = K\mu/q$ $\quad (cm^2/K/s)$

$B_2 = K\mu_h/q$ $\quad (cm^2/K/s)$

$$B_3 = \left(\frac{32\pi^3 K^3}{h^6} (m_e m_h)^{3/2}\right)^{1/2} \qquad (K^{-3/2} \cdot cm^{-3})$$

$B_4 = (8.46 - 2.29x + 0.00342T)10^{14}E_g^{3/4}$ $(K^{-3/2} \cdot cm^{-3})$

$B_5 = \mu + \mu_h$ $(cm^2/V/s)$

$B_6 = 10\mu q \tau_c \eta/(11hcv_p)$ (cm/V)

β = grating diffraction angle (rad)

$C_3 = (Z_F/Z_d)[A_o Z_d/(Z_d(1 + A_o) + Z_F)]$

$C_4 = 1/[1 + F_c R_F C_F - (R_F/(A_o R_d))(1 + F_c R_d C_d)]$

c = speed of light (cm/s)

C_d = detector capacitance (F)

C_F = feedback resistor capacitance (F)

D* = detector detectivity ($cm\sqrt{Hz}/W$)

E_g = bandgap energy (eV)

ε_d = dewar emissivity

$\varepsilon_{c\beta}$ = exit collimator emissivity

ε_g = grating emissivity

ε_{gm} = grating mask emissivity

$\varepsilon_{c\alpha}$ = inlet collimator emissivity

ε_{sm} = slit mask emissivity

ε_s = scene emissivity

ε_i = emissivity of background source i

ε_j = emissivity of background source j

ε_k = emissivity of background source k

η = quantum efficiency

$F_c = 2\pi \cdot$ chopping frequency (Hz)

F_s = slit factor = $S_{w\beta}/S_{w\alpha i}$

$G_{w\alpha}$ = projected grating width with respect to α (cm)

$G_{H\alpha}$ = projected grating height with respect to α (cm)

H = detector height (cm)

h = Planck's constant (J•s)

K = Boltzmann's constant (J/K)

K_b = Boltzmann's constant (eV/K)

l = total number of background source i's

m = total number of background source j's

m_e = reduced electron mass (kg)

m_h = reduced hole mass (kg)

μ = electron mobility ($cm^2/V/s$)

μ_h = hole mobility ($cm^2/V/s$)

n = total number of background source k's

NA = acceptor concentration (cm^{-3})

ND = donor concentration (cm^{-3})

$N_{c\beta}$ = blackbody radiance at the exit collimator temp. ($W/cm^2/sr/cm^{-1}$)

N_g = blackbody radiance at the grating temp. ($W/cm^2/sr/cm^{-1}$)

N_{gm} = blackbody radiance at the grating mask temp. ($W/cm^2/sr/cm^{-1}$)

$N_{c\alpha}$ = blackbody radiance at the inlet collimator temp. ($W/cm^2/sr/cm^{-1}$)

N_{sm} = blackbody radiance at the slit mask temp. ($W/cm^2/sr/cm^{-1}$)

N_T = blackbody radiance at the telescope temp. ($W/cm^2/sr/cm^{-1}$)

N_s = blackbody radiance at the scene temp. ($W/cm^2/sr/cm^{-1}$)

υ_p = peak spectral response of detector (cm^{-1})

υ = wavenumber (cm^{-1})

υ_{co} = detector cut-off wavenumber (cm^{-1})

$\Delta\upsilon$ = half power spectral bandwidth (cm^{-1})

$\Delta\upsilon_{OF}$ = order filter bandwidth (cm^{-1})

$\delta\nu$ = the wavenumber increment ($\nu_i - \nu_{i-1}$)

P_o = hole concentration (cm^{-3})

q = charge of an electron (A•s)

q_i = photon flux from background source i (photons/cm^2/sr/s)

q_d = photon flux from dewar (photons/cm^2/sr/s)

R_d = detector dark resistance (Ω)

R_F = feedback resistance (Ω)

R_s = shunt resistance (Ω)

$R = q\eta/(hc\upsilon_p)$ = responsivity (A/W)

$S_{w\beta}$ = exit slit width (cm)

$S_{w\alpha i}$ = image of inlet slit width (cm)

σ = detector conductivity ($1/\Omega$)

T = detector temperature (K)

T_s = scene equivalent temperature (K)

T_{RF} = feedback resistor temperature (K)

T_i = temperature of background source i (K)

T_j = temperature of background source j (K)

T_k = temperature of background source k (K)

t = detector thickness (cm)

τ_c = carrier lifetime (s)

τ_{FL} = transmissivity from ahead of field lens to detector

$\tau_{c\beta}$ = transmissivity from ahead of exit collimator to detector

τ_g = transmissivity from ahead of grating to detector

$\tau_{c\alpha}$ = transmissivity from ahead of inlet collimator to detector

τ_T = transmissivity from ahead of telescope to detector

τ_i = transmissivity from background source i to detector

τ_j = transmissivity from background source j to detector

τ_k = transmissivity from background source k to detector

V_b = detector bias voltage (V)

$V_b' = V_b/W$ (V/cm)

V_p = preamp noise voltage ($V/\sqrt{Hz}$)

W = detector width (cm)

x = mole fraction CdTe:(CdTe + HgTe)

Z_d = detector impedance (Ω)

Z_F = feedback impedance (Ω)

3.1.1.4.1 PC Detectors (HgCdTe)

The reciprocal of D* for the PC detector/TIA preamp combination can be expressed as

$$\frac{1}{D^*} = \left[\left(\frac{1}{D^*_{JN}}\right)^2 + \left(\frac{1}{D^*_{BGi}}\right)^2 + \left(\frac{1}{D^*_{BGs}}\right)^2 + \left(\frac{1}{D^*_{BGd}}\right)^2 + \left(\frac{1}{D^*_{JNfb}}\right)^2 + \left(\frac{1}{D^*_{GR}}\right)^2 + \left(\frac{1}{D^*_{PA}}\right)^2\right]^{1/2} \quad (3.26)$$

where

D^*_{JN} = Johnson noise limited D*

D^*_{BGi} = instrument background (shot) noise limited D*

D^*_{BGs} = scene background noise limited D*

D^*_{BGd} = dewar background noise limited D*

D^*_{JNfb} = feedback resistor Johnson noise limited D*

D^*_{GR} = generation/recombination (GR) noise limited D* (for PC detectors only)

D^*_{PA} = preamp noise limited D*

Each of these component D*'s can be viewed as the D* calculated as though only one noise type existed, where

$$\frac{1}{D^*_{JN}} = \left[\frac{4KTqt}{(B_6 V_b')^2 P_o}\left(\mu B_4{}^2 T^3 e^{-Eg/K_b T} + \mu_h P_o{}^2\right)\right]^{1/2} \quad (3.27a)$$

$$\frac{1}{D^*_{BGi}} = \left[\frac{(2q\upsilon B_5\tau_c)^2\eta A\Omega_\alpha c}{B_6{}^2A_d}\left(\sum_{ijk}^{lmn}\frac{\Delta\upsilon_{OF}F_sG_{i\alpha}G_{w\alpha}\tau_i\varepsilon_i}{A_{g\alpha}(e^{h\upsilon/KT_i}-1)}\right.\right.$$

$$\left.\left.+\frac{\Delta\upsilon_{OF}F_s\tau_j\varepsilon_j}{e^{h\upsilon/KT_j}-1}+\frac{\Delta\upsilon\tau_k\varepsilon_k}{e^{h\upsilon/KT_k}-1}\right)\right]^{1/2} \qquad (3.27b)$$

$$\frac{1}{D^*_{BGs}} = \left[\frac{(2q\upsilon B_5\tau_c)^2\eta A\Omega_\alpha c\Delta\upsilon\tau_T}{B_6{}^2A_d(e^{h\upsilon/KT_s}-1)}\right]^{1/2} \qquad (3.27c)$$

$$\frac{1}{D^*_{BGd}} = \left[\frac{(2q\upsilon B_5\tau_c)^2\eta A\Omega_\alpha c}{B_6{}^2A_d}\sum_{i=\upsilon_\infty}^{\infty}\frac{(\delta\upsilon)\upsilon_i}{e^{h\upsilon(i+1)/KT}-1}\right]^{1/2} \qquad (3.27d)$$

$$\frac{1}{D^*_{JNfb}} = \left[\frac{0.4T_{RF}qt}{(B_6V_b')^2P_o}(\mu B_4{}^2T^3e^{-Eg/KT}+\mu_hP_o{}^2)\right]^{1/2} \qquad (3.27e)$$

$$\frac{1}{D^*_{GR}} = \left[\frac{(2qB_5)^2\tau_cP_ot}{B_6{}^2}\right]^{1/2} \qquad (3.27f)$$

$$\frac{1}{D^*_{PA}} = \left[\left(\frac{V_pC_3tq}{B_6A_1V_b'P_o}\right)^2\left(\frac{H}{W}\right)(\mu B_4{}^2T^3e^{-Eg/KT}+\mu_hP_o{}^2)^2\right]^{1/2} \qquad (3.27g)$$

The interrelationship of $1/D^*$ and the optics term, $\sqrt{A_d}/A\Omega_\alpha$, is shown in Table 3-5 for each of these parametric equations for PC detectors. The NEN proportionality is the product of the $1/D^*$ proportionality and $\sqrt{A_d}/A\Omega$. Conceptually, optical immersion of the detector would reduce detector/preamp noise for all except the background noise components for PC HgCdTe detectors. The overall effectiveness of immersion depends upon the relative amplitudes of the individual noise components.

C-2

1/D* for the noise components of a 15 μm PC HgCdTe detector are plotted in Fig 3-15 for selected detector/preamp parameters and operating conditions. For this detector NEN due to the major noise components—GR, PA, JN and JNfb—are reduced by detector immersion. PA, JN, JNfb and BGd noise components are a relatively fast function of detector temperature. For the data plotted in Fig 3-15, the mole fraction of the material was varied as a function of detector temperature to hold υ_p constant. In addition, the feedback resistance was varied as a function of detector temperature to maintain the ratio of R_F/R_d equal to 10. A 1/f noise component is not included in the PC detector model. In general, this noise component is best treated in terms of equivalent noise bandwidth (Para 3.1.1.3.1).

The detector performance illustrated in Fig 3-15 is not necessarily typical of all detectors and all frequency ranges. This figure represents the nominal detector design for Baseline V channel 8, including detector immersion.

3.1.1.4.2 PV Detectors (HgCdTe and InSb)

The reciprocal of D* for these PV detector/TIA preamp combinations can be expressed as

$$\frac{1}{D^*} = \left[\left(\frac{1}{D^*_{JN}}\right)^2 + \left(\frac{1}{D^*_{BGi}}\right)^2 + \left(\frac{1}{D^*_{BGs}}\right)^2 + \left(\frac{1}{D^*_{BGd}}\right)^2 + \left(\frac{1}{D^*_{JNfb}}\right)^2 + \left(\frac{1}{D^*_{PA}}\right)^2\right]^{1/2} \quad (3.28)$$

where

$$\frac{1}{D^*_{JN}} = \left[\frac{2KT(1 + B_x T^{5/2} R_s e^{-Eg/K_b T})\ (1 + e^{qV_b/KT})}{R^2 R_s}\right]^{1/2} \quad (3.29a)$$

and

$$B_x = B_{InSb} \text{ or } B_{HgCdTe}$$

$$\frac{1}{D^*_{BGi}} = \left[\frac{4c(\upsilon q)^2 \eta A \Omega_\alpha}{A_d R^2} \cdot \left(\sum_{ijk}^{lmn} \frac{\Delta\upsilon_{OF} F_s G_{w\alpha} G_{H\alpha} \varepsilon_i \tau_i}{A_{g\alpha}(e^{h c\upsilon/KT_i} - 1)} + \frac{\Delta\upsilon_{OF} F_s \varepsilon_j \tau_j}{e^{h c\upsilon/KT_j} - 1} + \frac{\Delta\upsilon \varepsilon_k \tau_k}{e^{h c\upsilon/KT_k} - 1}\right)\right]^{1/2} \quad (3.29b)$$

Table 3-5 Interrelationship between 1/D* and NEN in terms of $\sqrt{A_d}/A\Omega_\alpha$

Noise Source	For PC HgCdTe			For PV HgCdTe & Pv InSb		
	1/D*	NEN	(?)[1]	1/D*	NEN	(?)[1]
Johnson noise	independent of $\frac{\sqrt{A_d}}{A\Omega_\alpha}$	$\propto \frac{\sqrt{A_d}}{A\Omega_\alpha}$	yes	independent of $\frac{\sqrt{A_d}}{A\Omega_\alpha}$	$\propto \frac{\sqrt{A_d}}{A\Omega_\alpha}$	yes
Instrument background noise	$\propto \sqrt{\frac{A\Omega_\alpha}{A_d}}$	$\propto \frac{1}{\sqrt{A\Omega_\alpha}}$	no	$\propto \sqrt{\frac{A\Omega_\alpha}{A_d}}$	$\propto \frac{1}{\sqrt{A\Omega_\alpha}}$	no
Scene background noise	$\propto \sqrt{\frac{A\Omega_\alpha}{A_d}}$	$\propto \frac{1}{\sqrt{A\Omega_\alpha}}$	no	$\propto \sqrt{\frac{A\Omega_\alpha}{A_d}}$	$\propto \frac{1}{\sqrt{A\Omega_\alpha}}$	no
Dewar background noise	$\propto \sqrt{\frac{A_{un}}{A_d}}$	$\propto \frac{\sqrt{A_{un}}}{A\Omega_\alpha}$	no	$\propto \sqrt{\frac{A_{un}}{A_d}}$	$\propto \frac{\sqrt{A_{un}}}{A\Omega_\alpha}$	no
Feedback resistor Johnson noise	independent of $\frac{\sqrt{A_d}}{A\Omega_\alpha}$	$\propto \frac{\sqrt{A_d}}{A\Omega_\alpha}$	yes	$\propto \sqrt{\frac{1}{A_d}}$	$\propto \frac{1}{A\Omega_\alpha}$	no
GR noise	independent of $\frac{\sqrt{A_d}}{A\Omega_\alpha}$	$\propto \frac{\sqrt{A_d}}{A\Omega_\alpha}$	yes	—	—	—
Preamp noise	independent of $\frac{\sqrt{A_d}}{A\Omega_\alpha}$	$\propto \frac{\sqrt{A_d}}{A\Omega_\alpha}$	yes	$\propto \sqrt{\frac{1}{A_d}}$	$\propto \frac{1}{A\Omega_\alpha}$	no

[1]This column answers the question, "Does immersion of the detector improve NEN?"

$$\frac{1}{D^*_{BGs}} = \left[\frac{4c(\upsilon q)^2 \eta A\Omega_\alpha \Delta\upsilon \tau_T}{A_d R^2 (e^{hc\upsilon/KT_s} - 1)}\right]^{1/2} \tag{3.29c}$$

$$\frac{1}{D^*_{BGd}} = \left[\frac{4c(\upsilon q)^2 \eta A\Omega_\alpha}{A_d R^2} \sum_{i=\upsilon_{co}}^{\infty} \frac{(\delta\upsilon)\upsilon_i}{e^{hc\upsilon(i+1)/KT} - 1}\right]^{1/2} \tag{3.29d}$$

$$\frac{1}{D^*_{JNfb}} = \left[\frac{4KT_{RF}}{A_d R_F R^2}\right]^{1/2} \tag{3.29e}$$

$$\frac{1}{D^*_{PA}} = \left[\frac{(V_p C_3 C_4)^2}{A_d (RR_F)^2}\right]^{1/2} \tag{3.29f}$$

The interrelationship of $1/D^*$ and the optics term, $\sqrt{A_d}/A\Omega_\alpha$, is shown in Table 3-5 for each of these parametric equations for PV detectors. For these detectors, detector immersion would affect only the detector Johnson noise component.

$1/D^*$ for the noise components of a 10 μm PV HgCdTe detector is plotted in Fig 3-16 and of a 4 μm PV InSb detector in Fig 3-17 for selected detector/preamp parameters and operating conditions. The PV HgCdTe detector performance of Fig 3-16 would not be significantly improved by optical immersion nor would junction bias significantly improve its overall performance. Conceptually, however, this detector performance could be improved significantly if the feedback resistance value could be increased, and the instrument optics cooled to <110 K. Under such conditions, the detector would approach scene background limited performance. Conceptually, the PV InSb detector performance of Fig 3-17 would be improved by optical immersion, by reverse biasing the detector junction, by increasing the feedback resistance, and by cooling the optics to <130 K. It would probably not be possible to approach scene background limited performance with this detector.

Detector/preamp circuit frequency response and pulse transient response characteristics place an upper limit upon the value of the feedback resistor in a particular application. This limit is related to the dark resistance of the detector, to the stray capacitance distributed throughout the circuit, and to the degree to which these capacitances can

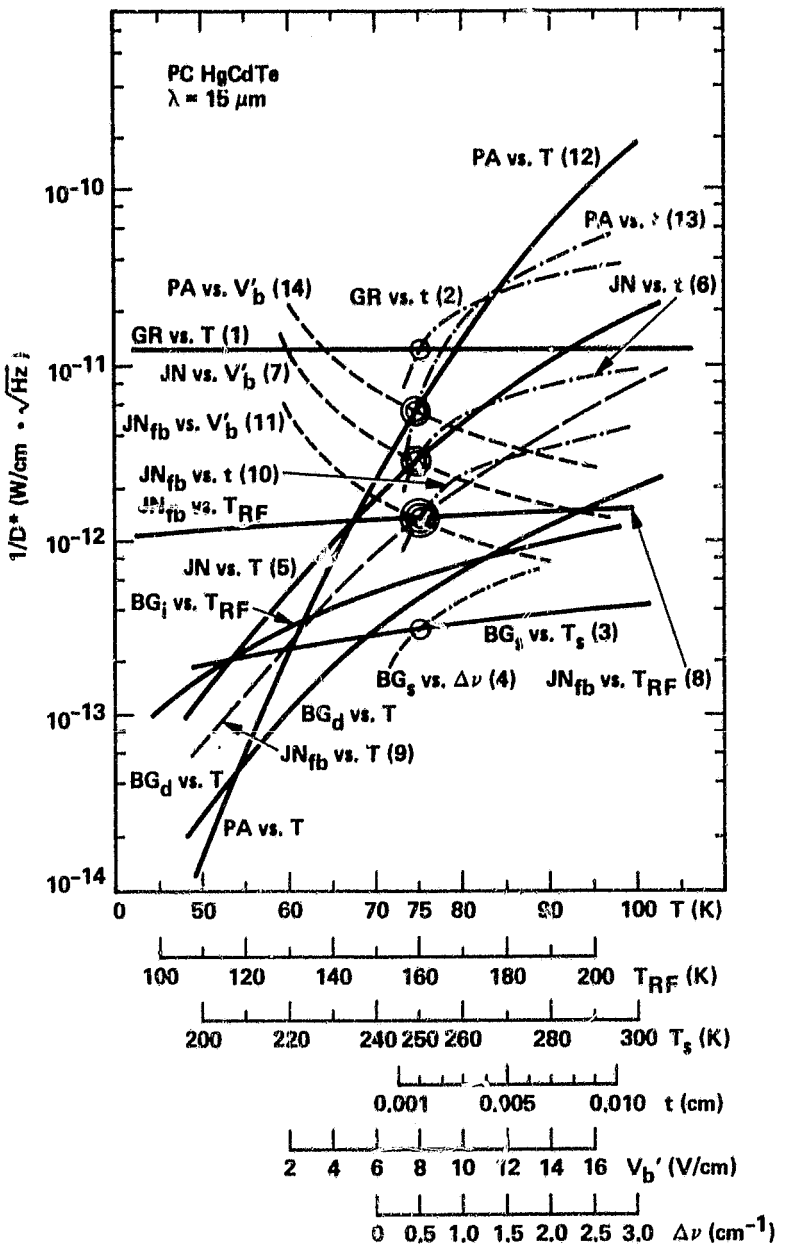

Notes:

(1) t = 0.001 cm
(2) T = 75 K
(3) $\Delta\upsilon$ = 0.5 cm^{-1}
(4) T_S = 250 K
(5) t = 0.001 cm, V_b' = 8 V/cm
(6) T = 75 K, V_b' = 8 V/cm
(7) T = 75 K, t = 0.001 cm
(8) T = 75 K, t = 0.001 cm, V_b' = 8 V/cm
(9) T_{RF} = 160 K, t = 0.001 cm, V_b' = 8 V/cm
(10) T_{RF} = 160 K, T = 75 K, V_b' = 8 V/cm
(11) T_{RF} = 160 K, T = 75 K, t = 0.001 cm
(12) t = 0.001 cm, V_b' = 8 V/cm
(13) T = 75 K, V_b' = 8 V/cm
(14) T = 75 K, t = 0.001 cm

Figure 3-15 PC HgCdTe detector performance. Solid lines represent 1/D* noise component vs temperature. Broken lines represent 1/D* noise component vs another detector parameter.

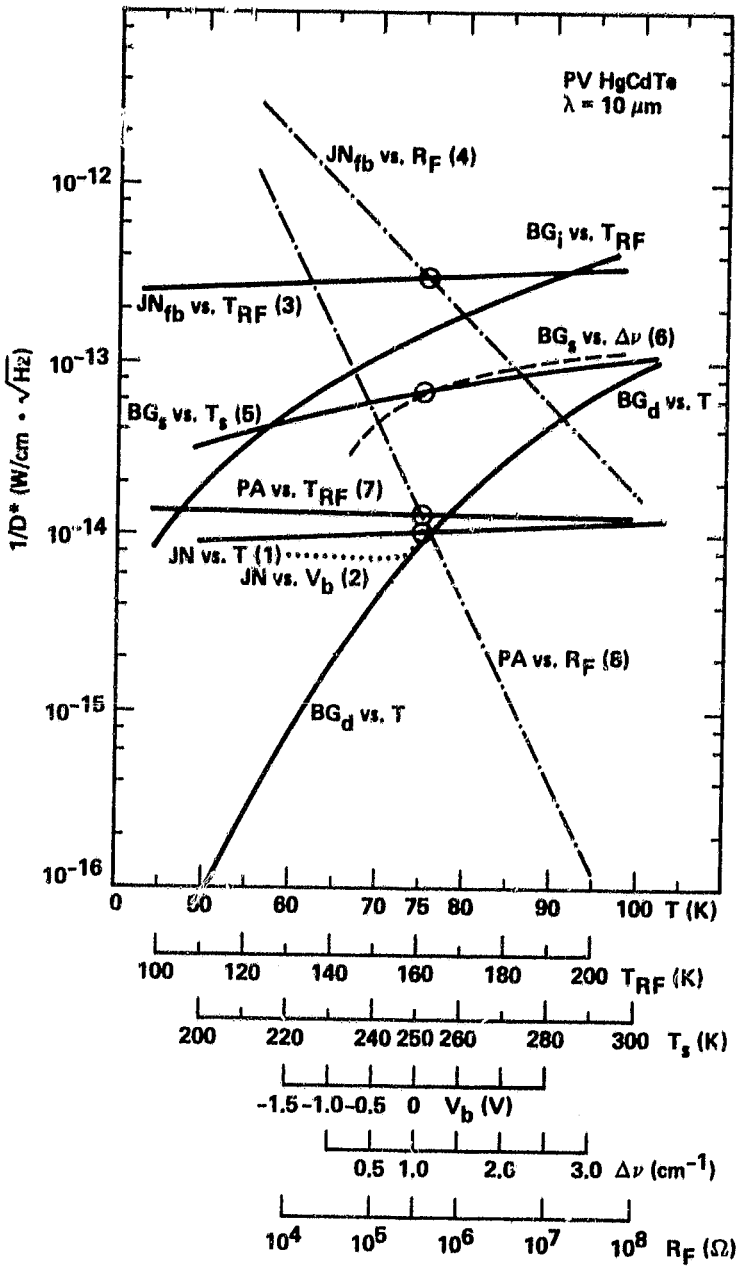

Notes:

(1) V_b = 0.0 V
(2) T = 75 K
(3) $R_F = 5 \times 10^5\ \Omega$
(4) T_{RF} = 160 K
(5) $\Delta\upsilon = 1.0\ cm^{-1}$
(6) T_S = 250 K
(7) $R_F = 5 \times 10^5\ \Omega$
(8) T_{RF} = 160 K

Figure 3-16 PV HgCdTe detector performance. Solid lines represent 1/D* noise component vs temperature. Broken lines represent 1/D* noise component vs another detector parameter.

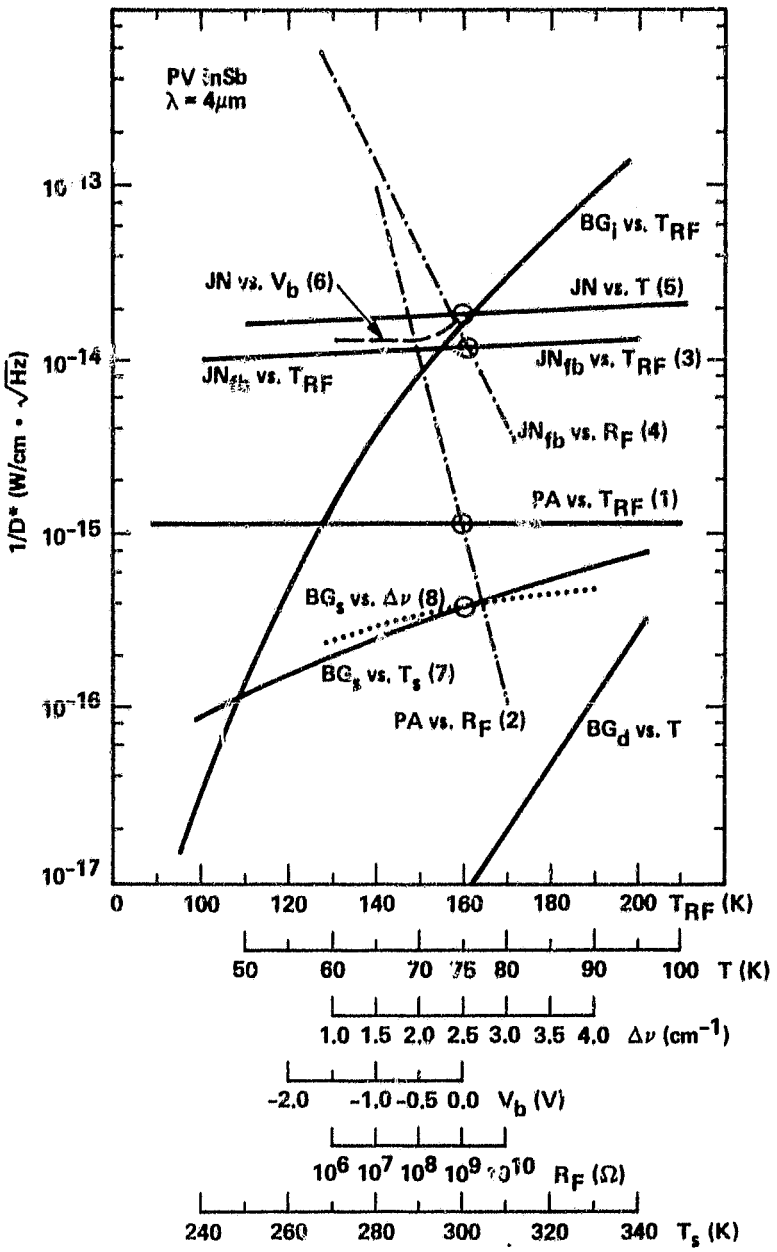

Notes:

(1) $R_F = 10^9\Omega$
(2) $T_{RF} = 160$ K
(3) $R_F = 10^9\Omega$
(4) $T_{RF} = 160$ K
(5) $V_b = 0.0$ V
(6) T = 75 K
(7) $\Delta\upsilon = 2.5$ cm^{-1}
(8) $T_s = 300$ K

Figure 3-17 PV InSb detector performance. Solid lines represent 1/D* noise component vs temperature. Broken lines represent 1/D* noise component vs another detector parameter.

be minimized and compensated for in circuit design and layout. For resistance values of the order of 10^9 to 10^{11} ohms, contamination and leakage current effects, as well as resistor linearity as a function of voltage and temperature, will also place a practical limit on the maximum value of the feedback resistor.

The detector performance illustrated in Fig 3-16 and 3-17 is not necessarily typical of all detectors and all frequency ranges. These figures represent the nominal detector design for Baseline V channels 12 and 26 respectively.

3.1.1.4.3 Background Calculation

For the instrument optical configuration of Fig 3-1 total background flux upon the detector is made up of unfocused flux from within the detector dewar plus flux focused upon the detector within the optical system ray bundle. The effects of unfocused dewar flux are represented by parametric Eq 3.27d and 3.29d; the effects of scene focused flux originating outside the instrument are represented by parametric Eq 3.27c and 3.29c; and the effects of focused flux originating within the instrument are represented by parametric Eq 3.27b and 3.29b. The method of calculating the focused flux from within the instrument is as follows:

The blackbody photon flux at an instrument source, i, is

$$q_i = \frac{N_i \, \Delta\upsilon_i}{hc\upsilon_i} \quad \text{(photons/(cm}^2\text{·sr·s))} \tag{3.30}$$

and the true photon flux at the detector is

$$Q_i = q_i \, \epsilon_i \, A\Omega_i \, \tau_i \quad \text{(photons/s)} \tag{3.31}$$

and the sum of all the sources within the instrument is:

$$\begin{aligned} \sum Q_i = \frac{1}{hc\upsilon} \Big[& N_{c\beta} \, \epsilon_{c\beta} \, A\Omega_{DET} \, \Delta\upsilon_{OF} \, \tau_{FL} \\ & + N_g \, \epsilon_g \, F_s \, A\Omega_\alpha \, \Delta\upsilon_{OF} \, \tau_{c\beta} \\ & + N_{gm} \, \epsilon_{gm} \, (A\Omega_{DET} - F_s \, A\Omega_\alpha) \, \Delta\upsilon_{OF} \, \tau_{c\beta} \\ & + N_{c\alpha} \, \epsilon_{c\alpha} \, F_s \, A\Omega_\alpha \, \Delta\upsilon_{OF} \, \tau_g \\ & + N_{sm} \, \epsilon_{sm} \, (F_s \, A\Omega_\alpha \, \Delta\upsilon_{OF} - A\Omega_\alpha \, \Delta\upsilon) \, \tau_{c\alpha} \\ & + N_T \, \epsilon_T \, A\Omega_\alpha \, \Delta\upsilon \, \tau_{c\alpha} \Big] \end{aligned} \tag{3.32}$$

Equation 3.32 illustrates the method for the general optical configuration of Fig 3-1, assuming that only the emitting elements pictured in Fig 3-1 exist in the instrument. In Eqs 3.27b and 3.29b, the i^{th} terms correspond to those elements which in Eq 3.32 contain the product $A\Omega_{DET}\ \Delta\upsilon_{OF}$ in their background contribution expression; the j^{th} terms correspond to $A\Omega_{\alpha}\ \Delta\upsilon_{OF}$; and the k^{th} terms correspond to $A\Omega_{\alpha}\ \Delta\upsilon$. For a particular instrument configuration, the method illustrated in Eq 3.32 can be used to develop an expression containing all sources of focused background originating within that instrument.

3.1.1.4.4 Conclusions (Detector Considerations)

In terms of NEN performance, the optical and thermal design of the instrument, the detector design, and the detector/preamp circuit design are strongly interrelated. Figures 3-15, 3-16 and 3-17 illustrate the importance of a well integrated design effort to optimize these parameters on a system basis where optimization of overall instrument performance is important. Performance gains of 2 to possibly 3 times might be achievable in this fashion which would be impossible or impractical to achieve in any other way. Such an effort must involve the detector manufacturer as well as the instrument designers.

3.1.1.5 Instrument Slit Function Considerations

Two AMTS requirements place constraints upon the instrument slit funtion response: 1) control of radiometric error due to slit function wing response crosstalk, and 2) the instrument line function of a channel for all footprint elements within a spatial array should have the same amplitude vs. frequency response within narrows limits (Para 2.3.6).

3.1.1.5.1 Spectrometer Slit Function Effects

The spectrometer slit function, defined between inlet and exit slits, is closely approximated by the convolution in the image plane of:

- The image of the inlet slit
- The geometric point spread distribution of the spectrometer optics between the inlet and exit slits
- The diffraction line function of the instrument aperture
- The exit slit width

The convolution of the inlet slit image with the exit slit results in the "ideal", or distortion free, slit function. Spreading of this ideal function is entirely due to the effects of geometric optics aberrations and of instrument aperture diffraction. The spreading due to the geometric point spread distribution is bounded, and is restricted to the near frequency field. Spreading of the instrument slit function response into the far frequency field is entirely due to the instrument aperture diffraction spread function, and is bounded by the channel order filter bandwidth.

Where a rectangular unobscured grating forms the system aperture stop, the diffraction spread distribution for a coherent monochromatic source is represented by the grating line function

$$\frac{I}{I_o} = \text{sinc}^2 \left\{ \frac{\pi L}{\lambda} [\sin \beta_o - \sin (\beta_o + \Delta\beta)] \right\} \qquad (3.33)$$

where

I_o = maximum line intensity ($\Delta\beta = 0$)

I = line intensity as a function of β

L = grating length (normal to grooves)

λ = wavelength

β_o = nominal diffraction angle for wavelength λ

β = grating diffraction angle

$\Delta\beta = \beta - \beta_o$

In the limit, as $\Delta\beta$ approaches zero, I/I_o approaches unity.

When the grating is illuminated by an area source, where each point source within the area has a coherence time, τ_o, then the overall grating line function is the summation of the autocorrelation line functions for all of the individual point sources. It is shown in Para 4.3.3 that this can modify the effective grating line function for long, high dispersion gratings. Widening of the overall instrument slit function response is not particularly severe, but the slit function wing response may be increased by two to four times.

Slit function wing response crosstalk is a function of the wing response of the slit function and of the spectral energy distribution of the channel within the bandwidth of the order filter (Para 4.3.3). Slit function wing response requirements effectively place a lower limit upon the acceptable grating length. The requirement that the slit function response for any given channel be the same within narrow limits for all footprint elements within an array implies that the point spread distribution of the spectrometer should be relatively independent of field angle.

3.1.1.5.2 Foreoptics Slit Function Effects

To the extent that the foreoptics point spread distribution due to the geometric aberrations and aperture diffraction effects is contained within the width of the spectrometer inlet slit, its effect will be to modify the overall point spread distribution at the spectrometer image plane. To the extent that this modified point spread begins to fall outside the exit slit width (while the foreoptic point spread is within the

inlet slit width) the principal effect will be a modification of the overall bandwidth of the instrument slit function response. As energy within the foreoptics point spread falls outside the inlet slit width, the object point energy distribution upon the grating is spatially weighted. The principal effect of this weighting will be to increase the slit function wing response. Vignetting anywhere ahead of the exit slit of the instrument can cause a similar effect.

Chromatic aberrations in the foreoptics will affect footprint spatial simultaneity as well as overall instrument slit function response. Variations of foreoptics aberrations vs field angle will affect the accuracy with which the system can be tuned in orbit.

Effects due to foreoptics aberrations can be minimized by:

- Using foreoptics having small geometric aberrations.
- Using low F/NO optics for the foreoptics (and spectrometer inlet collimator).
- Avoiding chromatic effects in the foreoptics.
- Focusing the foreoptics sharply on the inlet slit jaws.
- Using foreoptics whose point spread distribution is independent of field angle.

3.1.1.6 Orbit Considerations

Orbit and earth coverage parameters for a single satellite are listed in Table 3-6. The sun synchronous orbits listed above the line are also harmonically related to the solar day, and their ground tracks would repeat from day to day. Earth coverage for the three sun synchronous orbits listed below the line is illustrated in Fig 3-18.

For ±45 degree crosstrack scan, the Baseline V (TIROS) orbit provides full earth coverage once in each 24 hour period. Coverage on successive orbits is not contiguous near the equator, but gaps between the ascending orbits (orbits 1 and 2 for example) would be covered by descending orbits (orbit 8 for example) about one-half day later. If the ascending orbits provide daytime coverage, then the descending orbits provide nighttime coverage. In this intermediate altitude range, only orbits very near the 833 km altitude can provide full earth coverage once in each 24 hour period.

The 705 km altitude orbit has been proposed for the Earth Observing System (EOS). For ±45 degree crosstrack scan, this orbit would provide full earth coverage once in each 36 hour period.

Note that two satellites, both at the same altitude in synchronous orbits between 700 km and 1350 km and with their equatorial crossings properly time phased, could provide full earth coverage twice in each 24 hour period, once on the nightside and once on the sunlit side of the earth.

Table 3-6 Orbit and earth coverage parameters

Orbits/day	Altitude (km)	Swath Width (km) (±45° Scan)	Normal Distance Between (ascending) Orbits near Equator (km)
12	1693	4117	3334
13	1274	2902	3077
14	905	1972	2858
15	579	1218	2667
16	287	588	2500
12.81	1350[1]	3108	3123
14.21	833[2]	1799	2815
14.60	705[3]	1502	2740

[1]Minimum altitude for contiguous coverage at equator on successive orbits. Full earth coverage twice in each 24 hour period.

[2]TIROS / Baseline V orbit. Required altitude for full earth coverage in each 24 hour period.

[3]EOS orbit.

705 km ALTITUDE
98.22° INCLINATION
14.60 orbits/day

EOS ORBIT

833 km ALTITUDE
98.75° INCLINATION
14.21 orbits/day

TIROS/BASELINE V ORBIT

1350 km ALTITUDE
101.18° INCLINATION
12.81 orbits/day

ORIGINAL PAGE IS
OF POOR QUALITY

Figure 3-18 Earth coverage for sun synchronous orbits

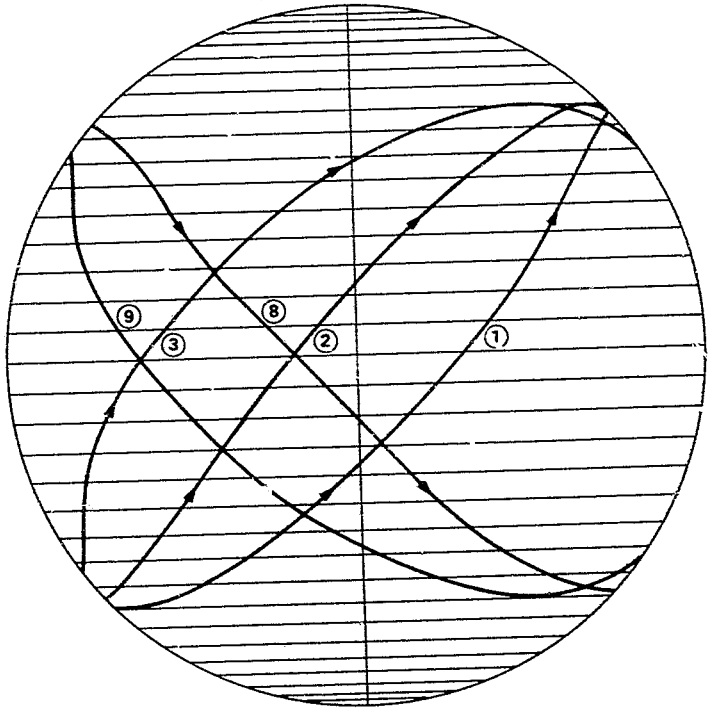

906 km ALTITUDE
45° INCLINATION
14 orbits/day

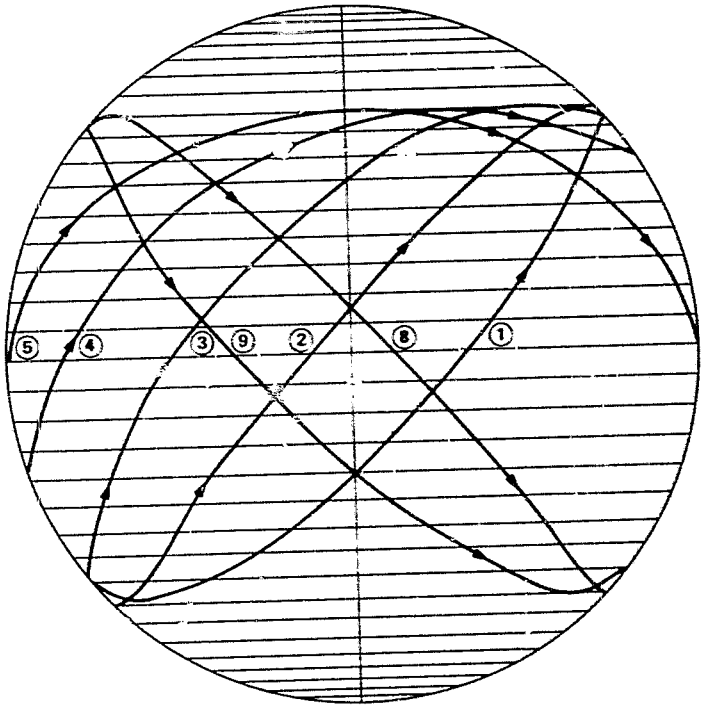

1274 km ALTITUDE
45° INCLINATION
13 orbits/day

Figure 3-19 Orbit ground tracks for medium inclination orbits

The 1350 km altitude orbit represents the minimum altitude for full earth coverage twice in each 24 hour period from a single satellite. Coverage would be contiguous between successive orbits. If ascending orbits provided daytime coverage, the descending orbits would provide nighttime coverage. This type of coverage could be provided by all higher orbits. For such orbits, the crosstrack scan angle could be reduced to minimize overlap between successive orbits and to maximize dwell time.

Orbit ground tracks for 45 degree inclination orbits are illustrated in Fig 3-19. In conjunction with Table 3-6, Fig 3-19 is useful for visualizing the type of coverage possible with medium inclination orbits.

3.1.1.7 Optical Design Criteria Summary

Optical design criteria developed in Para 3.1.1.1 through 3.1.1.6 are summarized in Table 3-7.

3.1.2 Optical Configuration

The conceptual optical design for a Baseline V instrument is based upon the optical design criteria of Table 3-7. A layout of the instrument optics is presented in Fig 3-20 (page 3-71). Details of the inlet slit mask and image plane assembly are shown in Fig 3-21. Optical design parameters common to all signal channels are listed in Table 3-8. Signal channel dependent parameters are listed in Table 3-9. Spectral alignment channel parameters are listed in Table 3-10.

A fixed R2 echelle grating is used in an in-plane, off-littrow, multichannel spectrometer configuration in the 3rd through the 13th orders. Sixteen element linear detector arrays are used for each spectral channel. An off-axis Bouwers concentric catadioptric system is used for the grating inlet and exit collimator. The extended center line of the grating passes through the center of curvature of the monocentric collimator optics; consequently, optical performance is relatively independent of grating angle. The grating mask forms the aperture stop of the instrument.

The linear inlet slit array is 16 elements high. The unmasked height of each element is 0.7 times the slit width. Premasks, 0.3 times the slit width, are provided between individual elements of the inlet slit array to spatially define each footprint element. Channel 10 controls the inlet slit width, the width of the image of the inlet slit in the image plane being equal to the channel 10 slit width. The exit slit widths for all other channels are wider than the inlet slit image.

The image plane of the Baseline V spectrometer contains 28 spectral channels. Each spectral channel is 16 detector assemblies high. Each detector optical assembly consists of a 1 percent bandwidth interference order filter, nominally vertical slit jaws located in the image plane which determine channel spectral frequency and bandwidth, a nominal F/1 field lens, and a detector. In addition, photoconductive detector channels--channels 1 through 11--contain a hemispheric detector immersion lens. The axes of the field lenses are aligned with the center rays of the off axis ray bundles converging upon the center of the image plane slits.

Table 3-7 Summary of optical design criteria

A. To minimize NEN per composite footprint within limitations of a given optical bandwidth:

1) Use a high dispersion grating
2) Operate the grating off Littrow (optimize grating angles, considering effects on grating efficiency)
3) Use a large, rectangular, unobscured grating
4) Use a long linear array of footprint elements
5) Use a separate image plane array for each spectral channel
6) Use a low pass electrical filter to limit high frequency noise bandwidth
7) If possible, use scene background limited detectors; else for temperature limited detectors:
   - Use a low F/NO detector field lens
   - Use a high index immersion lens
8) If possible, use detectors having a low (<1 Hz) 1/f noise frequency knee with a simple low pass integrator; else use an optical chopper and synchronous demodulator at a frequency considerably higher than that of the 1/f knee
9) Use a large composite footprint area

B. To Maximize Cloud Filtering Capability:

1) Use high spatial resolution. (NEN for a given composite footprint area is nominally independent of individual footprint size.)

C. To Control Slit Function Response:

1) Use a long grating
2) Use spectrometer collimator optics whose aberrations are independent of field angle
3) Use a foreoptics telescope whose aberrations are independent of field angle
4) Use low F/NO telescope and grating collimator optics
5) Use foreoptics having small geometric aberrations
6) Focus foreoptics sharply upon the entrance slit jaws
7) Avoid chromatic effects in the foreoptics
8) Avoid chopper configurations which modulate the point source illuminated length of the grating

D. To Control Spatial Weighting of the Footprint:

1) Use nominally square individual inlet slit array elements in a step-and-stare crosstrack scan mode
2) Use chopper wheel (if a chopper is used)

E. To minimize scene polarization induced radiometric errors:

1) Operate the grating in the scaler region (high grating orders)

Table 3-8 Baseline V spectrometer common optical parameters

Parameter	Value
Baseline V conditions	
Altitude	833 km
Nominal nadir footprint size	10 x 10 km
Optical design parameters	
Crosstrack scan angle	±44.34°
Individual footprint size (actual)	10 x 7 km
Foreoptics telescope focal length	189.26 mm
Effective foreoptics aperture (per individual footprint)	32.6 mm wide 30.3 mm high
Inlet slit (element) size	2.272 mm wide 1.590 mm high
No. of inlet slit array elements	16
Inlet slit interelement mask height	0.682 mm
Grating pitch	36.850 grooves/mm
Grating incident angle	71°
Grating diffraction angles	(See Table 3-9)
Grating blaze angle	64.0°
Grating antiblaze angle	42.0°
Grating mask size	317.5 mm wide 96 mm high
Collimator focal length	600 mm
Detector field lens focal length	3.16 mm
HgCdTe immersion lens index	4.0 (Ge CH 1-11)
HgCdTe immersion lens radius	2.0 mm (CH 1-11)
Exit slit size(s)	(See Table 3.9)
Detector size(s)	(See Table 3.9)

Table 3-9 Baseline V spectrometer channel dependent parameters

CH	Frequency $\upsilon(cm^{-1})$	Bandwidth $\Delta\upsilon_{1/2}(cm^{-1})$	Grating Order m	Grating Diffracting Angle β (deg)	Relative Grating Efficiency (%)	Exit Slit Width (mm)	Inlet Slit Width Image (mm)	Detector Width (mm)
1	606.95	0.50	3	61.137	40.0	1.8649	1.5330	0.199
2	623.20	0.50	3	55.923	40.0	1.5240	1.3207	0.231
3	627.80	0.50	3	54.616	40.0	1.4531	1.2780	0.239
4	634.30	0.50	3	52.868	40.0	1.3655	1.2259	0.249
5	646.60	0.50	3	49.827	40.0	1.2296	1.1471	0.266
6	654.35	0.50	3	48.060	40.0	1.1589	1.1072	0.275
7	665.55	0.50	3	45.677	40.0	1.0715	1.0591	0.288
8	666.85	0.50	3	45.413	40.0	1.0623	1.4267	0.290
9	668.15	0.50	3	45.150	40.0	1.0533	1.0493	0.291
10	669.45	0.50	3	44.890	40.0	1.0445	1.0445	0.292
11	875.00	0.75	4	47.649	40.0	1.2860	1.0980	0.319
12	1040.80	1.00	5	55.519	40.0	1.8018	1.3071	0.945
13	1231.60	1.00	6	58.137	40.0	1.6561	1.4018	0.882
14	1650.10	1.30	8	57.248	52.0	1.5610	1.3672	0.904
15	1700.30	1.30	8	52.024	56.0	1.2926	1.2021	1.028
16	1839.40	1.50	9	59.027	49.0	1.7142	1.4380	0.860
17	1850.90	1.50	9	57.802	50.0	1.6350	1.3888	0.890
18	1930.10	1.50	9	50.596	47.0	1.2622	1.1658	1.061
19	2384.00	2.00	11	48.997	41.0	1.3044	1.1279	1.096
20	2386.10	2.00	12	65.177	40.0	2.2199	1.7627	0.701
21	2388.20	2.00	11	48.737	40.0	1.2931	1.1221	1.102
22	2390.20	2.00	12	64.747	42.0	2.1770	1.7346	0.712
23	2392.35	2.00	11	48.482	40.0	1.2821	1.1164	1.108
24	2394.50	2.00	12	64.304	43.0	2.1343	1.7067	0.724
25	2424.00	2.50	12	61.478	51.0	2.3640	1.5498	0.798
26	2505.00	2.50	12	55.050	49.0	1.8451	1.2918	0.957
27	2616.50	2.50	13	62.283	48.0	2.2566	1.5911	0.776
28	2686.00	2.50	13	56.918	50.0	1.8246	1.3557	0.912

Grating incident angle (α) = 71°
Detector Height (mm): CH 1-11, 0.136; CH 12-28, 0.530
Detector linear dimensions are 93% of nominal projected grating dimensions.

Table 3-10 Spectrometer spectral alignment channel parameters

CH	λ (μm)	m	α_o(°)	β_o(°)	Relative Grating Efficiency (%)
S1	0.6929[illegible]72	67	78.0764	47.0883	18.2
S2	0.783908	62	67.9300	59.7967	72.0

As a result the detector planes are skewed with respect to the optical axes of the spectrometer and are approximately normal to the axes of the field lenses. The field lenses image the grating upon the detectors; i.e., the detectors essentially lie in a pupil plane of the instrument. This results in a uniform distribution of the radiance from each point in the scene over the entire area of the detector. The Baseline V detectors slightly underfill the nominal grating image in order to reduce the effects of field lens geometric aberrations upon the uniformity of energy distribution near the edges of the detectors. Consequently, the effects of local variations in detector responsivity over the area of the detector are minimized. In addition, spatial misalignment of the detector with respect to the exit slit can result in some loss in SNR but would have minimum effects upon the spectral performance and spatial simultaneity of the instrument. Alignment of the image plane mask slit jaws with respect to the spectral axis of the grating is critical to instrument spectral performance. The inlet slit premasks between footprint array elements, however, mask the junctions between detector optical assemblies. Consequently, limited misalignment normal to the spectral axis will have no effect upon footprint spatial simultaneity. The grating diffraction angle is given by

$$\beta = \sin^{-1}\left(\frac{m}{\upsilon a \cos\theta} - \sin\alpha\right) \qquad (3.34)$$

where

α = grating incident angle

β = grating diffraction angle

θ = grating out-of-plane angle

υ = spectral wavenumber

a = grating groove spacing

m = grating order

The out-of-plane angle for slit positions above or below the optical axis of the system results in curvature of the exit slit arrays, as shown in Fig 3-21.

Photoconductive HgCdTe detectors are used for the long wavelength channels -- 1 through 11 -- photovoltaic HgCdTe detectors are used for the intermediate wavelength channels -- 12 through 17 -- and InSb detectors are used for the short wavelength channels--18 through 28. The D* of the long wavelength detectors is a relatively strong function of detector temperature, and the D* of the short wavelength detectors is a relatively strong function of background photon flux. All detector assemblies are contained in a common thermal dewar having a design temperature of 75 K. Instrument background

photon flux is minimized by locating the detectors within the cold dewar; by using field lenses to restrict the flux falling upon the detector from outside the dewar to the optical ray bundle; by using cold (75 K) order filters to restrict the spectral bandwidth of the flux falling upon the detector from outside the dewar; and by cooling the spectrometer optics to a design temperature of 160 K. It is particularly important to cool the inlet slit, since the detector in a grating instrument sees the radiance within the bandwidth of the order filter from the area on either side of the inlet slit. This radiance is diffracted by the grating into the image plane slit.

The foreoptics telescope is an off-axis Schwarzschild. This is an all reflecting, monocentric optic; consequently, no chromatic aberration is introduced by the telescope to compromise spatial simultaneity, and telescope performance is relatively independent of IFOV element field angle. The grating pupil stop is imaged into foreoptics space as a skewed, curved surface, and lies within the converging ray bundle of the Schwarzschild telescope. There is some interference of the ray bundle between the secondary and primary mirrors of the Schwarzschild and the imaged instrument pupil; consequently, the foreoptics glare stop is partially formed by the edge of the primary telescope mirror and some light is incident upon the surface of the grating mask.

The image surfaces of both the Bouwers collimator and the Schwarzschild telescope are spherical, and are concave toward the center of curvature. The focal length of the telescope is less than that of the collimator in the Baseline V instrument and the inlet slit array is placed upon the telescope focal surface. This results in an excess object distance for the entrance collimator, and a very slight decollimation, for slits near the ends of the array. This effect is compensated for in the exit collimator by decreasing its image distance for image plane slits near the ends of the slit arrays. This effect converts the spherical image surface into a cylinderical surface.

A plane parallel KBr window is placed ahead of the foreoptics telescope. Its purpose is to provide a gas check into that portion of the optical assembly containing the cold detector cryostat in order to control contamination of the cold optical surfaces. This window is in collimated optical space, and introduces no geometric optical aberrations.

The foreoptics telescope may be visualized as projecting the inlet slit array upon the scene, or visa versa. At nadir, each footprint element is 7 km high and 10 km wide. These footprint elements are spaced 10 km center-to-center along the length of the array. Total array length is 160 km. The entrance slit array is projected onto the earth by a 45 degree scan mirror located ahead of the foreoptics. This mirror is mounted at 45 degrees with respect to its shaft axis which is parallel to the spacecraft velocity vector. At nadir the linear array of footprint elements is parallel to the spacecraft velocity vector. The array is scanned across track in a push-broom fashion by rotating the shaft of the scan mirror. This causes a skewing of the footprint array with respect to its nadir alignment, and results in a scan swath width which is almost constant as a function of scan angle. The instrument uses approximately

square individual IFOV elements; consequently, its scan mirror is step scanned. IFOV elements are nominally contiguous along the across track scan direction, and 130 16-element footprint arrays are contained in a single push-broom line scan. Total scan angle is approximately ± 45 degrees with respect to nadir. The AMTS footprint geometry projected onto a nonrotating earth is illustrated in Fig 3-22. Orbit and earth coverage parameters are listed in Table 3-11.

Radiometric calibration is achieved in orbit by having the scan mirror view a pair of on-board blackbody targets -- a cold target at ≈200 K and a hot target at ≈310 K -- between successive across track line scans. Calibration radiance values for a given line scan are obtained by averaging an equal number of calibration target looks that both precede and follow in time the line scan in question. This eliminates the effects of linear signal channel amplitude variations vs time. Only the nonlinearity of the variations over the averaging period results in radiometric errors. In addition, the random radiometric errors in the calibration radiance values are reduced by a factor of $\sqrt{N}$, where N is the number of calibration looks in the averaging period.

The spectrometer uses an optical chopper wheel operating at a frequency selected to be above the 1/f noise knee of the PC HgCdTe detectors. The chopper wheel is located on the foreoptics side of the inlet slit array and is equidistant from all slit array elements. The axis of the chopper wheel lies in a plane normal to the entrance slit array length so that the chopper blades tend to move along the length of the slit array to minimize spectral weighting effects. The inlet slit mask is toroidal. It has a radius of curvature equal to the foreoptics focal length along the length of the slit array, and a radius of curvature equal to the collimator focal length normal to the length of the slit array. The chopper wheel is a segment of a sphere whose radius is slightly less than the foreoptics focal length. The axis of the chopper wheel passes through the center of curvature of the foreoptics. Chopper blades operate at case temperature, without active thermal control. Blade temperature is stabilized with respect to scene radiance variations, however, by masking ahead of the blades and by a mirror surface on the input surface of the blades. An integral number of chopper cycles are contained within each IFOV dwell period.

A set of reference pulses for synchronous demodulation of the chopped IR signal channel voltage waveforms are derived from an optical chopper reference generator (Fig 3-27). Light from an inlet slit array, identical in size to the IR inlet slit array and illuminated by an on-board source, falls upon a linear array of detectors 16 elements long. This assembly is displaced from the IR inlet slit array around the periphery of the chopper wheel by an angle equal to an integer number of chopper blade cycles so that the reference generator slits are chopped in synchronism with the IR signal slits.

A capability is provided for in-orbit spectral monitoring and alignment, using relatively isolated lines of neon as the spectral reference source. An amplitude modulated, optically filtered, neon bulb source supplies illumination to two sets of spectral alignment inlet slits. These

Table 3-11 Baseline V (LEO) orbit and earth coverage parameters

Parameter	Baseline V
Orbit altitude	833 km
Orbit inclination	98.75°
No. orbits/day	14.21
S/C ground velocity	6.5812 km/sec
Distance between equator crossings (successive ascending orbits)	2815 km
Crosstrack swath width	1799 km
Swath coverage along equator	1820 km
Adjacent swath gap along equator	995 km
No. footprint array elements	16
Nominal nadir footprint	10 x 10 km
No. footprints per line scan	130
No. cal. target dwells per line scan	2
Line scan interval (T_{LINE})[1]	24.3117 sec
Footprint dwell time (T_d)[2]	0.1273 sec

[1]From Equation (3.18)

[2]From Equation (3.19). T_{SLEW} = 7.5015 sec (Fig 3-28)

slits are spatially displaced to the sides of the signal inlet slit array, as shown in Fig 3-21, in a common, thermally stable, inlet slit mask which contains the signal inlet slit array. Relative inlet slit positions are accurately known. Two 2 x 2 element spatial discriminator detector arrays are located on the image plane mask, as shown in Fig 3-21. The relative positions of these detector arrays are accurately known with respect to the image plane signal slit positions. A single wide detector is located below each spatial discriminator array to allow measurement of the slope of the grating power mode over the width of the spatial discriminator array. Grating power modes are rather narrow for high grating orders; consequently, the positions of the alignment channel entrance slits and detector arrays are chosen so that the grating is operated near the peak of its power mode in each alignment channel order. Redundant neon bulb sources are provided. Optical fibers are used to transport light from the neon bulb housing to the individual spectral alignment entrance slits.

The grating angle can be controlled by command. By stepping the grating over a small angular range, the spectral alignment channel data can be ground processed to yield:

- Slope of the grating power mode at the alignment detector array.
- Relative amplitude sensitivity of each spectral alignment channel detector. In essence, this allows an in-orbit recalibration of the spectral alignment system.
- Amplitude vs angle response of the essentially monochromatic inlet alignment slit images. This allows monitoring changes in the geometric blur pattern width due to instrument defocusing at two points on the image plane mask. Amplitude vs frequency response of the IR channels can be deduced from the measured amplitude vs. angle response of the monochromatic alignment slit images, based upon prelaunch calibration data.

For a fixed grating angle, the spectral alignment channel data can be ground processed to yield:

- The "apparent" angular offset of the alignment channel diffraction angles from the nominal design values. The individual detector outputs for an adjacent pair of detectors (in the 2 x 2 array) are differenced to effectively form a high resolution spatial position discriminator. The 2 x 2 detector arrays allow detection of spatial shifts in both the spectral and spatial image plane axes. In addition, these 2 x 2 arrays provide redundant measurements for both improved resolution and improved reliability.

In-orbit recalibration of the spectral alignment channels requires stepping the grating, and interferes with normal sounder operation. Normal spectral monitoring is a continuous process, however, and does not interfere with sounder operation. Spectral misalignment in orbit can be corrected by adjusting the grating angle within limits imposed by nonlinearity of grating spectral dispersion vs grating angle.

Conceptually, a rather elegant method exists for determining channel frequency for the IR channels. Given the knowledge of relative slit positions in the inlet slit mask, of relative slit positions with respect to the spatial discriminator arrays in the image plane mask, of grating groove spacing, alignment channel wavelength, and measured spatial displacements of the spectral reference slit images, solution of the following simultaneous equations provides the data necessary to determine the spectral alignment channel(s) incident and diffracted grating angles:

$$\frac{m_1 \lambda_1}{a} = \sin(\alpha_1 + \varepsilon_{\alpha s}) + \sin(\beta_1 + \varepsilon_{\beta s} + \varepsilon_{\beta 1}) \qquad (3.35a)$$

$$\frac{m_2 \lambda_2}{a} = \sin(\alpha_2 + \varepsilon_{\alpha s}) + \sin(\beta_2 + \varepsilon_{\beta s} + \varepsilon_{\beta 2}) \qquad (3.35b)$$

where

a = grating groove spacing

m = grating order

λ = wavelength

α = nominal design value of grating incident angle

β = nominal design value of grating diffracted angle

$\varepsilon_{\alpha s}$ = equivalent angular shift in inlet slit mask

$\varepsilon_{\beta s}$ = equivalent angular shift in image plane mask

ε_{β} = measured "apparent" angular offset in grating diffracted angle

Subscripts 1 and 2 in the set of Eq 3.35 differentiate between parameters for spectral alignment channels S1 and S2. $\varepsilon_{\beta 1}$ and $\varepsilon_{\beta 2}$ are measured parameters. ε_{α} and $\varepsilon_{\beta s}$ are the unknown parameters. Actual incident and diffracted angles for the spectral alignment channels are:

$$\alpha' = \alpha + \varepsilon_{\alpha s} \qquad (3.36a)$$

$$\beta' = \beta + \varepsilon_{\beta s} + \varepsilon_{\beta} \qquad (3.36b)$$

Actual IR channel frequency, υ, is

$$\upsilon = \frac{m}{a[\sin(\alpha + \varepsilon_{\alpha s}) + \sin(\beta + \varepsilon_{\beta s})]} \qquad (3.37)$$

This method depends upon the difference in grating dispersion between the two spectral reference channels. To be successful, the apparent shift in reference channel angular offset, ε_β, must be measured with a high degree of precision.

Narrow bandwidth elements — order filters, field lenses, immersion lenses, and detectors — are effectively A.R. coated for their design wavelength. The very broadband collimator corrector lens and the foreoptics gas check are not A.R. coated. Surface reflections from the corrector lens, however, are directed out of the optical system. The uncoated parallel plate gas check in effect forms a low Q Fabry-Perot filter. Its maximum rejection over the AMTS frequency range is approximately 8 percent. If the frequency response of the gas check is the same when viewing the radiometric calibration sources as when viewing the scene, it will not affect radiometric accuracy. Stray light crosstalk due to bulk scatter of the refractive materials of the corrector lens and gas check is minimized by using homogenous refractive material. Stray light crosstalk due to surface scatter is minimized by using a high surface polish on these materials. Crosstalk due to mirror BRDF is minimized by using "super polished" 6 to 8 Å RMS mirror surfaces. In addition, a floating light shield is used with the scan mirror in order to reduce the scene solid angle viewed by this mirror. This light shield is within a cylinder which rotates with the scan mirror. A reflective surface on the OD of the cylinder provides thermal isolation to the foreoptics compartment and to the calibration target cavities. In addition this temperature controlled shield prevents uncontrolled radiation from falling upon the emissive target surfaces and resulting in a varying "apparent" emissivity for the calibration targets. Spatial crosstalk due to multiple reflections within the detector assembly can, if necessary, be eliminated by using light baffles around each field lens, detector, and detector immersion lens assembly.

The off-axis optical configuration allows use of a reflective surface upon the image plane mask in order to reduce optical port thermal loading upon the detector cooler. Reflections from the image plane mask and order filter surfaces are directed out of the optical system. The off-axis configuration also avoids multiple passes of energy from the image plane back to the grating to be rediffracted onto the image plane at different diffraction angles. This avoids some order crosstalk.

3.1.3 Optical Configuration Rationale

Major drivers for the off-axis configuration are the need to use an unobscured grating and the need to have reasonable optical access to the inlet slit and exit slit assemblies.

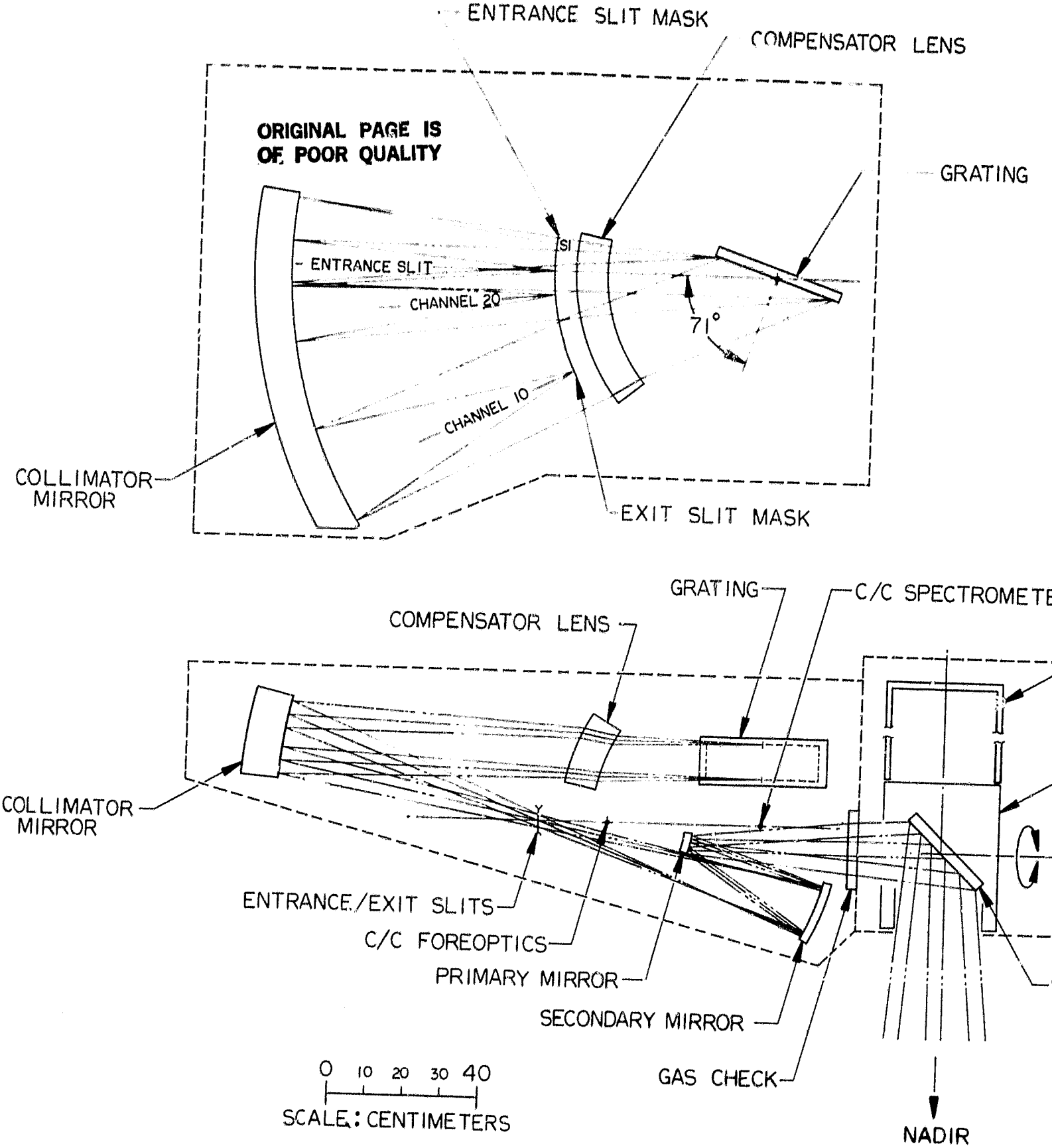

FOLDOUT FRAME

Figure 1

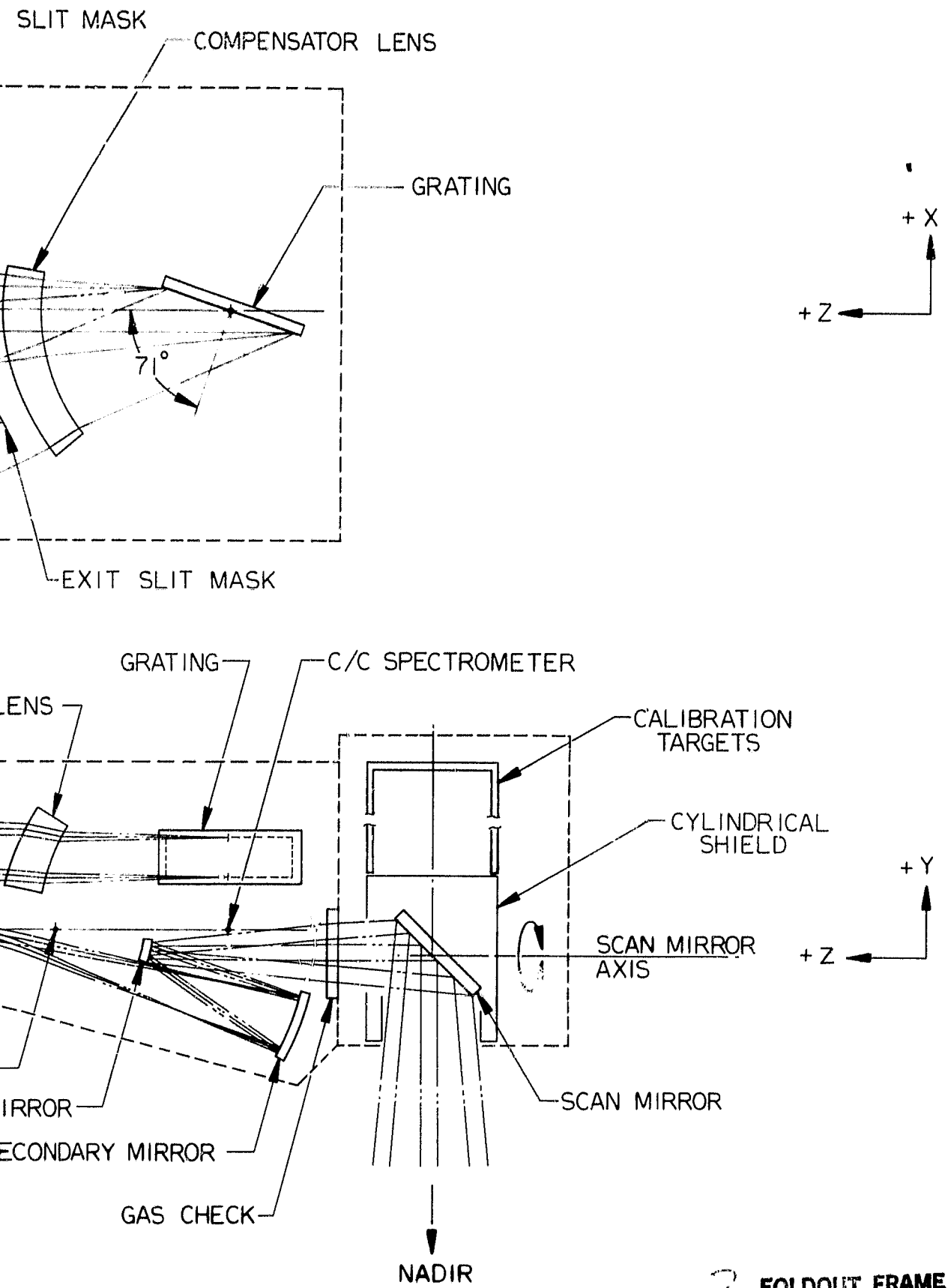

2 FOLDOUT FRAME

Figure 3-20 Baseline V optical layout

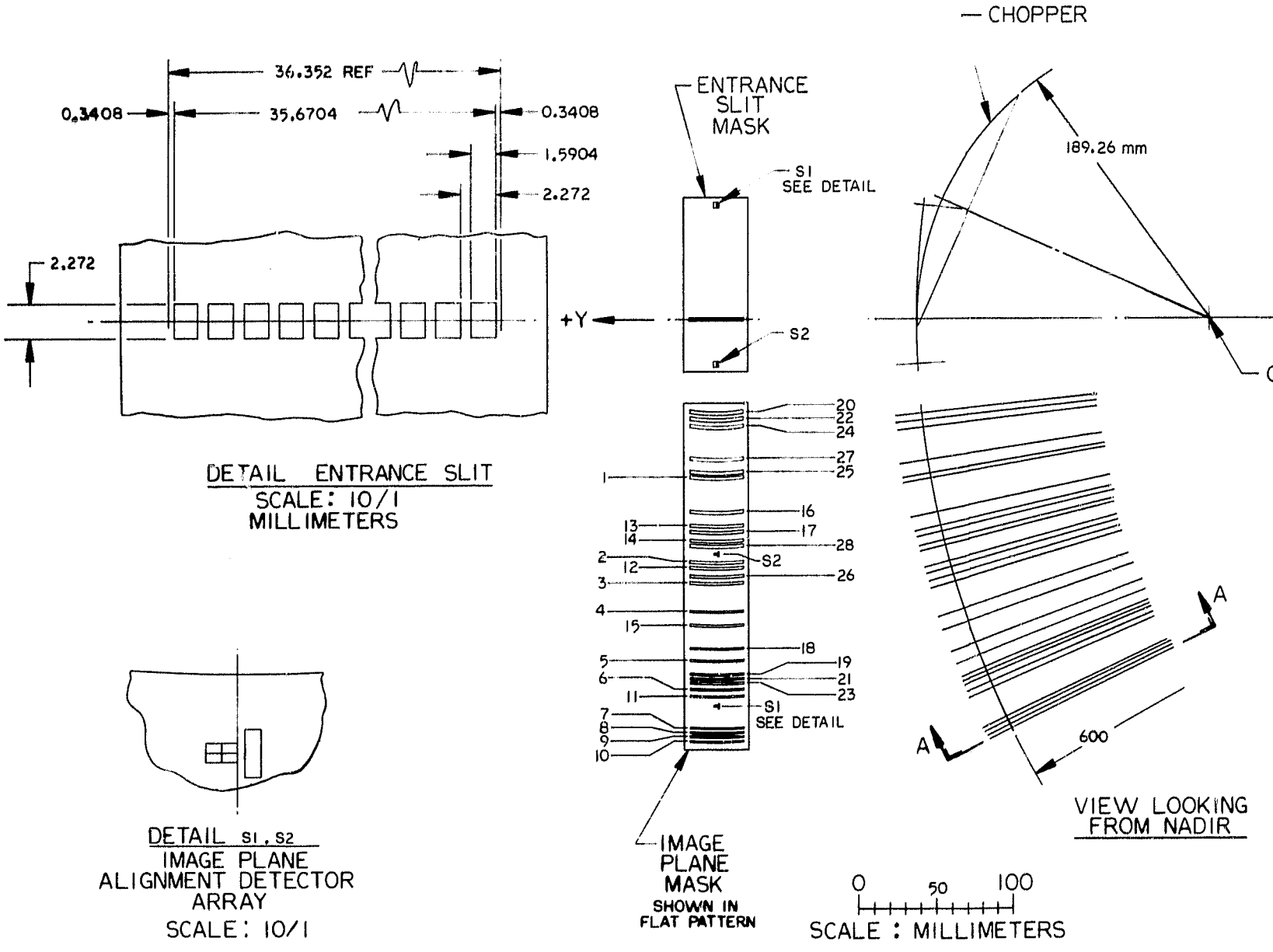

FOLDOUT FRAME

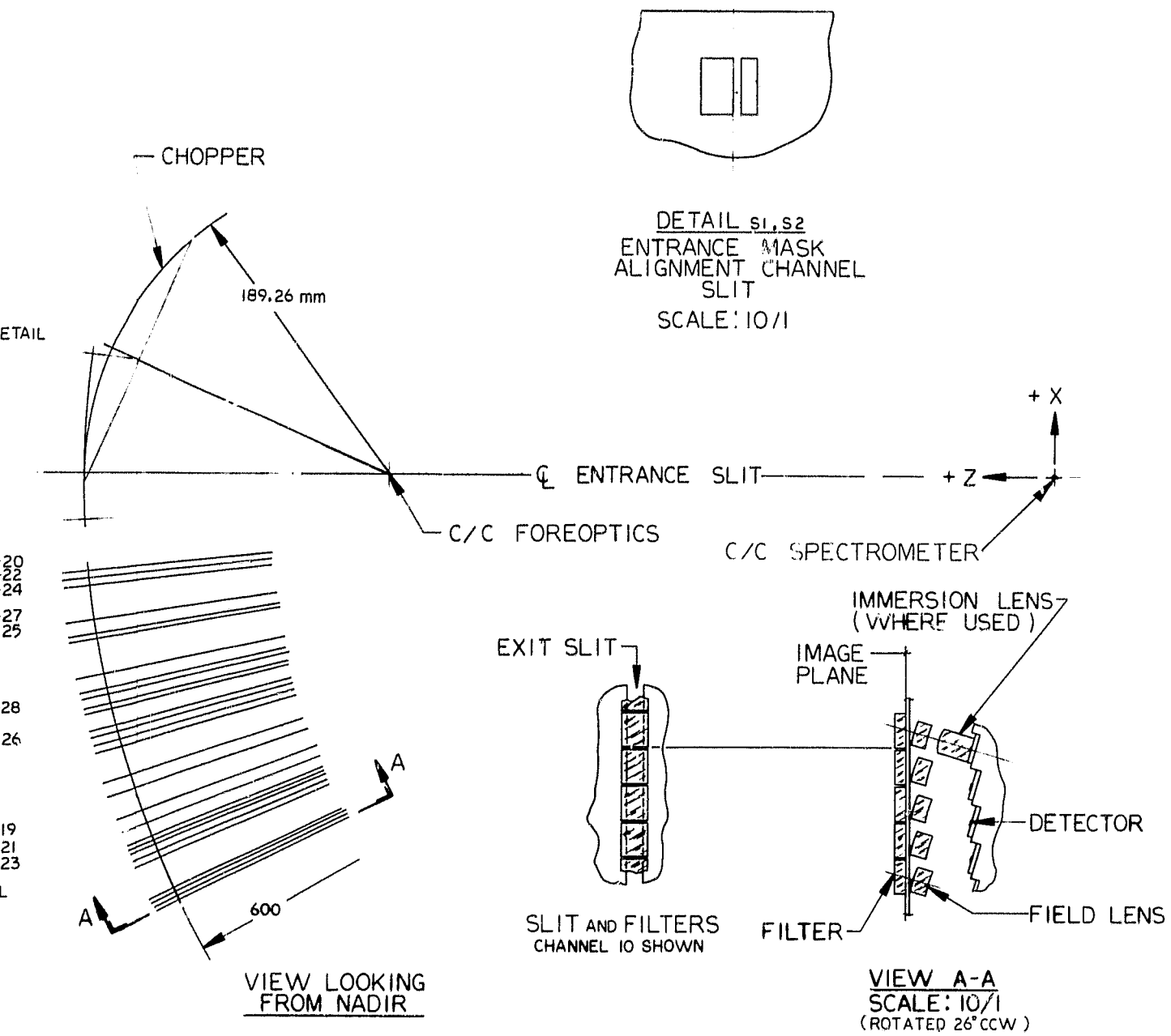

Figure 3-21 Inlet slit mask and image plane assembly optical layout

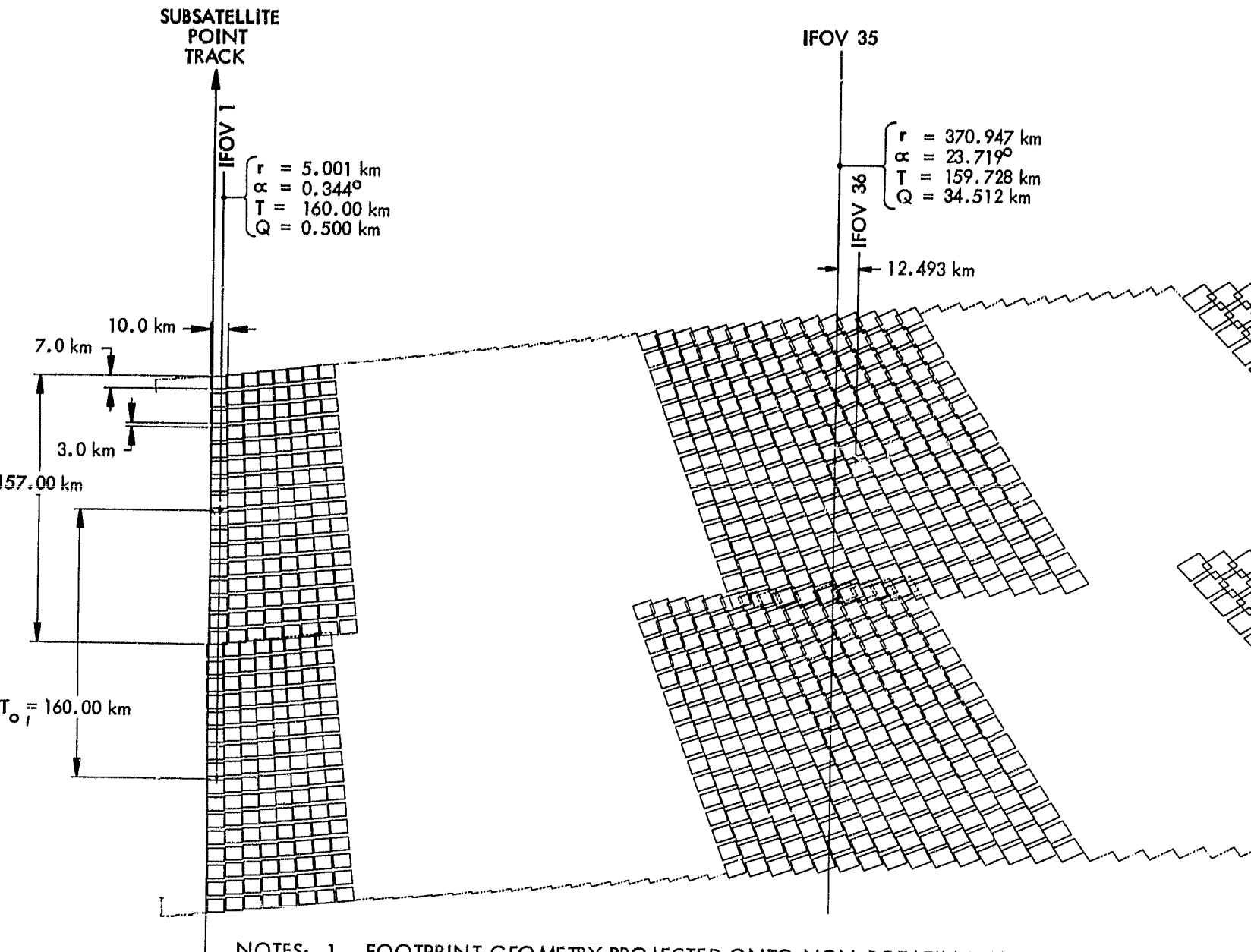

NOTES: 1. FOOTPRINT GEOMETRY PROJECTED ONTO NON-ROTATING EARTH FOR THE CASE FOR WHICH THE SCAN MIRROR LEADS THE ENTRANCE SLIT ALONG THE SPACECRAFT VELOCITY VECTOR. TWO HALF LINE SCANS ARE SHOWN, FROM NADIR TO END OF SCAN. IF SPACECRAFT VELOCITY WERE NEGLECTED, THE LEFT HALF LINE SCANS, FROM START OF SCAN TO NADIR, WOULD BE MIRROR IMAGES OF THE HALF LINE SCANS PICTURED.

2

FOLDOUT FRAME

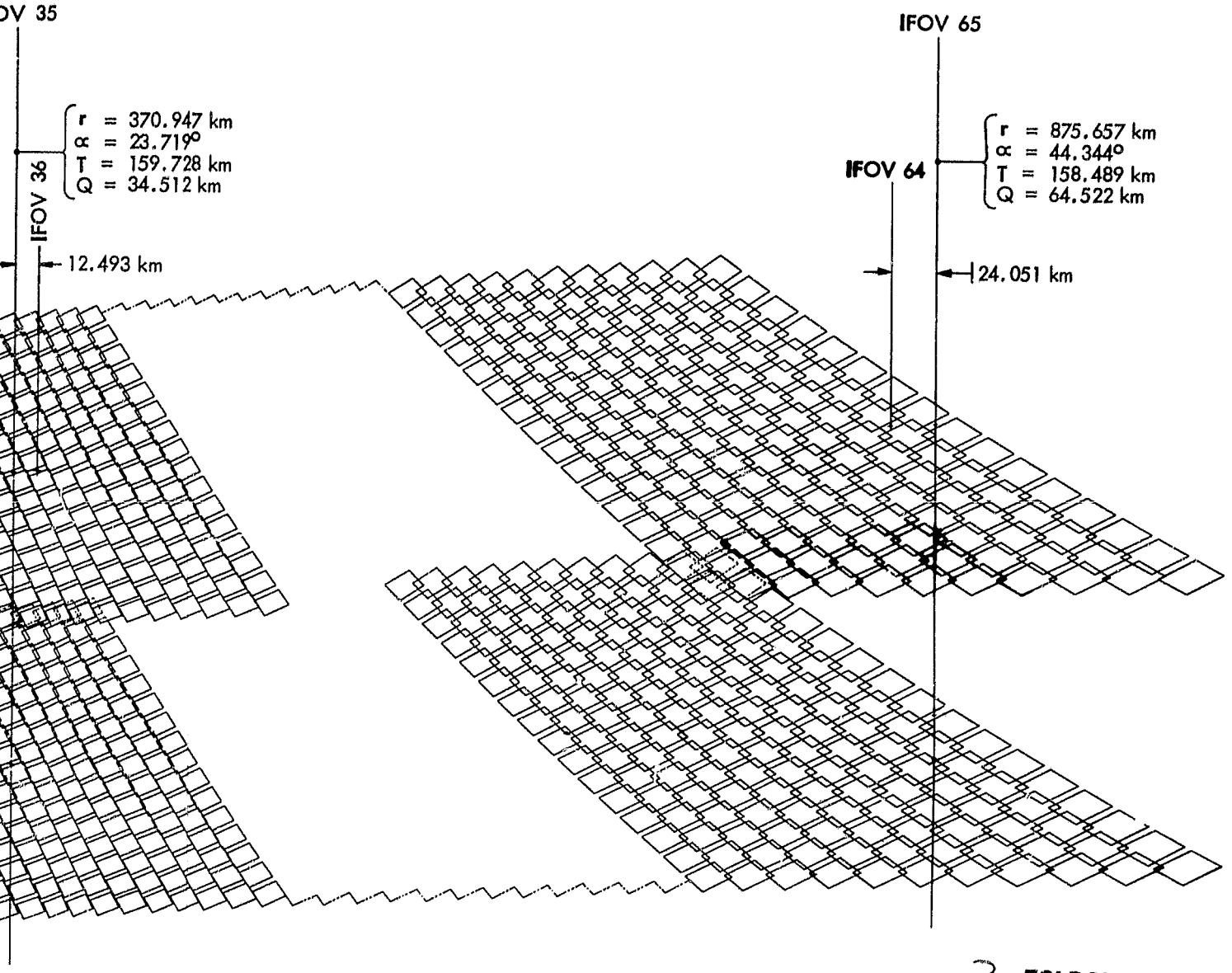

2 FOLDOUT FRAME

ON-ROTATING EARTH FOR
DS THE ENTRANCE SLIT ALONG
IALF LINE SCANS ARE SHOWN,
RAFT VELOCITY WERE NEGLECTED,
SCAN TO NADIR, WOULD BE
ICTURED.

2. SYMBOL DEFINITIONS
IFOV (FOOTPRINT) = INSTANTANEOUS FIELD OF VIEW

r = DISTANCE FROM NADIR TO CENTER LINE OF IFOV

α = ANGLE FROM SPACECRAFT NADIR LINE TO IFOV CENTERLINE ON EARTH

Ṫ = PITCH BETWEEN SUCCESSIVE LINE SCANS

Q = SKEW DISTANCE WITH RESPECT TO NADIR DUE TO SPACECRAFT VELOCITY

Figure 3-22 AMTS Baseline V footprint scan geometry

Use of the high dispersion grating is driven by the need to minimize instrument NEN.

The high dispersion grating results in wide field angles in the collimator. These wide field angles, coupled with the need to control relative slit function response vs. field angle for all elements within each channel array, are the drivers for use of a monocentric collimator. The Bouwers concentric optical system allows placing the grating at its center of curvature in collimated optical space.

The Schwarzschild foreoptic is used because it introduces no chromatic aberrations ahead of the entrance slit, it has very good optical performance which is relatively independent of field angle along the length of the inlet slit array, and the sign of curvature of its spherical image surface matches that of the Bouwers collimator. The fact that placing the inlet slit array upon the image surface of this foreoptic results in a cylindrical surface for the image plane for the Baseline V altitude and spatial resolution is a fortuitous circumstance.

Use of germanium immersion lenses for the long wavelength PC HgCdTe detectors results in approximately a factor of four reduction in NEN. This long wavelength performance is required to make the AMTS system viable, and we have found no other practical way to achieve it. In addition, germanium immersion lenses reduce the PC detector joule heat loading upon the detector cryostat by a factor of 16. Large radii immersion lenses are used to prevent total reflection of some rays at the immersion lens/detector interface.

The linear array is used to minimize NEN by increasing footprint dwell time and to obtain a dwell time which is compatible with optical chopping and signal processing requirements. A 16 element array is necessary for 10 km spatial resolution (Fig 3-3).

The use of the 16 element linear array results in nominally square pixel elements. This, in turn, requires use of the step-and-stare across track scan approach. Premasking at the inlet slit array — which results in rectangular actual footprint elements — along with the absence of chromatic aberrations in the foreoptics is required to satisfy footprint spatial simultaneity requirements.

The use of an optical chopper is driven by the relatively high 1/f noise frequency knee of PC HgCdTe detectors. A chopper wheel, chopping nominally along the length of the inlet slit array, is used to minimize relative slit function variations between array elements and to eliminate chopper induced spatial footprint weighting.

The nominally in-plane off-Littrow grating configuration results in grating angles which minimize $\sqrt{A_d}/A\Omega$, and which tend to equalize relative grating efficiency for the AMTS channel set over the length of the image plane with improved performance at the ends of the image plane. It also results in the most regular spatial layout of the image plane.

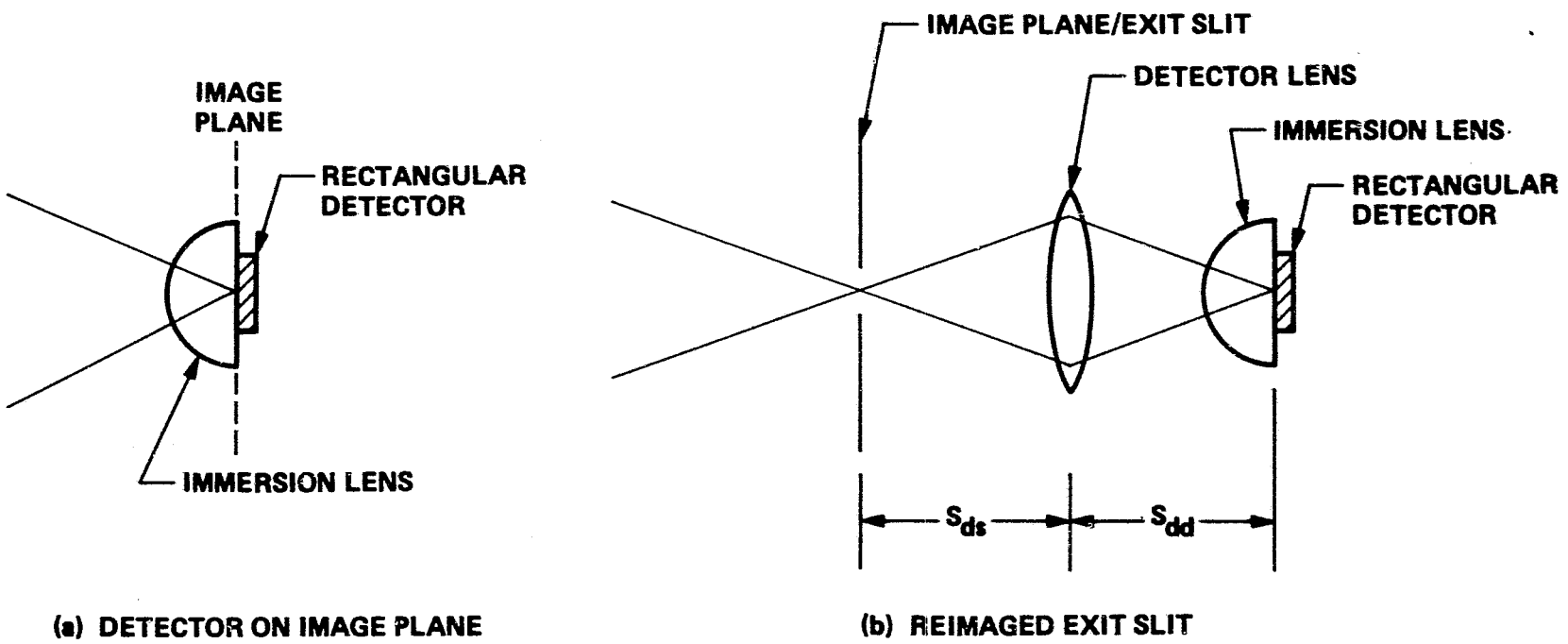

Figure 3-23 Alternate image plane configuration (ref. Fig. 3-1)

An out-of-plane grating configuration would result in rotation of the exit slit arrays over the length of the image plane. While an out-of-plane configuration would conceptually allow the grating to be operated closer to Littrow conditions, the chopper wheel as used in Baseline V would mask the image plane for reasonable out-of-plane angles.

Distributed radiometric calibration targets are used in a way that introduces no additional optical surfaces — with their uncertain radiometric calibration effects — into the system. Matched dual targets are used so that radiometric bias effects due to the defocused target surfaces are the same for both targets. This minimizes slope error in the radiometric calibration of the instrument. In-orbit system tuning — essential for a passive sounder — can easily compensate for radiometric offset error, but it cannot easily compensate for slope error. The calibration targets are symmetrically placed about the zenith to balance scan mirror polarization effects for the two targets. An angle of 30° off zenith would minimize polarization effects upon radiometric calibration. The targets are placed as close as possible to the 30° angle; i.e., at ≈45°.

Optical transmissivity has been maximized by use of a very clean optical configuration. The gas check introduces the only optical surfaces which do not perform a critical optical function.

Within limits imposed by a practical instrument size, long wavelength detectors having a relatively high 1/f noise frequency knee, and a grating configuration optimized for minimum NEN (rather than minimum polarization sensitivity), the conceptual optical design for the Baseline V instrument is believed to be near optimum in terms of the optical design criteria listed in Table 3-7.

What remains is to examine the generality of the grating spectrometer configuration of Fig 3-1. At this point a reasonable basis has been established for doing so.

Two alternate image plane configurations are shown in Fig 3-23. In Fig 3-23a the detector is mounted upon the image plane and forms the effective exit slit of the spectrometer. In Fig 3-23b the exit slit is reimaged onto the detector. For the detector upon the image plane, NEN per pixel can be written (Appendix B):

$$NEN_p' = \frac{f_{c\beta}}{A_{g\alpha}} \cdot \frac{\cos\alpha}{\sin\alpha + \sin\beta} \sqrt{\frac{\cos\alpha}{\cos\beta}\left(F_s \frac{S_{w\alpha}}{S_{h\alpha}}\right)} \cdot \frac{1}{E_g} \cdot \frac{1}{n} \cdot \frac{1}{\tau} \cdot \frac{\sqrt{\Delta F}}{F_c} \cdot \frac{1}{D^*} \cdot \frac{\nu}{\Delta\nu_o} \qquad (3.38)$$

For the exit slit re-imaged onto the detector, NEN per pixel can be written (Appendix B):

$$NEN''_p = \frac{s_{dd}}{s_{ds}} \cdot \frac{f_{c\beta}}{A_{g\alpha}} \cdot \frac{\cos\alpha}{\sin\alpha + \sin\beta} \sqrt{\frac{\cos\alpha}{\cos\beta}\left(F_s \frac{S_{w\alpha}}{S_{h\alpha}}\right)}$$

$$\cdot \frac{1}{E_g} \cdot \frac{1}{n} \cdot \frac{1}{\tau} \cdot \frac{\sqrt{\Delta F}}{F_c} \cdot \frac{1}{D^*} \cdot \frac{\upsilon}{\Delta\upsilon_o} \qquad (3.39)$$

Except for the term s_{dd}/s_{ds}, Eq 3.39 is identical to Eq 3.38. For their respective configurations, these equations correspond to the parametric and scaling Eq 3.10 for the configuration of Fig 3-1. For the field lens configuration, NEN is a function of both grating area and grating form factor; for the configurations of Fig 3-23 NEN is a function of grating area and is independent of grating form factor.

Taking the ratio of NEN'_p for detectors on the image plane (Eq 3.38) to NEN_p for the field lens configuration (Eq 3.10) where the primed terms are used for detectors on the image plane

$$\frac{NEN'_p}{NEN_p} = \frac{\dfrac{f_{c\beta}}{A'_{g\alpha}}}{\dfrac{\sqrt{G_{H\alpha}\, G_{w\alpha}}}{A_{g\alpha}}} \cdot \sqrt{\frac{\dfrac{\cos\alpha}{\cos\beta}\left(F_s \dfrac{S_{w\alpha}}{S_{h\alpha}}\right)}{\dfrac{\cos\beta}{\cos\alpha} + \dfrac{\cos\alpha}{\cos\beta}\left(F_s \dfrac{S_{w\alpha}}{S_{h\alpha}}\right)^2}}$$

$$\cdot \frac{n}{n'\, F/NO} \cdot \frac{D^*}{D^{*\prime}} \qquad (3.40)$$

If the first term of Eq 3.40 is examined numerically for three sets of grating configurations:

1) Equal rectangular grating areas, single sided, off-axis:

$$\frac{NEN'_p}{NEN_p} \propto \frac{f_{c\beta}}{\sqrt{A_{g\alpha}}} \approx \frac{600\ \text{mm}}{\sqrt{9923\ \text{mm}^2}} = 6.02$$

2) Maximum usable (rectangular) grating areas, double sided, center obscuration:

$$\frac{NEN_p'}{NEN_p} \propto \frac{\frac{f_{c\beta}}{A_{g\alpha}}}{\frac{\sqrt{G_{H\alpha}\, G_{W\alpha}}}{A_{g\alpha}}} \approx \frac{f_{c\beta}}{\sqrt{G_{H\alpha}\, G_{W\alpha}}}$$

$$= \frac{600 \text{ mm}}{\sqrt{47{,}348 \text{ mm}^2}} = 2.76$$

3) Double sided rectangular grating configuration for detector on image plane; single sided rectangular grating configuration for field lens configuration:

$$\frac{NEN_p'}{NEN_p} \propto \frac{\frac{f_{c\beta}}{A_{g\alpha}'}}{\frac{1}{\sqrt{A_{g\alpha}}}} = \frac{\frac{600 \text{ mm}}{19{,}847 \text{ mm}^2}}{\frac{1}{\sqrt{9923 \text{ mm}^2}}} = 3.01$$

For the second term (Eq 3.40), for $F_s = 1$ and $S_{w\alpha}/S_{h\alpha} = 1.43$, $\alpha = 71°$ and $\beta = 45°$:

$$\frac{NEN_p'}{NEN_p} = 0.46$$

For the third term (Eq 3.40), for F/NO = 1, $n' = 1$ and $n = 4$:

$$\frac{NEN_p'}{NEN_p} = 4.00$$

For this term, $n' = 1$ because, in general, both an order filter and an immersion lens cannot be placed ahead of the detector without interfering with adjacent channel ray bundles. Combining ratios for the first three terms of Eq 3-40, for the three grating configurations:

Grating Configuration	NEN′/NEN	
	CH With Immersion Lens	CH Without Immersion Lens
1	11.08	2.77
2	5.08	1.27
3	5.54	1.39

For the fourth term (Eq 3.40), D*/D*′, in the limit:

- For PC detector limited channels, D* = D*′
- For background limited detector channels, D* > D*′

Grating configuration (1) is a practical one, in terms of instrument buildability. Configuration (2) presents difficulties in terms of scan mirror size, introduction of the foreoptics ray bundle into the spectrometer, spectrometer size, and reflected stray light from the image plane within the system. Configuration (3) represents a hybrid ratio.

For the instrument configuration which re-images the exit slit onto the detector (Eq 3-39) the immersion lens can be used. Conceptually, the first term of Eq 3-39 could be less than unity, and the NEN performance of the configuration could equal that of the field lens configuration. It would be difficult, if not impossible, however, to use this configuration for the multidetector AMTS image plane.

For an instrument configuration using the detector in the focal plane, variation in detector responsivity over the area of the detector can result in radiometric errors when viewing a scene having nonuniform radiant emittance over the area of the pixel. Placing the order filter very close to the detector, which is a necessity in the configuration of Fig 3-23a, could result in degradation of the effective out of band rejection of the order filter due to the "Stierwalt effect" (Ref 3-2). (Stierwalt has reported — in other communications — that the effect is very much reduced when the detector is placed some distance beyond the order filter.)

With the grating to collimator distances reduced to zero, the grating spectrometer configuration of Fig 3-1 is equivalent to a configuration using a concave spherical grating. The NEN parametric equations — 3.10, 3.38 and 3.39 — apply to such configurations. The difficulty of ruling a steep grating upon a concave substate and the astigmatic focus of a concave grating on the Rowland circle limit its utility for the AMTS. The astigmatic line length

$$\ell = L \cos \beta \left(\frac{\sin^2 \alpha}{\cos \alpha} + \frac{\sin^2 \beta}{\cos \beta} \right) \qquad (3\text{-}41)$$

where

ℓ = astigmatic line length

L = grating groove length (or height of the grating)

α = incident angle

β = diffraction angle

An imaging instrument like the AMTS, for example, would require a collimator F/NO greater than 12 for incident and diffraction angles in the range of 5 to 10 degrees.

Hyperimmersion of the detector has been considered as a possible means of increasing optical convergence. Ray trace analysis showed that, for an immersion cement index of refraction of 1.5, total reflection was a problem at the immersion lens/detector interface. Hyperimmersion could be used by increasing the F/NO of the field lens, but this results in no improvement in optical convergence over that of the hemispheric immersion lens in combination with the F/1 field lens.

In summary, the generalized grating configurations of Fig 3-1 and 3-23, using plane and concave gratings, is believed to represent the general set of configurations of possible interest for the AMTS application. The configuration of Fig 3-1, using steep echelle gratings, offers the best NEN performance by some margin.

3.1.4 Optical Performance

Slit function considerations (Para 3.1.1.5) rather than minimum overall geometric point spread considerations govern optimization of the instrument optics. The inlet slit array lies on the image surface of the foreoptics telescope. For the Baseline V altitude and spatial resolution, it is possible to place all exit slit arrays on a single cylinderical image surface. Conceptually, it would have been possible to refocus the individual exit slits to compensate for the chromatic effects of the KBr compensator lens. In the interest of buildability of the image surface mask assembly, Baseline V was focused for Channel 10--which has the widest collimated ray bundle along the spectral axis--and the other channels were not refocused. Optical dimensions for the Schwarzschild telescope and Bouwers collimator are listed in Table 3-12.

Ray trace dot diagrams at the inlet slit array for the telescope when traced from the object surface to the inlet slit, and at the image plane array for the spectrometer when traced from inlet slit to exit slit, are shown in Fig 3-24. Relative point spread energy distributions due to geometric aberrations are plotted in Fig 3-25 for the spectral axis and in Fig 3-26 for the spatial axis. Ratios of slit dimension to main lobe point spread distributions for geometric aberrations and aperture diffraction point spreads are listed in Table 3-13.

Table 3-12 Monocentric optics radii from centers of curvature

Parameter	Value
Schwarzschild telescope	
Image surface	189.26 mm
Primary mirror	232.10 mm
Secondary mirror	600.00 mm
Bouwers collimator	
Inlet slit[1]	601.20 mm
Exit slit[1,2]	600.54 mm
Compensator lens ID	453.37 mm
Compensator lens OD	540.00 mm
Mirror	1294.90 mm

[1]To center of slit array
[2]Includes (germanium) order filter substrate 0.5 mm thick

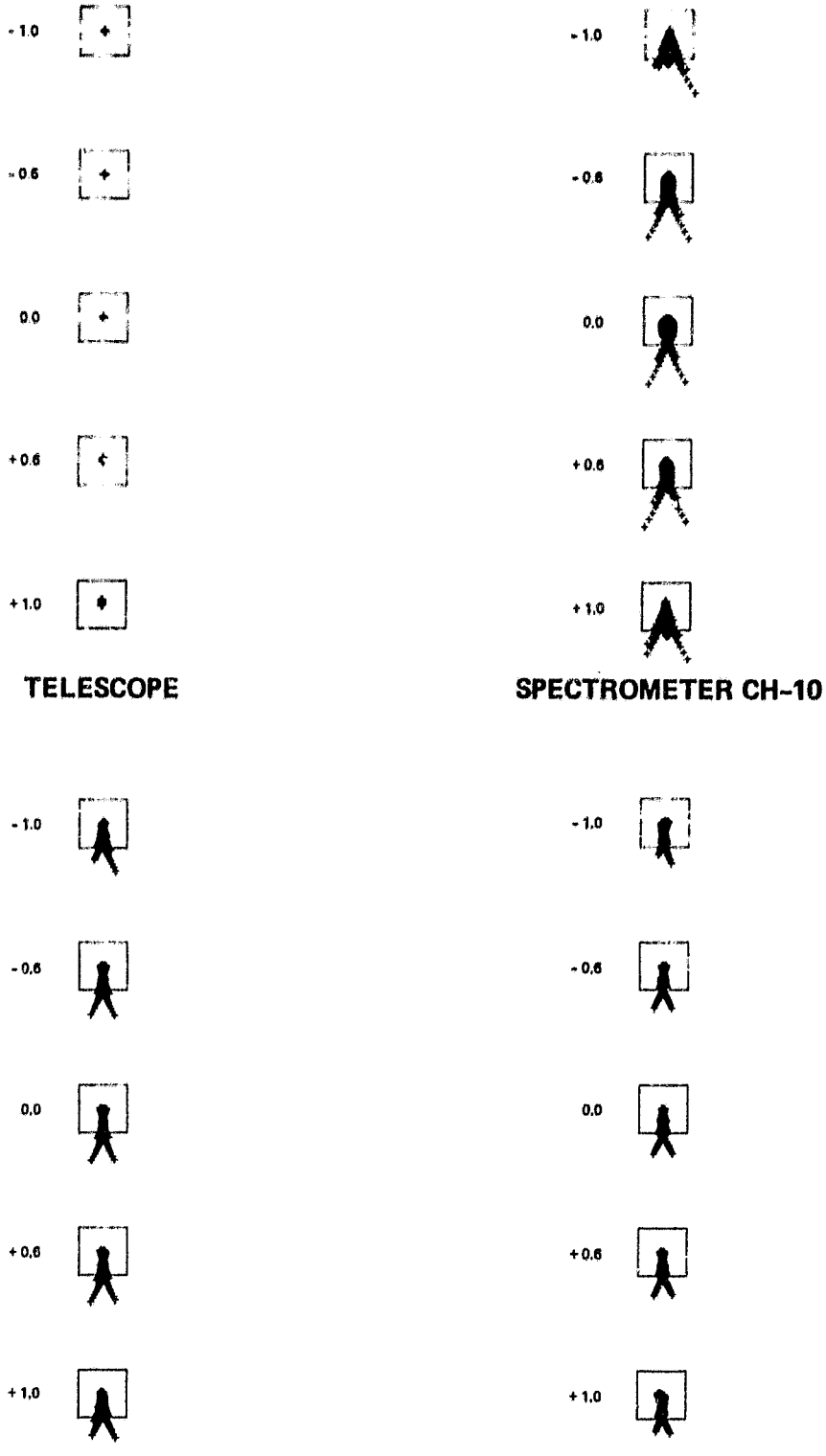

Figure 3-24 Dot diagrams vs field position — on axis, +/- full field, and 0.6 field points — of the inlet slit array. Reference squares are 200 μm per side.

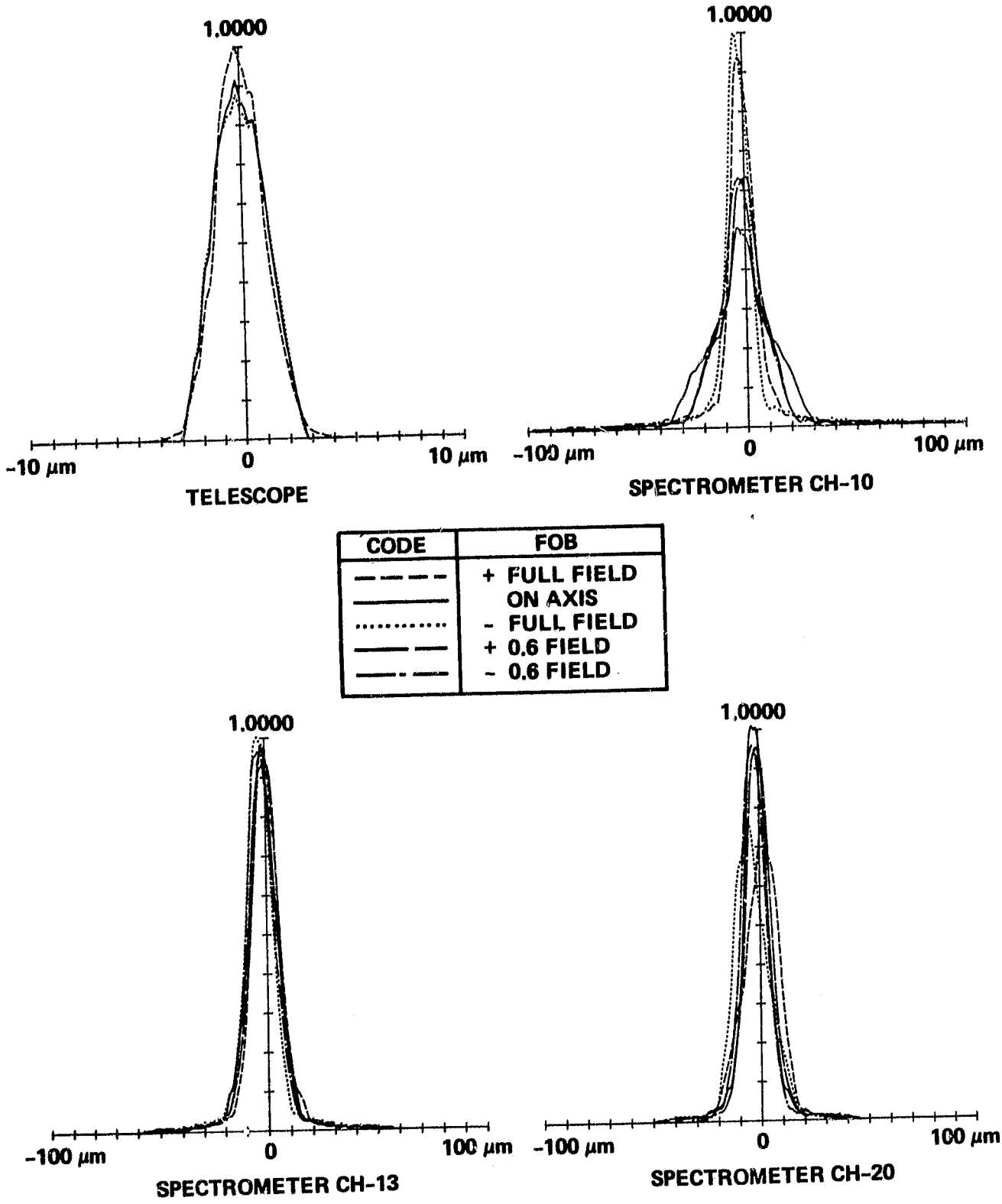

Figure 3-25 Relative point spread energy distribution along the spectral axis. (Note expanded scale for telescope.)

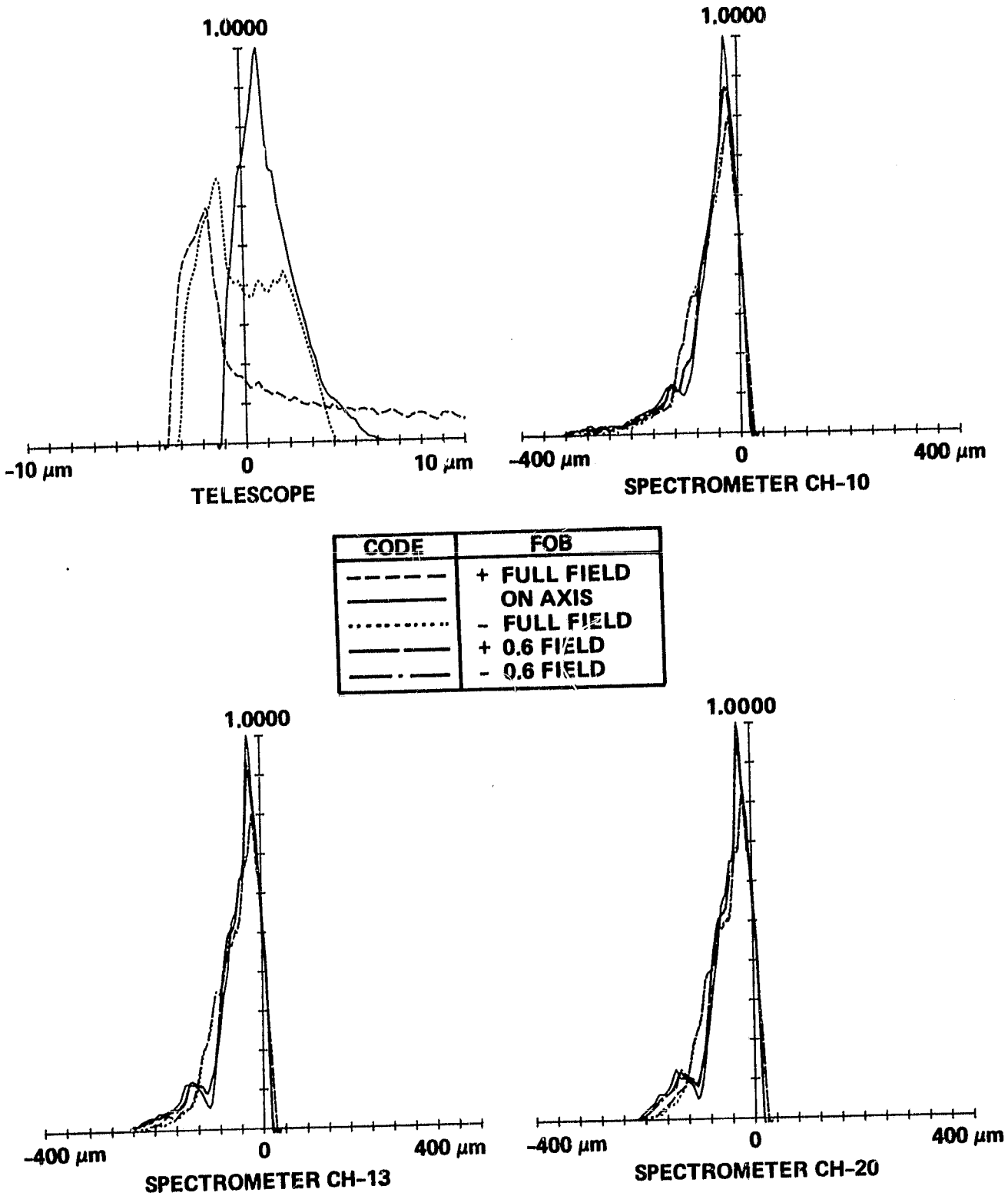

Figure 3-26 Relative point spread energy distribution along the spatial axis. (Note expanded scale for telescope.)

Table 3-13 Slit dimension to point spread ratios for geometric aberrations and aperture diffraction for foreoptics and spectrometer optics

	Spectral Axis			Spatial Axis		
	Slit Width (mm)	Slit Width to Point Spread Ratio		Slit Height (mm)	Slit Height to Point Spread Ratio	
		Geom[1]	Diff[2]		Geom[1]	Diff[2]
Foreoptics	2.272	379	13/46[3]	1.590	227	9/29[3]
Spectrometer						
CH 10	1.045	16	13	1.590	10	9
CH 13	1.659	47	28	1.590	10	16
CH 20	2.221	58	60	1.590	10	29

[1]For main lobe (less skirts) of geometric point spread
[2]For single point diffraction energy distribution within first nulls
[3]For CH 10/CH 20

Geometric aberrations of the Schwarzschild telescope are much smaller than the aperture diffraction point spread. Some variation in the geometric point spread distribution of the telescope as a function of field angle occurs because the image of the instrument pupil—the grating—does not lie at the center of curvature of the Schwarzschild, but the effect is so small that it is of little consequence for AMTS. Geometric aberrations for the spectrometer are effectively equal to or less than the diffraction point spread along the spectral axis, but are equal to or greater than the diffraction point spread along the spatial axis. In terms of AMTS requirements this nominal Baseline V optical aberration performance appears to be quite good. (This issue is examined further in Section 4.)

Geometric aberrations of the germanium single element F/1 field lenses result in some nonuniformity of energy density near the edges of the reflected pupil (the grating image). Consequently, linear dimensions of the Baseline V detectors are specified as 93 percent of the dimensions of the grating image. The net loss in $A\Omega$ is thus 14 percent, but the increase in $\sqrt{A_d}/A\Omega$—and in NEN—is only seven percent.

IR channel grating orders and estimated grating efficiencies are listed in Table 3-9. The use of multiple grating orders is necessary to fit the AMTS channel set within an acceptable range of diffraction angles. Channels 19 through 24 must be used in alternate adjacent orders to spatially fit them within the image plane. For a given set of grating incident and diffraction angles, both the blaze and the antiblaze grating angles must be adjusted to effectively balance relative grating efficiency between the individual channels.

For this Baseline V study a dual-vector grating efficiency model was used to specify grating blaze and antiblaze angles and to calculate relative grating efficiencies for AMTS grating incident and diffraction angles (Appendix C). Calculated relative efficiencies for the AMTS channel set for three antiblaze angles are listed in Table 3-14. This scalar grating efficiency model tells us nothing about grating polarization sensitivity (Para 3.1.1.2). In addition, it appears that for an R2 grating this model does not give useful results below about the sixth order. It appears that, for these low orders, the peak measured grating efficiency near Littrow is less than calculated, but that the angular width of the power mode tends to be greater than calculated. For the eighth through the thirteenth orders it appears that the model gives useful results (even though the grating is still not operating in the true scalar region) and that the measured angular power mode is greater than calculated. Consequently, for the Baseline V estimated grating efficiencies listed in Table 3-9, grating efficiencies for all channels for the third through the sixth order were assumed to be 40 percent, and calculated efficiencies were assumed for all channels in the 8th through the 13th orders. This is believed to be a conservative approach.

Measured efficiencies for R2 gratings under near-Littrow conditions show very high polarization sensitivity for the lower orders. Significant polarization sensitivity exists through the 13th order. For the

AMTS grating angles, polarization effects will probably be greater than those observed under near-Littrow conditions. Ultimately, the AMTS grating will have to be specified by testing a series of sample gratings, including polarization effects, under AMTS orders and angular operating conditions. We have procured several very clean micromachined sample gratings as a part of this study. Resources required to test these gratings under AMTS conditions, however, were not available.

Calculated grating efficiency as a function of grating angle is listed in Table 3-15 for the AMTS spectral alignment channels. For these high orders the grating is operated in the scalar region, and the grating efficiency model should give good results.

Baseline V optical transmissivities common to all channels are listed in Table 3-16. Baseline V spectrometer overall optical transmissivities are summarized in Table 3-17.

3.2 Mechanisms

3.2.1 Optical Chopper

The chopper wheel is located on the foreoptics side of the torodial inlet slit mask. It consists of a segment of a sphere spaced about 0.25 mm from the inlet slit mask along the length of the signal channel inlet slit array. Inlet slit jaws and chopper blades are tapered so that the flat sides of the slit jaws and chopper blades face each other. The axis of rotation of the chopper wheel passes through the center of curvature of the monocentric foreoptics. The wheel chops along the length of the inlet slit array (Fig 3-21). The chopper wheel configuration is shown in Fig 3-27. Reference signals for signal channel demodulation are derived from an optical source and reference detector array. This optical source is chopped by the optical chopper. Chopper wheel parameters are listed in Table 3-18, and chopper motor characteristics are listed in Table 3-19.

The face of the chopper wheel which is viewed by the spectrometer through the inlet slit array is a black emissive surface. The remainder of the wheel, front and back, can be reflective if required for thermal control. Temperature variations of the emissive surface of the chopper wheel must be extremely small over any 24 sec line scan interval. Within these limits, a linear thermal ramp variation is permitted over any 10 min radiometric calibration interval. Temperature of the wheel must always be less than the coldest scene or calibration target. A primary source of background photon flux from within the cold optics compartment is the entrance slit mask. This may place an additional constraint on the maximum permitted temperature of the chopper wheel. Estimated chopper wheel thermal control requirements are:

- Chopper wheel temperature <180 K

Table 3-14 Calculated Baseline V grating efficiencies

			Rel. Eff. (%) vs Antiblaze Angle		
CH	m	β°	$\bar{\phi}$=34°	$\bar{\phi}$=41°	$\bar{\phi}$=42°
1	3	61.137	68.8	45.2	41.0
2	3	55.923	56.1	49.7	62.9
3	3	54.616	51.5	78.3	70.9
4	3	52.868	45.6	86.1	81.5
5	3	49.827	37.2	81.9	88.8
6	3	48.060	33.7	69.5	80.6
7	3	45.677	30.5	51.3	61.3
8	3	45.413	30.3	49.5	59.2
9	3	45.150	30.1	47.8	57.1
10	3	44.890	30.0	46.1	55.0
11	4	47.649	30.6	37.1	41.3
12	5	55.519	31.5	43.0	45.2
13	6	58.137	42.8	44.7	49.4
14	8	57.248	54.7	50.8	51.7
15	8	52.024	71.3	59.8	56.3
16	9	59.027	55.1	48.4	48.6
17	9	57.802	52.5	50.2	50.0
18	9	50.596	52.6	49.0	47.2
19	11	48.997	34.4	41.9	40.9
20	12	65.177	33.8	40.9	40.1
21	11	48.737	34.2	41.2	40.4
22	12	64.747	35.5	42.4	41.7
23	11	48.482	34.2	40.4	39.9
24	12	64.304	37.5	43.7	43.4
25	12	61.478	53.4	49.0	51.1
26	12	55.050	52.0	50.0	49.2
27	13	62.283	51.4	45.9	47.9
28	13	56.918	51.3	50.9	50.3

α (Incident angle) = 71°
$\bar{\phi}$ (Blaze angle) = 64°

Table 3-15 Calculated relative grating efficiency vs grating angle for spectral alignment channels

CH S1			CH S2		
α(°)	β(°)	Rel Eff (%)	α(°)	β(°)	Rel Eff (%)
77.6	47.2359	15.58	67.4	60.1995	73.87
77.7	47.2044	16.10	67.5	60.1224	73.60
77.8	47.1732	16.63	67.6	60.0459	73.28
77.9	47.1422	17.19	67.7	59.9698	72.89
78.0	47.1116	17.78	67.8	59.8942	72.48
78.1	47.0811	18.39	67.9	59.8191	72.08
78.2	47.0510	18.99	68.0	59.7445	71.68
78.3	47.0211	19.55	68.1	59.6704	71.28
78.4	46.9915	20.05	68.2	59.5968	70.89
78.5	46.9622	20.48	68.3	59.5237	70.54
78.6	46.9331	20.84	68.4	59.4510	70.20

Table 3-16 Baseline V spectrometer common element optical transmissivi' es

"Common Elements"	Transmissivity, γ	
	CH 1 - 11	CH 12 - 28
Scan mirror	0.98	0.98
Gas check (KBr 1 pass)	0.92	0.92
Telescope primary	0.98	0.98
Telescope secondary	0.98	0.98
Collimator (1st pass)	0.98	0.98
Corrector lens (1st pass)	0.92	0.92
Grating (mirror loss)	0.97	0.97
Corrector lens (2nd pass)	0.92	0.92
Collimator (2nd pass)	0.98	0.98
Field lens (coated)	0.95	0.95
Immersion lens (coated)	0.95	—
Total (common)	0.62	0.65

Table 3-17 Baseline Y spectrometer overall optical transmissivities

CH	Relative Grating Efficiency	Detector Fill Factor	Transmissivity, γ		
			Common Elements	Order Filters	Overall Instrument
1	0.40	0.86	0.62	0.45	0.10
2	0.40	0.86	0.62	0.45	0.10
3	0.40	0.86	0.62	0.45	0.10
4	0.40	0.86	0.62	0.45	0.10
5	0.40	0.86	0.62	0.45	0.10
6	0.40	0.86	0.62	0.50	0.11
7	0.40	0.86	0.62	0.50	0.11
8	0.40	0.86	0.62	0.50	0.11
9	0.40	0.86	0.62	0.50	0.11
10	0.40	0.86	0.62	0.50	0.11
11	0.40	0.86	0.62	0.60	0.13
12	0.40	0.86	0.65	0.60	0.13
13	0.40	0.86	0.65	0.60	0.13
14	0.52	0.86	0.65	0.60	0.17
15	0.56	0.86	0.65	0.60	0.19
16	0.49	0.86	0.65	0.60	0.16
17	0.50	0.86	0.65	0.60	0.17
18	0.47	0.86	0.65	0.60	0.16
19	0.41	0.86	0.65	0.60	0.14
20	0.40	0.86	0.65	0.60	0.13
21	0.40	0.86	0.65	0.60	0.13
22	0.42	0.86	0.65	0.60	0.14
23	0.40	0.86	0.65	0.60	0.13
24	0.43	0.86	0.65	0.60	0.14
25	0.51	0.86	0.65	0.60	0.17
26	0.49	0.86	0.65	0.60	0.16
27	0.48	0.86	0.65	0.60	0.16
28	0.50	0.86	0.65	0.60	0.17

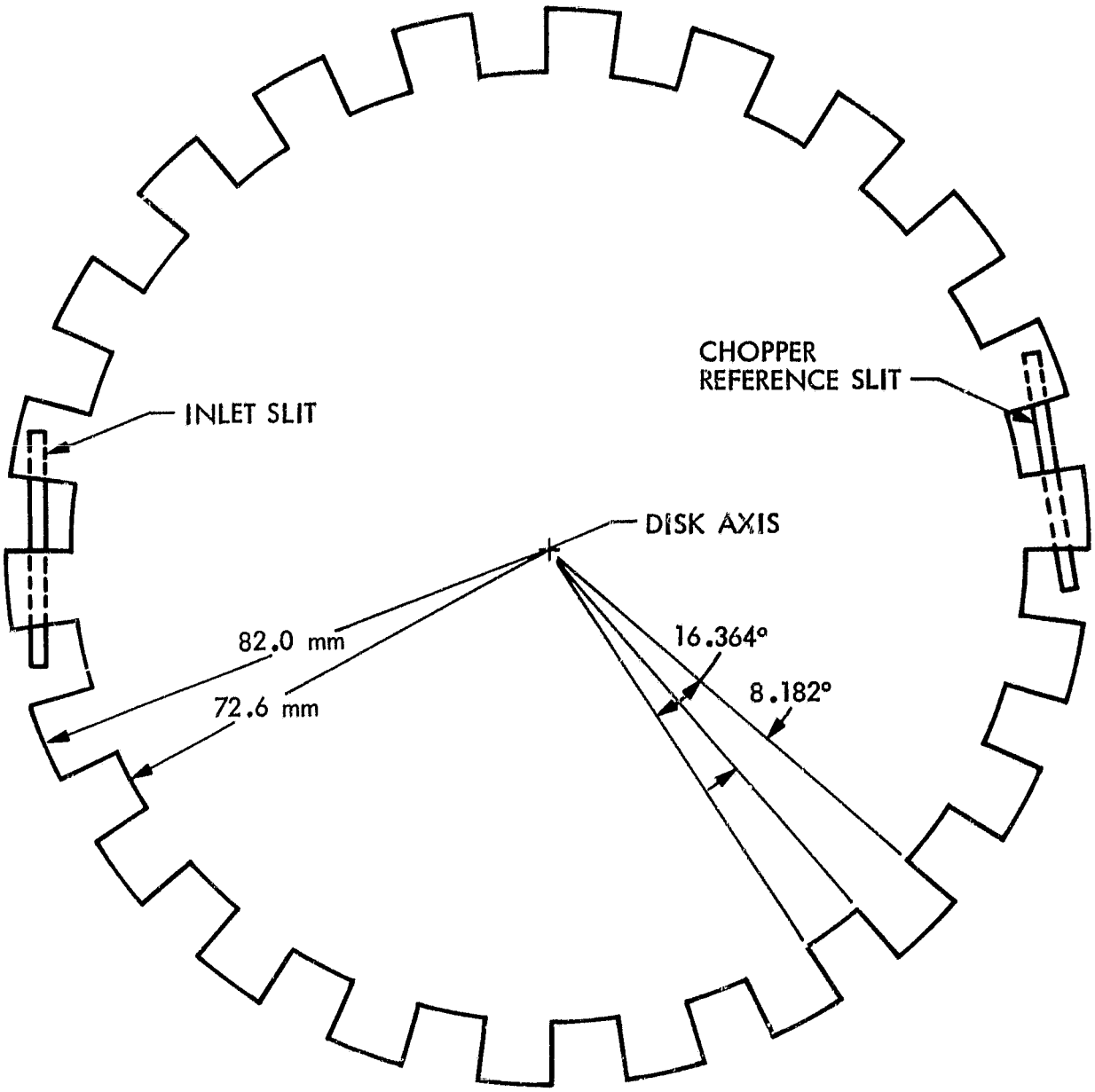

Figure 3-27 Chopper wheel configuration (projected view)

Table 3-18 Chopper wheel parameters

Parameters	Value
Inlet slit mask radius of curvature	
Along spectral axis	600 mm
Along spatial axis	189.26 mm
Chopper wheel spherical radius	189.00 mm
Overall wheel radius (projected)	82 mm
Inner cog radius	74.5 mm
Distance from center of wheel to center of inlet slit array	77.3 mm
Angular cog cycle width (Fig 3-27)	16.364°
Optical cycles per revolution	22
Optical chopper frequency	440 Hz
Chopper wheel speed	1200 rpm
Speed stability - over any 5 min interval	0.025%
Chopper wheel temperature	<185 K
Wheel temperature stability	
Over any 24 sec interval	±.01 K
Nonlinearity over any 10 min interval	0.135%
Long term	±2 K

Table 3-19 Chopper motor characteristics

Parameter	Value
Type	Hysteresis synchronous
No. phases	4
Input voltage	26/32 Vac
Input frequency	400 Hz
Input waveform	square wave
Maximum current	0.5 amp
Stall torque	36 cm-g (0.5 in-oz)
Speed	1200 ±0.3 rpm
Weight	≈28 g (≈10 oz)
Life - continuous operation	5 years
Operating temperature	-18 to 38°C
Bearings	Polyimide, self-lubricating

- Chopper wheel temperature stability (PP)
  - Over any 24 sec. interval ±0.01 K
  - Nonlinearity over any 10 min interval 0.135 %
  - Long term ±2 K

Passive temperature control of the chopper wheel can be achieved by:

- Thermal isolation of the chopper wheel from the motor shaft
- Thermal mass of the wheel
- A reflective surface on the inlet side of the wheel
- Masking ahead of the wheel with a large thermal mass

The chopper motor is placed outside the cooled optics compartment with the motor shaft passing through the compartment wall. A "turbine" type gas check is used on the motor shaft to inhibit contamination from entering the cooled optics case. This allows additional lubricants to be used for quieter motor bearing operation. Motor temperature can be controlled separately from cold case temperature to obtain near optimum bearing operating temperatures.

3.2.2 Spatial Scan Mechanism

For an 833 km altitude circular orbit, mean ground velocity of the subsatellite point is 6.5812 km/sec. For a mean IFOV array length of 160 km, total line scan cycle time is 24.3117 sec. The crosstrack scan mirror sequence is shown in Fig 3-28. A single line scan views 130 earth footprint arrays in a step-and-stare mode. The scan mirror then does a fast slew to the first calibration target, followed by a fast slew to the second calibration target, followed by a fast slew to the start of the next line scan position. Dwell times for each earth target and for each calibration target are identical. In addition, all fast slew angles and times are identical.

The rotating 45 degree plane scan mirror is a lightweight beryllium structure. The mirror is contained within a combination light shield and cylindrical thermal shield which rotates with the mirror. The mirror assembly is driven by a permanent magnet stepper motor through a 60:1 reduction gear drive. During each earth scan sequence step the motor is driven through 11 motor steps at a rate of 500 steps/sec. For the three fast slew sequences the motor step rate is ramped-up and ramped-down at an average rate of 1000 steps/sec.

Table 3-20 gives the mechanical specifications and performance of the scan system. The power dissipated is by the actuator and encoder only, not including any control electronics. The position tolerance and

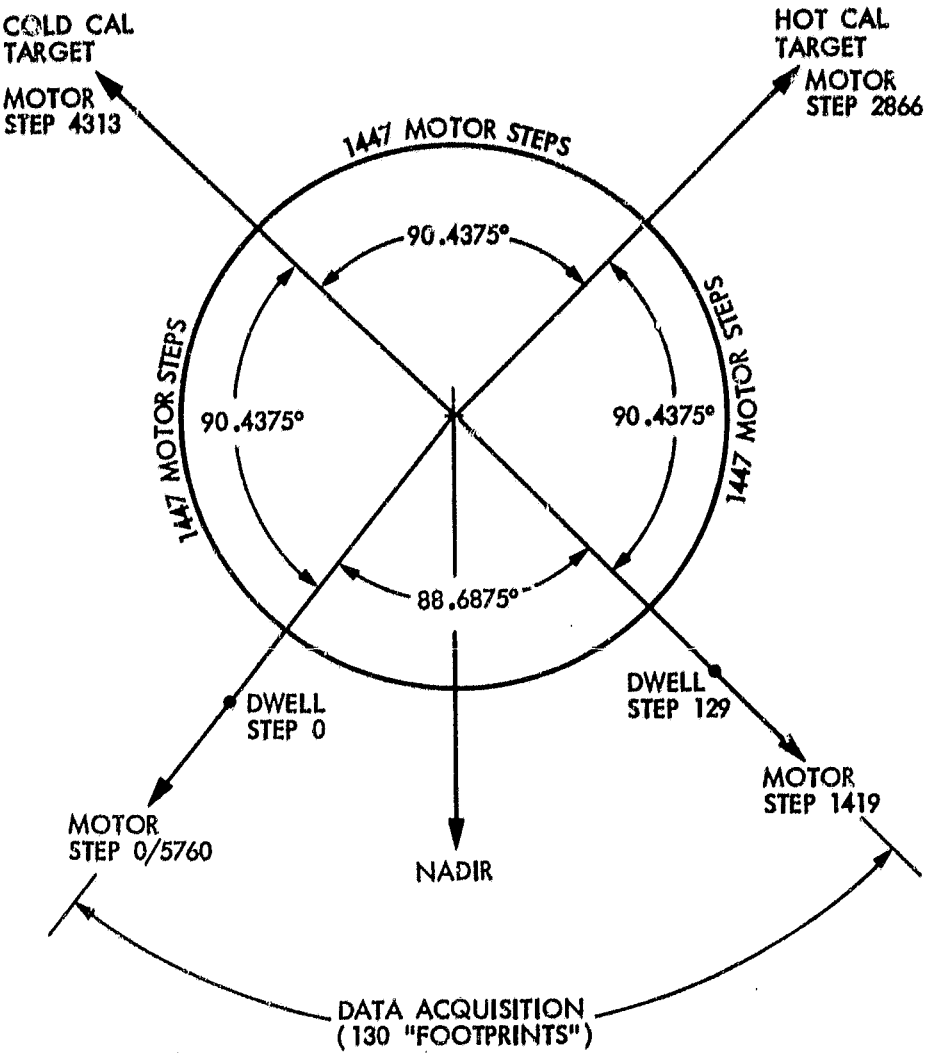

SCAN SEQUENCE	DURATION
• START OF LINE SCAN	
• 129 STEPS OF 0.6875°/STEP STEP TIME = 0.0245 sec/STEP DWELL TIME = 0.1273 sec/DWELL	19.7095 sec
• SLEW TO HOT CAL TARGET SLEW TIME = 1.4492 sec DWELL TIME = 0.1273 sec	1.5765 sec
• SLEW TO COLD CAL TARGET SLEW TIME = 1.4492 sec DWELL TIME = 0.1273 sec	1.5765 sec
• SLEW TO START OF LINE SCAN SLEW TIME = 1.4492 sec	1.4492 sec
	TOTAL CYCLE TIME - 24.3117 sec

Figure 3-28 Crosstrack scan mirror sequence

initial overshoot should be considered absolute maximums, while the position knowledge can be as gross or fine as necessary. Assumed here is a 0.5° knowledge encoder integral with the actuator and fixed to the motor shaft for finer resolution on the output. The actual mirror position knowledge would be a slightly greater value due to compliance in the harmonic gear drive. The settling time for the system is not given since it depends greatly on the specific motor and control electronics used (for electronic damping) and the amount of friction in the system. However, some damping is inherent in permanent magnet stepper motors, and electronic damping would be built into the control electronics. Figure 3-29 shows the conceptual design of the scan mirror assembly. The entire scan system is held by a mounting plate which supports the actuator and the rotating light shield and mirror. The light baffle allows the bearing support structure to penetrate close to the C.G. of the moving mass. Not shown is the integral encoder, which would increase the 75 mm reference dimension to approximately 120 mm. The permanent magnet actuator allows unenergized dwell positioning during testing. The encoder allows absolute position knowledge without counting steps or using feedback control, plus the necessary position knowledge after launch but before sequencing.

3.2.3 Grating Mount

Grating angle sensitivity corresponding to channel frequency knowledge requirements, channel frequency setability requirements, and to twice the specified channel half-power bandwidth are listed in Table 3-21 for the two end channels--10 and 20--and for an intermediate channel--13. The grating mount will include a mechanism which, in response to ground commands, will:

- Move the grating angle a specified number of steps to correct for channel frequency error.
- Rock the grating over a specified angular range in accordance with an on-board program to update calibration of the spectral monitoring circuit.

This mechanism will have the capability of changing the grating angle in 5 arc-sec increments over a total range of 150 increments. A telemetry sensor will indicate the grating actuator position in terms of step number. The mechanism controlling grating angle must not creep between command events--which will probably be very infrequent. It will probably be necessary to cage the grating mount assembly during launch of the satellite.

A detailed conceptual design of this mechanism was not undertaken, since it is expected that it will not present any special design difficulty.

3.2.4 Cooler Cover

A mechanism is required which is capable of repeatedly activating a roller-shade type radiative cooler cover upon ground command (Para 3.3.1 and 3.3.6). A detailed conceptual design for this mechanism was not undertaken. It is expected that it will not present any special design difficulty.

Table 3-20 AMTS scan mirror system parameters

Parameter	Value	
Total moving mass	1.64 kg	(3.61 lbs)
Moment of inertia	.024 kg-m^2	(82.27 lb-in^2)
Total nonmoving mass	1.48 kg	(3.26 lbs)
Power dissipated (incl. encoder)	7 watts	
Motor step size	3.75°	(65.45 mrad)
Actuator output step size	.0625°	(12.00 mrad)
Position tolerance (noncumulative)	<.012°	(.20 mrad)
Mirror position knowledge (1/2° knowledge encoder on motor shaft)	±.008°	(±.15 mrad)
Ringing (initial overshoot)	<.012° or less than 3.5% of dwell step	(.20 mrad)
Natural ringing frequency of system	18.9 Hz	

3.3 Optics Assembly Packaging, Cooling, and Contamination Control

3.3.1 Package Description

The Baseline V optics assembly package layout is shown in Fig 3-30 (page 3-107). All optical components are contained in a compartment cooled to ≈160 K to control background flux upon the short wavelength detectors. The detector cryostat is contained within this cold optics compartment. Design temperature for the cryostat is 75 K to improve D* performance of the long wavelength detectors. Passive radiative coolers are used to cool the instrument.

A single stage case cooler is thermally and mechanically coupled directly to the cooled optics case. The first stage of a three stage detector cooler is also thermally and mechanically coupled directly to the cooled optics case. The cold stage of the detector cooler is thermally coupled to the detector cryostat via a heat pipe. A single bend in the heat pipe allows the instrument to be oriented so that this heat pipe lies in a horizontal plane. This allows testing the radiative cooler and instrument assembly in a thermal test chamber within the earth's gravitational field. Sun shields are designed so that direct sunlight never falls within the aperture of the radiative cooler. (Sun angles for the Baseline V orbit are presented in Appendix E.) The detector cooler angle is chosen so that radiation from the earth does not fall upon the cooler emissive surfaces. Radiation from the earth that falls upon the specular surfaces of the cooler is reflected out of the cooler aperture. Outer surfaces of the optics case and of the radiative cooler are thermally insulated with MLI.

The portion of the case containing the detector cryostat, the spectrometer optics, and the foreoptics telescope is effectively sealed to control contamination of the cold cryostat optics. This portion of the case is isolated from the scan mirror compartment. The optical ray bundle enters through a KBr gas check. An outgassing port for this sealed compartment is provided through the tunnel through which the heat pipe enters the compartment. When the instrument is cooled down, the cold heat pipe tunnel assembly constitutes a cold trap for external contaminants. The chopper motor, which runs continuously, is located outside the sealed compartment in a well which projects into the sealed compartment. Contaminant flow into the sealed compartment along the chopper motor shaft is blocked by a "turbine" type noncontacting gas check. Isolation of the chopper motor from the cold optics compartment removes the major portion of the motor heat load from the case cooler, and allows temperature control and lubrication of the motor to be optimized for bearing life. The grating angle activator is operated intermittently and infrequently; consequently, it need not present a serious thermal or contamination design problem.

The scan mirror compartment contains the rotating 45° scan mirror, its associated rotating light and thermal shield, and its drive motor assembly. In addition, this compartment contains the two radiometric calibration targets. The temperatures of both the hot and cold targets are above the ambient temperature of the scan mirror compartment.

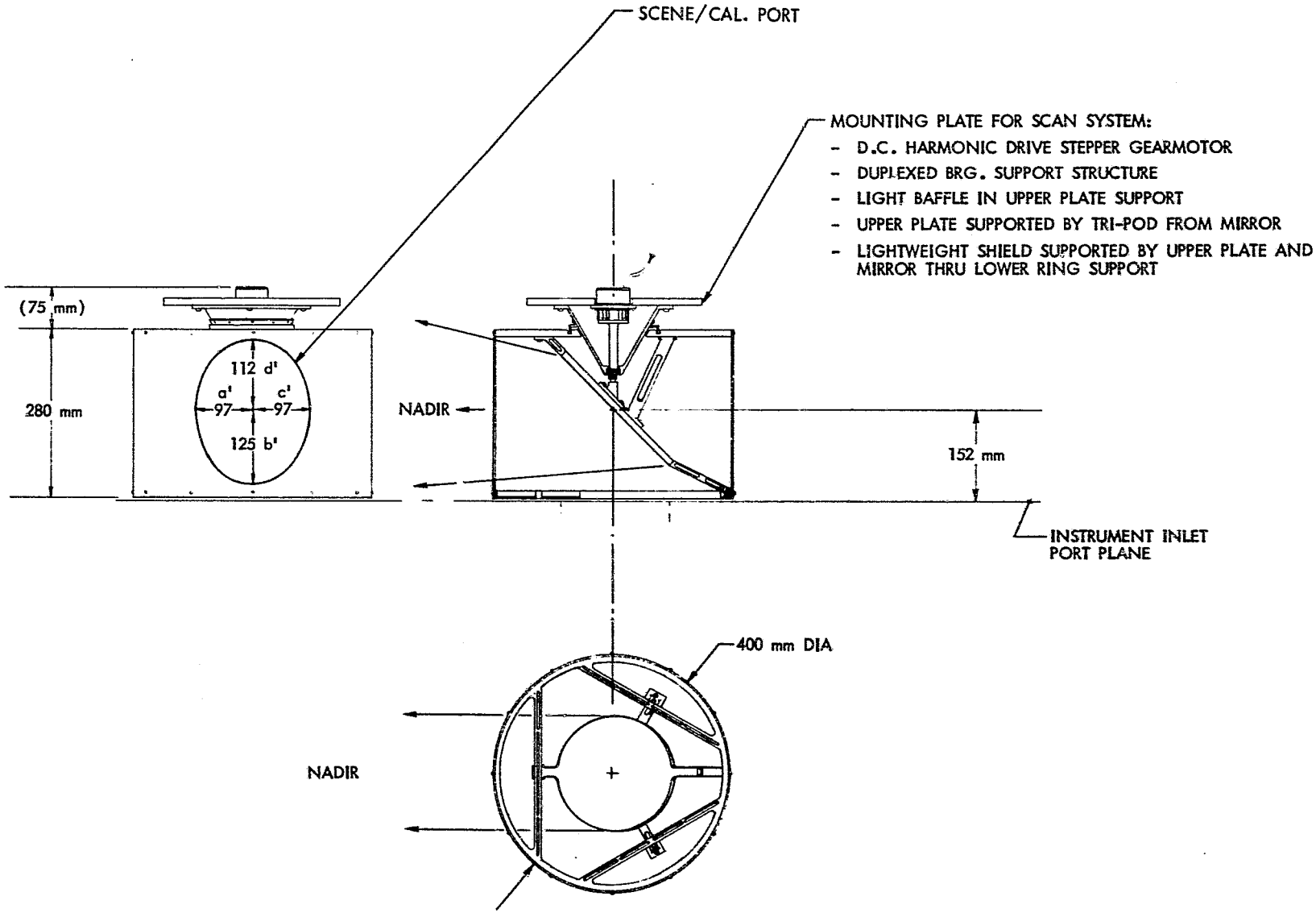

Figure 3-29 Scan mirror assembly

Table 3-21 Grating angle sensitivity corresponding to channel frequency knowledge, channel frequency setability, and twice channel bandwidth requirements

Parameter	Angle Sensitivity ~Δ	
Channel 10		
• Knowledge	0.00140°	5.04 arc sec
• Setability	0.00685°	24.66 arc sec
• 2 $\Delta\upsilon(cm^{-1})$	0.13620°	490.32 arc sec
Channel 13		
• Knowledge	0.00182°	6.55 arc sec
• Setability	0.00905°	32.58 arc sec
• 2 $\Delta\upsilon(cm^{-1})$	0.19480°	701.28 arc sec
Channel 20		
• Knowledge	0.00210°	7.56 arc sec
• Setability	0.01070°	38.52 arc sec
• 2 $\Delta\upsilon(cm^{-1})$	0.23720°	853.92 arc sec

$$\frac{\sin(\alpha + \Delta) + \sin(\beta + \Delta)}{\sin\alpha + \sin\beta} = \frac{\nu}{\nu - \Delta\nu'}$$

$\Delta\nu'$ = frequency increment of interest

The calibration targets are thermally insulated, and their internal temperature is controlled by heaters located within their thermal envelopes. The scan activator assembly temperature can be effectively controlled by thermal isolation from the cold case and through thermal coupling to an exterior, uninsulated surface. Two sun shields are provided to prevent direct sunlight from falling within the rotating light shield of the scan mirror (Appendix E).

A roller-shade-type thermal cover for the cooler aperture, actuated by ground command, is provided to prevent cool down of the instrument during an initial on-orbit decontamination interval and during possible subsequent decontamination intervals. The cooler cover is not pictured in Fig 3-30. Also not pictured are the thermal isolation mounts required to mount the optics case assembly to the spacecraft.

3.3.2 Detector Cryostat Assembly

A layout for the detector cryostat and heat pipe assembly is shown in Fig 3-31. The cryostat consists of a cryostat case operating at the temperature of the cold optics case, an intermediate reflective thermal shield supported within the cryostat case by thermal isolation supports, and a detector box assembly positioned within the intermediate shield and supported from the cryostat case by thermal isolation support bands. The detector box assembly is thermally coupled to the detector cooler heat pipe cold sink via flexible heat straps. Active heaters (not shown in Fig 3-31) within the detector box assembly control detector temperature. The temperature of the intermediate thermal shield is allowed to float. Detector preamplifiers are located on a preamplifier board which is mounted on the back of the cryostat case. Preamplifiers operate at the cold case temperature of 160 K. The preamplifier board is electrically interconnected with the detectors within the detector box assembly via high thermal impedance conductor assemblies. The front surface of the image plane mask between order filter assemblies is thermally reflective to reduce optical port thermal loading upon the detector cryostat. To reduce heat flow into the cryostat, the inner and outer surfaces of the cryostat case, the intermediate thermal shield, and the outer surface of the detector box are thermally reflective. The detector lead conduit assembly and the back surface of the preamp board are also thermally reflective. Detector lead conduits are thermally connected to the detector box only at the detector mounting plate.

The detector cryostat assembly is designed to be assembled, aligned, and bench tested as a unit apart from the optics assembly. Prior to installation of the heat pipe, the cryostat assembly would be installed within the optical bench of the optics assembly. It would be aligned as a unit as a part of overall optical assembly alignment. Access covers in the bottom of the optics case, the cryostat case, and the intermediate thermal shield provide access for installation of the heat pipe.

The heat pipe from the detector cooler cold stage passes through a dual wall tunnel to enter the detector cryostat. The outer wall of this tunnel is sealed against the outer wall of the optics case and operates at case temperature. There is no mechanical contact between the

end of the outer tunnel wall and the cryostat case. The inner wall of the tunnel is thermally coupled to the intermediate stage of the detector cooler. It passes through the outer tunnel to the intermediate thermal shield of the cryostat, but does not make contact with the cryostat. A gas check is used between inner and outer tunnel walls to prevent contaminant flow into the cooled optics case. The heat pipe is thermally coupled to the cold stage of the detector cooler and passes through the inner tunnel. The heat pipe is thermally coupled to the detector box assembly through heat straps distributed along the length of the heat pipe within the detector cryostat. All surfaces of the heat pipe and heat pipe tunnel assemblies within the cold optics case are thermally reflective. The heat pipe is supported by its attachment to the detector cooler cold stage and by thermal isolation support bands within the detector cryostat. The space between the inner tunnel wall and the heat pipe forms the outgassing port for the sealed portion of the cold optics case, and is a cold trap for contaminants entering this cold optics compartment.

The individual discrete detectors on their substrates are mounted upon a thermally stable detector mounting plate. Immersion lenses, where used, are mounted upon the detector and its substrate. The image plane mask is mounted ahead of the detectors. The field lenses are mounted upon the back of the image plane mask. (If necessary, stray light shields could be mounted upon the back of the image plane mask to enclose each individual field lens, immersion lens, and detector assembly.)

A twisted pair of 36 gauge low thermal conductance manganin wires is used to connect each detector with its preamplifier, which is located outside the detector cryostat. An individual tubular conduit having an outside diameter of 1.0 mm is used to shield and support each pair of manganin conductors. These conduits are formed of 0.025 mm (0.001 in.) thick titanium foil and have very low thermal conductance. The end of each conduit fits within a hole in the detector mounting plate. From the detector substrate the manganin leads pass through the detector mounting plate and conduit, through ports in the intermediate thermal shield and outer case of the detector cryostat, and through the preamplifer support board. (An alternate design approach would use very low thermal conductance kapton substrate ribbon conductors between the detector mounting plate and the detector preamplifiers. This approach may offer thermal and cost advantages. Issues of possible EMI and repair accessibility would have to be considered.)

The detector cryostat is designed to allow access to the detector assembly for repair purposes once the cryostat assembly has been removed from the optics case. After removal of front plates from the outer case and from the intermediate shield of the cryostat, the image plane mask can be removed to allow access to the detectors mounted upon the detector plate. Alignment pins are used to maintain repeatable alignment between the image plane mask and the detector assembly.

The spatial discriminator array detectors are mounted upon the image plane mask, and their relative positions with respect to the IR channel slits are accurately mapped. Signal leads from these detectors can leave the image plane mask via a hinge joint to allow displacement of the mask for repair purposes.

ORIGINAL PAGE IS
OF POOR QUALITY

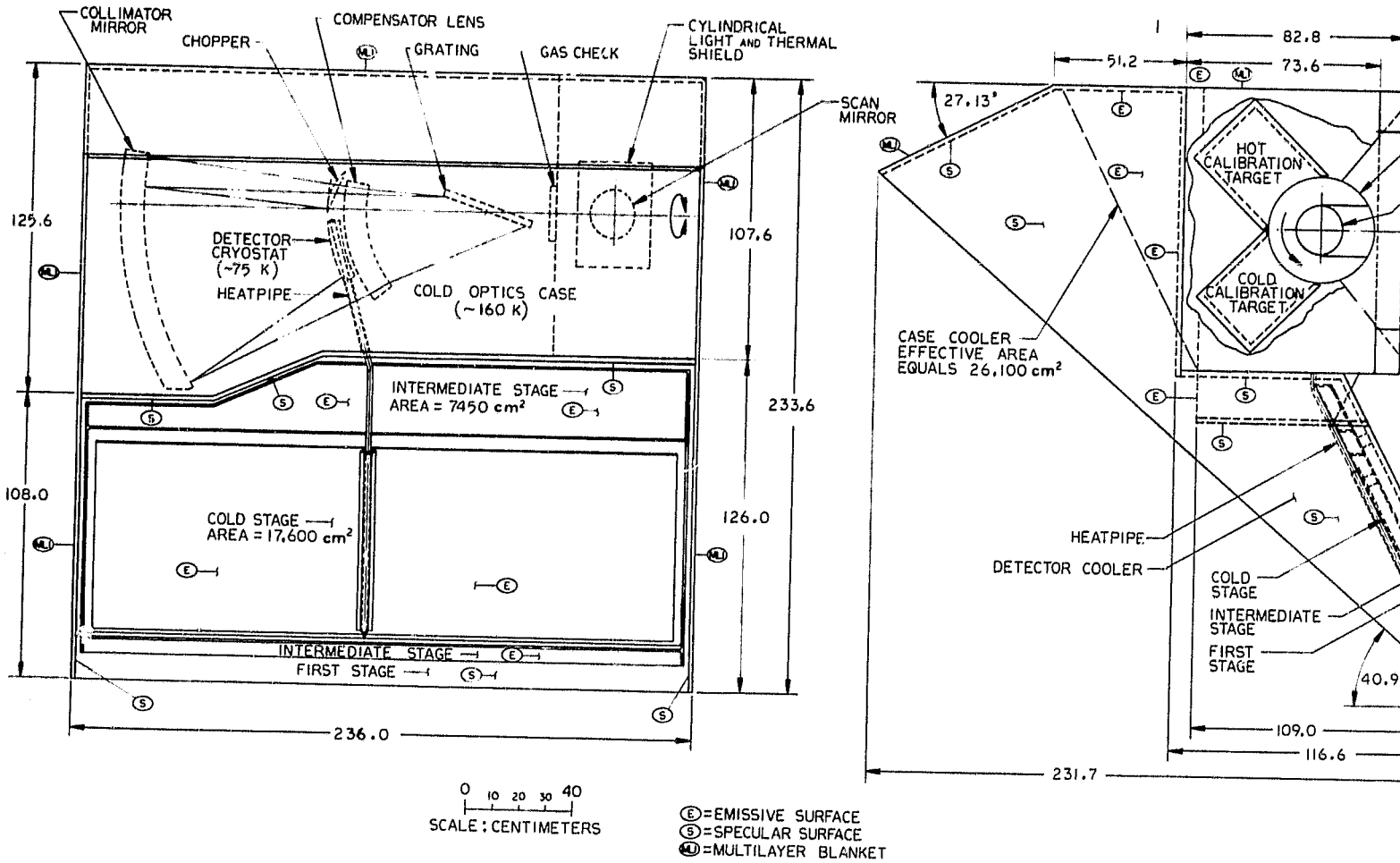

FOLDOUT FRAME

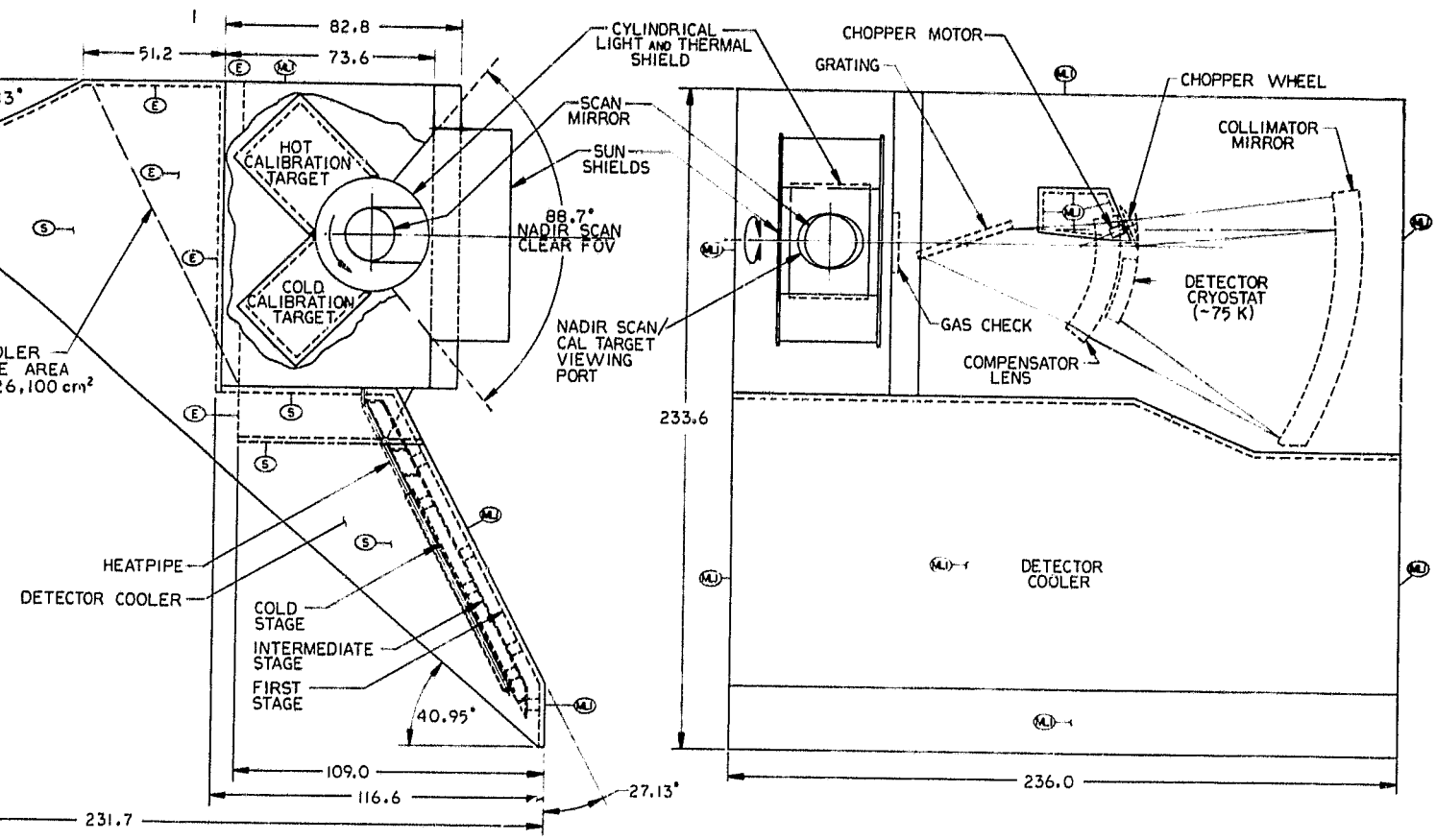

2 FOLDOUT FRAME

Figure 3-30 Baseline V radiative cooler and optical assembly

Page intentionally left blank

ORIGINAL PAGE IS
OF POOR QUALITY

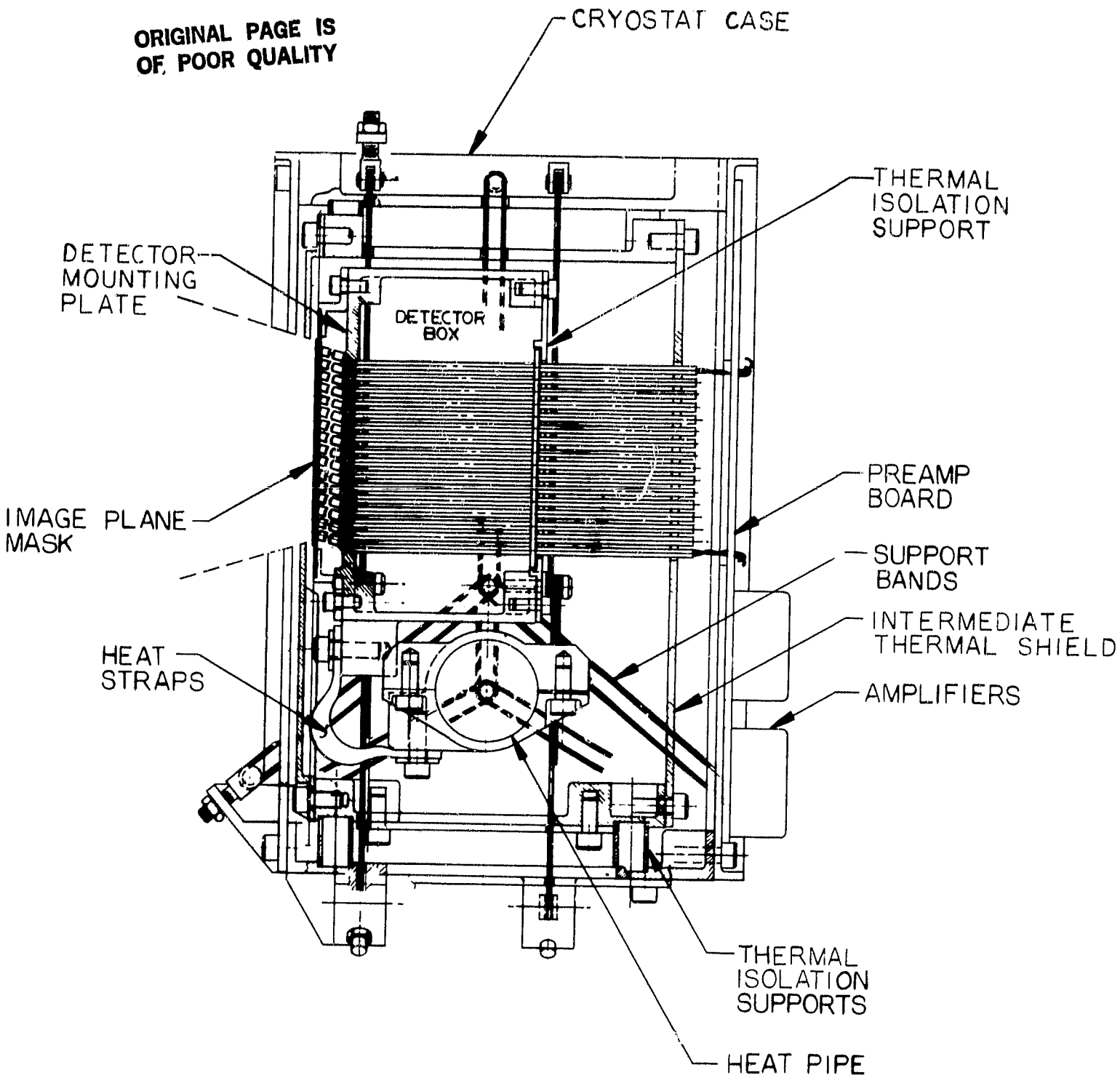

SECTION A-A

FOLDOUT FRAME

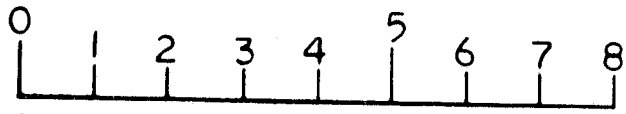

STAT CASE

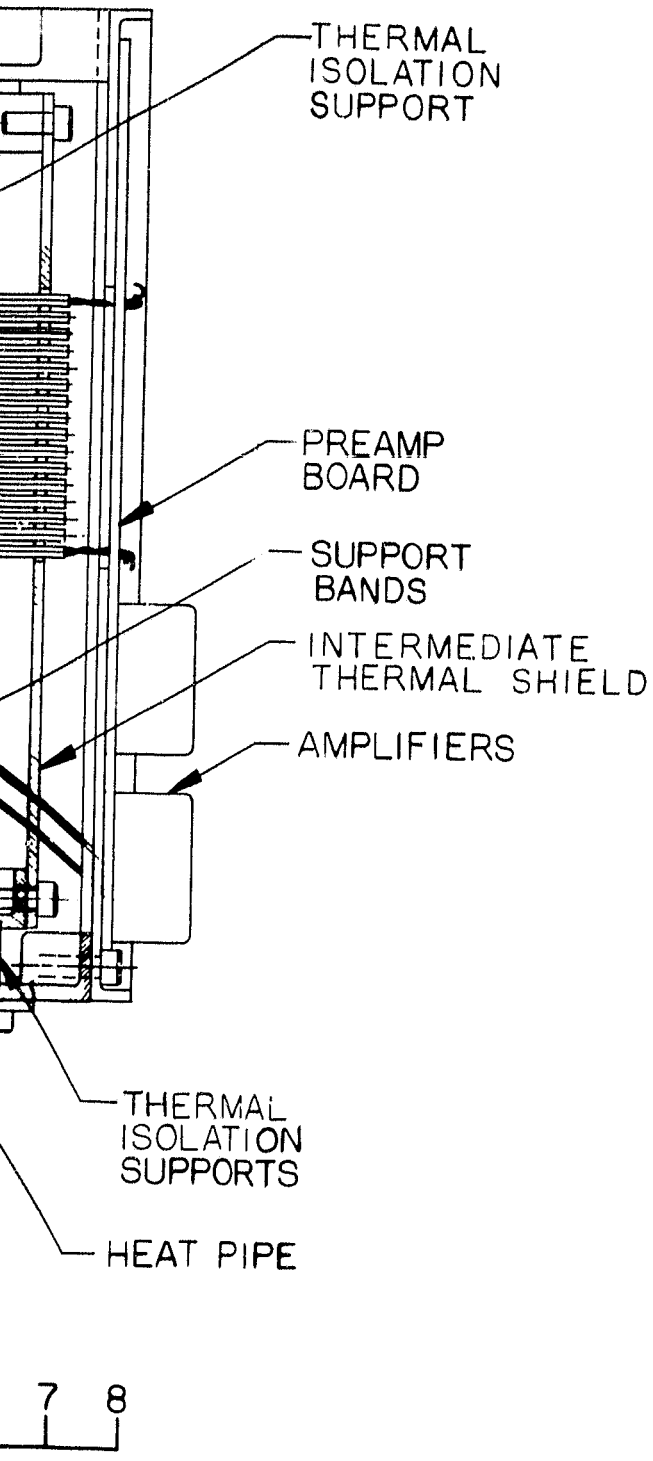

7 8

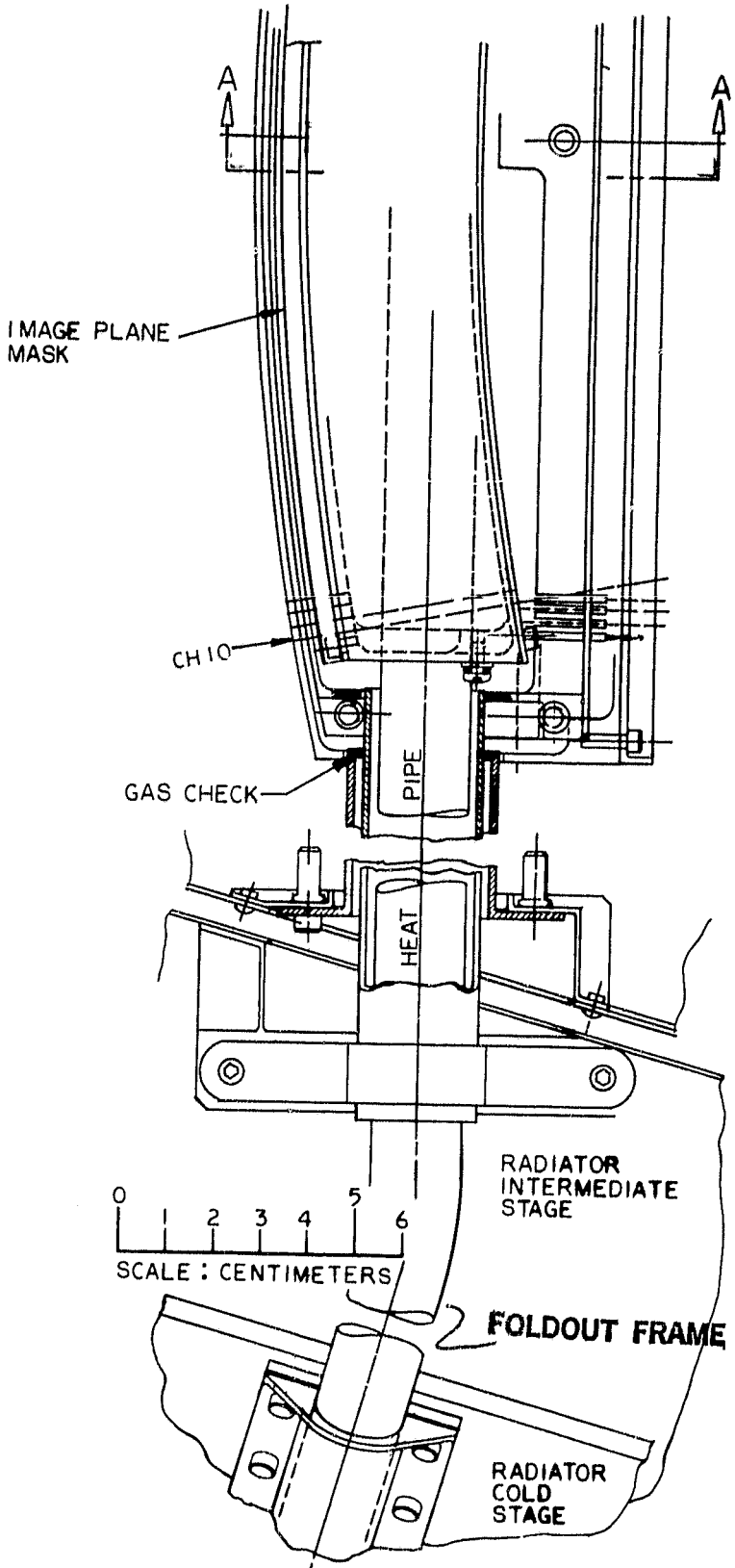

Figure 3-31 Baseline V detector cryostat and heat pipe assembly

Page intentionally left blank

Estimated joule heat loading within the detector cryostat—apart from the thermal control heaters—is:

- PC detector bias (176 detectors) 0.0367 W

Estimated cryostat thermal control requirements are:

- Detector temperature (nominal) 75 K
- Detector temperature stability (PP)
  - Over any 24 sec interval 0.05 K
  - Nonlinearity over any 10 minute interval 1.67 %
  - Long term ±2 K

It is not necessary that all detectors operate at exactly the same temperature. It is important, however, that the detector operating temperatures be stable. It is assumed that active thermal control of detector temperature using a proportional control loop will be required. Short term detector temperature variations will result in radiometric errors. Long term variations could require excessive dynamic range in the signal channel electronics.

3.3.3 Radiometric Calibration Targets

The two calibration targets are a matched pair, as far as their emitter surfaces, thermal baseplates, and scan angles with respect to grating alignment are concerned. The hot target runs at a temperature of ≈310 K; the cold target runs at ≈200 K. The absolute temperatures selected for these targets are not particularly critical but the spatial and temporal constancy of these temperatures is extremely critical. The targets consist of thick copper baseplates, both on the bottoms and sides of the targets. The internal surfaces consist of hexagonal copper cellular structures painted with 3M black velvet. Temperature sensors and heater elements are buried in the copper baseplates, on both bottoms and sides. The baseplates consist of a number of zones, each with its own sensor and heater. One bottom zone will be designated the absolute temperature control zone. Over-damped, proportionally controlled thermal control loops will be used to control zone temperatures relative to the reference zone temperature. Relative time constants of these control loops will be adjusted to maintain stable thermal control of the overall calibration target temperatures.

The effective radiance from the calibration target consists of the thermal blackbody radiance plus the scattered radiance from the blackbody surface from external sources—in this case from the sides of the blackbody target and from the scan mirror and its baffles. Radiometric precision requires that the total effective radiance per unit area from the bottom of the calibration target be constant over the target surface vs time. It also requires a constant temperature over the bottom of the calibration target. It requires that the temperature of the sides of the target be constant and close to that of the bottom and that the temperature of the scan mirror and its shield and baffle assembly remain relatively constant.

A cylindrical reflective thermal shield surrounds the scan mirror assembly and rotates with it. This shield minimizes variations in the temperature of the scan case--and scan mirror--due to variations in earth thermal radiation and albedo. It also stabilizes the calibration target effective surface temperature by minimizing radiative transfer between the target surfaces and the scan case components and the earth. Calibration target parameters and thermal requirements are listed in Table 3-22.

3.3.4 Optical Components

All mirror surfaces and the diffraction grating surface would be gold coated to maximize overall instrument optical transmissivity. The scan mirror would be a lightweight beryllium structure in order to minimize the moment of inertia of the scan assembly. For purposes of instrument weight estimates, all fixed mirrors are assumed to be machined beryllium assemblies. (Lightweight glass mirrors could also be used, and may be desirable in terms of cost and optical performance.)

The diffraction grating would be replicated onto a thermally stable "cer-vit" substrate. The grating would be ruled to have the design groove spacing at nominal case operating temperature.

The inlet slit mask and the image plane mask would use kovar from a selected heat which has a linear thermal coefficient of contraction down to 70 K. These masks would be etched to have the correct relative slit positions at their nominal design operating temperatures.

Sharp cutoff multilayer interference filters on a 0.635 mm (0.025 in.) thick germanium substrate would be used for the order filters. Since these filters are mounted flat against the front surface of the image plane mask, the center rays of the off axis converging ray bundles impinge upon the filters at an incident angle of 16.5 degrees. These ray angles must be taken into account when specifying filter spectral response requirements. Individual filters for each array element can be cut to size with a tolerance of ±0.025 mm (±0.001 in.). In addition, guard bands 0.127 mm (0.005 in.) wide for the long wavelength filters and 0.076 mm (0.003 in.) wide for the short wavelength filters must be provided along all filter edges to stay clear of cutting damage to the filter coatings. These filter tolerances place a lower limit upon the inlet slit array premask widths between array elements.

Germanium field lenses and (where used) germanium immersion lenses would be AR coated for the appropriate channel wavelength. At the immersion interface, both the immersion lens and the detector surface coatings should be designed to minimize reflections for the particular index ($\approx$1.5) of the immersion cement used. Incident ray angles upon the detector are minimized by using large immersion lens radii.

Because of the 4.5:1 wavelength range in the ray bundles incident upon the KBr corrector lens and gas check, these elements would not be coated. This will necessitate a humidity controlled environment for the instrument when it is within the earth's atmosphere. It is assumed that the corrector lens would be forged from a blank of KBr, primarily to obtain the improved mechanical properties that forging imparts to this material.

Table 3-22 Baseline V calibration target parameters and thermal requirements

Parameter	Value
Inside diameter	252 mm
Inside length (over scan cylinder)	173 mm
Honeycomb depth (sides)	13.5 mm
Honeycomb depth (bottom)	13.5 mm
Baseplate thickness (sides)	6.5 mm
Baseplate thickness (bottom)	9.5 mm
Insulation thickness	(as required)
Estimated (thermal) emissivity	0.998
Temperature uniformity, PP (bottom)	±0.10 K
Temperature stabilty, PP (bottom)	±0.05 K
Temperature uniformity, PP (sides)	(TBD) K
Temperature stability, PP (sides)	(TBD) K
Temperature stabilty of scan mirror/shield assembly, PP (for assumed nominal temperature of ~180 K)	
Over any 24 sec interval	(TBD) K
Nonlinearity over any 10 min interval	(TBD) %
Long term	±5 K

For the purpose of instrument weight estimates, a built-up beryllium structure was assumed for the optical bench. Other approaches--compatible with contamination control requirements--can be used for the optical bench, and from a cost basis they are probably desirable. Specifications of optical element surface tolerances and alignment requirements and detail conceptual design of the optical bench are tasks that were beyond the scope of available study resources. A preliminary look at performance sensitivity to optical element alignment, however, indicated that optical bench requirements for this instrument are relatively benign.

3.3.5 Radiative Cooler

The low temperature requirements, relatively low orbit, and large heat load present a challenge to radiative cooling, but one that is achievable with a large radiative cooler of an efficient design such as has been developed under military contracts (Ref 3-3). Radiative coolers are shown in the optics assembly layout of Fig 3-30.

3.3.5.1 Optics Case/Scan Mirror Compartment Cooling

Multilayer blanketing covers all outside surfaces of the instrument which do not face cold space, namely those facing spacecraft, earth and sun. The outside of the blanket is covered with Betacloth for high emittance and low solar absorptivity, 0.85 and 0.36 respectively, as well as low degradation under solar radiation. Conductive isolation from the spacecraft is achieved by the use of a truss of boron-epoxy composite struts sized for Shuttle dynamic launch loads. These are chosen for their combination of good mechanical properties and low thermal conductance. The top part of the optics case is shielded from the sun so that it sees only space. It is painted with a high emittance black paint. Using the entire top of the optics case for radiation results in an optics case effective radiator area of 26,100 cm^2.

The total heat load is made up of internal heat generation, conduction from the spacecraft, and radiation from the spacecraft, sun, earth IR and albedo. Conduction is made up from cables, of which there are approximately 1200 electrical conductors, and boron-epoxy supports. The boron-epoxy support structure to the spacecraft has a conductance of 9.3×10^{-3} W/K. For orbital heating, the following parameters were used: altitude of 833 km; 8:30 am or 3:30 pm sun synchronous orbit having an inclination of 98.8°. These parameters and the outside surfaces were used in LOHARP (Lockheed Orbital Heat Rate Program) to determine the average heating and the resulting temperature for the outside surfaces of the Betacloth. Heat loads to the optics case/scan mirror radiator are listed in Table 3-23.

Heat loads listed are based on the case design temperature of 160 K. The entire surface of the optics case/scan mirror compartment and all components thermally tied to it are assumed to be at the same temperature. The energy balance on the optics case/scan mirror predicts an uncontrolled equilibrium temperature of 158.1 K, assuming a radiator emittance of 0.85. This emittance value may easily be achieved with a simple

Table 3-23 Heat loads to optics case/scan mirror radiator[1]

Source	Heat Load (W)
1. Solar, albedo, planetshine transmitted through MLI (orbit average)	29.6
2. Calibration targets	4.2
3. Scan mirror motor	7.0
4. Chopper motor	5.0
5. Detector preamplifiers	5.0
6. Cable conduction from spacecraft	13.3
7. Support conduction from spacecraft	1.23
8. Radiation from spacecraft	5.0
9. Albedo, planetshine transmitted through optics	6.12
10. Scattered albedo + planetshine	0.90
	77.35 W

[1]Determined using T_{case} = 160 K

painted surface. A better radiator surface, similar to the intermediate and cold stage radiators, can provide an emittance of 0.95. The energy balance indicates that an uncontrolled equilibrium temperature of 154.1 K results with this higher radiator emittance. Table 3-24 shows the sensitivity of the optics case/scan mirror temperature to net heat input for radiator surface emittances of 0.85 and 0.95. They indicate that a substantial margin for growth of the heat loads may occur (≈15 W) before the design temperature is reached, using the present size of case cooler radiator and higher emittance value. Conversely, if more detailed preliminary analysis indicates insufficient heat loads to reach 160 K, the size of the effective case cooler may be decreased.

Incentives to thermally couple the scan mirror compartment and optics case include simplification of design and less variation over time of orbital heat loads to the case. Further, the scan mirror compartment temperature will be lower than both calibration targets, permitting simple and precise calibration target temperature control through heat addition alone. Calibration target temperatures may be achieved with the addition of 3 to 5 watts of heat in the steady state. The scan mirror motor should be operated at ≈300 K to achieve the long (5-year) lifetime goal. Room temperature operation of the motor may be achieved using its own power dissipation alone by proper combination of the design of its outer surface radiative properties and thermal contact to the compartment. High motor temperatures would result from enclosure within an MLI blanket and thermal conductive isolation from the compartment; low temperature operation would result from a high emittance on the outer surface and close thermal coupling to the compartment. Fine tuning of the motor temperature can thus be easily accomplished when its size, actual power dissipation, and desired operating temperature are more precisely known. Similar temperature control techniques may be employed with the chopper motor. Note that only 5 watts dissipated within the chopper motor are added in the Table 3-23 heat loads to the compartment, although up to 15 watts may be the actual motor dissipation. This is because the chopper motor is envisioned as mounted within a well in the compartment, with some heat loss directly to space.

This study has focused on temperature levels only, not on thermal gradients within the optical bench which could cause misalignment. When future study determines allowable and actual temperature gradients, then heaters (or heat pipes) may be placed in the colder parts of the instrument to equalize temperatures within the optics case. Since the outside of the case is covered with insulation except where it sees only space and because of its large mass, changes in temperature from one part of the orbit to another should be quite small.

3.3.5.2 Detector Radiative Cooler

The detector radiative cooler shown in Fig 3-30 is a two-stage design with a shielding system designed to protect it from solar and earth loads during every part of the orbit throughout the mission. The intermediate stage has 7450 cm^2 of radiative area; the cold stage 17,600 cm^2. The intermediate stage is supported off the optics case by low conductance fiberglass-epoxy tube supports as is the cold stage off the intermediate

Table 3-24 Optics case/scan mirror temperature sensitivity to net radiator heat loads[1]

	Temperature (K)	
Heat Load (W)	ε = .85	ε = .95
40.0	133.5	129.9
45.0	137.5	133.8
50.0	141.2	137.3
55.0	144.6	140.6
60.0	147.8	143.7
65.0	150.8	146.6
70.0	153.6	149.4
75.0	156.3	152.0
80.0	158.8	154.4
85.0	161.2	156.8
90.0	163.5	159.1
95.0	165.7	161.2
100.0	167.9	163.3

[1]Determined by steady state energy balance:

$$q = \sigma \varepsilon A_c T_c^4$$

where q = heat load (W)

σ = Stefan Boltzman constant = $5.67 \times 10^{-8} \left(\frac{W}{m^2 K^4}\right)$

ε = radiator emittance. taken as 0.85/0.95

A_c = case cooler radiator area, taken as 2.610 m^2

T_c = case radiator temperature

stage. The tube supports are a type which have been used on several radiative coolers flying in similar orbits. Radiative isolation between stages is achieved by covering the facing surfaces with sheets of aluminized mylar or with high specular vapor-deposited aluminum.

Each of the two radiative cooler stages can be treated separately, starting with the warmer of the two which is affected negligibly by the coldest stage. The geometry of the two-stage cooler design is shown in Fig 3-30. One of the goals of this design was to open up the gaps between cooler stages such that much radiation from one low emittance specular surface to the other would escape out the ends and not be absorbed by the colder stage. This represents a departure from previous cooler designs where every attempt was made to place the stages and/or shields as close as possible. The latter produces a situation which can be handled with the analytical solution for infinite parallel plates but is not necessarily optimum thermally. The cooler geometry was used with the Aerojet Monte Carlo program to determine radiative interchange factors between specular surfaces. The Monte Carlo analysis showed that approximately half of the radiation from the intermediate stage to the cold stage escaped out the end gaps. Between the optics compartment stage and intermediate stage nearly 40% escapes out the ends. The size and geometry of the gaps and end closures were not optimized.

Each of the cooler stages is suported on fiberglass-epoxy composite tubes such as have been used on many past cooler designs. Conductance from the optics stage to the intermediate stage is 3.45×10^{-2} W/K and from the intermediate stage to the cold stage, 1.46×10^{-2} W/K. These supports are subjected to calculated stresses under Shuttle launch loads which are only 10 to 12% of their maximum strength. This was done by design so that a large amount of conservatism would reside in this area, since this is where practical problems related to size and manufacturability are most likely to arise.

The dimensions of the cold stage radiator depth, width, and thickness were chosen such that the heat load comin in from the detector dewar heat pipe could be easily conducted all over _ te without the use of additional heat pipes i. the plate. This is po le becaus the useful heat load is only a small portion of the total he t rejected by the radiator.

Environmental heat loads from earth infrared and albedo which are diffusely reflected off the highly specular shields were calculated with the LOHARP orbital heating program.

Heat loads in the detector dewar consist of Joule heating by the PC HgCdTe detectors; conduction through a fiberglass tension band support system; conduction through ≈1000 detector leads; radiation from the gold plated cryostat case at optics case temperature with one intermediate radiative shield; and optics compartment radiation into the optical port. Heat loads into the gold plated heat pipe from detector head to radiator are due to conduction through fiberglass support bands and gold to gold radiation from the tunnel.

The heat loads on the intermediate stage are listed in Table 3-25, and those on the cold stage in Table 3-26. Heat loads itemized in these tables are based upon uncontrolled intermediate and final stage radiator temperatures. For analysis of the final cold stage temperature, it was assumed that components thermally tied to the radiator, including the detector assembly and the heat pipe, were all at the same temperature. Uncontrolled intermediate stage radiator temperature is predicted to be 100.4 K. Table 3-27 shows intermediate stage radiator temperature sensitivity to heat loads. The uncontrolled final (cold stage) radiator temperature is predicted to be 69.0 K. Table 3-28 shows cold stage radiator temperature sensitivity to heat loads. Control power is used to tightly control detector temperature to the design value. For 75 K detector temperature, ≈0.8 watts control heater power would be required.

It should be noted that the cooler radiator and shield are designed for one particular orbit altitude and orbit time. The cold temperatures obtained here could not be reached in more severe orbits, such as sun synchronous high noon where the sun shines directly down on the instrument from above.

3.3.6 Contamination Control

The cold temperatures of the instrument optics can result in contaminants freezing onto the optical surfaces. This is particularly true for the components within the detector dewar. In order to control contamination in orbit, the cold optics are contained in a closed compartment. The only openings into this compartment are through an insulated tunnel surrounding the detector cooler heat pipe and around the optical chopper shaft where it enters the optics compartment. Only clean low outgassing materials are used within this compartment. Before thermal pumpdown in orbit, a period of time must be allowed for outgassing of the compartment. (A detailed contamination analysis may indicate the desirability of providing an inert gas purge during the decontamination period.) After thermal pumpdown, most contaminants entering the optics case through the outgassing port will freeze out on the heat pipe within the tunnel. A "turbine-type" gas check is used where the optical chopper shaft enters the optics compartment. If after some time in orbit performance degradation does occur, the unit would be reheated to boil off most of the contaminants.

Reasonable levels of contaminants on the emissive surfaces of the radiative coolers have no effect upon cooler performance. Contamination on the specular surfaces of the cooler can have more serious effects. The optical case decontamination cycle described above would also decontaminate the cooler surfaces. Nevertheless, because of the cryogenic temperatures used on the instrument, it should be flown on a reasonably clean spacecraft.

A cover is required over the aperture of the cooler assembly to prevent cooldown of the instrument during decontamination periods. Conceptually, this cover would consist of a "roller shade" that could be deployed repeatedly over the cooler aperture by ground command. (This cover is not pictured in Fig 3.30). This cover forms a line-of-sight barrier and an infrared radiation shield over the full aperture of the detector and optics case coolers. Decontamination heaters are also provided.

Table 3-25 Summary of heat loads to intermediate stage detector radiator[1]

Source	Heat Load (W)
Radiator support conduction	2.056
Internal radiation	1.038
Sun shield radiation	0.255
Earth IR + planetshine (scattered from sun shield)	0.192
	3.541

[1]Calculated using:

T_{case} = 160 K

$T_{int.\ stage}$ = 100.4 K

Table 3-26 Summary of heat loads to cold stage detector radiator[1]

Source	Heat Load (W)
Wire conduction	0.526
PC detector bias	0.0367
Cryostat gold-gold radiation	0.0245
Cryostat support conduction	0.160
Optical port radiation	0.0830
Heat pipe parasitics	0.10
Radiator support conduction	0.458
Radiator internal radiation	0.1677
Sun shield radiation	0.3898
Scattered earth IR + planetshine	0.1766
	2.1223

[1]Calculated using:

T_{case} = 160 K

$T_{int.\ stage}$ = 100.4 K

$T_{cold\ stage}$ = 69.0 K

Table 3-27 AMTS intermediate stage radiator temperature sensitivity to net heat loads[1]

Heat Load (W)	Temperature (K)
2.00	87.0
2.25	89.6
2.50	92.0
2.75	94.2
3.00	96.3
3.25	98.2
3.50	100.1
3.75	101.8
4.00	103.5
4.25	105.1
4.50	106.6
4.75	108.0
5.00	109.4

[1]Determined by steady state energy balance:

$$q = \sigma\varepsilon \left[F_{1A-S} \cdot A_{1A} + F_{1B-S} \cdot A_{1B}\right] T_1^4$$

where:

q = heat load (W)

σ = Stefan-Boltzmann constant

ε = radiator emittance, taken as 0.95

A_{1A} = area of intermediate radiator section nearest optics compartment = 0.6130 m^2

A_{1B} = area of intermediate radiator section furthest from optics compartment = 0.1320 m^2

F_{1A-S} = view factor to space of intermediate radiator section nearest optics compartment, = 0.866

F_{1B-S} = view factor to space of intermediate radiator section furthest from optics compartment = 0.886

T_1 = intermediate stage radiator temperature

Table 3-28 AMTS cold stage radiator temperature sensitivity to net heat loads[1]

Heat Load (W)	Temperature (K)
1.0	57.1
1.1	58.5
1.2	59.7
1.3	61.0
1.4	62.1
1.5	63.2
1.6	64.2
1.7	65.2
1.8	66.1
1.9	67.0
2.0	67.9
2.1	68.7
2.2	69.5
2.3	70.3
2.4	71.1
2.5	71.8
2.6	72.5
2.7	73.2
2.8	73.9
2.9	74.5
3.0	75.1
3.1	75.8
3.2	76.4
3.3	77.0
3.4	77.5
3.5	78.1
3.6	78.7
3.7	79.2
3.8	79.7
3.9	80.2
4.0	80.8

[1]Determined by steady state energy balance:

$$q = \sigma \epsilon A_2 F_{2-s} T_2^4$$

where:

q = heat load (W)

σ = Stefan-Boltzmann constant

ϵ = radiator emittance, taken as 0.95

A_2 = cold stage radiator area, = 1.760 m^2

F_{2-s} = view factor to space, = 0.992

T_2 = cold stage radiator temperature

Table 3-29 Instrument operating states

Instrument State	Remarks
• Power off	• Replacement heater power only applied to the instrument. • Radiative cooler cover closed
• Decontaminate	• Radiative cooler cover closed • Decontamination optical case heaters active • IR detector circuits disabled • Downlink data circuits active (but signal channel data meaningless)
• Operate - normal sounding	• Instrument cooled down • IR detector circuits enabled • Normal spatial scan pattern • Spectral test circuits active
• Operate - spectral monitor scan	• Grating angle stepped over a pre-programmed range • Downlink committed to support spectral monitor channel data

The IR detectors, the KBr corrector lens and the KBr optical port must be protected from contamination—particularly from moisture—while in the atmosphere. Consequently, it will be necessary to maintain the instrument in a controlled environment prior to launch.

3.4 Electronics Assembly

3.4.1 Electronics Assembly Functional Requirements

Instrument operating states are listed in Table 3-29. Uplink commands required to select instrument operating states and control the instrument are listed in Table 3-30. Downlink data functions are listed in Table 3-31. The electronics assembly is required to control or perform the indicated functions.

3.4.2 Electronics Conceptual Design

The electronics assembly conceptual design for the Baseline V instrument has been completed through the functional block diagram level. Functional block diagrams are shown in Fig 3-32 and in Fig 3-35 through 3-38. Major electronics functional elements are listed in Table 3-32, with the applicable block diagrams indicated. Functional requirements for the clock and timing logic, data formatting logic, and command demodulator are highly interactive with the requirements of other functional elements. In each of the functional block diagrams of Fig 3-32 and of Fig 3-35 through 3-38, only those functions of the clock and timing logic, data formatting logic, and command demodulator which interface with the subject functional element are shown. Consequently, the overall requirements for these functional elements are the sum of the functions presented on the individual block diagrams.

3.4.2.1 Signal Channel Electronics

The block diagram of the signal channel electronics is shown in Fig 3-32. The signal channel electronics consists of the optical scan mirror control circuits, optical chopper control circuits, optical chopper reference generator circuits, and analog and digital signal channel circuits.

The scan mirror is step scanned, with identical dwell times for each footprint and for each calibration target look. It is necessary to both accelerate and decelerate the average scan mirror angular velocity to fast slew from the last scene footprint to the first calibration target, from the first calibration target to the second calibration target, and from the second calibration target to the first scene footprint. Scan mirror angular position is monitored for each dwell angle via telemetry. Scan mirror position is under the control of the clock and timing logic function. A "direct access" test scan mode is provided for prelaunch laboratory calibration of the instrument. In this test mode the scan dwell sequence would be: laboratory test target, first internal calibration target, second internal calibration target, laboratory test target, etc.

Table 3-30 Uplink commands

Commands	Remarks
Spacecraft	
• Instrument power off	• Replacement heaters on
• Instrument power on	• Replacement heaters off
Instrument	
• Cooler cover open	
• Cooler cover closed	
• Detector dewar temperature set point	
• Grating angle set point	• Set for correct channel frequencies
• Spectral monitor scan test	• Steps grating over a range of angles about grating set point for a specified number of cycles

Table 3-31 Downlink data functions

Parameter	Remarks
Operational Data[1]	
• Signal channel data	• (Fig 3-32)
• Scan mirror position	
• Calibration targets temperature	• ~12 sensors
• Spectral position monitor data	• (Fig 3-35)
Housekeeping Telemetry[2]	
• Grating angle position	
• Optical chopper speed	
• Radiative cooler cover position	
• Cold optical case temperature	• ~12 sensors
• Detector dewar temperature	• ~ 4 sensors
• Radiative cooler temperature	• ~12 sensors
• Electronics assembly temperature	• ~ 4 sensors
• Electronics assemblies - selected voltages and currents	• ~48 channels

[1]Required to reduce signal channel data

[2]Required for instrument control and performance analysis

Table 3-32 Major electronics functional elements[1]

	Function Element	Block Diagram Figure No(s)
1)	Signal channel electronics	3-32
2)	Spectral monitor and control	3-35
3)	Downlink telemetry	3-36
4)	Optical assembly temperature control	3-37
5)	Spacecraft/instrument prime power interface	3-38
6)	Clock and timing logic	3-32, 3-35
7)	Data formatting logic	3-32, 3-35, 3-36
8)	Command demodulator	3-32, 3-35, 3-37

[1]Functional requirements for elements 6, 7 and 8 are distributed over a number of different block diagrams. Overall functional requirements for these elements are the sum of those presented on the block diagrams indicated.

The optical chopper drive is synchronized with the spatial scan in the sense that detector output is integrated over a specified integer number of chopper cycles for each spatial dwell. Chopper wheel speed is synchronized with the system clock.

The analog portion of the signal channel electronics consists of all electrical circuit elements from the detectors through the analog multiplexers. There is a separate analog signal channel for each detector within a spectral channel array, for a total of 16 analog channels per spectral channel set. A separate analog multiplexer, 14 bit "Analog to Digital Converter" (ADC), and "First In First Out" (FIFO) data buffer are provided for each spectral channel set. There are 28 sets of signal channel analog circuits; one for each spectral channel.

The optical chopper reference generator circuits process the voltage waveform from the reference generator detectors to derive waveforms of the proper phase required to perform the functions of synchronous demodulation, integrated signal hold, and integrator reset. There are 16 waveforms--nominally square waves--derived from the chopper generator reference detectors; one for each element of the IR inlet slit array. From each of these 16 spatial channel waveforms, chopper clock, hold, and integrator reset waveforms are generated for the 28 spectral signal channels corresponding to the spatial channel.

A functional schematic of the analog signal channel is shown in Fig 3-33. A DC coupled switched integrator approach is used to avoid footprint to footprint baseline slew induced radiometric errors. Because of the close proximity of the 75 K focal plane and the 160 K cold optics case, it is not necessary to locate any electronics within the 75 K cryostat. Critical electrical components such as the input JFET and load resistor can be mounted in the cold optics case at 160 K, with the balance of the electronics at 300 K.

The preamp is a differential "Transimpedance Amplifier" (TIA) consisting of a balanced JFET followed by an operational amplifier. This differential configuration provides both thermal and electrical common mode rejection. It also minimizes the effects of thermally induced drifts in the offset voltage of the input JFET upon detector bias. For both minimum preamp noise and minimum detector cryostat joule heat load the input JFET is best located on the 160 K surface rather than directly within the 75 K detector cryostat. By making the TIA feedback resistor, R_L, 10 times the detector dark resistance, it can be located on the 160 K surface with minimal impact upon overall system noise. Bias voltage for the PC HgCdTe channels are listed in Table 3-33. Incremental signal photocurrents for the AMTS detectors are listed in Table 3-34.

The analog signal amplifier provides gain, low-pass band limiting of the chopped waveform and coarse DC offset adjustment. Both gain and DC offset would be adjusted on an individual channel basis during instrument alignment.

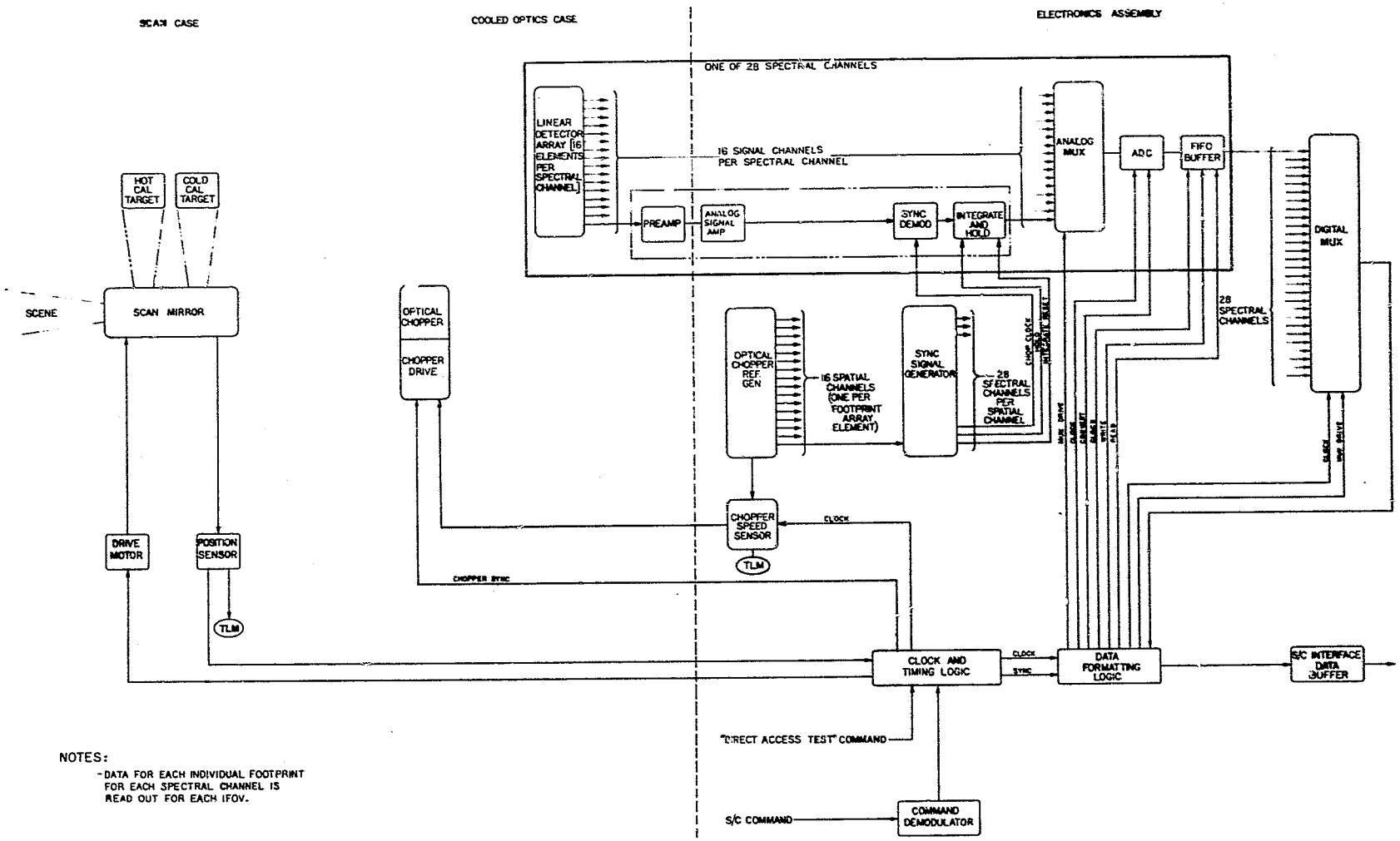

Figure 3-32. Signal channel electronics block diagram.

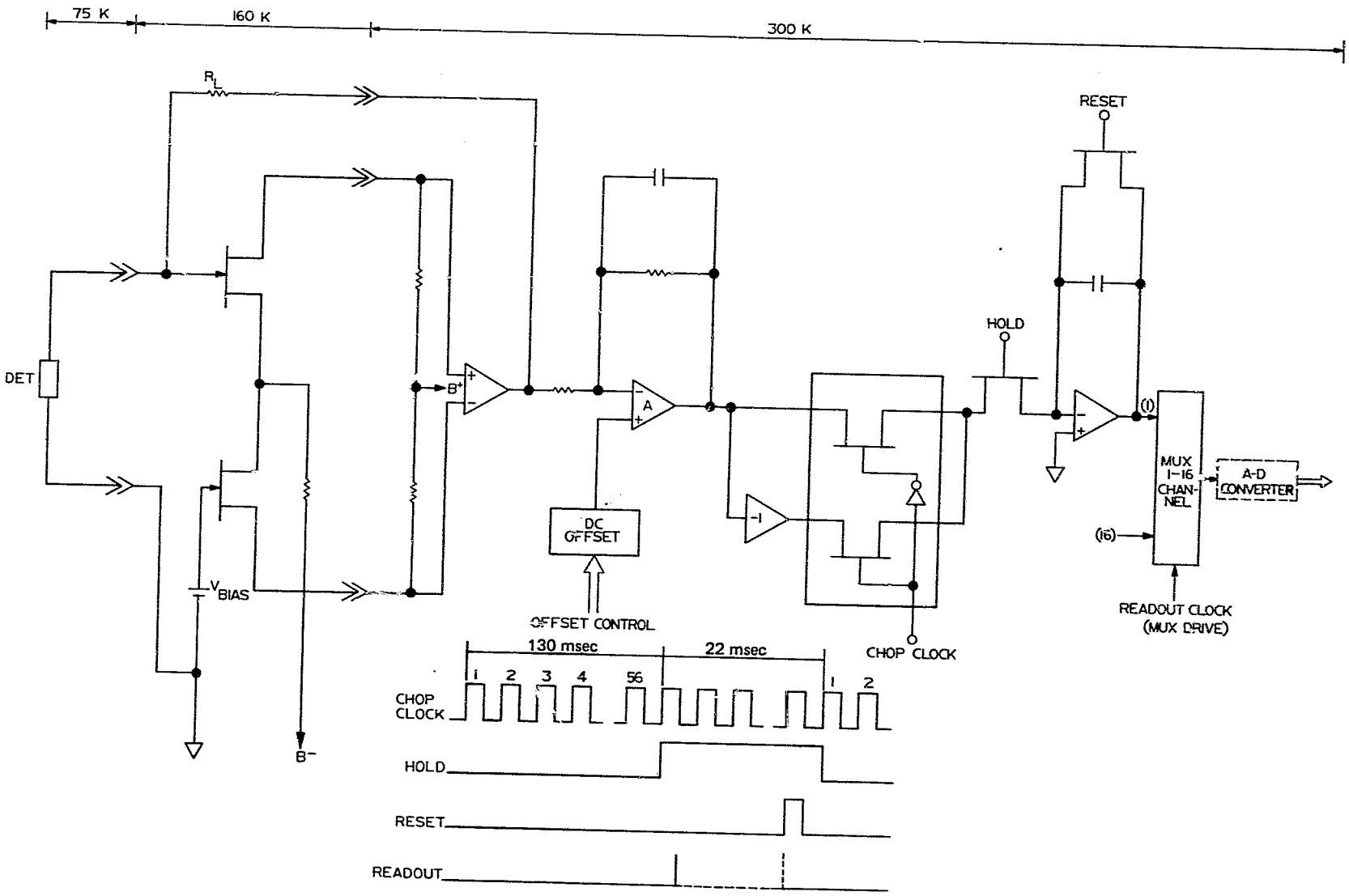

Figure 3-33 Functional schematic of analog signal channel

Table 3-33 Bias voltage across terminals of PC detectors

CH	λ (μm)	Bias Voltage (V)
1	16.476	0.159
2	16.046	0.185
3	15.929	0.191
4	15.765	0.199
5	15.466	0.213
6	15.282	0.220
7	15.025	0.230
8	14.996	0.232
9	14.967	0.233
10	14.938	0.234
11	11.429	0.255

Table 3-34 Incremental total signal photocurrents for AMTS detectors

CH	λ (μm)	Detector Type	Junction Capacitance (F)	Dark Resistance R_o (Ω)	Incremental Photocurrent (A) $T_{chopper}$	T_{min}	T_{max} or T_{cal} [1]
1	16.476	PC HgCdTe	—	3.40E2	$2.11E^{-8}$	$6.18E^{-8}$	$8.68E^{-8}$
2	16.046	|	—	3.94E2	$1.49E^{-8}$	$4.10E^{-8}$	$5.78E^{-8}$
3	15.929	|	—	4.08E2	$1.15E^{-8}$	$3.10E^{-8}$	$4.41E^{-8}$
4	15.765	|	—	4.25E2	$9.07E^{-9}$	$2.36E^{-8}$	$3.38E^{-8}$
5	15.466	|	—	4.54E2	$5.14E^{-9}$	$1.35E^{-8}$	$1.99E^{-8}$
6	15.282	|	—	4.69E2	$4.94E^{-9}$	$1.23E^{-8}$	$1.82E^{-8}$
7	15.025	|	—	4.91E2	$4.66E^{-9}$	$1.12E^{-8}$	$1.66E^{-8}$
8	14.996	|	—	4.95E2	$5.06E^{-9}$	$1.21E^{-8}$	$1.78E^{-8}$
9	14.967	▼	—	4.96E2	$5.15E^{-9}$	$1.21E^{-8}$	$1.78E^{-8}$
10	14.938	PC HgCdTe	—	4.98E2	$4.84E^{-9}$	$1.03E^{-8}$	$1.52E^{-8}$
11	11.429	PC HgCdTe	—	7.22E2	$7.12E^{-9}$	$1.29E^{-7}$	$1.42E^{-7}$
12	9.608	PV HgCdTe	$1.24E^{-10}$	2.08E8	$1.83E^{-9}$	$1.82E^{-8}$	$2.42E^{-8}$ [2]
13	8.120	|	$1.16E^{-10}$	2.23E8	$5.21E^{-10}$	$5.53E^{-9}$	$1.29E^{-8}$
14	6.060	▼	$2.66E^{-10}$	2.19E8	$1.41E^{-10}$	$5.44E^{-10}$	$2.46E^{-9}$ [2]
15	5.881	PV HgCdTe	$3.03E^{-10}$	1.93E8	$1.08E^{-10}$	$3.79E^{-10}$	$1.99E^{-9}$ [2]
16	5.437	PV HgCdTe	$5.18E^{-10}$	2.30E8	$7.93E^{-11}$	$1.42E^{-10}$	$1.44E^{-9}$ [2]
17	5.403	PV HgCdTe	$5.36E^{-10}$	2.23E8	$7.42E^{-11}$	$1.40E^{-10}$	$1.38E^{-9}$ [2]
18	5.181	PV InSb	$9.88E^{-11}$	1.86E8	$2.88E^{-11}$	$6.48E^{-11}$	$8.06E^{-10}$
19	4.195	PV InSb	$1.02E^{-10}$	1.81E8	$8.18E^{-13}$	$3.61E^{-12}$	$2.61E^{-10}$
20	4.191	|	$6.52E^{-11}$	2.82E8	$9.05E^{-13}$	$4.21E^{-12}$	$2.58E^{-10}$
21	4.187	|	$1.03E^{-10}$	1.80E8	$7.70E^{-13}$	$5.14E^{-12}$	$1.52E^{-10}$
22	4.184	|	$6.63E^{-11}$	2.78E8	$9.00E^{-13}$	$5.61E^{-12}$	$1.99E^{-10}$
23	4.180	|	$1.03E^{-10}$	1.79E8	$7.16E^{-13}$	$5.45E^{-12}$	$2.18E^{-10}$
24	4.176	|	$6.74E^{-11}$	2.73E8	$1.15E^{-12}$	$6.19E^{-12}$	$2.44E^{-10}$
25	4.125	|	$7.43E^{-11}$	2.48E8	$1.06E^{-12}$	$7.74E^{-12}$	$3.86E^{-10}$
26	3.992	|	$8.91E^{-11}$	2.07E8	$6.42E^{-13}$	$6.36E^{-12}$	$5.16E^{-10}$
27	3.822	▼	$7.22E^{-11}$	2.55E8	$1.84E^{-13}$	$2.60E^{-12}$	$3.69E^{-10}$
28	3.723	PV InSb	$8.49E^{-11}$	2.17E8	$1.49E^{-13}$	$2.57E^{-12}$	$5.48E^{-10}$

[1] Tcal = 310 K

[2] Values correspond to Tcal

The analog signal processing consists of synchronous demodulation and integration. The integrator doubles as an analog hold function. The maximum hold time could not exceed the 22 msec spatial scan slew interval. Hold times could be reduced to about 1.0 msec by operating the ADC near its minimum conversion time (≈50 μsec for a 14 bit ADC). The signal channel demodulation approach is pictured in Fig 3-34. Integrated values during shutter open and shutter closed intervals are differenced due to the synchronous switching of signal polarity to the integrator. (Para 3.1.1.3.1, Configuration d). Integration must be performed over an integer number of cycles. Within limits, slowly varying DC offset levels and clock vs signal voltage phase offsets will not affect radiometric performance of the system. The output vs input voltage characteristics of the integrator must be linear. Residual voltage in the integrator bucket after the "reset" command must be independent of the radiometric value of the preceding dwell period.

Digital outputs from each spectral channel are combined in a digital multiplexer. The data formatting circuit accepts the output data stream from the digital multiplexer, combines it with the telemetry and spectral monitor functions data streams, and adds the necessary synchronization words. The analog multiplexer, ADC, FIFO buffer, and digital multiplexer are controlled by the data formatting logic.

A spacecraft interface data buffer is probably required to buffer the composite data stream from the AMTS. Detail requirements for the buffer are, of course, dependent upon the requirements of the spacecraft data system. It is assumed that an AMTS command demodulator would be required to demodulate AMTS uplink command words received via the spacecraft uplink command system. Detail requirements for the command demodulator are dependent upon the characteristics of the spacecraft command system.

The scan mirror assembly, the optical chopper assembly, the chopper reference generator detector assembly, and the detector and first stage preamp assemblies are located within the cooled optics case. The remaining circuitry is located in the electronics assembly, removed from the optics case.

3.4.2.2 Spectral Monitor and Control

The block diagram of the spectral monitor and control circuit is shown in Fig 3-35. This circuit consists of an AC modulated redundant neon bulb spectral reference source, spectral monitoring detectors and their spectral channel electronics, and a grating angle control circuit.

The spectral monitor signal channel circuits consist of 10 detectors, in two groups of five each, used to detect selected neon spectral lines. The outputs of 10 individual analog channel circuits, one per detector, are combined in an analog multiplexer. Signal levels are digitized by a common 14 bit ADC, fed into a FIFO buffer, and then to the common AMTS data formatting circuit. The analog multiplexer, ADC, and FIFO buffer operate under control of the data formating logic. The analog channels of the spectral monitoring circuit are functionally identical with those of the IR signal channel electronics.

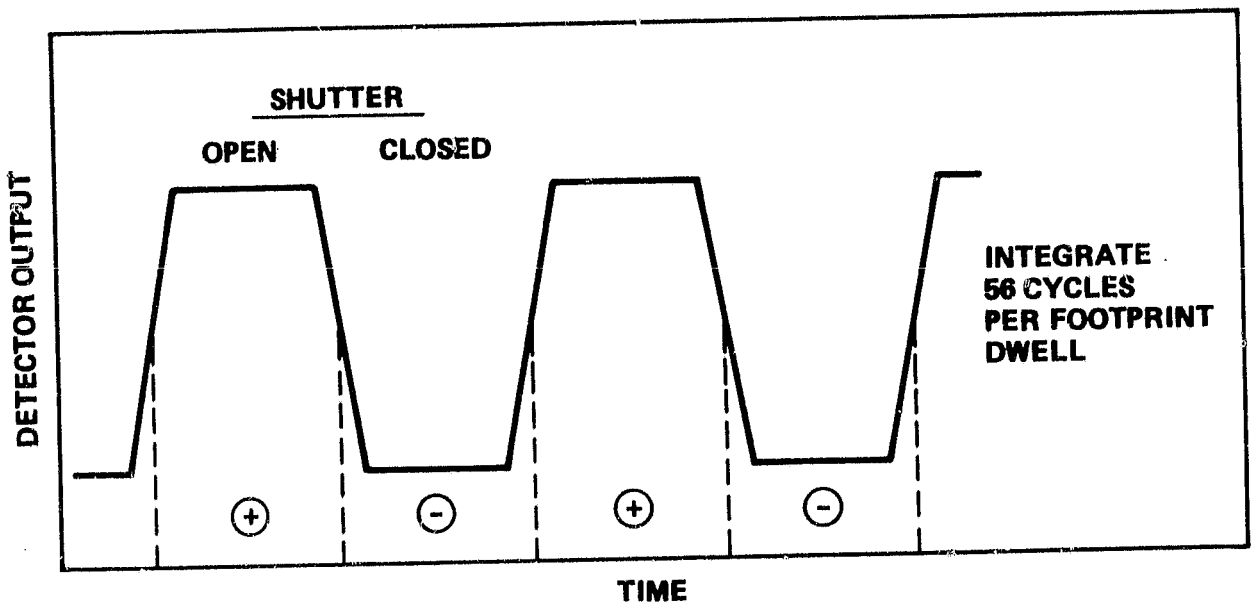

Figure 3-34 Signal channel demodulation approach .

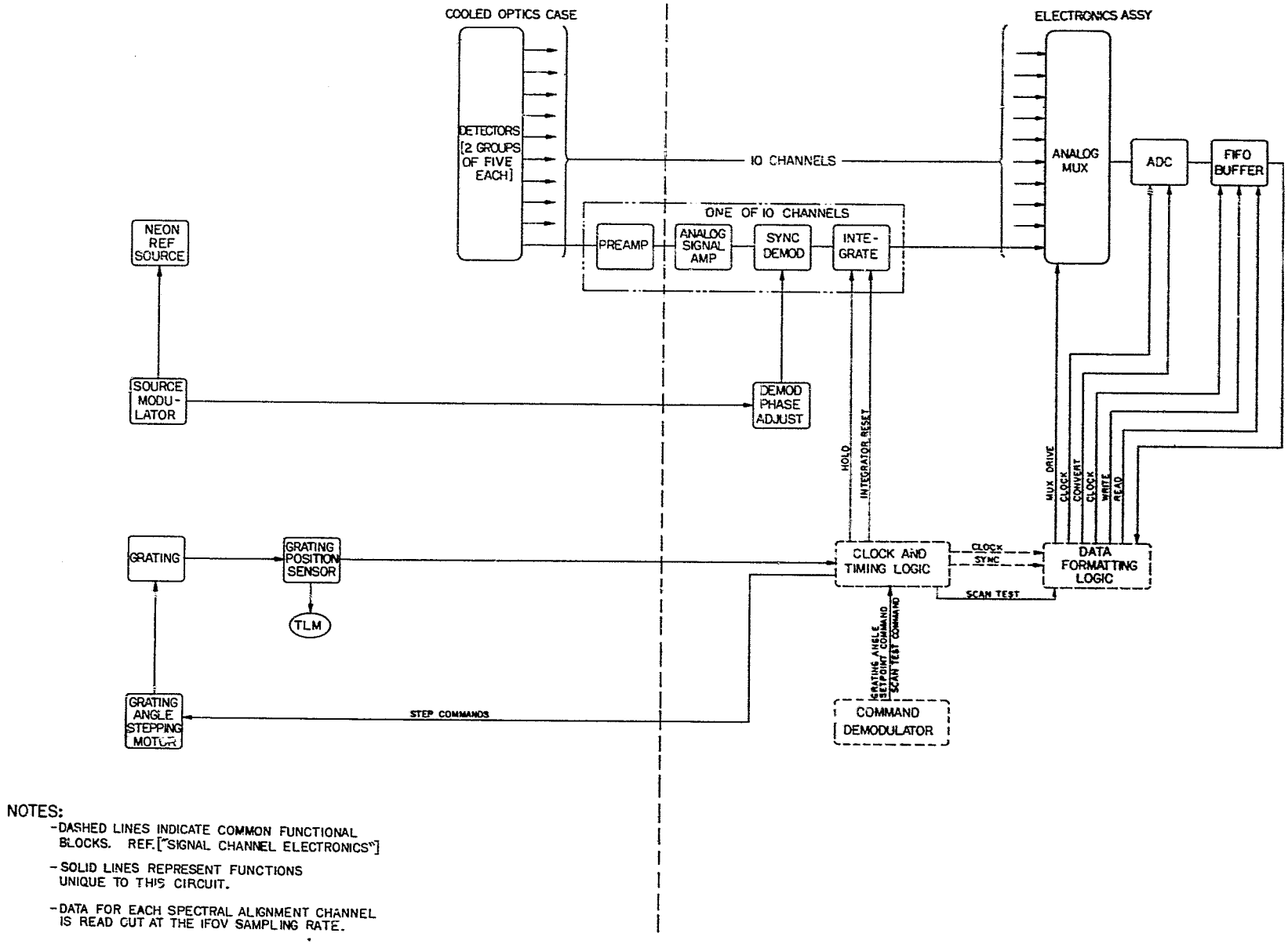

NOTES:

- DASHED LINES INDICATE COMMON FUNCTIONAL BLOCKS. REF.["SIGNAL CHANNEL ELECTRONICS"]
- SOLID LINES REPRESENT FUNCTIONS UNIQUE TO THIS CIRCUIT.
- DATA FOR EACH SPECTRAL ALIGNMENT CHANNEL IS READ OUT AT THE IFOV SAMPLING RATE.

Figure 3-35 Spectral monitor and control block diagram

A relative grating angular position sensor provides inputs to the downlink telemetry circuit and to the clock and timing logic circuit. Changes in grating angle are executed under control of the clock and timing logic upon receipt of appropriate ground commands.

In the normal monitor mode the spectral monitoring circuit operates continuously and without interfering with IR signal channel operation. The output data from the 10 spectral monitoring channels are merged into the downlink data stream by the data formatting logic. Data from the spectral monitoring channels is read out at the IFOV sampling rate.

In the IR channel "frequency adjust" mode the grating angle is changed under control of the clock and timing logic by an increment specified in the uplink command. The grating angular step would be accomplished during a scan slew period between line scan and calibration target dwell intervals, and no IR signal channel data would be lost.

Upon receipt of a "scan test" command, the grating angle would be stepped over a preprogrammed angular range. Spectral monitor data would be read out for each grating position. During the scan test interval, IR signal channel data is affected by the varying grating angles; consequently, it is of no value for atmospheric profile retrievals. During the scan test cycle, maximum utilization of the downlink for spectral monitor channel measurements would be instituted by the clock and timing logic and the data formatting logic. IR signal channel data would not be transmitted during the test cycle.

The neon lamp source and the grating angle drive circuitry are located in the cooled optics case. Spectral monitor detectors are located on the spectrometer image plane mask in the detector dewar. The remaining circuitry is located in the electronics assembly.

3.4.2.3 Telemetry Data Circuit

This circuit collects all downlink data except IR signal channel data and spectral monitor channel data. The telemetry data circuit block diagram is shown in Fig 3-36. Individual telemetry analog sensors are not shown in the diagram. All temperature sensor data is sampled by an analog multiplexer, digitized, and accumulated in a FIFO buffer. All other analog telemetry data is also sampled by an analog multiplexer, digitized, and accumulated in a separate FIFO buffer. Data is output from these buffers through a common digital multiplexer to the instrument data formatting logic. The analog multiplexers, ADCs, FIFO buffers and digital multiplexer operate under the control of the data formatting logic. Readout of the digital scan mirror shaft angle sensor is also under control of the data formatting logic. Scan mirror position is read out for every spatial dwell position, including the calibration target dwells. Other telemetry functions are read out once per line scan. With the exception of telemetry sensors, the telemetry data circuit is located in the electronics assembly.

3.4.2.4 Optics Assembly Temperature Control Circuits

The active optics assembly temperature control block diagram is shown in Fig 3-37.

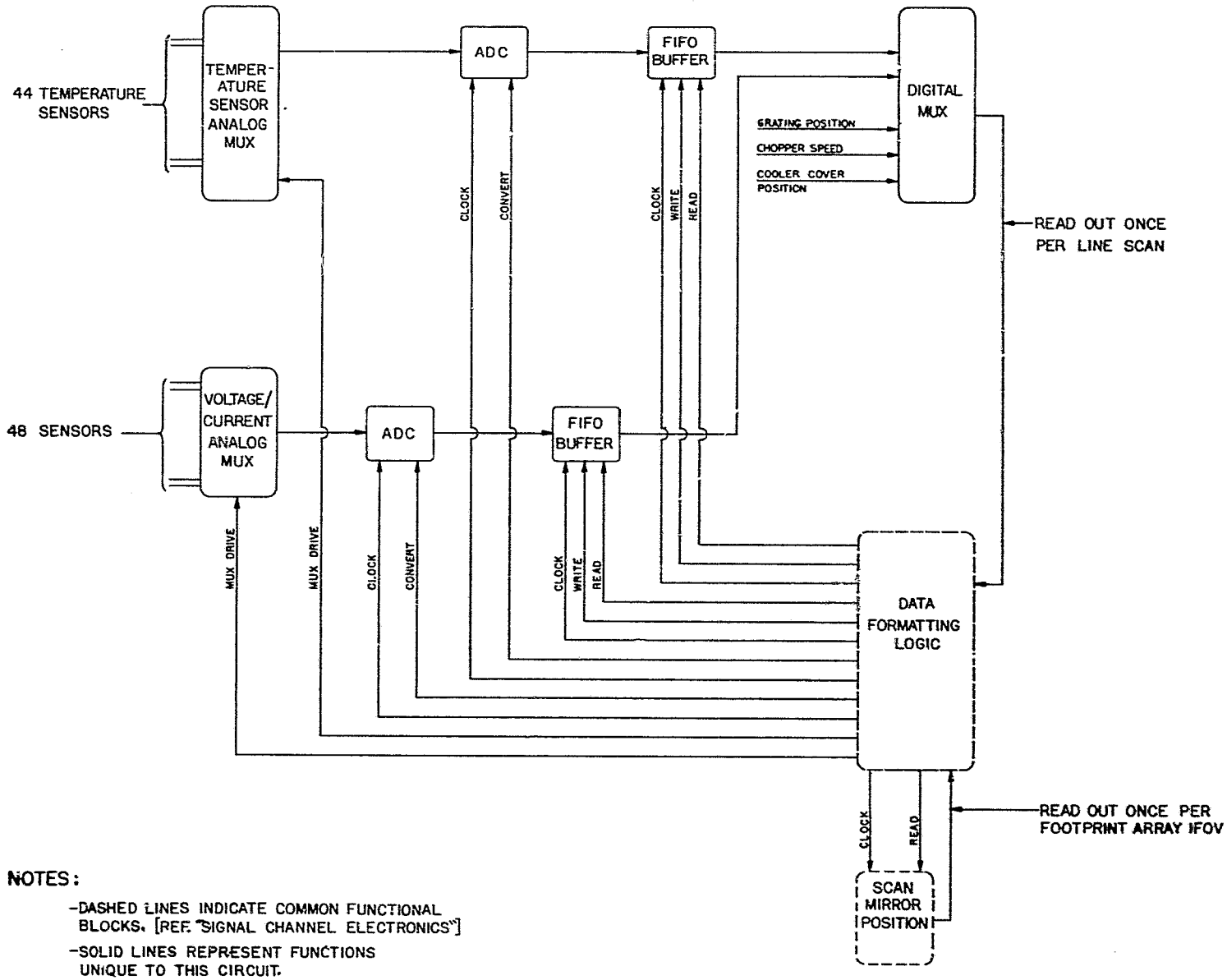

Figure 3-36 Telemetry data circuit block diagram

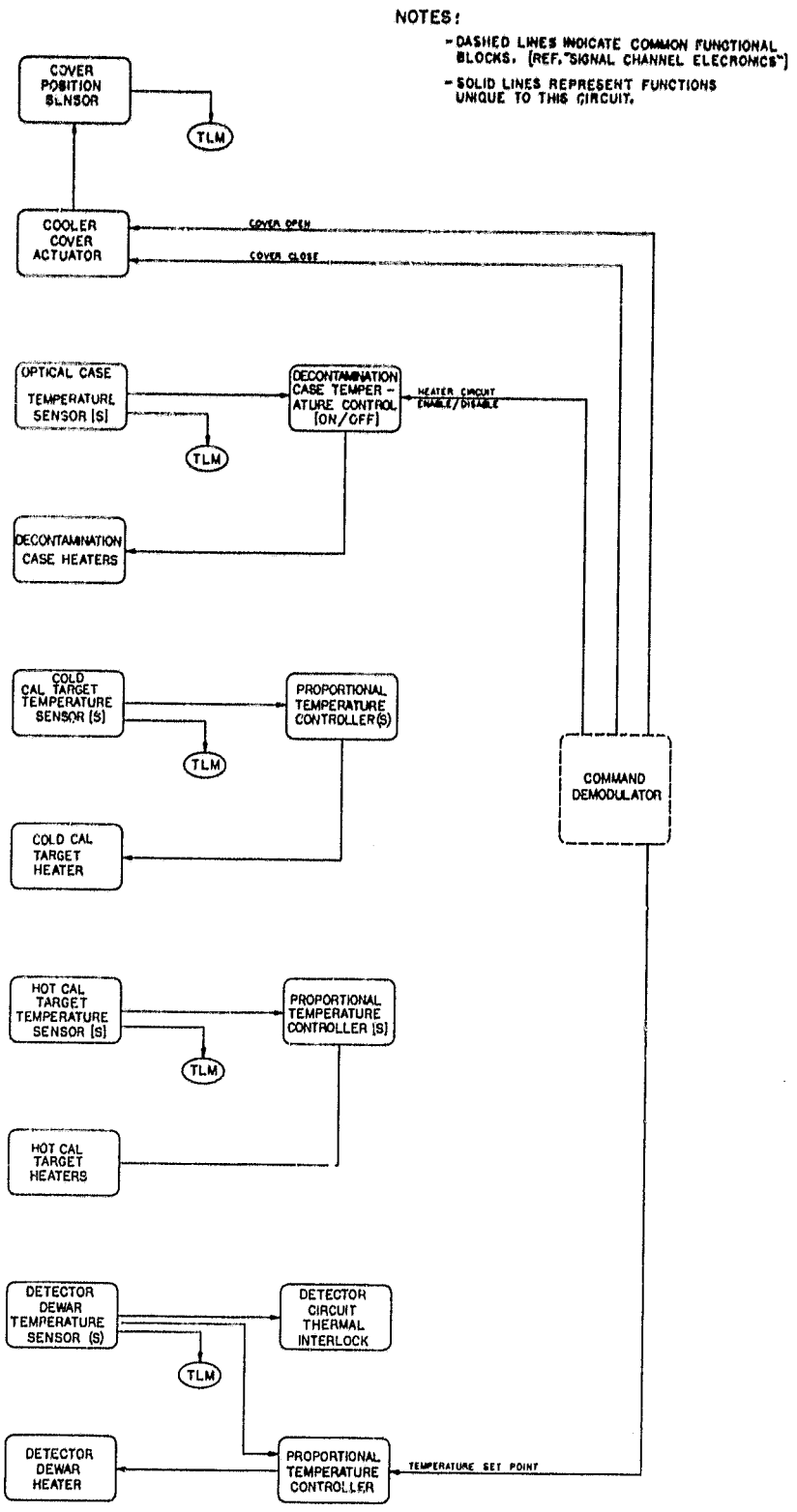

Figure 3-37 Optics assembly temperature control block diagram

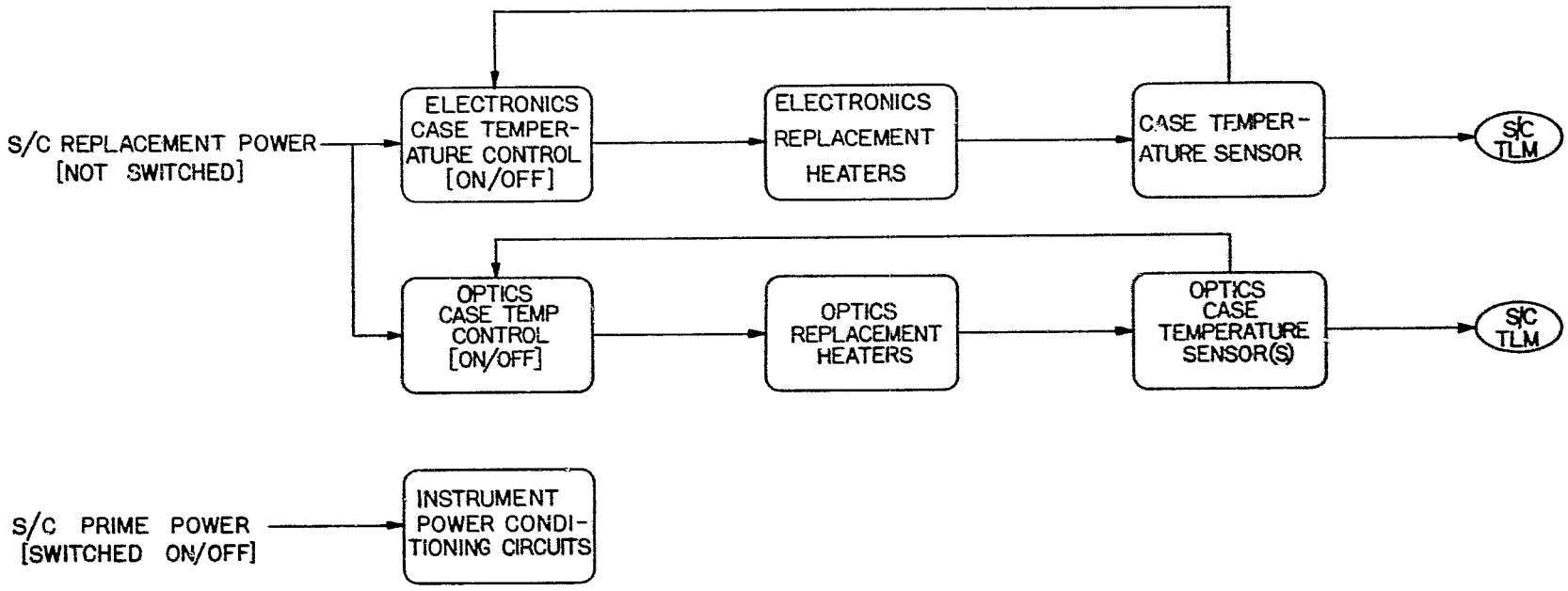

Figure 3-38 Spacecraft/Instrument prime power interface block diagram

The radiative cooler cover is opened and closed via ground command. Contamination within the optics assembly and the cooler can be largely boiled off by applying power to the decontamination case heaters with the radiative cooler cover closed. On/off control of these heaters is used to hold case temperature within the design range for decontamination.

The on-board calibration target temperatures are maintained constant within a high degree of precision by proportional temperature controllers.

The detector cryostat is cooled by the detector radiative cooler. Since HgCdTe detector responsivity is a function of detector temperature, an active cryostat heater is used in order to maintain temperature constant. A tight, over-damped, proportional temperature control loop is used in order to avoid relatively short term variations of detector temperature. The cryostat temperature set point can be changed via ground command in order to take full advantage of the cooling capacity of the radiative cooler. A detector circuit thermal interlock is provided to protect the detectors by disabling the detector bias circuits when the cryostat is not cooled down.

3.4.2.5 Spacecraft/Instrument Prime Power Functional Interface

A functional block diagram of the spacecraft/instrument prime power interface is shown in Fig 3-38. Details of this interface, of course, are dependent upon options and constraints imposed upon the AMTS instrument by the spacecraft. Spacecraft prime power to the instrument power conditioning circuits must be controlled by ground command on the spacecraft side of the interface. Spacecraft replacement power is always supplied to the instrument to maintain the optics assembly and the electronics assembly within a safe standby temperature range when spacecraft power to the instrument power conditioning circuits is switched off. Spacecraft telemetry channels should be provided to monitor critical AMTS standby temperatures when the spacecraft prime power to the instrument is off.

3.5 Instrument Data Rate, Size, Weight, and Prime Power Requirements

3.5.1 Downlink Data Rate

Downlink data rate requirements for the Baseline V instrument are listed in Table 3-35. The downlink data rate is 35.5 kbits/sec.

3.5.2 Size

The dimensions of the optics assembly, including the radiative cooler assembly, are shown in the layout drawing of Fig 3-30. Thermal isolation spacecraft mounts are not shown in the layout drawing. A detailed conceptual circuit design of the electronics and a detailed conceptual layout of the electronics assembly have not been done. The volume of this assembly is estimated to be 100,000 cm^3.

3.5.3 Weight

Weight estimates for the overall instrument are listed in Table 3-36. Thermal isolation spacecraft mounts are included in the weight estimate.

Optics assembly weights are based upon lightweight beryllium mirrors and a lightweight beryllium optical bench structure. This will result in minimum weight for the assembly. A more cost effective approach may be to use lightweight glass mirrors and an athermalized aluminum optical bench, for example. This is a trade-off that must be made when spacecraft options and constraints are known. A detailed conceptual design for the optical bench and overall optics assembly structure has not been done; neither has a detailed design of the electronics assembly package.

3.5.4 Prime Power Requirements.

Total prime power requirements for the AMTS instrument are estimated to be $\leq$ 250 watts. A detailed conceptual circuit design has not been made, however, beyond the functional block diagram level. In addition, details of the instrument/spacecraft prime power interface are not known.

C-3

Table 3-35 Downlink data requirements (Baseline V)

Downlink Data Item	No. of Words per Line Scan
Operational data	
IR signal channel data	59,136
Spectral monitor channel data	1,320
Scan mirror position (TLM)	132
Cal target temperatures (TLM)	12
Subtotal	60,600
Housekeeping data (TLM)	
Voltages and currents	48
Temperatures	32
Grating angle position	1
Optical chopper speed	1
Radiative cooler cover position	1
Subtotal	83
Sync words	≈1,000
Total (14 bit) words/line	61,683
Average words/sec	2,537
Average bits/sec	35,520

Table 3-36 Instrument weight estimates (Baseline V)

Assembly		Weight (kg)
Optical		
Optics		46
Structure		86
Radiative coolers		70
Thermal blankets		16
Miscellaneous Hardware[1]		36
	Subtotal	254
Electronics		
	Subtotal	45
	Total	299 (659 lbs)

[1]Includes spacecraft thermal isolation mounting provisions

REFERENCES - SECTION 3

3-1 Evans, Nathan L. and Valerie G. Wright, "A Dual-Vector Grating Efficiency Model," SPIE Volume 503, (1984).

3-2 Stierwalt, D.L., and W.L. Eisenman, "Problems in Using Cold Spectral Filters with LWIR Detectors," SPIE Volume 132, (1978).

3-3 Wright, J.P., "Development of a 5-Watt 70 K Passive Radiator," AIAA Paper 80-1512.

SECTION 4

4.0 BASELINE V AMTS ERROR ANALYSIS

This section identifies error sources which impact AMTS system performance. To the extent that a data base is available and error analysis can be performed, estimated error values are presented. All identified error sources are treated individually. This treatment generally provides additional insight into the requirements and constraints of a high precision IR atmospheric sounder. The results of the Baseline V error analysis are summarized in Para 4.12.

Error sources can be grouped into four broad categories:

- Spectral errors (Para 2.3.6 through 2.3.9)
- Nontunable radiometric errors (Para 2.3.10)
- Tunable radiometric errors (Para 2.1.6 and 2.3.11)
- Correlated relative radiometric errors (Para 2.3.12)

The overriding requirement for good AMTS system performance is high precision radiometry. Ultimately, spectral error components can be expressed in terms of equivalent radiometric errors.

Nontunable short term radiometric error components can have various kinds and degrees of correlation. The following correlation categories affect sounder system performance in different ways:

- Random footprint to footprint — These error components are reduced by a factor of $1/\sqrt{N}$ when N individual footprints are combined to form a composite footprint (Para 2.1.7).
- Correlated footprint to footprint — These error components are not reduced in the composite footprint.
- Random channel to channel.
- Correlated (tracking) channel to channel — The effects of individual error components upon cloud filtering capability are reduced with respect to random errors.
- Correlated (nontracking) channel to channel — These error components have a more detrimental effect upon cloud filtering capability than random errors.

The effects of long term systematic radiometric errors (tunable errors) can be reduced by in-orbit system tuning (Para 2.1.6).

Correlated relative radiometric errors are a subset of nontunable radiometric errors. They consist of the nontunable correlated channel to channel differential error components. In general, these errors also tend to

be correlated footprint to footprint over the area of the composite footprint, and are not necessarily reduced in the composite footprint. This instrument requirement error category is defined seperately because of its effect upon the cloud filtering capability of the sounder system (Para 2.1.7).

4.1 Spectral Errors

Spectral requirements consist of:

- Channel frequency (Para 2.3.7)
- Knowledge of channel frequency (Para 2.3.8)
- Channel bandwidth (Para 2.3.6)
- Knowledge of relative channel intensity vs frequency response (Para 2.3.9)

Uncertainties — or errors — in these spectral parameters affect system tuning (Para 2.1.6). Long term systematic instrument spectral errors are tunable errors. Short term temporal variation in instrument spectral parameters result in nontunable radiometric errors. The instrument error contribution can be analyzed in terms of spectral parameters. Converting these spectral error values to radiometric errors must be done through system level simulation.

4.1.1 Channel Frequency Setting

Channel frequency setting errors are a function of the following parameters defined at the operating temperature of the instrument:

- Grating pitch.
- Accuracy to which the relative slit positions of the inlet slit mask and exit slit mask are fabricated.
- Relative angular alignment of the entrance slit mask, exit slit mask, grating, and grating collimator.

Channel frequency setting errors resulting from optical alignment errors can be corrected within limits while in orbit by adjusting the grating angle (Para 3.1.2).

The equation used to calculate spectral setability error is:

$$\Delta\lambda = \frac{m \cos(\theta + \Delta\theta)}{a + \Delta a} [\sin(\alpha + \Delta\alpha) + \sin(\beta + \Delta\beta)] - \lambda \qquad (4.1)$$

where

a = grating pitch

Δa = error in grating pitch

α = grating incident angle

$\Delta\alpha$ = error in grating incident angle

β = grating diffraction angle

$\Delta\beta$ = error in grating diffraction angle

λ = channel wavelength

$\Delta\lambda$ = error in channel wavelength

m = grating order number

θ = grating out-of-plane angle

$\Delta\theta$ = error in grating out-of-plane angle

Part A of Table 4-1 shows the sources of prelaunch setability error. The values shown are fairly conservative. Part B shows the in orbit resetability error sources when using the spectral monitor. Part C shows setability errors in terms of wavelength for several channels. The second column is the setability design requirement expressed in terms of wavelength (Para 2.3.7). The third column shows that the prelaunch setability error is within the design requirement as is the reset error using the discriminators as shown in column four. Channel 10 is the most error sensitive channel.

4.1.2 Knowledge of Channel Frequency

Knowledge of the channel frequency setting depends upon prelaunch calibration data and, ultimately, upon the ability to monitor channel frequency in orbit (Para 3.1.2).

Table 4-2 part A shows the sources of error in spectral knowledge using the spectral monitor. The calculated spectral knowledge in terms of wavelength falls well within the design requirement (Para 2.3.8), as can be seen from part B. Channel 10 is the most sensitive to error and Channel 20 the least. Of the two discriminators, S2 is the more sensitive to errors. When nulling discriminator offsets, the S2 correction should be favored over the S1 correction.

Table 4-3 part A shows the results of testing an algorithm which calculates $\Delta\alpha$ and $\Delta\beta$ from the spatial discriminator data using Eq 3.35 and 3.36. The first column shows the number of significant digits used in the program. The second and third columns show the true errors in α and β, and the fourth and fifth columns show $\Delta\alpha$ and $\Delta\beta$ calculated by

Table 4-1 Channel frequency setability error
(for a 5 arc second grating step)

Error Sources	Δa (μm)	Δα (rad)	Δβ (rad)	Δθ (rad)
A. Setability - prelaunch				
Grating pitch error	5.22E-4	———	———	———
Grating thermal expansion uncertainity at 160 K	3.80E-6	———	———	———
Exit mask cutting error	———	———	3.33E-5	———
Exit mask thermal expansion uncertainity at 160 K	———	———	6.98E-8	———
Inlet mask cutting error	———	3.33E-5	———	———
Inlet mask thermal expansion uncertainity at 160 K	———	6.98E-8	———	———
Exit mask alignment error	———	———	3.33E-5	———
Inlet mask alignment error	———	3.33E-5	———	———
Grating alignment error	———	4.85E-6	4.85E-6	———
Collimator alignment error	———	1.62E-5	1.62E-5	———
Out-of-plane alignment error	———	———	———	2.43E-5
Total (RSS)	5.22E-4	5.00E-5	5.00E-5	2.43E-5
B. Discriminator reset - in orbit				
Relative position of exit slits and discriminators	———	4.71E-5	4.71E-5	———
Grating step size setability error	———	1.21E-5	1.21E-5	———
Detector relative response error	———	4.89E-7	4.89E-7	———
Grating pitch error	5.22E-4	———	———	———
Inlet/exit mask cutting error	———	3.33E-5	3.33E-5	———
Thermal expansion uncertainties at 160 K	3.80E-6	6.98E-8	6.98E-8	———
Total (RSS)	5.22E-4	5.89E-5	5.89E-5	———

C. Setability in Terms of Wavelength

CH	Required (μm)	Set. Prelaunch (μm)	Set. In Orbit (μm)
1	1.26E-3	6.82E-4	7.47E-4
10	1.12E-3	7.55E-4	8.38E-4
13	6.09E-4	3.49E-4	3.84E-4
20	3.14E-4	1.65E-4	1.80E-4
28	2.79E-4	1.62E-4	1.79E-4

Table 4-2 Channel frequency knowledge error
(for a 5 arc second grating step)

Error Sources	Δa (μm)	Δα (rad)	Δβ (rad)
A. Setability - prelaunch			
Grating pitch knowlege error	5.22E-6	-------	-------
Exit slit/discriminator relative position error	-------	9.44E-6	9.44E-6
Detector relative response error	-------	4.89E-7	4.89E-7
Digitization error	-------	8.48E-8	8.48E-8
Grating step size error	-------	2.42E-6	2.42E-6
Thermal expansion uncertainties	3.80E-6	4.00E-6	4.00E-6
Total (RSS)	5.23E-6	1.05E-5	1.05E-5

B. Setability Knowledge in Terms of Wavelength

CH	Required (μm)	Calculated (μm)
1	2.47E-4	7.97E-5
10	2.24E-4	1.01E-4
13	1.22E-4	4.24E-5
20	6.30E-5	1.87E-5
28	5.60E-5	1.98E-5

the algorithm. As can be seen, there is a limit beyond which increasing the number of significant digits does not improve the accuracy of the calculated numbers. Part B of Table 4-3 shows, for Channel 10, the errors in the calculated angles in terms of wavelength. Comparing the results to the design requirement for spectral knowledge shows that the inputs to the algorithm should be accurate to five decimal digits. Why this algorithm did not result in greater precision was not determined.

4.1.3 Channel Bandwidth

Channel bandwidth considerations are treated in Para 3.1.1.5. Possible spectral weighting effects due to optical chopping are treated in Para 3.1.1.3.2. Calculated channel amplitude vs. frequency response for a number of AMTS channels and the effects of wing response crosstalk upon system performance are treated in Para 4.3.3.

Satisfying the half-power channel bandwidth requirements (Para 2.3.6) is easy with the Baseline V instrument design approach.

The requirement that the channel amplitude vs. frequency response be the same within narrow limits for all elements of the spatial array (Para 2.3.6) is an important requirement that places constraints upon the optical design. The small variation in point spread distribution along the spectral axis vs. array position for the Baseline V optics (Para 3.1.4) is within the limits of resolution for the algorithm used to derive the slit function responses of Para 4.3.3. System tuning simulations having this degree of sensitivity have not been performed. We believe, however, that the requirement would be satisfied by Baseline V.

4.1.4 Knowledge of Relative Channel Intensity vs. Frequency Response

Knowledge of relative channel amplitude vs. frequency response must depend upon prelaunch calibration of the instrument. A change in this parameter after launch would primarily be caused by a shift in the optical focus of the instrument. No significant focus shift is anticipated with a well designed optical bench. The spectral alignment channels, however, provide a means of detecting a shift in instrument focus (Para 3.1.2). Amplitude vs. frequency response of the IR channels can be roughly deduced from the measured amplitude vs. angle response of the monochromatic alignment slit images, based upon prelaunch calibration data.

Radiometric errors corresponding to an error in knowledge of the integrated channel intensity vs frequency response are shown in Table 4-4 for selected band 1 and band 4 channels. Radiometric error values corresponding to differential channel areas resulting from a 5 percent change in geometric point spread distributions are listed. Radiance was calculated using the GSFC radiance tape for the U.S. Standard Atmosphere at a resolution of 0.005 cm^{-1} and assuming no clouds in the field of view. Radiometric error values normalized to an error in the area knowledge goal requirement of 0.15 percent are also listed in this table. This error is correlated footprint to footprint and is not reduced in the composite footprint. Table 4-4 shows that if the error component were nontunable it would be a significant source of error at the goal specification limit. It is believed, however, that a significant part of this error component is systematic and would be reduced by system tuning.

Table 4-3. Calculated grating angle errors

A. Test of an algorithm using the method specified in Eq 3.35 and 3.36

No. of Decimal Digits	True Δα (rad)	True Δβ (rad)	Calculated Δα (rad)	Calculated Δβ (rad)
10	0.0	0.01	3.50356E-6	9.99894E-3
6	0.0	0.01	2.40330E-6	9.99915E-3
5	0.0	0.01	1.94356E-5	1.00097E-2
4	0.0	0.01	7.86287E-6	9.90151E-3
6	0.0	0.001	2.40330E-6	9.99151E-4
6	0.0	0.0001	2.40330E-6	9.91514E-5
6	0.01	0.0	1.00107E-2	4.54333E-6
6	0.0001	0.0	9.89475E-5	3.49326E-5
6	0.01	0.01	1.00107E-2	1.00045E-2

B. For CH 10: Setability knowledge in terms of wavelength

No. of Decimal Digits	Error in Calculated Δα (rad)	Error in Calculated Δβ (rad)	Δλ Calculated Spectral Knowledge (μm)	Δλ Know. Required (μm)
10	3.50E-6	1.06E-6	4.50E-5	2.24E-4
6	2.40E-6	8.50E-7	4.04E-5	|
5	1.94E-5	9.7 E-6	1.47E-4	|
4	7.86E-6	4.85E-5	3.62E-4	|
6	2.40E-6	8.49E-7	4.04E-5	|
6	2.40E-6	8.47E-7	4.04E-5	|
6	1.07E-5	4.54E-6	8.85E-5	|
6	1.05E-6	3.49E-5	2.82E-4	|
6	1.07E-5	4.50E-6	8.82E-5	2.24E-4

4.1.5 Spectral Error Summary

Channel frequency setability, knowledge of channel frequency setability, and channel half-power bandwidth requirements can be satisfied by the Baseline V design. The prelaunch precision with which the channel amplitude vs. frequency response can be determined depends upon prelaunch calibration capability (Para 4.10.3).

Spectral errors will primarily result in equivalent systematic radiometric errors. Tuning tests using the AMTS physical method of profile retrieval with HIRS-2 data have shown that errors in knowledge of channel frequency and channel amplitude vs. frequency response can be reduced by system tuning. With careful design of the optical bench relatively short term nontunable errors should be quite small. The channel to channel correlated relative radiometric error component values should also be quite small. There is footprint to footprint and channel to channel correlation between these spectral error sources. They are uncorrelated with other error sources.

These spectral radiometric error component values could be better quantized through system tuning simulation tests specifically designed to determine the residual radiometric error as a function of the range of spectral error values. It is believed that the spectral errors estimated for Baseline V will not make a significant contribution to overall system radiometric error.

4.2 Signal Channel Random Radiometric Errors

Signal channel random radiometric errors consist of:

- Detector/preamp limited signal channel noise.
- Signal channel digitization error.
- Calibration channel noise contributions.

These error sources result in noise-like radiometric errors.

4.2.1 Detector/Preamp Limited Signal Channel Noise

Individual footprint signal channel detector/preamp limited random radiometric error for the Baseline V instrument is listed in Table 4-5. NEN_U is calculated using Eq 3.1 and 3.2. Detector area is calculated from detector dimensions listed in Table 3-9. $A\Omega$ is calculated from

$$A\Omega = \frac{S_{w\alpha}\, S_{h\alpha}\, G_{w\alpha}\, G_{H\alpha}}{f_{c\alpha}^{\,2}} \qquad (4.2)$$

using parameter values derived from Tables 3-8 and 3-9. Overall optical transmissivities, $E_g\tau$, are listed in Table 3-17.

Table 4-4 Sensitivity to knowledge of integrated channel intensity vs frequency response

CH No.	Freq. (cm^{-1})	Error in Channel Area Knowledge (%)	NEΔT (K)	NEΔT for 0.15% Area Uncertainty (K)
1	606.95	0.005	0.0027	0.081
7	665.55	0.140	0.0701	0.075
10	669.45	0.340	0.1882	0.083
19	2384.00	0.008	0.0005	0.009
22	2390.20	0.029	0.0061	0.032
26	2505.00	0.012	0.0024	0.030
28	2686.00	0.025	0.0054	0.032

Table 4-5 Baseline V signal channel detector/preamplifier limited random radiometric error

CH	ν (cm^{-1})	$\Delta\nu$ (cm^{-1})	A_d (cm^2)	τ	Eq. Scene Temp (K)			D^* ($cm\sqrt{Hz}/W$)			N_ν ($W/cm^2 \cdot sr \cdot cm^{-1}$)			NEN_ν ($W/cm^2 \cdot sr \cdot cm^{-1}$)			NEΔT (K)			Band NEAT (K)	
					T_{min}	T_{std}	T_{max}	T_{min}	T_{std}	T_{max}	T_{min}	T_{std}	T_{max}	T_{min}	T_{std}	T_{max}	T_{min}	T_{std}	T_{max}	Mean	Standard Deviation
1	606.95	0.50	2.71E-4	0.096	230	263.83	286	4.61E10	4.61E10	4.61E10	6.11E-6	1.01E-5	1.32E-5	4.22E-8	4.22E-8	4.22E-8	0.408	0.321	0.285		
2	623.20	0.50	3.14E-4	0.096	229	260.15	283	4.64E10	4.64E10	4.64E10	5.86E-6	9.48E-6	1.27E-5	4.51E-8	4.51E-8	4.51E-8	0.440	0.347	0.305		
3	627.60	0.50	3.25E-4	0.096	218	236.51	260	4.66E10	4.66E10	4.66E10	4.75E-6	6.61E-6	9.42E-6	4.57E-8	4.57E-8	4.57E-8	0.497	0.418	0.351		
4	634.30	0.50	3.39E-4	0.096	211	226.46	256	4.63E10	4.63E10	4.63E10	4.08E-6	5.50E-6	8.85E-6	4.69E-8	4.69E-8	4.69E-8	0.552	0.470	0.369		
5	646.60	0.50	3.62E-4	0.096	202	219.66	248	4.61E10	4.61E10	4.61E10	3.25E-6	4.73E-6	7.74E-6	4.89E-8	4.89E-8	4.89E-8	0.650	0.527	0.407		
6	654.35	0.50	3.78E-4	0.107	195	219.68	255	4.63E10	4.63E10	4.63E10	2.69E-6	4.66E-6	8.53E-6	4.43E-8	4.43E-8	4.43E-8	0.656	0.480	0.349	0.452	0.134
7	665.55	0.50	3.92E-4	0.107	197	222.69	266	4.61E10	4.61E10	4.61E10	2.74E-6	4.83E-6	9.86E-6	4.56E-8	4.56E-8	4.56E-8	0.666	0.481	0.332		
8	666.85	0.50	3.95E-4	0.107	194	223.38	279	4.60E10	4.60E10	4.61E10	2.53E-6	4.88E-6	1.17E-5	4.58E-8	4.58E-8	4.58E-8	0.701	0.480	0.307		
9	668.15	0.50	3.96E-4	0.107	196	254.00	300	4.61E10	4.61E10	4.61E10	2.79E-6	8.26E-6	1.50E-5	4.58E-8	4.58E-8	4.58E-8	0.661	0.363	0.274		
10	669.45	0.50	3.97E-4	0.107	199	233.04	285	4.61E10	4.61E10	4.61E10	2.85E-6	5.82E-6	1.26E-5	4.58E-8	4.58E-8	4.58E-8	0.[illegible]	0.436	0.296		
11	675.00	0.75	4.34E-4	0.128	231	285.00	327	8.07E10	8.07E10	8.07E10	3.44E-6	9.74E-6	1.73E-5	1.53E-8	1.53E-8	1.53E-8	0.187	0.100	0.073		
12	1040.80	1.00	5.01E-3	0.128	198	256.26	290	3.60E12	3.32E12	3.07E12	6.97E-7	3.90E-6	7.72E-6	8.72E-10	9.45E-10	1.02E-9	0.033	0.011	0.007		
13	1231.60	1.00	4.67E-3	0.128	231	285.40	327	5.76E12	4.51E12	3.79E12	1.04E-6	4.48E-6	9.90E-6	5.26E-10	6.72E-10	7.99E-10	0.015	0.007	0.001	0.037	0.050
14	1650.10	1.30	4.79E-3	0.166	220	239.30	261	1.19E13	1.10E13	9.57E12	1.10E-7	2.63E-7	6.00E-7	1.53E-10	1.65E-10	1.90E-10	0.028	0.015	0.009		
15	1700.30	1.30	5.45E-3	0.179	216	229.50	255	1.47E13	1.46E13	1.21E13	1.06E-8	1.37E-7	3.99E-7	1.22E-10	1.23E-10	1.49E-10	0.033	0.019	0.010		
16	1839.40	1.50	4.56E-3	0.157	232	259.32	282	1.75E13	1.35E13	1.03E13	8.24E-8	2.74E-7	6.23E-7	9.30E-11	1.20E-10	1.58E-10	0.023	0.011	0.008		
17	1850.90	1.50	4.72E-3	0.160	233	266.90	289	1.78E13	1.27E13	9.67E12	8.21E-8	3.51E-7	7.52E-7	9.13E-11	1.28E-10	1.68E-10	0.023	0.010	0.007	0.016	0.011
18	1930.10	1.50	5.62E-3	0.150	232	280.28	315	1.68E13	1.35E13	1.01E13	5.22E-[illegible]	4.27E-7	1.27E-6	1.12E-10	1.40E-10	1.87E-10	0.040	0.009	0.005		
19	2384.00	2.00	5.81E-3	0.131	214	229.56	274	3.59E13	3.56E13	3.15E13	1.77E-[illegible]	5.23E-9	5.90E-8	4.60E-11	4.64E-11	5.24E-11	0.344	0.136	0.019		
20	2386.10	2.00	3.72E-3	0.128	222	240.97	299	3.33E13	3.25E13	2.31E13	3.11E-9	1.05E-8	1.67E-7	4.06E-11	4.13E-11	5.85E-11	0.186	0.067	0.009		
21	2388.20	2.00	5.84E-3	0.128	229	254.69	313	3.57E13	3.42E13	2.33E13	4.94E-9	2.24E-8	2.77E-7	4.74E-11	4.9[illegible]E-11	7.27E-11	0.146	0.042	0.007		
22	2390.20	2.00	3.78E-3	0.134	231	265.88	321	3.34E13	2.99E13	1.81E13	5.57E-9	3.93E-8	3.62E-7	3.90E-11	4.25E-11	7.19E-11	0.108	0.023	0.006		
23	2392.35	2.00	5.88E-3	0.128	232	273.30	325	3.57E13	3.21E13	2.08E13	5.87E-9	5.53E-8	4.10E-7	4.76[illegible]11	5.30E-11	8.17E-11	0.126	0.021	0.006	0.083	0.124
24	2394.50	2.00	3.84E-3	0.138	232	276.20	326	3.31E13	2.80E13	1.68E13	5.81E-9	6.26E-8	4.21E-7	3.85[illegible]11	4.55E-11	7.58E-11	0.103	0.016	0.006		
25	2424.00	2.50	4.23E-3	0.163	232	281.38	331	3.30E13	2.60E13	1.45E13	5.02E-9	7.02E-8	4.50E-7	2.74E-11	3.48E-11	6.25E-11	0.084	0.011	0.004		
26	2505.00	2.50	5.07E-3	0.157	232	285.22	342	3.31E13	2.63E[illegible]	1.34E13	3.35E-9	6.09E-8	4.96E-7	3.11E-11	3.91E-11	7.68E-11	0.138	0.014	0.005		
27	2616.50	2.50	4.12E-3	0.154	232	286.57	354	3.07E13	2.65E13	1.32E13	1.91E-9	4.21E-8	5.14E-7	3.08E-11	3.57E-11	7.17E-11	0.228	0.019	0.005		
28	2686.00	2.50	4.84E-3	0.160	232	286.53	364	3.07E13	2.67E13	1.17E13	1.35E-9	3.20E-8	5.65E-7	3.21E-11	3.70E-11	8.44E-11	0.574	0.025	0.005		

$\frac{\sqrt{\Delta F}}{F_c} = 5.65$

$A\Omega = 9.955 \times 10^{-4}\ cm^2 \cdot sr$

Electrical noise bandwidth, ΔF, is calculated using the chopped square wave model of Appendix D. Baseline V uses 56 chopper cycles per footprint dwell interval. Integration time is reduced to 0.1273 sec to allow use of an integer number of cycles per footprint dwell. For a 1/f noise frequency knee of 100 Hz and using a value of 0.5 for the chopper factor, Fc, $\sqrt{\Delta F}/Fc$ = 5.65 (Table D-1, Appendix D). Note that the effect of 1/f noise is included in the equivalent noise bandwidth, ΔF, rather than in detector D* values. A value of 100 Hz for the 1/f knee is representative of good PC HgCdTe performance and is very conservative for the PV detectors which typically have a knee of ≈1 Hz.

Detector D* peak values are calculated using the D* models of Appendix F. Detector sizes are listed in Table 3-9. Detector temperature is 75 K. Background is calculated using the method of Para 3.1.1.4.3 for a detector cryostat temperature of 75 K, an optics case temperature of 160 K, and scene equivalent temperatures listed in Table 4-5. Signal photon flux density, total photon flux density, and the ratio of unfocused flux/total photon flux vs. equivalent scene temperature is listed in Table 4-6. Detector parameter and performance printouts are listed in Appendix F for all channels. Baseline V D* values listed in Table 4-5 for the AMTS channel frequencies were derived from D* peak values using the curve of Fig F-2 (Appendix F) for PC and PV HgCdTe detectors and of Fig F-3 for PV InSb detectors. In addition, D* values listed in Table 4-5 for PC and PV HgCdTe detectors are reduced by a factor of 1.5 from the calculated values. For PV InSb detectors, R_oA values assumed for calculation were less than R_oA values measured for detectors developed by Cincinatti Electronics for other JPL programs. Consequently, we believe that these D* values used for Baseline V error analysis are reasonably conservative.

Baseline V channel half-power bandwidths, $\Delta\upsilon$, are listed in Table 4-5.

The effects upon detector D* of increasing case and detector temperatures for selected channels are shown in Table 4-7. PC detector D* as a function of detector bias potential is shown in Table 4-8. The relative effect of preamp noise upon D* is shown in Table 4-9.

4.2.1.1 Detector/Preamp Limited Uncertainties, Design Options, and Constraints

Detector/preamp limited noise is an important error source in that it limits AMTS system performance. It effectively places a limit on the radiometric error per composite footprint or upon the minimum size of the composite footprint. This error may be minimized by optimizing instrument design using as guidelines the NEN parametric equations of Para 3.1.1.1 and the detector/preamp considerations and parametric equations of Para 3.1.1.4.

It appears to be impractical to achieve significant improvement in Baseline V performance by increasing instrument scale, by improving the optical performance, or by degrading the individual footprint spatial resolution. The greatest uncertainties, and possibly the greater opportunities for optimization, are associated with detector/preamp performance. For example, from Table 3-5 and from Fig 3-15, 3-16, and 3-17, we can make the following general observations concerning major noise sources and possible means for reducing them:

Table 4-6 Baseline V detector background flux vs equivalent scene temperature

CH	ν (cm^{-1})	Detector Type	Detector Area (cm^2)	Signal Photon Flux Density ($ph/cm^2 \cdot s$)			Total Photon Flux Density ($ph/cm^2 \cdot s$)			Unfocused Flux/ Total Photon Flux (%)		
				T_{min}	T_{std}	T_{max}	T_{min}	T_{std}	T_{max}	T_{min}	T_{std}	T_{max}
1	606.95	PC HgCdTe	3.12E-4	3.22E13	5.30E13	6.94E13	1.31E15	1.34E15	1.36E15	23.7	23.3	23.0
2	623.20		3.62E-4	2.48E13	4.02E13	5.37E13	1.04E15	1.05E15	1.07E15	30.2	29.8	29.4
3	627.80		3.75E-4	1.94E13	2.69E13	3.84E13	9.80E14	9.97E14	9.97E14	31.7	31.4	31.0
4	634.30		3.91E-4	1.54E13	1.82E13	3.36E13	9.01E14	9.10E14	9.19E14	34.7	34.5	34.1
5	646.60		4.18E-4	1.10E13	1.60E13	2.63E13	7.90E14	7.96E14	8.14E14	39.4	39.3	38.8
6	654.35		4.32E-4	9.71E12	1.68E13	3.09E13	7.90E14	8.02E14	8.14E14	39.6	39.1	38.4
7	665.55		4.53E-4	9.27E12	1.64E13	3.35E13	7.24E14	7.30E14	7.48E14	43.0	42.6	41.6
8	666.85		4.56E-4	8.50E12	1.64E13	3.94E13	7.18E14	7.24E14	7.48E14	43.4	43.0	41.6
9	668.15		4.57E-4	9.19E12	2.73E13	4.97E13	7.06E14	7.24E14	7.42E14	44.3	43.2	42.0
10	669.45	PC HgCdTe	4.58E-4	9.27E12	1.90E13	4.13E13	7.00E14	7.12E14	7.30E14	44.7	44.0	42.8
11	875.00	PC HgCdTe	3.44E-4	5.68E13	1.81E14	3.17E14	2.67E15	2.81E15	2.95E15	26.8	25.5	24.3
12	1040.80	PV HgCdTe	5.79E-3	1.12E12	6.32E12	1.25E13	3.02E13	3.55E13	4.15E13	3.22E-1	2.75E-1	2.34E-1
13	1231.60		5.40E-3	1.55E12	6.70E12	1.48E13	9.87E12	1.62E13	2.30E13	8.69E-2	5.71E-2	3.72E-2
14	1650.10		5.54E-3	1.38E11	3.31E11	7.54E11	9.47E11	1.14E12	1.56E12	1.94E-4	1.61E-4	1.18E-4
15	1700.30	PV HgCdTe	6.30E-3	7.60E10	9.01E10	4.29E11	5.79E11	5.93E11	9.32E11	3.18E-4	3.10E-4	1.97E-4
16	1839.40	PV HgCdTe	5.27E-3	1.17E11	3.91E11	8.84E11	2.59E11	5.33E11	1.03E12	3.88E-6	1.89E-6	9.76E-7
17	1850.90	PV HgCdTe	5.45E-3	1.17E11	4.99E11	1.07E12	2.48E11	6.27E11	1.20E12	4.07E-6	1.60E-6	8.40E-7
18	1930.10	PV InSb	6.50E-3	4.60E10	3.61E11	1.08E12	9.01E10	4.06E11	1.12E12	1.12E-5	2.48E-6	8.97E-7
19	2384.00	PV InSb	6.72E-3	1.33E9	3.94E9	4.44E10	4.85E9	7.48E9	4.79E10	2.08E-4	1.35E-4	2.10E-5
20	2386.10		4.30E-3	3.44E9	1.15E10	1.85E11	8.84E9	1.70E10	1.89E11	1.14E-4	5.93E-5	5.31E-6
21	2388.20		6.75E-3	3.59E9	1.63E10	2.01E11	6.88E9	1.05E10	2.04E11	1.46E-4	5.15E-5	4.94E-6
22	2390.20		4.37E-3	6.21E9	4.40E10	4.05E11	1.16E10	4.93E10	4.11E11	8.68E-5	2.04E-5	2.45E-6
23	2392.35		6.79E-3	4.10E9	3.86E10	2.86E11	7.24E9	4.17E10	2.90E11	1.39E-4	2.41E-5	3.48E-6
24	2394.50		4.44E-3	6.75E9	7.30E10	4.91E11	1.26E10	7.90E10	4.97E11	8.00E-5	1.28E-5	2.03E-6
25	2424.00		4.89E-3	7.90E9	1.10E11	7.06E11	1.43E10	1.17E11	7.12E11	7.06E-5	8.62E-6	1.41E-6
26	2505.00		5.86E-3	5.36E9	9.71E10	7.96E11	9.80E9	1.01E11	7.96E11	1.03E-4	9.91E-6	1.26E-6
27	2616.50		4.76E-3	2.59E9	5.69E10	6.94E11	4.94E9	5.92E10	7.00E11	2.04E-4	1.70E-5	1.45E-6
28	2686.00	PV InSb	5.59E-3	2.11E9	5.00E10	8.84E11	4.15E9	5.21E10	8.84E11	2.42E-4	1.93E-5	1.14E-6

$A\Omega = 9.955 \times 10^{-4}$ $cm^2 \cdot sr$
Case temperature 160 K
Detector temperature 75 K

Table 4-7 Detector D* (peak) vs case and detector temperature[1]

Band	CH	Detector Type	D* vs Case/Detector Temperature (K)				Max Change From 160/75 To 180/80
			160/75 ②	180/75	160/80	180/80	
1	1	PC HgCdTe	6.91E10	6.89E10	5.30E10	5.29E10	-23.4%
	11	PC HgCdTe	1.21E11	1.17E11	5.56E10	5.51E10	-54.5%
2	12	PV HgCdTe	4.98E12	3.18E12	4.11E12	2.92E12	-41.4%
	14	PV HgCdTe	1.65E13	8.93E12	1.65E13	8.93E12	-45.9%
3	16	PV HgCdTe	2.03E13	1.49E13	2.02E13	1.49E13	-26.6%
	19	PV InSb	4.16E13	3.98E13	4.07E13	3.90E13	- 6.2%
4	25	PV InSb	3.04E13	2.93E13	3.01E13	2.90E13	- 4.6%
	28	PV InSb	3.57E13	3.48E13	3.50E13	3.43E13	- 3.9%

[1]U.S. Std. Atmosphere; all detector feedback resistors and preamps at case temperature; PC HgCdTe feedback resistors are 10x detector dark resistances.

[2]Baseline V temperatures

Table 4-8 PC HgCdTe detector D* (peak) vs detector bias field potential[1]

Band	CH	Detector Bias[2] (V/cm)	Bias Power (W)	D* $\left(\frac{cm\sqrt{Hz}}{W}\right)$
1	1	2	4.67E-6	3.00E10
		4	1.87E-5	5.06E10
		6	4.20E-5	6.25E10
		8	7.46E-5	6.91E10
		10	1.17E-4	7.30E10
		12	1.68E-4	7.54E10
		14	2.29E-4	7.70E10
		16	2.99E-4	7.81E10
1	10	2	6.85E-6	3.40E10
		4	2.74E-5	5.53E10
		6	6.16E-5	6.63E10
		8	1.10E-4	7.20E10
		10	1.71E-4	7.52E10
		12	2.46E-4	7.71E10
		14	3.36E-4	7.83E10
		16	4.38E-4	7.92E10
2	11	2	5.64E-6	3.31E10
		4	2.26E-5	6.49E10
		6	5.08E-5	9.43E10
		8	9.03E-5	1.21E11
		10	1.41E-4	1.44E11
		12	2.03E-4	1.64E11
		14	2.76E-4	1.81E11
		16	3.61E-4	1.95E11

[1]U.S. Std. Atmosphere; case temp = 160 K; cryostat temp = 75 K

[2]Baseline V bias potential = 8 V/cm

Table 4-9 D* sensitivity to preamp noise

Detector Type	Preamp Noise ($V/\sqrt{Hz}$)	D* Det/Preamp ($cm\sqrt{Hz}/W$)
PC HgCdTe	1×10^{-9}	7.8×10^{10}
	1×10^{-8}	4.1×10^{10}
	5×10^{-8}	9.6×10^{9}
	1×10^{-7}	4.8×10^{9}
PV HgCdTe	1×10^{-9}	2.2×10^{13}
	1×10^{-8}	2.1×10^{13}
	1×10^{-7}	8.2×10^{12}
	5×10^{-7}	1.8×10^{12}
	1×10^{-6}	8.9×10^{11}
PV InSb	1×10^{-9}	3.8×10^{13}
	1×10^{-8}	3.6×10^{13}
	1×10^{-7}	3.6×10^{13}
	1×10^{-6}	1.2×10^{13}

1) For long wavelength PC HgCdTe detectors

   a) GR Noise
      - Decrease detector thickness

   b) Preamp Noise
      - Decrease detector thickness
      - Increase detector bias
      - Decrease detector temperature

2) For PV HgCdTe intermediate range detectors

   a) Feedback resistor Johnson noise
      - Increase feedback resistance

   b) Instrument background noise
      - Decrease optics case temperature

3) For PV InSb short wavelength detectors

   a) Johnson noise
      - Bias the photodiode junction
      - Immerse the detector

   b) Instrument background noise
      - Decrease optics case temperature

   c) Feedback resistor Johnson noise
      - Increase feedback resistance

Clearly, there are a number of complex interactive trade-offs necessary to further optimize detector/preamp limited instrument performance. They involve investigations at the detector and preamp device levels and at the circuit level, as well as at the overall instrument level. Some of these issues must be addressed on the bench, by building and testing devices and circuits; they cannot be resolved at the study level.

We believe there is a very good chance that the Baseline V detector/preamp noise limited performance listed in Table 4-5 can be achieved or bettered. At this point, we would guess that the performance cannot be bettered by more than about a factor of 2. It must be remembered, when optimizing the detector/preamp for minimum noise, that possible effects upon amplitude linearity and 1/f noise frequency knee must be considered. We have considered use of PV HgCdTe detectors for the short wavelength channels where channel frequencies are some distance removed from the D* peak frequency of InSb. For detector parameter values used in the D* models, calculated instrument D* values for the two detector types were virtually identical.

4.2.2 Signal Channel Digitization Error

Radiometric errors due to signal channel digitization step size are listed in Table 4-10. Maximum radiance values, N_{max}, listed correspond to maximum equivalent scene temperature, T_{max}, or to the hot calibration target

Table 4-10 Baseline V signal channel digitization random radiometric error[1]

CH	υ (cm^{-1})	Max. Eq. Target Temp (K)		N_{max} $\left(\frac{W}{cm^2\ sr\ cm^{-1}}\right)$	NEN_υ (1σ) $\left(\frac{W}{cm^2\ sr\ cm^{-1}}\right)$	NEΔT (1σ) (K)		
		T_{max}	T_{cal}			T_{min}	T_{std}	T_{max}
1	606.95		310	1.69×10^{-5}	3.57×10^{-10}	0.003	0.003	0.002
2	623.20		310	1.69×10^{-5}	3.57×10^{-10}	0.003	0.003	0.002
3	627.80		310	1.69×10^{-5}	3.57×10^{-10}	0.004	0.003	0.003
4	634.30		310	1.69×10^{-5}	3.57×10^{-10}	0.004	0.004	0.003
5	646.60		310	1.69×10^{-5}	3.57×10^{-10}	0.005	0.004	0.003
6	654.35		310	1.68×10^{-5}	3.55×10^{-10}	0.005	0.004	0.003
7	665.55		310	1.68×10^{-5}	3.55×10^{-10}	0.005	0.004	0.003
8	666.85		310	1.67×10^{-5}	3.53×10^{-10}	0.005	0.004	0.002
9	668.15		310	1.67×10^{-5}	3.53×10^{-10}	0.005	0.003	0.002
10	669.45		310	1.67×10^{-5}	3.53×10^{-10}	0.005	0.003	0.002
11	875.00	327		1.73×10^{-5}	3.66×10^{-10}	0.004	0.002	0.002
12	1040.80		310	1.08×10^{-5}	2.28×10^{-10}	0.009	0.003	0.002
13	1231.60	327		9.90×10^{-6}	2.09×10^{-10}	0.006	0.002	0.001
14	1650.10		310	2.53×10^{-6}	5.35×10^{-11}	0.010	0.005	0.002
15	1700.30		310	2.19×10^{-6}	4.63×10^{-11}	0.013	0.011	0.003
16	1839.40		310	1.45×10^{-6}	3.07×10^{-11}	0.008	0.003	0.001
17	1850.90		310	1.40×10^{-6}	2.96×10^{-11}	0.007	0.002	0.001
18	1930.10	315		1.27×10^{-6}	2.69×10^{-11}	0.010	0.002	0.001
19	2384.00		310	2.53×10^{-7}	5.35×10^{-12}	0.040	0.016	0.002
20	2386.10		310	2.51×10^{-7}	5.31×10^{-12}	0.024	0.009	0.001
21	2388.20	313		2.77×10^{-7}	5.86×10^{-12}	0.018	0.005	0.001
22	2390.20	321		3.62×10^{-7}	7.65×10^{-12}	0.021	0.004	0.001
23	2392.35	325		4.10×10^{-7}	8.67×10^{-12}	0.023	0.003	0.001
24	2394.50	326		4.21×10^{-7}	8.90×10^{-12}	0.024	0.003	0.001
25	2424.00	331		4.50×10^{-7}	9.51×10^{-12}	0.029	0.003	0.001
26	2505.00	342		4.96×10^{-7}	1.05×10^{-11}	0.047	0.004	0.001
27	2616.50	354		5.14×10^{-7}	1.09×10^{-11}	0.081	0.006	0.001
28	2686.00	364		5.65×10^{-7}	1.19×10^{-11}	0.123	0.008	0.001

[1]For a 14 bit ADC and a signal channel dynamic range design margin of 20%

temperature, T_{cal}, whichever is greater (Table 3-34). The design dynamic range for Baseline V has been taken as 120 percent of these maximum radiance values. The DC offset bias (Fig 3-33) employed to prevent a signal voltage sign reversal at the ADC input effectively corresponds to a radiance below that representing chopper blade temperature. (Note that channel gains for individual detectors would be set at assembly for nominal detector responsivity.) Digitization error distribution is rectangular. The standard deviation of this rectangular distribution is defined as

$$\text{Standard deviation} = \frac{\text{Digitization step size}}{\sqrt{12}} \qquad (4.3)$$

Baseline V uses 14 bit ADC's for all channels.

4.2.3 Calibration Channel Detector/Preamp Limited Random Radiometric Errors

A schematic diagram of the radiometric calibration timing sequence is shown in Fig 4-1. The average radiance readings of 10 sets of calibration target looks are used in Baseline V to obtain slope and offset values for reducing the scene radiances for one scene line scan. For the scene looks in line scan i, for example, calibration looks for (i - 5) through (i + 5) are averaged. Calibration target look dwell times are the same as scene dwell times. Consequently, detector/preamp noise limited random radiometric calibration error values and calibration channel digitization error values are reduced by a factor of $\sqrt{10}$. To a very close approximation the detector/preamp noise limited random radiometric calibration error component and the calibration channel digitization error component are equal to the corresponding signal channel error values listed in Tables 4-5 and 4-10 divided by $\sqrt{10}$.

The "look ahead" feature, using calibration data from calibration looks (i + 1) through (i + 5) in the traveling average, is used to eliminate ramp errors in the calibrated signal channel radiances (Para 3.1.2). Ramp errors are not part of the "noise like" random radiometric errors discussed in Para 4.2. There is no compelling reason to choose a traveling average of 10 calibration looks for Baseline V. Increasing the length of the traveling average would further reduce the calibration look contribution to the random radiometric error but would probably increase the ramp error contribution.

4.2.4 Detector/Preamp Limited Random Radiometric Error Summary

Random radiometric errors in terms of NEΔT are summarized in Table 4-11 for the Baseline V instrument configuration. Detector signal channel noise predominates. Values listed in Table 4-11 represent the standard deviation of brightness temperature errors of a single footprint (10 x 10 km nominal at nadir) basis. Since the error sources within this group are uncorrelated footprint to footprint, NEΔT for these errors is proportional to $1/\sqrt{N}$, where N is the number of individual footprint elements combined within a composite footprint. The correlated channel to channel error component is negligible. Errors due to these sources are uncorrelated with respect to each other and to other error sources.

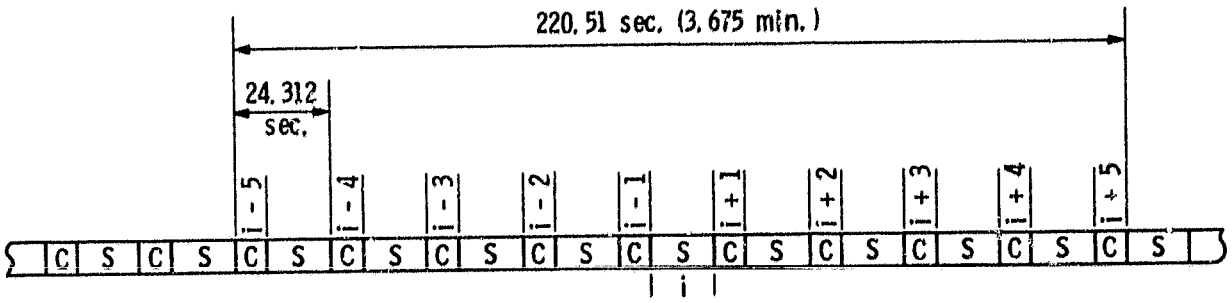

"C" REPRESENTS ONE COLD AND ONE HOT CALIBRATION TARGET DWELL PER SPECTRAL CHANNEL PER DETECTOR WHICH OCCUR BETWEEN SCENE SCANS

"S" REPRESENTS 130 SCENE DWELLS PER SPECTRAL CHANNEL PER DETECTOR PER LINE SCAN.

Figure 4-1 Schematic diagram of radiometric calibration timing sequence

Table 4-11 Baseline V random radiometric error summary per individual footprint element in terms of NEΔT vs equivalent target temperature

		NEΔT (1σ) (K)														
		Detector Signal Channel Noise			Signal Channel Digitization Error			Detector Calibration Channel Noise			Calibration Channel Digitization Error			Total Channel Noise			Mean and Standard Deviation for Total Channel Noise
CH	ν (cm^{-1})	T_{min}	T_{std}	T_{max}	T_{min}	T_{std}	T_{max}	T_{min}	T_{std}	T_{max}	T_{min}	T_{std}	T_{max}	T_{min}	T_{std}	T_{max}	$\bar{x}$/SD
1	605.95	0.408	0.321	0.285	0.003	0.003	0.002	0.129	0.102	0.090	0.001	0.001	0.001	0.428	0.337	0.299	
2	623.20	0.440	0.347	0.305	0.003	0.003	0.002	0.139	0.110	0.096	0.001	0.001	0.001	0.461	0.364	0.320	
3	627.80	0.497	0.418	0.351	0.004	0.003	0.003	0.157	0.132	0.111	0.001	0.001	0.001	0.521	0.438	0.368	
4	634.30	0.552	0.470	0.369	0.004	0.004	0.003	0.175	0.149	0.117	0.001	0.001	0.001	0.579	0.493	0.387	
5	646.60	0.650	0.527	0.407	0.005	0.004	0.003	0.206	0.167	0.129	0.002	0.001	0.001	0.682	0.553	0.427	
6	654.35	0.656	0.480	0.349	0.005	0.004	0.003	0.207	0.152	0.110	0.002	0.001	0.001	0.688	0.504	0.366	0.471/0.128
7	665.55	0.666	0.481	0.332	0.005	0.004	0.003	0.211	0.152	0.105	0.002	0.001	0.001	0.699	0.504	0.348	
8	666.85	0.701	0.480	0.307	0.005	0.004	0.002	0.222	0.152	0.097	0.002	0.001	0.001	0.735	0.504	0.322	
9	668.15	0.661	0.363	0.274	0.005	0.003	0.002	0.209	0.115	0.087	0.002	0.001	0.001	0.693	0.381	0.287	
10	669.45	0.653	0.436	0.296	0.005	0.003	0.002	0.206	0.138	0.094	0.002	0.001	0.001	0.685	0.457	0.311	
11	875.00	0.187	0.100	0.073	0.004	0.002	0.002	0.059	0.032	0.023	0.001	0.001	0.001	0.200	0.105	0.077	
12	1040.80	0.033	0.011	0.007	0.009	0.003	0.002	0.010	0.003	0.002	0.003	0.001	0.001	0.036	0.012	0.008	
13	1231.60	0.015	0.007	0.001	0.006	0.002	0.001	0.005	0.002	0.000	0.002	0.001	0.000	0.017	0.008	0.001	0.040/0.053
14	1650.10	0.028	0.015	0.009	0.010	0.005	0.002	0.009	0.005	0.003	0.003	0.002	0.001	0.031	0.017	0.010	
15	1700.30	0.033	0.019	0.010	0.013	0.011	0.003	0.010	0.006	0.003	0.004	0.003	0.001	0.037	0.023	0.011	
16	1839.40	0.023	0.011	0.008	0.008	0.003	0.001	0.007	0.003	0.003	0.003	0.001	0.000	0.026	0.012	0.009	
17	1850.90	0.023	0.010	0.007	0.007	0.002	0.001	0.007	0.003	0.002	0.002	0.001	0.000	0.025	0.011	0.007	0.016/0.012
18	1930.10	0.040	0.009	0.005	0.010	0.002	0.001	0.013	0.003	0.002	0.003	0.001	0.000	0.043	0.010	0.005	
19	2384.00	0.344	0.136	0.019	0.040	0.016	0.002	0.109	0.043	0.006	0.013	0.005	0.001	0.363	0.144	0.020	
20	2386.10	0.135	0.067	0.009	0.024	0.009	0.001	0.059	0.021	0.003	0.008	0.003	0.000	0.197	0.073	0.010	
21	2388.20	0.146	0.042	0.007	0.018	0.005	0.001	0.046	0.013	0.002	0.006	0.002	0.000	0.154	0.044	0.007	
22	2390.20	0.108	0.023	0.006	0.021	0.004	0.001	0.034	0.007	0.002	0.007	0.001	0.000	0.115	0.024	0.006	
23	2392.35	0.126	0.021	0.006	0.023	0.003	0.001	0.040	0.007	0.002	0.007	0.001	0.000	0.134	0.022	0.006	0.089/0.132
24	2394.50	0.103	0.016	0.006	0.024	0.003	0.001	0.033	0.005	0.002	0.008	0.001	0.000	0.111	0.017	0.006	
25	2424.00	0.084	0.011	0.004	0.029	0.003	0.001	0.027	0.003	0.001	0.009	0.001	0.000	0.093	0.012	0.004	
26	2505.00	0.138	0.014	0.005	0.047	0.004	0.001	0.044	0.004	0.002	0.015	0.001	0.000	0.153	0.015	0.005	
27	2616.50	0.228	0.019	0.005	0.081	0.006	0.001	0.072	0.006	0.002	0.026	0.002	0.000	0.254	0.021	0.005	
28	2686.00	0.574	0.025	0.005	0.123	0.008	0.001	0.182	0.008	0.002	0.039	0.003	0.000	0.616	0.028	0.005	

4.3 Spectral Crosstalk Radiometric Errors

Spectral crosstalk radiometric errors are a function of the scene spectral profile within the bandwidth of the spectral channel order filters.

Spectral crosstalk errors are not correlated with errors in other groups. There is a high degree of correlation from channel to channel and from footprint to footprint for scenes having a high degree of homogeneity. Consequently, in the limit, these errors are not reduced by spatial integration of a number of individual footprints to form a larger composite footprint. Errors in this group are considered nontunable for purposes of analysis. Spectral crosstalk radiometric errors consist of:

- Grating order crosstalk
- Grating grass crosstalk
- Slit function wing response crosstalk

4.3.1 Grating Order Crosstalk

Order crosstalk in the grating spectrometer can occur when wavelengths corresponding to grating orders other than the desired order fall upon the exit slit. Radiation at a given wavelength, λ, from the inlet slit at an incident angle, α, will be diffracted by the grating and will impinge upon the image plane at a diffracted angle, β_1, in a given grating order, m_1. Since the AMTS spectrometer uses an echelle grating operating in relatively high orders, radiation at a number of undesired wavelengths corresponding to other than the desired order will fall upon the spatial filter represented by the exit slit. A spectral bandpass order filter is inserted ahead of the exit slit to reject these unwanted wavelengths. In addition, for some optical configurations, radiation can fall upon the exit slit after a number of passes, n, through the system. For example, radiation scattered from the image plane at angle β_1 will pass back through the system at a grating incident angle of β_1 and be rediffracted by the grating. Rediffracted radiation in order m_1 will, of course, fall on the inlet slit at grating angle α. Rediffracted radiation may, however, fall back upon the image plane at grating angle β_2 in order m_2. For a spectral channel corresponding to a grating incident angle of α and a diffraction angle of β, the interfering wavelength for n passes through the spectrometer when n is odd is:

$$\lambda_n = \frac{a(\sin\beta + \sin\alpha)}{m_n - m_{n-1} + \cdots + m_1} \qquad (4.4a)$$

The interfering wavelength when n is even is:

$$\lambda_n = \frac{a(\sin\beta - \sin\alpha)}{m_n - m_{n-1} + \cdots - m_1} \qquad (4.4b)$$

where "a" is the grating line spacing. The numerators in Eq 4.4a and 4.4b are constants for a given spectral channel for all applicable values of n. The denominators can have only integer values of 1, 2, 3, ••• n or -1, -2, -3, ••• n, depending upon whether the numerator is a positive or negative constant, for realizable (positive) wavelengths. Consequently, from Eq 4.4a and 4.4b, all wavelengths which could possibly result in grating order crosstalk can be readily determined. (Note that in Baseline V, where the reflective image plane mask — or an out-of-band order filter — directs scattered energy out of the optical system, all possible interfering wavelengths are defined by Eq 4.4a where n is unity.)

The bandwidth of the interfering signal, $\Delta\upsilon_i$, is:

$$\Delta\upsilon_i = \Delta\upsilon \frac{\upsilon_i}{\upsilon} \qquad (4.5)$$

where:

υ_i = interfering wavenumber

υ = channel design wavenumber

$\Delta\upsilon$ = channel design bandwidth

The spectral interference ratio incident upon the spectrometer from the target scene for a particular interfering order is the ratio of the spectral radiance at the interfering frequency integrated over the interfering order bandwidth to the spectral radiance at the design channel frequency integrated over the design channel bandwidth. (Note that this spectral interference ratio is a function of the scene spectral profile.) Consequently, the resulting spectral crosstalk ratio of the system for a particular interfering order is the product of:

- The spectral interference ratio incident upon the instrument.
- The relative order filter transmissivity for the interfering order with respect to the design order.
- The relative detector response to the interfering order with respect to the design order.
- The relative transmissivity of the spectrometer optics — excluding the order filter — at the interfering order with respect to the design order.

The overall order crosstalk ratio for a particular channel is the ratio of the sum of the crosstalk ratios for all interfering orders to the relative response of the channel in the design order.

Grating order crosstalk errors for the Baseline V instrument are listed in Table 4-12. For the spectral interference ratio, the sum radiances were calculated using a line-by-line atmospheric program developed

Table 4-12 Baseline V grating order crosstalk errors

CH	ν (cm-1)	Crosstalk Ratio	NEΔT (K)
1	606.95	1.568E-6	1.205E-4
2	623.20	1.417E-6	1.036E-4
3	627.80	2.056E-6	1.245E-4
4	634.30	2.325E-6	1.284E-4
5	646.60	2.799E-6	1.431E-4
6	654.35	2.747E-6	1.388E-4
7	665.55	2.529E-6	1.292E-4
8	666.85	2.454E-6	1.258E-4
9	668.15	1.402E-6	9.190E-5
10	669.45	2.035E-6	1.128E-4
11	875.00	—	—
12	1040.80	8.873E-7	3.880E-5
13	1231.60	1.259E-6	5.780E-5
14	1650.10	—	—
15	1700.30	—	—
16	1839.40	1.780E-6	4.520E-5
17	1850.90	1.469E-6	3.430E-5
18	1930.10	6.934E-6	1.960E-5
19	2384.00	1.332E-4	2.046E-3
20	2386.10	4.605E-5	7.789E-4
21	2388.20	2.768E-5	5.225E-4
22	2390.20	1.778E-5	3.655E-4
23	2392.35	1.109E-5	2.406E-4
24	2394.50	1.021E-5	2.261E-4
25	2424.00	9.472E-6	2.149E-4
26	2505.00	1.115E-5	2.517E-4
27	2616.50	1.714E-5	3.738E-4
28	2686.00	2.253E-5	4.786E-4

by J. Susskind at the Goddard Space Flight Center. The 1976 McClotchey Lire Parameter Tape was used as input to the program and the following conditions were used for the calculation:

- U.S. Standard Atmosphere.
- Gaussian slit functions truncated at the 3 sigma level. Baseline V half-power channel bandwidths were used.
- A spectral resolution of 0.005 cm^{-1} was used for integration.
- Effects of atmospheric species H_2O, CO_2, O_3, N_2O, CO, CH_4, and O_2 were included.
- H_2O and N_2 continuum effects were included.
- Analytic CHI molecular bandshape function was used.
- Above approximately 4500 cm^{-1} all emission was assumed to come from the surface; i.e., Planck radiance at a surface temperature of 286.8 K.

To assess the degree of variability in the spectral interference ratios due to differing atmospheric conditions, a limited series of line-by-line calculations were performed using a hot and humid tropical atmosphere. These calculations showed that a few spectral interference ratios in the 4.3 micron wavelength region decreased by approximately 40 percent. Similarly, in the 15 micron region, a few spectral interference ratios increased by approximately 40 percent. It is estimated that the spectral interference ratio values can probably vary by a factor of 2 due to atmospheric conditions extremely different from the U.S. Standard Atmosphere.

All interfering orders with wavelengths greater than the cutoff wavelength of the order filter germanium substrates were included. State-of-the-art 1 percent half-power bandwidth order filter amplitude vs frequency response characteristics having a steep skirt rolloff were used. The normalized amplitude vs frequency response for these filters is shown in Fig 4-2. Relative response in the far field of these filters was taken to be 10^{-6}. Relative detector response at the interfering order wavelength with respect to detector response at the design order wavelength was taken into account. Relative optical transmissivity of the spectrometer, excluding the order filter transmissivity, for the interfering order with respect to the design order was assumed to be unity. In general, the transmissivity at the design order wavelength is greater than at the interfering order wavelength. In the worst case, the transmissivity at the interfering order wavelength will probably not exceed the design order transmissivity by more than 2:1.

It is estimated that the worst case grating order crosstalk errors will not exceed 4 times the NEΔT values listed in Table 4-12 for all atmospheric profiles and for actual spectrometer optics relative transmissivities. (Note that NEΔT values in Table 4-12 are not 1σ values, since the

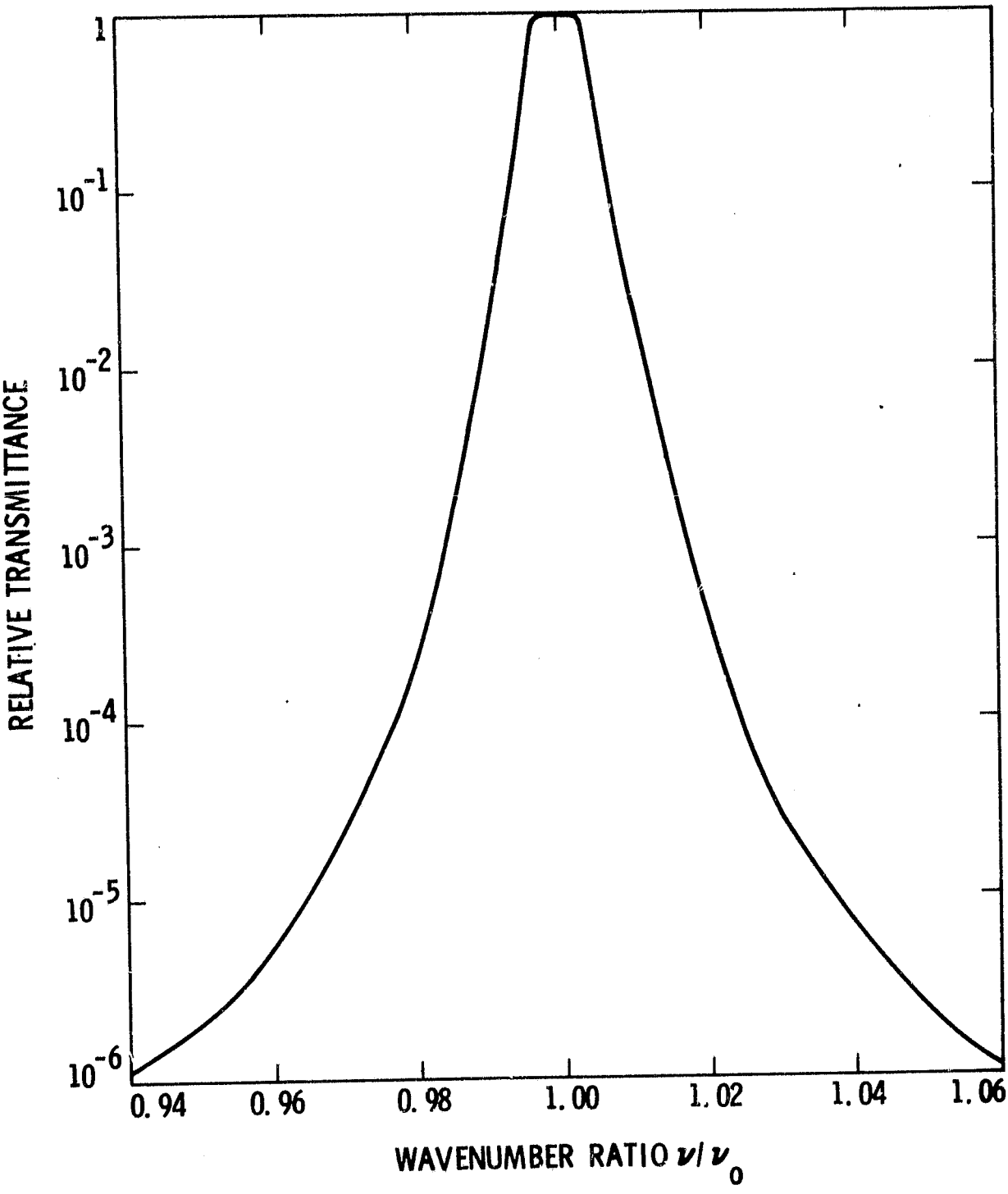

Figure 4-2 Relative transmissivity of 1% half-power bandwidth order filters

error distribution for all atmospheric profiles is not known. These are calculated values for a particular profile.) Consequently, in terms of grating order crosstalk errors, a considerable design margin exists for all channels for the Baseline V grating spectrometer.

4.3.2 Grating Grass Crosstalk

A ruled grating displays grass (band) scatter which is due to random errors in groove position and depth. Grass scatter from a monochromatic source appears in the image plane of the spectrometer as a band of radiation connecting the entrance slit images due to different grating orders. (Grass scatter does not lie outside the plane of the diffracted radiation.) This scatter in effect spreads radiation from every wavelength incident upon the inlet slit over the full width of the image plane. The scatter ratio is the amount of radiance scattered into the exit slit within the bandwidth of the order filter divided by the radiance diffracted into the exit slit in the design order. Consequently, the scatter ratio is a function of the scene spectral profile.

The grass scatter ratio for a scene having a constant amplitude vs. frequency spectral profile can be estimated using the equation:

$$\frac{P_g'}{P_o} \langle \lambda_1, \alpha_1, \beta_1 \rangle = \frac{P_g}{P_i} \langle \lambda_2, \alpha_2, \beta_2 \rangle \cdot \left(\frac{\lambda_2}{\lambda_1} \frac{\sin \alpha_1 + \sin \beta_1}{\sin \alpha_2 + \sin \beta_2} \right)^2 \frac{BW_{OF}}{E_{ff} \cdot \Delta\upsilon} \frac{S_{w\beta}}{f_{c\beta}} \qquad (4.6)$$

where:

P_g' = (Grass) scattered radiance incident on the detector; i.e., scatter within the angle subtended by the exit slit and within the spectral bandwidth of the order filter

P_g = (Grass) scattered radiance per unit angle per unit bandwidth of radiance incident upon the grating

P_o = Signal radiance incident upon the detector

P_i = Radiance incident upon the grating per unit bandwidth

α = Grating incident angle

β = Grating diffraction angle

λ = Wavelength

BW_{OF} = Order filter bandwidth

E_{ff} = Grating efficiency

$\Delta\upsilon$ = Channel slit function half-power bandwidth

$f_{c\beta}$ = Focal length of spectrometer exit collimator

$s_{w\beta}$ = Spectrometer exit slit width

Subscript 1 (for λ, α, β,) refers to the design grating operating parameters

Substript 2 (for λ, α, β,) refers to grating operating parameters for measured grating grass scatter

The grass scatter ratio, P''_g/P_o, for a specific atmospheric profile is:

$$\frac{P''_g}{P_o} = \frac{P'_g}{P_o} \frac{R_s}{R_{BB}} \tag{4.7}$$

where:

$$R = \frac{\int_{BW_{OF}} I\, d\upsilon - \int_{\Delta\upsilon} I\, d\upsilon}{\int_{\Delta\upsilon} I\, d\upsilon} \tag{4.8}$$

and:

R_s = value of R for the atmospheric profile

R_{BB} = value of R for a blackbody source

Estimated values for the Baseline V grating grass crosstalk are presented in Table 4-13. Grating grass scatter errors are listed for all channels for minimum equivalent target temperatures, assuming a blackbody spectral profile within the bandwidth of the order filter for each channel. Scatter errors are also listed for band 1 and band 4 channels for the spectral profile corresponding to the Standard U.S. Atmosphere, using 0.005 cm^{-1} spectral resolution for integration, and including the effects of CO_2, H_2O, and O_3 absorption. $\Delta\upsilon$ was taken as the channel half-power bandwidth. Note that the NEΔT values listed in Table 4-13 are not 1σ values, since the error distribution for all atmospheric profiles has not been determined.

A number of approximations were involved in estimating the grating grass crosstalk errors listed in Table 4-13. Measured data for P_g/P_i $< \lambda_2, \alpha_2, \beta_2 >$ was taken from Dunning and Minder (Ref 4-1) for a 37° blaze grating, since no scattering data for an R2 echelle grating was available. Values used were:

$$\frac{P_g}{P_i} = 1.5 \times 10^{-5} \text{ rad}^{-1}$$

$$\lambda_2 = 10.6\mu m$$

$$\alpha_2 = 60°$$

$$\beta_2 = 42.2°$$

In addition, the scaling factor used in Eq 4.6 to scale the effect of λ, α, and β is based on grating scalar theory, which is only an approximation for low grating orders where grating polarization effects are significant. It is believed, however, that the results obtained give the correct order of magnitude for a Baseline V grating ruled on a modern interferometrically controlled ruling engine. Grating grass crosstalk errors listed in Table 4-13 can be increased by two to three orders of magnitude before they become significant in AMTS system performance. (Atmospheric spectral tapes were not available for calculating crosstalk error for bands 2 and 3. Based upon the calculated blackbody errors, however, it is evident that atmospheric errors for these bands would be insignificant.)

4.3.3 Slit Function Wing Response Crosstalk

The spectrometer slit function describes how the instrument responds to a constant amplitude signal as a function of wavelength. When the Baseline V instrument views a scene, the spectral channel response is proportional to the multiplication of the scene spectral profile with the instrument slit function within the order filter bandwidth of the channel. Since a priori knowledge of the relative spectral radiance of the scene is inadaquate to allow consideration of the full order filter bandwidth slit function during atmospheric profile recovery, it must be assumed that channel radiance measured by the instrument lies within a narrower "truncation bandwidth" as illustrated in Fig 4-3(a). For Baseline V, the channel truncation bandwidths are taken as 2.548 times the channel half-power bandwidths, $\Delta\upsilon_{1/2}$. The channel radiance transfer calibration procedure is illustrated in Fig 4-3(b). This procedure compares scene radiance with an interpolated blackbody standard radiance, and returns the estimated integrated scene radiance within the channel truncation bandwidth, N_{ST}'. The actual time integrated scene radiance within the truncation bandwidth, N_{ST}, cannot be determined; consequently

$$\text{Radiance error} = |N_{ST} - N_{ST}'| \tag{4.9a}$$

and

$$\text{Fractional radiance error} = \frac{|N_{ST} - N_{ST}'|}{N_{ST}} \tag{4.9b}$$

It is generally accepted (Para 3.1.1.5) that the instrument slit function is closely approximated by the convolution in the image plane of:

Table 4-13 Baseline V grating grass crosstalk errors

CH	υ (cm^{-1})	Grass Scatter Error				
		For BB at T_{min}		For U.S. Std. Atmosphere		
		P_g'/P_o (1)	NEΔT(K)	R_s/R_{BB} (2)	P_g''/P_o (2)	NEΔT(K)
1	606.95	6.305E-7	3.73E-5	0.829	5.227E-7	4.02E-5
2	623.20	5.501E-7	3.15E-5	0.707	3.889E-7	2.85E-5
3	627.80	5.328E-7	2.76E-5	0.902	4.806E-7	2.91E-5
4	634.30	5.106E-7	2.46E-5	0.959	4.897E-7	2.70E-5
5	646.60	4.768E-7	2.07E-5	1.092	5.207E-7	2.66E-5
6	654.35	4.588E-7	1.84E-5	1.074	4.928E-7	2.49E-5
7	665.55	4.364E-7	1.76E-5	1.225	5.346E-7	2.73E-5
8	666.85	4.326E-7	1.69E-5	1.200	5.191E-7	2.66E-5
9	668.15	4.307E-7	1.74E-5	0.667	2.873E-7	1.88E-5
10	669.45	4.279E-7	1.74E-5	0.981	4.198E-7	2.33E-5
11	875.00	9.679E-7	4.09E-5			
12	1040.80	1.384E-7	3.62E-5			
13	1231.60	2.129E-6	6.40E-5			
14	1650.10	5.114E-6	1.04E-4			
15	1700.30	4.363E-6	8.32E-5			
16	1839.40	5.264E-6	1.07E-4			
17	1850.90	4.922E-6	1.00E-4			
18	1930.10	5.266E-6	1.02E-4			
19	2384.00	8.947E-6	1.20E-4	4.742	4.243E-5	6.52E-4
20	2386.10	1.922E-5	2.76E-4	2.734	5.255E-5	8.89E-4
21	2388.20	9.106E-6	1.39E-4	1.471	1.339E-5	2.53E-4
22	2390.20	1.814E-5	2.81E-4	0.967	1.754E-5	3.61E-4
23	2392.35	9.266E-6	1.45E-4	0.734	6.801E-6	1.48E-4
24	2394.50	1.720E-5	2.69E-4	0.745	1.281E-5	2.84E-4
25	2424.00	1.262E-5	1.95E-4	0.994	1.254E-5	2.85E-4
26	2505.00	8.125E-6	1.21E-4	0.999	8.117E-6	1.83E-4
27	2616.50	1.705E-5	2.44E-4	0.960	1.637E-5	3.57E-4
28	2686.00	1.015E-5	1.41E-4	0.955	9.693E-6	2.06E-4

[1]Reference Eq 4.6

[2]Reference Eq 4.7

- The image of the entrance slit, with
- The geometric point spread distribution of the spectrometer optics (between the entrance and exit slits), with
- The diffraction line spread function of the instrument aperture, with
- The exit slit width.

Note that foreoptics slit function effects (Para 3.1.1.5.2) are not included in this slit function approximation. This is justified for Baseline V by the very good optical performance possible with the Schwarzschild foreoptics telescope.

If the grating effectively forms the system aperture, and if there is no vignetting ahead of the exit slit of the ray bundle passing through the instrument, then the aperture diffraction line spread distribution for a coherent monochromatic source is represented by the grating line function characterized by Eq 3.33. When the grating is illuminated by a set of monochromatic point sources, however, where each point source has a coherence time, τ_o, then the overall grating line function is the summation of the autocorrelation line functions for all of the individual point sources. Figure 4-4 illustrates the effective length of the grating -- in terms of the number of grating lines, N -- vs time for a single coherence time interval, τ_o, for a single point source. The maximum optical path difference, OPD, is

$$OPD = aN_o(\sin \alpha_o + \sin \beta_o) \tag{4.10}$$

where N_o is the maximum number of grating lines, "a" is the grating line spacing, and α_o is the grating incident angle. All grating lines are effective for a period, τ_1, where

$$\tau_1 = \tau_o \frac{\tau_o c - OPD}{\tau_o c} = \tau_o - \frac{OPD}{c} \tag{4.11}$$

where c is the velocity of light. As a coherent length of radiation sweeps on to and off of the grating, a lesser number of grating lines, N_i, are effective for a period, $\Delta\tau$:

$$\Delta\tau = \frac{\tau_o - \tau_1}{n} = \frac{OPD}{nc} \tag{4.12}$$

where n is the number of $\Delta\tau$ intervals each side of τ_1.

$$N_i = N_o \frac{(i-1)\Delta\tau + \frac{\Delta\tau}{2}}{\tau_o - \tau_1} = \frac{N_o}{2n}(2i-1) \tag{4.13}$$

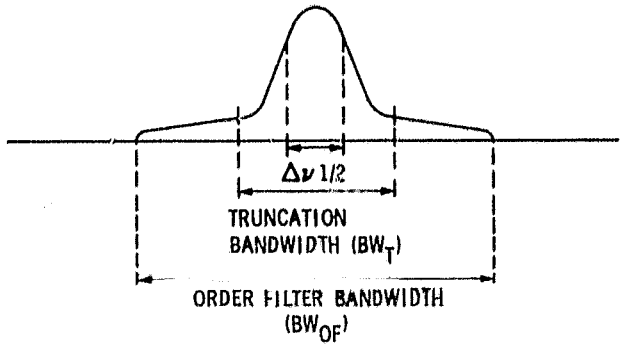

(a) RELATIVE SLIT FUNCTION
BANDWIDTH RELATIONSHIPS

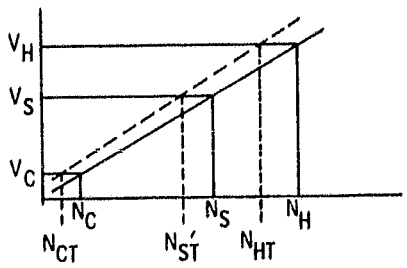

$$N_{ST}' = N_{CT} + (N_{HT} - N_{CT}) \frac{N_S - N_C}{N_H - N_C}$$

WHERE:

- N'_{ST} = ESTIMATED INTEGRATED SCENE RADIANCE WITHIN TRUNCATION BANDWIDTH
- N_{ST} = TRUE INTEGRATED SCENE RADIANCE WITHIN TRUNCATION BANDWIDTH
- N_S = TRUE INTEGRATED SCENE RADIANCE WITHIN ORDER FILTER BANDWIDTH
- N_C = COLD CALIBRATION TARGET INTEGRATED RADIANCE WITHIN ORDER FILTER BANDWIDTH
- N_H = HOT CALIBRATION TARGET INTEGRATED RADIANCE WITHIN ORDER FILTER BANDWIDTH
- N_{CT} = TRUE COLD CALIBRATION TARGET INTEGRATED RADIANCE WITHIN TRUNCATION BANDWIDTH
- N_{HT} = TRUE HOT CALIBRATION TARGET INTEGRATED RADIANCE WITHIN TRUNCATION BANDWIDTH
- V_C, V_S, V_H = INSTRUMENT SIGNAL CHANNEL VOLTAGES CORRESPONDING TO N_C, N_S, N_H

(b) CHANNEL RADIOMETRIC
TRANSFER CALIBRATION
PARAMETERS

Figure 4-3 Slit function wing response crosstalk parameters

when i represents the i^{th} $\Delta\tau$ interval and N_i is an integer. The area-solid angle product, $A\Omega$, at any time is proportional to N_i; consequently, relative power equals N_i/N_o. The normalized relative intensity of the grating line function as a function of the i^{th} $\Delta\tau$ interval, $(I/I_0)_{N_i}$, can be calculated from Eq 3.33 with L replaced by $N_i a$. The overall relative grating line function is then

$$\frac{I}{I_o} = \left[\sum_{i=1}^{n} W_i \left(\frac{I}{I_o} \right)_{N_i} \right] + W_o \left(\frac{I}{I_o} \right)_{N_o} \qquad (4.14)$$

where the weighting functions, W_i and W_o, are

$$W_i = 2 \frac{N_i}{N_o} \frac{\Delta\tau}{\tau_o} = \frac{2N_i}{N_o} \frac{OPD}{n\tau_o c}, \qquad N_i < N_o$$

$$W_o = \frac{\tau_1}{\tau_o} = 1 - \frac{OPD}{\tau_o c}, \qquad N = N_o$$

For an average coherence time, τ_o, of 10^{-8}sec, solution of Eq 4.14 shows that noncoherent source radiation increases the half-power line width of the Baseline V diffraction line function by a factor of ≈1.1 and increases the relative wing response by a factor of ≈4.

A representative set of Baseline V slit function response plots are shown in Fig 4-5. An average cohrence time, τ_o, of 10^{-8} sec was used. The geometric point spread distribution was represented by a cosine function, defined between $-\pi/2$ and $\pi/2$, which was a "best fit" to the ray trace determined geometric point spread distribution for each channel. The inverse Fourier transform required by the convolution theorem was computationally illdefined using all four functions. The approach used was to apply the convolution theorem to the entrance and exit slit functions and to the geometric point spread distribution, and then to numerically evaluate the convolution of this function and the aperture diffraction function as defined by Eq 4.14.

Calculated slit function wing response crosstalk errors for the Standard U.S. Atmosphere are listed in terms of percent radiance and NEΔT in Table 4-14 for selected channels. A spectral resolution of 0.005 cm^{-1} was used for integration for all channels. (No Band 2 and Band 3 channels were included because spectral profile tapes having the required spectral resolution were not available at JPL.) Errors were not calculated for all channels in Band 1 and Band 4 because of the computer time required. An effort was made, however, to select the "worst case" channels for analysis. (Note that NEΔT values listed in Table 4-14 are not 1σ values, since the error distribution for all atmospheric profiles is not known. These are calculated values for a particular profile.)

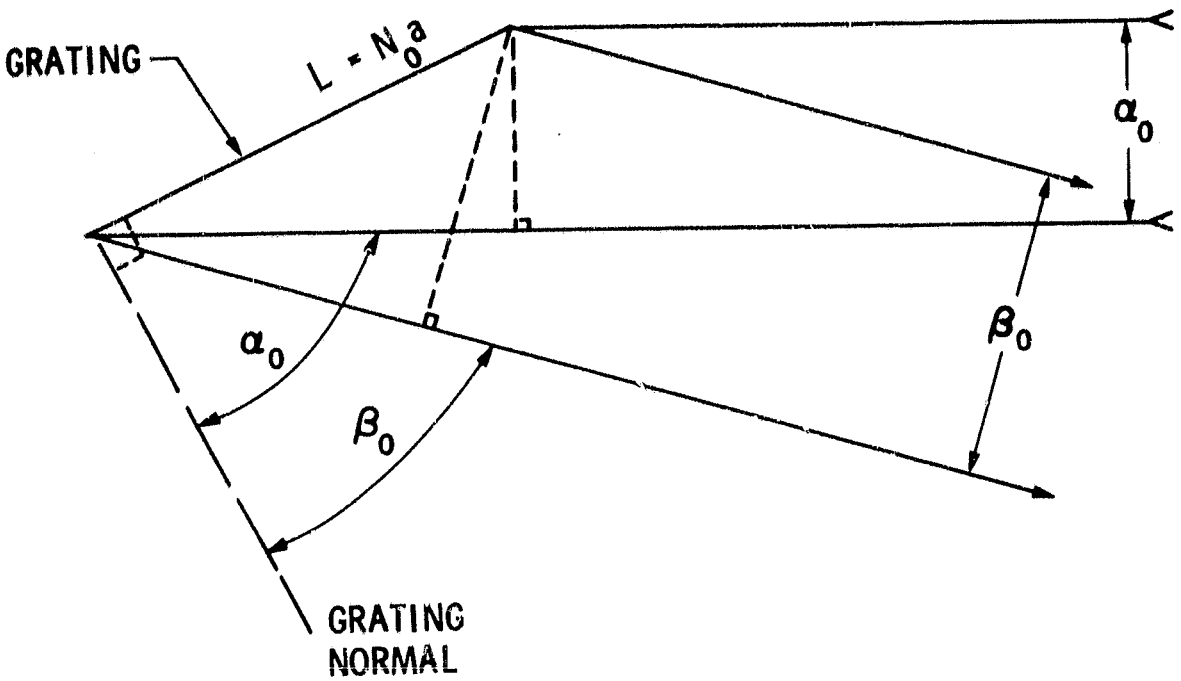

(a) GRATING GEOMETRY

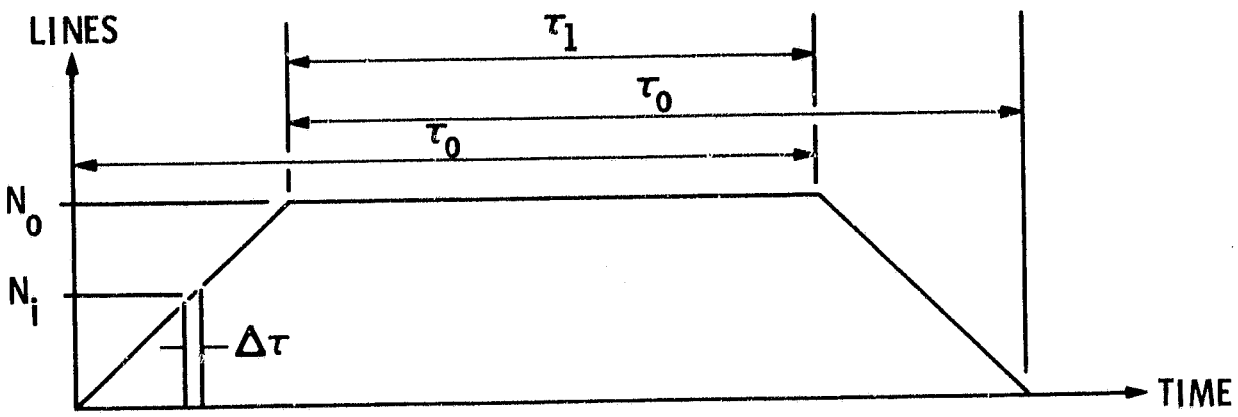

(b) GRATING EFFECTIVE LENGTH vs TIME

Figure 4-4 Baseline V grating coherence time parameters

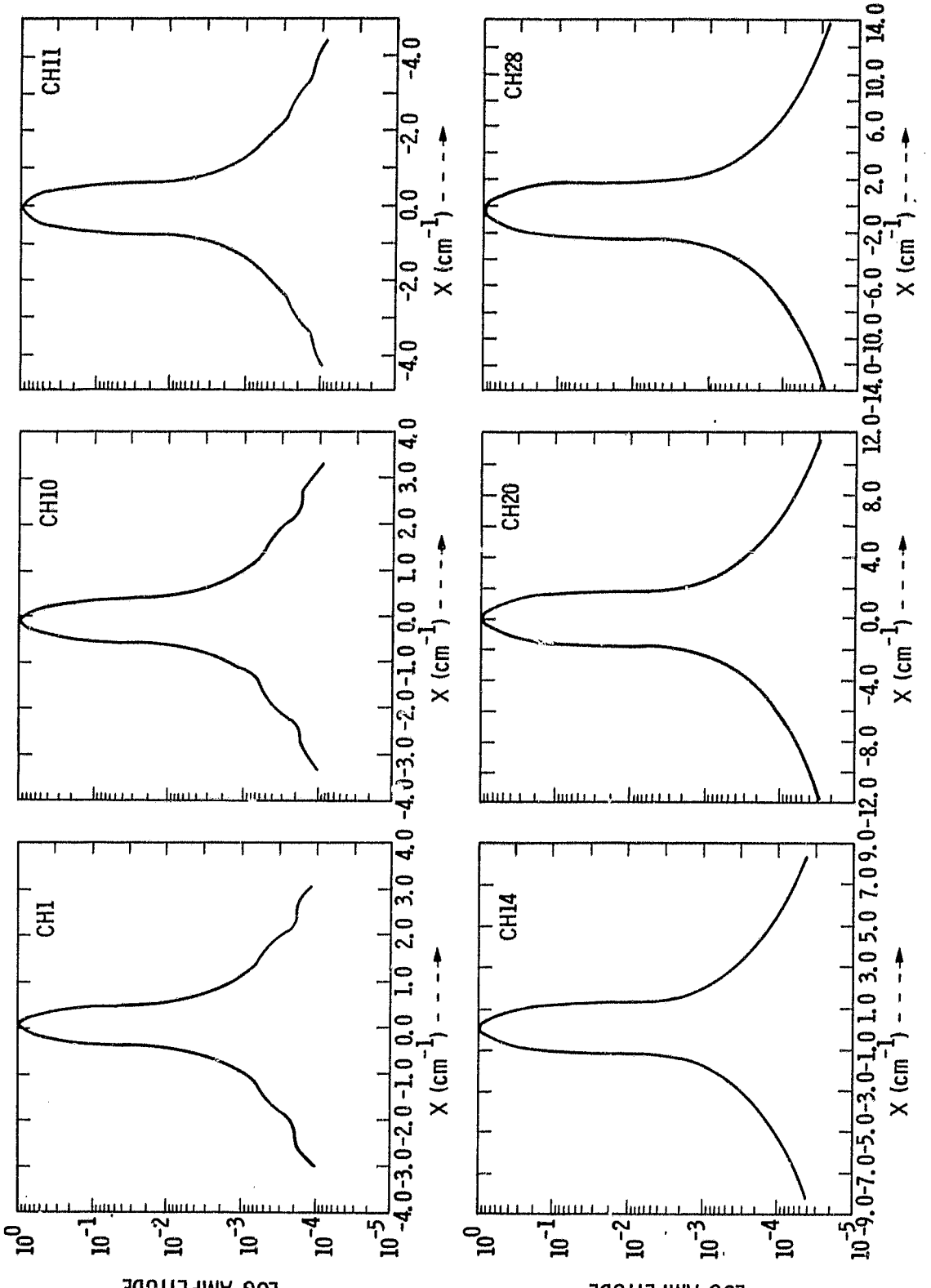

Figure 4-5 Baseline V slit function log relative amplitude vs spectral frequency

Table 4-14 Baseline V slit function wing response crosstalk errors

CH	ν (cm^{-1})	$\Delta\upsilon$ (cm^{-1})	Truncation Bandwidth (cm^{-1})	Order Filter Bandwidth (cm^{-1})	Crosstalk Error[1] Radiance Error (%)	NEΔT (K)
1	606.95	0.50	1.274	6.0695	0.1380	0.1069
2	623.20	0.50	1.274	6.2320		
3	627.80	0.50	1.274	6.2780		
4	634.30	0.50	1.274	6.3430		
5	646.60	0.50	1.274	6.4660		
6	654.35	0.50	1.274	6.5435		
7	665.55	0.50	1.274	6.6555		
8	666.85	0.50	1.274	6.6685		
9	668.15	0.50	1.274	6.6815		
10	669.45	0.50	1.274	6.6945	0.0679	0.0381
11	875.00	0.75	1.911	8.7500		
12	1040.80	1.00	2.548	10.4100		
13	1231.60	1.00	2.548	12.3100		
14	1650.10	1.30	3.312	16.5010		
15	1700.30	1.30	3.312	17.0030		
16	1839.40	1.50	3.822	18.3940		
17	1850.90	1.50	3.822	18.5090		
18	1930.10	1.50	3.822	19.3010		
19	2384.00	2.00	5.096	23.8400		
20	2386.10	2.00	5.096	23.8610	0.2095	0.0357
21	2388.20	2.00	5.096	23.8820		
22	2390.20	2.00	5.096	23.9020		
23	2392.35	2.00	5.096	23.9235		
24	2394.50	2.00	5.096	23.9450		
25	2424.00	2.50	6.370	24.2400		
26	2505.00	2.50	6.370	25.0500		
27	2616.50	2.50	6.370	26.1650		
28	2686.00	2.50	6.370	26.8600	0.0227	0.0046

[1]For U.S. Standard Atmosphere

4.3.3.1 Wing Response Crosstalk Uncertainties, Design Options, and Constraints

Wing response crosstalk errors are uncorrelated with other error sources, but they can have a high degree of correlation from footprint to footprint. In general, these errors are not significantly reduced in the composite footprint.

The wing response crosstalk error values listed in Table 4-14 are total residual errors following the channel radiometric calibration procedure. These errors will be somewhat reduced by the sytem tuning procedures of Para 2.1.6. The estimated integrated scene radiance within the truncation bandwidth will be in error to the extent that interpolated blackbody wing spectral distribution (within the bandwidth of the order filter and outside the truncation bandwidth) differs from that of the scene. The system tuning procedure can compensate for the mean difference of the set of profiles used for tuning. The variation in scene wing spectral distribution from this mean results in a nontunable radiometric error. For given slit function responses within the bandwidth of the order filter (when viewing the scene and when viewing the blackbody calibration sources) and a set of scene spectral distributions corresponding to a statistical set of atmospheric profiles, tunable and nontunable radiometric error values could be determined through computer modeling of the calibration procedure. Such modeling has not been performed.

The method used to calculate the effect of viewing spatially distributed noncoherent sources upon the grating line function is an approximation. The individual point source amplitude vs. time function is not a simple constant amplitude pulse, but tends to have an exponential-like decay. The average coherence time is not necessarily the value estimated for the calculations for sources at different pressure levels within the atmosphere or upon the surface. These approximations primarily affect the wing response of the instrument slit function rather than its half-power bandwidth.

The instrument slit function for a coherent point source is not necessarily the same when viewing the highly defocused on-board calibration targets as when viewing the focused scene. The physics of the spectrometer operation are quite different for the two cases. The inlet slit is a highly diffracting aperture for wavefronts originating at a point within the calibration target. The grating is illuminated by these diffracted fields which have their phase centers at the center of the inlet slit. The main lobe of each of these fields covers a comparatively short length of the grating for each point source. The entire length of the grating is covered, of course, by fields originating at different spatial positions within the calibration targets. Computer modeling shows that if about 10 or more sidelobes on either side of the main lobe fall upon the grating, an image of the inlet slit is formed at the image plane of the instrument for each monochromatic point source on the calibration target. For a focused monochromatic point source, on the other hand, a diffraction pattern in the spectral dimension corresponding to the grating line function is formed at the image plane. For spatially distributed polychromatic sources, the resulting instrument slit functions are very similar for both cases. At the

detail radiometric level, however, there is some spatial weighting of the illumination over the grating aperture, and there are probably some differences in the equivalent half-power bandwidths and in the wing responses of the slit functions. The effects are stable and, except for some residual wing response crosstalk error, could be corrected via prelaunch radiometric calibration of the apparent emissivity of the hot and cold calibration targets or could be compensated by system tuning. A more detailed evaluation of these error components could be performed by computer modeling. Again, such modeling has not been performed.

The basic method of calculating slit function response presented in Para 3.1.1.5 was used to determine Baseline V slit function characteristics plotted in Fig 4-5 and to estimate slit function wing response crosstalk errors listed in Table 4-14. This generally accepted method is valid for optical configurations which use the detector in the image plane. Subsequent to the conceptual design for Baseline V, however, we have begun to have doubts about the validity of this method when the detector is in a pupil plane; i.e., when the grating is imaged upon the detector as in Baseline V. When the collimated field from a coherent point source falls upon a diffraction grating it is disassociated into a set of individual fields, one for each grating groove. Each of these fields is spread over a relatively wide spatial angle in a plane normal to the length of the grating grooves (for a zero out-of-plane incident angle). At infinity the individual fields from all grating grooves become spatially coincident and add vectorially to produce the relatively narrow grating line function defined by Eq 3.33. The integrated amplitude of this line function contains radiometric information and its angular position contains spectral information. For the purpose of argument, assume that an exit decollimator is now placed one focal length from the grating. The individual fields from the grating grooves are converted into plane waves which pass through a common area in the image plane of the instrument. The individual fields from all grating grooves, when summed vectorially in the image plane, produce the narrow grating line function whose integrated amplitude contains radiometric information and whose angular position contains spectral information. When a field lens is used behind the image plane to focus the grating image upon a detector the individual groove fields are spatially disassociated and, in the limit, are focused upon the detector as parallel lines. Under these conditions the integrated detector output would contain radiometric information but no spectral information. If a relatively narrow exit slit is now placed in the image plane it acts as a diffracting aperture for the individual groove fields. These individual diffracted fields with phase centers at the center of the exit slit width now overlap a number of equivalent groove widths in the pupil plane. The detected vectorial sums of the overlapping fields contain both radiometric and spectral information. For the Baseline V instrument, the number of grooves whose fields overlap at any given point at the detector is considerably less than the total number of grooves on the grating. Consequently, for this alternate model of slit function formation, we suspect that the instrument slit function half-power bandwidths would be somewhat wider and the wing responses would be considerably higher than originally calculated.

Assuming that the alternate slit function model is the correct one for the Baseline V configuration, it is believed that the effect on half-power channel bandwidth would not be a problem but that the effect on slit response

crosstalk error could be a problem. This problem could be effectively eliminated if the order filter bandwidth could be reduced from 1 percent to ≈0.25 percent. In-band transmissivities would be less for narrower bandwidth order filters. In addition, it would be more difficult to control center frequency and frequency response characteristics for these very narrow filters when used in the converging beam and at the operating temperatures to be encountered in the instrument. Order filter bandwidths as narrow as 0.25 percent are probably impractical for this application.

Spectrometers have been built with detectors in a pupil plane. At JPL, the TOSCA (or multidetector) spectroradiometer used for balloon and aircraft tests during the early phases of the AMTS study used this configuration. Channel half-power bandwidths measured for this instrument were close to the values expected using the conventional method to determine slit function response. Wing responses for this instrument were not measured. We have not found anyone who has measured slit function wing response for a spectrometer having this configuration. This uncertainty could be resolved by measurements on a suitable laboratory test instrument and/or by computer modeling.

Even if the instrument slit function wing response is significantly degraded with respect to the performance estimated in Para 4.3.3, the effect upon system performance may not be serious. To the extent that the ratio of the integrated energy within the wings of the slit function (outside the truncation bandwidth) to the integrated energy within the truncation bandwidth is a constant for a given channel for all profiles, the effect is tunable. This ratio, in turn, is a function of the width of the truncation bandwidth and of the width of the order filter bandwidth. These ratio and bandwidth limits have not been explored.

4.3.4 Spectral Crosstalk Radiometric Error Summary

Grating order crosstalk errors and grating grass crosstalk errors are negligible, even taking into account the uncertainties in the data bases and the computational accuracy limitations for these error sources. Slit function wing response crosstalk errors may be significant in terms of limiting AMTS performance. Whether or not this is the case depends upon uncertainties in the calculation of overall wing response crosstalk values, and upon what portion of the overall error could be reduced by system tuning.

4.4 Polarization Radiometric Errors

Polarization radiometric errors consist of:

- Scene polarization effects
- Scan mirror polarization effects

These error sources result in nontunable individual footprint radiometric errors which, in general, are not reduced in the composite footprint. In addition, these error sources can result in a significant channel to channel correlated error component.

4.4.1 Scene Polarization Effects

Scene polarization radiometric errors are a function of both scene polarization and of instrument polarization sensitivity. Scene polarization is primarily due to the presence of sunlit clouds or ground haze in the footprint field of view, and occurs primarily at the shorter wavelengths (bands 3 and 4). Scene polarization error is a function of the sun/scene/spacecraft angle. There is a high degree of correlation from channel to channel and from footprint to footprint for scenes which have a high degree of homogeneity; consequently, in the limit, these errors are not reduced in the composite footprint.

If specular reflection of solar radiation from the surface is neglected then the primary source of scene polarization is due to scattering of solar radiation from clouds and ground haze. For purposes of this AMTS error analysis it is assumed that specular surface reflection can be ignored because of the relatively small number of footprints affected. It is also assumed that the circular polarization component from the planetary atmosphere is negligible (Ref 4-2). Consequently, scene radiation consists of solar radiation scattered from clouds or haze plus thermal radiation. The scattered radiation consists of an unpolarized component and a linearly polarized component. The thermal radiation is unpolarized.

The degree of scene polarization is defined as:

$$\text{Scene Polarization} = \frac{P_{pol}}{P_{unpol} + P_{pol}} \tag{4.15}$$

where

P_{pol} = linearly polarized part of source radiant flux

P_{unpol} = unpolarized part of source radiant flux

For the AMTS satellite instrument viewing the atmosphere

$$\frac{P_{pol}}{P_{unpol} + P_{pol}} = \frac{\frac{H_\nu}{\pi}\,\gamma_{in}\,\gamma_{out}\,\frac{N_\nu(s)}{N_\nu(o)}\,\frac{N_{\nu pol}(s)}{N_\nu(s)}}{N_\nu(TH) + \frac{H_\nu}{\pi}\,\gamma_{in}\,\gamma_{out}\,\frac{N_\nu(s)}{N_\nu(o)}} \tag{4.16}$$

where

H_ν = spectral solar irradiance at the top of the atmosphere ($W/cm^2 \cdot cm^{-1}$)

γ_{in} = atmospheric transmittance from the top of the atmosphere to the cloud top

γ_{out} = atmospheric transmittance from the cloud top to the top of the atmosphere

$N_{\nu(s)}$ = actual total reflected spectral solar radiance ($W/cm^2 \cdot sr \cdot cm^{-1}$)

$N_{\nu(o)}$ = reflected spectral solar radiance, assuming a Lambertian reflection with a reflectively of unity

$N_{\nu pol(s)}$ = linearily polarized component of reflected spectral solar radiance

$N_{\nu(TH)}$ = unpolarized thermal spectral radiance

The ratio, $N_{\nu pol(s)}/N_{\nu(s)}$, is the polarization factor of the scattered solar spectral radiance and the ratio $N_{\nu(s)}/N_{\nu(o)}$ is the relative scattered solar spectral radiance at the cloud top. Equation 4.16 defines the total scene polarization at the top of the atmosphere.

The relative radiometric polarization error for a grating is:

$$\text{Rel. Error} = \frac{P_{pol}}{P_{unpol} + P_{pol}} \left| \frac{E\perp - E\parallel}{E\perp + E\parallel} \right| (2 \cos^2 \phi - 1) \qquad (4.17)$$

where

$\frac{P_{pol}}{P_{unpol} + P_{pol}}$ = polarization of the radiation incident on the grating (Eq 4.16)

$\left| \frac{E\perp - E\parallel}{E\perp + E\parallel} \right|$ = grating polarization factor

$E\perp$ = relative grating efficiency for radiation polarized perpendicular to the grating grooves (S-plane)

$E\parallel$ = relative grating efficiency for radiation polarized parallel to the grating grooves (P-plane)

ϕ = angular displacement of the linear polarization vector aligment with respect to the P-plane, (where ϕ is defined between 0 and 90 degrees)

For $\phi = 45°$, the scene polarization radiometric error is zero, regardless of scene polarization. For $\phi = 0°$ or $90°$ the polarization radiometric error contribution of the instrument is a maximum. Under these conditions, Eq 4.17 reduces to

$$\text{Rel. Error (max)} = \frac{P_{pol}}{P_{unpol} + P_{pol}} \left| \frac{E\perp - E\parallel}{E\perp + E\parallel} \right| \qquad (4.18)$$

The relative radiometric scene polarization error for the AMTS with the instrument grating effects maximized can be calculated by substituting Eq 4.16 into Eq 4.18.

Estimated Baseline V worst case scene polarization radiometric errors due to sunlit clouds are developed in Table 4-15 for bands 3 and 4. Atmospheric transmissivity was calculated for clouds at a pressure height of 250 mbar for the tropics, 500 mbar for midlatitudes, and 700 mbar in the polar regions. The cloud top scatter ratio and cloud top scatter polarization factor for optical thicknesses of 4 or greater were taken from Hansen (Ref 4-3) for a wavelength of 3.4 μm. (Hansen's results for typical clouds are shown in Fig 4-6.) Single scattering results from Hansen were compared with single scattering results calculated by JPL over the AMTS frequency range as an aid in interpolating Hansen's multiple scattering data. The AMTS can encounter all scattering angles between approximately 20 and 160 degrees. In general, this includes the scattering angles corresponding to relatively large scene polarization. The scattering ratio and cloud top polarization ratio for channels 16 through 28 were assumed to be the same as at 3.4 μm. These assumptions may be pessimistic for the 3.7 μm to 5.4 μm wavelength region. (These values could be better determined by performing multiple scattering calculations over the AMTS wavelength range of interest for a statistical set of cloud types and ground haze.) It was assumed that the relative scattered intensity for the longer wavelengths of bands 1 and 2 would be very small so that polarization effects could be neglected. In view of the relatively large grating polarization factors expected in the low grating orders used for the Baseline V long wavelength channels (Para 3.1.1.2) this assumption may be optimistic. We have no model for calculating grating polarization factors for the grating angular relationships used in the Baseline V instrument. The grating polarization factors listed in Table 4-15 are rough estimates made from available measured polarization data on a number of Bausch and Lomb R2 gratings used in a near-littrow monochromator configuration (Fig 3-12). More accurate grating polarization factor values could be obtained by measuring sample gratings at the AMTS grating orders and angles.

Table 4-15 Baseline V scene polarization radiometric error (clouds)

CH (No.)	Frequency ν (cm^{-1})	Thermal Radiance N_ν (T_{min}) $\left(\frac{W}{cm^2\ sr\ cm^{-1}}\right)$	Solar Irradiance At Top Atmos. H_ν $\left(\frac{W}{cm^2\ cm^{-1}}\right)$	Atmospheric Transmissivity τ	Cloud Top Scatter Ratio $\frac{N_\nu(s)}{N_\nu(o)}$	Cloud Top Polarization Factor $\frac{N_{vpol}(s)}{N_\nu(s)}$	Total Scene Polarization Factor $\frac{N_{vpol}}{N_{vunpol} + N_{vpol}}$	Grating Polarization Factor $\left\lvert\frac{E\perp - E\parallel}{E\perp + E\parallel}\right\rvert$	Fractional Radiance Error	Total Radiance $N_{vunpol} + N_{vpol}$ $\left(\frac{W}{cm^2\ sr\ cm^{-1}}\right)$	$= 3\sigma$ Polarization NEAT (K)
16	1839.40	8.24×10^{-8}	9.15×10^{-7}	0.998	≈0.06	≈0.13	0.023	0.119	0.0027	9.98×10^{-8}	0.057
17	1850.90	8.21×10^{-8}	9.25×10^{-7}	0.999	≈0.06	≈0.13	0.023	0.159	0.0037	9.97×10^{-8}	0.078
18	1930.10	5.42×10^{-8}	9.95×10^{-7}	0.997	≈0.06	≈0.13	0.034	0.500	0.0168	7.31×10^{-8}	0.340
19	2384.00	1.77×10^{-9}	1.43×10^{-6}	0.497	≈0.06	≈0.13	0.103	0.333	0.0343	0.85×10^{-8}	0.555
20	2386.10	3.11×10^{-9}	1.43×10^{-6}	0.717	≈0.06	≈0.13	0.106	0.259	0.0276	1.72×10^{-8}	0.495
21	2388.20	4.94×10^{-9}	1.44×10^{-6}	0.853	≈0.06	≈0.13	0.104	0.333	0.0347	2.50×10^{-8}	0.656
22	2390.20	5.57×10^{-9}	1.44×10^{-6}	0.924	≈0.06	≈0.13	0.105	0.195	0.0205	2.91×10^{-8}	0.399
23	2392.35	5.87×10^{-9}	1.44×10^{-6}	0.954	≈0.06	≈0.13	0.105	0.333	0.0351	3.09×10^{-8}	0.686
24	2394.50	5.81×10^{-9}	1.44×10^{-6}	0.962	≈0.06	≈0.13	0.106	0.130	0.0138	3.13×10^{-8}	0.273
25	2424.00	5.02×10^{-9}	1.47×10^{-6}	0.979	≈0.06	≈0.13	0.110	0.109	0.0119	3.19×10^{-8}	0.238
26	2505.00	3.35×10^{-9}	1.56×10^{-6}	0.992	≈0.06	≈0.13	0.117	0.400	0.0467	3.27×10^{-8}	0.939
27	2616.50	1.91×10^{-9}	1.67×10^{-6}	0.998	≈0.06	≈0.13	0.123	0.101	0.0124	3.37×10^{-8}	0.260
28	2686.00	1.35×10^{-9}	1.75×10^{-6}	0.998	≈0.06	≈0.13	0.125	0.114	0.0142	3.46×10^{-8}	0.303

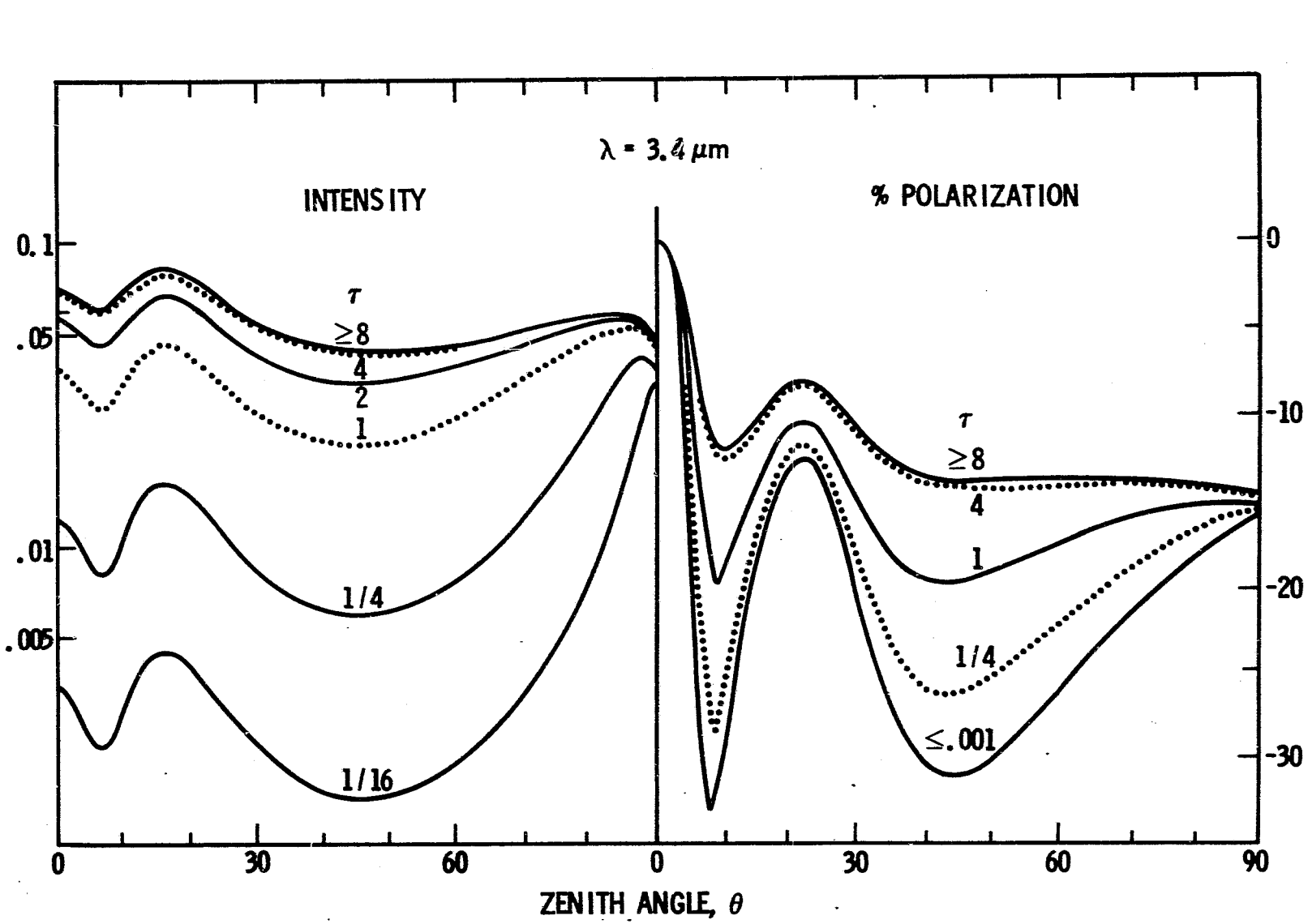

Figure 4-6 Intensity and percent polarization of sunlight reflected by a plane parallel cloud with the sun at the zenith ($\theta_o = 0$). Results are shown vs optical thickness, τ. The horizontal axis represents the zenith angle of the scattered radiation.

Actual polarization errors are a function of

- Cloud cover
- Cloud type
- Sun/scene/satellite angle
- Scan angle

Insufficient data are available to accurately determine polarization error statistics. The 3σ polarization errors in Table 4-15 are very rough statistical estimates.

Table 4-15 shows that the channel to channel relative radiometric error due to scene polarization can be rather large. Note that the sign of the grating polarization factor is not necessarily the same for all channels (Fig 3-12). In addition, cloud top scatter ratios and polarization factors are not the same for all channels, as assumed in Table 4-15. The channel to channel correlated error component for this error source could approach the algebraic sum of the individual channel scene polarization radiometric error components.

4.4.2 Scan Mirror Polarization Effects

For an unpolarized scene some polarization is introduced into the radiation incident upon the grating by reflection from the metal mirror surfaces. To the extent that this induced polarization is the same for the scene and for the calibration targets no residual radiometric error is introduced. This condition holds for all mirrors except the 45 degree scan mirror.

The polarization introduced by the scan mirror is a constant. The polarization angle incident upon the grating, however, is a function of scan mirror position. The relative polarization radiometric error as a function of scan mirror angle is defined by Eq 4.17 when ϕ is taken as the scan mirror angular position with respect to the nadir or zenith. Relative error as a function of scan mirror position is listed in Table 4-16. Note that scan mirror polarization error is zero for a scan angle of 45 degrees, and maximum for a scan angle of zero. When the calibration targets are placed at 45 degrees — as in Baseline V — there is no residual error at the ends of the crosstrack line scan and the residual error is a maximum at nadir. The peak error could be halved if calibration targets were placed at 30 degrees, but the layout does not allow this (Fig 3-30). If calibration targets were placed at 90 degrees, the Baseline V peak error would be doubled at nadir, and would be one half the peak value at the ends of the line scan. In any case, the effects of scan mirror induced polarization error as a function of scan angle could be removed using prelaunch calibration data.

Scan mirror induced polarization radiometric error estimates are listed in Table 4-17. The scan mirror polarization factor and the grating polarization factor were taken as the worst case channel values

Table 4-16 Relative scan mirror induced polarization radiometric error as a function of scan angle

Scan Angle ϕ (deg)	Relative Error $2\cos^2\phi - 1$	Remarks
0	1	Nadir or zenith scan angle
30	0.5	Optimum calibration target angle
45	0	"End of line scan" angle. Actual calibration target angles
90	-1	

Table 4-17 Baseline V scan mirror polarization error estimates

Frequency Band	Scan Mirror Polarization Factor[1]	Grating Polarization Factor[1]	Fractional Radiance Error	≈3σ Scan Mirror Polarization Error NEΔT (K)		
				T_{min}	T_{std}	T_{max}
1	2.0×10^{-3}	0.6	1.2×10^{-3}	0.052	0.061	0.094
2	2.5×10^{-3}	0.3	7.5×10^{-4}	0.023	0.035	0.046
3	7.4×10^{-4}	0.6	4.4×10^{-4}	0.008	0.009	0.011
4	4.8×10^{-4}	0.4	1.9×10^{-4}	0.003	0.004	0.006

[1]Estimated worst case values within each band

for each band. The worse case relative peak scan mirror polarization error corresponds to the nadir scan angle. The resulting worst case ($\approx 3\sigma$) radiometric error components are relatively small, and it is probably not worth while to attempt to calibrate operational data vs. scan angle.

The channel to channel correlated error component for this error source could approach the algebraic sum of the individual channel scan mirror induced radiometric error components.

4.4.3 Polarization Error Uncertainties, Design Options, and Constraints

Uncertainties in the relative intensity and polarization factor of radiation scattered from cloud tops could be reduced by performing multiple scattering calculations for the AMTS channels for a statistical set of cloud and ground haze characteristics and sun/satellite/scene angles. Uncertainties in instrument polarization sensitivity could be reduced by measuring sample gratings under AMTS angular conditions. Finally, to evaluate the operational system significance of scene polarization errors, the spatial and temporal distribution of sunlit cloud fields should be considered.

Three approaches have been identified for effectively eliminating the effects of scene polarization error.

The first approach would increase satellite altitude to the point where successive crosstrack swaths at the equator were contiguous. This would result in full earth coverage twice in each 24 hour period, once on the dark side and once on the sunlit side of the planet. Night side coverage is free of scene polarization effects. Paragraph 3.1.1.6 shows that full earth coverage could be obtained twice a day for an altitude of 1350 km or higher. The scaling equations, 3.10 and 3.22, show that this would result in a detector/preamp limited random radiometric error penalty of 18 percent for the spatial resolution of Baseline V. Note that if two satellites were used in properly synchronized orbits, this same twice-daily coverage could be obtained with no radiometric error penalty for orbits between approximately 700 and 1350 km.

The second approach would use the grating in the scalar domain -- i.e., in higher orders -- where the polarization sensitivity of the instrument would be effectively eliminated. This approach would require a multiblazed grating in order to maintain an adequate angular bandwidth for the higher orders (Para 3.1.1.2). This approach would result in more parasitic grating orders with significant output power levels which could reduce grating efficiency significantly in the desired orders. The use of higher orders, however, would allow more flexibility in the layout of the image plane. It might be possible to group higher order channels into a more narrow angular bandwidth than that of Baseline V. A rough estimate is that this approach would approximately double the detector/preamp limited random radiometric error calculated for Baseline V. A multiblaze dual vector grating efficiency model could be developed, using the approach of Para 3.1.1.2 and Appendix C, which would allow an accurate performance evaluation for this instrument approach.

A third approach would use a wire grid polarizer in the diverging beam of the spectrometer between the inlet slit and the inlet collimator. This polarizer would be spatially rotated (switched) 90 degrees during each IFOV dwell interval. Thus each footprint would be viewed twice in order to measure orthogonal polarization components of the scene — or calibration target — radiation. These two orthogonal components would be summed during ground based data reduction to yield correct total radiance values for each footprint. Insertion of the wire grid polarizer would significantly reduce the optical transmissivity of the instrument. The required slew time for rotating the polarizer would reduce the effective footprint dwell time. It is estimated that this approach would increase detector/preamp limited random radiometric error calculated for Baseline V by approximately a factor of 3. The downlink date rate (Table 3-35) would be increased by almost a factor of 2.

4.4.4 Polarization Radiometric Error Summary

Scan mirror induced radiometric errors are negligable. Based upon estimated values for scene polarization errors, it appears that this error source would be a limiting factor on system performance in the presence of sunlit clouds. This is particularly true because of the relatively large channel to channel correlated error component. It is believed that the polarization sensitivity for the Baseline V instrument — which operates at grating orders below the scalar region — would be much greater than that of the HIRS-2 filter wheel instrument. Techniques are available for effectively eliminating these polarization radiometric errors. These approaches require trade-offs involving either significant constraints upon orbit selection or a significant increase in detector/preamp limited random radiometric errors.

4.5 Spatial Crosstalk Radiometric Errors

Spatial crosstalk occurs when a portion of the energy originating within a pixel is scattered into other pixels. Energy from other pixels is also scattered into the first pixel. Crosstalk error is the difference between total energy scattered out of the pixel and total energy scattered into the pixel. Spatial crosstalk errors are scene dependent, with error values a function of relative pixel radiances and relative pixel locations. Spatial crosstalk error is zero for a scene having no contrast.

Spatial crosstalk error sources consist of:

- Aperture diffraction
- Gas check scatter
- Scan mirror BRDF
- Telescope and collimator mirror BRDF
- Collimator corrector lens scatter
- Grating diffuse scatter

- Grating mask scatter
- Image plane mask scatter

Spatial crosstalk due to aperture diffraction and to scattering from surfaces ahead of the field stop (inlet slit array) includes the effects of many pixels. The remaining error components include only the effects of the 16 pixels defined by the inlet slit array. Spatial crosstalk errors from all of these sources are correlated with each other, but are not correlated with other error sources. Some spatial crosstalk error sources result in error values which are a function of channel wavelength; consequently, there can be a relatively large spatial crosstalk channel to channel correlated error component. Spatial crosstalk errors are not reduced by system tuning. In general, individual footprint spatial crosstalk errors would be somewhat reduced in the composite footprint. The degree of this error reduction would be scene dependent. Under suitable conditions spatial crosstalk errors can be effectively eliminated by a deconvolution of the image during ground data processing.

Spatial crosstalk errors can be treated component by component. Since the total system crosstalk error is effectively the algebraic sum of the individual component errors, for some purposes it is more appropriate to treat it in terms of total system error. Measured radiance values can be expressed in terms of true scene radiance values and instrument radiance transfer ratios as

$$N_o' = N_o + \sum_i TR_i \, (N_i - N_o) \qquad (4.19)$$

where

N_o' = contaminated (measured) radiance value in footprint o

N_o = true radiance value in footprint o

N_i = true radiance value in footprint i

TR_i = fraction of energy originating in footprint o that spreads into footprint i, or vice versa (radiance transfer ratio)

Consequently, spatial crosstalk radiance error can be expressed as

$$NEN = \left| N_o' - N_o \right| = \left| \sum_i TR_i \, (N_i - N_o) \right| \qquad (4.20)$$

In order to simplify estimation of Baseline V spatial crosstalk error components, a worst case condition is assumed where a clear footprint (pixel) having an effective channel temperature corresponding to T_{min} (Table 2-1) is completely surrounded by sunlit clouds. The effective channel thermal radiance of the cloudy pixels is assumed equal to that of the clear pixel. For such conditions, from Eq 4.20

$$NEN(3\sigma) \approx |TR\ (N_T + N_{RS} - N_T)|$$

which reduces to

$$NEN(3\sigma) \approx TR\ N_{RS} \tag{4.21}$$

where

N_T = thermal radiance from each pixel

N_{RS} = reflected solar radiance from each cloudy pixel

$TR = \sum_i TRi$

4.5.1 Aperture Diffraction Spatial Crosstalk

Diffraction spreads the energy emitted from a source into a pattern that stretches from plus to minus infinity. In an optical system, the aperture causes diffraction of the energy in each footprint (pixel) that is seen by the system.

In the calculation of the AMTS aperture diffraction spatial crosstalk, the grating mask aperture was projected forward into the Fraunhofer region in front of the foreoptics. The first order diffraction spread from the image of the aperture is equivalent to the diffraction spread from the aperture itself. The Fraunhofer diffraction spread for a particular wavelength from a rectangular aperture is

$$\frac{I(\theta,\phi)}{I(0,0)} = \left(\frac{\sin m}{m}\right)^2 \left(\frac{\sin n}{n}\right)^2 \tag{4.22}$$

where

$$m = \frac{\pi x \sin \theta}{\lambda}$$

$$n = \frac{\pi y \sin \phi}{\lambda}$$

$I(\theta,\phi)$ = normalized intensity at (θ,ϕ)

θ = diffraction angle in the x direction

ϕ = diffraction angle in the y direction

λ = wavelength

x = width of the aperture

y = height of the aperture

The aperture diffraction radiance transfer ratios are found by convolving the diffraction spread pattern (Eq 4.22) with an entrance slit element and then integrating over the angular limits of the pixels. Figure 4-7 shows the diffraction spread from a rectangular aperture. Most of the energy lies along the perpendicular arms of the coordinate system. For reasons of symmetry, only the transfer ratios for one quadrant need be calculated. Some of the outer pixel transfer ratio values were extrapolated from the inner pixel data.

Aperture diffraction spatial crosstalk errors for selected channels are listed in Table 4-18. Worst case radiance errors were estimated using Eq 4.21. This worst case calculation was assumed to be the 3σ condition. The NEΔT values shown in Table 4-18 are the worst case values divided by three.

4.5.2 Gas Check Scatter Spatial Crosstalk

Refractive elements display two different types of scatter, bulk scatter and surface scatter. The scatter from transparent materials travels both forwards and backwards, so the total amount of scattered radiance is the sum of the radiance that scatters forward and the radiance that scatters backward from the material. The backscatter from the gas check does not contribute to the radiance scattered into a pixel since the backscatter travels out of the instrument and never reaches the image plane. Backscatter from a pixel merely affects instrument transmittance. Consequently, only forward scatter contributes to spatial crosstalk.

Scheele (Ref 4-4) has measured the scatter of several infrared transparent materials. The Baseline V gas check is made of KBr (potassium bromide). KBr was not one of the materials Scheele measured. However, all the materials given in the paper had scatter characteristics that were similar, so it was assumed that KBr had a scatter characteristic similar to the measured data.

The gas check's position is in front of the field stop which means that it views many footprints. Transfer ratios were calculated by integrating the normalized scatter curves over the angles of interest for two wavelengths (usually HeNe lines). The transfer ratios were assumed to vary linearly with wavelength.

Spatial crosstalk worst case radiance error components were calculated using Eq 4-21. Table 4-19 shows the transfer ratios and the estimated 1σ NEΔT errors. The estimated 1σ value is the worst case value divided by three.

4.5.3 Scan Mirror BRDF Spatial Crosstalk

The Bidirectional Reflectance Distribution Function (BRDF) is a measure of the amount of incident energy on a surface scattered out of the reflected specular direction. BRDF is defined as the reflected radiance from a mirror divided by the incident irradiance on the mirror,

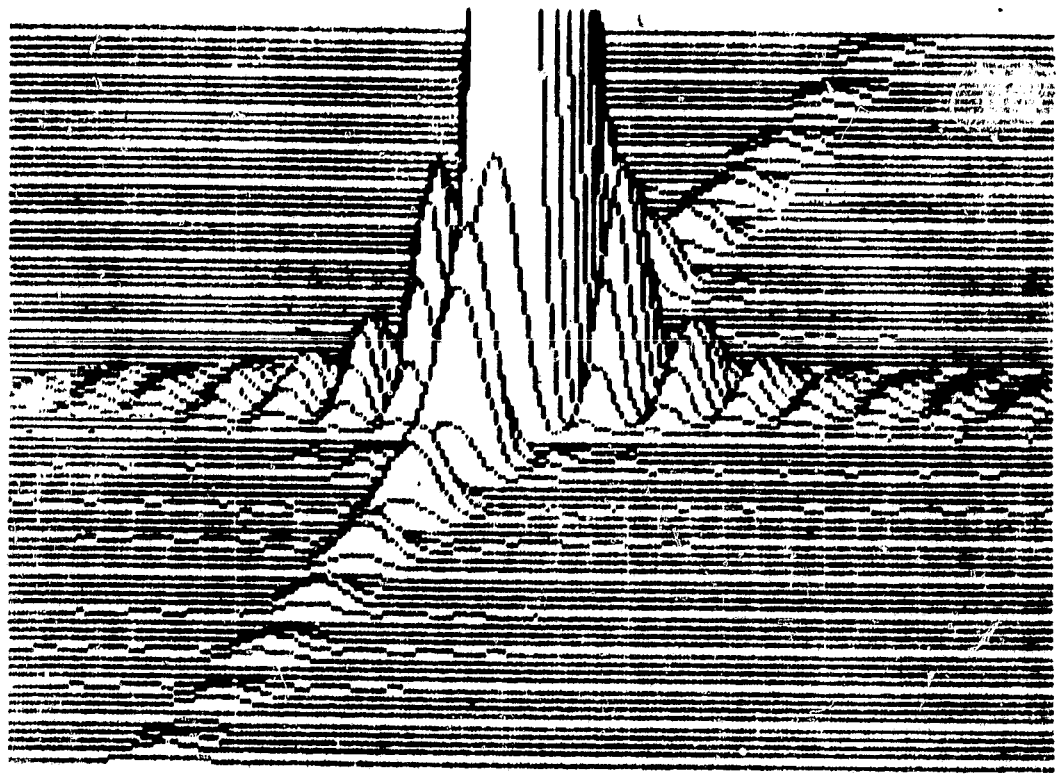

Figure 4-7 Fraunhofer diffraction spread for a rectangular aperture

Table 4-18 Baseline V aperture diffraction spatial crosstalk

CH	ν (cm^{-1})	N_{RS} $\left(\frac{W}{cm^2\ sr\ cm^{-1}}\right)$	Radiance Transfer Ratio TR	T_{min} (K)	NEΔT 1σ (K)
1	606.95	3.30×10^{-10}	3.84×10^{-2}	230	<0.001
10	669.45	5.28×10^{-10}	3.33×10^{-2}	199	<0.001
12	1040.80	3.59×10^{-9}	1.98×10^{-2}	198	0.001
17	1850.90	1.79×10^{-8}	1.20×10^{-2}	233	0.095
20	2386.10	1.10×10^{-7}	6.87×10^{-3}	222	1.056
28	2686.00	2.24×10^{-7}	5.81×10^{-3}	232	3.274

Table 4-19 Baseline V corrector lens and gas check scatter

CH	ν (cm^{-1})	T_{min} (K)	N_{RS} $\left(\frac{W}{cm^2\ sr\ cm^{-1}}\right)$	Transfer Ratio TR		NEΔT (K) 1σ	
				Gas Check	Corrector Lens	Gas Check	Corrector Lens
1	606.95	230	3.3×10^{-10}	4.5×10^{-4}	1.0×10^{-4}	<0.001	<0.001
2	623.20	229	3.72×10^{-10}		1.2×10^{-4}	<0.001	<0.001
3	627.80	218	4.08×10^{-10}		1.2×10^{-4}	<0.001	<0.001
4	634.30	211	4.19×10^{-10}		1.2×10^{-4}	<0.001	<0.001
5	646.60	202	4.69×10^{-10}		1.3×10^{-4}	<0.001	<0.001
6	654.35	195	4.79×10^{-10}		1.3×10^{-4}	<0.001	<0.001
7	665.55	197	5.26×10^{-10}		1.5×10^{-4}	<0.001	<0.001
8	666.85	194	5.28×10^{-10}		1.5×10^{-4}	<0.001	<0.001
9	668.15	198	5.28×10^{-10}		1.5×10^{-4}	<0.001	<0.001
10	669.45	199	5.28×10^{-10}	4.5×10^{-4}	1.5×10^{-4}	<0.001	<0.001
11	875.00	231	1.61×10^{-9}	4.7×10^{-4}	1.7×10^{-4}	<0.001	<0.001
12	1040.80	198	3.59×10^{-9}	4.8×10^{-4}	1.8×10^{-4}	<0.001	<0.001
13	1231.60	231	5.20×10^{-9}	5.0×10^{-4}	2.0×10^{-4}	<0.001	<0.001
14	1650.10	220	2.96×10^{-8}	5.2×10^{-4}	2.7×10^{-4}	0.001	<0.001
15	1700.30	216	3.37×10^{-8}	5.3×10^{-4}	2.8×10^{-4}	0.001	0.001
16	1839.40	232	4.88×10^{-8}	5.4×10^{-4}	3.0×10^{-4}	0.002	0.001
17	1850.90	233	1.79×10^{-8}	5.4×10^{-4}	3.0×10^{-4}	0.001	<0.001
18	1930.10	232	5.62×10^{-8}	5.4×10^{-4}	3.1×10^{-4}	0.004	0.002
19	2384.00	214	1.10×10^{-7}	5.8×10^{-4}	5.0×10^{-4}	0.159	0.137
20	2386.10	222	1.10×10^{-7}	5.8×10^{-4}	5.0×10^{-4}	0.097	0.084
21	2388.20	229	1.11×10^{-7}	5.8×10^{-4}	5.0×10^{-4}	0.066	0.057
22	2390.20	231	1.12×10^{-7}	5.8×10^{-4}	5.0×10^{-4}	0.059	0.052
23	2392.35	232	1.12×10^{-7}	5.8×10^{-4}	5.0×10^{-4}	0.055	0.049
24	2394.50	232	1.12×10^{-7}	5.8×10^{-4}	5.0×10^{-4}	0.058	0.050
25	2424.00	232	1.20×10^{-7}	5.8×10^{-4}	5.2×10^{-4}	0.071	0.064
26	2505.00	232	1.41×10^{-7}	5.9×10^{-4}	5.5×10^{-4}	0.122	0.114
27	2616.50	232	1.73×10^{-7}	5.9×10^{-4}	6.5×10^{-4}	0.248	0.273
28	2686.00	232	2.24×10^{-7}	6.0×10^{-4}	7.0×10^{-4}	0.444	0.515

$$BDRF = f(\theta_i,\phi_i;\theta_r,\phi_r) = \frac{dN_r(\theta_r,\phi_r)}{dH_i(\theta_i,\phi_i)} = \frac{dN_r(\theta_r,\phi_r)}{N_i(\theta_i,\phi_i)d\Omega_i} \qquad (4.23)$$

where

$H_i(\theta_i,\phi_i)$ = Irradiance incident on the mirror from the θ_i,ϕ_i direction (Fig 4-8)

$N_i(\theta_i,\phi_i)$ = Radiance incident on the mirror from the θ_i,ϕ_i direction

$N_r(\theta_r,\phi_r)$ = Radiance reflected or scattered from the mirror in the θ_r,ϕ_r direction (Fig 4-8)

$d\Omega_i$ = Projected solid angle = $(\cos\theta_i \sin\theta_i)\, d\theta_i\, d\phi_i$

BRDF has the units of (sr^{-1}). Equation 4-23 can be rewritten

$$N_r(\theta_r,\phi_r) = \int f(\theta_i,\phi_i;\theta_r,\phi_r)\, N_i(\theta_i,\phi_i)\, d\Omega_1 \qquad (4.24)$$

To simplify the integral the scan mirror was assumed isotropic (no ϕ_i dependence) and $N_i(\theta_i,\phi_i)$ was assumed constant. Measured BRDF data was found in a report by Scheele (Ref 4-5). Unfortunately, the BRDF was measured with the reflected angles in the mirror normal direction only. (The incident angles were varied.) A transform can be performed, however, to approximate the BRDF with other reflected angles

$$f(\theta_i,\theta_r,\phi_r) \approx f(\beta,0,0) \qquad (4.25)$$

where

$$\beta = \cos^{-1}(\cos\theta_i \cos\theta_r - \sin\theta_i \sin\theta_r \cos\phi_r)$$

The solid angle containing the specular reflection was excluded from the integral calculation. This means $N_r(\theta_r,\phi_r)$ represents only the scattered radiance.

The radiance transfer ratio was calculated for two wavelengths that more or less bound the AMTS channel set. By assuming that the transfer ratios vary linearly with wavelength, the AMTS channel set transfer ratios were determined. The total number of footprints that contribute to the error is restricted by a light shield around the mirror.

The worst case crosstalk radiance error was calculated from Eq 4-21. Table 4-20 shows the transfer ratios for the scan mirror and also for the four remaining mirrors. NEΔT was calculated using the total transfer ratio. The worst case condition is assumed to be the 3σ case so the 1σ NEΔT's given are the worst case values divided by three. BRDF was calculated using data for silica mirrors. It is believed to be similar for beryllium mirrors.

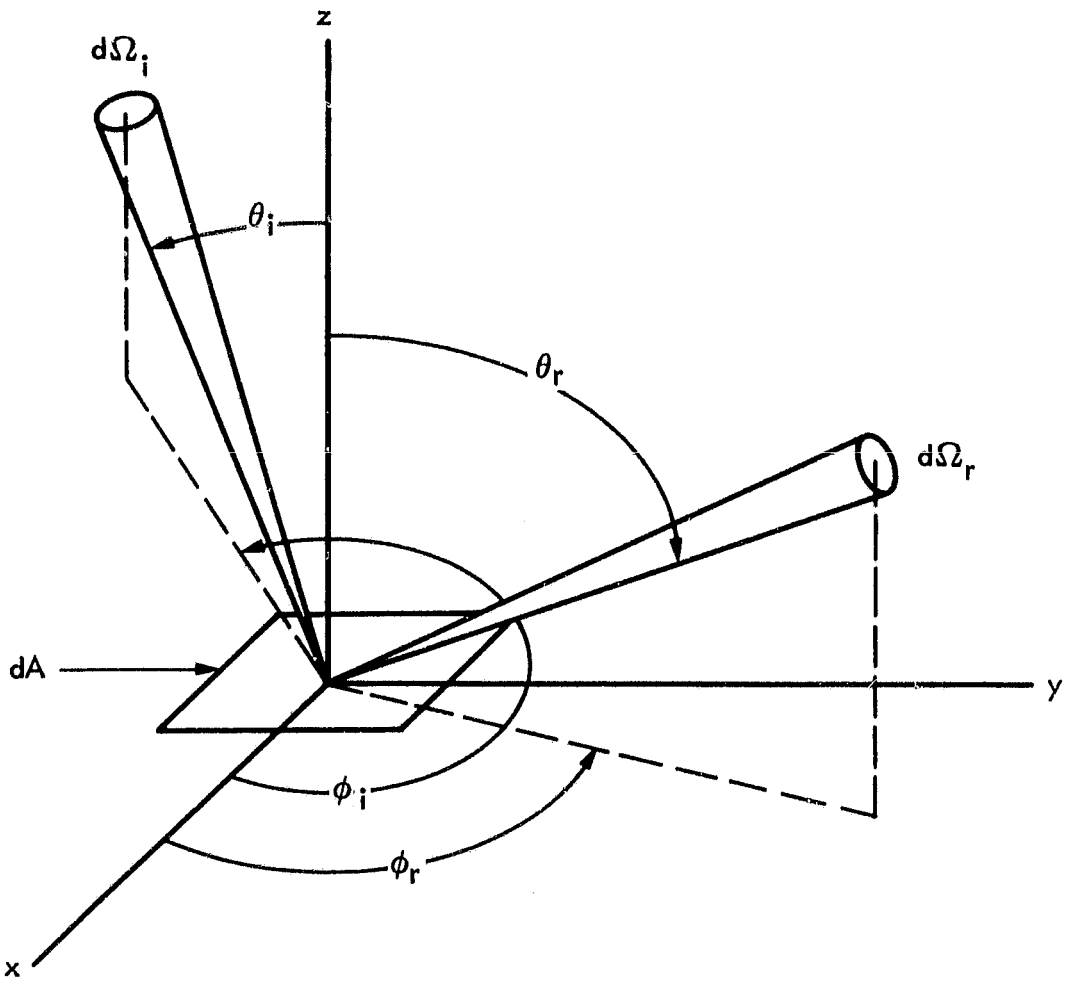

Figure 4-8 BRDF scatter geometry

Table 4-20 Baseline V NEΔT due to mirror BRDF

CH	ν (cm^{-1})	T_{min} (K)	N_{RS} $\left(\frac{W}{cm^2\ sr\ cm^{-1}}\right)$	Transfer Ratio TR: Scan Mirror	Transfer Ratio TR: Other Mirrors	Total Transfer Ratio TR	NEΔT (K) 1σ
1	606.95	230	3.30×10^{-10}	5.25×10^{-4}	5.75×10^{-7}	5.26×10^{-4}	<0.001
2	623.20	229	3.72×10^{-10}	5.32×10^{-4}	5.75×10^{-7}	5.33×10^{-4}	<0.001
3	627.80	218	4.08×10^{-10}	5.32×10^{-4}	5.75×10^{-7}	5.33×10^{-4}	<0.001
4	634.30	211	4.19×10^{-10}	5.36×10^{-4}	5.80×10^{-7}	5.37×10^{-4}	<0.001
5	646.60	202	4.69×10^{-10}	5.41×10^{-4}	5.80×10^{-7}	5.42×10^{-4}	<0.001
6	654.35	195	4.79×10^{-10}	5.44×10^{-4}	5.80×10^{-7}	5.45×10^{-4}	<0.001
7	665.55	197	5.26×10^{-10}	5.49×10^{-4}	5.80×10^{-7}	5.50×10^{-4}	<0.001
8	666.85	194	5.28×10^{-10}	5.50×10^{-4}	5.80×10^{-7}	5.51×10^{-4}	<0.001
9	668.15	198	5.28×10^{-10}	5.50×10^{-4}	5.80×10^{-7}	5.51×10^{-4}	<0.001
10	669.45	199	5.28×10^{-10}	5.50×10^{-4}	5.80×10^{-7}	5.51×10^{-4}	<0.001
11	875.00	231	1.61×10^{-9}	6.33×10^{-4}	6.02×10^{-7}	6.34×10^{-4}	<0.001
12	1040.80	198	3.59×10^{-9}	7.00×10^{-4}	6.20×10^{-7}	7.01×10^{-4}	<0.001
13	1231.60	231	5.20×10^{-9}	7.77×10^{-4}	6.50×10^{-7}	7.78×10^{-4}	<0.001
14	1650.10	220	2.96×10^{-8}	9.46×10^{-4}	7.05×10^{-7}	9.47×10^{-4}	0.002
15	1700.30	216	3.37×10^{-8}	9.66×10^{-4}	7.12×10^{-7}	9.67×10^{-4}	0.003
16	1839.40	232	4.88×10^{-8}	1.02×10^{-3}	7.30×10^{-7}	1.02×10^{-3}	0.004
17	1850.90	233	1.79×10^{-8}	1.03×10^{-3}	7.35×10^{-7}	1.03×10^{-3}	0.002
18	1930.10	232	5.62×10^{-8}	1.06×10^{-3}	7.45×10^{-7}	1.06×10^{-3}	0.007
19	2384.00	214	1.10×10^{-7}	1.24×10^{-3}	8.20×10^{-7}	1.24×10^{-3}	0.333
20	2386.10	222	1.10×10^{-7}	1.24×10^{-3}	8.20×10^{-7}	1.24×10^{-3}	0.206
21	2388.20	229	1.11×10^{-7}	1.24×10^{-3}	8.20×10^{-7}	1.24×10^{-3}	0.140
22	2390.20	231	1.12×10^{-7}	1.24×10^{-3}	8.20×10^{-7}	1.24×10^{-3}	0.128
23	2392.35	232	1.12×10^{-7}	1.24×10^{-3}	8.20×10^{-7}	1.24×10^{-3}	0.122
24	2394.50	232	1.12×10^{-7}	1.25×10^{-3}	8.20×10^{-7}	1.25×10^{-3}	0.124
25	2424.00	232	1.20×10^{-7}	1.26×10^{-3}	8.20×10^{-7}	1.26×10^{-3}	0.153
26	2505.00	232	1.41×10^{-7}	1.29×10^{-3}	8.40×10^{-7}	1.29×10^{-3}	0.264
27	2616.50	232	1.73×10^{-7}	1.34×10^{-3}	8.55×10^{-7}	1.34×10^{-3}	0.549
28	2686.00	232	2.24×10^{-7}	1.36×10^{-3}	8.70×10^{-7}	1.36×10^{-3}	0.959

4.5.4 Telescope and Collimator Mirrors BRDF Spatial Crosstalk

The calculation of the BRDF scatter is essentially the same as for the scan mirror (Para 4.5.3). The collimator mirror views only the 16 footprints within the field stop. The transfer ratio was calculated for each mirror and then summed to obtain the remaining mirror transfer ratio shown in Table 4-20. The collimator transfer ratio was doubled because the mirror is used twice (as both the entrance and exit collimator). The total estimated 1σ NEΔT BRDF mirror crosstalk errors are shown in Table 4-20. These are worst case values divided by three.

4.5.5 Corrector Lens Scatter Spatial Crosstalk

The corrector lens scatter is basically the same problem as the gas check scatter (Para 4.5.2). Major differences in the calculation of the transfer ratio were a reduction in scatter angles because only the 16 field stop pixels need to be included, both forward and backscatter are included, and the crosstalk ratio was increased by a factor of three to account for the thickness of the lens. Table 4-19 gives the transfer ratio and the NEΔT's for corrector lens scatter. The NEΔT's are estimated 1σ values found by dividing the worst case NEΔT by three.

4.5.6 Grating Diffuse Scatter Spatial Crosstalk

Diffuse scatter is caused by the small scale random surface roughness of a ruled grating. It spreads into 2π steradians. The transfer ratio is the fraction of radiance scattered from/into a particular pixel by the grating that reaches the detector. The crosstalk error is the difference between the radiance scattered out of a pixel and the radiance scattered into the pixel.

The transfer ratio can be calculated from

$$\frac{P_d}{P_o}\langle\lambda_1\rangle = \frac{P_d}{P_i}\langle\lambda_2\rangle \frac{\lambda_1 + k}{\lambda_2 + k} \frac{BW_{OF}}{E_{ff}\,\Delta\nu} \frac{W_o h_o}{f_o^2} \qquad (4.26)$$

where

P_d = radiance scattered from the grating

P_o = signal radiance incident on the detector

P_i = radiance incident on the detector.

λ = wavelength

BW_{OF} = order filter bandwidth

E_{ff} = grating efficiency

$\Delta\nu$ = channel half power bandwidth

k = constant

W_o = exit slit width

h_o = exit slit height

f_o = focal length of collimator

Base scatter data were obtained from a paper by Dunning and Minder (Ref 4-1). The constant, k, was found by assuming P_d/P_i varies linearly with wavelength, so P_d/P_i <10.6> = 2.5 x 10^{-3} sr^{-1} and k = -0.64. The estimated 1σ NEΔT errors are shown in Table 4-21. Estimated 1σ NEΔT values are estimated by taking one third of the NEΔT of the worst case situation.

4.5.7 Grating Mask Scatter Spatial Crosstalk

The foreoptics of the AMTS spectrometer cannot be fully masked, so that about 6 percent of the radiance incident on the instrument from a particular pixel hits the grating mask. Some of the energy scattered from the mask will be a source of crosstalk error.

The only way scatter from the grating mask can reach a detector is through the optical aberrations of the collimator. This greatly reduces the crosstalk scatter error. Using BRDF measurements for a Martin Black coated surface found in a paper by Smith (Ref 4-6), the transfer ratio was calculated. NEΔT values shown in Table 4-22 are worst case values divided by three.

4.5.8 Image Plane Mask Scatter Spatial Crosstalk

Energy scattered from the specular image plane mask of the AMTS spectrometer will travel back through the instrument to the grating where it will be diffracted back to the image plane and the detectors, causing crosstalk. The specular reflection from the image plane does not return to the grating (Fig 3-20 and 3-21). Only one scatter radiance pass through the spectrometer is included in this error analysis.

Measured BRDF data were found in a report by Scheele (Ref 4-5). Transfer ratios were calculated by integrating scatter ratios over angles that lead back to a detector, for wavelengths that fall within the passband of the order filter. Table 4-22 lists NEΔT values. The estimated 1σ value is the worst case value divided by three.

4.5.9 Spatial Crosstalk Error Correction

Given a measured radiance image of a scene and a knowledge of the radiance transfer ratios of the instrument, it is conceptionally possible to reduce spatial crosstalk errors in the image by several orders of magnitude. The image matrix must be larger than the necessary radiance transfer ratio matrix. Maximum error correction is only possible over a

Table 4-21 Baseline V grating diffuse scatter

CH	ν (cm^{-1})	T_{min} (K)	N_{RS} ($W/cm^2/sr/cm^{-1}$)	Transfer Ratio TR	NEΔT (K) 1σ
1	606.95	230	3.30E-10	8.36E-7	<0.001
10	669.45	199	5.28E-10	5.14E-7	<0.001
12	1040.80	198	3.59E-9	3.96E-7	<0.001
14	1650.10	220	2.96E-8	3.02E-7	<0.001
16	1839.40	232	4.88E-8	2.76E-7	<0.001
18	1930.10	232	5.62E-8	2.63E-7	<0.001
20	2386.10	222	1.10E-7	4.49E-7	<0.001
28	2686.00	232	2.24E-7	1.82E-7	<0.001

Table 4-22 Baseline V NEΔT due to scatter from the grating and image plane masks

CH	ν (cm^{-1})	T_{min} (K)	N_{RS} ($w/cm^2/sr/cm^{-i}$)	Transfer Ratios, TR		NEΔT (K) 1σ	
				Grating Mask	Image Plane Mask	Grating Mask	Image Plane Mask
1	606.95	230	3.30E-10	9.44E-10	5.33E-10	<0.0001	<0.0001
10	669.45	199	5.28E-10	9.05E-10	5.04E-10	<0.0001	<0.0001
12	1040.80	198	3.59E-9	8.42E-10	4.40E-10	<0.0001	<0.0001
14	1650.10	220	2.96E-8	8.60E-10	3.93E-10	<0.0001	<0.0001
16	1839.40	232	4.88E-8	9.27E-10	3.86E-10	<0.0001	<0.0001
18	1930.10	232	5.62E-8	9.17E-10	3.77E-10	<0.0001	<0.0001
20	2386.10	222	1.10E-7	9.02E-10	3.72E-10	<0.0001	<0.0001
28	2686.00	232	2.24E-7	8.87E-10	3.55E-10	<0.0001	<0.0001

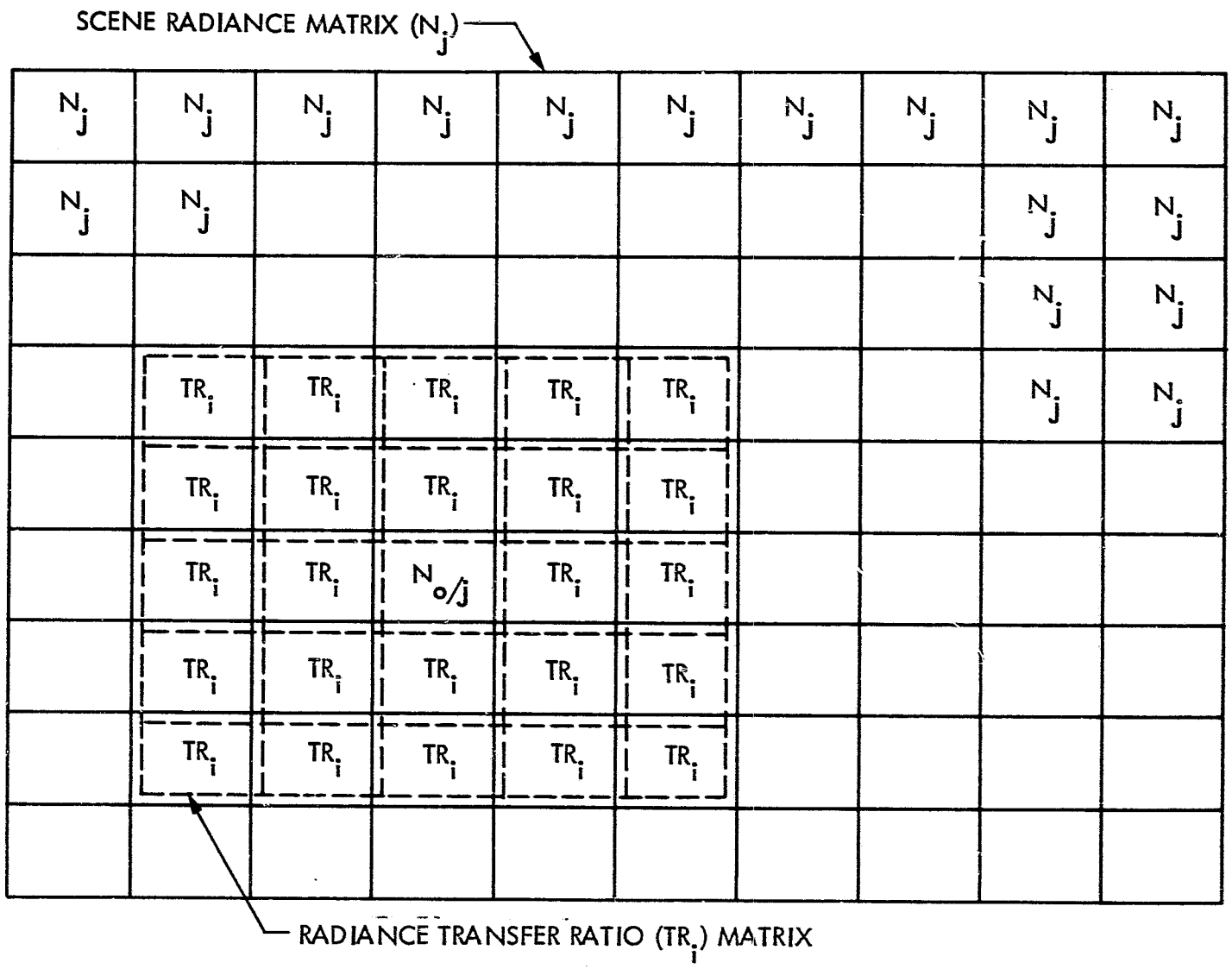

Figure 4-9 Illustration of radiance transfer matrix (i-matrix) superimposed upon scene radiance matrix (j-matrix). The i-matrix is centered over each j-matrix footprint in turn.

portion of the image matrix. This paragraph develops the argument and the algorithm for spatial crosstalk correction through a deconvolution of the measured image radiance values.

Figure 4-9 illustrates a radiance transfer ratio matrix (i-matrix) centered over a scene — or image — radiance matrix (j-matrix). Given true scene radiance values, measured radiance values in the image are

$$N'_{o/j} = N_{o/j} + \sum_i TR_i \, (N_{i/j} - N_{o/j}) \tag{4.27}$$

where

$N'_{o/j}$ = measured radiance value for the j-matrix footprint corresponding to the 0 position (center) of the i-matrix

$N_{o/j}$ = true radiance value of the j-matrix footprint corresponding to the 0 position of the i-matrix

$N_{i/j}$ = true radiance value of the j-matrix footprint corresponding to the i^{th} position of the i-matrix

TR_i = radiance transfer ratio for the i^{th} position of the i-matrix

Measured radiance values in the image can be determined by centering the i-matrix over each footprint of the true radiance j-matrix in turn and applying Eq 4.27. Error-free measured radiance values can be determined only for that portion of the j-matrix for which the i-matrix is completely contained within the border of the j-matrix.

Given an image whose radiance values are contaminated by spatial crosstalk errors, true radiance values can be approximated by deconvolving the image using a two-pass algorithm. The first pass of the i-matrix over the j-matrix yields two matrices in j-space whose values are calculated using the following equations:

$$\bar{N}_{o/j} = \frac{N'_{o/j} - \sum_i TR_i \, N'_{i/j}}{1 - \sum_i TR_i} \tag{4.28a}$$

$$\varepsilon_{o/j} = N'_{o/j} - \frac{N'_{o/j} - \sum_i TR_i N'_{i/j}}{1 - \sum_i TR_i} \qquad (4.28b)$$

The second pass of the i-matrix over the partially corrected radiance matrix ($\bar{N}_j$-matrix) yields a corrected radiance image in j-space whose values are estimated using the following equation:

$$N_{o/j} = \bar{N}_{o/j} + \frac{\sum_i TR_i \varepsilon_{i/j}}{1 - \sum_i TR_i} \qquad (4.28c)$$

where

$N'_{i/j}$ = measured (contaminated) radiance value of the j-matrix footprint corresponding to the i^{th} position of the i-matrix

$\varepsilon_{i/j}$ = estimated error term of the j-matrix footprint corresponding to the i^{th} position of the i-matrix

Residual crosstalk errors in the corrected image radiance values are due to the fact that the ε_j values calculated using Eq 4.28b are approximations for $\varepsilon_j(\text{true}) = N'_j - N_j$. These true values, of course, are not determinable starting with the contaminated radiance image.

An example illustrating spatial crosstalk correction is presented in Tables 4-23 through 4-29. Table 4-23 represents true footprint radiance values for a 21 x 21 element two-tone scene. The boxed radiance values represent cloudy footprints and the remaining values represent clear footprints. Table 4-24 represents a 5 x 5 element radiance transfer ratio matrix. Table 4-25 represents the contaminated radiance image matrix which results when the true radiance matrix is convolved with the radiance transfer ratio matrix per Eq 4.27. (This 17 x 17 element matrix is the maximum size that can be obtained from this convolution without encountering edge effect inaccuracies.) Relatively large crosstalk errors, due to a relatively small amount of cloud cover, accrue in this image matrix in pixels corresponding to clear cold footprints.

The contaminated radiance image matrix of Table 4-25 is the starting point for application of the crosstalk error correction algorithm. The first pass of the radiance transfer ratio matrix over the contaminated radiance image matrix results in the radiance error approximation matrix of Table 4-26 per Eq 4.28b and in the partially corrected radiance matrix of Table 4-27 per Eq 4.28a. (A 13 x 13 element matrix is the maximum size that can be obtained in Tables 4-26 and 4-27 without encountering edge effects. Table 4-27 shows only the 9 × 9 element matrix needed for this exercise.)

ORIGINAL PAGE IS
OF POOR QUALITY

Table 4-23 True radiance value matrix

Table 4-24 Radiance transfer ratio, TR, matrix

0. 204E-06	0. 447E-05	0. 495E-03	0. 447E-05	0. 204E-06
0. 120E-05	0. 262E-04	0. 290E-02	0. 262E-04	0. 120E-05
0. 412E-03	0. 903E-02	0. 000E+00	0. 903E-02	0. 412E-03
0. 120E-05	0. 262E-04	0. 290E-02	0. 262E-04	0. 120E-05
0. 204E-06	0. 447E-05	0. 495E-02	0. 447E-05	0. 204E-06

Table 4-25 Contaminated/measured radiance image matrix

0. 156E-07	0. 537E-06	0. 130E-07	0. 539E-06	0. 815E-08	0. 616E-08	0. 328E-08	0. 329E-08	0. 750E-08	0. 330E-08	0. 506E-08	0. 841E-08	0. 540E-06	0. 130E-07	0. 538E-06	0. 815E-08	0 532E-08			
0. 486E-08	0. 751E-08	0. 331E-08	0. 510E-08	0. 330E-08	0. 483E-08	0. 351E-08	0. 815E-08	0. 541E-06	0. 157E-07	0. 537E-06	0. 816E-08	0. 661E-08	0. 772E-08	0. 484E-08	0 595E-08	0 376E-08			
0. 540E-06	0. 996E-08	0. 351E-08	0. 376E-08	0. 813E-08	0. 540E-06	0. 835E-08	0. 838E-08	0. 540E-06	0. 973E-08	0. 929E-08	0. 815E-08	0. 537E-06	0. 813E-08	0. 377E-08	0. 483E-08	0 329E-08			
0. 113E-07	0. 540E-06	0. 813E-08	0. 350E-08	0. 596E-08	0. 639E-08	0. 352E-08	0. 837E-08	0. 544E-06	0. 542E-06	0. 113E-07	0. 352E-08	0. 749E-08	0. 351E-08	0. 108E-07	0. 537E-06	0 835E-08			
0. 537E-06	0. 139E-07	0. 353E-08	0. 351E-08	0. 969E-08	0. 537E-06	0. 108E-07	0. 352E-08	0. 778E-08	0. 487E-08	0. 485E-08	0. 330E-08	0. 510E-08	0. 330E-08	0. 485E-08	0. 485E-08	0. 329E-08			
0. 971E-08	0. 539E-06	0. 110E-07	0. 110E-07	0. 537E-06	0. 970E-08	0. 507E-08	0. 597E-08	0. 533E-08	0. 841E-08	0. 540E-06	0. 130E-07	0. 540E-06	0. 130E-07	0. 537E-06	0. 8[illegible]E-08	0 350E-08			
0. 841E-08	0. 539E-06	0. 972E-08	0. 508E-08	0. 507E-08	0. 841E-08	0. 537E-06	0. 172E-07	0. 537E-06	0. 108E-07	0. 662E-08	0. 599E-08	0. 640E-08	0. 332E-08	0. 750E-08	0. 329E-08	0. 327E-08			
0. 353E-08	0. 128E-07	0. 542E-06	0. 542E-06	0. 862E-08	0. 640E-08	0. 971E-08	0. 539E-06	0. 994E-08	0. 993E-08	0. 540E-06	0. 146E-07	0. 538E-06	0. 108E-07	0. 532E-08	0. 329E-08	0. 328E-08			
0. 815E-08	0. 533E-08	0. 486E-08	0. 485E-08	0. 330E-08	0. 506E-08	0. 842E-08	0. 539E-06	0. 133E-07	0. 537E-06	0. 161E-07	0. 540E-06	0. 993E-08	0. 992E-08	0. 537E-06	0. 813E-08	0. 351E-08			
0. 815E-08	0. 540E-06	0. 111E-07	0. 399E-08	0. 813E-08	0. 537E-06	0. 815E-08	0. 352E-08	0. 969E-08	0. 537E-06	0. 115E-07	0. 113E-07	0. 537E-06	0. 969E-08	0. 373E-08	0. 835E-08				
0. 354E-08	0. 641E-08	0. 486E-08	0. 329E-08	0. 595E-08	0. 483E-08	0. 329E-08	0. 620E-08	0. 594E-08	0. 378E-08	0. 969E-08	0. 537E-06	0. 124E-07	0. 774E-08	0. 622E-08	0. 328E-08	0. 329E-08			
0. 134E-07	0. 545E-06	0. 542E-06	0. 837E-08	0. 772E-08	0. 356E-08	0. 329E-08	0. 485E-08	0. 485E-08	0. 329E-08	0. 644E-08	0. 124E-07	0. 539E-06	0. 998E-08	0. 307E-08	0. 595E-08	0. 328E-08			
0. 622E-08	0. 641E-08	0. 508E-08	0. 816E-08	0. 539E-06	0. 836E-08	0. 857E-08	0. 542E-06	0. 542E-06	0. 837E-08	0. 529E-08	0. 102E-07	0. 544E-06	0. 549E-06	0. 545E-06	0. 126E-07	0 351E-08			
0. 146E-07	0. 538E-06	0. 862E-08	0. 837E-08	0. 539E-06	0. 814E-08	0. 351E-08	0. 485E-08	0. 507E-08	0. 837E-08	0. 545E-06	0. 545E-06	0. 102E-07	0. 954E-08	0. 113E-07	0. 539E-06	0. 108E-07			
0. 542E-06	0. 126E-07	0. 351E-08	0. 329E-08	0. 510E-08	0. 595E-08	0. 328E-08	0. 354E-08	0. 355E-08	0. 597E-08	0. 642E-08	0. 664E-08	0. 866E-08	0. 545E-06	0. 547E-06	0. 544E-06	0. 148E-07			
0. 488E-08	0. 512E-08	0. 595E-08	0. 328E-08	0. 622E-08	0. 750E-08	0. 595E-08	0. 328E-08	0. 351E-08	0. 126E-07	0. 542E-06	0. 542E-06	0. 132E-07	0. 539E-06	0. 994E-08	0. 102E-07	0. 540E-06			
0. 133E-07	0. 537E-06	0. 969E-08	0. 375E-08	0. 124E-07	0. 541E-06	0. 971E-08	0. 373E-08	0. 615E-08	0. 541E-06	0. 972E-08	0. 507E-08	0. 330E-08	0. 510E-08	0. 356E-08	0. 623E-08	0. 640E-08			

Table 4-26 Radiance error approximation, ε_j, matrix

0.403E-09	0.619E-09	0.497E-08	-0.123E-08	0.523E-08	0.525E-08	-0.703E-09	0.659E-08	0.222E-08	0.496E-08	-0.399E-08	0.492E-08	0.666E-09
0.497E-08	0.412E-09	0.281E-08	0.324E-08	0.449E-09	0.523E-08	-0.278E-08	0.105E-08	0.810E-08	0.495E-09	0.430E-08	0.483E-09	0.755E-08
0.497E-09	0.409E-09	0.647E-08	-0.352E-08	0.756E-08	0.522E-09	0.459E-08	0.178E-08	0.171E-08	0.183E-09	0.193E-08	0.170E-09	0.170E-08
0.791E-08	0.786E-08	-0.376E-08	0.651E-08	0.200E-08	0.284E-08	0.224E-08	0.529E-08	-0.942E-08	0.984E-08	-0.700E-08	0.979E-08	-0.359E-08
0.655E-08	0.199E-08	0.195E-08	0.524E-08	-0.351E-08	0.139E-07	-0.346E-08	0.764E-08	0.357E-08	0.291E-08	0.325E-08	0.271E-09	0.428E-08
0.106E-08	0.960E-09	0.549E-08	0.331E-08	0.655E-08	-0.222E-08	0.680E-08	0.684E-08	-0.607E-09	0.114E-07	-0.323E-08	0.761E-08	0.222E-08
0.174E-08	0.167E-08	0.181E-09	0.191E-08	0.526E-08	-0.203E-08	0.101E-07	-0.325E-08	0.129E-07	-0.834E-09	0.684E-08	0.678E-08	-0.381E-08
0.788E-08	0.933E-09	0.494E-08	-0.388E-08	0.495E-08	0.218E-08	0.453E-09	0.646E-08	-0.346E-08	0.836E-08	0.818E-08	-0.379E-08	0.647E-08
0.173E-08	0.177E-09	0.278E-08	0.168E-08	0.180E-09	0.305E-08	0.279E-08	0.705E-09	0.649E-08	-0.345E-08	0.922E-08	0.470E-09	0.311E-08
0.101E-08	0.786E-08	0.456E-08	0.444E-09	0.132E-09	0.168E-08	0.168E-08	0.188E-09	0.337E-08	0.921E-08	-0.217E-08	0.685E-08	0.202E-08
0.198E-08	0.499E-08	-0.231E-08	0.522E-08	0.543E-08	0.949E-09	0.947E-09	0.523E-08	0.224E-08	0.711E-08	0.286E-08	0.853E-08	0.400E-08
0.546E-08	0.521E-08	-0.231E-08	0.497E-08	0.399E-09	0.168E-08	0.194E-08	0.529E-08	0.365E-08	0.370E-08	0.718E-08	0.651E-08	0.820E-08
0.456E-09	0.136E-09	0.197E-08	0.280E-08	0.152E-09	0.356E-09	0.407E-09	0.285E-08	0.333E-08	0.355E-08	0.558E-08	0.306E-08	0.614E-08

Table 4-27 Partially corrected radiance matrix

0.3219E-08	0.5408E-06	0.3235E-08	0.2994E-08	0.3183E-08	0.3084E-08	0.3142E-08	0.3121E-08	0.3172E-08
0.5408E-06	0.3192E-08	0.3072E-08	0.3126E-08	0.3089E-08	0.3124E-08	0.5408E-06	0.3146E-08	0.5408E-06
0.3126E-08	0.3174E-08	0.5408E-06	0.3272E-08	0.5407E-06	0.3177E-08	0.3045E-08	0.3080E-08	0.3148E-08
0.3131E-08	0.3088E-08	0.3157E-08	0.5408E-06	0.3136E-08	0.3095E-08	0.5408E-06	0.3181E-08	0.5408E-06
0.3120E-08	0.3143E-08	0.3167E-08	0.5408E-06	0.3211E-08	0.5407E-06	0.3213E-08	0.5408E-06	0.3083E-08
0.3190E-08	0.5409E-06	0.3195E-08	0.3141E-08	0.3072E-08	0.3230E-08	0.5408E-06	0.3120E-08	0.3126E-08
0.3168E-08	0.3156E-08	0.3111E-08	0.3159E-08	0.3149E-08	0.3073E-08	0.3207E-08	0.5408E-06	0.3154E-08
0.3158E-08	0.3112E-08	0.3159E-08	0.3163E-08	0.3162E-08	0.3105E-08	0.3075E-08	0.3157E-08	0.5408E-06
0.5409E-06	0.3141E-08	0.3144E-08	0.5409E-06	0.5409E-06	0.3140E-08	0.3049E-08	0.3098E-08	0.5408E-06

Table 4-28 Fully corrected radiance matrix

0.3204E-08	0.5410E-06	0.3205E-08	0.3200E-08	0.3205E-08	0.3202E-08	0.3203E-08	0.3202E-08	0.3202E-08
0.5410E-06	0.3204E-08	0.3202E-08	0.3204E-08	0.3203E-08	0.3203E-08	0.5408E-06	0.3204E-08	0.5408E-06
0.3203E-08	0.3204E-08	0.5410E-06	0.3206E-08	0.5410E-06	0.3206E-08	0.3202E-08	0.3203E-08	0.3204E-08
0.3202E-08	0.3202E-08	0.3203E-08	0.5410E-06	0.3204E-08	0.3203E-08	0.5408E-06	0.3205E-08	0.5410E-06
0.3201E-08	0.3202E-08	0.3203E-08	0.5410E-06	0.3205E-08	0.5410E-06	0.3206E-08	0.5408E-06	0.3204E-08
0.3203E-08	0.5410E-06	0.3202E-08	0.3202E-08	0.3201E-08	0.3205E-08	0.5410E-06	0.3204E-08	0.3204E-08
0.3202E-08	0.3202E-08	0.3201E-08	0.3202E-08	0.3202E-08	0.3201E-08	0.3205E-08	0.5410E-06	0.3206E-08
0.3203E-08	0.3201E-08	0.3202E-08	0.3201E-08	0.3202E-08	0.3203E-08	0.3202E-08	0.3205E-08	0.5410E-06
0.5410E-06	0.3202E-08	0.3202E-08	0.5409E-06	0.5409E-06	0.3203E-08	0.3203E-08	0.3204E-08	0.5410E-06

Table 4-29 NEAT errors (K)

CONTAMINED/MEASURED VALUES (REF. TABLE 4-25)

18.46841	-0.23309	20.41635	1.46970	14.57895	6.67023	6.61206	0.49634	7.44244
-0.24988	18.49020	7.34970	10.05084	8.15750	15.95993	-0.06879	23.82712	-0.05505
7.34933	15.95261	-0.23572	29.17831	-0.23566	20.45865	11.80862	10.12146	11.22583
16.38516	11.22238	18.49564	-0.15063	18.92233	18.90628	-0.05042	25.96390	-0.21899
0.48553	7.30569	15.97934	-0.13812	24.22116	-0.22095	27.90231	-0.06628	18.90189
15.36057	-0.25092	15.39041	8.14221	1.50821	18.47195	-0.23145	21.53653	21.26328
10.00403	6.56787	0.43921	10.70966	9.98462	2.59775	18.47421	-0.23212	22.91788
14.45078	1.64603	0.43344	6.60696	6.60733	0.44479	11.34207	22.91776	-0.15033
-0.15240	15.85611	16.28867	0.05499	0.05499	15.85770	8.05447	19.39725	0.16785

FINAL CORRECTED VALUES (REF. TABLE 4-28)

0.01788	0.00000	0.02643	0.00024	0.02399	0.00793	0.01523	0.01641	0.01080
0.00006	0.01996	0.00833	0.01694	0.01309	0.01682	-0.00958	0.01840	-0.01105
0.01212	0.01700	0.00006	0.03021	0.00000	0.02811	0.01175	0.01614	0.02119
0.01184	0.00922	0.01691	0.00012	0.01984	0.01520	-0.01227	0.02643	0.00006
0.00595	0.00958	0.01315	0.00006	0.02295	0.00006	0.02707	-0.01385	0.01843
0.01389	0.00006	0.01038	0.01016	0.00342	0.02313	0.00006	0.02039	0.02136
0.00974	0.00989	0.00604	0.01004	0.01166	0.00552	0.02438	0.00012	0.02661
0.01303	0.00638	0.00989	0.00635	0.00992	0.01291	0.01181	0.02405	0.00018
0.00012	0.01065	0.01013	-0.00464	-0.00452	0.01556	0.01358	0.02130	0.00024

The second pass of the radiance transfer ratio matrix over this partially corrected radiance matrix per Eq 4.28c results in the fully corrected radiance matrix of Table 4-28. (This 9 x 9 element matrix is the maximum size that can be obtained without encountering edge effects.) Table 4-29 shows crosstalk errors in terms of NEΔT in the uncorrected image (corresponding to Table 4-25) and in the corrected image (corresponding to Table 4-28). In this example, application of the spatial crosstalk error correction algorithm resulted in an error reduction of approximately three orders of magnitude.

The above example was used to illustrate the principle of spatial crosstalk correction by deconvolution of the radiance image. Numeric values and matrix sizes in the example do not correspond to the Baseline V instrument.

The only Baseline V error sources which result in significant spatial crosstalk errors are aperture diffraction, corrector lens and gas check scatter, and scan mirror BRDF. As shown in Tables 4-18, 4-19 and 4-20, crosstalk correction is needed only for the band 3 and band 4 channels. For a worst case condition of a clear footprint surrounded by an unbroken cloud field, a 27 x 27 element i-matrix would result in $\approx$0.1 K NEΔT in the worst case channel (channel 28).

Edge effects can limit the area over which maximum spatial crosstalk correction is possible. In the limit, full earth coverage crosstalk correction would require a continuous image — i.e., no edges — for the crosstalk correction algorithm to be applied everywhere. In addition, to realize the full error correction capability of the algorithm, all measured pixel values within the i-matrix at any one time should effectively have temporal simultaneity. For the Baseline V altitude of 833 km, successive swaths in the equatorial regions are not contiguous and full earth coverage data contains both nighttime and daytime image segments measured approximately 12 hours apart (Fig 3-18).

For an altitude of 1350 km, successive swaths are contiguous and seperated in time by 112 minutes. For slightly higher orbits successive swaths could be made to overlap. For error correction purposes this would represent an image without edges having temporal simultaneity. For nighttime only full earth coverage, available with orbital altitudes of 1350 km or higher, high scene contrast due to reflection of solar radiation from broken cloud fields would be eliminated with a corresponding decrease in spatial crosstalk errors. It is possible under these conditions that spatial crosstalk correction would seldom, if ever, be necessary.

The crosstrack scan angle affects the spatial registration of scene (j-matrix) pixel elements with the elements of the radiance transfer ratio i-matrix. The i-matrix is aligned with its axes along the length of the linear inlet slit array and normal to the length of the inlet slit array respectively. The effect of the rotating 45 degree scan mirror used on Baseline V is to displace successive linear footprint arrays in object space with respect to each other as a function of scan angle (Fig 3-22). In applying the spatial crosstalk correction algorithm, this effect must be taken into account in selecting the image pixels in j-space which correspond to the i-matrix positions. In general, there will not be a one-to-one spatial registration between j-space and i-space pixel areas for linear

footprint arrays on either side of the center of the i-matrix. This problem can be resolved using reimaging techniques with no loss in crosstalk correction accuracy. If the scattering characteristics of the scan mirror are not isotropic, it could be necessary to calibrate the radiance transfer ratio values of the i-matrix as a function of scan angle.

Ideally, the image pixels should have a 100 percent fill factor to maximize spatial crosstalk error correction capability. As a practical matter, for the 70 percent pixel fill factor of Baseline V, a very unique scene contrast pattern would be required to cause significant crosstalk correction degradation.

4.5.10 Spatial Crosstalk Radiometric Error Summary

Spatial crosstalk error values are scene dependent. Spatial crosstalk is most severe for high contrast scenes; generally for solar reflection from broken cloud cover. Significant spatial crosstalk error can occur in band 4 due to instrument aperture diffraction, gas check and corrector lens scatter, and scan mirror BRDF. Spatial crosstalk errors from various scattering sources are correlated with each other, but are not correlated with other nontunable radiometric errors. Spatial crosstalk errors are nontunable. In general, individual footprint spatial crosstalk errors would be somewhat reduced in the composite footprint. The degree of this reduction would be scene pattern dependent. Since spatial crosstalk error values are a function of channel wavelength, there can be a relatively large channel to channel correlated error component due to this uncorrected error source.

Spatial crosstalk error can be reduced to a level that is no longer significant in terms of AMTS performance capability by image processing of the measured channel radiance images for selected channels and for selected scenes. Spatial crosstalk correction requires prelaunch calibration of overall instrument radiance transfer ratio matrix values.

4.6 Spatial Simultaneity Radiometric Errors

If all channels do not simultaneously view the same IFOV a scene dependent channel to channel relative radiometric error can occur. In terms of geometric optics, spatial simultaneity error can occur unless

- The scene images at all channel wavelengths coincide at the inlet slit (field stop).
- Geometric aberrations are identical for all channel wavelengths at the inlet slit.
- No relative channel to channel image vignetting occurs along the spatial axis — normal to the spectral axis — ahead of the channel detectors.

For Baseline V, the first two conditions are satisfied by using all reflecting elements in the foreoptics. The last condition is satisfied by premasking along the spatial axis at the inlet slit to compensate for relative geometric aberration effects and for relative misalignment of the image plane mask in the spatial dimension. Since the detectors are normally in a pupil plane, relative detector misalignment can cause no significant spatial simultaneity radiometric error component.

In terms of physical optics, aperture diffraction can result in a wavelength dependent spatial simultaneity radiometric error (Para 4.5.1). This is true of all spatial crosstalk error sources. The effects of these error sources are evaluated in Para 4.5, and in this study are treated as spatial crosstalk radiometric errors.

4.7 Chopper and Electronics Radiometric Errors

Electronics and optical chopper induced radiometric error sources are:

- Chopper induced spectral weighting of pixels.
- Chopper induced spatial weighting of pixels.
- Signal channel electronics errors.

4.7.1 Chopper Induced Spectral Weighting of Pixels

If the blades of the optical chopper were placed precisely in an image plane no chopper induced spectral weighting could occur. When the blades are placed forward of the image plane spectral weighting can occur (Para 3.1.1.3.2). For the chopper wheel configuration of Baseline V (Para 3.1.2 and 3.2.1) this weighting is a maximum at the ends of the slit array and approaches zero for the center array elements. For a chopper wheel to slit jaw spacing of 0.25 mm some degree of point source differential shadowing along the length of the grating -- normal to the grating grooves -- occurs only ≈0.2 percent of the time for the worst case end array elements. The resulting contribution to channel passband characteristics variation over the length of the slit array would be negligable.

4.7.2 Chopper Induced Spatial Weighting of Pixels

The Baseline V chopper wheel configuration does not result in radiometric errors due to spatial weighting of the footprint (Para 3.1.1.3.2).

4.7.3 Signal Channel Electronics Errors

The signal channel electronics consists of the optical scan mirror control circuits, optical chopper control circuits, optical chopper reference generator circuits, and analog and digital signal channel circuits (Para 3.4.2.1; Fig 3-32 and 3-33). Possible signal channel electronics radiometric error sources include:

- Chopper synchronization error.
- Synchronous demodulator phase error.
- Input/output amplitude linearity.
- Input/output amplitude stability.
- DC offset stability.
- Integrator hold stability.
- Integrator memory.
- EMI.

4.7.3.1 Chopper Synchronization Error

Average chopper wheel angular velocity is synchronized with the system clock. There are 56 (integer) chopper cycles per footprint dwell interval, or ≈2.56 chopper wheel revolutions per dwell interval. Integrated signal energy is directly proportional to the footprint signal integration time. Consequently, the footprint chopper speed radiometric error component is a function of the average chopper speed per dwell interval. The calibration target reference signal values used for individual footprint data reduction are averaged over 10 individual calibration target looks corresponding to ≈9 line scan intervals, or 3.67 minutes (Para 3.1.2 and 4.2.3; Fig 3-28 and 4-1). Consequently, the chopper speed error component due to these calibration reference signal values is a function of the average chopper speed over the 10 sets of calibration target looks. The total chopper speed error per footprint is the algebraic sum of these two error components.

Practically, the average speed variation over the 10 sets of calibration target looks spread over a 3.67 minute interval would be much less than that of the 0.1273 sec footprint dwell interval. Clock frequency stability over the 3.67 minute interval should be very good. Consequently, chopper speed error can be approximated using only footprint dwell interval average speed errors. Table 4-30 lists the average chopper speed synchronization error per footprint dwell interval which would result in a radiometric error of ≈0.1 K NEΔT (Table 2-9). By holding the maximum per footprint synchronization error to <0.1 percent the 1σ error contribution due to chopper speed variation effects would be <0.03 K, and would not significantly limit AMTS system performance capability.

4.7.3.2 Synchronous Demodulator Phase Error

Synchronization and relative phase relationships between signal channel and reference channel pulses is inherent in the chopper/reference signal generation configuration (Para 3.1.2; Fig 3-27). Reference channel phase with respect to that of the signal channel can be controlled by adjusting the angular position of the reference slit array. In terms of out-of-band noise rejection by the synchronous demodulation process, it is

important that signal channel integration occur over an integer number of complete chopper cycles per footprint dwell interval. In the nominal design, signal channel integration starts and stops at a zero crossing of the same sign (Fig 3-34). Within limits, a reference phase offset should have very little effect upon radiometric performance. To the extent that they are linear, slowly varying reference phase shifts in terms of the 3.67 minute radiometric calibration cycle tend to cancel out in the calibration process (Para 4.2.3).

4.7.3.3 Input/Output Amplitude Linearity

Conceptually, given enough data points, the in-orbit system tuning approach outlined in Para 2.1.6 should be able to correct for non-linearity in input/output amplitude response of the signal channel. As a practical matter, system tuning can only be relied on to correct for linear systematic errors (Para 2.3.11). The effects of signal channel nonlinearity are illustrated in Fig 4-10. The channel input/output response is anchored radiometrically at radiance values corresponding to those of the calibration targets. System tuning tends to establish a best straight line fit to that portion of a nonlinear response which lies between the calibration radiance values. The total instrument calibration error then consists of a systematic component which is tunable, plus a residual nontunable component. The peak nontunable radiance error component is proportional to 1/2 the peak instrument signal channel linearity error.

Discreet PC and PV IR detectors tend to be quite linear. The degree of linearity can be a function of the conditions under which the detector is operated, including the interaction of the detector/preamplifier circuits. The linearity of the signal channel electronics through the ADC is a function of the detail design of the circuits. Here, as for chopper wheel synchronization error (Table 4-30), 0.1% peak nontunable signal channel linearity error would not significantly affect overall AMTS system performance.

Detector manufacturers and circuit designers consulted during the course of this study have no reason to believe that this degree of linearity cannot be achieved. No measured data base was found, however, with this precision. Techniques are becoming available which allow this measurement precision (Ref 4-7). It is believed that this error source need not be a problem for the AMTS.

4.7.3.4 Input/Output Amplitude Stability

Only short term input/output instability, within the time frame of the 3.67 minute reference averaging period of the instrument calibration cycle, could result in a radiometric error (Para 4.2.3). Linear drifts within this interval would be removed by the calibration process during data reduction. This error source need not be a problem for the AMTS.

4.7.3.5 DC Offset Stability

Long term DC offset drifts must be held within acceptable limits to maintain the full dynamic range of the channel within the voltage window of the data system. Only short term DC drifts within the

Table 4-30 Average percent chopper wheel synchronization error per 130 msec interval which would result in 0.1 K NEΔT

Band	CH	Speed Sync. Error (%)	
		T_{min}	T_{max}
1	1	0.17	0.11
	10	0.25	0.12
2	11	0.24	0.12
	15	0.53	0.38
3	16	0.49	0.33
	18	0.54	0.28
4	19	0.75	0.46
	28	0.72	0.29

3.67 minute reference averaging period of the instrument calibration cycle could result in a radiometric error. Linear drifts within this interval would be removed by the calibration process during data reduction. DC offset drifts are primarily caused by temperature drifts. Differential TIA's are used in Baseline V to provide thermal common mode rejection. If necessary, active thermal control could be employed, but it is believed that this would not be necessary. This error source need not be a problem for the AMTS.

4.7.3.6 Integrator Hold Stability

Per footprint drift in the channel integrated voltage does not result in a radiometric error provided the elapsed time between the dwell interval and the integrator readout cycle for a particular channel are the same where viewing the calibration targets as when viewing the scene. Longer term drifts within the 3.67 minute reference averaging period of the instrument calibration cycle could result in a radiometric error. Linear drifts within the interval would be removed by the calibration process during data reduction. This error source need not be a problem for the AMTS.

4.7.3.7 Integrator Memory

A "last scene" dependent residual voltage in the integrator capacitor following the reset cycle could result in a scene dependent radiometric error. Should this be a problem, it could be eliminated by subjecting the storage capacitor to a short charge/discharge cycle from a fixed, stable, relatively high voltage source between the footprint integrate/read/dump cycles. This error source need not be a problem for the AMTS.

4.7.3.8 EMI

Several general categories of EMI could be encountered which affect radiometric performance in different ways. Effects of EMI which is stable, periodic, and synchronous on a footprint to footprint basis with the footprint sampling rate of both the calibration targets and the scene would be removed by the radiometric calibration process during data reduction. Conceptually, the effects of EMI which is scene dependent, stable, and synchronous with footprint sampling — such as that caused by crosstalk between signal channels — is a form of spatial crosstalk and could be removed through image processing (Para 4.5.9). EMI which is assynchronous with the footprint sampling rate or whose effects are not stable or linear over the 3.67 minute instrument calibration cycle could result in radiometric error. Relatively large transient events are particularly undesirable. The first line of defense against EMI is avoidance at the system design and detail circuit design levels. The choice of relative frequencies at the system design level is important. In Baseline V, for example, the optical chopper frequency is set at 440 Hz to keep the 400 Hz chopper motor frequency out of the signal channel passband. At the circuit design level, the use of differential amplifiers for common mode rejection, circuit and cable layout, grounding, and shielding are important. This is particularly true for the relatively low signal level circuitry associated with the image

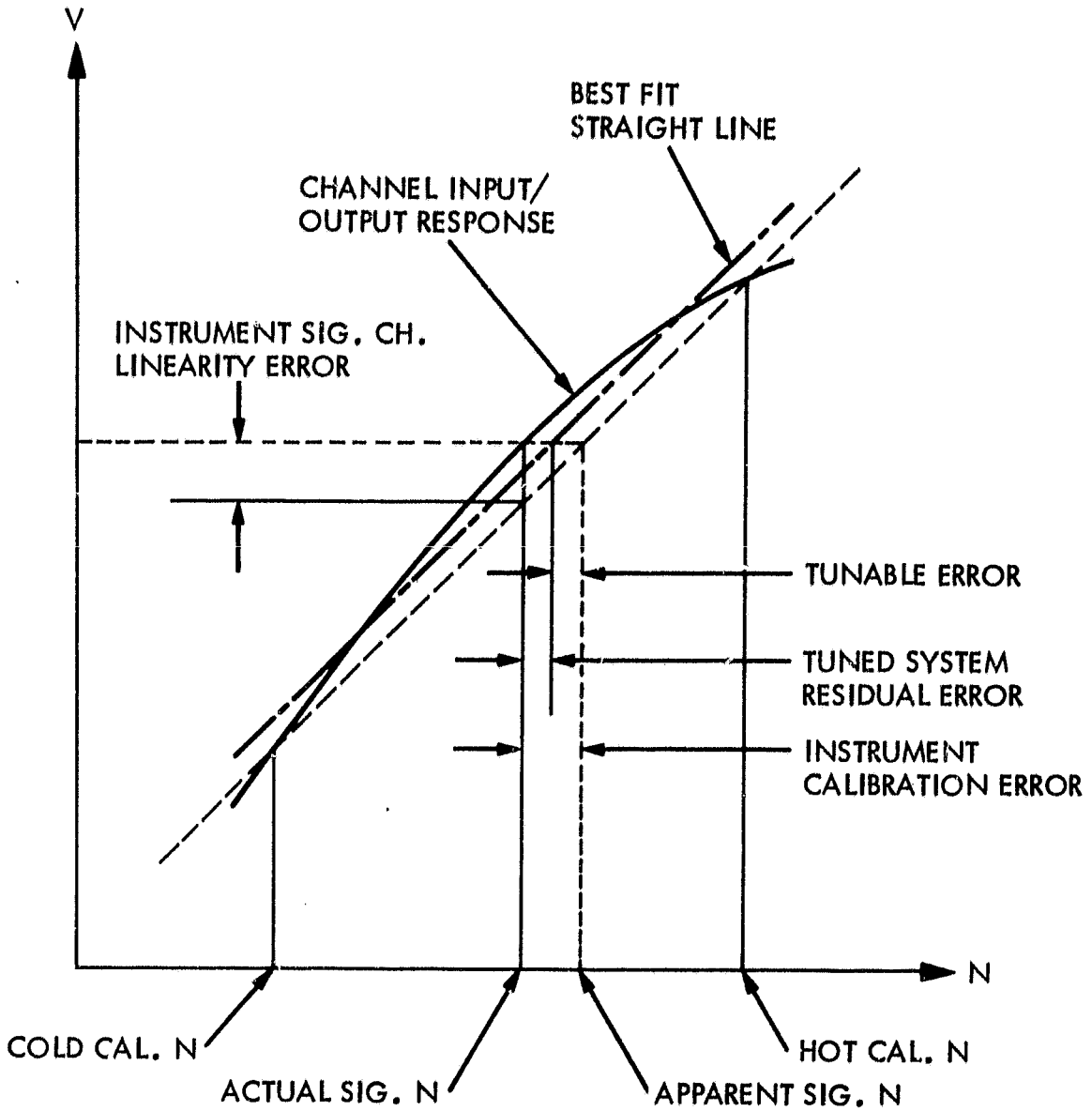

Figure 4-10 Signal channel input/output amplitude linearity error effects

plane assembly. To the extent that detail circuit design concepts were developed for Baseline V, these EMI avoidance techniques were employed. RMS EMI voltage errors within the signal channel should be held to <0.025 percent of signal voltage. This error source need not be a problem for the AMTS.

4.7.4 Chopper and Electronics Radiometric Error Summary

Baseline V chopper induced spectral and spatial weighting errors do not significantly affect AMTS system performance capability. With a careful and well integrated detail design, involving detector and signal channel electronics circuits and thermal control, the signal channel electronics should not significantly limit radiometric system performance capability. Subsystem specification performance limits for selected overall system error contributions can be developed in terms of percent of signal radiance or of signal channel voltage using Table 2-9.

4.8 Nuclear Radiation Induced Radiometric Errors

High detectivity infrared detectors are effective detectors of nuclear radiation. PC HgCdTe detectors display two kinds of performance degradation — an overall change in responsivity (Ref 4-8) and random fast rise time pulses (Ref 4-9). PV HgCdTe detectors degrade by increased rms noise (transients), increased leakage current, and an increase in the optical response of the detector (Ref 4-10). PV InSb detectors degrade by increased rms noise (transients), increased leakage current, and decreased optical response (Ref 4-11). The degradation of detector performance due to transient pulses is not permanent and in general will clear in a few microseconds. All other sources of degradation are considered permanent.

The Baseline V AMTS design assumes a TIROS orbit (833 km). This error analysis also includes calculations showing the nuclear radiation effects for a 1350 km orbit. The radiation encountered in these orbits (Ref 4-12) only slightly degrades the AMTS overall performance.

For the Baseline V AMTS a change in detector response causes radiometric error when the time rate of response change is not linear over the 3.67 minute calibration averaging interval. The fast rise time pulses or transients cause radiometric error when the integrated pulse output voltage while viewing the chopper does not equal the integrated pulse output voltage while viewing the scene.

For PC HgCdTe detectors the change in responsivity at 833 km during one orbit through the South Atlantic Anomaly (SAA) is about 0.003% for protons and 0.004% for electrons. This change in responsivity is permanent and affects both the dynamic range of the instrument and the detectivity (D*) of the detectors. After 5 years in space these very small responsivity changes add up to a total response change of 0.040% for protons and 5.2% for electrons. The corresponding change in D* would produce a 0.034 K change in NEΔT. At 1350 km, the responsivity change after one orbit through the SAA is 0.004% for protons and 18.2% for electrons for

a corresponding 0.119 K change in NEΔT. The rise and fall times of the random pulses are on the order of 5 μsec. The event rate for the worst dwell inside the SAA is 1.4 events/sec at 833 km and 6.14 events/sec at 1350 km. The average pulse height is 1.5×10^{-4} V. If it is assumed that this one second average number of events all occur within one dwell time (0.1273 sec) and that all events occur either while viewing the scene or while viewing the chopper, the resultant change in NEΔT is 0.008 K for 833 km and 0.037 K for 1350 km. This is by far a worst case calculation and statistically the error would be much smaller during the actual flight of the instrument.

For PV HgCdTe change in responsivity after one orbit through the SAA is 0.016% at 833 km and 0.079% at 1350 km. These changes cause insignificant radiometric error. The leakage current of the detector increases after one pass through the SAA which also affects the responsivity of the detector. The change in response due to increased leakage current is 0.14% at 833 km and 0.20% at 1350 km. Both these changes in responsivity produce changes in D* and the dynamic range of the instrument. The magnitude of these changes is such that they produce no perceptable radiometric errors. The transient pulses within the SAA produce 0.004 K and 0.033 K changes in NEΔT for 833 km and 1350 km respectively, again assuming the maximum differential integrated pulse output voltage.

For PV InSb, the general responsivity changes due to nuclear radiation are a function of wavelength. At 5 μm, the responsivity change after one orbit through the SAA is 0.6% (<0.001 K NEΔT) at 833 km and 1.2% (<0.001 K NEΔT) at 1350 km. After 5 years, the cumulative response change is 18.45% (0.007 K NEΔT) at 833 km and 19.0% (0.008 K NEΔT) at 1350 km. At 4 μm, the same calculation as above produces errors of 0.26% (<0.001 K NEΔT) at 833 km and 0.54% (0.001 K NEΔT) at 1350 km. After 5 years the cumulative responsivity change is 8.2% (0.011 K NEΔT) at 833 km and 8.4% (0.011 K NEΔT) at 1350 km. Increased leakage current after one pass through the SAA at both altitudes results in an imperceptable radiometric error.

While radiometric performance errors due to nuclear radiation effects are quite small the dynamic range of signal channel circuits should be designed taking expected changes in detector responsivity into account. Transient events peak during passage through the SAA and are much smaller elsewhere. D* changes due to changes in responsivity would be significant only for the PC HgCdTe detectors after some years in space at the higher 1350 km orbit. These errors are random footprint to footprint and channel to channel, and are reduced in the composite footprint. PC HgCdTe detectors have been found which are radiation resistant (Ref 4-8). Radiation hard detectors were not assumed for this error analysis.

4.9 Microphonics Induced Radiometric Errors

Microphonic induced radiometric error can occur due to vibration of the optical ray bundle with respect to the detector. This can occur where detector responsivity is uniform over the area of the detector if the edge of the optical ray bundle moves across an edge of the detector. Where detector responsivity is nonuniform over the area of

the detector, radiometric error can occur if the detector views the edge of a ray bundle where energy density has been modified by optical aberrations. An additional source of microphonic error could be electromagnetic coupling within the signal channel which is vibration modulated.

In general, detector responsivity varies significantly over the detector area, particularly for PC HgCdTe detectors. Consequently, detectors should be specified to minimize area responsivity variations. The Baseline V detectors are very near a pupil plane so that relative energy density per unit area is nominally independent of scene contrast and pattern. These Baseline V detectors underfill the optical ray bundle to minimize the effects of optical aberrations and optical misalignment. In addition, relative chopper frequency and possible microphonic source frequencies should be selected to keep microphonic source frequencies out of the signal channel passband. This would also minimize microphonic effects due to electromagetic coupling. Minimizing EMI, of course, would also minimize radiometric error due to microphonically modulated electromagnetic coupling.

With careful design, microphonic induced radiometric errors need not be a problem for the AMTS.

4.10 Instrument Calibration

Instrument calibration errors can be encountered both in the on-board calibration procedures which reduce raw instrument data to calibrated radiance values and in prelaunch calibration of the instrument.

4.10.1 On-board Instrument Calibration

The Baseline V instrument design contains provisions for in-orbit spectral monitoring and control. In addition, on-board radiometric reference sources are provided. Spectral monitor and control design features are described in Para 3.1.2 and 3.4.2.2. The radiometric transfer design features are described in Para 3.1.2, 3.1.3, 3.3.1 and 3.3.3.

Conceptually, the spectral monitor and control features would allow self-contained calibration of channel frequency setting, both prelaunch and in-orbit, without use of external calibration equipment. In addition, slit function relative response characteristics could be monitored in orbit, based upon prelaunch calibration data obtained using external calibration equipment.

At the risk of greater radiometric offset errors, measured signal channel radiance values could be determined using only the on-board blackbody calibration sources without resorting to prelaunch calibration using external calibration equipment. Correction of measured image radiance values to remove spatial crosstalk errors, however, requires prelaunch measurement of footprint radiance transfer ratios using external calibration equipment.

4.10.2 Prelaunch Calibration

In the normal course of events, one would expect to perform the following prelaunch calibration functions on the AMTS instrument:

- Spectral channel frequency verification.
- Spectral channel slit function (relative amplitude response) calibration, including wing response.
- Spectral monitor performance verification.
- Absolute radiometric calibration.
- Footprint radiance transfer ratios calibration.
- Instrument polarization sensitivity verification.

Prelaunch spectral channel slit function verification and footprint radiance transfer ratio measurements are considered to be essential. It would be incautious to omit the remaining prelaunch calibrations without a risk assessment of the final detail design based upon:

- Analysis of residual errors using detailed instrument design tolerances and uncertainties.
- System tuning simulation to determine residual tuning errors as a function of the range of uncorrected individual systematic error components.

4.10.3 Instrument Spectral Calibration Radiometric Errors

Channel frequency setting goal instrument requirements are specified in Para 2.3.7 and 2.3.8. Error analysis of the applicable on-board channel frequency calibration capability is treated in Para 4.1.1 and 4.1.2. Prelaunch channel frequency setting verification and calibration using a tunable narrow band frequency source — test monochromator or possibly a tunable laser -- is a relatively straightforward procedure. The precision of this approach is primarily dependent upon the absolute accuracy to which the tunable source frequency is known. Commercial monochromators have a specified frequency accuracy in the range of 1 part in 10^3 to 1 part in 10^4. When used with an external white cell it is believed that calibrating the frequency of a test monochromator with an accuracy of 1 part in 10^5 or better would be possible.

Channel relative intensity vs. frequency response goal instrument requirements are specified in Para 2.3.6 and 2.3.9. These requirements must be interpreted to include a slit function wing response within the bandwidth of the order filter which results in acceptable wing response crosstalk errors (Para 3.1.1.5 and 4.3.3). Uncertainties in the calculation of the extended slit function response plus the inability of the on-board

spectral monitor to determine the characteristic without prelaunch spectral calibration makes prelaunch calibration essential. Direct measurement of the overall instrument slit function response requires a tunable laboratory source having the following characteristics:

- Monochromatic, or very narrow, frequency bandwidth with respect to channel half-power bandwidth.
- Temporally noncoherent, with coherence times near those of the AMTS scene footprints.
- A spatially distributed source must fill the instrument aperture and be imaged upon the inlet slit of the spectrometer. This source image must spatially fill the inlet slit. A high quality test collimator would be required so that its optical aberrations would not significantly affect overall slit function response (Para 3.1.1.5.2).
- Relative amplitude vs. frequency response of the source must be accurately known within the order filter bandwidth.

Calibration of the wings of the slit function would require a relative amplitude measurement resolution of about 10^{-5} (Fig 4-5). A relatively wider source bandwidth could be used to measure wing response outside the slit function truncation bandwidth (Fig 4-3). It is questionable whether the integrated slit function response can be determined to the goal precision specified in Para 2.3.9 by direct measurement of the slit function.

In order to be able to estimate relative shifts in the slit function response in orbit, it would be necessary to measure prelaunch correlated slit function effects for the IR signal channels and for the spectral alignment channels (Para 3.1.2) as a function of spectrometer focus shifts at the image plane. Special provisions to allow such focus shifts during calibration should be made in the design of the spectrometer image plane mounting within the optical bench.

In general, systematic spectral errors result in corresponding effective radiometric errors which are reduced by system tuning (Para 4.1.5). We suspect that the specified goal spectral requirements are unnecessarily severe.

4.10.4 Radiometric Calibration Errors

The Baseline V instrument measures scene radiance via a substitution process. For each footprint during the crosstrack line scan relative radiance of the scene is measured with respect to that of the chopper wheel reference surface. Between successive line scans the relative radiance of hot and cold on-board blackbody calibration targets is also measured with respect to that of the reference surface of the chopper wheel. The radiance of the scene with respect to that of the calibration targets is determined by interpolation (Para 4.2.3). Effective radiance values of the calibration targets are referenced to a secondary standard blackbody during prelaunch instrument calibration. Radiometric error sources associated with this process consist of:

- Absolute error of the laboratory blackbody secondary standard.
- Prelaunch calibration transfer error, from laboratory standard to on-board reference standards.
- Radiometric interpolation error.
- Relative slope error associated with on-board, calibrated, reference standards.
- Radiometric calibration stability.

4.10.4.1 Absolute Error of Laboratory Blackbody Standard

We are told (by C. R. Yokley of the National Bureau of Standards) that regular off-the-shelf blackbodies usually have about 1 percent absolute radiometric error in the AMTS wavelength range. We assume a 1 percent 1σ absolute spectral radiance error for an AMTS laboratory secondary blackbody standard.

4.10.4.2 Prelaunch Radiometric Calibration Transfer Error

A prelaunch radiometric calibration setup must satisfy the following requirements:

- The surface of the secondary standard blackbody must be imaged upon the inlet slit of the instrument in order to avoid slit function pertubation effects and instrument aperture weighting effects which can occur when viewing a defocused source (Para 3.1.1.5 and 4.3.3.1). The secondary standard radiance must fill the instrument aperture; the blackbody image must fill the inlet slit. A relatively high quality test collimator is required.
- Spatial crosstalk effects must be avoided. This is probably best accomplished by holding all surfaces within the extended instrument field of view, which could cause significant crosstalk effects, near the temperature of the blackbody standard. With the exception of the collimator mirror aperture all surfaces should have relatively high emissivity. Note that transmissivity plus emissivity of the collimator is unity. Thermal flux emitted from the surface of the collimator and from the surrounding extended field of view is not collimated at the instrument input nor focused at the inlet slit; consequently, the collimator should have a relatively large aperture, corresponding to an 18 x 18 degree instrument field of view (Para 4.5.9). The relatively small amount of unfocused flux emitted from the surface of the collimator would result in a relatively small crosstalk radiometric error component. BRDF scatter from the collimator mirror surface into and out of a given footprint element is about the same and should introduce no significant radiometric error component from a wide angle collimator.

- The entire test setup, including the instrument, must be in vacuum.

We assume a 0.2 percent 1σ calibration transfer radiance error component from such a test setup.

4.10.4.3 Radiometric Interpolation Error/Radiometric Slope Error

In this paragraph offset errors and slope errors are treated seperately for convenience. In point of fact, one would expect to find offset error components, slope error components, and linearity error components associated with any given radiometric calibration characteristic.

Figure 4-11 illustrates the effects of equal systematic radiometric error offsets for both the hot and cold calibration targets. For this condition, the apparent absolute radiance curve is parallel to the true curve, and all of the offset error component is tunable.

The effects of instrument input/output amplitude linearity errors are discussed in Para 4.7.3.3 and are illustrated in Fig 4-10. The relative input/output amplitude characteristic could be calibrated prelaunch, using the method of Ref 4-7, for example. To the extent that the curvature of the characteristic is stable with time, only the residual linearity calibration error would remain.

Figure 4-12 illustrates the effects of offset calibration error in the cold calibration target only, resulting in a slope error in the apparent calibration characteristic. A portion of the slope error is tunable, and a portion is nontunable. System tuning tends to establish a best straight line parallel to the true slope having an offset error corresponding to the mean slope error for the set of atmospheric profiles used for tuning.

Residual prelaunch calibration errors for nonlinearity and slope result from relative errors in the calibration process. We estimate a peak nonlinearity residual error of 0.1 percent of radiance, and a peak slope residual error of 0.2 percent of radiance. The corresponding nontunable systematic error components would be 0.05 and 0.1 percent of radiance, respectively.

4.10.4.4 Radiometric Calibration Stability

Changes in the signal channel linearity characteristic or in the apparent emissivity of the on-board calibration targets after prelaunch calibration could result in both tunable and nontunable error components. Short term changes in these characteristics would tend to be very small and their effects should be negligible.

We assume that the postcalibration nontunable 1σ error component due to long term drift in signal channel linearity would not exceed 0.05 percent of radiance (Para 4.7.3.3).

Prelaunch radiometric calibration establishes an "apparent emissivity" for the on-board calibration targets. In addition to uncertainties in the laboratory reference blackbody and the prelaunch radiometric calibration transfer process, the apparent emissivity of the on-board targets is a function of:

- True emissivity of calibration targets.
- Knowledge of calibration target temperatures.
- Reflected radiance from the surface of the calibration targets.
- Calibration target defocusing.
- Instrument polarization sensitivity.

Very slow drifts in apparent emissivity will result in tunable errors to the extent that offset error drifts are the same for both the hot and cold targets. The aim of the Baseline V design was to reduce slope errors to a minimum. Mechanically, the calibration targets should be built as a matched pair in all respects except for the degree of thermal insulation. Coating the emissive surfaces should also be done as a matched pair -- the same batch of material applied by the same person at the same time. Calibration target placements at the same distance from the scan mirror and at the same relative absolute angle with respect to nadir insure that calibration target defocusing effects (Para 4.3.3.1) and -- assuming correct grating alignment -- instrument polariziation sensitivity effects are practically the same for both targets.

The radiance reflected from the active surface area of the calibration target viewed by the instrument, as a percent of total radiance, is balanced as much as possible by using deep targets to restrict the external solid angle viewed by this active surface area and by maintaining the calibration target wall temperature the same as that of this active surface area. In addition, the reflective rotating light and thermal shield (Para 3.1.2 and 3.3.1) prevents external radiation from other than the shield/scan mirror assembly from entering the calibration target aperture. The reflected radiance originating from the external source is calculated to be 0.09 percent of calibration target radiance for the cold target and 0.01 percent of radiance for the hot target, corresponding to a peak slope error of 0.08 percent. Most of this external background radiation is from the black sides of the scan mirror light shield aperture. Conceptually, this unbalanced offset error component could be eliminated by operating a zone around the side walls of the hot calibration target at a slightly higher temperature than its active surface area.

Calibration targets would be divided into a number of thermal zones, with each zone having its individual proportionally controlled active heater and temperature sensors (Para 3.3.3). The reflective rotating thermal shield would tend to thermally isolate the active surfaces of the targets except during the very brief calibration dwell interval occuring once in each line scan period. Small temperature variations over the active surface area of the target can result in some uncertainty with

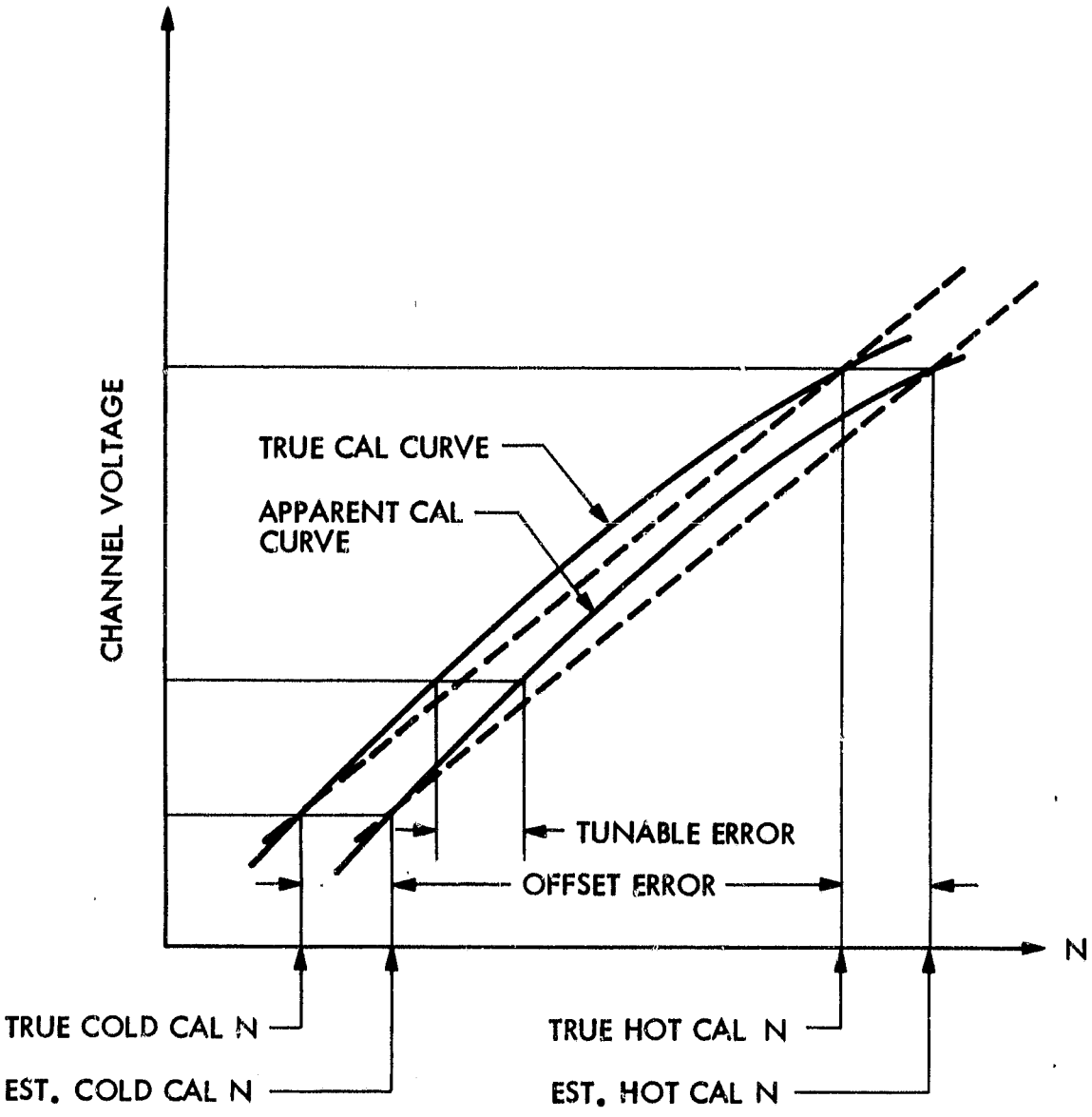

Figure 4-11 Effects of equal calibration target percent offset radiometric errors

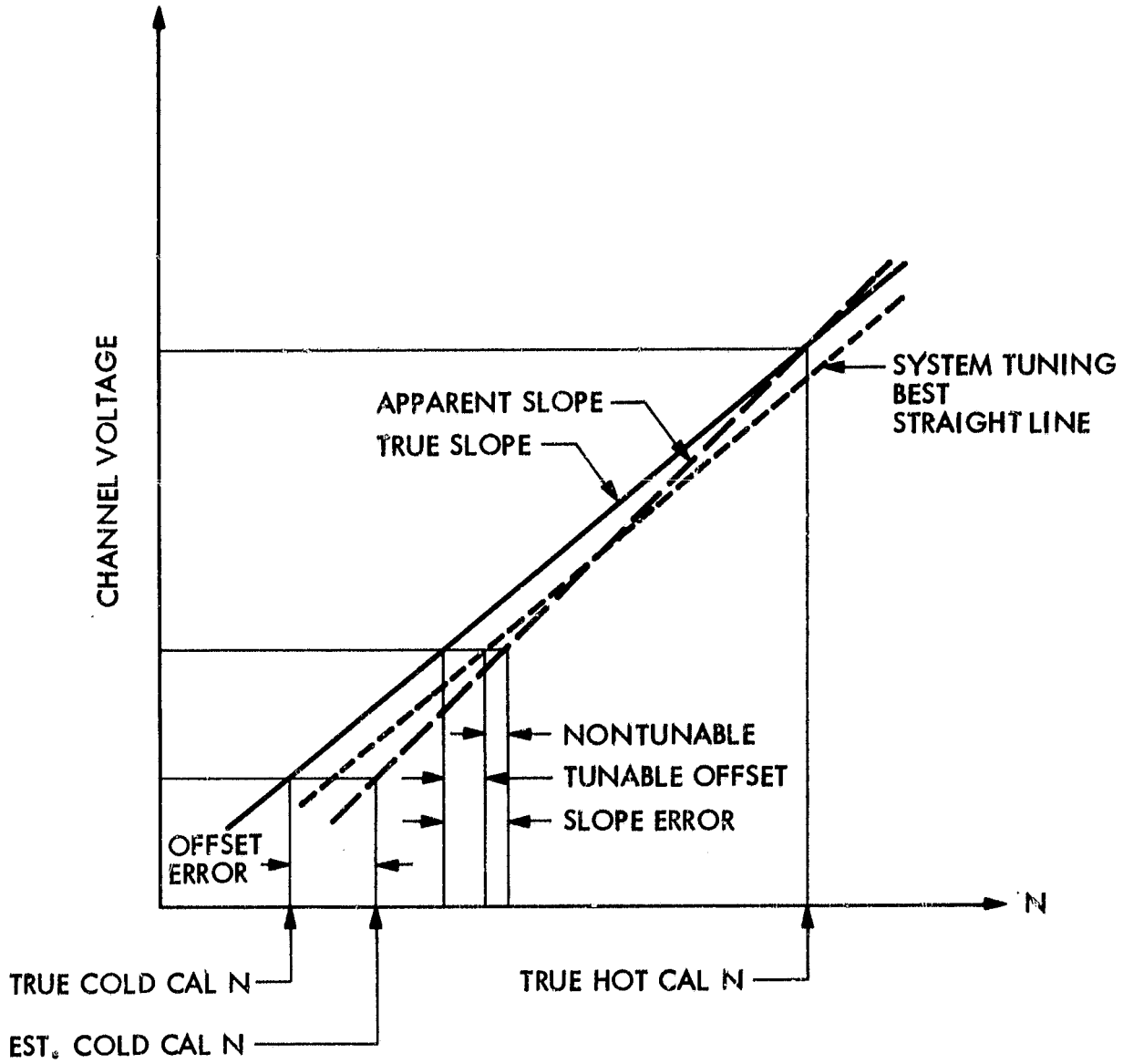

Figure 4-12 Effects of calibration target slope radiometric error

respect to the absolute effective target temperature. With matched targets, however, it should be possible to reduce the slope error due to uncertainty in calibration target temperatures to a very small value.

It is possible that very long term contamination of the calibration target surfaces could change the true emissivity. The rate of change should be such that the effect on calibration within any 30 day interval should be negligible. A long term slope error would occur if the cumulative effect in terms of target emissivity were not the same for the hot and cold targets. Effects of calibration target contamination could probably be reduced if the instrument were subjected to an in-orbit decontamination cycle.

Chopper wheel reference surface temperature would change slowly within the 24.3 second time frame of a single line scan and the 3.67 minute time frame of the calibration target averaging period (Para 3.2.1). It would be possible, though probably unnecessary, to take chopper wheel temperature slope within an individual line scan interval into account when reducing instrument data to calibrated scene radiance values. Radiometric error introduced by chopper wheel temperature variations would be nontunable.

4.10.5 Footprint Radiance Transfer Ratios Calibration

Correction of measured image radiance values to remove spatial crosstalk errors requires high precision prelaunch calibration of radiance transfer ratios of the i-matrix (Para 4.5.9). A rather large aperture test collimator is required, filling an instrument field of view of about 18 x 18 degrees, to correctly calibrate instrument diffraction spatial crosstalk effects (Para 4.10.4.2). An isotropic mirror surface exhibiting low BRDF effects — compared to total instrument scatter — should be used to allow radiance transfer ratio product terms of the collimator and instrument to be dropped from the radiance balance calibration equations. Geometric aberrations introduced by the collimator should be small compared to the instrument inlet slit over the full field of view of the collimator. A relatively hot blackbody calibration target — whose image size at the instrument inlet slit corresponds to an individual pixel element, i.e., a full 10 x 10 km footprint equivalent — should be embedded into a much larger area relatively low temperature background reference target. The area of the cold target should be such that it fills the full field of view corresponding to the i-matrix when the hot target is in any footprint location of the i-matrix. In addition, a means must be provided to effectively remove or mask the hot target from the extended field of view of the instrument. Hot and cold target temperatures must be within the dynamic range of the instrument for all channels to be calibrated (Table 2-9).

Let

$N_{\bar{c}}$ = Measured radiance for footprint (o), hot target not in the i-matrix

$N'_{o(i)}$ = Measured radiance for footprint (o), hot target at position (i)

$N'_{o(o)}$ = Measured radiance for footprint (o), hot target at position (o)

N_B = Background (cold target) radiance

N_H = Hot target radiance

TR_i = Instrument radiance transfer ratio, matrix positions (i/o)

TR_{ic} = Test collimator radiance transfer ratio, matrix positions (i/o)

Neglecting all radiance transfer ratio product terms, in the absence of the hot target

$$N'_o = N_B + \sum_i TR_i N_B - \sum_i TR_i N_B + \sum_i TR_{ic} N_B - \sum_i TR_{ic} N_B$$

which reduces to

$$N'_o = N_B \tag{4.29}$$

With the hot footprint at position (i)

$$N'_{o(i)} = N_B + \sum_i TR_i N_B - TR_i N_B + TR_i N_H - \sum_i TR_i N_B + \sum_i TR_{ic} N_B - TR_{ic} N_B + TR_{ic} N_H - \sum_i TR_{ic} N_B$$

which reduces to

$$N'_{o(i)} = N_B + (N_H - N_B)(TR_i + TR_{ic}) \tag{4.30}$$

Now

$$N_H - N_B = \frac{N'_{o(i)} - N_B}{TR_i + TR_{ic}} \tag{4.31}$$

and

$$TR_i + TR_{ic} = \frac{N'_{O(i)} - N_B}{N_H - N_B} \tag{4.32}$$

With the hot footprint at position (o)

$$N'_{O(o)} = N_H + \sum_i TR_i N_B - \sum_i TR_i N_H + \sum_i TR_{ic} N_B - \sum_i TR_{ic} N_H$$

which reduces to

$$N'_{O(o)} = N_H - \sum_i (TR_i + TR_{ic})(N_H - N_B) \tag{4.33}$$

From Eq 4.29, 4.31, and 4.33

$$N_H = N'_{O(o)} - N'_O + \sum_i N'_{O(i)} \tag{4.34}$$

From Eq 4.32 and 4.34

$$TR_i + TR_{ic} = \frac{N'_{O(i)} - N'_O}{N'_{O(o)} - 2N'_O + \sum_i N'_{O(i)}} \tag{4.35}$$

Significant effects due to scattering by the test collimator can be removed by subtraction from the measured overall transfer ratios of Eq 4.35. This requires a seperate calibration (or calculation) of the BRDF of the test collimator. The relatively large physical aperture of the collimator with respect to that of the instrument effectively assures that diffraction spatial crosstalk effects from the test collimator would be negligible. If instrument scan mirror scatter characteristics were isotropic, instrument transfer ratio calibration for a single scan mirror position is all that would be required; otherwise, the calibration would have to be repeated at a number of instrument scan angles.

The test collimator should probably be a Schwarzschild. This monocentric optic could provide very small geometric aberrations over very wide field angles. A superpolished surface on a glass substrate would provide very low BRDF. A single test collimator could satisfy the requirements for radiance transfer ratios calibration, absolute radiometric calibration (Para 4.10.4.2), and spectral calibration (Para 4.10.3).

The extended radiance transfer target surfaces should be spherical, with a radius of curvature approximately equal to that of the focal length of the collimator. This would result in the same required hot target footprint size, and the same normal incidence angle radiance characteristics for all positions within the i-matrix. Such a target would also match the Schwarzschild image surface. Temperature and emissivity must be uniform over the extended surface of the cold background target. Temperature stability of both target surfaces must be very good over the time period of the overall calibration sequence (Eq 4.35). Actual absolute target temperatures and emissivity are not critical, and knowledge of these parameters is not required. The calibration would have to be performed in a vacuum.

In the limit, accuracy of this method for calibrating radiance transfer ratios would be limited only by slope and nonlinearity errors of the instrument (Para 4.10.4.3). Calibration errors due to the calibration setup could, with effort, be reduced to quite small values. High precision calibration of radiance transfer ratios would require a large, relatively complex calibration setup.

4.10.6 Instrument Polarization Sensitivity Characterization

It is very doubtful that scene polarization could be determined with sufficient accuracy to allow polarization induced radiometric errors to be removed from measured radiance data based upon a knowledge of instrument polarization sensitivity characteristics. Nevertheless, instrument polarization sensitivity characteristics should be determined prior to launch. Instrument polarization sensitivity is primarily a function of the grating polarization sensitivity, although it is modified slightly by polarization upon reflection from mirror surfaces -- particularly from the 45 degree scan mirror (Para 4.4.2). Consequently, overall instrument polarization sensitivity characteristics are a relatively weak function of the across track spatial scan angle.

Instrument polarization sensitivity could be characterized with a relatively small error from grating polarization effects measured at the grating component level. It would also be relatively simple to add a polarizer to the instrument radiometric calibration test setup and characterize overall instrument polarization response as a function of scan angle.

4.10.7 Prelaunch Calibration Summary

Calibration error estimates have, in general, been expressed in terms of percent of radiance. For reference, Table 4-31 lists radiometric errors in terms of NEΔT vs. 1, 3, and 5 percent radiance errors for the Baseline V channel set.

Baseline V prelaunch calibration special equipment requirements to satisfy calibration functions are summarized in Table 4-32.

Baseline V prelaunch calibration to satisfy Baseline V goal instrument requirements would be relatively expensive. At this point, however, we feel that a better understanding of system performance sensitivity in terms of instrument requirements -- particularly in terms of

Table 4-31 Radiometric errors in NEΔT vs percent radiometric error for the Baseline V channel set

CH	υ (cm^{-1})	NEΔT for 1% N_υ error (K)					NEΔT for 3% N_υ error (K)					NEΔT for 5% N_υ error (K)				
		T_{min}	T_{std}	T_{max}	Mean	Std. Dev.	T_{min}	T_{std}	T_{max}	Mean	Std. Dev.	T_{min}	T_{std}	T_{max}	Mean	Std. Dev.
1	606.95	0.59	0.77	0.89			1.76	2.29	2.66			2.92	3.80	4.42		
2	623.20	0.57	0.73	0.85			1.71	2.18	2.55			2.83	3.61	4.23		
3	627.80	0.52	0.60	0.72			1.54	1.80	2.16			2.55	2.99	3.58		
4	634.30	0.48	0.55	0.70			1.43	1.64	2.08			2.37	2.72	3.45		
5	646.60	0.43	0.51	0.64			1.29	1.52	1.92			2.14	2.52	3.19		
6	654.35	0.40	0.50	0.67	0.61	0.15	1.19	1.50	2.01	1.81	0.46	1.97	2.49	3.33	3.00	0.77
7	665.55	0.40	0.51	0.72			1.20	1.52	2.14			1.98	2.52	3.55		
8	666.85	0.39	0.51	0.78			1.16	1.53	2.34			1.92	2.53	3.87		
9	668.15	0.40	0.65	0.90			1.20	1.95	2.68			1.99	3.24	4.44		
10	669.45	0.41	0.55	0.81			1.21	1.65	2.43			2.01	2.74	4.03		
11	875.00	0.42	0.64	0.83			1.25	1.90	2.47			2.08	3.14	4.10		
12	1040.80	0.26	0.44	0.56			0.78	1.30	1.66			1.28	2.15	2.75		
13	1231.60	0.30	0.46	0.60	0.39	0.19	0.89	1.36	1.79	1.17	0.57	1.48	2.26	2.96	1.94	0.95
14	1650.10	0.20	0.24	0.29			0.60	0.72	0.85			1.00	1.18	1.41		
15	1700.30	0.19	0.21	0.26			0.57	0.64	0.79			0.93	1.06	1.30		
16	1839.40	0.20	0.25	0.30			0.60	0.75	0.89			1.00	1.25	1.47		
17	1850.90	0.20	0.27	0.31	0.26	0.06	0.60	0.79	0.93	0.78	0.17	1.00	1.31	1.54	1.30	0.27
18	1930.10	0.19	0.28	0.36			0.57	0.84	1.06			0.95	1.39	1.75		
19	2384.00	0.13	0.15	0.22			0.40	0.46	0.65			0.65	0.75	1.07		
20	2386.10	0.14	0.17	0.26			0.43	0.50	0.77			0.70	0.83	1.28		
21	2388.20	0.15	0.19	0.28			0.45	0.56	0.85			0.75	0.92	1.40		
22	2390.20	0.15	0.20	0.30			0.46	0.61	0.89			0.76	1.01	1.47		
23	2392.35	0.16	0.22	0.31	0.22	0.07	0.46	0.64	0.91	0.64	0.20	0.73	1.06	1.50	1.06	0.34
24	2394.50	0.16	0.22	0.31			0.46	0.66	0.91			0.76	1.08	1.51		
25	2424.00	0.15	0.23	0.31			0.46	0.67	0.93			0.76	1.11	1.54		
26	2505.00	0.15	0.22	0.32			0.44	0.67	0.96			0.73	1.11	1.59		
27	2616.50	0.14	0.22	0.33			0.42	0.65	0.99			0.70	1.07	1.63		
28	2686.00	0.14	0.21	0.34			0.41	0.63	1.02			0.68	1.04	1.68		

Table 4-32 Baseline V prelaunch calibration special equipment requirements[1]

Equipment Requirements	Calibration Functions					
	CH frequency	Slit function	Spectral monitor	Radiometric	Transfer ratios	Polarization
Optical/radiometric						
• Monochromator (variable slit)	X	X	X			
• White cell (wavelength ref.)	X		X			
• Black body (high temp.)	X	X	X			
• Secondary std. blackbody (var. temp)				X		2
• Distributed two temp. wide angle Source (controllable spatial position)					X	
• Collimator (large aperture)	2	X	2	X	X	2
• Wide bandwidth wire grid polarizer						X
Vacuum environmental chamber (large)	X	X	X	X	X	X
Thermal						
• Instrument assembly bench cooler	X	X	X	X	X	X
Instrument direct access functions						
• Test scan control (programmable scan angles; no. dwells)	X	X	X	X	X	X
• Focal plane offset control			X			
• Detector circuit disable	X	X	X	X	X	X

[1]Electronics GSE and data handling/data reduction GSE not included

[2]Could use less elaborate equipment if not required for other tests

in-orbit system tuning capability — could result in relaxation of some instrument performance requirements which, in turn, could result in relaxation of prelaunch calibration requirements.

Prelaunch spectral calibration to verify channel frequency setting is desirable; it is believed essential to verify instrument slit function response. Uncertainties in the effective absolute radiance error without prelaunch radiometric calibration, coupled with uncertainties in the range of absolute systematic errors that could be effectively corrected via in-orbit system tuning make prelaunch calibration of instrument offset error appear desirable. It is possible that the on-board radiometric calibration provisions, without prelaunch calibration, would result in slope error performance equal to or better than that with prelaunch calibration. Uncertainties in achievable instrument input/output amplitude linearity make prelaunch verification of instrument performance appear desirable. Prelaunch calibration to determine spatial radiometric transfer ratios is essential. Measurement of instrument polarization sensitivity could probably be performed at the grating level.

4.11 System Tuning

System tuning (Para 2.1.6) is used in-orbit to reduce the effects of systematic system errors. The residual system tuning error is a function of the following system error components:

- Reference errors
  - Radiosonde calibration errors (Ref 4-13)
  - Sampled field profile prediction errors
    - — Clear column temperature
    - — Surface temperature
- Atmospheric/surface parameter uncertainties
  - Transmissivity values
    - — Clear column, standard atmosphere, at nadir
    - — Effects vs. look angle
    - — Effects of water vapor and other atmospheric constituents
  - Atmospheric emmissivity
  - Surface emissivity
  - Surface reflectivity

C-4

- Instrument systematic errors
  - Knowledge of channel frequency
  - Knowledge of slit function response
  - Radiometric offset
  - Radiometric slope
  - Amplitude linearity
- Other limiting uncertainties
  - "Ideal" profile retrieval precision
  - Equivalent nontunable instrument radiometric error effects

Reference errors and other limiting uncertainties would place a lower limit on the residual system tuning error, even if atmospheric/surface parameter uncertainties and instrument systematic errors did not exist, and regardless of the size of the set of profiles used for tuning.

Tuning can reduce only radiance errors or radiance error equivalents. Since sounder system measurements are nominally linear in terms of radiance but grossly nonlinear in terms of brightness temperature (Fig 4-13, for example), tuning should be performed in terms of atmospheric transmissivity to reduce the effects of atmospheric/surface parameter uncertainties and of instrument equivalent radiometric offset errors. Conceptually, system tuning by adjusting only atmospheric transmissivity values could compensate for instrument mean slope error (Fig 4-12) and mean amplitude linearity error (Fig 4-10).

Baseline V assumes a single pass tuning algorithm which adjusts atmospheric transmissivity values. Conceptually, given a large enough set of tuning profiles, a second pass tuning algorithm in terms of radiance and of the form

$$N_O'' = N_O' + (AN_O' + B) \tag{4.36}$$

where

N_O'' = second pass corrected radiance values

N_O' = first pass corrected radiance values

A and B = channel dependent matrices

could reduce instrument slope error. A second pass algorithm of the form

$$N''_O = N'_O + [A(N'_O)^2 + BN'_O + C] \qquad (4.37)$$

could reduce both instrument slope and amplitude linearity error.

It has been established, by practice and by system simulation, that system tuning is effective. An evaluation of the residual system tuning error and its effect upon overall system performance — and ultimately upon system design trade-offs — was beyond the scope of the Baseline V study effort. The results of Baseline V error analysis, however, indicate the desirability of determining overall system performance sensitivity in terms of the range of system tuning error components. It is conceivable that system tuning performance would allow prelaunch full-up instrument level calibration requirements to be significantly reduced or, for certain system design options, virtually eliminated. It is also conceivable that system tuning performance would impose limits on the overall system performance such that instrument requirements could be relaxed without significant degradation of achievable overall system performance.

4.12 Baseline V Error Summary

Baseline V sounder system single footprint element radiometric errors are summarized in Table 4-33. Estimated mean and standard deviation radiometric error values for all channels and all profiles are listed for each frequency band. Where, based upon a qualitative analysis, error component values were judged to be negligible, the table is marked "N". Data quality flags are shown in the table. Where a reasonable numeric data base was available and we had confidence in the data analysis the data is marked as a "good value". Where a good numeric data base was not available or there were significant uncertainties in the error analysis method, data quality is marked as an "estimate".

Error components are flagged as tunable or nontunable. Nontunable errors are further flagged as:

- Random footprint to footprint — These error components are reduced by a factor of $1/\sqrt{N}$ in the composite footprint, where N is the number of individual footprints summed to form the composite.
- Correlated footprint to footprint — These error components are not reduced in the composite footprint.
- Correlated channel to channel — These relative channel to channel error components can be detrimental to the cloud filtering capability of the system.

Tunable error components are long term systematic errors whose effects upon profile retrieval performance can be reduced by in-orbit system tuning (Para 2.1.6). Some error components can be further divided into tunable and nontunable components. Some nontunable components exhibit

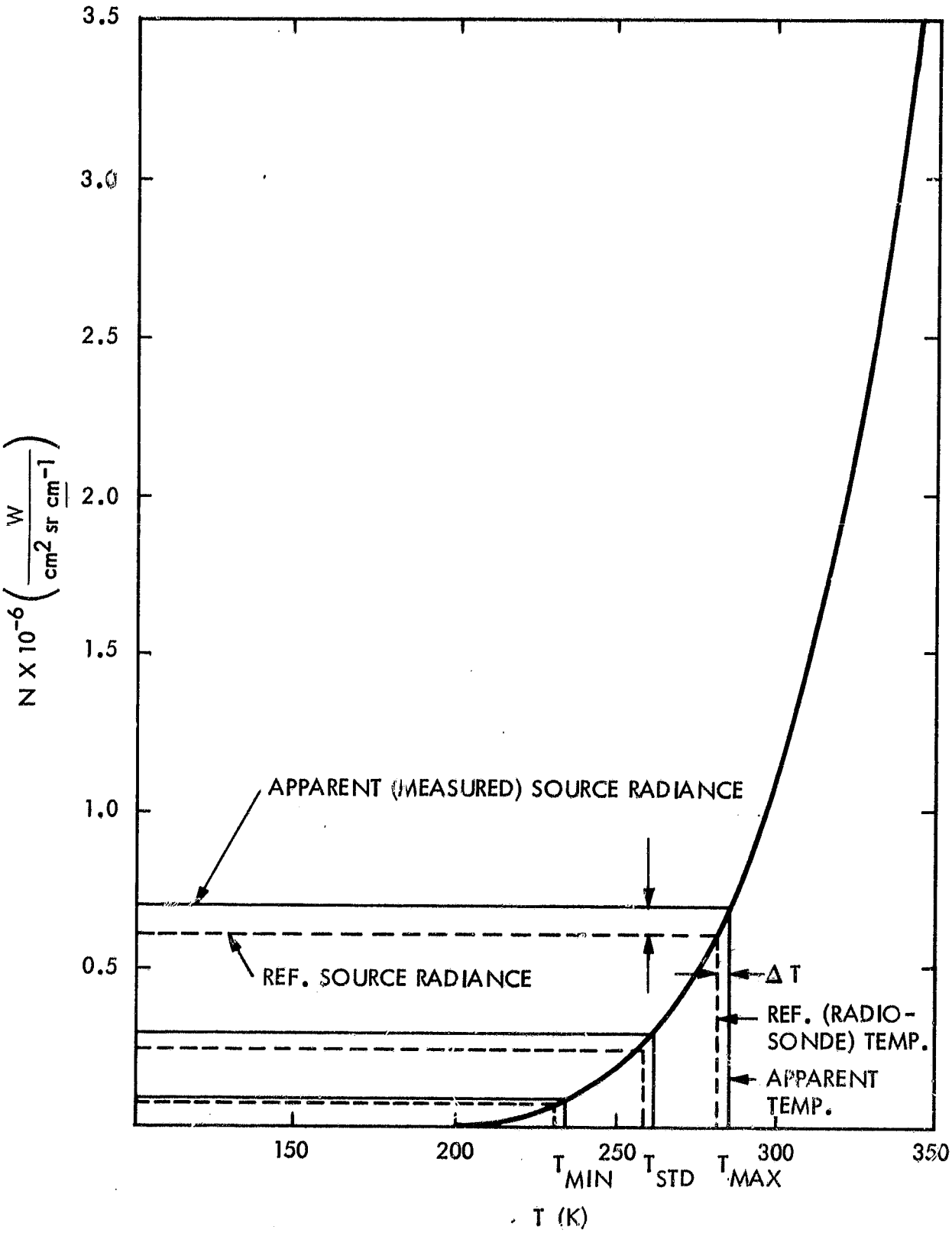

Figure 4-13 Radiance vs brightness temperature (above atmosphere) for channel 16

Table 4-33 Radiometric error summary per footprint element

ERROR SOURCE	NEΔT (1σ) Mean and Standard Deviation (K)								Data Quality		Error Component Type				Reference Paragraph
	Band 1		Band 2		Band 3		Band 4				Nontunable				
	$\bar{x}$	s	$\bar{x}$	s	$\bar{x}$	s	$\bar{x}$	s	Estimate	Good Value	Random FP to FP[1]	Correlated FP to FP[2]	Correlated CH to CH[3]	Tunable[4] Systematic	
1) Spectral Errors															4.1; 4.1.5
Channel frequency setting	N		N		N		N		X			S		L	4.1.1
Knowledge of channel frequency	N		N		N		N		X			S		L	4.1.2
Channel bandwidth	N		N		N		N		X			S		L	4.1.3
Channel intensity vs. frequency response	0.080	0.004	—		—		0.026	0.011	X			S		L	4.1.4
2) Sig. Channel Random Error															4.2; 4.2.4
Det/PA limited sig. Channel noise	0.452	0.134	0.037	0.050	0.016	0.011	0.083	0.124		X	L				4.2.1
Sig. Channel digitization error	0.003	0.001	0.007	0.004	0.004	0.003	0.017	0.027		X	L				4.2.2
Cal. Channel det/PA limited noise	0.142	0.042	0.011	0.016	0.005	0.004	0.028	0.039		X	L				4.2.3
Cal. Channel digitization error	0.001	<0.001	0.002	0.001	0.001	0.001	0.005	0.009		X	L				4.2.3
TOTAL (RSS)	0.471	0.138	0.040	0.053	0.016	0.012	0.089	0.132							
3) Spectral Crosstalk															4.3; 4.3.4
Grating order crosstalk	<0.001	<0.001	<0.001	<0.001	<0.001	<0.001	<0.001	<0.001		X	S	E		E	4.3.1
Grating grass crosstalk	<0.001	<0.001	<0.001	<0.001	<0.001	<0.001	<0.001	<0.001		X	S	E		E	4.3.2
Slit reaction wing response crosstalk	0.073	0.049	—	—	—	—	0.020	0.022	X		S	E		E	4.3.3
TOTAL (RSS)	0.073	0.049	—	—	—	—	0.020	0.022							
4) Polarization Errors															4.4; 4.4.4
Scene polarization	N		N		0.053	0.053	0.160	0.077	X		S	L	L		4.4.1
Scan mirror polarization	0.023	0.007	0.012	0.004	0.003	0.001	0.001	0.001		X	S	L	L		4.4.2
TOTAL (RSS)	0.023	0.007	0.012	0.004	0.053	0.053	0.160	0.077							
5) Spatial Crosstalk															4.5; 4.5.10
Aperture diffraction	<0.001	<0.001	0.001	<0.001	0.095	0.008	2.165	1.568		X	S	L	L		4.5.1
Gas check scatter	<0.001	<0.001	<0.001	<0.001	0.002	0.002	0.138	0.124		X	S	L	L		4.5.2
Scan mirror BRDF	<0.001	<0.001	0.001	0.001	0.004	0.003	0.298	0.268		X	S	L	L		4.5.3
Telescope & collimator mirror BRDF	<0.001	<0.001	<0.001	<0.001	<0.001	<0.001	<0.001	<0.001		X	S	L	L		4.5.4
Corrector lens scatter	<0.001	<0.001	<0.001	<0.001	0.001	0.001	0.140	0.149		X	S	L	L		4.5.5
Grating diffuse scatter	<0.001	<0.001	<0.001	<0.001	<0.001	<0.001	<0.001	<0.001		X	S	L	L		4.5.6
Grating mask scatter	<0.001	<0.001	<0.001	<0.001	<0.001	<0.001	<0.001	<0.001		X	S	L	L		4.5.7
Image plane mask scatter	<0.001	<0.001	<0.001	<0.001	<0.001	<0.001	<0.001	<0.001		X	S	L	L		4.5.8
TOTAL (algebraic)	<0.001	<0.001	0.002	0.001	0.102	0.014	2.741	2.109							
6) Spatial Simultaneity	N		N		N		N		X				S		4.6

7) Chopper & Electronics Errors																				4.7; 4.7.4
Chopper spectral weighting	N		N		N		N		X			E			E					4.7.1
Chopper spatial weighting	0		0		0		0			X										4.7.2
Chopper sync	0.020	0.005	0.013	0.006	0.009	0.002	0.007	0.002	X		E	E								4.7.3.1
Demod. phase	N		N		N		N		X			L								4.7.3.2
Amplitude linearity	0.031	0.010	0.023	0.008	0.012	0.004	0.011	0.004	X			S^7			L^7					4.7.3.3
I/O amplitude stability	N		N		N		N		X		L									4.7.3.4
DC offset stability	N		N		N		N		X			L								4.7.3.5
Hold stability	N		N		N		N		X		L									4.7.3.6
"Last scene" memory	N		N		N		N		X		E	E								4.7.3.7
EMI	N		N		N		N		X		E	E								4.7.3.8
8) Nuclear Radiation	0.034	—	0.004	—	0.004	—	0.011	—		X	L									4.8
9) Microphonics	N		N		N		N		X		E	E								4.9
10) Instrument Calibration																				4.10; 4.10.7
• Instr. Spectral Cal. Rad. Errors																				4.10.3
Channel freq. setting cal.[5]																				
Slit function response cal.[5]																				4.10.4
• Radiometric Cal. Errors										X										4.10.4.1
Absolute blackbody error	0.610	0.150	0.450	0.130	0.240	0.060	0.220	0.070	X						L					4.10.4.2
Prelaunch cal. transfer error	0.121	0.031	0.090	0.026	0.048	0.011	0.043	0.014	X			S^7			L^7					4.10.4.3
Interpolation/slope error	0.061	0.020	0.045	0.015	0.024	0.006	0.022	0.007	X			E			E					4.10.4.4
Rad. cal. stability	N		N		N		N		X		L									4.10.5
Transfer ratio measurement	N		N		N		N		X			L								4.10.6
Polarization sensitivity	N		N		N		N		X											
11) System Tuning[6]																				4.11
Radiosonde cal. errors												L								
Sampled field temperature prediction errors												L								
Transmissivity values												L								
Atmospheric emissivity values												L								
Surface emissivity values												L								
Surface reflectivity values												L								
Knowledge of CH frequency												L								
Knowledge of slit function response												L								
Radiometric offset												L								
Radiometric slope												L								
Amplitude linearity												L								
Ideal profile retrieval precision												L								
Equivalent nontunable instrument radiometric errors												L								

1 NEΔT reduced by $1/\sqrt{N}$ in composite footprint
2 NEΔT not reduced in composite footprint
3 Affects system cloud filtering performance
4 NEΔT reduced by system tuning
5 Radiometric errors are included in Source 1) above
6 System tuning numeric values have not been determined
7 Assumes mean component tunable; ≈ 1/3 mean nontunable

E: Approximately equal error components
L: The larger error component(s)
N: Error value negligible
S: The smaller error component(s)

more than one degree of correlation. Error component type flags in Table 4-33 are largely qualitative. (They are used as guides, however, for making engineering estimates of the relative allocation of error components for the purpose of estimating overall system performance capability.)

System tuning error component numeric values were not determined during this Baseline V study. Neither were residual equivalent nontunable error values remaining after system tuning evaluated as a function of the range of these system tuning systematic error source values. System tuning error components are listed in Table 4-33 for completeness.

Error components listed in Table 4-33 are further categorized and summarized in terms of their effects upon overall system profile retrieval performance in Section 5 of this report.

REFERENCES - SECTION 4

4-1 Dunning, G.J. and M.L. Minder, "Scattering From High Efficiency Diffraction Gratings," Applied Optics, Vol. 19, No. 14, 15 July 1980.

4-2 Hansen, James E. and Larry D. Travis, "Light Scattering in Planetary Atmospheres," Space Science Reviews 16 (1974), pp. 527-610.

4-3 Hansen, James E., "Multiple Scattering of Polarized Light in Planetary Atmospheres. Part II. Sunlight Reflected by Terrestrial Water Clouds," Journal of the Atmospheric Sciences, Vol. 28 (1971), pp. 1400-1426.

4-4 Scheele, S.R., "Scattering from Infrared Transparent Materials," SPIE Proceedings, Vol. 107, 1977.

4-5 Scheele, S.R., "Scattering Characteristics of Mirrors and the Inverse Scattering Problem," Hughes Report, Ref. No. MS 73-82, Nov. 1973.

4-6 Smith, Sheldon M., "Far-Infrared (FIR) Optical Black Bidirectional Reflectance Distribution Function BRDF," SPIE Proceedings, Vol. 257, 1980.

4-7 Saunders, Robert D. and J.B. Shumaker, "Automated Radiometric Linearity Tester," Applied Optics, Vol. 23, No. 20, October 1984.

4-8 Mallon, C.E., B.A. Green, R.E. Leadon, and J.A. Naber, "Radiation Effects in $Hg_{(1-x)}$ Cd_x Te," IEEE Transactions on Nuclear Science, Vol. NS-22, No. 6, Dec. 1975, pp. 2283-88.

4-9 Pickel, J.C., and M.S. Petroff, "Nuclear Radiation Induced Noise in Infrared Detector," IEEE Transactions on Nuclear Science, Vol. NS-22, No. 6, Dec. 1975, pp. 2456-61.

4-10 Kalma, A.H., and R.A. Cesena; "Radiation Testing of Trimetal Infrared Detectors," IEEE Transactions on Nuclear Science, Vol. NS-26, 1979, pp. 4833-39.

4-11 Wilsey, N.D., C.S. Guenzer, B. Molnar, and W.J. Moore, "A Comparison of Fast Neutron Irradiation Effects in Photoconductive and Photovoltaic InSb Infrared Detectors," IEEE Transactions on Nuclear Science, Vol. NS-22, No. 6, Dec. 1975, pp. 2448-55.

4-12 Stassinopoulos, E.G., "The IRAS Environment," NASA-Goddard Space Flight Center Report No. X-601-79-7, Dec. 1978.

4-13 Nestler, M.S., "A Comparative Study of Measurements from Radiosondes, Rocketsondes, and Satellites," NASA Contractor Report 168343, Contract No. NAS 6-2726, GSFC Wallops Flight Facility, April 1983.

SECTION 5

5.0 SYSTEM PERFORMANCE SUMMARY

For this Baseline V study, instrument requirements for an AMTS all IR passive sounder system were defined based upon results of system profile retrieval simulation and upon profile retrieval experience using the physical method with operational HIRS data. Goal instrument requirements were chosen which would minimize instrument error contributions to overall AMTS system performance. The Baseline V instrument concept was developed in an all-out attempt to satisfy these goal instrument requirements.

This section evaluates the extent to which the Baseline V approach -- and certain indicated modifications to the Baseline V approach -- could satisfy the Baseline V goal instrument requirements. It also summarizes significant risk areas and uncertainties associated with the Baseline V concept.

5.1 Estimated Baseline V Performance vs. Goal Instrument Requirements and vs. Estimated AMTS Instrument Performance used for NASA/NOAA Tests

Estimated mean, nontunable, radiometric error component values per composite footprint for each frequency band for those Baseline V error components which were numerically evaluated in Section 4.0 on an individual footprint basis are summarized in Table 5-1(A). By using all individual footprints within a 100 x 100 km earth grid element for a three footprint cloud filtering algorithm, each composite footprint near nadir contains 33 individual footprints and, near the end of scan, 9 individual footprints. For spectral errors and spectral crosstalk errors, numeric values were not calculated for bands 2 and 3. Estimated (interpolated) values for these bands are listed in Table 5-1. Estimated composite footprint nontunable error values in Table 5-1 were derived from Table 4-33 with relative nontunable vs. tunable error contributions and relative random vs. correlated footprint-to-footprint error contributions taken into account. (It was necessary to use some "Kentucky windage" in the process. Residual uncertainties could be removed if the "Data Needs/Performance Questions" listed in Table 6-1 were satisfied.)

Estimated total nontunable composite footprint errors for three AMTS configurations are listed in Table 5-1(B). For comparison, estimated total AMTS nontunable composite footprint errors used for the NASA/NOAA tests are listed in Table 5-1(C) (Ref 2-1; Para 2.2.2; Tables 2-5, 2-6, 2-7; Fig 2-6, 2-7, 2-8).

The AMTS configuration of B.1 (Table 5-1) is the Baseline V configuration. In the presence of sunlit clouds (B.1.a) instrument NEΔT is unsatisfactory in band 4 and marginal in band 3 due to scene polarization induced errors and spatial crosstalk errors. (These error components would be very small for soundings on the nightside of the Earth). For footprints near the end of the crosstrack scan, NEΔT for band 1 is greater than the goal requirement of 0.1 K but close to the values used in the NASA/NOAA tests.

In the presence of sunlit clouds but using image processing to remove spatial crosstalk errors (B.1.b), band 4 NEΔT is still excessive due to scene polarization effects. (Note in Tables 4-15 and 4-33 that the channel to channel correlated relative radiometric errors for both bands 3 and 4 could be quite large, and could still be detrimental to system cloud filtering capability.)

In the absence of clouds, but using image processing (B.1.c) — which may not be necessary under these conditions — NEΔT for bands 2, 3, and 4 is significantly below the goal instrument requirement and approaches the values used for the NASA/NOAA tests. NEΔT in band 1 still exceeds the goal instrument requirement near the end of scan. It is significantly less than the value used for the clear column NASA/NOAA tests and approaches the value used for the cloudy profile NASA/NOAA tests.

The AMTS configuration of B.2 (Table 5-1) uses a higher order multiblaze grating in the instrument to reduce polarization errors and image processing to eliminate spatial crosstalk errors. NEΔT in bands 2, 3, and 4 is significantly less than the goal instrument requirement but greater than the NEΔT values used in the NASA/NOAA tests. NEΔT in band 1 is significantly greater than the goal instrument requirement and is significantly greater than the value used for the cloudy NASA/NOAA tests.

The AMTS configuration of B.3 (Table 5-1) uses the basic Baseline V spectrometer with a longer focal length telescope to give 10 x 10 km spatial resolution at an altitude of 1350 km. By using only nightside soundings — which will give full earth coverage once in each 24 hour period — the effects of scene polarization are eliminated. Image processing, if required, would be used to eliminate residual effects of spatial crosstalk. NEΔT performance for bands 2, 3, and 4 is well below the goal instrument requirement and approaches the NEΔT values used for the NASA/NOAA tests. NEΔT for band 1 is greater than the goal instrument requirement, but is comparable with the values used for the NASA/NOAA tests. (Nightside soundings only from two Baseline V instruments on two satellites near the Baseline V orbit altitude would result in the same performance listed for the clear condition with image processing in line B.1.c of Table 5-1.)

Table 4-33 shows that tunable radiometric errors due to the instrument are less than the goal instrument requirement of 1.0 K ΔT. They are equal to or less than the systematic error components assumed for the NASA/NOAA tests (Para 2.2.2; Table 4-31). Noninstrument system tuning radiometric errors were not numerically evaluated as a part of the Baseline V study effort. If these systematic error components were included, it is believed that nontunable error components would equal or possibly exceed the values used for the NASA/NOAA tests. It is believed that, with system tuning, these systematic radiometric errors do not present a problem in terms of overall system performance capability.

System simulation results, including the NASA/NOAA tests, show a graceful degradation in the accuracy of profile retrievals as a function of instrument radiometric performance degradation. Based upon Baseline V instrument error analysis, the unmodified Baseline V configuration, including image processing, probably would not satisfy the overall performance

goals of the AMTS system. Modification of the sounder system to use primarily nightside sounding data -- either by using a higher orbit altitude or by using two satellites near the current TIROS altitude -- or modification of the basic instrument to reduce its polarization sensitivity in the presence of sunlit clouds would effectively satisfy the profile retrieval performance goals for the AMTS.

5.2 Baseline V Approach - Risk Areas and Uncertainties

A major purpose of the Baseline V instrument study was to determine the limits and constraints imposed upon a passive IR AMTS system by achievable instrument technology. This paragraph addresses what, at one time or another, have been considered to be significant technological risks in terms of achieving estimated instrument performance.

5.2.1 Wing Response Crosstalk

Uncertainties in wing response crosstalk on system performance are discussed in Para 4.3.3.1. This uncertainty contains two issues:

- The obtainable instrument slit function response.
- The residual nontunable system radiometric error component for a given slit function response.

The first issue could be resolved through analysis and computer modeling, supported by laboratory tests using setups based upon a standard laboratory grating monochomator. The second issue could be resolved through computer modeling using a statistical set of atmospheric profiles.

It is believed that this uncertainty does not represent a high risk. It is significant in the sense that, if there is a problem, there is no obvious way to correct it through instrument design or system tradeoffs.

5.2.2 Grating Efficiency and Polarization Sensitivity

Uncertainties in the Baseline V grating efficiency and polarization sensitivity are discussed in Para 3.1.1.2. Resolution of these performance uncertainties for the relatively low order Baseline V grating would require building sample gratings and testing them using AMTS angles. For a higher order multiblaze grating, residual performance uncertainties could be effectively removed through analysis. The buildability of a rather coarse pitch multiblaze grating could be a problem. This uncertainty could be removed through consultation with grating manufacturers and possibly through fabrication and test of a coarse sample grating. (The degree of relative phase control required between blaze sections of a multiblaze grating could be influenced by resolution of the issue of obtainable instrument slit function response (Para 5.2.1).)

5.2.3 Image Plane Complexity

Concern has been expressed that the instrument image plane assembly, discussed in Para 3.3.2, would be both complex and expensive. Relative to a single detector instrument this image plane is complex, but it is not particularly complex compared to some military image plane assemblies. It would be a significant cost factor in overall instrument cost. We believe this study has shown, however, that for an all IR passive sounder capable of improved vertical resolution, image plane complexity is unavoidable, whatever the instrument approach.

Image plane requirements do not represent a technical constraint upon buildability of an AMTS instrument.

5.2.4 Detector Performance

The basis for detector/preamp limited performance estimates is discussed in Para 4.2.1. Detector/preamp limited performance uncertainties are discussed in Para 4.2.1.1. We believe detector/preamp D* values estimated for Baseline V are reasonably conservative. Nevertheless, an element of black art remains in the fabrication of IR detectors. One cannot actually know what D*'s can be achieved for the AMTS until the detectors are actually built for the AMTS. Without too much effort, however, the uncertainty associated with AMTS D* estimates could be reduced by working with detector manufacturers to test the validity of detector/preamp D* models of Appendix F and the parametric equations of Para 3.1.1.4. In effect, known detector material and operational parameters would be used to calculate D* performance for existing detectors under conditions for which existing performance data was measured.

It is believed that detector/preamp performance would not represent a technical constraint upon the feasibility of an AMTS instrument. It is quite possible that effort expended to optimize detector performance within the detector operating environmental constraints imposed by the instrument would prove to be cost effective.

5.2.5 Detector Immersion

Germanium immersion lenses are used for the PC HgCdTe detectors of channels 1 through 11. Failure to immerse these detectors would result in an increase in NEΔT by a factor of ≈ 4. This study has established the necessity for immersion, both to control NEΔT and to control detector bias power thermal loading upon the detector cryostat.

The preferred method of immersion is to use an immersion cement to mount the lens upon the detector and its substrate. Detector manufacturers point out that the basic problems of glue line thickness and thermal compatibility associated with mounting these detectors upon their substrate have been solved. To immerse the AMTS detectors, it would be necessary to find an otherwise suitable cement which has an appropriate index of refraction (> 1.5), is optically transparent at the desired wavelengths, and is

Table 5-1 Summa

		Mean N		
		BAND 1		
		Near Nadir	End Scan	N N
A.	Nontunable error components			
1)	Spectral errors	0.020	0.020	≈0
2)	Signal channel random errors	0.083	0.157	0
3)	Spectral crosstalk	0.037	0.037	≈0
4)	Polarization error	0.023	0.023	0
5)	Spatial crosstalk	<.001	<.001	0
7)	Chopper and electronic errors	0.014	0.015	0
8)	Nuclear radiation (after 5 years in orbit)	0.006	0.011	0
10)	Prelaunch radiometric calibration	0.020	0.020	0
B.	Total (RSS) nontunable errors vs system configuration			
1)	Baseline V Spectrometer; 833 km altitude			
	a) Clouds	0.099	0.166	0
	b) Clouds; image processing	0.099	0.166	0
	c) Clear; image processing	0.099	0.166	0
2)	Higher order multiblaze grating spectrometer; 833 km alt.; clouds; image processing	0.173	0.318	0
3)	Baseline V spectrometer; 1350 km altitude; clouds; nightside soundings; image processing	0.112	0.193	0
C.	Total (RSS) nontunable errors used for NASA/NOAA tests			
1)	Clear (20 x 20 km composite footprint)	0.231		0
2)	Clear (noise doubled)	0.462		0.
3)	Cloudy (30 x 30 km composite footprint)	0.154		0.

[1]For Baseline V; 33 individual footprints per composite near nadir; 9 near end of scan

FOLDOUT FRAME

Table 5-1 Summary estimates of nontunable NEΔT per composite footprint[1]

	Mean NEΔT (K) for All Channels and Profiles							
	BAND 1		BAND 2		BAND 3		BAND 4	
	Near Nadir	End Scan	Near Nadir	End Scan	Near Nadir	End Scan	Near Nadir	End Scan
	0.020	0.020	≈0.016	≈0.016	≈0.011	≈0.011	0.007	0.007
	0.083	0.157	0.007	0.013	0.003	0.005	0.016	0.030
	0.037	0.037	≈0.028	≈0.028	≈0.019	≈0.019	0.010	0.010
	0.023	0.023	0.012	0.012	0.053	0.053	0.160	0.160
	<.001	<.001	0.002	0.002	0.102	0.102	2.741	2.741
	0.014	0.015	0.010	0.011	0.006	0.006	0.005	0.005
	0.006	0.011	0.001	0.001	0.001	0.001	0.002	0.004
	0.020	0.020	0.015	0.015	0.008	0.008	0.007	0.007
	0.099	0.166	0.040	0.042	0.117	0.118	2.746	2.746
	0.099	0.166	0.040	0.042	0.057	0.059	0.162	0.164
	0.099	0.166	0.040	0.042	0.021	0.026	0.025	0.036
lt.;	0.173	0.318	0.040	0.046	0.022	0.027	0.037	0.063
	0.112	0.193	0.040	0.043	0.021	0.026	0.026	0.040
	0.231		0.014		0.022		0.043	
	0.462		0.028		0.043		0.085	
	0.154		0.009		0.014		0.028	

ar nadir;

2 FOLDOUT FRAME

Page intentionally left blank

compatible with the necessary AR coatings used upon the immersion lens and the detector surfaces. Detector manufacturers stated that many candidate materials having an index of refraction in the desired range are available. It would be necessary to test their optical transmissivity at the desired wavelengths until suitable materials are found. Finally, it would be necessary to design the AR coatings for the detector and the mounting surface of the immersion lens to be compatible with the index of refraction of the immersion cement. Another immersion method being used by detector manufacturers consists of mechanically holding the immersion lens in very close contact with the detector surface without use of an immersion interface medium. This would present a more challenging mechanical problem for the AMTS, but it does represent a bail-out if suitable immersion cements could not be found.

It is believed that detector immersion does not represent a technical constraint upon the buildability of an AMTS instrument. The residual uncertainity could be resolved by searching for suitable immersion cements and demonstrating the performance of an immersed interface.

5.2.6 Collimator Corrector Lens

Concerns have been expressed about the availability and cost, optical mounting, and prelaunch environmental protection requirements associated with the Baseline V instrument KBr Bouwers collimator corrector lens.

The following information was obtained in telephone conversations with the Harshaw Chemical Company:

- KBr is the preferred material for the AMTS application. The cesium compounds (CsBr and CsI) grow as one crystal, but the crystal structure changes during cooling. More than one lattice structure is possible; consequently, the crystal axis changes over the volume of the boule with resultant changes in crystal properties.

- Transmissivity of KBr improves as the material is cooled. The thermal expansion coefficient as a function of temperature has been measured as:

Temp. (K)	Thermal Expansion Coefficient
223	42×10^{-6}
253	41×10^{-6}
273	40×10^{-6}
293	41×10^{-6}
313	45×10^{-6}

- Harshaw has furnaces capable of growing a boule of KBr 76 cm (30 in.) in diameter. It is difficult to grow a single crystal of this size, however. The primary concern is with mechanical properties at crystal boundaries. There tends to be 3rd or 4th decimal place variation in mechanical properties between different crystals. Harshaw is comfortable with crystals up to 25 to 30 cm (10 to 12 in.) in diameter.

- The ROM cost for a large single crystal of KBr is $100K for the first run. Subsequent runs would probably cost less, since the material is salvagable. A finished Baseline V ground and polished lens would cost about $150K. The bulk of this cost is in the material. It could take a number of tries to obtain a suitable boule of KBr.

- An alternate approach for building the large AMTS lens is to forge it from a block of KBr using pressure and temperature. Harshaw has the presses and they have forged NaCl up to 51 cm (20 in.) in diameter. They have little experiencce forging KBr. Since both NaCl and KBr are cubic crystals, however, they would expect similarity in forging characteristics. A forged lens would be pressed close to the final dimensions. Some final grinding and finishing would be required to finish the lens. The forged diameter is larger than the diameter of the blank from which the lens is forged — by a factor of about 1.25. Forging results in a material consisting of 20 to 60 μm particle sizes, where each particle is a single crystal. Optical properties of the material are unchanged. Forged material does not have cleavage planes; its mechanical properties are improved. Harshaw is not too concerned about being able to grow blanks suitable for forging.

Collimator spherical aberrations were examined as a function of error in compensator lens radii and index of refraction. These exploratory ray trace results showed that the collimator optical performance is relatively a very slow function of corrector lens fabrication and alignment errors. "Soft" mounting of the KBr lens within the optical bench is feasible.

KBr is successfully used in critical applications in other instruments — ATMOS, for example. Even if the KBr corrector lens could be eliminated, the KBr gas check window would still require environmental protection for the instrument prior to launch.

It is believed that the KBr corrector lens does not represent a technical constraint upon the buildability of an AMTS instrument.

A satisfactory all reflecting collimator configuration for the AMTS grating has not been found. A monocentric Schwarzschild double pass collimator configuration would not allow the grating to be placed at its center of curvature, resulting in a very wide physical aperture with optical aberrations being a function of field angle. The spherical image surfaces of a Schwarzschild collimator used with a Schwarzschild telescope

would be mismatched at the inlet slit, since they curve in opposite directions. A Schwarzschild collimator would be much larger than the Bouwers. The Schwarzschild has an overall length to focal length ratio of about 4.3:1, compared to about 2.1:1 for the Bouwers. Wide field all reflecting aspheric optical systems also tend to be quite large. The optical system described in Ref 5-1, for example, would have an overall length to focal length ratio between 3:1 and 4:1. Since this optical system has a relatively flat field, image surfaces would tend to match at the inlet slit for an instrument using this optical system for both the collimator and the foreoptics telescope. Like the Schwarzschild, this optical system would not allow the grating to be placed in a "natural" pupil plane, which would further limit its useful field angle where used in a double pass collimator configuration. A Schmidt collimator would require that the grating be ruled upon a figured substrate. This is believed to be impractical for a system using a high dispersion eschelle grating. In addition, the degree of grating groove shape control needed for the AMTS favors a micromachined grating (Para 3.1.1.2 and 3.1.4). A multiblaze grating for this application would almost certainly require micromaching. Currently, it is not feasible to micromachine a grating upon a figured substrate.

5.2.7 Radiative Coolers

Concerns have been expressed that the 75 K detector cryostat temperature could not be obtained using passive radiative coolers. Neither the basic physics governing cooler performance nor experience with building and testing large radiative coolers (Ref 3-3) support this viewpoint. The Baseline V detector cooler (Para 3.3.5.2) is conservatively designed, with parasitic heat loads that scale closely to those of the test cooler described in Ref 3-3. JPL is currently testing an advanced radiative cooler design that is much more efficient than this Baseline V design.

For instruments which can be serviced in orbit, various active cooling approaches could be used. Where a suitable orbit is available, however, and where a suitable field of view is available for the cooler, radiative coolers are still probably the preferred approach. It is believed that cooling requirements do not represent a technical constraint upon the buildability of an AMTS instrument.

5.3 System Feasibility Summary and Conclusions - Baseline V Concept

Within the constaints of the AMTS Baseline V study concept, study results lead to high confidence that an all IR sounder system using a grating spectrometer instrument approach is technically feasible. It is believed that the only significant physical uncertainties concern wing response crosstalk (Para 5.2.1) and possibly multiblaze grating buildability (Para 5.2.2). Both of these uncertainties would be relatively easy to resolve. All identified additional uncertainties, including those identified in Para 5.2.3 through 5.2.7, are engineering type problems which are normally resolved at the detail design level; indeed, most of them could only be resolved at the detail design level.

Far more is now known about the Baseline V instrument approach than is normally known when committing to an instrument hardware program. Prior to building an instrument using the Baseline V concept, however, another pass should be made at optimizing the instrument detailed conceptual design, including instrument cost as a consideration. Most of the analytic tools needed for performance optimization are described in this study report. Cost considerations could be made visible by developing a detailed cost model for the Baseline V instrument design. This cost model should show cost slopes for those instrument parameters where cost/performance trade-offs could be considered. The availability of a consistent detailed conceptual design and cost model would provide a powerful tool for evaluating design trade-offs, including possible alternate design approaches.

This Baseline V study has provided insights into options and trade-offs for passive atmospheric sounder systems beyond the constraints of the Baseline V study concept. Some of these considerations are identified in Section 6.0.

REFERENCES - SECTION 5

5-1 Egdall, Ira M., "Manufacture of a Three-Mirror Wide-Field Optical System," Optical Engineering, Vol. 24, No. 2, pp. 285-289, March/April 1985.

SECTION 6

6.0 ADVANCED SYSTEM DESIGN CONSIDERATIONS

IR instrument options and constraints are reasonably well understood. It is now possible to seriously explore advanced sounder system aspects beyond hardware design. The system design selected from the possible options can have an impact on system performance, instrument complexity, the satellite vehicle, ground processing software, and system development costs and risks. Trade-offs necessary to arrive at an acceptable — and reasonably optimal — system design involve manipulation of a multidimensional, interactive set of considerations:

- System performance requirements
  - Hardware
    - -Satellite instrument
    - -Radiosondes/rocketsondes
  - Software/computer capability
- System costs
  - Hardware
  - Software
- Options and constraints
  - Hardware design
  - System design

Some of these considerations are identified in Table 6-1. In the left hand column of this table, considerations are listed in sections A through L as they apply to the corresponding instrument requirement specified in Para 2.3. Questions concerning the corresponding table section data needs are listed in the right hand column of the table. These are items which could be considered; they may or may not offer an advantage in terms of performance or cost. Most of the residual uncertainties in the Baseline V study results could be resolved, however, if the "Data Needs/ Performance Questions" listed in Table 6-1 were satisfied.

While the considerations listed in Table 6-1 retain a Baseline V flavor, the basic principles involved tend to be common to other instrument approaches. Spatial crosstalk, for example, will be present in any instrument approach, and significant scene polarization sensitivity will be present in any instrument using a beam splitter or angled dichroic beam divider as well as in a grating instrument.

The Baseline V performance is near the limit of what is practically obtainable from a grating spectrometer instrument approach providing full earth coverage once in each 24 hour period. Parametric and scaling equations (Eq 3.10 and 3.22) allow Baseline V detector/preamp noise limited performance to be scaled in terms of:

- Earth coverage
  - Altitude
  - Crosstrack scan width
- Spatial resolution
  - Pixel size
  - Composite footprint area/earth coverage grid size
- Instrument parameters
  - Instrument scale
  - Number of elements in the pushbroom array
  - Grating optimization criteria

Table 6-2 is an example of scaling the relative detector noise limited performance of a number of IR sounder system configurations. Footprint configurations considered in Table 6-2 are illustrated in Fig 6-1. Sources and characteristics of radiometric error in addition to detector/preamp error must be considered when evaluating alternate sounder system approaches (Tables 4-33, 5-1). This is particularly important for configurations for which detector/preamp limited performance for the composite footprint is no longer the major error component in limiting overall system performance.

Initial cost factors for instrument cost/performance trade-off studies are best derived from a built-up cost model of a well defined baseline instrument (Para 5.3). The instrument cost model can then evolve as the baseline evolves. Cost factors for a wider range of system issues are probably best derived from a cost model of a total system baseline. Again, this cost model can evolve as the baseline system evolves. For this wider range of system issues, what cost factors are and what cost factors are not to be included in the cost/performance trade-off must be defined.

Whatever the instrument approach, this study illustrates the importance of identifying all sources of system error and of understanding their impact upon overall system performance as a basis for committing to major hardware or software development. The results of this study also suggest that the overriding requirement for the next generation atmospheric sounder will remain high precision radiometry, and that the basic physics of the problem will require a relatively complex instrument.

Table 6-1 Some possible considerations for an advanced sounder system design

Instrument Requirements/System Considerations	Data Needs/Performance Questions
A. In-Orbit Lifetime (Para 2.3.1)	
• If the instrument could be serviced in orbit then:	
- The option of using active coolers or stored cryogens becomes more attractive.	
- The use of doped silicon detectors cooled to near liquid helium temperature could be considered.	
- Use of a continuous low flow rate inert gas purge could be considered for the cold instrument compartments (Para 3.3.6).	
B. Orbit (Para 2.3.2)	
• Below 1350 km only orbit altitudes near that of the 833 km TIROS orbit can provide full earth coverage once in each 24 hour period from a single satellite (Para 3.1.1.6). (The proposed EOS 705 km orbit could provide full earth coverage once in each 36 hour period).	• What are the advantages to end users of sounder data of having contiguous coverage on successive swaths?
• Orbit altitudes > 1350 km (Para 3.1.1.6) would, from a single satellite:	• What is the impact of getting full earth coverage only once in each 36 hour period (EOS orbit) vs once in each 24 hour period (TIROS orbit) vs once in each 24 hour period (nightside only) vs twice in each 24 hour period (once on nightside and once on sunlit side)?

Table 6-1 (continued)

Instrument Requirements/System Considerations	Data Needs/Performance Questions
- Provide contiguous coverage between successive orbit passes. (Contiguous coverage would reduce or eliminate swath edge effects encountered in image processing) (Para 4.5.9).	
- Provide full earth coverage twice in each 24 hour period, once on the sunlit side of earth and once on the nightside.	
- Provide good radiometric data for both the sunlit side and nightside of the earth if the instrument is made insensitive to scene polarization effects (Para 4.4.3) and image processing is used to reduce effects of spatial crosstalk.	
- Provide good radiometric data only for the nightside of the earth for an instrument which is sensitive to scene polarization effects.	
• Two satellites, both at the same altitude in sun synchronous orbits between ≈ 700 km and 1350 km and with their equatorial crossings properly time phased, could provide full earth coverage twice in each 24 hour period, once on the nightside and once on the sunlit side of the earth (Para 3.1.1.6).	
• If active coolers or stored cryogens are feasible (see A above) then orbit times nearer noon or even orbits which are not sun synchronous could be used.	

Table 6-1 (continued)

Instrument Requirements/System Considerations	Data Needs/Performance Questions
C. Spatial Coverage (Para 2.3.3)	
• (For repeat coverage considerations see B above.	
• With a 16 element footprint array, acceptable square pixel sizes are from 10 km to 28 km; with 8 element arrays, from ≈ 20 km to 45 km (Para 3.1.1.1; Fig 3-3).	
• For a given array length, there is no significant composite footprint NEN advantage in making the pixel size larger than the acceptable minimum size. (Minimum pixel size is believed to result in best cloud filtering performance) (Para 3.1.1.1; Fig 3-3).	
• No spatial sampling approach can significantly improve performance or reduce cost for a given performance over that of an imaging system having as high a ratio of footprint area/pixel area as possible (Para 3.1.1.1).	
• It is assumed that clear column profiles are identical in the two or more composite footprints used for cloud filtering, and that observed radiance differences are entirely due to differences in cloud density (Para 2.1.7). As a practical matter, this constraint would place an upper limit on the area that could be used to build the set of composite footprints.	• In terms of cloud filtering performance: - Considering expected worldwide statistical cloud field pattern granularity distributions, what would be the effect vs individual pixel size? - What would be the effect vs variations in clear column profiles over the area of the (two or more) composite footprints? - Considering expected worldwide statistical mesoscale clear column profile distributions, what are the limits on maximum composite footprint area? Is this maximum area greater than or less than the 100 x 100 km grid size requirement for Baseline V? Is this maximum area a function of the scene image such that a machine algorithm could optimize composite footprint generation for each grid area? - What would be the effect upon overall system performance of increasing the earth coverage grid size?

Table 6-1 (continued)

Instrument Requirements/System Considerations	Data Needs/Performance Questions
• Detector noise limited performance is a function of composite footprint area (see J below). This, in turn, may be a function of the earth coverage grid size (100 x 100 km for Baseline V).	
D. Spectral IR Channels (Para 2.3.4)	
• If all channels requiring PC detectors (which have relatively high 1/f noise frequency knees) could be eliminated (Channels 1 through 11) then the optical chopper could be eliminated. This would reduce detector/preamp noise limited NEN by a factor of 2 or greater (Para 3.1.1.3.1). This would probably require use of microwave sounding data to supplement the IR sounding data.	• What would be the impact on overall profile retrieval performance if IR channels 1 through 11 were eliminated and microwave sounding data were used instead? (All sources of error for an IR/microwave sounding system should be evaluated.)
• If alternate spectral lines could be found for selected channels then it would become physically possible to use wider exit slits in the image plane of a grating spectrometer. This would represent lower spectral resolution and lower detector noise limited NEN (see F below).	
E. Equivalent Scene Temperature (Para 2.3.5)	
• The maximum equivalent scene temperature effectively determines the required dynamic range for the instrument. Excessive dynamic range requirements could result in either a larger than necessary digitization radiometric error or a larger than necessary number of bits for the ADC (Para 4.2.2).	• Verify expected equivalent scene temperature limit requirements on a worldwide basis, taking into account solar reflection from clouds and from the surface of the earth.

Table 6-1 (continued)

Instrument Requirements/System Considerations	Data Needs/Performance Questions
F. Channel Bandwidth (Para 2.3.6)	
• Detector noise limited NEN for all channels can be a function of the highest spectral resolution channel (Para 3.1.1.1). If the same field lens F/NO were used for all channels, then minimum NEN would result if all channels had the same spectral resolution and if this spectral resolution were as low as possible. (On the other hand, there may be some cost advantage in maintaining some commonality in the focal lengths of the field lenses, with some degradation in performance.)	• How does profile retrieval performance vary as a function of channel spectral resolution? • What would be the impact on profile retrieval performance of making spectral resolution the same for all channels?
• Slit function wing response crosstalk requirements are a function of the extent to which wing response crosstalk is systematic — and tunable — for all profiles. To the extent that slit function wing response requirements can be relaxed, the grating width could be reduced without compromising this requirement (Para 3.1.1.5.1, 4.3.3, 4.3.3.1).	• What is the actual blackbody wing response characteristic of the instrument, considering temporal coherence effects of the source and the effects of having the detector near a pupil plane? • What are the channel mean and standard deviation values for wing response crosstalk for a statistical distribution of atmospheric profiles?
• If the system could be tuned in orbit for each footprint array element for each channel — rather than for just each channel — then the requirement that the slit function responses for all array elements of a channel be the same within very narrow limits could be relaxed (see K below).	• (See K below for system tuning data needs.)

Table 6-1 (continued)

Instrument Requirements/System Considerations	Data Needs/Performance Questions
G. Absolute Channel Frequency Tolerance (Para 2.3.7) • This requirement imposes constraints upon the design of the optical bench and upon optical alignment requirements (Para 3.3.4, 4.1.1).	• (See H below for data needs.)
H. Knowledge of Channel Frequency (Para 2.3.8) • This requirement either imposes constraints in terms of very long term stability upon the optical bench design and the optical alignment and/or it requires in-orbit monitoring of channel frequency (Para 3.1.2, 4.1.2). It also requires a high precision prelaunch calibration of the instrument (Para 4.10.3).	• What is the effect upon system performance as a function of absolute channel frequency error and as a function of error in the knowledge of channel frequency? • To what extent can the effects of systematic errors in channel frequency setting and knowledge of channel frequency be reduced by system tuning?
I. Knowledge of Channel Intensity vs Frequency Response (Para 2.3.9) • This requirement makes a difficult, high precision, prelaunch instrument calibration procedure necessary (Para 3.1.1.5, 4.1.3, 4.3.3, 4.10.3).	• (See F above for wing response data needs.) • What is the effect upon system performance as a function of error in the knowledge of slit function response: - Within the truncation bandwidth? - Within the wings of the response (outside truncation bandwidth but within order filter bandwidth)?

Table 6-1 (continued)

Instrument Requirements/System Considerations	Data Needs/Performance Questions
	• To what extent can the effect of systematic errors in the knowledge of slit function response be reduced by system tuning?
J. Nontunable Radiometric Error (Para 2.3.10)	
• Detector/preamp limited performance is a function of composite footprint area. NEΔT would be:	• What are the effects upon profile retrieval — with and without clouds — as a function of range and distribution of:
- Decreased if all channels had the same spectral resolution (Para 3.1.1.1).	- Random footprint to footprint nontunable radiometric instrument errors?
- Decreased if spectral resolution were decreased (Para 3.1.1.1).	- Correlated footprint to footprint nontunable radiometric instrument errors?
- Decreased if detector D* were optimized (Para 3.1.1.4, 4.2.1.1).	- Correlated (nontracking) channel to channel nontunable radiometric instrument errors?
- Decreased if larger composite footprint area could be used (Para 3.1.1.1; see C above).	- Nontunable spectral instrument errors — channel frequency and slit function response?
- Decreased if optical chopper could be eliminated (see D above).	- Residual system tuning errors?
- Increased if higher order multiblaze grating is used (Para 3.1.1.2, 4.4.3).	

Table 6-1 (continued)

Instrument Requirements/System Considerations	Data Needs/Performance Questions
- Increased if instrument scale is reduced. Limitations are buildability of a small image plane assembly (Para 3.1.2) and the slit function wing response of a shorter grating (Para 3.1.1.5.1; see F above). - Increased if number of elements in footprint array — and number of detectors — are decreased (see C above). - Increased if composite footprint area must be reduced below values assumed for Baseline V (Para 2.3.3, 3.1.1.1; see C above). - Increased if detectors are placed in the image plane (Para 3.1.3). This would remove most of the uncertainty in instrument slit function wing response (Para 4.3.3.1). On the other hand, PC HgCdTe channels could not be used due to excess detector noise; detector noise would increase for remaining channels due to the configuration NEN penalty (Eq 3.40) and to increased detector background; the system would become sensitive to nonuniform responsivity over the detector area; and the "Stierwalt Effect" in the order filters may become a problem (Ref 3-2). • Other system performance limiting nontunable error sources — which in general are a function of composite footprint area — are: - Spatial crosstalk must be corrected via image processing (Para 4.5.9).	• What are the practical limits upon spatial crosstalk correction as a function of: - The ability to calibrate the instrument prelaunch for radiance transfer ratios? - The precision of the spatial crosstalk correction algorithm as a function of the expected range of scene contrast and pattern? - Expected computer time required for spatial crosstalk correction during data reduction as a function of the statistical distribution of worldwide 24 hour data sets? • Since polarization error is primarily a function of grating polarization sensitivity and scene polarization: - What is the actual grating polarization ratios vs spectral channel frequency? - What is the range and distribution — spatial and temporal — of scene polarization vs. spectral channel frequencies and scene/spacecraft/sun angles due to the scattering of sunlight from clouds and ground haze, considering expected worldwide statistical cloud field distributions?

Table 6-1 (continued)

Instrument Requirements/System Considerations	Data Needs/Performance Questions
- Scene polarization effects — for Baseline V — must be corrected by making the instrument insensitive to scene polarization or by depending upon nightside data only (Para 4.4.3). - Slit function wing response crosstalk (uncertainty) (see F above). - Residual system tuning error (Para 4.11; see K below).	
K. "Tunable" Radiometric Error (Para 2.3.11) • Baseline V assumed that system tuning — by adjusting atmospheric transmissivity values — could only reduce systematic radiometric offset errors, and that slope errors and linearity errors as a function of brightness temperature could not be reduced (Para 2.1.6, 4.11). • Baseline V assumed that it would not be practical to tune the system separately for each footprint array element for each spectral channel (Para 2.3.6). • While it appears at this point to be a bit far-fetched, one could consider: - Considerably reducing the scope of prelaunch instrument calibration if in-orbit system tuning had sufficient range and accurancy.	• What is the range of each of the system tuning systematic error components (Para 4.11)? • What is the residual system tuning error component — when tuning by adjusting only atmospheric transmissivity values — as a function of the range of system tuning error component values? (See H and I above.) • Would it be practical — in terms of the number and quality of tuning data sets required — to employ a second pass in the tuning algorithm to: - Correct for instrument radiometric slope error (Para 4.11)?

Table 6-1 (continued)

Instrument Requirements/System Considerations	Data Needs/Performance Questions
- Deleting in-orbit system tuning and the need for radiosondes, if atmospheric radiance transfer parameter values could be established with sufficient accuracy, if prelaunch instrument calibration accuracy was acceptable, and if long term in-orbit calibration stability could be assured (Para 4.10, 4.11).	- Correct for both instrument slope and amplitude linearity error (Para 4.11)? • Would it be practical — in terms of the number of tuning data sets required and in terms of operational data reduction requirements — to tune the system for each individual spatial array element?
L. Correlated Relative Radiometric Errors (Para 2.3.12)	
• Cloud filtering requirements impose constraints on relative channel to channel radiometric errors, particularly nontracking errors with a high degree of footprint to footprint and channel to channel correlation (such as spatial crosstalk errors and scene polarization errors, for example) (Para 2.1.2, 2.1.3.3, 2.1.7, 4.4, 4.5)	• (See J above for spatial crosstalk and scene polarization data needs.)
• The footprint spatial simultaneity requirement results in a constraint on:	• What is the effect upon profile retrieval performance as a function of the range of footprint simultaneity error when using composite footprints and considering a statistical set of cloud field density distributions?
- Relative foreoptics aberrations (Para 3.1.1.5.2, 4.6).	
- Relative channel to channel inlet slit pre-masking, inlet slit to exit slit optical alignment, and inlet slit to exit slit optical aberrations (Para 3.1.1.5.1, 4.6).	

Table 6-2 Relative detector noise limited composite footprint NEN for some possible AMTS system configurations with respect to that of the Baseline V system configuration

System Configuration	Composite Footprint NEN/NEN$_{(Ref)}$[1] Ratio							
	Altitude							
	1350 km		833 km		705 km		287 km	
	Full scale	0.7 scale	Full scale	0.7 scale	Full scale	0.7 scale	Full scale	0.7 scale
N_{ARRAY} = 16 Pixel = 10 x 10 km IFOV = 10 W x 7 L (km) Step scan	1.18	1.69	1.0①	1.43	0.94	1.34	0.65	0.93
N_{ARRAY} = 8 Pixel = 10 x 10 km IFOV = 5 W x 8.5 L (km) Constant velocity scan	1.40	2.00	1.19	1.70	1.12	1.60	0.78	1.11
Pixel = 10 x 10 km IFOV = 5 W x 8.5 L (km) Step Scan	1.69	2.41	1.49	2.13	1.42	2.03	1.05	1.50
Pixel = 10 x 20 km IFOV = 10 W x 10 L (km) Step scan	1.61	2.29	1.38	1.98	1.30	1.86	0.92	1.32

[1]Baseline V (reference)

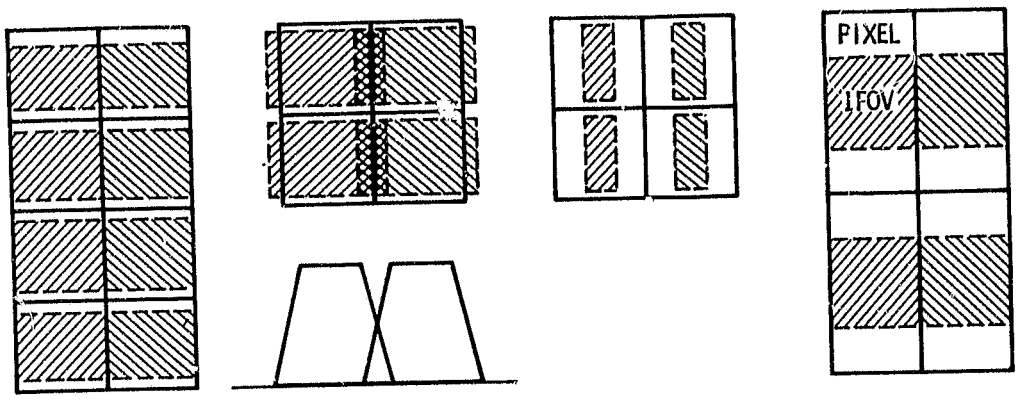

(BASELINE V)			
N_{ARRAY} = 16	8	8	8
PIXEL = 10 X 10 km	10 X 10 km	10 X 10 km	10 X 20 km
IFOV = 10 X 7 km	5 X 8.5 km	5 X 8.5 km	10 X 10 km
S_{Wa}/S_{ha} = 1.43	0.59	0.59	1
T_{SLEW} = 7.179 sec	4.341 sec	7.179 sec	7.179 sec
STEP AND STARE	CONSTANT ANGULAR VELOCITY	STEP AND STARE	STEP AND STARE

Figure 6-1 Some possible AMTS footprint configurations

SECTION 7

7.0 STUDY SUMMARY AND CONCLUSIONS

This report summarizes the results of a study covering the past eight years. The ultimate objective of this study was to develop an advanced infrared atmospheric sounder system which could meet the requirements of the numerical weather prediction models of the 1990s.

This study has defined a passive infrared baseline sounding system and has identified a set of goal instrument performance requirements. A set of parametric equations has been developed which define instrument detector noise limited performance for a grating spectrometer in terms of instrument and system parameters. These equations identify the degrees of freedom available for instrument design. Optical design criteria for a state-of-the-art instrument have been specified, and a detailed conceptual design of a baseline grating spectrometer instrument has been developed in accordance with these criteria. End-to-End system performance has been estimated based upon an error analysis of all identified sources of instrument and system errors.

The study has demonstrated with a high degree of confidence that implementation of a passive infrared Advanced Moisture and Temperature Sounder (AMTS) is technically feasible. This sounder would be capable of substantially increasing the vertical resolution of atmospheric temperature profiles and of improving their accuracy, even in the presence of broken clouds. This Baseline V AMTS study report, within narrow limits, establishes the highest level of performance achievable with a stand-alone infrared sounder using current state-of-the-art technology.

Basic principles established during this study have a high degree of applicability to any high precision passive infrared sounder capable of full global daily coverage. They show that the next generation sounder system will require an instrument capable of: 1) multispectral observations of the atmosphere and surface, 2) relatively high spectral and spatial resolution, and 3) high radiometric precision. It will of necessity require arrays of detectors to simultaneously achieve spectral resolution, spatial coverage, and radiometric precision. In-orbit system tuning, using radiosondes and predictive fields as a reference, will be required to reduce systematic errors. A number of error sources identified for the Baseline V system and the order of magnitude of the resulting system errors are believed predictive of the performance achievable with the next generation passive infrared sounder, whatever the exact system and instrument approach.

While a Baseline V AMTS sounder is technically feasible and would achieve superior performance compared to current operational sounders, it is also, compared to these sounders, a large and complex instrument. The design concepts and parametric equations presented in this report could be used to explore a middle ground between the higher performance and complexity of a Baseline V AMTS and the lower performance and complexity of current sounders.

APPENDIX A

JPL Summary Analysis of P.E. FTS Study Report (Ref 1-1)

JPL Comments on Perkin-Elmer Report #15407

(January 24, 1983)

Two instrument approaches for a LEO AMTS have been examined in some detail. The system performance capability of a multi-channel grating spectrometer baseline design has been examined in-house by JPL. A comprehensive report detailing grating spectrometer options and constraints upon an AMTS system is currently being prepared. No un-resolved problems have been identified for the grating spectrometer approach, which we believe to be the lower risk AMTS instrument approach by some margin. Consequently, the grating spectrometer is currently the baseline instrument being used for the AMTS system study effort.

The feasibility of using a Fourier Transform Spectrometer (FTS) for the AMTS instrument was also investigated. The major portion of the effort was performed by Perkin-Elmer Electro-Optical Division under contract to JPL. The use of a Fourier Transform Spectrometer as the very high precision radiometer required by a LEO AMTS represents a problem of considerable complexity. All issues relating to this problem could not be resolved by this initial study, and additional issues have been identified after the study was completed. Major identified problems and uncertainties which can discriminate against use of the Fourier Transform Spectrometer for this application are listed below. A more detailed comparison of the Fourier Transform Spectrometer approach with the baseline grating spectrometer for the LEO AMTS would require updating and extending this initial FTS study to arrive at a baseline FTS instrument having a maturity comparable with that of the grating spectrometer baseline design. This would be a task of considerable magnitude. Currently, this effort does not appear to be justified.

1) Detectors and Preamplifiers

The requirements for amplitude output vs input linearity for the FTS signal channels are rather severe. We know of no available data base for detector linearity at the level of precision required by the AMTS. The possibility of using multiple calibration targets to calibrate for a non-linear response can be used with a grating instrument, but we do not believe it can be used with the FTS.

The requirement to provide heavy pre-emphasis to correct the amplitude-frequency and phase-frequency distortion introduced by the Band 3 and Band 4 detector/preamps which will remain accurate and stable over the dynamic range, environmental conditions, and lifetime of the AMTS instrument is cause for concern.

The JPL detector D* model predicts values of D* that are less than those listed in the P.E. study report. There is a risk that acceptable signal-to-noise ratios may not be achievable for the Band 4 Channels.

2) Residual Image Motion During a Spectral Scan

The baseline interferometer provides image motion compensation (IMC) only for spacecraft motion with respect to a plane tangent to the

earth's surface at nadir. This does not correct for the following sources of image motion:

- Variation of land surface above mean sea level. (≈0 to 9km)
- Cloud height above mean sea level. (≈0 to 15km)
- Distance below the nadir horizon of the earth's surface as a function of scan angle. This is ≈78km at a scan angle of 48 degrees. If IMC as a function of scan angle were provided, a residual error due to tilt of the local horizon plane with respect to the nadir horizon plane would remain. Over the area of the footprint array, this would amount to about ±33km equivalent altitude error at a scan angle of ±48 degrees for the near and far corner footprint elements of a 10 x 10 array of 10km by 10km footprint elements.
- Earth rotation effects vs latitude and the spacecraft velocity vector. Earth rotational velocity is ≈0.463km/sec at the equator. This represents about a 5 percent area displacement at approximately right angles to the spacecraft velocity vector for a 1 sec dwell time for a 10 x 10km footprint. In theory, IMC could remove these effects at the price of increased instrument complexity.
- Spacecraft altitude and attitude effects. In theory, IMC could remove these effects at the price of instrument complexity provided spacecraft altitude and attitude parameters were available to the instrument from on-board the spacecraft in real time.
- Possible footprint rotation effects due to IMC implementation.

Radiometric errors due to uncompensated image motion would be dependent upon scene contrast and pattern. The magnitude of these errors has not been determined.

3) Scene Polarization

Current analysis indicates that scene polarization due to the scattering of solar radiation from clouds and ground haze can result in significant instrument radiometric error. At this point, we do not know how to eliminate this error in an AMTS FTS instrument.

4) Instrument Line Function Wing Response Spatial Crosstalk.

Perkin-Elmer has shown that on-board data processing of the number of interferograms required by a LEO AMTS using a Fast Fourier Transform (FFT) would result in excessive circuit and power requirements; consequently, the baseline FTS uses a Discreet Fourier Transform (DFT) algorithm. JPL modeling indicates that the proposed DFT algorithm is perfectly orthogonal only at the design wavelength. Unless the interferogram is properly compensated and phased, the DFT algorithm will yield a different radiometric value for other wavelengths within the passband for an interferogram scanned left-to-right vs one scanned right-to-left.

JPL analysis of line function wing response spectral crosstalk for an FTS instrument shows that with proper apodization an FFT algorithm can produce satisfactory performance. Preliminary JPL modeling of the DFT algorithm, however, indicates that excessive wing response crosstalk may be encountered. This issue has not been resolved.

5) Radiometric Calibration

A distributed blackbody calibration source within the near field of an instrument focused at infinity will not be imaged at the normal input image plane. Consequently, the ray bundles within an interferometer cavity corresponding to individual point sources in the calibration source will be grossly decollimated. The radiometric implications of this for an interferometer are not clear. (We have an intuitive feeling that the approach will work, though possibly with some radiometric offset compared to normal scene radiance which, hopefully, could be calibrated out. This case has been examined for a grating spectrometer for the case of a plane wave incident upon the inlet slit of the instrument. Under these conditions a grating spectrometer continues to function, but the physics of its operation are entirely different from the case where an image is formed at its entrance slit.)

There is concern about the radiometric precision of a calibration approach that would only check signal channel responsivity slopes--via space looks--twice per orbit. This places very severe stability requirements upon a system that may exhibit sensitivity to nuclear radiation encountered in its environment, which is sensitive to thermal variation of its internal self-emission and in which detector responsivity is a fast function of detector temperature. There is a further concern about obtaining adequate repeat radiometric calibration of all gain steps in a system using gain switching amplifiers.

6) Interferometer Cavity Alignment

Interferometer cavity alignment shifts can result in both a shift in the center frequency and in the instrument line shape in an imaging interferometer. The proposal to use a plane mirror system with no means of monitoring or correcting cavity alignment after launch means that there would be no in-orbit update of knowledge about these AMTS system critical parameters. It may be very difficult to establish confidence in such an approach. It appears that, at the cost of considerable complexity, cavity alignment could be monitored by using an expanded and diffused helium-neon laser beam within both interferometer cavities in conjunction with 10 x 11 element laser frequency detector arrays. It might even be possible to obtain sufficient alignment data from a much smaller number of laser frequency detectors properly placed within the overall array geometry.

7) Signal Handling Electronics

Conditioning and processing 550 interferograms per second requires far more complex interferometer instrument signal handling electronics

than are required by a grating spectrometer. This results in concerns of prime power requirements, cooling requirements, and in-orbit reliability for the interferometer instrument as compared with the grating spectrometer.

8) Laser Reliability

Mil Handbook 217 Rev. C lists 12000 hr. MTBF for helium-neon lasers. 12000 hr. MTBF means that 67 percent of a group of lasers would have failed after 18 months continuous operation. Hughes Aircraft claims 37000 hr. MTBF with 60 percent confidence, based upon life test on 26 hard seal helium-neon lasers. 37,000 hr. MTBF means that 30 percent of a group of lasers would have failed after 18 months continuous operation. This corresponds to 50 percent after 3 years, and 69 percent after 5 years.

APPENDIX B

Development of Parametric Expansion of $\sqrt{A_d}/A\Omega$

Development of Parametric Expansion of $\sqrt{A_d}/A\Omega$

This appendix develops the parametric expansion of $\sqrt{A_d}/A\Omega$ for three configurations. The first configuration is shown in Fig 3-1; a field lens lies in the image plane and the detector is in a pupil plane. The second configuration is where the detector lies on the image plane (Fig B-2a) and the third configuration is where the ray bundle has been re-imaged onto a detector plane behind the image plane (Fig B-2b). The grating parameters are shown in Fig B-1. The variables used are:

A_d = detector area
A_g = true grating area
$A_{g\alpha}$ = projected grating area with respect to α
$A\Omega$ = area-solid angle product of instrument
α = grating incident angle
β = grating diffraction angle
$\left|\frac{d\alpha}{d\upsilon}\right|, \left|\frac{d\beta}{d\upsilon}\right|$ = grating spectral dispersions
d = distance between the field lens and the exit collimator
D_H = detector height
D_W = detector width
$f_{c\alpha}$ = inlet collimator focal length
$f_{c\beta}$ = exit collimator focal length
f_d = field lens focal length

$$F_d = 1 \Big/ \left[\frac{f_d}{f_{c\beta}^2} (s_{\beta o} - f_{c\beta}) + 1 \right] = \text{detector size factor}$$

$$F_s = \frac{S_{w\beta}}{S_{w\alpha i}} = \text{slit factor}$$

F/NO = field lens F/NO
$G_{H\alpha}$ = projected grating height with respect to α
$G_{W\alpha}$ = projected grating width with respect to α
$G_{H\beta}$ = projected grating height with respect to β
$G_{W\beta}$ = projected grating width with respect to β
H_g = true grating height
L_g = true grating width (normal to grating grooves)
M_d = magnification of field lens
M_β = magnification of exit collimator
M_T = total magnification of field lens and exit collimator
n = index of refraction of a hemispherical immersion lens
υ = optical channel wavenumber
$\Delta\upsilon$ = optical channel bandwidth
$\Delta\upsilon_o$ = optical channel bandwidth when $F_s = 1$
$s_{\alpha o}$ = distance from the inlet collimator to the grating
$s_{\beta i}$ = distance from the exit collimator to the (real or virtual) image of the grating formed by the exit collimator
$s_{\beta o}$ = distance from the exit collimator to the grating

s_{dd} = distance from detector lens to detector (Fig B-2b)
s_{di} = distance from the field lens to the image of the grating formed by the field lens and the exit collimator
s_{do} = distance from the field lens to the image of the grating formed by the exit collimator
s_{ds} = distance from the exit slit to the detector lens (Fig B-2b)
$S_{h\alpha}$ = inlet slit height
$S_{w\alpha}$ = inlet slit width
$S_{h\beta}$ = exit slit height
$S_{w\beta}$ = exit slit width
$S_{w\alpha i}$ = width of the inlet slit image
$S_{w\beta i}$ = width of the exit slit image
θ = grating out-of-plane angle

For the first configuration, it is assumed that the detector is rectangular, that the principle plane of the field lens is in the image plane of the instrument and that the exit slit width is greater than or equal to the image of the inlet slit width. The area of the detector is determined by the size of the image of the aperture stop (i.e., grating) in the detector plane. (The grating dimensions are imaged through the exit collimator and the field lens.)

Treating the lenses one at a time, the total magnification of the two lenses can be written:

$$M_\beta = -\frac{s_{\beta i}}{s_{\beta o}}$$

$$M_d = \frac{s_{di}}{s_{do}}$$

and

$$M_T = M_\beta M_d = -\frac{s_{\beta i}}{s_{\beta o}}\frac{s_{di}}{s_{do}} \qquad (1)$$

The detector dimensions are

$$D_H = G_{H\beta} M_T \qquad (2)$$

$$D_W = G_{W\beta} M_T \qquad (3)$$

Using the thin lens relationship, $\frac{1}{i} = \frac{1}{f} - \frac{1}{o}$, and assuming $s_{\beta o} > f_{c\beta}$ and $s_{\beta i} > d$,

$$\frac{1}{s_{\beta i}} = \frac{1}{f_{c\beta}} - \frac{1}{s_{\beta o}} \qquad (4)$$

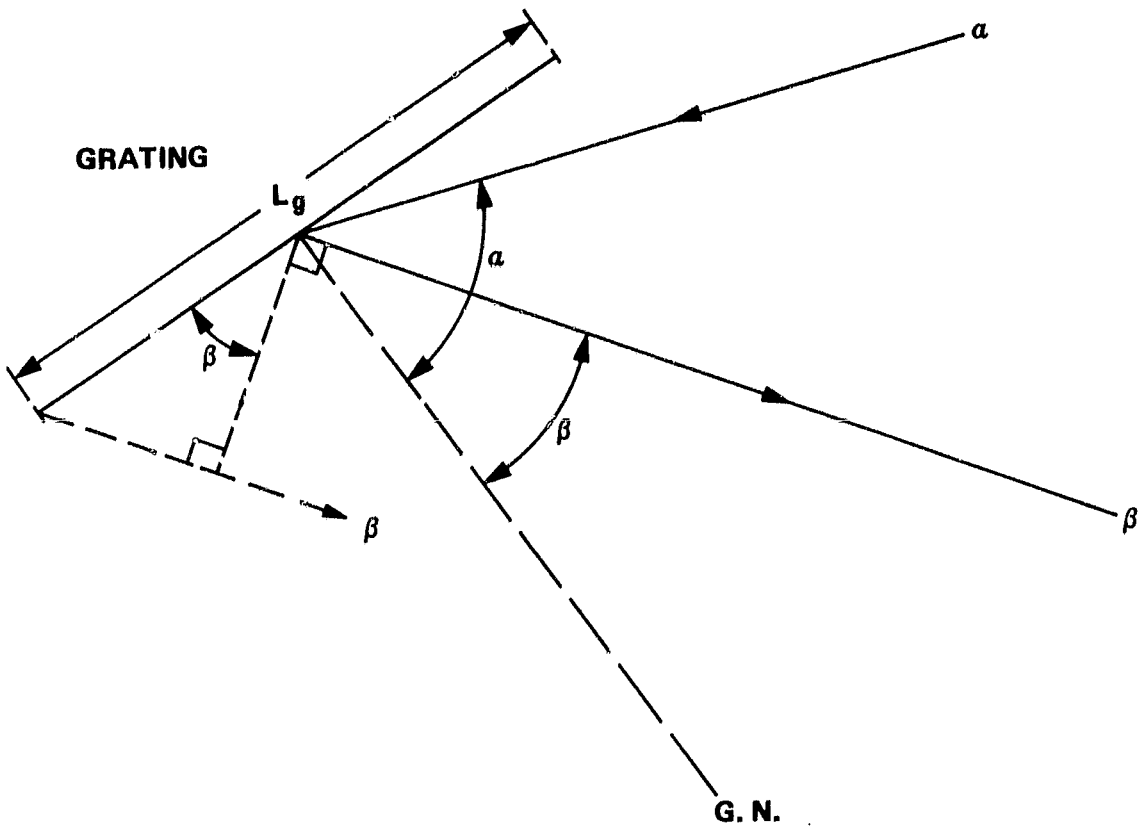

$G_{\omega a} = L_g \cos a$

$G_{\omega \beta} = L_g \cos \beta$

Figure B-1 Projected grating widths

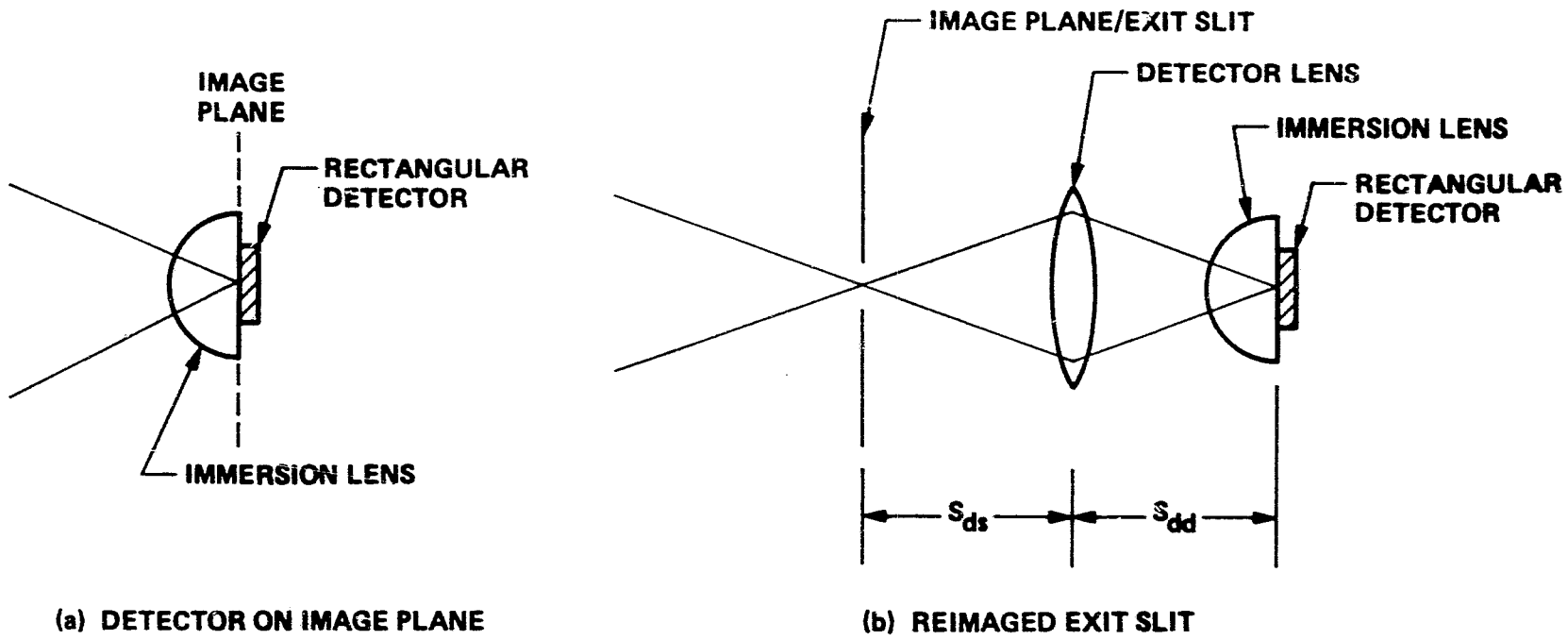

Figure B-2 Alternate image plane configurations

and

$$\frac{1}{s_{di}} = \frac{1}{f_d} + \frac{1}{s_{do}} \tag{5}$$

and

$$s_{do} = s_{\beta i} - d \tag{6}$$

Substituting Eq 6 into Eq 5 with rearrangement yields

$$s_{di} = \frac{f_d\,(s_{\beta i} - d)}{s_{\beta i} - d + f_d} \tag{7}$$

Rearranging Eq 4,

$$s_{\beta i} = \frac{f_{c\beta}\, s_{\beta o}}{s_{\beta o} - f_{c\beta}} \tag{8}$$

Substituting Eq 8 into Eq 7 with rearrangement yields

$$s_{di} = f_d \frac{f_{c\beta}\left[s_{\beta o} - d\left(\frac{s_{\beta o}}{f_{c\beta}} - 1\right)\right]}{f_{c\beta} s_{\beta o} + (s_{\beta o} - f_{c\beta})(f_d - d)} \tag{9}$$

Finally, substituting Eq 6, 8 and 9 into Eq 1,

$$M_T = \frac{f_d}{f_{c\beta}} \left| \frac{-f_{c\beta}^2}{f_{c\beta}\, s_{\beta o} + (f_d - d)\,(s_{\beta o} - f_{c\beta})} \right| \tag{10}$$

Similarly, for the case where $s_{\beta o} < f_{c\beta}$, the thin lens equations are

$$\frac{1}{s_{\beta i}} = \frac{1}{s_{\beta o}} - \frac{1}{f_{c\beta}} \tag{11}$$

$$\frac{1}{s_{di}} = \frac{1}{f_d} - \frac{1}{s_{do}} \tag{12}$$

$$s_{do} = d + s_{\beta i} \tag{13}$$

which combine to give the same M_T as Eq 10.

Defining a detector size factor,

$$F_d = \frac{f_{c\beta}^2}{f_{c\beta}\, s_{\beta o} + (f_d - d)(s_{\beta o} - f_{c\beta})} \tag{14}$$

For the configuration of Fig 3-1,

$$d = f_{c\beta}$$

$$F_d = \frac{1}{\frac{f_d}{f_{c\beta}^2}\,(s_{\beta o} - f_{c\beta}) + 1} \tag{15}$$

Under normal conditions this factor, F_d, is very close to unity.

Consequently,

$$M_T = \frac{f_d}{f_{c\beta}} \tag{16}$$

and

$$D_H = \frac{G_{H\beta}\, f_d}{f_{c\beta}} \tag{17}$$

$$D_W = \frac{G_{W\beta}\, f_d}{f_{c\beta}} \tag{18}$$

If the detector is immersed with a hemispherical immersion lens,

$$D_H = \frac{G_{H\beta}\, f_d}{n\, f_{c\beta}} \tag{19}$$

$$D_W = \frac{G_{W\beta}\, f_d}{n\, f_{c\beta}} \tag{20}$$

Inspection of Fig B-1 shows that

$$G_{W\alpha} = \frac{\cos\,\alpha}{\cos\,\beta}\, G_{W\beta} \tag{21}$$

and

$$G_{H\beta} \approx G_{H\alpha} \tag{22}$$

So,

$$D_W = G_{W\alpha} \left(\frac{f_d}{f_{c\beta}\, n}\right) \left(\frac{\cos\beta}{\cos\alpha}\right) \tag{23}$$

Therefore, detector area from Eq 19, 22, and 23 is

$$A_d = G_{W\alpha}\, G_{H\alpha} \left(\frac{f_d}{f_{c\beta}\, n}\right)^2 \left(\frac{\cos\beta}{\cos\alpha}\right) \tag{24}$$

Assuming a rectangular detector following a field lens whose principle plane is in the image plane and whose effective diameter is the diagonal of the exit slit aperture, the field lens focal length can be expressed:

$$f_d = F/NO \sqrt{S_{h\beta}^2 + S_{w\beta}^2} \tag{25}$$

When the exit slit width is greater than or equal to the inlet slit width image, a slit factor, F_s, may be defined

$$F_s = \frac{S_{w\beta}}{S_{w\alpha i}} = \frac{S_{w\beta i}}{S_{w\alpha}} = \frac{\Delta\upsilon}{\Delta\upsilon_o} > 1 \tag{26}$$

where

$$S_{w\alpha} = \Delta\upsilon_o \left|\frac{d\alpha}{d\upsilon}\right| f_{c\alpha} \tag{27}$$

$$S_{w\beta} = \Delta\upsilon \left|\frac{d\beta}{d\upsilon}\right| f_{c\beta} \tag{28}$$

$$S_{w\alpha i} = \Delta\upsilon_o \left|\frac{d\beta}{d\upsilon}\right| f_{c\beta} \tag{29}$$

$$S_{w\beta i} = \Delta\upsilon \left|\frac{d\alpha}{d\upsilon}\right| f_{c\alpha} \tag{30}$$

By inspection of Fig 3-1,

$$S_{h\beta} = \frac{f_{c\beta}}{f_{c\alpha}} S_{h\alpha} \tag{31}$$

The spectral dispersions are

$$\left|\frac{d\alpha}{d\upsilon}\right| = \frac{1}{\upsilon} \cdot \frac{\sin\alpha + \sin\beta}{\cos\alpha} \tag{32}$$

$$\left|\frac{d\beta}{d\upsilon}\right| = \frac{1}{\upsilon} \cdot \frac{\sin\alpha + \sin\beta}{\cos\beta} \tag{33}$$

Substituting Eq 31 and 26 into Eq 25 yields

$$f_d = F/NO \sqrt{\left(\frac{f_{c\beta}}{f_{c\alpha}} S_{h\alpha}\right)^2 + (S_{w\alpha i} F_s)^2} \tag{34}$$

Writing Eq 29 in terms of $S_{w\alpha}$ (using Eq 27),

$$S_{w\alpha i} = \frac{\cos\alpha}{\cos\beta} \frac{f_{c\beta}}{f_{c\alpha}} S_{w\alpha} \tag{35}$$

Now Eq 34 can be written

$$f_d = F/NO \sqrt{\left(\frac{f_{c\beta}}{f_{c\alpha}} S_{h\alpha}\right)^2 + \left(\frac{\cos\alpha}{\cos\beta} \frac{f_{c\beta}}{f_{c\alpha}} F_s S_{w\alpha}\right)^2} \tag{36}$$

Substituting Eq. 36 into 24 with rearrangement gives

$$A_d = G_{W\alpha} G_{H\alpha} \frac{S_{h\alpha}^2}{f_{c\alpha}^2} \frac{F/NO^2}{n^2} \left[\frac{\cos\beta}{\cos\alpha} + \frac{\cos\alpha}{\cos\beta}\left(\frac{S_{w\alpha}}{S_{h\alpha}} F_s\right)^2\right] \tag{37}$$

The area-solid angle product is

$$A\Omega = \frac{A_{g\alpha} S_{h\alpha} S_{w\alpha}}{f_{c\alpha}^2} \tag{38}$$

Combining Eq 37 and 38 into $\sqrt{A_d}/A\Omega$,

$$\frac{\sqrt{A_d}}{A\Omega} = \frac{\sqrt{G_{W\alpha} G_{H\alpha}}}{A_{g\alpha}} \frac{f_{c\alpha}}{S_{w\alpha}} \frac{F/NO}{n} \sqrt{\frac{\cos\beta}{\cos\alpha} + \frac{\cos\alpha}{\cos\beta}\left(\frac{S_{w\alpha}}{S_{h\alpha}} F_s\right)^2} \tag{39}$$

Substituting Eq 30 into Eq 26 and rearranging, using Eq 26 and 32, gives

$$\frac{f_{c\alpha}}{S_{w\alpha}} = \frac{F_s}{\Delta\upsilon \left|\frac{d\alpha}{d\upsilon}\right|} = \frac{\upsilon}{\Delta\upsilon_o} \frac{\cos\alpha}{\sin\alpha + \sin\beta} \tag{40}$$

and

$$\frac{\sqrt{A_d}}{A\Omega} = \frac{\sqrt{G_{W\alpha}\, G_{H\alpha}}}{A_{g\alpha}} \cdot \frac{\cos\alpha}{\sin\alpha + \sin\beta} \sqrt{\frac{\cos\beta}{\cos\alpha} + \frac{\cos\alpha}{\cos\beta}\left(\frac{S_{w\alpha}}{S_{h\alpha}} F_s\right)^2} \cdot \frac{F/NO}{n} \cdot \frac{\upsilon}{\Delta\upsilon_o} \tag{41}$$

In terms of true grating dimensions (on the surface of the grating)

$$G_{W\alpha} = L_g \cos\alpha \tag{42}$$

$$G_{H\alpha} = H_g \cos\theta \tag{43}$$

$$A_{g\alpha} = A_g \cos\alpha \cos\theta \tag{44}$$

$$\frac{\sqrt{A_d}}{A\Omega} = \frac{\sqrt{H_g\, L_g}}{A_g} \cdot \frac{1}{\sin\alpha + \sin\beta} \sqrt{\frac{\cos\alpha}{\cos\theta}\left[\frac{\cos\beta}{\cos\alpha} + \frac{\cos\alpha}{\cos\beta}\left(\frac{S_{w\alpha}}{S_{h\alpha}} F_s\right)^2\right]} \cdot \frac{F/NO}{n} \cdot \frac{\upsilon}{\Delta\upsilon_o} \tag{45}$$

For the second configuration (Fig B-2a) a rectangular detector lies on the image plane. The detector width is greater than or equal to the image of the inlet slit width.

The detector area is

$$A_d = S_{h\beta}\, S_{w\beta} \tag{46}$$

Writing Eq 28 in terms of $S_{w\beta i}$,

$$S_{w\beta} = \frac{\cos\alpha}{\cos\beta} \frac{f_{c\beta}}{f_{c\alpha}} S_{w\beta i} \tag{47}$$

Substituting Eq 30 into Eq 47,

$$S_{w\beta} = \frac{\cos\alpha}{\cos\beta} f_{c\beta}\, \Delta\upsilon \left|\frac{d\alpha}{d\upsilon}\right| \tag{48}$$

Substituting Eq 31 and 48 into Eq 46,

$$A_d = S_{h\alpha} \frac{f_{c\beta}^2}{f_{c\alpha}} \Delta\upsilon \left|\frac{d\alpha}{d\upsilon}\right| \frac{\cos \alpha}{\cos \beta} \tag{49}$$

The area-solid angle product is

$$A\Omega = S_{h\alpha} S_{w\alpha} \frac{A_{g\alpha}}{f_{c\alpha}^2} \tag{50}$$

Using Eq 26

$$A\Omega = \frac{S_{h\alpha} S_{w\beta i}}{F_s} \frac{A_{g\alpha}}{f_{c\alpha}^2} \tag{51}$$

Using Eq 30,

$$A\Omega = S_{h\alpha} \frac{\Delta\upsilon \left|\frac{d\alpha}{d\upsilon}\right|}{F_s} \frac{A_{g\alpha}}{f_{c\alpha}} \tag{52}$$

Using Eq 26 and 27 to write $f_{c\alpha}$ in terms of $S_{w\alpha}$,

$$f_{c\alpha} = \frac{F_s S_{w\alpha}}{\Delta\upsilon \left|\frac{d\alpha}{d\upsilon}\right|} \tag{53}$$

Substituting Eq 53 into Eq 49 and 52 gives

$$A_d = \frac{S_{h\alpha}}{S_{w\alpha}} \frac{f_{c\beta}^2}{F_s} \Delta\upsilon^2 \left|\frac{d\alpha}{d\upsilon}\right|^2 \frac{\cos \alpha}{\cos \beta} \tag{54}$$

and

$$A\Omega = \frac{S_{h\alpha}}{S_{w\alpha}} \left(\frac{\Delta\upsilon \left|\frac{d\alpha}{d\upsilon}\right|}{F_s} \right)^2 A_{g\alpha} \tag{55}$$

Therefore, $\sqrt{A_d}/A\Omega$ (including the effect of a hemispheric immersion lens) is

$$\frac{\sqrt{A_d}}{A\Omega} = \frac{1}{A_{g\alpha}} \frac{f_{c\beta}}{n} \frac{F_s}{\Delta\upsilon \left| \frac{d\alpha}{d\upsilon} \right|} \sqrt{\frac{\cos\alpha}{\cos\beta} \frac{S_{w\alpha}}{S_{h\alpha}} F_s} \tag{56}$$

or, using Eq 26 and 32 and rearranging,

$$\frac{\sqrt{A_d}}{A\Omega} = \frac{f_{c\beta}}{A_{g\alpha}} \cdot \frac{\cos\alpha}{\sin\alpha + \sin\beta} \sqrt{\frac{\cos\alpha}{\cos\beta} \frac{S_{w\alpha}}{S_{h\alpha}} F_s} \cdot \frac{1}{n} \cdot \frac{\nu}{\Delta\nu_o} \tag{57}$$

Figure B-2b shows a generalized grating spectrometer that refocuses the ray bundle onto a detector plane behind the image plane. For this configuration it is assumed that the detector is rectangular and that the exit slit width is greater than or equal to the image of the inlet slit width.

By inspection,

$$D_H = \frac{s_{dd}}{s_{ds}} S_{h\beta} \tag{58}$$

and

$$D_W = \frac{s_{dd}}{s_{ds}} S_{w\beta} \tag{59}$$

so the detector area is

$$A_d = \left(\frac{s_{dd}}{s_{ds}} \right)^2 S_{h\beta} \; S_{w\beta} \tag{60}$$

Substituting Eq 31 and 4[illegible],

$$A_d = \left(\frac{s_{dd}}{s_{ds}} \right)^2 S_{h\alpha} \frac{f_{c\beta}^2}{f_{c\alpha}} \Delta\upsilon \left| \frac{d\alpha}{d\upsilon} \right| \frac{\cos\alpha}{\cos\beta} \tag{61}$$

The area-solid angle product is

$$A\Omega = \frac{S_{h\alpha}\, S_{w\alpha}\, A_{g\alpha}}{f_{c\alpha}^{\,2}} \tag{62}$$

Using the same development as Eq 50 to 52,

$$A\Omega = \frac{A_{g\alpha}}{f_{c\alpha}}\, S_{h\alpha}\, \frac{\Delta\upsilon}{F_s}\, \left|\frac{d\alpha}{d\upsilon}\right| \tag{63}$$

Therefore, $\sqrt{A_d}/A\Omega$ is

$$\frac{\sqrt{A_d}}{A\Omega} = \frac{s_{dd}}{s_{ds}}\, \frac{f_{c\beta}}{A_{g\alpha}}\, F_s \sqrt{\frac{f_{c\alpha}}{S_{h\alpha}}\, \frac{1}{\Delta\upsilon \left|\frac{d\alpha}{d\upsilon}\right|}\, \frac{\cos\alpha}{\cos\beta}} \tag{64}$$

Substituting Eq 53 (and including the effect of a hemispherical immersion lens)

$$\frac{\sqrt{A_d}}{A\Omega} = \frac{s_{dd}}{s_{ds}}\, \frac{f_{c\beta}}{A_{g\alpha}}\, \frac{F_s}{\Delta\nu \left|\frac{d\alpha}{d\nu}\right|} \sqrt{\frac{\cos\alpha}{\cos\beta}\, \frac{s_{w\alpha}}{s_{h\alpha}}\, F_s\, \frac{1}{n}} \tag{65}$$

or, using Eq 26 and 32 and rearranging,

$$\frac{\sqrt{A_d}}{A\Omega} = \frac{s_{dd}}{s_{ds}} \cdot \frac{f_{c\beta}}{A_{g\alpha}} \cdot \frac{\cos\alpha}{\sin\alpha + \sin\beta} \sqrt{\frac{\cos\alpha}{\cos\beta}\, \frac{s_{w\alpha}}{s_{h\alpha}}\, F_s} \cdot \frac{1}{n} \cdot \frac{\nu}{\Delta\nu_o} \tag{66}$$

APPENDIX C

A Dual-Vector Grating Efficiency Model (Ref 3-1)

A dual-vector grating efficiency model

Nathan L. Evans and Valerie G. Wright

Jet Propulsion Laboratory, California Institute of Technology,
4800 Oak Grove Drive, Pasadena, California 91109

Abstract

A scalar grating efficiency model is developed primarily for use with Echelle gratings when the incident beam does not directly illuminate the antiblaze facet. Relative field intensities are calculated as the square of the vector sum of the direct diffraction field from the blaze facet and the reflected diffraction field from the antiblaze facet. Relative grating efficiency is the ratio of the relative intensity in the desired order to the summation of the relative intensities in all possible orders. Calculated efficiencies are compared with measured efficiencies for Echelle gratings.

Introduction

We have shown that there is a class of grating instruments for which there is a throughput advantage in using Echelle gratings in relatively low orders.[1] A scalar model for calculating relative grating efficiency has been developed for use in first-order design of the Advanced Moisture and Temperature Sounder (AMTS) instrument.[1,2] This instrument design uses a fixed R2 Echelle grating at an incident angle of 71° so that the antiblaze facets are not directly illuminated by the incident wave. Desired diffraction angles lie between 45° and 65° in the 3rd through the 13th orders.

Relative grating efficiency at a given wavelength can be defined as the ratio between the relative grating intensity in the desired order to the sum of the relative intensities in all possible grating orders.[3] An efficiency model, which considers only the direct diffracted wave from the blaze facet (β in Figure 1), results in calculated efficiencies for Echelle gratings that are significantly higher than measured efficiencies under near-Littrow conditions. The blaze facet diffracted field reflected from the antiblaze facet will also satisfy the grating equation when $\beta' = \beta$ (refer to Figure 1). A dual-vector efficiency model in which relative intensities are based upon the vector sum of the relative amplitude of the direct, β, and reflected, β', amplitudes results in calculated efficiencies that are a function of both the blaze and antiblaze grating angles. This model results in calculated efficiencies in the scalar region that are closer to measured efficiencies for plausible values of blaze and antiblaze angles.

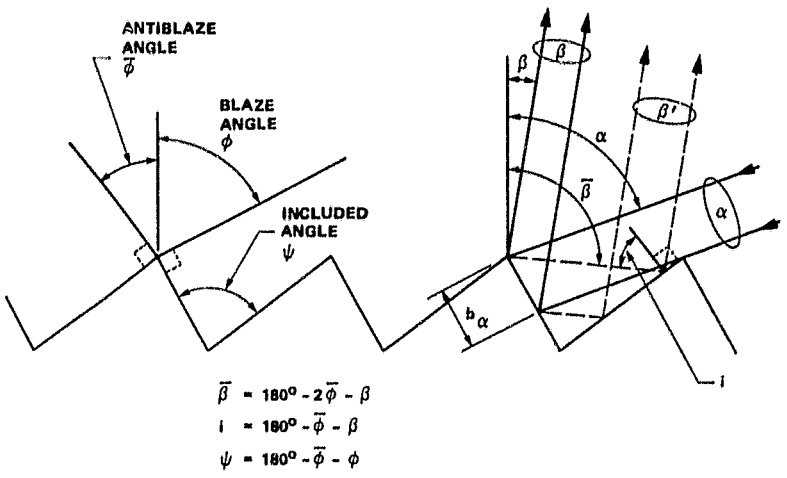

Figure 1. Grating angles.

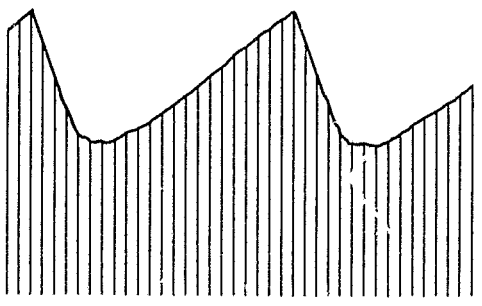

Figure 2. Typical groove shape for a (negative) replica of an embossed grating with a pitch of ≈32 g/mm.

The mathematical model

This model is valid for the condition that $\alpha \geq (90° - \bar{\phi})$; i.e., when the antiblaze facet not directly illuminated by the wave incident upon the grating.

Considering direct scalar diffraction from the blaze facets

$$\frac{I}{I_o} = \text{sinc}^2 \left\{ \frac{\pi b}{\lambda} \left[\sin (\alpha_o - \phi) + \sin (\beta_o - \phi) \right] \right\} \cdot \text{sinc}^2 \left\{ \frac{\pi L}{\lambda} \left[\sin \beta_o - \sin (\beta_o + \Delta\beta) \right] \right\} \tag{1}$$

where

I = intensity of diffracted line function

I_o = intensity of diffracted line function when $(\alpha - \phi) = -(\beta - \phi)$

b = effective illuminated width of blaze facet

λ = wavelength

α_o = grating incident angle

β_o = grating diffraction angle for maximum I/I_o at wavelength λ

$\Delta\beta$ = diffraction angle offset with respect to β_o

ϕ = blaze angle

L = grating length normal to grating grooves.

The first term of Equation 1 defines the envelope of the maximum intensity of all line functions. The second term defines the normalized grating line function.

The relative width of the blaze facet illuminated by the incident wave is

$$\frac{b_\alpha}{a} = \cos \phi - \sin \phi \tan (\alpha_o - \phi) \tag{2}$$

where

a = grating groove spacing.

Since

$$\frac{a}{\lambda} = \frac{m_o}{\cos \theta \, (\sin \alpha_o + \sin \beta_o)} \tag{3}$$

where

m_o = grating order

θ = out of plane angle,

the relative amplitude corresponding to the first term of Equation 1 can be expressed in terms of grating orders and angles[4]:

$$\frac{A}{A_o} = \text{sinc} \left\{ \frac{\pi m_o [\cos \phi - \sin \phi \tan (\alpha_o - \phi)]}{\cos \theta \, (\sin \alpha_o + \sin \beta_o)} \cdot [\sin (\alpha_o - \phi) + \sin (\beta - \phi)] \right\}. \tag{4}$$

The value of $\pi b_\alpha/\lambda$--the first term within the brackets--is a constant for fixed values of θ, α, λ, and a for all grating orders.

Relative grating line width as a function of β is related to the line width at Littrow by the factor $\cos \alpha/\cos \beta$. The width of a grating spectrometer entrance slit image as a function of β is also related to the image width at Littrow by the factor $\cos \alpha/\cos \beta$. When a spatially distributed noncoherent source is imaged onto the entrance slit of the instrument, the relative image point density distribution at the exit slit with respect to that at the entrance slit is thus $\cos \beta/\cos \alpha$. Where slit widths are relatively wide with

respect to the grating line widths, the peak values of I/I_o from Equation 1 are proportional to the normalized integrated intensity in each grating order at a given wavelength. It follows that the relative grating efficiency (neglecting shadowing) is

$$E_r = \frac{\frac{I_d}{I_o}}{\sum \frac{I_m}{I_o}} \tag{5}$$

where the numerator in Equation 5 is proportional to the normalized integrated intensity in the desired grating order, and the denominator is proportional to the sum of the normalized integrated intensities in all possible grating orders at a given wavelength. In order to build an efficiency model for Echelle gratings, both the shadowing effects and the reflection effects from the antiblaze facet must be taken into account when evaluating I/I_o terms for use in Equation 5.

For this model, an amplitude weighting factor is defined as

$$W = \frac{b_\beta}{b_\alpha} \tag{6}$$

where

b_α = width of the blaze facet illuminated by the incident wave

b_β = unshadowed portion of b_α at a given diffraction angle, β.

The relative weighted amplitude of the diffracted wave is taken as

$$\frac{A_W}{A_o} = W \frac{A}{A_o} \tag{7}$$

where A/A_o is the unweighted relative amplitude calculated from Equation 4.

When $(\phi - 90°) < \beta_o < \alpha_o$, the direct diffracted wave from the blaze facet is unshadowed, $b_\beta/a = b_\alpha/a$ and $W = 1$. A/A_o is calculated from Equation 4 with β_o substituted for β.

When $\alpha_o < \beta_o < 90°$, the direct diffracted wave is shadowed. The relative effective unshadowed width of the blaze facet at the diffraction angle is

$$\frac{b_\beta}{a} = \cos \phi - \sin \phi \tan (\beta_o - \phi). \tag{8}$$

W is calculated from Equations 2, 6 and 8. A/A_o is calculated from Equation 4, with β_o substituted for β.

The wave reflected from the antiblaze facet leaves the grating at angle β_o; the diffraction angle from the blaze facet, however, is

$$\bar{\beta} = 180° - 2\bar{\phi} - \beta_o \tag{9}$$

where $\bar{\phi}$ is the antiblaze angle as defined in Figure 1. The unweighted value of A/A_o for this reflected wave is calculated from Equation 4, with $\bar{\beta}$ substituted for β (but not for β_o).

The relative intensity of the grating orders, taking into account the effects of shadowing and of reflection from the antiblaze facet, is

$$\frac{\bar{I}}{I_o} = \left(W_1 \frac{A_1}{A_o} + W_2 \frac{A_2}{A_o} \cos \Delta P \right)^2 + \left(W_2 \frac{A_2}{A_o} \sin \Delta P \right)^2 \tag{10}$$

where

$\frac{A_1}{A_o}$ = relative direct diffraction amplitude ratio

$\frac{A_2}{A_o}$ = relative reflected diffraction amplitude ratio

W_1 = weighting factor for direct diffracted wave

W_2 = weighting factor for reflected diffracted wave

ΔP = relative phase difference between the direct and reflected diffracted waves.

The relative phase difference (in degrees) is

$$\Delta P = \frac{\Delta d}{a} \cdot \frac{a}{\lambda} \cdot \frac{360°}{\cos \theta} \tag{11}$$

where

$\frac{\Delta d}{a}$ = relative path difference between the direct and reflected diffracted waves.

When $\alpha_o < \bar{\beta} < 90°$, the corresponding range of β_o is $(90° - 2\bar{\phi}) < \beta_o < (180° - \alpha_o - 2\bar{\phi})$.

$$\frac{b_{\bar{\beta}}}{a} = \sin \phi \, [\tan (\bar{\beta} - \phi) - \tan (\alpha_o - \phi)] \tag{12}$$

and W is calculated from Equation 6, with $b_{\bar{\beta}}$ substituted for b_β. The relative path difference

$$\frac{\Delta d}{a} = \frac{2 \sin \phi - \sin (180° - \phi - \bar{\phi}) [\cos \phi - \sin \phi \tan (\alpha_o - \phi)]}{2 \sin (\bar{\phi} + \bar{\beta} - 90°)} \cdot [1 - \cos (\bar{\beta} - \beta_o)] \, . \tag{13}$$

When $(\phi + \bar{\phi}) \geq 90°$, $\bar{\beta}$ has a range of $90° \leq \bar{\beta} < (180° - \bar{\phi})$, and the corresponding range of β_o is $(-\bar{\phi}) < \beta_o \leq (90° - 2\bar{\phi})$. When $(\phi + \bar{\phi}) < 90°$, $\bar{\beta}$ has a range of $90° \leq \bar{\beta} < (90° + \phi)$, and the corresponding range of β_o is $(90° - \phi - 2\bar{\phi}) < \beta_o \leq (90° - 2\bar{\phi})$. For both sets of ranges, $b_{\bar{\beta}}/a = b_\alpha/a$ and $W = 1$. The relative path difference, $\Delta d/a$, is given by Equation 13.

Finally, relative grating efficiency is calculated from Equation 5, using appropriate values of I/I_o calculated from Equation 10.

Calculated vs measured grating performance

This grating relative efficiency model was tested against measured efficiencies of embossed R2 Echelle gratings. In all cases, grating performance was measured under near-Littrow conditions with 7.5° between incident and diffraction angles. The diffraction angle was greater than the incident angle. We do not know the actual blaze and antiblaze angles of these gratings. The typical groove shape of a replica of an embossed grating is shown in Figure 2. The rounded bottom of the groove and curvature of the antiblaze surface is a deviation from the ideal groove shape of Figure 1 for which the model was developed. A complete set of data was not available for any single grating.

Relative groove spacings and relative illuminated blaze facet widths for R2 Echelles as a function of grating order are listed in Table 1. Plots of grating order power modes for P and S plane waves, available through the 12th order, show considerable polarization sensitivity through the 12th order. We expect that good scaler performance would begin to be obtained near the 20th order.

Calculated relative grating efficiency vs wavelength, for both a single-vector and dual-vector efficiency model, is shown in Figure 3 with respect to measured efficiency for a 31.6 groove/mm R2 Echelle grating in the 25th order. An actual blaze angle of 62.7° was used for calculation. Antiblaze angles of 34° and 38° were used with the dual-vector model. The antiblaze facet for an antiblaze angle of 34° is directly illuminated by the incident wave for data points corresponding to wavelengths of 2.18 μm or less. The dual-

vector model predicts an effective blaze angle of 63.0° vs a measured effective blaze angle of 63.3° for an antiblaze angle of 34°. Calculated relative efficiency vs antiblaze angle is shown in Figure 4 at a wavelength of 2.25 μm. An example of energy distribution among the grating orders predicted by both the single-vector and dual-vector efficiency models is shown in Table 2 for an antiblaze angle of 34° and a wavelength of 2.25 μm. The most significant difference in I/I_o values between the two models occurs in the 20th, 21st, and 22nd orders. The dual-vector model predicts much higher energy in these parasitic orders due to reflection from the antiblaze facet.

Calculated vs measured peak relative efficiency and effective blaze angle vs grating order for a 316 groove/mm R2 Echelle grating are shown in Figure 5. Measured results are for unpolarized radiation. Calculated relative efficiency using a single-vector model is shown for comparison. Calculated relative efficiency vs wavelength in the 10th order, using the dual-vector model, is shown in Figure 6. Measured relative efficiency is for unpolarized radiation. The antiblaze facet is directly illuminated for data points at 0.53 μm and less. Table 1 indicates that this grating is not really operating within the scaler region in the 10th order. We would be more comfortable with the blaze and antiblaze angles used for calculating performance of this grating if measured performance vs wavelength for an order within the scaler region had been available.

Table 1. Relative Grating Groove Spacing and Illuminated Blaze Facet Width Near Peak Efficiency for R2 Echelle Gratings

Order	a/λ	b_α/λ	Order	a/λ	b_α/λ
4	2.24	1.14	15	8.41	4.26
5	2.80	1.42	16	8.97	4.54
6	3.36	1.70	17	9.53	4.82
7	3.92	1.99	18	10.09	5.11
8	4.48	2.27	19	10.65	5.39
9	5.04	2.55	20	11.21	5.68
10	5.60	2.84	21	11.77	5.69
11	6.16	3.12	22	12.33	6.24
12	6.72	3.41	23	12.89	6.53
13	7.29	3.69	24	13.45	6.81
14	7.85	3.97	25	14.01	7.09

Table 2. Example of Calculated Energy Distribution Among Grating Orders for 31.6 g/mm Grating at λ = 2.25 μm

α_o (deg) = 59.210
β_o (deg) = 66.701
m_o = 25
θ (deg) = 0
ϕ (deg) = 62.7
$\bar{\phi}$ (deg) = 34
a/λ = 14.07
b_α/λ = 7.22

Single-Vector Model				Dual-Vector Model				
m	β	I/I_o	Eff	m	β	$\bar{\beta}$	I/I_o	Eff
6	-25.62	0.0014	0.0021	5	-30.23	142.23	0.0018	0.0022
7	-21.18	0.0015	0.0023	6	-25.62	137.62	0.0060 *	0.0074
8	-16.87	0.0018 *	0.0027	7	-21.18	133.18	0.0063 *	0.0077
9	-12.66	0.0017	0.0026	8	-16.87	128.87	0.0004	0.0004
10	-8.51	0.0011	0.0016	9	-12.66	124.66	0.0011	0.0013
11	-4.41	0.0001	0.0002	10	-8.51	120.51	0.0061 *	0.0075
12	-0.33	0.0003	0.0005	11	-4.41	116.41	0.0018 *	0.0022
13	3.74	0.0020	0.0030	12	-0.33	112.33	0.0002	0.0003
14	7.84	0.0019	0.0029	13	3.74	108.26	0.0087 *	0.0106
15	11.97	0.0000	0.0000	14	7.84	104.16	0.0048 *	0.0059
16	16.18	0.0023	0.0034	15	11.97	100.03	0.0004	0.0005
17	20.47	0.0023 *	0.0034	16	16.18	95.82	0.0029	0.0036
18	24.88	0.0007	0.0011	17	20.47	91.53	0.0016	0.0020
19	29.46	0.0047	0.0071	18	24.88	87.12	0.0106 **	0.0130
20	34.26	0.0010	0.0015	19	29.46	82.54	0.0084 *	0.0104
21	39.35	0.0061	0.0092	20	34.26	77.74	0.0214 **	0.0262
22	44.84	0.0113	0.0171	21	39.35	72.65	0.0806 **	0.0990
23	50.92	0.0020	0.0030	22	44.84	67.16	0.0205 **	0.0252
24	57.93	0.0015	0.0023	23	50.92	61.08	0.0097 **	0.0119
25	66.70	0.5927	0.8940	24	57.93		0.0015	0.0019
26	81.71	0.0265	0.0400	25	66.70		0.5927	0.7281
				26	81.71		0.0265	0.0326

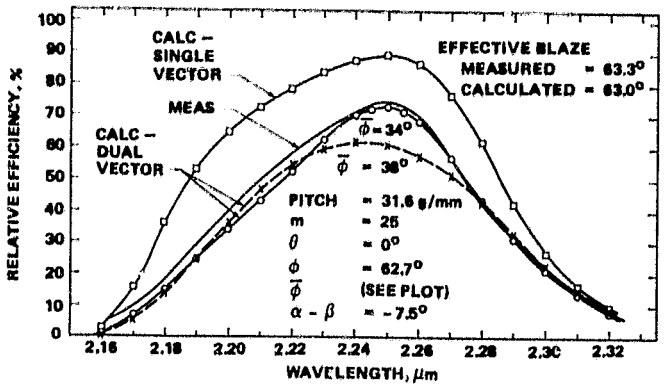

Figure 3. Relative efficiency vs wavelength vs antiblaze angle for an R2 Echelle grating in the scalar region.

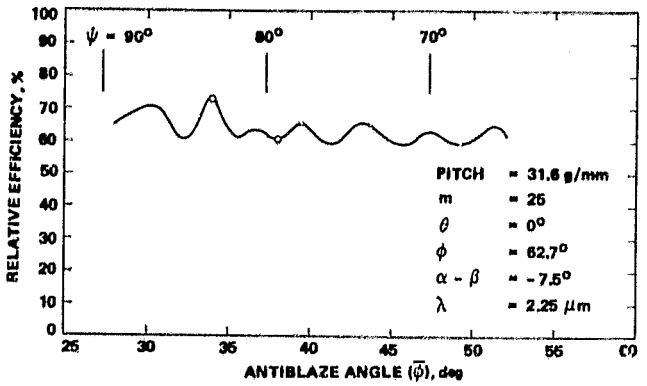

Figure 4. Calculated relative efficiency vs antiblaze angle for an R2 Echelle grating in the scalar region.

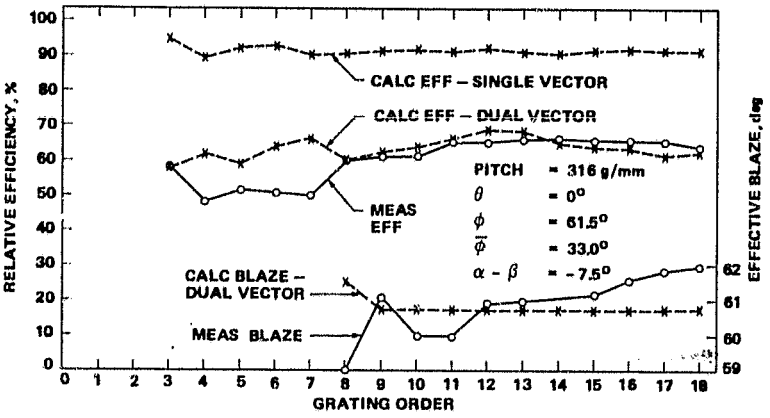

Figure 5. Relative efficiency and effective blaze angle for an R2 Echelle grating.

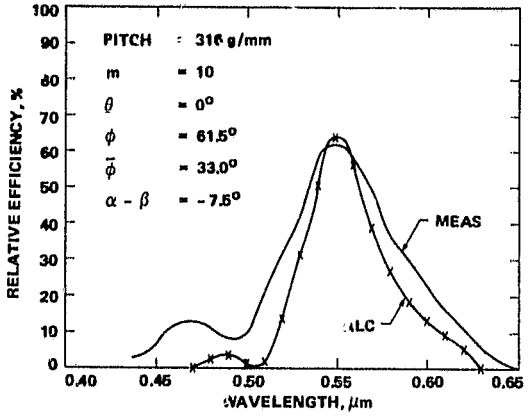

Figure 6. Relative efficiency vs wavelength for an R2 Echelle grating.

Analysis

The current dual-vector efficiency model assumes that (1) the relative phase shift due to reflection of the diffracted wave from the antiblaze facet is not significant, and (2) the diffraction pattern depends upon b_α even where shadowing results in $b_\beta < b_\alpha$. Consequently, the phase center for the diffracted wave is taken at the center of b_α. Table 2 shows that for this particular example the first assumption has some first-order validity. For the major parasitic orders--20, 21, 22--the reflection from the antiblaze facet tends to dominate the direct diffracted wave so that the effects of differential phase shifts between direct and reflected waves from whatever source tend to be second order. The phase shift upon reflection is a function of the complex index of refraction and can be different for P and S waves. Estimates of the relative phase shift between the P and S reflected waves show them to be approximately in quadrature with each other for these major parasitic orders. It appears that this effect alone, if taken into account in the model, would increase calculated efficiency in the example by several percentage points. We now believe that including the phase shifts due to reflection separately for the P and S waves would improve the model. The second assumption grew out of a concern that using the unshadowed width of the blaze facet, b_β, to calculate diffraction patterns might result in false wings upon the order power modes for small values of b_β. We now believe that this assumption has not been adequately tested.

The dual-vector model is not necessarily valid when the antiblaze facet is directly illuminated by the incident wave. The model could be expanded into a four-vector model to include the direct wave diffracted from the antiblaze facet and the diffracted wave from the antiblaze facet which is reflected from the blaze facet. Conceptually, this four-vector scaler model would be valid for all angles of incidence.

To expand the dual-vector model into a four-vector model and/or to fine tune the assumptions included in the model, we would like to have measured relative efficiency vs wavelength and measured effective blaze angles for a number of orders in the scaler region. Ideally, these data would be for a micromachined grating having flat blaze and antiblaze facets of known angles. Conceptually, however, if we had only measured relative efficiencies and effective blaze angles for a number of orders, it should be possible through iterative calculations to infer the actual blaze and antiblaze grating angles. This suggests that the model could be used to extrapolate grating performance to any set of incident and diffracted angles from a standard set of measured data.

Conclusions

Tests of a grating dual-vector relative efficiency model against available measured data for R2 Echelle gratings have indicated that the model has validity within the scaler region. These tests have indicated how the model could possibly be expanded and fine tuned.

We have used the dual-vector model for first-order design of the AMTS instrument for the 6th through 13th grating orders. For these low orders, the model yields only rough approximations. From the point of view of the instrument designer, there is a need for a grating efficiency model which, ideally, would accurately predict relative grating efficiencies for given blaze and antiblaze angles in both the P and S planes for all grating orders as a function of arbitrary incident angles, diffraction angles, and out-of-plane angles. Such a model is beyond the capability of scaler theory. We believe it would require a scattering model for the grating groove that exhibited considerable rigor.

Acknowledgments

Experimental data were provided by Dr. E. G. Lowen of Bausch and Lomb. The research described in this paper was carried out by the Jet Propulsion Laboratory, California Institute of Technology, under a contract with the National Aeronautics and Space Administration.

References

1. Evans, N. L., and V. G. Wright, "Optical Design Criteria for Grating Spectroradiometers," SPIE Proceedings, Vol. 503, August 1984.
2. Chahine, M. T., N. L. Evans, V. Gilbert, and R. D. Haskins, "Requirements for a Passive IR Advanced Moisture and Temperature Sounder," Applied Optics, Vol. 22, No. 7, 1 April 1984.
3. Schroeder, David J., and R. L. Hilliard, "Echelle Efficiencies: Theory and Experiment," Applied Optics, Vol. 19, No. 16, 15 August 1980.
4. Bottema, M., "Echelle Efficiency and Blaze Characteristics," SPIE Proceedings, Vol. 240, August 1980.

APPENDIX D

Equivalent Noise Bandwidth Models

Equivalent Noise Bandwidth Models

In this appendix, equations are developed for computer simulation modeling of the equivalent noise bandwidth for IR radiometers using square law detectors. Configurations using simple integration without optical chopping, and chopped configurations with synchronous demodulation, for both symmetric and assymmetric chopped waveforms, are considered. The effects of 1/f noise and low pass filters upon equivalent noise bandwidth are included. Numeric examples are presented. It is concluded that in the absence of 1/f noise, and for integration over a frequency range of zero to infinity, noise bandwidth for simple integration without optical chopping is approximately equal to $1/4T_d$, where T_d is total sample dwell time. For a square wave chopper and synchronous demodulator, noise bandwidth is approximately equal to $1/T_d$ (rather than $1/2T_d$, which is often used). The square wave chopper with synchronous demodulator configuration results are checked using a Laplace transform model.

For square law IR detectors, the voltage (or current) output from the detector is proportional to the IR signal power incident upon the detector. The responsivity of the detector is defined as:

$$R = \frac{V_s}{P_s} \tag{1}$$

where

P_s = IR signal power incident upon the detector

V_s = output voltage from the detector (due to P_s)

If the signal channel electronics integrates the detector output voltage,

$$\int V_s(t)\, dt \propto \int P_s(t)\, dt \tag{2}$$

Noise equivalent power is

$$NEP = H A_d \frac{V_{I(n)}}{V_{I(s)}} \tag{3}$$

Where

H = radiant flux per unit area incident upon the detector

A_d = detector area

$V_{I(n)}$ = RMS value of the integrated noise voltage

$V_{I(s)}$ = RMS value of the integrated signal voltage

Detectivity is then

$$D^* = \frac{\sqrt{A_d\ \Delta F}}{NEP} = \frac{R\ \sqrt{A_d\ \Delta F}}{V_n} \tag{4}$$

where the equivalent signal channel electrical noise bandwidth is

$$\Delta F = \frac{1}{G(Fo)} \int_0^\infty G(F)dF \tag{5}$$

and

$G(F)$ = power gain at frequency F

$G(Fo)$ = maximum power gain

Where detector/preamplifier noise power density is constant vs. frequency, system noise equivalent radiance

$$NEN \propto \frac{\sqrt{\Delta F}}{D^*} \tag{6}$$

When noise power density is a function of frequency, however, D* becomes a function of frequency and evaluation of system NEN can present a problem. This difficulty can be overcome by using a constant value of D* and re-defining ΔF:

$$\Delta F' = \frac{1}{G(Fo)\ Po} \int_\Theta^\infty G(F)\ P_n(F)\ dF \tag{7}$$

where

$P_n(F)$ = noise power density at frequency F

Po = noise power density for which D* is evaluated

For the simple gated integrator of Table D-1a, in which only the light interval is integrated, the fixed integration interval

$$T_d = To/2 \tag{8}$$

The integrated value of a sine wave voltage

$$V_{I(sin)} = \int_{t=T}^{T+To/2} V_p \sin(2\pi Ft)\, dt$$

$$= \frac{V_p}{2\pi F} [\cos 2\pi FT - \cos 2\pi F(T + To/2)] \qquad (9)$$

where

V_p = peak sine wave voltage

As F approaches zero, the maximum value of the integrated sine wave voltage approaches $V_pTo/2$. The normalized value of the integrated sine wave voltage is then

$$\frac{2V_{I(sin)}}{V_pTo} = \frac{1}{\pi FTo} [\cos 2\pi FT - \cos 2\pi F(T + To/2)] \qquad (10)$$

and its variance -- as a function of the phase of F -- is

$$\sigma^2 = \frac{1}{N(\pi FTo)^2} \sum_{T=0}^{\frac{N-1}{NF}} [\cos 2\pi FT - \cos 2\pi F(T + To/2)]^2 \qquad (11)$$

where

$T = 1/F$

N = number of equal intervals within T

$\frac{1}{NF} = \Delta T$

If detector/preamp noise power density consists of a component which is constant with frequency plus a 1/f noise component (Fig D-1)

$$P_{1/f} = \frac{C_1}{F^b} \qquad (12)$$

Table D-1 Comparison of noise bandwidth and figures-of-merit for typical chopper/integrator configurations as a function of 1/F noise frequency knee

		$F_K = 0, b = 1$		$F_K = 1, b = 1$		$F_K = 100, b = 1$	
		ΔF (Hz)	$\sqrt{\Delta F}/F_c$	ΔF (Hz)	$\sqrt{\Delta F}/F_c$	ΔF (Hz)	$\sqrt{\Delta F}/F_c$
a 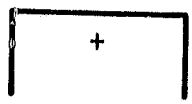	$T_d = 0.12$ $F_c = 1.0$	2.06	1.44	5.48	2.34	343.1	18.5
a' 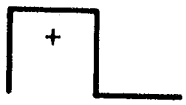	$T_d = 0.12$ $F_c = 0.5$	4.12	4.06	7.89	5.61	379.8	39.0
b 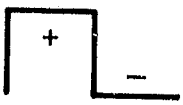	$T_d = 0.12$ $F_c = 0.5$	8.14	5.71	9.51	6.17	143.4	24.0
c 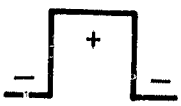	$T_d = 0.12$ $F_c = 0.5$	8.07	5.68	8.84	5.95	85.6	18.5
c' 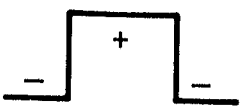	$T_d = 0.16$ $F_c = 0.67$	6.08	3.68	6.86	3.91	83.7	13.7
d 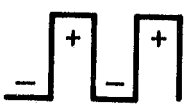	$T_d = 0.12$ $F_c = 0.5$ $C = 6$	7.93	5.63	8.10	5.69	24.8	9.96
	$C = 12$	7.52	5.48	7.60	5.51	15.3	7.82
	$C = 24$	6.77	5.20	6.81	5.22	10.4	6.44
	$C = 48$	6.76	5.20	6.78	5.21	8.51	5.83
	$T_d = 0.1278$ $C = 46$	6.72	5.18	6.75	5.20	8.47	5.82
	* $T_d = 0.1273$ $C = 56$					7.97	5.65
e 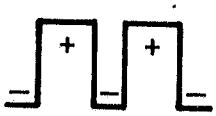	$T_0 = 0.1267$ $C = 6$ $F_c = 0.67$	13.55	5.49			37.16	9.10

T_d = DWELL TIME (sec)

C = NUMBER OF CYCLES IN T_0

F_c = CHOPPER FACTOR

1/f NOISE $\propto \left(\frac{F_K}{F}\right)^b$

F_K = 1/f NOISE FREQUENCY KNEE (Hz)

* BASELINE ∇ CHOPPING CONFIGURATION

where

C_1 = constant

F = noise frequency

b = exponent (typically between 0.8 and 1.5)

$P_{1/f}$ = 1/f spectral noise density

At the knee of the total spectral noise density curve

$$P_{det} = \frac{C_1}{F_k{}^b}$$

or

$$C_1 = P_{det}\, F_k{}^b \tag{13}$$

therefore

$$P_{1/f} = P_{det} \left(\frac{F_k}{F}\right)^b \tag{14}$$

Total noise spectral power density is

$$P_t = P_{det} + P_{1/f} = P_{det}\left[1 + \left(\frac{F_k}{F}\right)^b\right] \tag{15}$$

The variance in integrated noise voltage is proportional to noise power. The total normalized variance in the integrated voltage of a test signal consisting of a component whose power spectral density is constant vs frequency plus a component which is a function of 1/f, from Eq 11 and 15, is

$$\sigma_t{}^2 = \frac{1}{N(\pi F To)^2}\left[1 + \left(\frac{F_k}{F}\right)^b\right] \cdot \sum_{T=0}^{\frac{N-1}{NF}} [\cos 2\pi FT - \cos 2\pi F(T + To/2)]^2 \tag{16}$$

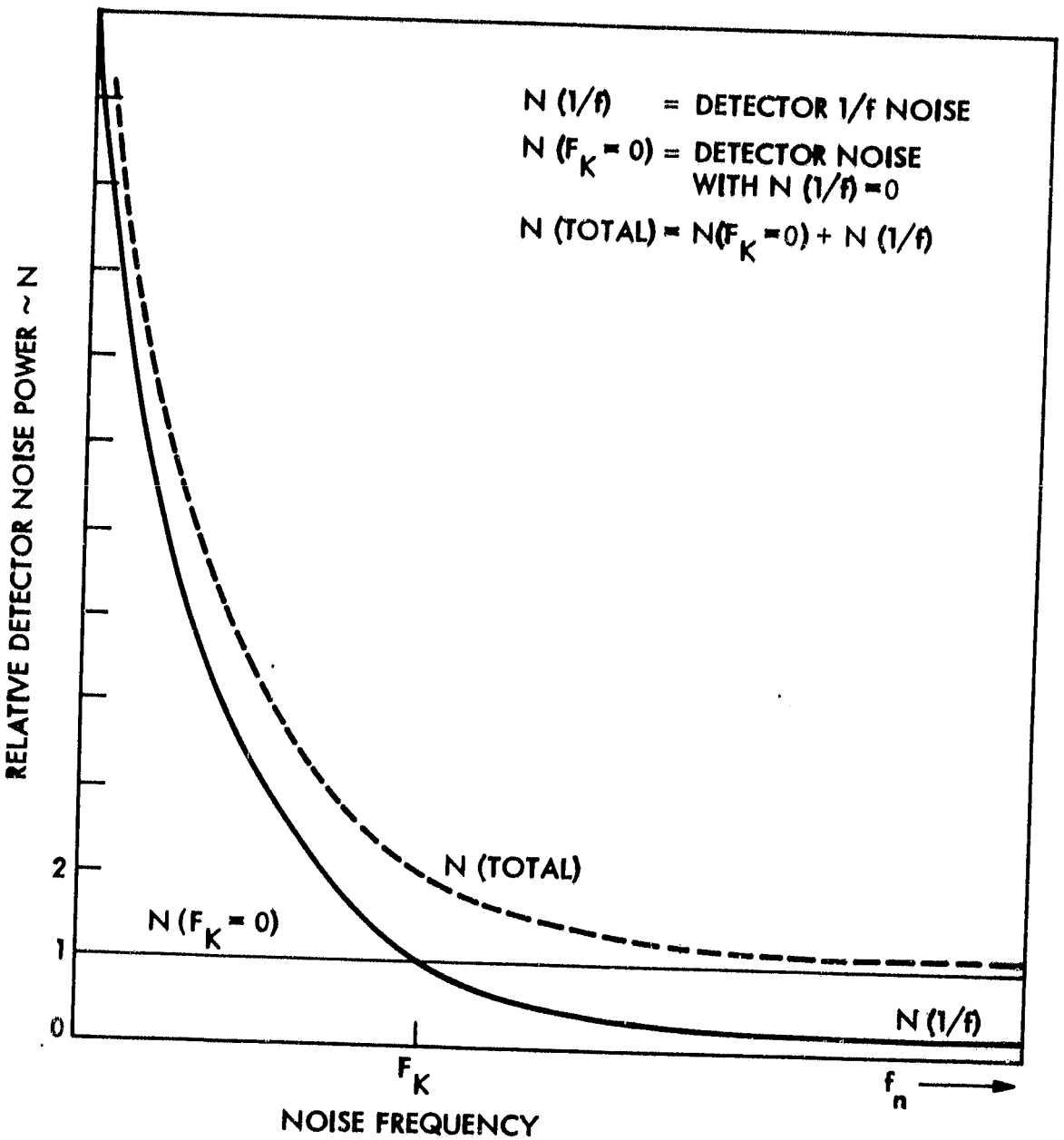

Figure D-1 Relative detector noise power vs noise frequency

The equivalent noise power bandwidth, as defined in Eq 7, is then

$$\Delta F' = \int_{F=0}^{\infty} \sigma_t^2 \, dF \tag{17}$$

For the simple gated integrator only, numerical evaluation of Eq 11 shows that the RMS value of the integrated sine wave is equal to

$$\frac{V_{I(sin)\ Max}}{\sqrt{2}}$$

where $V_{I(sin)\ Max}$ is evaluated using Eq 9 with

$$T = \frac{1}{4F} - \frac{To}{4} \tag{18}$$

For the square wave integrator of Table D-1b, the integrated value for the To/2 dark interval is subtracted from the integrated value of the To/2 light interval, where

$$V_{I(sin)} = \int_{t=T}^{T+To/2} V_p \sin 2\pi Ft \, dt - \int_{T+To/2}^{T+To} V_p \sin 2\pi Ft \, dt \tag{19}$$

Following the argument of Eq 9 through 16, the variance for the square wave integrator is

$$\sigma_t^2 = \frac{1}{N(\pi FTo)^2} \left[1 + \left(\frac{F_k}{F} \right)^b \right] \cdot \sum_{T=0}^{\frac{N-1}{NF}} [\cos 2\pi FT - 2 \cos 2\pi F(T + To/2) + \cos 2\pi F(T + To)]^2 \tag{20}$$

For the split square wave integrator of Table D-1c, the integrated values of the two To/4 dark intervals are subtracted from the integrated value of the To/2 light interval, where

$$V_{I(sin)} = -\int_{t=T}^{T+To/4} V_p \sin 2\pi Ft\, dt + \int_{T+To/4}^{T+3To/4} V_p \sin 2\pi Ft\, dt$$

$$- \int_{T+3To/4}^{T+To} V_p \sin 2\pi Ft\, dt \qquad (21)$$

Following the argument of Eq 9 through 16, the variance for the split square wave integrator is

$$\sigma_t^2 = \frac{1}{N(\pi FTo)^2} \left[1 + \left(\frac{F_k}{F}\right)^b\right]$$

$$\cdot \sum_{T=0}^{\frac{N-1}{NF}} [-\cos 2\pi FT + 2\cos 2\pi F(T + To/4)$$

$$- 2\cos 2\pi F(T + 3To/4) + \cos 2\pi F(T + To)]^2 \qquad (22)$$

For the square wave chopper of Table D-1d, the integrated values of the To/2C dark intervals are subtracted from the To/2C light intervals, where C is the number of cycles and

$$V_{I(sin)} = \sum_{J=0}^{J} \int_{t=T+(To/C)(J)}^{T+(To/C)(J+1/2)} V_p \sin 2\pi Ft\, dt - \int_{T+(To/C)(J+1/2)}^{T+(To/C)(J+1)} V_p \sin 2\pi Ft\, dt \qquad (23)$$

Following the arguments of Eq 9 through 16, the variance for the square wave chopper is

$$\sigma_t^2 = \frac{1}{N(\pi FTo)^2}\left[1 + \left(\frac{F_k}{F}\right)^b\right]$$

$$\cdot \sum_{T=0}^{\frac{N-1}{NF}} \left\{ \sum_{J=0}^{J} [\cos 2\pi F(T + (To/C)(J)) - 2 \cos 2\pi F(T + (To/C)(J + 1/2)) + \cos 2\pi F(T + (To/C)(J + 1))] \right\}^2 \qquad (24)$$

For the split square wave chopper of Table D-1e, the integrated values of the two C1/3 dark intervals on either side of the 2C1/3 light interval are subtracted from the light interval, where C1 = 3To/(3C + 1) and

$$V_{I(sin)} = \sum_{J=0}^{C-1} - \int_{T+C1(J)}^{T+C1/3+(J\cdot C1)} V_p \sin(2\pi Ft)\, dt + \int_{T+C1/3+(J\cdot C1)}^{T+C1(J+1)} V_p \sin(2\pi Ft)\, dt$$

$$- \int_{T+C1(J+1)}^{T+4C1/3+(J\cdot CI)} V_p \sin(2\pi Ft)\, dt \qquad (25)$$

Following the arguments of Eq 9 through 16, the variance for the split square wave chopper is

$$\sigma_t^2 = \frac{1}{N(\pi FTo)^2}\left[1 + \left(\frac{F_k}{F}\right)^b\right] \sum_{T=0}^{\frac{N-1}{NF}} \left\{ \sum_{J=0}^{C-1} \cos(2\pi F(T + 4C1/3 + (J \cdot C1))) \right.$$

$$+ 2[\cos(2\pi F(T + C1/3 + (J \cdot C1))) - \cos(2\pi F(T + C1(J + 1)))]$$

$$\left. - \cos(2\pi F(T + C1(J))) \right\}^2 \qquad (26)$$

The results of numerically integrating Eq 17 for the various configurations are shown in Table D-1. A discussion of these results can be found in Para 3.1.1.3 of the main text.

Another way to calculate the electrical noise bandwidth, excluding 1/f noise effects, is to use a Laplace transform to approximate the amplitude function or the integrated value of the sine wave voltage. A square wave chopped waveform consisting of n half cycles is shown in Fig D-2. The Laplace transform (or amplitude function) of this function is

$$V_{I(sin)} \approx H(s) = \frac{1}{s\tau} \quad \frac{(1 - e^{-sT})\ (1 - e^{-nsT})}{(1 + e^{-sT})} \qquad (27)$$

where

$H(s)$ = amplitude function

τ = gated integrator time constant

n = number of half cycles

T = dwell time divided by number of half cycles = T_d/n

s = Laplace frequency domain variable

The mean sum of the amplitudes is found by substituting $i\omega$ for s in Eq 27 and taking the complex conjugate

$$\sigma^2 \approx H^2(\omega) = \frac{n^2T^2}{\tau^2} \quad \frac{\sin^2(n\omega T/2)}{(n\omega T/2)^2} \quad \tan^2\left(\frac{\omega T}{2}\right) \qquad (28)$$

where

$$\omega = 2\pi f$$

Figure D-3 shows plots of this function. The equivalent noise bandwidth is obtained by integrating this function (Eq 28) over all frequencies and dividing by the maximum value of the function

$$\Delta F \approx \frac{\int_0^\infty H^2(\omega)\ d\omega}{H^2\ Max} \qquad (29)$$

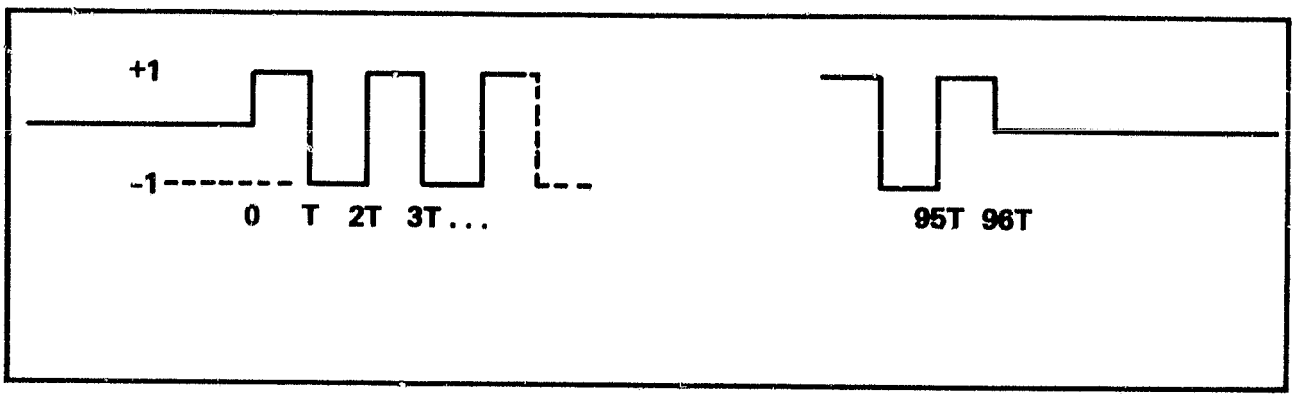

Figure D-2 Square wave chopped waveform consisting of n = 96 half cycles

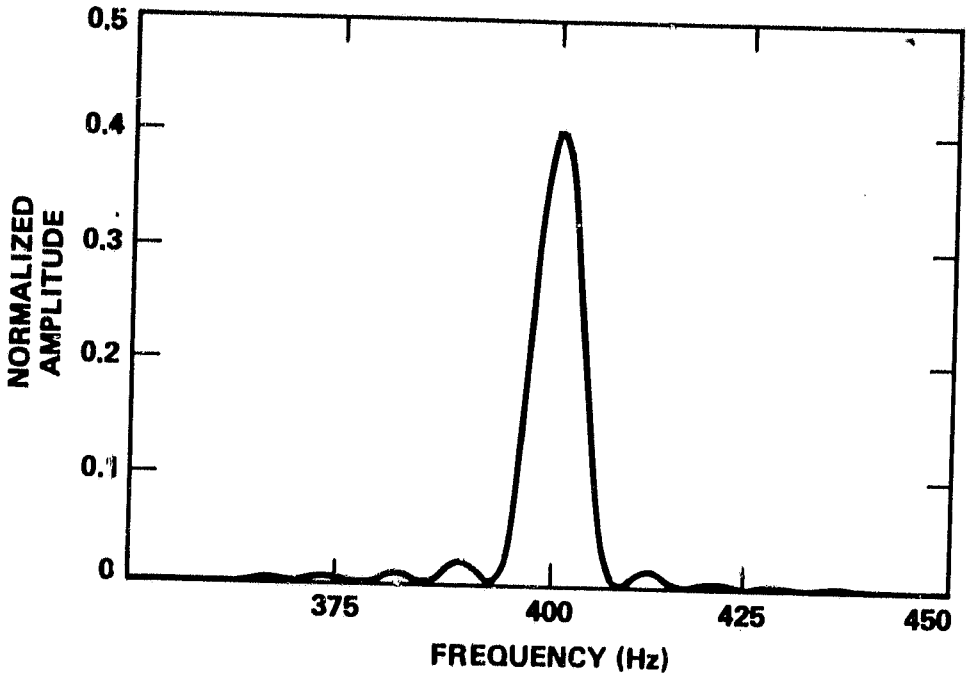

EXPANDED SCALE AROUND MAIN PEAK

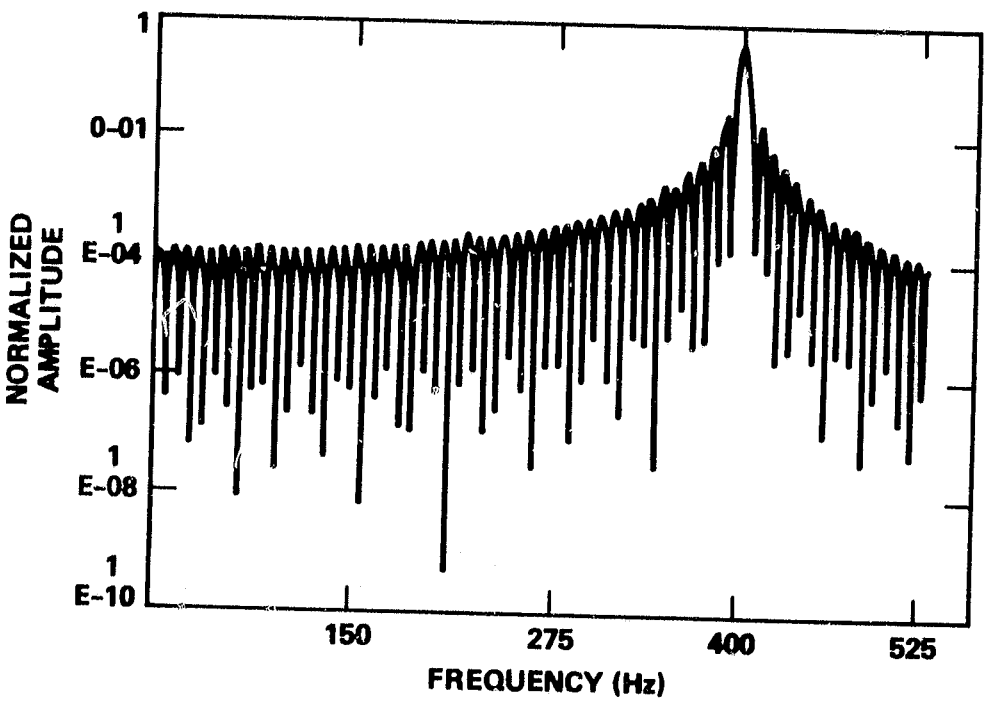

SEMI-LOGARITHMIC PLOT SHOWING NUMEROUS SIDEBANDS

Figure D-3 Mean sum variance for the square wave chopper; F_c = 400 Hz, T = 0.125 msec, n = 96

The maximum of Eq 28 (H^2 Max) occurs when f equals the chopping frequency (400 Hz in Figure D-3). At this point the sine term is zero and the tangent term is undefined. Approaching the limit from either side of 400 Hz yields

$$\lim_{f \to 400} \frac{\sin^2(n\pi ft)}{(n\pi ft)^2} \tan^2(\pi ft) \approx 0.405$$

where

$$n = 96$$

$$t = 1.25 \text{ msec}$$

The integral part of Eq 29 was calculated by numerical means from 0 to 1000 Hz and found to be about 3.381, so the equivalent noise bandwidth is

$$\Delta F \approx \frac{3.381}{0.405} = 8.35 \text{ Hz}$$

For no 1/f noise and for integration over a frequency range of 0 to ∞, the straight integrator configuration of Table D-1a (without optical chopper) would result in a noise bandwidth of

$$\Delta F \approx \frac{1}{4T_d}$$

Numeric values listed in the table for this configuration were obtained by integrating over a frequency range of 0.02 to 200 Hz. The square wave synchronous demodulator configurations of Table D-1b and D-1d would result in a noise bandwidth of

$$\Delta F \approx \frac{1}{T_d}$$

Numeric values listed in the table for configuration (b) were obtained by integrating over a frequency range of 0.05 to 200 Hz. For configuration (d) integration was from 0.5 Hz to 400 Hz for 6, 12, and 24 cycles per dwell interval, and from 0.5 Hz to 600 Hz for 48 cycles. The reduced noise bandwidth for these configurations is believed primarily due to the effective low pass filter used for these numeric examples. It is believed that the computer simulation models provide the more accurate results. They also allow 1/f noise effects to be accurately modeled.

APPENDIX E

Sun Angles Incident Upon the AMTS Baseline V Instrument

Sun Angles Incident Upon the AMTS Baseline V Instrument

The TIROS orbit is assumed for the Baseline V instrument. The TIROS-N orbit is at an altitude of 833 km. It is reported to be an 8:30 a.m. or 3:30 p.m. orbit, corresponding to a ΔT_o of 3.5 hours. Sun angles for this orbit are listed in Table E-1. The following interrelated parameters are presented in this table:

- ΔT_o — The longitude difference, in hours, between the orbit equatorial longitude and the longitude of the sun. A positive value represents a satellite ascending orbit equatorial crossing west of the sun; i.e., a morning orbit.
- ΔT — The longitude difference, in hours, between the local satellite longitude and the longitude of the sun. A positive value represents a satellite position west of the sun.
- SUN ELE — Sun elevation with respect to the equatorial plane. A positive value represents a sun position north of the equator.
- SAT LAT — Satellite latitude. A positive value represents a local satellite position north of the equator.
- ϕ — Sun azimuth, measured cw from the satellite velocity vector.
- ψ — Incident angle of sunlight with respect to the satellite zenith.

The coordinate system used is shown in Fig E-1. In Fig E-1a,

- V — represents the spacecraft velocity vector.
- Z — represents the spacecraft zenith; Z is normal to V.
- X — is an axis normal to the VZ plane.
- S — is a line from the upper limb of the sun to the spacecraft.
- ψ — is the incident angle of the sun line with respect to Z, measured in the SZ plane.
- ϕ — is the azimuth of the sun with respect to V, measured in the XV plane.
- R — is the distance from the origin to an arbitrary point, P, in the XV plane; R lies in both the XV and the ZS planes.
- H — is the height of the sun line above point P; H lies in the ZS plane and is parallel to Z.

Table E-1 TIROS orbit sun angles†

ΔT_0 (hr) / SUN ELE.°	3.5 / 23.45			3.5 / 12			3.5 / 0			3.5 / -12			3.5 / -23.45		
SAT. LAT.°	ΔT(hr)	Ø°	ψ°	ΔT(hr)	Ø°	ψ°	ΔT(hr)	Ø°	ψ°	ΔT(hr)	Ø°	ψ°	ΔT(hr)	Ø°	ψ°
81.25	9.50	125.61	73.32	9.50	126.71	84.72	9.50	127.82	96.67	9.50	129.00	108.61	9.50	130.29	120.00*
70.00	5.17	119.62	63.52	5.17	124.02	74.21	5.17	128.16	85.50	5.17	132.18	96.80	5.17	136.21	107.56
60.00	4.53	114.36	58.62	4.53	120.99	68.42	4.53	127.03	78.92	4.53	132.66	89.54	4.53	138.02	99.67
50.00	4.20	108.06	54.85	4.20	116.96	63.37	4.20	124.95	72.81	4.20	132.16	82.53	4.20	138.75	91.90
40.00	3.99	100.78	52.29	3.99	111.89	59.13	3.99	121.87	67.16	3.99	130.72	75.74	3.99	138.55	84.20
30.00	3.84	92.85	51.07	3.84	105.79	55.83	3.84	117.72	62.09	3.84	128.28	69.25	3.84	137.43	76.63
20.00	3.71	84.73	51.29	3.71	98.83	53.65	3.71	112.44	57.77	3.71	124.72	63.20	3.71	135.32	69.28
10.00	3.60	77.00	52.91	3.60	91.33	52.75	3.60	106.06	54.42	3.60	119.92	57.77	3.60	132.05	62.27
0	3.50	70.08	55.78	3.50	83.75	53.19	3.50	98.75	52.24	3.50	113.75	53.19	3.50	127.42	55.79
-10.00	3.40	62.24	59.73	3.40	76.57	54.93	3.40	90.86	51.38	3.40	106.22	49.72	3.40	121.14	50.07
-20.00	3.29	59.55	64.51	3.29	70.16	57.84	3.29	82.92	51.94	3.29	97.55	47.62	3.29	113.00	45.44
-30.00	3.16	55.99	69.93	3.16	64.75	61.74	3.16	75.43	53.85	3.16	88.27	47.10	3.16	103.01	42.28
-40.00	3.01	53.46	75.82	3.01	60.40	66.44	3.01	68.79	56.99	3.01	79.11	48.23	3.01	91.71	40.97
-50.00	2.80	51.90	82.04	2.80	57.09	71.77	2.80	63.23	61.17	2.80	70.73	50.90	2.80	80.15	41.71
-60.00	2.47	51.27	88.50	2.47	54.77	77.59	2.47	58.78	66.21	2.47	63.55	54.95	2.47	69.49	44.44
-70.00	1.83	51.58	95.22	1.83	53.39	83.92	1.83	55.38	72.07	1.83	57.65	60.25	1.83	60.37	49.02
-81.25	-2.50	54.39	106.15	-2.50	53.29	94.75	-2.50	52.18	82.81	-2.50	51.00	70.86	-2.50	49.71	59.47
(ψ MIN) -41.47													2.98	90.00	40.95

* Satellite is within the earth shadow.
† Orbit inclination is 98.75°. Orbit is sun synchronous.

In Fig E-1b, a plane X'V, inclined to the plane XV, has been added. In this figure,

X' lies in the XZ plane; it is normal to V, but not to X or to Z.

Θ is the angle between the XV and X'V planes, measured between normals to the V axis.

h is the height above point P at which the X'V plane cuts H.

The following relationships exist:

$$H = \frac{R}{\tan \psi} \tag{1}$$

$$h = R \tan \Theta \sin \phi \tag{2}$$

$$H - h = R \left(\frac{1}{\tan \psi} - \tan \Theta \sin \phi \right) \tag{3}$$

If h = H, then:

$$\Theta = \tan^{-1} \frac{1}{\tan \psi \sin \phi} \tag{4}$$

By choosing the origin at appropriate points in the XV or X'V planes, the intersection of the sun lines with the XV or X'V planes can be determined for shield positions defined by R, ϕ, and H. Conversely, required shield positions can be calculated.

Table E-1 is for an ascending morning orbit. Parameter values for an ascending afternoon orbit can be obtained from the table as follows:

- For positive satellite latitudes, use negative latitude values from the table.
- For positive sun elevations, use negative elevation values from the table.
- For sun azimuth, use 180 - ϕ, measured ccw with respect to the satellite velocity vector.
- Let positive values of ΔT represent positions east of the sun.

The table only lists values for half orbits, between maximum values of north and south satellite latitudes. When necessary, sun azimuth and sun incident angles can be obtained for the extended orbit by noting that the magnitude of these parameter deltas are symmetric about the minimum values of ψ and about 90° for ϕ.

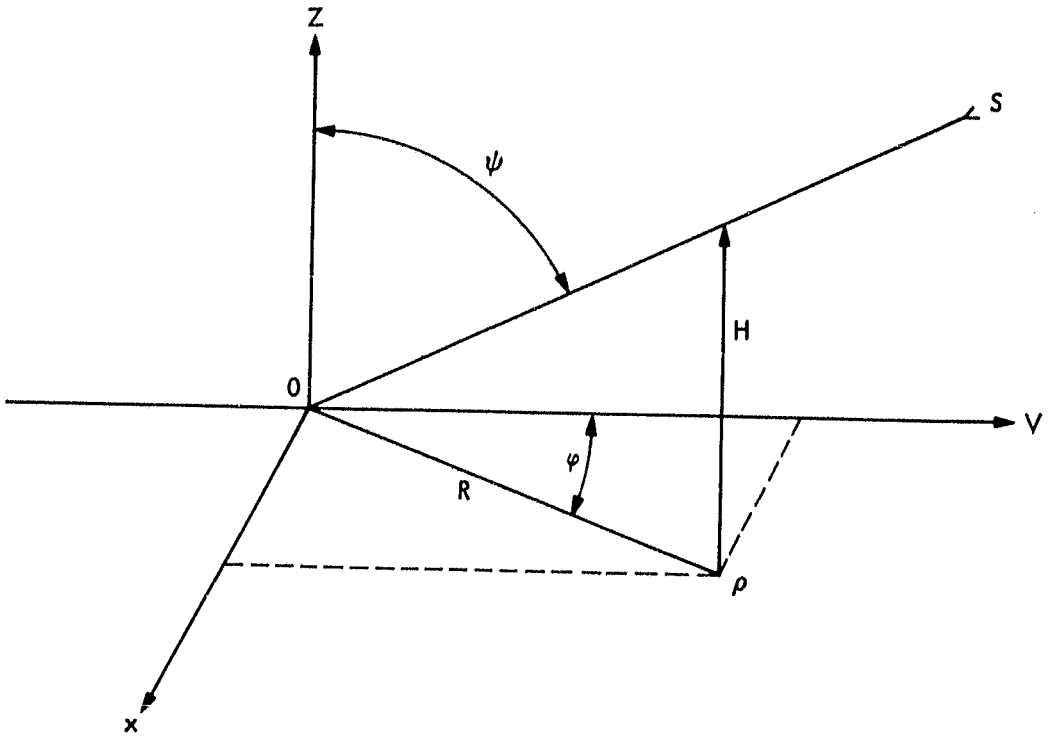

Figure E-1a

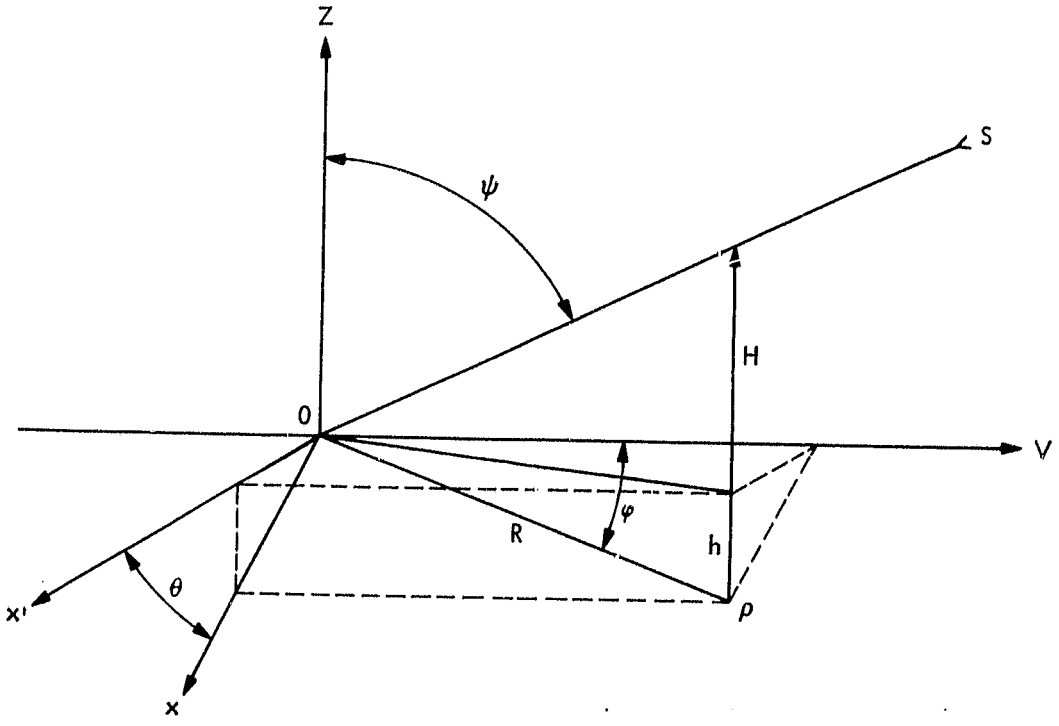

Figure E-1b

Figure E-1 Spacecraft instrument coordinates

The angle of incidence of rays from the limb of the earth with respect to the satellite zenith for a 900 km satellite altitude is 118.81°. If the limb of the earth is defined to be 100 km above the surface, the angle is 117.13°. The offset from the limb of the sun to the center of the sun is 0.27°. The offset of the angle of incidence of the sun from the satellite altitude to the surface of the earth is 0.003°. Consequently, the angle of incidence of the sun at the subsatellite point can be taken from the values of ψ in the table for determining earth lighting corresponding to each orbit. (This argument will hold for the 833 km Baseline V orbit.)

All sun synchronous orbits must have inclinations greater than 90°. The appropriate inclination, θ_i, for such an orbit depends on A, the average of the altitudes at perigee and at apogee. If the eccentricity of the orbit is e, and the radius of the earth is R_e then

$$\theta_i \approx \cos^{-1} \left[-0.098951(1 + A/R_e)^{3.5}(1 - e^2)^2\right] \qquad (5)$$

APPENDIX F

AMTS Baseline V Detector D* Performance Models

AMTS Baseline V Detector D* Performance Models

Three types of detectors, PC HgCdTe, PV HgCdTe, and PV InSb are used to cover the AMTS baseline V spectral range. The first part of this appendix gives a brief description of each of these detector materials and their associated noise sources. The preamplifier configuration and preamp noise is also discussed. Next, there is a short summary of how the background flux densities were calculated for the Baseline V instrument. Finally, the actual models are presented along with some demonstration computer runs. The math models are presented without complete development, but most of the equations used are found in the literature.

PC HgCdTe DETECTORS

HgCdTe Material Considerations

Baseline V channels 1 through 11 use photoconductive HgCdTe. This material has the property of having a bandgap that is controlled by the mole ratio of CdTe to HgTe and detector temperature. Two alloys of varying CdTe:HgTe mole ratios are used to cover the broad spectral band of these channels. The mole ratios or mole fractions where chosen so that at the dewar temperature the detector cut-off wavelength would be just beyond the channel with the longest wavelength in that particular band. The peak response of the detector always falls at a shorter wavelength. The exact peak location is a function of the detector quantum efficiency which, in turn, is a function of the material index of refraction, the reflectivity of the passivation layer, the antireflective coatings (if any), and other second-order physical characteristics. Improving the quantum efficiency, by whatever means, moves the peak closer to the cut-off wavelength. For purposes of simplification, the AMTS Baseline V detectors were peaked at wavelengths that are shorter than cut-off by ≈10 percent and a quantum efficiency of 0.70 was chosen for the data sets. This efficiency is probably a realistic value. Table F-1 gives the mole fraction, calculated bandgap energy, cut-off wavenumber, and estimated peak wavenumber for some HgCdTe detector alloys at 75 K.

Detector dark resistance is a function of the distance between the electrical contacts of the detector, its cross-sectional area, and resistivity. Resistivity, in turn, is controlled by the minority carrier concentration; fewer numbers of minority carriers mean a higher conductivity and less resistivity. The intrinsic carrier concentration, the initial concentrations of electrons and holes in undoped HgCdTe, is calculated directly from the bandgap energy and detector temperature.

In pure HgCdTe, the mole ratios used by the two AMTS detector materials are p-type. Electron mobilities are several orders of magnitude higher than hole mobilities. It is, therefore, advantageous to make use of the higher electron mobility and fabricate the detector as an n-type device. This can be done through doping either a bulk boule of material or by forming a thick epitaxial layer on a substrate. As a general rule, it is more difficult to control the minority carrier concentrations in the long wavelength 16 μm material than it is in the shorter wavelength materials.

Table F-1 Baseline V HgCdTe detector material characteristics

CH	Mole fraction CdTe:HgTe	Bandgap energy (eV)	Cut-off wave-number (cm^{-1})	Peak wave-number (cm^{-1})
1-10	0.1838	0.06847	551.52	606.80
11	0.2035	0.0988	787.45	874.5
12-13	0.2143	0.1156	932.66	1036.27
14-15	0.2573	0.1829	1475.36	1639.34
16-17	0.2707	0.2040	1645.28	1828.15

Table F-2 Baseline V PC HgCdTe detector parameters

CH	Minority carrier conc. (cm^{-3})	Carrier lifetime (s)	Electron mobility ($cm^2/V/s$)	Hole mobility ($cm^2/V/s$)
1-10	$1x10^{14}$	$1x10^{-6}$	$2.06x10^4$	295.00
11	$2x10^{12}$	$1x10^{-6}$	$2.01x10^4$	292.00

Table F-3 Baseline V PV HgCdTe detector parameters

CH	Acceptor Conc. (cm^{-3})	Donor conc. (cm^{-3})	Carrier lifetime (s)	Electron mobility ($cm^2/V/s$)	Hole mobility ($cm^2/V/s$)
12-13	$2x10^{14}$	$1x10^{15}$	$5x10^{-7}$	$1.98x10^4$	289.00
14-15	$7x10^{14}$	$1x10^{16}$	$5x10^{-7}$	$1.87x10^4$	277.00
16-17	$2x10^{15}$	$5x10^{16}$	$5x10^{-7}$	$1.84x10^4$	273.00

For purposes of modelling, the minority carrier concentrations were chosen so that the resulting dark resistivities were consistant with detector manufacturers' catalog values, which often quote dark resistivities in the range of 40 to 400 ohm/sq at 77 K for long wavelength HgCdTe material. Table F-2 lists the minority carrier concentrations used in the Baseline V data sets. Generation-recombination (G-R) noise is the dominate source of noise in the long wavelength alloys and is directly related to the concentration of minority carriers (holes). On the other hand, the detector responsivity is inversely related to this concentration through the dark resistivity. This indicates that there is a trade-off between detector G-R noise and detector response in terms of total detector performance.

Dark resistivity is also controlled by carrier mobilities and carrier lifetimes. The majority carrier, or electron, is the predominate carrier here. Neither parameter is very sensitive to temperature, but both are very dependent on the make-up of the material. Mobilities must be measured. Carrier lifetimes can be calculated for various trapping mechanisms, but they must ultimately be derived from measurements. Table F-2 also lists these parameters.

PC HgCdTe Detector Biasing

The Baseline V photoconductive HgCdTe detectors must be biased to function. The photoconductive gain of the detector is directly dependent on a constant bias field. This necessitates the use of a load resistor. The circuit configuration used in the modelling uses the load resistor as a voltage divider to drop the supply voltage to a controlled voltage level, and the photosignal current is read from it. As such, it is desirable to make the load resistor value at least ten times the dark resistance of the detector, for reasons of detector Joule heat loading and responsivity. (This is shown in the data set of Table F-5.) This bias level seems to give the best heat load vs detector response for these detector materials and parameters.

PC HgCdTe Detector and Preamplifier Noises

The PC HgCdTe detectors were modelled with three sources of noise:

- Johnson or thermal noise
- Background or photoinduced carrier noise
- Generation-recombination (G-R) noise

In addition, there are two sources of preamp noise; Johnson noise from the load resistor and preamplifier noise. With the exception of preamplifier noise, all of the noises are calculated from their basic sources: temperatures, minority carrier concentrations, and total background photon flux densities. Johnson noise calculations are based upon both detector and load resistor temperatures. As earlier stated, G-R noise is related to the minority carrier concentration, specifically, to the square root of the concentration.

Since a photoconductor's gain is dependent on the dimensions of the detector, i.e. the distance between electrical contacts and cross-sectional area, the background noise is area dependent. The electrical contacts of the Baseline V detectors are at the opposite sides of the channel's width dimension. A short description of the sources and quantities of background photon flux follows the PV HgCdTe detector section.

A differential transimpedance amplifier (TIA) is used as the preamplifier for the PC HgCdTe detectors (Fig F-1). The differential TIA amplifies the difference between the measured signal and a reference signal. The noise of a differential TIA is assumed to be $\sqrt{2}$ ($2X10^{-9}$) $nV/\sqrt{Hz}$. Transimpedance is a function of open loop gain, detector and feedback resistor impedances, and associated stray capacitances. Each detector noise current is multiplied by the transimpedance to arrive at the individual equivalent detector noise voltages at the output of the preamp. The total noise voltage is then the RSS of the individual detector noises and the preamp output noise.

PV InSb DETECTORS

Detector Diode Characteristics

Channels 18 through 28 of the AMTS Baseline V instrument utilize a single detector material, PV InSb, to cover the short wavelength band from 5.18 to 3.72 μm. The InSb detector is a diode structure with a bandgap and cutoff wavelength that is totally temperature dependent. At an operating temperature of 75 K, the cut-off wavelength is 5.45 μm. Again, the peak wavenumber was very conservatively put at a wavelength that is 10% shorter than the cut-off wavelength. With a quantum efficiency of 0.80, the peak should lie much closer to cutoff. Cincinnati Electronics has quoted quantum efficiencies of 0.80 and greater.

Typically a high impedance device, the InSb detector's so-called dark resistance at zero bias, R_O, can be altered by a suitable dopant. The Baseline V detectors were modelled as p-type semiconductors with p-type acceptor and n-type donor dopants added in concentrations of 1×10^{17} and 5×10^{14} cm^{-3}, respectively. These values are probably readily available using present liquid phase epitaxy (LPE) or molecular beam epitaxy (MBE) techniques. Good numbers for the carrier mobilities and lifetimes are difficult to obtain. Carrier mobilities of 80000 and 5000 $cm^2/V/s$ for electrons and holes, respectively, and lifetimes of 5×10^{-7} s were used in the modelling. The dark resistance is calculated from these parameters, but the calculated values are much too high to represent the true dark resistance at zero bias of a real-world diode. Most typically quoted resistance values, in terms of the product of the dark resistance at zero bias and detector area ($R_O \cdot A$), are in the range of 1 to 2×10^8 $ohm \cdot cm^2$ at 77 K. This indicates that there is a form of parallel leakage resistance that has to be accounted for in the model. Actual dark resistance must be inferred from the measurement of the current-voltage diode characteristics at operating temperatures. However, diode leakage current measurements made on Cincinnati Electronics InSb diodes imply that dark, zero-biased

resistivities can be one to two magnitudes higher. Since the methodology of these measurements was not established, the lower values of $R_o \cdot A$ were used. To accomplish this, a shunt $R_o \cdot A$ factor 1×10^6 ohm$\cdot$cm^2 was artificially added in parallel to the calculated $R_o \cdot A$ product values in the model.

The model calculates the impedances and relative phase angles of the detector and feedback loop. Measurements taken on the NIMS InSb detectors, indicated the presence of a shunt capacitance of a few picofarads. A ballpark value of 6.0 pF was added to the calculated AMTS detector capacitances. Total capacitance estimates are well within the ranges noted for the NIMS detectors.

PV InSb Detector and Preamplifier Noises

Photovoltaic detectors exhibit three principle types of noise. These include:

- Thermally-generated noise (Johnson noise)
- Current-generated noise (G-R noise)
- Photoinduced carrier noise (Background noise)

When operated under a zero-biased condition, as is the case in the Baseline V design, the first two forms of noise are identical, so that the sum of the two equations equals the familiar Johnson noise equation used in the photoconductors. Photoinduced noise is the same as the background noise found in the photoconductors with two exceptions: the gain is unity and the noise is less by a factor of $\sqrt{2}$.

The preamplifier type used in modelling is a differential transimpedance amplifier (TIA), utilizing an operational amplifier (OA) with resistive feedback. Each of the detector/preamp noise components is individually passed through the TIA and expressed as TIA-modified equivalent components. The transimpedance equation used to modify the noises is a function of the detector and feedback resistor impedances and the RC time constants associated with stray circuit capacitances. Stray capacitance was set at 0.3 pF. The feedback resistor value was set at 1×10^9 ohm for channels 18 through 28.

PV HgCdTe DETECTORS

PV HgCdTe detectors cover the middle range of AMTS wavelengths (9.6 to 5.4 μm). Like the PC HgCdTe detectors, bandgap energy and cut-off wavelength depend on the mole fraction and the temperature of the material. The PV HgCdTe detector material parameters are given in Table F-1. Quantum efficiency for these detectors was set at 0.75.

Baseline V PV HgCdTe detectors are n-type, with p-type acceptor and n-type donor dopant concentrations listed in Table F-3. The calculated dark resistance is too large so, like in the InSb model, a shunt $R_o \cdot A$ factor of $\approx 10^4$ ohm$\cdot$cm^2 and a shunt capacitance of 6 pF are added.

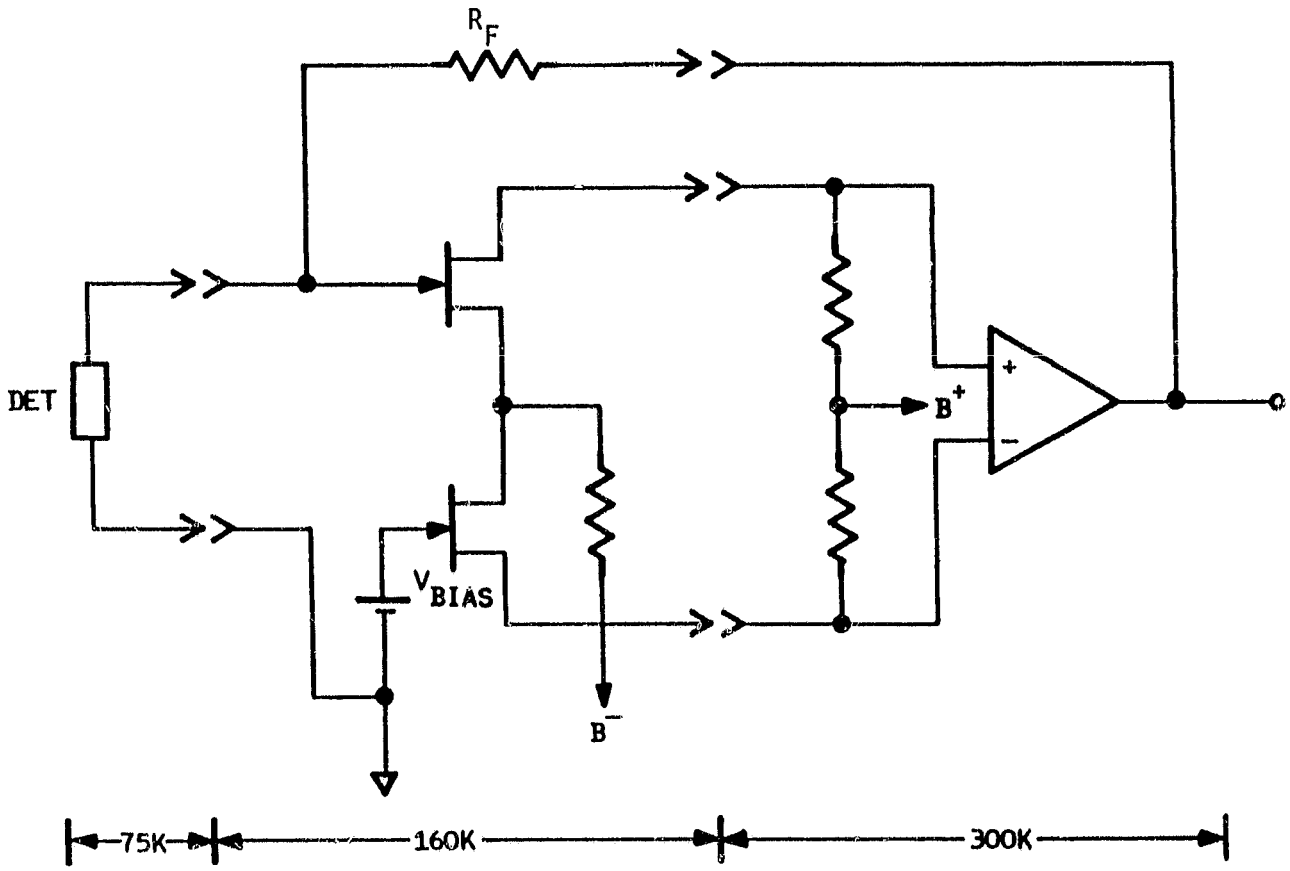

Figure F-1 Functional schematic of differential transimpedance amplifier

PV HgCdTe Detector and Preamplific Noises

These photovoltaic detectors exhibit the same noises as InSb detectors:

- Thermally-generated noise
- Current-generated noise
- Photoinduced carrier noise

The PV HgCdTe model treats these noises in exactly the same manner as the InSb model. The preamp is once again a differential transimpedance amplifier.

BACKGROUND PHOTON FLUX DENSITIES

Background scene and instrument photon fluxes dramatically affect the performance of the PV InSb and PV HgCdTe detectors and, to a very limited extent, the PC HgCdTe detectors. Including the scene, each and every optical or structural surface that lies within the optical path or that can be "seen" by the detector is a source of background photon-induced noise. Photon flux density is defined as the quantity of photon flux:

- Emitted by a surface at some given temperature.
- Having a given emissivity.
- Within a given optical bandwidth.
- Contained within a given $A\Omega$.
- Reduced by the optical transmission losses of the intervening optical surfaces.
- Falling upon a given detector area.

The background photon fluxes reaching the detector can be divided into three optical bands. These bands and their associated groups of surfaces are:

- Channel half-power bandwidth: scene and all optical surfaces up to the inlet slit.
- Order filter half-power bandwidth: all optical surfaces from the inlet slit to the order filters.
- Detector band of photosensitivity (from 1 μm to cutoff): the "dewar surround" which includes each channel order filter, field lens, and dewar.

Starting from the scene, the irradiance produced by each surface is found from the Planck equations at the surface temperature. The following points should be noted:

- It is assumed that each surface, including the scene, is a Lambertian radiator.
- The scene temperatures are T_{min}, T_{std}, and T_{max}.
- The scan mirror, telescope, and spectrometer optics are at the case temperature.
- The total irradiance within an optical band is constant over that band, except for the irradiance within the detector dewar which is integrated over the portion of the Planck curve from the detector cutoff wavelength to 1 μm.
- It is assumed that the chopper is fully open; therefore, no chopper factor is included.
- For the scene and for all surfaces ahead of the inlet slit, photon flux is calculated within the signal area-solid angle product of the instrument, $A\Omega_\alpha$.
- For surfaces interim to the inlet slit and ahead of the exit slit, photon flux is calculated within an area-solid angle product $A\Omega_\beta = A\Omega_\alpha F_s$, where F_s is the ratio of the exit slit width to the inlet slit image width.
- For unfocused flux within the dewar, photon flux is considered to be the unimmersed detector area time Pi.

PC HgCdTe DETECTOR PERFORMANCE MODEL

The bandgap energy of a PC HgCdTe detector depends on the relative proportions of HgTe and CdTe in the detector alloy. Photons with energies greater than or equal to the bandgap energy will allow an electron or hole to leave the valence band and enter the conduction band (i.e., ionize). The minimum photon energy required to photoionize the material is described by the cutoff wavelength.

$$\lambda_c = \frac{10^4\ hc}{q\ Eg} \quad \text{or} \quad \upsilon_c = \frac{q\ Eg}{hc} \qquad (1)$$

where

c = speed of light (cm/s)

Eg = bandgap energy (eV)

h = Planck's constant (J•s)

q = electron charge (A•s)

λ_c = cutoff wavelength (μm)

υ_c = cutoff wavenumber (cm^{-1})

The bandgap energy for HgCdTe has been empirically determined to be

$$Eg = 0.327x^3 + 1.59x - 0.00109xT + 0.000523T - 0.25 \qquad (2)$$

where

x = mole fraction (CdTe: (CdTe + HgTe))

T = temperature of detector (K)

In the absence of light, the number of electrons and holes available in the valence and conduction bands (the intrinsic carrier concentration) is empirically determined by

$$n_i = (8.46 - 2.29x + 0.00342T)10^{14}\ Eg^{3/4}\ T^{3/2}\ e^{-Eg/2K_bT} \qquad (3)$$

where

K_b = Boltzmann's constant (eV/K)

n_i = intrinsic carrier concentration (cm^{-3})

In its natural intrinsic state, HgCdTe is a p-type material whereby holes are the majority carrier. Electrons have a much greater mobility than holes, so HgCdTe is usually doped to a n-type material (electron majority carrier) to lower the overall resistivity of the material. The concentration of donor (electron) carriers is then

$$N_D = \frac{n_i^2}{P_o} \qquad (4)$$

where

N_D = concentration of donors (cm^{-3})

P_o = hole concentration (cm^{-3})

Responsivity Development

Naturally occuring p-type impurities place a lower limit on the number of hole (minority carriers) found in n-type doped material. This lower limit is usually within two orders of magnitude of the hole concentration found in undoped intrinsic material. The detector dark conductivity is

$$\sigma = q\ (N_D\ \mu + P_o\ \mu_h) \qquad (5)$$

where

σ = detector dark conductivity $((\Omega \cdot cm)^{-1})$

μ = electron mobility $(cm^2/V/s)$

μ_h = hole mobility $(cm^2/V/s)$

The detector dark resistance is

$$R_d = W/(\sigma H t) \tag{6}$$

where

R_d = detector dark resistance (Ω)

H = detector height (cm)

t = detector thickness (cm)

W = detector width between terminals (cm)

The load or feedback resistor is set at a value 10 times the dark resistor,

$$R_F = 10\ R_d \tag{7}$$

where

R_F = feedback resistance (Ω)

A transimpedance amplifier is used as the preamp in the AMTS baseline V configuration. The transimpedance is

$$A_z = \frac{R_F}{(1 + F_o\ R_F\ C_F) - \frac{R_F}{A_o\ R_d}(1 + F_o\ R_d\ C_d)} \tag{8}$$

where

$F_o = 2\pi F_c = 2\pi \cdot$ chopping frequency (Hz)

A_z = transimpedance (Ω)

C_F = capacitance of feedback resistor (F)

A_o = open loop gain of preamplifier

C_d = capacitance of detector (F)

The supply voltage to the feedback resistor and detector is

$$V_s = V_b \frac{R_d + R_F}{R_d} \tag{9}$$

where

V_s = supply voltage (V)

V_b = bias voltage across detector (V)

The responsivity of the detector/preamp at the output of the preamp can be calculated from

$$R = \frac{V_s R_F R_d A_z q \mu \tau \eta F_k}{(R_F + R_d)^2 W^2 h c \nu_p} \tag{10}$$

where

R = responsivity at the output of the preamp (V/W)

τ = carrier lifetime (s)

η = quantum efficiency

$F_k = [1 + (F_o \gamma)^2]^{1/2}$

ν_p = peak wavenumber (cm^{-1})

The responsivity at the output of the detector is

$$RE = \frac{R R_d}{A_z} \tag{11}$$

Detector Noise Development

There are four types of detector noise in PC HgCdTe detectors. These noise components are calculated as currents in units of $A/\sqrt{Hz}$:

Background noise

$$I_{BG} = [4(q G)^2 \eta Q_{BG} H W]^{1/2} \tag{12}$$

Johnson noise

$$I_{JN} = (4KT/R_d)^{1/2} \tag{13}$$

Generation-recombination noise

$$I_{GR} = [4(q\ G)^2\ P_o\ t\ H\ W/\tau]^{1/2} \quad (14)$$

Feedback resistor Johnson noise

$$I_{JNfb} = (4K\ T_{RF}/R_F)^{1/2} \quad (15)$$

where

$G = V_b\ (\mu + \mu_h)\ \tau/W^2$ = photoconductive gain

K = Boltzmann's constant (J/K)

T_{RF} = feedback resistor temperature (K)

Q_{BG} = total background photon flux density (photons/cm^2/s)

Each noise current is then multiplied by the transimpedance to get the noise voltage in V/$\sqrt{\text{Hz}}$ at the output of the preamp or

$$V_{BG} = I_{BG}\ A_Z \quad (16)$$

$$V_{JN} = I_{JN}\ A_Z \quad (17)$$

$$V_{GR} = I_{GR}\ A_Z \quad (18)$$

$$V_{JNfb} = I_{JNfb}\ A_Z \quad (19)$$

Preamplifier Noise Development

Modeling the detector as a parallel resistor and capacitor, the detector impedance magnitude, phase angle, and real impedance component are

$$|Z| = \frac{R_d}{(1 + F_o\ R_d\ C_d)} \quad (20)$$

where

$|Z|$ = impedance magnitude (Ω)

C_d = detector capacitance (F)

The detector phase angle (in radians) is

$$\phi = \tan^{-1} \frac{F_o\ C_d}{R_d} \quad (21)$$

The real component of Z (in ohms) is

$$\mathrm{Re}\,(Z) = |Z| \cos \phi \tag{22}$$

Similarly, the feedback resistor impedance magnitude, phase angle, and real impedance component can be calculated by substituting R_F and C_F into Eq 20, 21 and 22.

The preamp output noise voltage is

$$V_{PA} = V_P \frac{Z_F}{Z} \frac{A_O Z}{Z (1 + A_O) + Z_F} \tag{23}$$

where

V_{PA} = output preamp noise voltage ($V/\sqrt{Hz}$)

V_P = preamp noise voltage ($V/\sqrt{Hz}$

Z = real detector impedance component (Ω)

Z_F = real feedback resistor impedance component (Ω)

D* Development

The total noise voltage ($V/\sqrt{Hz}$) at the output of the preamp is the RSS value of the individual noise components.

$$V_T = \left(V_{BG}^2 + V_{JN}^2 + V_{GR}^2 + V_{JNfb}^2 + V_{PA}^2 \right)^{1/2} \tag{24}$$

The noise equivalent power is then

$$NEP = V_T/R \tag{25}$$

and D* peak in units of cm $\sqrt{Hz}/W$ is

$$D^* = \sqrt{WH}/NEP \tag{26}$$

Signal output voltage is

$$V_O = R\, Q_S\, H\, W\, h\, c\, G\, \nu_p \tag{27}$$

where

V_O = signal photovoltage ($V/\sqrt{Hz}$)

Q_S = signal photon flux density (photons/cm^2/s)

Signal-to-noise ratio is

$$SNR = \frac{V_O}{V_T\, \Delta f} \tag{28}$$

where

Δf = noise power (electrical) bandwidth (Hz)

Detector Joule heat in watts is

$$P_w = V_b^2/R_d \tag{29}$$

Load resistor Joule heat in (w) is

$$P_{RF} = (V_s - V_b)^2/R_F \tag{30}$$

PV HgCdTe AND PV InSb DETECTOR PERFORMANCE MODELS

The PV HgCdTe and PV InSb detector models are very similar. The bandgap energy in both models is calculated from Eq 1. λ_c for HgCdTe is calculated using Eq 1 and 2. The intrinsic carrier concentration for the PV HgCdTe model is calculated from Eq 2 and 3 while the intrinsic carrier concentration for PV InSb is

$$n_i = \left[4\left(\frac{2\pi KT}{h^2}\right)^3 (m_e\, m_h)^{3/2}\ e^{-Eg/K_bT} \right]^{1/2} \tag{31}$$

where

$m_e = 1.366 \times 10^{-32}$ (kg) = reduced electron mass

$m_h = 3.5516 \times 10^{-31}$ (kg) = reduced hole mass

In form, the two models now proceed identically. Photovoltaic detectors are photodiodes. A diode junction is created in the material by doping one side of the material with a p-type dopant and the other side with a n-type dopant. The concentration of electrons on the p-type side of the diode, given a doping of N_A acceptors, is

$$n_p = \frac{n_i^2}{N_A} \tag{32}$$

where

n_p = concentration of electrons on the p-type side (cm^{-3})

N_A = concentration of acceptors (holes) (cm^{-3})

Likewise, the concentration of holes on the n-type side of the diode, given a doping of N_D donors, is

$$P_n = \frac{n_i^2}{N_D} \tag{33}$$

where

p_n = concentration of holes on the n-type side (cm^{-3})

N_D = concentration of donors (cm^{-3})

Parameters which describe the behavior of electrons and holes within the junction are

$$D_e = \frac{KT\ \mu}{q} \tag{34}$$

$$L_e = (De\tau)^{1/2} \tag{35}$$

$$D_h = \frac{KT\ \mu_h}{q} \tag{36}$$

$$L_h = (D_h\ \tau)^{1/2} \tag{37}$$

where

D_e = electron diffusion constant (cm^2/s)

D_h = hole diffusion constant (cm^2/s)

L_e = electron diffusion length (cm)

L_h = hole diffusion length (cm)

Responsivity Development

The dark resistance times the area of the diode junction, $R_o{\cdot}A$, is often used to compare the performance of different detectors.

$$RA = \frac{K_b T}{q^2} \quad \frac{L_e\ L_h}{p_n\ D_h\ L_e + n_p\ D_e\ L_h} \tag{38}$$

and

$$R_o{\cdot}A = RA\ RS/(RA + RS) \tag{39}$$

where

RA = resistance area product excluding the effects of shunt resistance ($\Omega\ cm^2$)

RS = shunt resistance (Ω)

The junction capacitance can be derived from the following development:

Contact potential

$$V_c = \frac{KT}{q} \ln \frac{N_D N_A}{n_i^2} \tag{40}$$

Junction barrier potential

$$V_j = V_c - V_b \tag{41}$$

Space charge layer width

$$w_j = \left(\frac{2V_j \kappa \varepsilon_o}{q N_D} \right)^{1/2} \tag{42}$$

Junction capacitance

$$c_j = \frac{\kappa \varepsilon_o A_d}{w_j} \tag{43}$$

where

A_d = detector area (cm^2)

$\varepsilon_o = 8.85 \times 10^{-14}$ (F/cm) = permittivity of free space

κ = dielectric constant (HgCdTe or InSb)

V_c = contact potential (V)

V_j = junction barrier potential (V)

w_j = space charge layer width (cm)

C_j = junction capacitance (F)

This model assumes the use of transimpedance amplifiers as the preamplifiers for the system. The transimpedance of these amplifiers is

$$A_Z = \frac{R_F}{(1 + F_o R_F C_F) - \frac{R_F}{A_o R_o} (1 + F_o R_o C_o)} \tag{44}$$

where

$R_o = R_o \cdot A/A_d$ = detector dark resistance (Ω)

$C_o = C_j + C_s$ = detector capacitance (F)

C_s = stray capacitance (F)

The responsivity at the output of the TIA

$$R = \frac{q\eta A_z}{hc\ \nu_p} \tag{45}$$

where

R = responsivity (V/W)

Detector Noise Development

The PV detector noise components are presented as noise currents in units of $(A/\sqrt{Hz})$:

Johnson noise

$$I_{JN} = \left(\frac{2KT}{R_o}\right)^{1/2} \tag{46}$$

Generation-recombination noise

$$I_{GR} = \left(\frac{2KT}{R_o}\ e^{qV_b/KT}\right)^{1/2} \tag{47}$$

PV detectors are often operated at zero bias, $V_b = 0$. It is common practice to sum I_{JN} and I_{GR} and label the sum as Johnson noise.

Background noise

$$I_{BG} = \left(2\ q^2\ \eta\ \Omega_{BG}\ A_d\right)^{1/2} \tag{48}$$

Feedback resistor Johnson noise

$$I_{JNfb} = \left(\frac{4K\ T_{RF}}{R_F}\right)^{1/2} \tag{49}$$

These noise currents are converted to noise voltages at the output of the preamp by multiplying by the transimpedance:

$$V_{JN} = I_{JN}\ Az \tag{50}$$

$$V_{GR} = I_{GR}\ Az \tag{51}$$

$$V_{BG} = I_{BG}\, Az \tag{52}$$

$$V_{JNfb} = I_{JNfb}\, Az \tag{53}$$

All the noise voltages are in units of $V/\sqrt{Hz}$.

Preamplifier Noise Development

Since the same type of preamp is used in the PC HgCdTe model as in the PV HgCdTe and PV InSb models, the preamp noise is handled in the same way. The detector impedance magnitude, phase angle, and real impedance component are described by Eq (20-22). Substituting R_F for R_d and C_F for C_d in Eq (20-22) allows the calculation of feedback resistor impedance magnitude, phase angle, and real impedance component. Equation 23 describes the output preamp noise voltage in $V/\sqrt{Hz}$.

D* Development

The total noise voltage is

$$V_T = \left(V_{JN}^2 + V_{GR}^2 + V_{BG}^2 + V_{JNfb}^2 + V_{PA}^2\right)^{1/2} \tag{54}$$

The noise equivalent power is

$$NEP = \frac{V_T\, hc\, \nu_p}{q\eta A_z} \tag{55}$$

and D* peak in units of cm $\sqrt{Hz}/W$ is

$$D^* = \sqrt{A_d}/NEP \tag{56}$$

The output signal current is

$$I_s = q\, \eta\, Q_s\, A_d \tag{57}$$

where

I_s = signal photo current $(A/\sqrt{Hz})$

TRUE D*

Detector response is a function of wavelength. The math models above calculate D* as if the detector response were the same for all wavelengths. Figures F-2 and F-3 show the relative response of HgCdTe and InSb detectors vs wavenumber. These figures have been used for the Baseline V calculations to obtain true D* values.

C-5

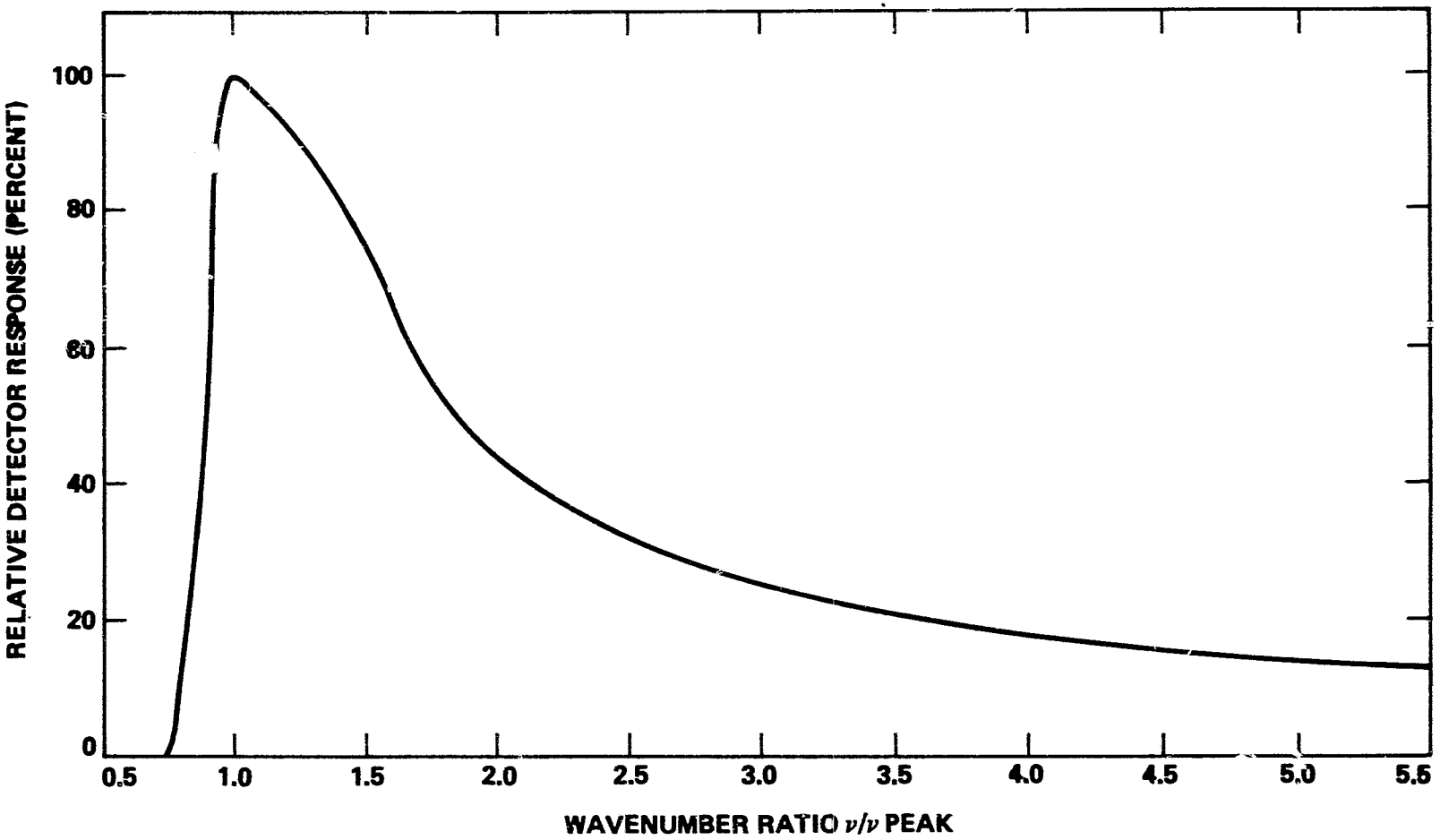

Figure F-2 HgCdTe detector response vs relative wavenumber

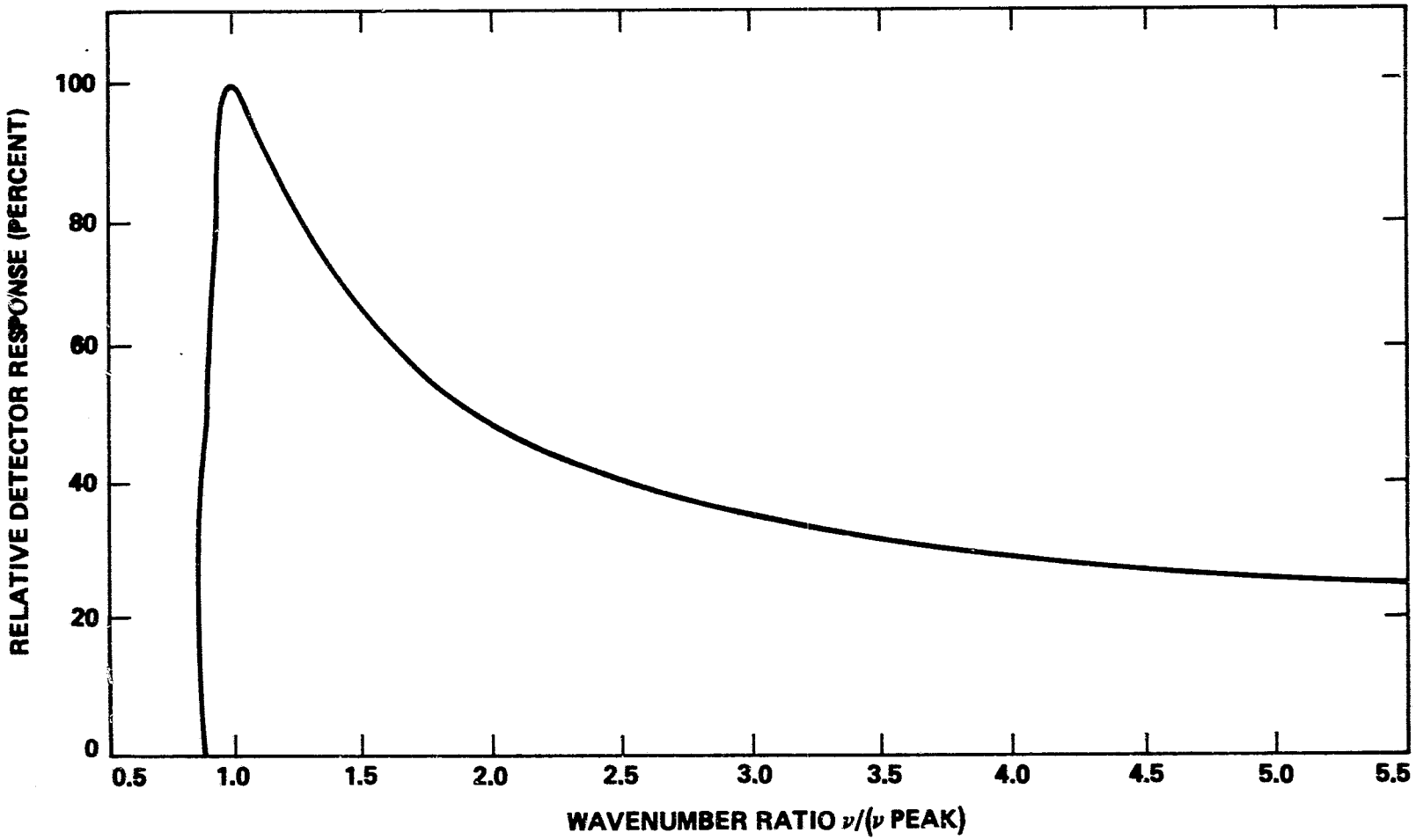

Figure F-3 InSb detector response vs relative wavenumber

MODEL RESULTS FOR BASELINE V DETECTOR PERFORMANCE

Table F-4 lists detector model parameters used for all channels, corresponding to min, std, and max scene temperatures, and used under Baseline V conditions.

Table F-5 lists photoconductive detector model parameters for channels 1, 10, and 11 as a function of detector bias potential.

Table F-6 lists detector model parameters for channels 1, 11, 12, 14, 16, 19, 25, and 28 for detector/case temperature combinations of 75 K/160 K, 75 K/180 K, 80 K/160 K, and 80 K/180 K, respectively.

Because of the variety and importance of the assumptions upon which baseline detector performance estimates are based, these model printouts are presented in their entirety. This material can provide a point of departure for future trade-offs and analysis or for preparation and negotiation of detector procurement performance specifications.

Table F-4. Detector performance for all channels under Baseline V conditions vs min, std, and max equivalent scene temperature

Table F-4 (CH 1)

PC HGCDTE DETECTOR PERFORMANCE CHANNEL 1 75/160/MIN 8 V/CM

CH = CHANNEL NUMBER	0.1000E+01
T = DET. TEMP	0.7500E+02
HD = DET. HEIGHT CM	0.1360E-01
WD = DET. WIDTH CM	0.1990E-01
TD = DETECTOR THICKNESS CM	0.1000E-02
VB = DETECTOR BIAS VOLTAGE V	0.1592E+00
CD = DETECTOR CAPACITANCE F	0.1500E-10
RD = DETECTOR DARK RESISTANCE OHM	0.3395E+03
ZD = DETECTOR IMPEDANCE OHM	0.3395E+03
PD = DETECTOR PHASE ANGLE RAD	0.1221E-09
X = MOLE FRACTION	0.1838E+00
PO = HOLE CONC. N-TYPE DOPING CM**-3	0.1000E+15
ND = DONAR CARRIER CONC. CM**-3	0.1305E+16
NI = INTRINSIC CARRIER CONC. CM**-3	0.3612E+15
TAU= CARRIER LIFETIME S	0.1000E-05
ETA= QUANTUM EFFICIENCY	0.7000E+00
NUP= PEAK WAVENUMBER 1/CM	0.6068E+03
EG = BAND GAP ENERGY EV	0.6847E-01
SIGMA = CONDUCTIVITY 1/OHM/CM	0.4310E+01
MU = ELECTRON MOBILITY CM**2/V/S	0.2060E+05
MUH= HOLE MOBILITY CM**2/V/S	0.2950E+03
QBG= BKGD PHOTON FLUX DENSITY P/CM**2/S	0.1310E+16
QS = SGNL PHOTON FLUX DENSITY P/CM**2/S	0.3220E+14
TRF= FEEDBACK RESISTOR TEMP. K	0.1600E+03
CF = FDBK RESISTOR CAPACITANCE F	0.3000E-12
RF = FEEDBACK RESISTANCE OHM	0.3395E+04
PF = FDBK RESISTOR PHASE ANGLE RAD	0.2443E-12
ZF = FDBK RESISTOR IMPEDANCE OHM	0.3395E+04
VS = SUPPLY VOLTAGE TO RF/DET. V	0.1751E+01
AO = OPEN LOOP GAIN	0.1000E+04
VP = PREAMP NOISE (INPUT) V/HZ**.5	0.2800E-08
FC = CHOPPING FREQUENCY HZ	0.4400E+03
PW = DETECTOR BIAS POWER W	0.7465E-04
PRF= FEEDBACK RESISTOR BIAS POWER W	0.7465E-03
SIGV = SIGNAL VOLTAGE V	0.2119E-03
RE = DET. RESPONSIVITY V/W	0.2379E+05
AZ = TRANSIMPEDANCE OHM	0.3429E+04
R = DET./PREAMP RESPONSIVITY V/W	0.2402E+06
VBG= BACKGROUND NOISE V/HZ**.5	0.4598E-08
VJN= JOHNSON NOISE V/HZ**.5	0.1198E-07
VGR= GR NOISE V/HZ**.5	0.4802E-07
VRF= FDBK RESISTOR NOISE V/HZ**.5	0.5532E-08
VPA= PREAMP NOISE V/HZ**.5	0.2770E-07
VT = TOTAL NOISE V/HZ**.5	0.5716E-07
NEP= NOISE EQUIVALENT POWER W/HZ**.5	0.2300E-12
DSTAR = PEAK DSTAR CM*HZ**.5/W	0.6912E+11

PC HGCDTE DETECTOR PERFORMANCE CHANNEL 1 75/160/STD 8 V/CM

CH = CHANNEL NUMBER	0.1000E+01
T = DET. TEMP	0.7500E+02
HD = DET. HEIGHT CM	0.1360E-01
WD = DET. WIDTH CM	0.1990E-01
TD = DETECTOR THICKNESS CM	0.1000E-02
VB = DETECTOR BIAS VOLTAGE V	0.1592E+00
CD = DETECTOR CAPACITANCE F	0.1500E-10
RD = DETECTOR DARK RESISTANCE OHM	0.3395E+03
ZD = DETECTOR IMPEDANCE OHM	0.3395E+03
PD = DETECTOR PHASE ANGLE RAD	0.1221E-09
X = MOLE FRACTION	0.1838E+00
PO = HOLE CONC. N-TYPE DOPING CM**-3	0.1000E+15
ND = DONAR CARRIER CONC. CM**-3	0.1305E+16
NI = INTRINSIC CARRIER CONC. CM**-3	0.3612E+15
TAU= CARRIER LIFETIME S	0.1000E-05
ETA= QUANTUM EFFICIENCY	0.7000E+00
NUP= PEAK WAVENUMBER 1/CM	0.6068E+03
EG = BAND GAP ENERGY EV	0.6847E-01
SIGMA = CONDUCTIVITY 1/OHM/CM	0.4310E+01
MU = ELECTRON MOBILITY CM**2/V/S	0.2060E+05
MUH= HOLE MOBILITY CM**2/V/S	0.2950E+03
QBG= BKGD PHOTON FLUX DENSITY P/CM**2/S	0.1340E+16
QS = SGNL PHOTON FLUX DENSITY P/CM**2/S	0.5300E+14
TRF= FEEDBACK RESISTOR TEMP. K	0.1600E+03
CF = FDBK RESISTOR CAPACITANCE F	0.3000E-12
RF = FEEDBACK RESISTANCE OHM	0.3395E+04
PF = FDBK RESISTOR PHASE ANGLE RAD	0.2443E-12
ZF = FDBK RESISTOR IMPEDANCE OHM	0.3395E+04
VS = SUPPLY VOLTAGE TO RF/DET. V	0.1751E+01
AO = OPEN LOOP GAIN	0.1000E+04
VP = PREAMP NOISE (INPUT) V/HZ**.5	0.2800E-08
FC = CHOPPING FREQUENCY HZ	0.4400E+03
PW = DETECTOR BIAS POWER W	0.7465E-04
PRF= FEEDBACK RESISTOR BIAS POWER W	0.7465E-03
SIGV = SIGNAL VOLTAGE V	0.3488E-03
RE = DET. RESPONSIVITY V/W	0.2378E+05
AZ = TRANSIMPEDANCE OHM	0.3429E+04
R = DET./PREAMP RESPONSIVITY V/W	0.2402E+06
VBG= BACKGROUND NOISE V/HZ**.5	0.4658E-08
VJN= JOHNSON NOISE V/HZ**.5	0.1198E-07
VGR= GR NOISE V/HZ**.5	0.4802E-07
VRF= FDBK RESISTOR JOHNSON NOISE V/HZ**.5	0.5532E-08
VPA= PREAMP NOISE V/HZ**.5	0.2770E-07
VT = TOTAL NOISE V/HZ**.5	0.5717E-07
NEP= NOISE EQUIVALENT POWER W/HZ**.5	0.2300E-12
DSTAR = PEAK DSTAR CM*HZ**.5/W	0.6912E+11

PC HGCDTE DETECTOR PERFORMANCE CHANNEL 1 75/160/MAX 8 V/CM

CH = CHANNEL NUMBER	0.1000E+01
T = DET. TEMP	0.7500E+02
HD = DET. HEIGHT CM	0.1360E-01
WD = DET. WIDTH CM	0.1990E-01
TD = DETECTOR THICKNESS CM	0.1000E-02
VB = DETECTOR BIAS VOLTAGE V	0.1592E+00
CD = DETECTOR CAPACITANCE F	0.1500E-10
RD = DETECTOR DARK RESISTANCE OHM	0.3395E+03
ZD = DETECTOR IMPEDANCE OHM	0.3395E+03
PD = DETECTOR PHASE ANGLE RAD	0.1221E-09
X = MOLE FRACTION	0.1838E+00
PO = HOLE CONC. N-TYPE DOPING CM**-3	0.1000E+15
ND = DONAR CARRIER CONC. CM**-3	0.1305E+16
NI = INTRINSIC CARRIER CONC. CM**-3	0.3612E+15
TAU= CARRIER LIFETIME S	0.1000E-05
ETA= QUANTUM EFFICIENCY	0.7000E+00
NUP= PEAK WAVENUMBER 1/CM	0.6068E+03
EG = BAND GAP ENERGY EV	0.6847E-01
SIGMA = CONDUCTIVITY 1/OHM/CM	0.4310E+01
MU = ELECTRON MOBILITY CM**2/V/S	0.2060E+05
MUH= HOLE MOBILITY CM**2/V/S	0.2950E+03
QBG= BKGD PHOTON FLUX DENSITY P/CM**2/S	0.1360E+16
QS = SGNL PHOTON FLUX DENSITY P/CM**2/S	0.6940E+14
TRF= FEEDBACK RESISTOR TEMP. K	0.1600E+03
CF = FDBK RESISTOR CAPACITANCE F	0.3000E-12
RF = FEEDBACK RESISTANCE OHM	0.3395E+04
PF = FDBK RESISTOR PHASE ANGLE RAD	0.2443E-12
ZF = FDBK RESISTOR IMPEDANCE OHM	0.3395E+04
VS = SUPPLY VOLTAGE TO RF/DET. V	0.1751E+01
AO = OPEN LOOP GAIN	0.1000E+04
VP = PREAMP NOISE (INPUT) V/HZ**.5	0.2800E-08
FC = CHOPPING FREQUENCY HZ	0.4400E+03
PW = DETECTOR BIAS POWER W	0.7465E-04
PRF= FEEDBACK RESISTOR BIAS POWER W	0.7465E-03
SIGV = SIGNAL VOLTAGE V	0.4568E-03
RE = DET. RESPONSIVITY V/W	0.2379E+05
AZ = TRANSIMPEDANCE OHM	0.3429E+04
R = DET./PREAMP RESPONSIVITY V/W	0.2402E+06
VBG= BACKGROUND NOISE V/HZ**.5	0.4658E-08
VJN= JOHNSON NOISE V/HZ**.5	0.1198E-07
VGR= GR NOISE V/HZ**.5	0.4802E-07
VRF= FDBK RESISTOR JOHNSON NOISE V/HZ**.5	0.5532E-08
VPA= PREAMP NOISE V/HZ**.5	0.2778E-07
VT = TOTAL NOISE V/HZ**.5	0.5717E-07
NEP= NOISE EQUIVALENT POWER W/HZ**.5	0.2300E-12
DSTAR = PEAK DSTAR CM*HZ**.5/W	0.6912E+11

Table F-4 (CH 2)

PC HGCDTE DETECTOR PERFORMANCE CHANNEL 2 75/160/MIN 8 V/CM		PC HGCDTE DETECTOR PERFORMANCE CHANNEL 2 75/160/STD 8 V/CM		PC HGCDTE DETECTOR PERFORMANCE CHANNEL 2 75/160/MAX 8 V/CM	
CH = CHANNEL NUMBER	0.2000E+01	CH = CHANNEL NUMBER	0.2000E+01	CH = CHANNEL NUMBER	0.2000E+01
T = DET. TEMP	0.7500E+02	T = DET. TEMP	0.7500E+02	T = DET. TEMP	0.7500E+02
HD = DET. HEIGHT CM	0.1360E-01	HD = DET. HEIGHT CM	0.1360E-01	HD = DET. HEIGHT CM	0.1360E-01
WD = DET. WIDTH CM	0.2310E-01	WD = DET. WIDTH CM	0.2310E-01	WD = DET. WIDTH CM	0.2310E-01
TD = DETECTOR THICKNESS CM	0.1000E-02	TD = DETECTOR THICKNESS CM	0.1000E-02	TD = DETECTOR THICKNESS CM	0.1000E-02
VB = DETECTOR BIAS VOLTAGE V	0.1848E+00	VB = DETECTOR BIAS VOLTAGE V	0.1848E+00	VB = DETECTOR BIAS VOLTAGE V	0.1848E+00
CD = DETECTOR CAPACITANCE F	0.1500E-10	CD = DETECTOR CAPACITANCE F	0.1500E-10	CD = DETECTOR CAPACITANCE F	0.1500E-10
RD = DETECTOR DARK RESISTANCE OHM	0.3941E+03	RD = DETECTOR DARK RESISTANCE OHM	0.3941E+03	RD = DETECTOR DARK RESISTANCE OHM	0.3941E+03
ZD = DETECTOR IMPEDANCE OHM	0.3941E+03	ZD = DETECTOR IMPEDANCE OHM	0.3941E+03	ZD = DETECTOR IMPEDANCE OHM	0.3941E+03
PD = DETECTOR PHASE ANGLE RAD	0.1052E-09	PD = DETECTOR PHASE ANGLE RAD	0.1052E-09	PD = DETECTOR PHASE ANGLE RAD	0.1052E-09
X = MOLE FRACTION	0.1838E+00	X = MOLE FRACTION	0.1838E+00	X = MOLE FRACTION	0.1838E+00
PO = HOLE CONC. N-TYPE DOPING CM**-3	0.1000E+15	PO = HOLE CONC. N-TYPE DOPING CM**-3	0.1000E+15	PO = HOLE CONC. N-TYPE DOPING CM**-3	0.1000E+15
ND = DONAR CARRIER CONC. CM**-3	0.1305E+16	ND = DONAR CARRIER CONC. CM**-3	0.1305E+16	ND = DONAR CARRIER CONC. CM**-3	0.1305E+16
NI = INTRINSIC CARRIER CONC. CM**-3	0.3612E+15	NI = INTRINSIC CARRIER CONC. CM**-3	0.3612E+15	NI = INTRINSIC CARRIER CONC. CM**-3	0.3612E+15
TAU= CARRIER LIFETIME S	0.1000E-05	TAU= CARRIER LIFETIME S	0.1000E-05	TAU= CARRIER LIFETIME S	0.1000E-05
ETA= QUANTUM EFFICIENCY	0.7000E+00	ETA= QUANTUM EFFICIENCY	0.7000E+00	ETA= QUANTUM EFFICIENCY	0.7000E+00
NUP= PEAK WAVENUMBER 1/CM	0.6068E+03	NUP= PEAK WAVENUMBER 1/CM	0.6068E+03	NUP= PEAK WAVENUMBER 1/CM	0.6068E+03
EG = BAND GAP ENERGY EV	0.6847E-01	EG = BAND GAP ENERGY EV	0.6847E-01	EG = BAND GAP ENERGY EV	0.6847E-01
SIGMA = CONDUCTIVITY 1/OHM/CM	0.4310E+01	SIGMA = CONDUCTIVITY 1/OHM/CM	0.4310E+01	SIGMA = CONDUCTIVITY 1/OHM/CM	0.4310E+01
MU = ELECTRON MOBILITY CM**2/V/S	0.2060E+05	MU = ELECTRON MOBILITY CM**2/V/S	0.2060E+05	MU = ELECTRON MOBILITY CM**2/V/S	0.2060E+05
MUH= HOLE MOBILITY CM**2/V/S	0.2950E+03	MUH= HOLE MOBILITY CM**2/V/S	0.2950E+03	MUH= HOLE MOBILITY CM**2/V/S	0.2950E+03
QBG= BKGD PHOTON FLUX DENSITY P/CM**2/S	0.1840E+16	QBG= BKGD PHOTON FLUX DENSITY P/CM**2/S	0.1050E+16	QBG= BKGD PHOTON FLUX DENSITY P/CM**2/S	0.1070E+16
QS = SGNL PHOTON FLUX DENSITY P/CM**2/S	0.2480E+14	QS = SGNL PHOTON FLUX DENSITY P/CM**2/S	0.4020E+14	QS = SGNL PHOTON FLUX DENSITY P/CM**2/S	0.5370E+14
TRF= FEEDBACK RESISTOR TEMP. K	0.1600E+03	TRF= FEEDBACK RESISTOR TEMP. K	0.1600E+03	TRF= FEEDBACK RESISTOR TEMP. K	0.1600E+03
CF = FDBK RESISTOR CAPACITANCE F	0.3000E-12	CF = FDBK RESISTOR CAPACITANCE F	0.3000E-12	CF = FDBK RESISTOR CAPACITANCE F	0.3000E-12
RF = FEEDBACK RESISTANCE OHM	0.3941E+04	RF = FEEDBACK RESISTANCE OHM	0.3941E+04	RF = FEEDBACK RESISTANCE OHM	0.3941E+04
PF = FDBK RESISTOR PHASE ANGLE RAD	0.2104E-12	PF = FDBK RESISTOR PHASE ANGLE RAD	0.2104E-12	PF = FDBK RESISTOR PHASE ANGLE RAD	0.2104E-12
ZF = FDBK RESISTOR IMPEDANCE OHM	0.3941E+04	ZF = FDBK RESISTOR IMPEDANCE OHM	0.3941E+04	ZF = FDBK RESISTOR IMPEDANCE OHM	0.3941E+04
VS = SUPPLY VOLTAGE TO RF/DET. V	0.2833E+01	VS = SUPPLY VOLTAGE TO RF/DET. V	0.2833E+01	VS = SUPPLY VOLTAGE TO RF/DET. V	0.2833E+01
AO = OPEN LOOP GAIN	0.1000E+04	AO = OPEN LOOP GAIN	0.1000E+04	AO = OPEN LOOP GAIN	0.1000E+04
VP = PREAMP NOISE (INPUT) V/HZ**.5	0.2000E-08	VP = PREAMP NOISE (INPUT) V/HZ**.5	0.2000E-08	VP = PREAMP NOISE (INPUT) V/HZ**.5	0.2000E-08
FC = CHOPPING FREQUENCY HZ	0.4400E+03	FC = CHOPPING FREQUENCY HZ	0.4400E+03	FC = CHOPPING FREQUENCY HZ	0.4400E+03
PW = DETECTOR BIAS POWER W	0.8666E-04	PW = DETECTOR BIAS POWER W	0.8666E-04	PW = DETECTOR BIAS POWER W	0.8666E-04
PRF= FEEDBACK RESISTOR BIAS POWER W	0.8666E-03	PRF= FEEDBACK RESISTOR BIAS POWER W	0.8666E-03	PRF= FEEDBACK RESISTOR BIAS POWER W	0.8666E-03
SIGV = SIGNAL VOLTAGE V	0.1632E-03	SIGV = SIGNAL VOLTAGE V	0.2646E-03	SIGV = SIGNAL VOLTAGE V	0.3535E-03
RE = DET. RESPONSIVITY V/W	0.2378E+05	RE = DET. RESPONSIVITY V/W	0.2378E+05	RE = DET. RESPONSIVITY V/W	0.2378E+05
AZ = TRANSIMPEDANCE OHM	0.3981E+04	AZ = TRANSIMPEDANCE OHM	0.3981E+04	AZ = TRANSIMPEDANCE OHM	0.3981E+04
R = DET./PREAMP RESPONSIVITY V/W	0.2402E+06	R = DET./PREAMP RESPONSIVITY V/W	0.2402E+06	R = DET./PREAMP RESPONSIVITY V/W	0.2402E+06
VBG= BACKGROUND NOISE V/HZ**.5	0.4414E-08	VBG= BACKGROUND NOISE V/HZ**.5	0.4435E-08	VBG= BACKGROUND NOISE V/HZ**.5	0.4477E-08
VJN= JOHNSON NOISE V/HZ**.5	0.1291E-07	VJN= JOHNSON NOISE V/HZ**.5	0.1291E-07	VJN= JOHNSON NOISE V/HZ**.5	0.1291E-07
VGR= GR NOISE V/HZ**.5	0.5173E-07	VGR= GR NOISE V/HZ**.5	0.5173E-07	VGR= GR NOISE V/HZ**.5	0.5173E-07
VRF= FDBK RESISTOR JOHNSON NOISE V/HZ**.5	0.5961E-08	VRF= FDBK RESISTOR JOHNSON NOISE V/HZ**.5	0.5961E-08	VRF= FDBK RESISTOR JOHNSON NOISE V/HZ**.5	0.5961E-08
VPA= PREAMP NOISE V/HZ**.5	0.2770E-07	VPA= PREAMP NOISE V/HZ**.5	0.2770E-07	VPA= PREAMP NOISE V/HZ**.5	0.2770E-07
VT = TOTAL NOISE V/HZ**.5	0.6054E-07	VT = TOTAL NOISE V/HZ**.5	0.6054E-07	VT = TOTAL NOISE V/HZ**.5	0.6054E-07
NEP= NOISE EQUIVALENT POWER W/HZ**.5	0.2520E-12	NEP= NOISE EQUIVALENT POWER W/HZ**.5	0.2520E-12	NEP= NOISE EQUIVALENT POWER W/HZ**.5	0.2521E-12
DSTAR = PEAK DSTAR CM*HZ**.5/W	0.7032E+11	DSTAR = PEAK DSTAR CM*HZ**.5/W	0.7032E+11	DSTAR = PEAK DSTAR CM*HZ**.5/W	0.7032E+11

Table F-4 (CH 3)

PC HGCDTE DETECTOR PERFORMANCE CHANNEL 3 75/160/MIN 8 V/CM

CH = CHANNEL NUMBER	0.3000E+01
T = DET. TEMP	0.7500E+02
HD = DET. HEIGHT CM	0.1360E-01
WD = DET. WIDTH CM	0.2390E-01
TD = DETECTOR THICKNESS CM	0.1000E-02
VB = DETECTOR BIAS VOLTAGE V	0.1912E+00
CD = DETECTOR CAPACITANCE F	0.1500E-10
RD = DETECTOR DARK RESISTANCE OHM	0.4078E+03
ZD = DETECTOR IMPEDANCE OHM	0.4077E+03
PD = DETECTOR PHASE ANGLE RAD	0.1017E-09
X = MOLE FRACTION	0.1838E+00
PO = HOLE CONC. N-TYPE DOPING CM**-3	0.1000E+15
ND = DONAR CARRIER CONC. CM**-3	0.1305E+16
NI = INTRINSIC CARRIER CONC. CM**-3	0.3612E+15
TAU= CARRIER LIFETIME S	0.1000E-05
ETA= QUANTUM EFFICIENCY	0.7000E+00
NUP= PEAK WAVENUMBER 1/CM	0.6068E+03
EG = BAND GAP ENERGY EV	0.6847E-01
SIGMA = CONDUCTIVITY 1/OHM/CM	0.4318E+01
MU = ELECTRON MOBILITY CM**2/V/S	0.2060E+05
MUH= HOLE MOBILITY CM**2/V/S	0.2950E+03
QBG= BKGD PHOTON FLUX DENSITY P/CM**2/S	0.9900E+15
QS = SGNL PHOTON FLUX DENSITY P/CM**2/S	0.1940E+14
TRF= FEEDBACK RESISTOR TEMP. K	0.1600E+03
CF = FDBK RESISTOR CAPACITANCE F	0.3000E-12
RF = FEEDBACK RESISTANCE OHM	0.4078E+04
PF = FDBK RESISTOR PHASE ANGLE RAD	0.2034E-12
ZF = FDBK RESISTOR IMPEDANCE OHM	0.4077E+04
VS = SUPPLY VOLTAGE TO RF/DET. V	0.2183E+01
AO = OPEN LOOP GAIN	0.1000E+04
VP = PREAMP NOISE (INPUT) V/HZ**.5	0.2900E-08
FC = CHOPPING FREQUENCY HZ	0.4400E+03
PW = DETECTOR BIAS POWER W	0.8966E-04
PRF= FEEDBACK RESISTOR BIAS POWER W	0.8966E-03
SIGV = SIGNAL VOLTAGE V	0.1277E-03
RE = DET. RESPONSIVITY V/W	0.2378E+05
AZ = TRANSIMPEDANCE OHM	0.4119E+04
R = DET./PREAMP RESPONSIVITY V/W	0.2402E+06
VBG= BACKGROUND NOISE V/HZ**.5	0.4358E-08
VJN= JOHNSON NOISE V/HZ**.5	0.1313E-07
VGR= GR NOISE V/HZ**.5	0.5262E-07
VRF= FDBK RESISTOR NOISE V/HZ**.5	0.6063E-08
VPA= PREAMP NOISE V/HZ**.5	0.2770E-07
VT = TOTAL NOISE V/HZ**.5	0.6135E-07
NEP= NOISE EQUIVALENT POWER W/HZ**.5	0.2554E-12
DSTAR = PEAK DSTAR CM*HZ**.5/W	0.7858E+11

PC HGCDTE DETECTOR PERFORMANCE CHANNEL 3 75/160/STD 8 V/CM

CH = CHANNEL NUMBER	0.3000E+01
T = DET. TEMP	0.7500E+02
HD = DET. HEIGHT CM	0.1360E-01
WD = DET. WIDTH CM	0.2390E-01
TD = DETECTOR THICKNESS CM	0.1000E-02
VB = DETECTOR BIAS VOLTAGE V	0.1912E+00
CD = DETECTOR CAPACITANCE F	0.1500E-10
RD = DETECTOR DARK RESISTANCE OHM	0.4078E+03
ZD = DETECTOR IMPEDANCE OHM	0.4077E+03
PD = DETECTOR PHASE ANGLE RAD	0.1017E-09
X = MOLE FRACTION	0.1838E+00
PO = HOLE CONC. N-TYPE DOPING CM**-3	0.1000E+15
ND = DONAR CARRIER CONC. CM**-3	0.1305E+16
NI = INTRINSIC CARRIER CONC. CM**-3	0.3612E+15
TAU= CARRIER LIFETIME S	0.1000E-05
ETA= QUANTUM EFFICIENCY	0.7000E+00
NUP= PEAK WAVENUMBER 1/CM	0.6068E+03
EG = BAND GAP ENERGY EV	0.6847E-01
SIGMA = CONDUCTIVITY 1/OHM/CM	0.4318E+01
MU = ELECTRON MOBILITY CM**2/V/S	0.2060E+05
MUH= HOLE MOBILITY CM**2/V/S	0.2950E+03
QBG= BKGD PHOTON FLUX DENSITY P/CM**2/S	0.9970E+15
QS = SGNL PHOTON FLUX DENSITY P/CM**2/S	0.2690E+14
TRF= FEEDBACK RESISTOR TEMP. K	0.1600E+03
CF = FDBK RESISTOR CAPACITANCE F	0.3000E-12
RF = FEEDBACK RESISTANCE OHM	0.4078E+04
PF = FDBK RESISTOR PHASE ANGLE RAD	0.2034E-12
ZF = FDBK RESISTOR IMPEDANCE OHM	0.4077E+04
VS = SUPPLY VOLTAGE TO RF/DET. V	0.2183E+01
AO = OPEN LOOP GAIN	0.1000E+04
VP = PREAMP NOISE (INPUT) V/HZ**.5	0.2900E-08
FC = CHOPPING FREQUENCY HZ	0.4400E+03
PW = DETECTOR BIAS POWER W	0.8966E-04
PRF= FEEDBACK RESISTOR BIAS POWER W	0.8966E-03
SIGV = SIGNAL VOLTAGE V	0.1771E-03
RE = DET. RESPONSIVITY V/W	0.2378E+05
AZ = TRANSIMPEDANCE OHM	0.4119E+04
R = DET./PREAMP RESPONSIVITY V/W	0.2402E+06
VBG= BACKGROUND NOISE V/HZ**.5	0.4396E-08
VJN= JOHNSON NOISE V/HZ**.5	0.1313E-07
VGR= GR NOISE V/HZ**.5	0.5262E-07
VRF= FDBK RESISTOR JOHNSON NOISE V/HZ**.5	0.6063E-08
VPA= PREAMP NOISE V/HZ**.5	0.2770E-07
VT = TOTAL NOISE V/HZ**.5	0.6135E-07
NEP= NOISE EQUIVALENT POWER W/HZ**.5	0.2554E-12
DSTAR = PEAK DSTAR CM*HZ**.5/W	0.7858E+11

PC HGCDTE DETECTOR PERFORMANCE CHANNEL 3 75/160/MAX 8 V/CM

CH = CHANNEL NUMBER	0.3000E+01
T = DET. TEMP	0.7500E+02
HD = DET. HEIGHT CM	0.1360E-01
WD = DET. WIDTH CM	0.2390E-01
TD = DETECTOR THICKNESS CM	0.1000E-02
VB = DETECTOR BIAS VOLTAGE V	0.1912E+00
CD = DETECTOR CAPACITANCE F	0.1500E-10
RD = DETECTOR DARK RESISTANCE OHM	0.4078E+03
ZD = DETECTOR IMPEDANCE OHM	0.4077E+03
PD = DETECTOR PHASE ANGLE RAD	0.1017E-09
X = MOLE FRACTION	0.1838E+00
PO = HOLE CONC. N-TYPE DOPING CM**-3	0.1000E+15
ND = DONAR CARRIER CONC. CM**-3	0.1305E+16
NI = INTRINSIC CARRIER CONC. CM**-3	0.3612E+15
TAU= CARRIER LIFETIME S	0.1000E-05
ETA= QUANTUM EFFICIENCY	0.7000E+00
NUP= PEAK WAVENUMBER 1/CM	0.6068E+03
EG = BAND GAP ENERGY EV	0.6847E-01
SIGMA = CONDUCTIVITY 1/OHM/CM	0.4318E+01
MU = ELECTRON MOBILITY CM**2/V/S	0.2060E+05
MUH= HOLE MOBILITY CM**2/V/S	0.2950E+03
QBG= BKGD PHOTON FLUX DENSITY P/CM**2/S	0.9970E+15
QS = SGNL PHOTON FLUX DENSITY P/CM**2/S	0.3840E+14
TRF= FEEDBACK RESISTOR TEMP. K	0.1600E+03
CF = FDBK RESISTOR CAPACITANCE F	0.3000E-12
RF = FEEDBACK RESISTANCE OHM	0.4078E+04
PF = FDBK RESISTOR PHASE ANGLE RAD	0.2034E-12
ZF = FDBK RESISTOR IMPEDANCE OHM	0.4077E+04
VS = SUPPLY VOLTAGE TO RF/DET. V	0.2183E+01
AO = OPEN LOOP GAIN	0.1000E+04
VP = PREAMP NOISE (INPUT) V/HZ**.5	0.2900E-08
FC = CHOPPING FREQUENCY HZ	0.4400E+03
PW = DETECTOR BIAS POWER W	0.8966E-04
PRF= FEEDBACK RESISTOR BIAS POWER W	0.8966E-03
SIGV = SIGNAL VOLTAGE V	0.2527E-03
RE = DET. RESPONSIVITY V/W	0.2378E+05
AZ = TRANSIMPEDANCE OHM	0.4119E+04
R = DET./PREAMP RESPONSIVITY V/W	0.2402E+06
VBG= BACKGROUND NOISE V/HZ**.5	0.4396E-08
VJN= JOHNSON NOISE V/HZ**.5	0.1313E-07
VGR= GR NOISE V/HZ**.5	0.5262E-07
VRF= FDBK RESISTOR NOISE V/HZ**.5	0.6063E-08
VPA= PREAMP NOISE V/HZ**.5	0.2770E-07
VT = TOTAL NOISE V/HZ**.5	0.6135E-07
NEP= NOISE EQUIVALENT POWER W/HZ**.5	0.2554E-12
DSTAR = PEAK DSTAR CM*HZ**.5/W	0.7858E+11

Table F-4 (CH 4)

PC HGCDTE DETECTOR PERFORMANCE CHANNEL 4 75/160/MIN 8 V/CM

CH = CHANNEL NUMBER	0.4000E+01
T = DET. TEMP	0.7500E+02
HD = DET. HEIGHT CM	0.1360E-01
WD = DET. WIDTH CM	0.2490E-01
TD = DETECTOR THICKNESS CM	0.1000E-02
VB = DETECTOR BIAS VOLTAGE V	0.1992E+00
CD = DETECTOR CAPACITANCE F	0.1500E-10
RD = DETECTOR DARK RESISTANCE OHM	0.4249E+03
ZD = DETECTOR IMPEDANCE OHM	0.4249E+03
PD = DETECTOR PHASE ANGLE RAD	0.9762E-10
X = MOLE FRACTION	0.1839E+00
PO = HOLE CONC. N-TYPE DOPING CM**-3	0.1000E+15
ND = DONAR CARRIER CONC. CM**-3	0.1305E+16
NI = INTRINSIC CARRIER CONC. CM**-3	0.3612E+15
TAU= CARRIER LIFETIME S	0.1000E-05
ETA= QUANTUM EFFICIENCY	0.7000E+00
NUP= PEAK WAVENUMBER 1/CM	0.6068E+03
EG = BAND GAP ENERGY EV	0.6847E-01
SIGMA = CONDUCTIVITY 1/OHM/CM	0.4318E+01
MU = ELECTRON MOBILITY CM**2/V/S	0.2068E+05
MUH= HOLE MOBILITY CM**2/V/S	0.2950E+03
QBG= BKGD PHOTON FLUX DENSITY P/CM**2/S	0.9018E+15
QS = SGNL PHOTON FLUX DENSITY P/CM**2/S	0.1540E+14
TRF= FEEDBACK RESISTOR TEMP. K	0.1600E+03
CF = FDBK RESISTOR CAPACITANCE F	0.3000E-12
RF = FEEDBACK RESISTANCE OHM	0.4248E+04
PF = FDBK RESISTOR PHASE ANGLE RAD	0.1952E-12
ZF = FDBK RESISTOR IMPEDANCE OHM	0.4248E+04
VS = SUPPLY VOLTAGE TO RF/DET. V	0.2191E+01
AO = OPEN LOOP GAIN	0.1000E+04
VP = PREAMP NOISE (INPUT) V/HZ**.5	0.2800E-08
FC = CHOPPING FREQUENCY HZ	0.4400E+03
PW = DETECTOR BIAS POWER W	0.9341E-04
PRF= FEEDBACK RESISTOR BIAS POWER W	0.9341E-03
SIGV = SIGNAL VOLTAGE V	0.1014E-03
RE = DET. RESPONSIVITY V/W	0.2378E+05
AZ = TRANSIMPEDANCE OHM	0.4291E+04
R = DET./PREAMP RESPONSIVITY V/W	0.2402E+06
VBG= BACKGROUND NOISE V/HZ**.5	0.4265E-08
VJN= JOHNSON NOISE V/HZ**.5	0.1340E-07
VGR= GR NOISE V/HZ**.5	0.5371E-07
VRF= FDBK RESISTOR NOISE V/HZ**.5	0.6189E-08
VPA= PREAMP NOISE V/HZ**.5	0.2778E-07
VT = TOTAL NOISE V/HZ**.5	0.6235E-07
NEP= NOISE EQUIVALENT POWER W/HZ**.5	0.2596E-12
DSTAR = PEAK DSTAR CM*HZ**.5/W	0.7885E+11

PC HGCDTE DETECTOR PERFORMANCE CHANNEL 4 75/160/STD 8 V/CM

CH = CHANNEL NUMBER	0.4000E+01
T = DET. TEMP	0.7500E+02
HD = DET. HEIGHT CM	0.1360E-01
WD = DET. WIDTH CM	0.2430E-01
TD = DETECTOR THICKNESS CM	0.1000E-02
VB = DETECTOR BIAS VOLTAGE V	0.1992E+00
CD = DETECTOR CAPACITANCE F	0.1500E-10
RD = DETECTOR DARK RESISTANCE OHM	0.4248E+03
ZD = DETECTOR IMPEDANCE OHM	0.4248E+03
PD = DETECTOR PHASE ANGLE RAD	0.9762E-10
X = MOLE FRACTION	0.1839E+00
PO = HOLE CONC. N-TYPE DOPING CM**-3	0.1000E+15
ND = DONAR CARRIER CONC. CM**-3	0.1305E+16
NI = INTRINSIC CARRIER CONC. CM**-3	0.3612E+15
TAU= CARRIER LIFETIME S	0.1000E-05
ETA= QUANTUM EFFICIENCY	0.7000E+00
NUP= PEAK WAVENUMBER 1/CM	0.6068E+03
EG = BAND GAP ENERGY EV	0.6847E-01
SIGMA = CONDUCTIVITY 1/OHM/CM	0.4318E+01
MU = ELECTRON MOBILITY CM**2/V/S	0.2068E+05
MUH= HOLE MOBILITY CM**2/V/S	0.2950E+03
QBG= BKGD PHOTON FLUX DENSITY P/CM**2/S	0.9100E+15
QS = SGNL PHOTON FLUX DENSITY P/CM**2/S	0.1870E+14
TRF= FEEDBACK RESISTOR TEMP. K	0.1600E+03
CF = FDBK RESISTOR CAPACITANCE F	0.3000E-12
RF = FEEDBACK RESISTANCE OHM	0.4248E+04
PF = FDBK RESISTOR PHASE ANGLE RAD	0.1952E-12
ZF = FDBK RESISTOR IMPEDANCE OHM	0.4248E+04
VS = SUPPLY VOLTAGE TO RF/DET. V	0.2191E+01
AO = OPEN LOOP GAIN	0.1000E+04
VP = PREAMP NOISE (INPUT) V/HZ**.5	0.2900E-08
FC = CHOPPING FREQUENCY HZ	0.4400E+03
PW = DETECTOR BIAS POWER W	0.9341E-04
PRF= FEEDBACK RESISTOR BIAS POWER W	0.9341E-03
SIGV = SIGNAL VOLTAGE V	0.1231E-03
RE = DET. RESPONSIVITY V/W	0.2378E+05
AZ = TRANSIMPEDANCE OHM	0.4291E+04
R = DET./PREAMP RESPONSIVITY V/W	0.2402E+06
VBG= BACKGROUND NOISE V/HZ**.5	0.4287E-08
VJN= JOHNSON NOISE V/HZ**.5	0.1340E-07
VGR= GR NOISE V/HZ**.5	0.5371E-07
VRF= FDBK RESISTOR NOISE V/HZ**.5	0.6189E-08
VPA= PREAMP NOISE V/HZ**.5	0.2778E-07
VT = TOTAL NOISE V/HZ**.5	0.6235E-07
NEP= NOISE EQUIVALENT POWER W/HZ**.5	0.2596E-12
DSTAR = PEAK DSTAR CM*HZ**.5/W	0.7889E+11

PC HGCDTE DETECTOR PERFORMANCE CHANNEL 4 75/160/MAX 8 V/CM

CH = CHANNEL NUMBER	0.4000E+01
T = DET. TEMP	0.7500E+02
HD = DET. HEIGHT CM	0.1360E-01
WD = DET. WIDTH CM	0.2490E-01
TD = DETECTOR THICKNESS CM	0.1000E-02
VB = DETECTOR BIAS VOLTAGE V	0.1992E+00
CD = DETECTOR CAPACITANCE F	0.1500E-10
RD = DETECTOR DARK RESISTANCE OHM	0.4248E+03
ZD = DETECTOR IMPEDANCE OHM	0.4248E+03
PD = DETECTOR PHASE ANGLE RAD	0.9762E-10
X = MOLE FRACTION	0.1839E+00
PO = HOLE CONC. N-TYPE DOPING CM**-3	0.1000E+15
ND = DONAR CARRIER CONC. CM**-3	0.1305E+16
NI = INTRINSIC CARRIER CONC. CM**-3	0.3612E+15
TAU= CARRIER LIFETIME S	0.1000E-05
ETA= QUANTUM EFFICIENCY	0.7000E+00
NUP= PEAK WAVENUMBER 1/CM	0.6068E+03
EG = BAND GAP ENERGY EV	0.6847E-01
SIGMA = CONDUCTIVITY 1/OHM/CM	0.4318E+01
MU = ELECTRON MOBILITY CM**2/V/S	0.2068E+05
MUH= HOLE MOBILITY CM**2/V/S	0.2958E+03
QBG= BKGD PHOTON FLUX DENSITY P/CM**2/S	0.9198E+15
QS = SGNL PHOTON FLUX DENSITY P/CM**2/S	0.3368E+14
TRF= FEEDBACK RESISTOR TEMP. K	0.1600E+03
CF = FDBK RESISTOR CAPACITANCE F	0.3000E-12
RF = FEEDBACK RESISTANCE OHM	0.4248E+04
PF = FDBK RESISTOR PHASE ANGLE RAD	0.1952E-12
ZF = FDBK RESISTOR IMPEDANCE OHM	0.4248E+04
VS = SUPPLY VOLTAGE TO RF/DET. V	0.2191E+01
AO = OPEN LOOP GAIN	0.1000E+04
VP = PREAMP NOISE (INPUT) V/HZ**.5	0.2800E-08
FC = CHOPPING FREQUENCY HZ	0.4400E+03
PW = DETECTOR BIAS POWER W	0.9341E-04
PRF= FEEDBACK RESISTOR BIAS POWER W	0.9341E-03
SIGV = SIGNAL VOLTAGE V	0.2212E-03
RE = DET. RESPONSIVITY V/W	0.2378E+05
AZ = TRANSIMPEDANCE OHM	0.4291E+04
R = DET./PREAMP RESPONSIVITY V/W	0.2402E+06
VBG= BACKGROUND NOISE V/HZ**.5	0.4308E-08
VJN= JOHNSON NOISE V/HZ**.5	0.1340E-07
VGR= GR NOISE V/HZ**.5	0.5371E-07
VRF= FDBK RESISTOR NOISE V/HZ**.5	0.6189E-08
VPA= PREAMP NOISE V/HZ**.5	0.2778E-07
VT = TOTAL NOISE V/HZ**.5	0.6236E-07
NEP= NOISE EQUIVALENT POWER W/HZ**.5	0.2596E-12
DSTAR = PEAK DSTAR CM*HZ**.5/W	0.7889E+11

Table F-4 (CH 5)

PC HGCDTE DETECTOR PERFORMANCE CHANNEL 5 75/160/MIN 8 V/CM

CH = CHANNEL NUMBER	0.5000E+01
T = DET. TEMP	0.7500E+02
HD = DET. HEIGHT CM	0.1360E-01
WD = DET. WIDTH CM	0.2660E-01
TD = DETECTOR THICKNESS CM	0.1000E-02
VB = DETECTOR BIAS VOLTAGE V	0.2120E+00
CD = DETECTOR CAPACITANCE F	0.1500E-10
RD = DETECTOR DARK RESISTANCE OHM	0.4530E+03
ZD = DETECTOR IMPEDANCE OHM	0.4530E+03
PD = DETECTOR PHASE ANGLE RAD	0.9130E-10
X = MOLE FRACTION	0.1830E+00
PO = HOLE CONC. N-TYPE DOPING CM**-3	0.1000E+15
ND = DONAR CARRIER CONC. CM**-3	0.1305E+16
NI = INTRINSIC CARRIER CONC. CM**-3	0.3612E+15
TAU= CARRIER LIFETIME S	0.1000E-05
ETA= QUANTUM EFFICIENCY	0.7000E+00
NUP= PEAK WAVENUMBER 1/CM	0.6068E+03
EG = BAND GAP ENERGY EV	0.6847E-01
SIGMA = CONDUCTIVITY 1/OHM/CM	0.4310E+01
MU = ELECTRON MOBILITY CM**2/V/S	0.2060E+05
MUH= HOLE MOBILITY CM**2/V/S	0.2900E+03
QBG= BKGD PHOTON FLUX DENSITY P/CM**2/S	0.7900E+15
QS = SGNL PHOTON FLUX DENSITY P/CM**2/S	0.1100E+14
TR1= FEEDBACK RESISTOR TEMP. K	0.1600E+03
C1 = FDBK RESISTOR CAPACITANCE F	0.3000E-12
R1 = FEEDBACK RESISTANCE OHM	0.4530E+04
P1 = FDBK RESISTOR PHASE ANGLE RAD	0.1828E-12
Z1 = FDBK RESISTOR IMPEDANCE OHM	0.4530E+04
VS = SUPPLY VOLTAGE TO R1/DET. V	0.2341E+01
AO = OPEN LOOP GAIN	0.1000E+04
VP = PREAMP NOISE (INPUT) V/HZ**.5	0.2800E-08
FC = CHOPPING FREQUENCY HZ	0.4400E+03
PW = DETECTOR BIAS POWER W	0.9979E-04
PR1= FEEDBACK RESISTOR BIAS POWER W	0.9979E-03
SIGV = SIGNAL VOLTAGE V	0.7241E-04
RE = DET. RESPONSIVITY V/W	0.2378E+05
AZ = TRANSIMPEDANCE OHM	0.4584E+04
R = DET./PREAMP RESPONSIVITY V/W	0.2402E+06
VBG= BACKGROUND NOISE V/HZ**.5	0.4129E-08
VJN= JOHNSON NOISE V/HZ**.5	0.1385E-07
VGR= GR NOISE V/HZ**.5	0.5552E-07
VNR= FDBK RESISTOR NOISE V/HZ**.5	0.6396E-08
VPA= PREAMP NOISE V/HZ**.5	0.2772E-07
VT = TOTAL NOISE V/HZ**.5	0.6403E-07
NEP= NOISE EQUIVALENT POWER W/HZ**.5	0.2666E-12
DSTAR = PEAK DSTAR CM*HZ**.5/W	0.7135E+11

PC HGCDTE DETECTOR PERFORMANCE CHANNEL 5 75/160/STD 8 V/CM

CH = CHANNEL NUMBER	0.5000E+01
T = DET. TEMP	0.7500E+02
HD = DET. HEIGHT CM	0.1360E-01
WD = DET. WIDTH CM	0.2660E-01
TD = DETECTOR THICKNESS CM	0.1000E-02
VB = DETECTOR BIAS VOLTAGE V	0.2120E+00
CD = DETECTOR CAPACITANCE F	0.1500E-10
RD = DETECTOR DARK RESISTANCE OHM	0.4530E+03
ZD = DETECTOR IMPEDANCE OHM	0.4530E+03
PD = DETECTOR PHASE ANGLE RAD	0.9130E-10
X = MOLE FRACTION	0.1830E+00
PO = HOLE CONC. N-TYPE DOPING CM**-3	0.1000E+15
ND = DONAR CARRIER CONC. CM**-3	0.1305E+16
NI = INTRINSIC CARRIER CONC. CM**-3	0.3612E+15
TAU= CARRIER LIFETIME S	0.1000E-05
ETA= QUANTUM EFFICIENCY	0.7000E+00
NUP= PEAK WAVENUMBER 1/CM	0.6068E+03
EG = BAND GAP ENERGY EV	0.6847E-01
SIGMA = CONDUCTIVITY 1/OHM/CM	0.4310E+01
MU = ELECTRON MOBILITY CM**2/V/S	0.2060E+05
MUH= HOLE MOBILITY CM**2/V/S	0.2900E+03
QBG= BKGD PHOTON FLUX DENSITY P/CM**2/S	0.7960E+15
QS = SGNL PHOTON FLUX DENSITY P/CM**2/S	0.1600E+14
TR1= FEEDBACK RESISTOR TEMP. K	0.1600E+03
C1 = FDBK RESISTOR CAPACITANCE F	0.3000E-12
R1 = FEEDBACK RESISTANCE OHM	0.4530E+04
P1 = FDBK RESISTOR PHASE ANGLE RAD	0.1828E-12
Z1 = FDBK RESISTOR IMPEDANCE OHM	0.4530E+04
VS = SUPPLY VOLTAGE TO R1/DET. V	0.2341E+01
AO = OPEN LOOP GAIN	0.1000E+04
VP = PREAMP NOISE (INPUT) V/HZ**.5	0.2800E-08
FC = CHOPPING FREQUENCY HZ	0.4400E+03
PW = DETECTOR BIAS POWER W	0.9979E-04
PR1= FEEDBACK RESISTOR BIAS POWER W	0.9979E-03
SIGV = SIGNAL VOLTAGE V	0.1053E-03
RE = DET. RESPONSIVITY V/W	0.2378E+05
AZ = TRANSIMPEDANCE OHM	0.4584E+04
R = DET./PREAMP RESPONSIVITY V/W	0.2402E+06
VBG= BACKGROUND NOISE V/HZ**.5	0.4144E-08
VJN= JOHNSON NOISE V/HZ**.5	0.1385E-07
VGR= GR NOISE V/HZ**.5	0.5552E-07
VNR= FDBK RESISTOR NOISE V/HZ**.5	0.6396E-08
VPA= PREAMP NOISE V/HZ**.5	0.2770E-07
VT = TOTAL NOISE V/HZ**.5	0.6403E-07
NEP= NOISE EQUIVALENT POWER W/HZ**.5	0.2666E-12
DSTAR = PEAK DSTAR CM*HZ**.5/W	0.7135E+11

PC HGCDTE DETECTOR PERFORMANCE CHANNEL 5 75/160/MAX 8 V/CM

CH = CHANNEL NUMBER	0.5000E+01
T = DET. TEMP	0.7500E+02
HD = DET. HEIGHT CM	0.1360E-01
WD = DET. WIDTH CM	0.2660E-01
TD = DETECTOR THICKNESS CM	0.1000E-02
VB = DETECTOR BIAS VOLTAGE V	0.2120E+00
CD = DETECTOR CAPACITANCE F	0.1500E-10
RD = DETECTOR DARK RESISTANCE OHM	0.4530E+03
ZD = DETECTOR IMPEDANCE OHM	0.4530E+03
PD = DETECTOR PHASE ANGLE RAD	0.9130E-10
X = MOLE FRACTION	0.1830E+00
PO = HOLE CONC. N-TYPE DOPING CM**-3	0.1000E+15
ND = DONAR CARRIER CONC. CM**-3	0.1305E+16
NI = INTRINSIC CARRIER CONC. CM**-3	0.3612E+15
TAU= CARRIER LIFETIME S	0.1000E-05
ETA= QUANTUM EFFICIENCY	0.7000E+00
NUP= PEAK WAVENUMBER 1/CM	0.6068E+03
EG = BAND GAP ENERGY EV	0.6847E-01
SIGMA = CONDUCTIVITY 1/OHM/CM	0.4310E+01
MU = ELECTRON MOBILITY CM**2/V/S	0.2060E+05
MUH= HOLE MOBILITY CM**2/V/S	0.2900E+03
QBG= BKGD PHOTON FLUX DENSITY P/CM**2/S	0.8148E+15
QS = SGNL PHOTON FLUX DENSITY P/CM**2/S	0.2630E+14
TR1= FEEDBACK RESISTOR TEMP. K	0.1600E+03
C1 = FDBK RESISTOR CAPACITANCE F	0.3000E-12
R1 = FEEDBACK RESISTANCE OHM	0.4530E+04
P1 = FDBK RESISTOR PHASE ANGLE RAD	0.1828E-12
Z1 = FDBK RESISTOR IMPEDANCE OHM	0.4530E+04
VS = SUPPLY VOLTAGE TO R1/DET. V	0.2341E+01
AO = OPEN LOOP GAIN	0.1000E+04
VP = PREAMP NOISE (INPUT) V/HZ**.5	0.2800E-08
FC = CHOPPING FREQUENCY HZ	0.4400E+03
PW = DETECTOR BIAS POWER W	0.9979E-04
PR1= FEEDBACK RESISTOR BIAS POWER W	0.9979E-03
SIGV = SIGNAL VOLTAGE V	0.1731E-03
RE = DET. RESPONSIVITY V/W	0.2378E+05
AZ = TRANSIMPEDANCE OHM	0.4584E+04
R = DET./PREAMP RESPONSIVITY V/W	0.2402E+06
VBG= BACKGROUND NOISE V/HZ**.5	0.4191E-08
VJN= JOHNSON NOISE V/HZ**.5	0.1385E-07
VGR= GR NOISE V/HZ**.5	0.5552E-07
VNR= FDBK RESISTOR NOISE V/HZ**.5	0.6396E-08
VPA= PREAMP NOISE V/HZ**.5	0.2773E-07
VT = TOTAL NOISE V/HZ**.5	0.6403E-07
NEP= NOISE EQUIVALENT POWER W/HZ**.5	0.2666E-12
DSTAR = PEAK DSTAR CM*HZ**.5/W	0.7135E+11

Table F-4 (CH 6)

PC HGCDTE DETECTOR PERFORMANCE CHANNEL 6 75/160/MIN 8 V/CM

CH = CHANNEL NUMBER	0.6000E+01
T = DET. TEMP	0.7500E+02
HD = DET. HEIGHT CM	0.1360E-01
WD = DET. WIDTH CM	0.2750E-01
TD = DETECTOR THICKNESS CM	0.1000E-02
VB = DETECTOR BIAS VOLTAGE V	0.2200E+00
CD = DETECTOR CAPACITANCE F	0.1500E-10
RD = DETECTOR DARK RESISTANCE OHM	0.4692E+03
ZD = DETECTOR IMPEDANCE OHM	0.4692E+03
PD = DETECTOR PHASE ANGLE RAD	0.8839E-10
X = MOLE FRACTION	0.1838E+00
PO = HOLE CONC. N-TYPE DOPING CM**-3	0.1000E+15
ND = DONAR CARRIER CONC. CM**-3	0.1305E+16
NI = INTRINSIC CARRIER CONC. CM**-3	0.3612E+15
TAU= CARRIER LIFETIME S	0.1000E-05
ETA= QUANTUM EFFICIENCY	0.7000E+00
NUP= PEAK WAVENUMBER 1/CM	0.6068E+03
EG = BAND GAP ENERGY EV	0.6847E-01
SIGMA = CONDUCTIVITY 1/OHM/CM	0.4310E+01
MU = ELECTRON MOBILITY CM**2/V/S	0.2060E+05
MUH= HOLE MOBILITY CM**2/V/S	0.2950E+03
QBG= BKGD PHOTON FLUX DENSITY P/CM**2/S	0.7900E+15
QS = SGNL PHOTON FLUX DENSITY P/CM**2/S	0.9710E+13
TR1= FEEDBACK RESISTOR TEMP. K	0.1600E+03
C1 = FDBK RESISTOR CAPACITANCE F	0.3000E-12
R1 = FEEDBACK RESISTANCE OHM	0.4692E+04
P1 = FDBK RESISTOR PHASE ANGLE RAD	0.1768E-12
Z1 = FDBK RESISTOR IMPEDANCE OHM	0.4692E+04
VS = SUPPLY VOLTAGE TO R1/DET. V	0.2420E+01
AO = OPEN LOOP GAIN	0.1000E+04
VP = PREAMP NOISE (INPUT) V/HZ**.5	0.2000E-08
FC = CHOPPING FREQUENCY HZ	0.4400E+03
PW = DETECTOR BIAS POWER W	0.1032E-03
PR1= FEEDBACK RESISTOR BIAS POWER W	0.1032E-02
SIGV = SIGNAL VOLTAGE V	0.6391E-04
RE = DET. RESPONSIVITY V/W	0.2378E+05
AZ = TRANSIMPEDANCE OHM	0.4739E+04
R = DET./PREAMP RESPONSIVITY V/W	0.2402E+06
VBG= BACKGROUND NOISE V/HZ**.5	0.4197E-08
VJN= JOHNSON NOISE V/HZ**.5	0.1408E-07
VGR= GR NOISE V/HZ**.5	0.5644E-07
VNR= FDBK RESISTOR NOISE V/HZ**.5	0.6584E-08
VPA= PREAMP NOISE V/HZ**.5	0.2778E-07
VT = TOTAL NOISE V/HZ**.5	0.6489E-07
NEP= NOISE EQUIVALENT POWER W/HZ**.5	0.2782E-12
DSTAR = PEAK DSTAR CM*HZ**.5/W	0.7158E+11

PC HGCDTE DETECTOR PERFORMANCE CHANNEL 6 75/160/STD 8 V/CM

CH = CHANNEL NUMBER	0.6000E+01
T = DET. TEMP	0.7500E+02
HD = DET. HEIGHT CM	0.1360E-01
WD = DET. WIDTH CM	0.2750E-01
TD = DETECTOR THICKNESS CM	0.1000E-02
VB = DETECTOR BIAS VOLTAGE V	0.2200E+00
CD = DETECTOR CAPACITANCE F	0.1500E-10
RD = DETECTOR DARK RESISTANCE OHM	0.4692E+03
ZD = DETECTOR IMPEDANCE OHM	0.4692E+03
PD = DETECTOR PHASE ANGLE RAD	0.8839E-10
X = MOLE FRACTION	0.1838E+00
PO = HOLE CONC. N-TYPE DOPING CM**-3	0.1000E+15
ND = DONAR CARRIER CONC. CM**-3	0.1305E+16
NI = INTRINSIC CARRIER CONC. CM**-3	0.3612E+15
TAU= CARRIER LIFETIME S	0.1000E-05
ETA= QUANTUM EFFICIENCY	0.7000E+00
NUP= PEAK WAVENUMBER 1/CM	0.6068E+03
EG = BAND GAP ENERGY EV	0.6847E-01
SIGMA = CONDUCTIVITY 1/OHM/CM	0.4310E+01
MU = ELECTRON MOBILITY CM**2/V/S	0.2060E+05
MUH= HOLE MOBILITY CM**2/V/S	0.2950E+03
QBG= BKGD PHOTON FLUX DENSITY P/CM**2/S	0.8020E+15
QS = SGNL PHOTON FLUX DENSITY P/CM**2/S	0.1680E+14
TR1= FEEDBACK RESISTOR TEMP. K	0.1600E+03
C1 = FDBK RESISTOR CAPACITANCE F	0.3000E-12
R1 = FEEDBACK RESISTANCE OHM	0.4692E+04
P1 = FDBK RESISTOR PHASE ANGLE RAD	0.1768E-12
Z1 = FDBK RESISTOR IMPEDANCE OHM	0.4692E+04
VS = SUPPLY VOLTAGE TO R1/DET. V	0.2420E+01
AO = OPEN LOOP GAIN	0.1000E+04
VP = PREAMP NOISE (INPUT) V/HZ**.5	0.2000E-08
FC = CHOPPING FREQUENCY HZ	0.4400E+03
PW = DETECTOR BIAS POWER W	0.1032E-03
PR1= FEEDBACK RESISTOR BIAS POWER W	0.1032E-02
SIGV = SIGNAL VOLTAGE V	0.1105E-03
RE = DET. RESPONSIVITY V/W	0.2378E+05
AZ = TRANSIMPEDANCE OHM	0.4739E+04
R = DET./PREAMP RESPONSIVITY V/W	0.2402E+06
VBG= BACKGROUND NOISE V/HZ**.5	0.4229E-08
VJN= JOHNSON NOISE V/HZ**.5	0.1408E-07
VGR= GR NOISE V/HZ**.5	0.5644E-07
VNR= FDBK RESISTOR NOISE V/HZ**.5	0.6584E-08
VPA= PREAMP NOISE V/HZ**.5	0.2778E-07
VT = TOTAL NOISE V/HZ**.5	0.6490E-07
NEP= NOISE EQUIVALENT POWER W/HZ**.5	0.2782E-12
DSTAR = PEAK DSTAR CM*HZ**.5/W	0.7158E+11

PC HGCDTE DETECTOR PERFORMANCE CHANNEL 6 75/160/MAX 8 V/CM

CH = CHANNEL NUMBER	0.6000E+01
T = DET. TEMP	0.7500E+02
HD = DET. HEIGHT CM	0.1360E-01
WD = DET. WIDTH CM	0.2750E-01
TD = DETECTOR THICKNESS CM	0.1000E-02
VB = DETECTOR BIAS VOLTAGE V	0.2200E+00
CD = DETECTOR CAPACITANCE F	0.1500E-10
RD = DETECTOR DARK RESISTANCE OHM	0.4692E+03
ZD = DETECTOR IMPEDANCE OHM	0.4692E+03
PD = DETECTOR PHASE ANGLE RAD	0.8839E-10
X = MOLE FRACTION	0.1838E+00
PO = HOLE CONC. N-TYPE DOPING CM**-3	0.1000E+15
ND = DONAR CARRIER CONC. CM**-3	0.1305E+16
NI = INTRINSIC CARRIER CONC. CM**-3	0.3612E+15
TAU= CARRIER LIFETIME S	0.1000E-05
ETA= QUANTUM EFFICIENCY	0.7000E+00
NUP= PEAK WAVENUMBER 1/CM	0.6068E+03
EG = BAND GAP ENERGY EV	0.6847E-01
SIGMA = CONDUCTIVITY 1/OHM/CM	0.4310E+01
MU = ELECTRON MOBILITY CM**2/V/S	0.2060E+05
MUH= HOLE MOBILITY CM**2/V/S	0.2950E+03
QBG= BKGD PHOTON FLUX DENSITY P/CM**2/S	0.[illegible]E+15
QS = SGNL PHOTON FLUX DENSITY P/CM**2/S	0.[illegible]E+14
TR1= FEEDBACK RESISTOR TEMP. K	0.1600E+03
C1 = FDBK RESISTOR CAPACITANCE F	0.3000E-12
R1 = FEEDBACK RESISTANCE OHM	0.4692E+04
P1 = FDBK RESISTOR PHASE ANGLE RAD	0.1768E-12
Z1 = FDBK RESISTOR IMPEDANCE OHM	0.4692E+04
VS = SUPPLY VOLTAGE TO R1/DET. V	0.2420E+01
AO = OPEN LOOP GAIN	0.1000E+04
VP = PREAMP NOISE (INPUT) V/HZ**.5	0.2000E-08
FC = CHOPPING FREQUENCY HZ	0.4400E+03
PW = DETECTOR BIAS POWER W	0.1032E-03
PR1= FEEDBACK RESISTOR BIAS POWER W	0.1032E-02
SIGV = SIGNAL VOLTAGE V	0.2834E-03
RE = DET. RESPONSIVITY V/W	0.2378E+05
AZ = TRANSIMPEDANCE OHM	0.4739E+04
R = DET./PREAMP RESPONSIVITY V/W	0.2402E+06
VBG= BACKGROUND NOISE V/HZ**.5	0.4261E-08
VJN= JOHNSON NOISE V/HZ**.5	0.1408E-07
VGR= GR NOISE V/HZ**.5	0.5644E-07
VNR= FDBK RESISTOR NOISE V/HZ**.5	0.6584E-08
VPA= PREAMP NOISE V/HZ**.5	0.2778E-07
VT = TOTAL NOISE V/HZ**.5	0.6490E-07
NEP= NOISE EQUIVALENT POWER W/HZ**.5	0.2782E-12
DSTAR = PEAK DSTAR CM*HZ**.5/W	0.7158E+11

Table F-4 (CH 7)

PC HGCDTE DETECTOR PERFORMANCE CHANNEL 7 75/168/MIN 8 V/CM

CH = CHANNEL NUMBER	0.7000E+01
T = DET. TEMP	0.7500E+02
HD = DET. HEIGHT CM	0.1360E-01
WD = DET. WIDTH CM	0.2000E-01
TD = DETECTOR THICKNESS CM	0.1000E-02
VB = DETECTOR BIAS VOLTAGE V	0.2304E+00
CD = DETECTOR CAPACITANCE F	0.1500E-10
RD = DETECTOR DARK RESISTANCE OHM	0.4913E+03
ZD = DETECTOR IMPEDANCE OHM	0.4913E+03
PD = DETECTOR PHASE ANGLE RAD	0.8440E-10
X = MOLE FRACTION	0.1838E+00
PO = HOLE CONC. N-TYPE DOPING CM**-3	0.1000E+15
ND = DONAR CARRIER CONC. CM**-3	0.1305E+16
NI = INTRINSIC CARRIER CONC. CM**-3	0.3612E+15
TAU= CARRIER LIFETIME S	0.1000E-05
ETA= QUANTUM EFFICIENCY	0.7000E+00
NUP= PEAK WAVENUMBER 1/CM	0.6068E+03
EG = BAND GAP ENERGY EV	0.6847E-01
SIGMA = CONDUCTIVITY 1/OHM/CM	0.4310E+01
MU = ELECTRON MOBILITY CM**2/V/S	0.2060E+05
MUH= HOLE MOBILITY CM**2/V/S	0.2950E+03
QBG= BKGD PHOTON FLUX DENSITY P/CM**2/S	0.7240E+14
QS = SGNL PHOTON FLUX DENSITY P/CM**2/S	0.9270E+13
TR1= FEEDBACK RESISTOR TEMP. K	0.1600E+03
C1 = FDBK RESISTOR CAPACITANCE F	0.3000E-12
R1 = FEEDBACK RESISTANCE OHM	0.4913E+04
P1 = FDBK RESISTOR PHASE ANGLE RAD	0.1688E-12
Z1 = FDBK RESISTOR IMPEDANCE OHM	0.4913E+04
VS = SUPPLY VOLTAGE TO R1/DET. V	0.2534E+01
AO = OPEN LOOP GAIN	0.1000E+04
VP = PREAMP NOISE (INPUT) V/HZ**.5	0.2000E-08
FC = CHOPPING FREQUENCY HZ	0.4400E+03
PW = DETECTOR BIAS POWER W	0.1000E-03
PR1= FEEDBACK RESISTOR BIAS POWER W	0.1000E-02
SIGV = SIGNAL VOLTAGE V	0.6102E-04
RE = DET. RESPONSIVITY V/W	0.2376E+05
AZ = TRANSIMPEDANCE OHM	0.4963E+04
R = DET./PREAMP RESPONSIVITY V/W	0.2402E+06
VBG= BACKGROUND NOISE V/HZ**.5	0.1300E-08
VJN= JOHNSON NOISE V/HZ**.5	0.1441E-07
VGR= GR NOISE V/HZ**.5	0.5776E-07
VNR= FDBK RESISTOR NOISE V/HZ**.5	0.6656E-08
VPA= PREAMP NOISE V/HZ**.5	0.2770E-07
VT = TOTAL NOISE V/HZ**.5	0.6601E-07
NEP= NOISE EQUIVALENT POWER W/HZ**.5	0.2748E-12
DSTAR = PEAK DSTAR CM*HZ**.5/W	0.7201E+11

PC HGCDTE DETECTOR PERFORMANCE CHANNEL 7 75/168/STD 8 V/CM

CH = CHANNEL NUMBER	0.7000E+01
T = DET. TEMP	0.7500E+02
HD = DET. HEIGHT CM	0.1360E-01
WD = DET. WIDTH CM	0.2000E-01
TD = DETECTOR THICKNESS CM	0.1000E-02
VB = DETECTOR BIAS VOLTAGE V	0.2304E+00
CD = DETECTOR CAPACITANCE F	0.1500E-10
RD = DETECTOR DARK RESISTANCE OHM	0.4913E+03
ZD = DETECTOR IMPEDANCE OHM	0.4913E+03
PD = DETECTOR PHASE ANGLE RAD	0.8440E-10
X = MOLE FRACTION	0.1838E+00
PO = HOLE CONC. N-TYPE DOPING CM**-3	0.1000E+15
ND = DONAR CARRIER CONC. CM**-3	0.1305E+16
NI = INTRINSIC CARRIER CONC. CM**-3	0.3612E+15
TAU= CARRIER LIFETIME S	0.1000E-05
ETA= QUANTUM EFFICIENCY	0.7000E+00
NUP= PEAK WAVENUMBER 1/CM	0.6068E+03
EG = BAND GAP ENERGY EV	0.6847E-01
SIGMA = CONDUCTIVITY 1/OHM/CM	0.4310E+01
MU = ELECTRON MOBILITY CM**2/V/S	0.2060E+05
MUH= HOLE MOBILITY CM**2/V/S	0.2950E+03
QBG= BKGD PHOTON FLUX DENSITY P/CM**2/S	0.7300E+15
QS = SGNL PHOTON FLUX DENSITY P/CM**2/S	0.1640E+14
TR1= FEEDBACK RESISTOR TEMP. K	0.1600E+03
C1 = FDBK RESISTOR CAPACITANCE F	0.3000E-12
R1 = FEEDBACK RESISTANCE OHM	0.4913E+04
P1 = FDBK RESISTOR PHASE ANGLE RAD	0.1688E-12
Z1 = FDBK RESISTOR IMPEDANCE OHM	0.4913E+04
VS = SUPPLY VOLTAGE TO R1/DET. V	0.2534E+01
AO = OPEN LOOP GAIN	0.1000E+04
VP = PREAMP NOISE (INPUT) V/HZ**.5	0.2000E-08
FC = CHOPPING FREQUENCY HZ	0.4400E+03
PW = DETECTOR BIAS POWER W	0.1000E-03
PR1= FEEDBACK RESISTOR BIAS POWER W	0.1000E-02
SIGV = SIGNAL VOLTAGE V	0.1079E-03
RE = DET. RESPONSIVITY V/W	0.2378E+05
AZ = TRANSIMPEDANCE OHM	0.4963E+04
R = DET./PREAMP RESPONSIVITY V/W	0.2402E+06
VBG= BACKGROUND NOISE V/HZ**.5	0.4129E-08
VJN= JOHNSON NOISE V/HZ**.5	0.1441E-07
VGR= GR NOISE V/HZ**.5	0.5776E-07
VNR= FDBK RESISTOR NOISE V/HZ**.5	0.6656E-08
VPA= PREAMP NOISE V/HZ**.5	0.2770E-07
VT = TOTAL NOISE V/HZ**.5	0.6613E-07
NEP= NOISE EQUIVALENT POWER W/HZ**.5	0.2753E-12
DSTAR = PEAK DSTAR CM*HZ**.5/W	0.7189E+11

PC HGCDTE DETECTOR PERFORMANCE CHANNEL 7 75/168/MAX 8 V/CM

CH = CHANNEL NUMBER	0.7000E+01
T = DET. TEMP	0.7500E+02
HD = DET. HEIGHT CM	0.1360E-01
WD = DET. WIDTH CM	0.2000E-01
TD = DETECTOR THICKNESS CM	0.1000E-02
VB = DETECTOR BIAS VOLTAGE V	0.2304E+00
CD = DETECTOR CAPACITANCE F	0.1500E-10
RD = DETECTOR DARK RESISTANCE OHM	0.4913E+03
ZD = DETECTOR IMPEDANCE OHM	0.4913E+03
PD = DETECTOR PHASE ANGLE RAD	0.8440E-10
X = MOLE FRACTION	0.1838E+00
PO = HOLE CONC. N-TYPE DOPING CM**-3	0.1000E+15
ND = DONAR CARRIER CONC. CM**-3	0.1305E+16
NI = INTRINSIC CARRIER CONC. CM**-3	0.3612E+15
TAU= CARRIER LIFETIME S	0.1000E-05
ETA= QUANTUM EFFICIENCY	0.7000E+00
NUP= PEAK WAVENUMBER 1/CM	0.6068E+03
EG = BAND GAP ENERGY EV	0.6847E-01
SIGMA = CONDUCTIVITY 1/OHM/CM	0.4310E+01
MU = ELECTRON MOBILITY CM**2/V/S	0.2060E+05
MUH= HOLE MOBILITY CM**2/V/S	0.2950E+03
QBG= BKGD PHOTON FLUX DENSITY P/CM**2/S	0.7400E+15
QS = SGNL PHOTON FLUX DENSITY P/CM**2/S	0.3350E+14
TR1= FEEDBACK RESISTOR TEMP. K	0.1600E+03
C1 = FDBK RESISTOR CAPACITANCE F	0.3000E-12
R1 = FEEDBACK RESISTANCE OHM	0.4913E+04
P1 = FDBK RESISTOR PHASE ANGLE RAD	0.1688E-12
Z1 = FDBK RESISTOR IMPEDANCE OHM	0.4913E+04
VS = SUPPLY VOLTAGE TO R1/DET. V	0.2534E+01
AO = OPEN LOOP GAIN	0.1000E+04
VP = PREAMP NOISE (INPUT) V/HZ**.5	0.2000E-08
FC = CHOPPING FREQUENCY HZ	0.4400E+03
PW = DETECTOR BIAS POWER W	0.1000E-03
PR1= FEEDBACK RESISTOR BIAS POWER W	0.1000E-02
SIGV = SIGNAL VOLTAGE V	0.2205E-03
RE = DET. RESPONSIVITY V/W	0.2378E+05
AZ = TRANSIMPEDANCE OHM	0.4963E+04
R = DET./PREAMP RESPONSIVITY V/W	0.2402E+06
VBG= BACKGROUND NOISE V/HZ**.5	0.4100E-08
VJN= JOHNSON NOISE V/HZ**.5	0.1441E-07
VGR= GR NOISE V/HZ**.5	0.5776E-07
VNR= FDBK RESISTOR NOISE V/HZ**.5	0.6656E-08
VPA= PREAMP NOISE V/HZ**.5	0.2770E-07
VT = TOTAL NOISE V/HZ**.5	0.6613E-07
NEP= NOISE EQUIVALENT POWER W/HZ**.5	0.2753E-12
DSTAR = PEAK DSTAR CM*HZ**.5/W	0.7188E+11

Table F-4 (CH 8)

PC HGCDTE DETECTOR PERFORMANCE CHANNEL 8 75/160/MIN 8 V/CM

CH = CHANNEL NUMBER	8.0000E+01
T = DET. TEMP	8.7500E+02
HD = DET. HEIGHT CM	8.1360E-01
WD = DET. WIDTH CM	8.2900E-01
TD = DETECTOR THICKNESS CM	8.1000E-02
VB = DETECTOR BIAS VOLTAGE V	8.2320E+00
CD = DETECTOR CAPACITANCE F	8.1500E-10
RD = DETECTOR DARK RESISTANCE OHM	8.4940E+03
ZD = DETECTOR IMPEDANCE OHM	8.4940E+03
PD = DETECTOR PHASE ANGLE RAD	8.6382E-10
X = MOLE FRACTION	8.1830E+00
PO = HOLE CONC. N-TYPE DOPING CM**-3	8.1000E+15
ND = DONAR CARRIER CONC. CM**-3	8.1305E+16
NI = INTRINSIC CARRIER CONC. CM**-3	8.3612E+15
TAU= CARRIER LIFETIME S	8.1000E-05
ETA= QUANTUM EFFICIENCY	8.7000E+00
NUP= PEAK WAVENUMBER 1/CM	8.6868E+03
EG = BAND GAP ENERGY EV	8.6847E-01
SIGMA = CONDUCTIVITY 1/OHM/CM	8.4318E+01
MU = ELECTRON MOBILITY CM**2/V/S	8.2868E+05
MUH= HOLE MOBILITY CM**2/V/S	8.2958E+03
QBG= BKGD PHOTON FLUX DENSITY P/CM**2/S	8.7188E+15
QS = SGNL PHOTON FLUX DENSITY P/CM**2/S	8.8500E+13
TR1= FEEDBACK RESISTOR TEMP. K	8.1600E+03
C1 = FDBK RESISTOR CAPACITANCE F	8.3000E-12
R1 = FEEDBACK RESISTANCE OHM	8.4948E+04
P1 = FDBK RESISTOR PHASE ANGLE RAD	8.1676E-12
Z1 = FDBK RESISTOR IMPEDANCE OHM	8.4948E+04
VS = SUPPLY VOLTAGE TO R1/DET. V	8.2552E+01
AO = OPEN LOOP GAIN	8.1000E+04
VP = PREAMP NOISE (INPUT) V/HZ**.5	8.2300E-08
FC = CHOPPING FREQUENCY HZ	8.4400E+03
PW = DETECTOR BIAS POWER W	8.1088E-03
PR1= FEEDBACK RESISTOR BIAS POWER W	8.1088E-02
SIGV = SIGNAL VOLTAGE V	8.5595E-04
RE = DET. RESPONSIVITY V/W	8.2378E+05
AZ = TRANSIMPEDANCE OHM	8.4998E+04
R = DET./PREAMP RESPONSIVITY V/W	8.2402E+06
VBG= BACKGROUND NOISE V/HZ**.5	8.4105E-08
VJN= JOHNSON NOISE V/HZ**.5	8.1446E-07
VGR= GR NOISE V/HZ**.5	8.5795E-07
VNR= FDBK RESISTOR NOISE V/HZ**.5	8.6679E-08
VPA= PREAMP NOISE V/HZ**.5	8.2778E-07
VT = TOTAL NOISE V/HZ**.5	8.6631E-07
NEP= NOISE EQUIVALENT POWER W/HZ**.5	8.2761E-12
DSTAR = PEAK DSTAR CM*HZ**.5/W	8.7193E+11

PC HGCDTE DETECTOR PERFORMANCE CHANNEL 8 75/160/STD 8 V/CM

CH = CHANNEL NUMBER	8.0000E+01
T = DET. TEMP	8.7500E+02
HD = DET. HEIGHT CM	8.1360E-01
WD = DET. WIDTH CM	8.2900E-01
TD = DETECTOR THICKNESS CM	8.1000E-02
VB = DETECTOR BIAS VOLTAGE V	8.2320E+00
CD = DETECTOR CAPACITANCE F	8.1500E-10
RD = DETECTOR DARK RESISTANCE OHM	8.4940E+03
ZD = DETECTOR IMPEDANCE OHM	8.4940E+03
PD = DETECTOR PHASE ANGLE RAD	8.8382E-10
X = MOLE FRACTION	8.1830E+00
PO = HOLE CONC. N-TYPE DOPING CM**-3	8.1000E+15
ND = DONAR CARRIER CONC. CM**-3	8.1305E+16
NI = INTRINSIC CARRIER CONC. CM**-3	8.3612E+15
TAU= CARRIER LIFETIME S	8.1000E-05
ETA= QUANTUM EFFICIENCY	8.7000E+00
NUP= PEAK WAVENUMBER 1/CM	8.6868E+03
EG = BAND GAP ENERGY EV	8.6847E-01
SIGMA = CONDUCTIVITY 1/OHM/CM	8.4318E+01
MU = ELECTRON MOBILITY CM**2/V/S	8.2868E+05
MUH= HOLE MOBILITY CM**2/V/S	8.2958E+03
QBG= BKGD PHOTON FLUX DENSITY P/CM**2/S	8.7248E+15
QS = SGNL PHOTON FLUX DENSITY P/CM**2/S	8.1648E+14
TR1= FEEDBACK RESISTOR TEMP. K	8.1600E+03
C1 = FDBK RESISTOR CAPACITANCE F	8.3000E-12
R1 = FEEDBACK RESISTANCE OHM	8.4948E+04
P1 = FDBK RESISTOR PHASE ANGLE RAD	8.1676E-12
Z1 = FDBK RESISTOR IMPEDANCE OHM	8.4948E+04
VS = SUPPLY VOLTAGE TO R1/DET. V	8.2552E+01
AO = OPEN LOOP GAIN	8.1000E+04
VP = PREAMP NOISE (INPUT) V/HZ**.5	8.2000E-08
FC = CHOPPING FREQUENCY HZ	8.4400E+03
PW = DETECTOR BIAS POWER W	8.1088E-03
PR1= FEEDBACK RESISTOR BIAS POWER W	8.1088E-02
SIGV = SIGNAL VOLTAGE V	8.1879E-03
RE = DET. RESPONSIVITY V/W	8.2378E+05
AZ = TRANSIMPEDANCE OHM	8.4998E+04
R = DET./PREAMP RESPONSIVITY V/W	8.2402E+06
VBG= BACKGROUND NOISE V/HZ**.5	8.4126E-08
VJN= JOHNSON NOISE V/HZ**.5	8.1446E-07
VGR= GR NOISE V/HZ**.5	8.5796E-07
VNR= FDBK RESISTOR NOISE V/HZ**.5	8.6679E-08
VPA= PREAMP NOISE V/HZ**.5	8.2778E-07
VT = TOTAL NOISE V/HZ**.5	8.6631E-07
NEP= NOISE EQUIVALENT POWER W/HZ**.5	8.2761E-12
DSTAR = PEAK DSTAR CM*HZ**.5/W	8.7193E+11

PC HGCDTE DETECTOR PERFORMANCE CHANNEL 8 75/160/MAX 8 V/CM

CH = CHANNEL NUMBER	8.0000E+01
T = DET. TEMP	8.7500E+02
HD = DET. HEIGHT CM	8.1360E-01
WD = DET. WIDTH CM	8.2900E-01
TD = DETECTOR THICKNESS CM	8.1000E-02
VB = DETECTOR BIAS VOLTAGE V	8.2320E+00
CD = DETECTOR CAPACITANCE F	8.1500E-10
RD = DETECTOR DARK RESISTANCE OHM	8.4940E+03
ZD = DETECTOR IMPEDANCE OHM	8.4940E+03
PD = DETECTOR PHASE ANGLE RAD	8.8382E-10
X = MOLE FRACTION	8.1830E+00
PO = HOLE CONC. N-TYPE DOPING CM**-3	8.1000E+15
ND = DONAR CARRIER CONC. CM**-3	8.1305E+16
NI = INTRINSIC CARRIER CONC. CM**-3	8.3612E+15
TAU= CARRIER LIFETIME S	8.1000E-05
ETA= QUANTUM EFFICIENCY	8.7000E+00
NUP= PEAK WAVENUMBER 1/CM	8.6868E+03
EG = BAND GAP ENERGY EV	8.6847E-01
SIGMA = CONDUCTIVITY 1/OHM/CM	8.4318E+01
MU = ELECTRON MOBILITY CM**2/V/S	8.2868E+05
MUH= HOLE MOBILITY CM**2/V/S	8.2958E+03
QBG= BKGD PHOTON FLUX DENSITY P/CM**2/S	8.7488E+15
QS = SGNL PHOTON FLUX DENSITY P/CM**2/S	8.3948E+14
TR1= FEEDBACK RESISTOR TEMP. K	8.1600E+03
C1 = FDBK RESISTOR CAPACITANCE F	8.3000E-12
R1 = FEEDBACK RESISTANCE OHM	8.4948E+04
P1 = FDBK RESISTOR PHASE ANGLE RAD	8.1676E-12
Z1 = FDBK RESISTOR IMPEDANCE OHM	8.4948E+04
VS = SUPPLY VOLTAGE TO R1/DET. V	8.2552E+01
AO = OPEN LOOP GAIN	8.1000E+04
VP = PREAMP NOISE (INPUT) V/HZ**.5	8.2000E-08
FC = CHOPPING FREQUENCY HZ	8.4400E+03
PW = DETECTOR BIAS POWER W	8.1088E-03
PR1= FEEDBACK RESISTOR BIAS POWER W	8.1088E-02
SIGV = SIGNAL VOLTAGE V	8.2593E-03
RE = DET. RESPONSIVITY V/W	8.2378E+05
AZ = TRANSIMPEDANCE OHM	8.4998E+04
R = DET./PREAMP RESPONSIVITY V/W	8.2402E+06
VBG= BACKGROUND NOISE V/HZ**.5	8.4194E-08
VJN= JOHNSON NOISE V/HZ**.5	8.1446E-07
VGR= GR NOISE V/HZ**.5	8.5796E-07
VNR= FDBK RESISTOR NOISE V/HZ**.5	8.6679E-08
VPA= PREAMP NOISE V/HZ**.5	8.2778E-07
VT = TOTAL NOISE V/HZ**.5	8.6632E-07
NEP= NOISE EQUIVALENT POWER W/HZ**.5	8.2761E-12
DSTAR = PEAK DSTAR CM*HZ**.5/W	8.7193E+11

Table F-4 (CH 9)

PC HGCDTE DETECTOR PERFORMANCE CHANNEL 9 75/160/MIN 8 V/CM

CH = CHANNEL NUMBER	0.9000E+01
T = DET. TEMP	0.7500E+02
HD = DET. HEIGHT CM	0.1360E-01
WD = DET. WIDTH CM	0.2910E-01
TD = DETECTOR THICKNESS CM	0.1000E-02
VB = DETECTOR BIAS VOLTAGE V	0.2328E+00
CD = DETECTOR CAPACITANCE F	0.1500E-10
RD = DETECTOR DARK RESISTANCE OHM	0.4965E+03
ZD = DETECTOR IMPEDANCE OHM	0.4965E+03
PD = DETECTOR PHASE ANGLE RAD	0.8353E-10
X = HOLE FRACTION	0.1838E+00
PO = HOLE CONC. N-TYPE DOPING CM**-3	0.1000E+15
ND = DONAR CARRIER CONC. CM**-3	0.1305E+16
NI = INTRINSIC CARRIER CONC. CM**-3	0.3612E+15
TAU= CARRIER LIFETIME S	0.1000E-05
ETA= QUANTUM EFFICIENCY	0.7000E+00
NUP= PEAK WAVENUMBER 1/CM	0.6068E+03
EG = BAND GAP ENERGY EV	0.6847E-01
SIGMA = CONDUCTIVITY 1/OHM/CM	0.4310E+01
MU = ELECTRON MOBILITY CM**2/V/S	0.2060E+05
MUH= HOLE MOBILITY CM**2/V/S	0.2958E+03
QBG= BKGD PHOTON FLUX DENSITY P/CM**2/S	0.7068E+15
QS = SGNL PHOTON FLUX DENSITY P/CM**2/S	0.9190E+13
TR1= FEEDBACK RESISTOR TEMP. K	0.1600E+03
C1 = FDBK RESISTOR CAPACITANCE F	0.3000E-12
R1 = FEEDBACK RESISTANCE OHM	0.4965E+04
P1 = FDBK RESISTOR PHASE ANGLE RAD	0.1671E-12
Z1 = FDBK RESISTOR IMPEDANCE OHM	0.4965E+04
VS = SUPPLY VOLTAGE TO R1/DET. V	0.2561E+01
AO = OPEN LOOP GAIN	0.1000E+04
VP = PREAMP NOISE (INPUT) V/HZ**.5	0.2000E-08
FC = CHOPPING FREQUENCY HZ	0.4400E+03
PW = DETECTOR BIAS POWER W	0.1092E-03
PR1= FEEDBACK RESISTOR BIAS POWER W	0.1092E-02
SIGV = SIGNAL VOLTAGE V	0.6049E-04
RE = DET. RESPONSIVITY V/W	0.2378E+05
AZ = TRANSIMPEDANCE OHM	0.5015E+04
R = DET./PREAMP RESPONSIVITY V/W	0.2402E+06
VBG= BACKGROUND NOISE V/HZ**.5	0.4082E-08
VJN= JOHNSON NOISE V/HZ**.5	0.1448E-07
VGR= GR NOISE V/HZ**.5	0.5806E-07
VNR= FDBK RESISTOR NOISE V/HZ**.5	0.6690E-08
VPA= PREAMP NOISE V/HZ**.5	0.2770E-07
VT = TOTAL NOISE V/HZ**.5	0.6640E-07
NEP= NOISE EQUIVALENT POWER W/HZ**.5	0.2765E-12
DSTAR = PEAK DSTAR CM*HZ**.5/W	0.7196E+11

PC HGCDTE DETECTOR PERFORMANCE CHANNEL 9 75/160/STD 8 V/CM

CH = CHANNEL NUMBER	0.9000E+01
T = DET. TEMP	0.7500E+02
HD = DET. HEIGHT CM	0.1360E-01
WD = DET. WIDTH CM	0.2910E-01
TD = DETECTOR THICKNESS CM	0.1000E-02
VB = DETECTOR BIAS VOLTAGE V	0.2328E+00
CD = DETECTOR CAPACITANCE F	0.1500E-10
RD = DETECTOR DARK RESISTANCE OHM	0.4965E+03
ZD = DETECTOR IMPEDANCE OHM	0.4965E+03
PD = DETECTOR PHASE ANGLE RAD	0.8353E-10
X = HOLE FRACTION	0.1838E+00
PO = HOLE CONC. N-TYPE DOPING CM**-3	0.1000E+15
ND = DONAR CARRIER CONC. CM**-3	0.1305E+16
NI = INTRINSIC CARRIER CONC. CM**-3	0.3612E+15
TAU= CARRIER LIFETIME S	0.1000E-05
ETA= QUANTUM EFFICIENCY	0.7000E+00
NUP= PEAK WAVENUMBER 1/CM	0.6068E+03
EG = BAND GAP ENERGY EV	0.6847E-01
SIGMA = CONDUCTIVITY 1/OHM/CM	0.4310E+01
MU = ELECTRON MOBILITY CM**2/V/S	0.2060E+05
MUH= HOLE MOBILITY CM**2/V/S	0.2958E+03
QBG= BKGD PHOTON FLUX DENSITY P/CM**2/S	0.7240E+15
QS = SGNL PHOTON FLUX DENSITY P/CM**2/S	0.2730E+14
TR1= FEEDBACK RESISTOR TEMP. K	0.1600E+03
C1 = FDBK RESISTOR CAPACITANCE F	0.3000E-12
R1 = FEEDBACK RESISTANCE OHM	0.4965E+04
P1 = FDBK RESISTOR PHASE ANGLE RAD	0.1671E-12
Z1 = FDBK RESISTOR IMPEDANCE OHM	0.4965E+04
VS = SUPPLY VOLTAGE TO R1/DET. V	0.2561E+01
AO = OPEN LOOP GAIN	0.1000E+04
VP = PREAMP NOISE (INPUT) V/HZ**.5	0.2000E-08
FC = CHOPPING FREQUENCY HZ	0.4400E+03
PW = DETECTOR BIAS POWER W	0.1092E-03
PR1= FEEDBACK RESISTOR BIAS POWER W	0.1092E-02
SIGV = SIGNAL VOLTAGE V	0.1797E-03
RE = DET. RESPONSIVITY V/W	0.2378E+05
AZ = TRANSIMPEDANCE OHM	0.5015E+04
R = DET./PREAMP RESPONSIVITY V/W	0.2402E+06
VBG= BACKGROUND NOISE V/HZ**.5	0.4134E-08
VJN= JOHNSON NOISE V/HZ**.5	0.1448E-07
VGR= GR NOISE V/HZ**.5	0.5806E-07
VNR= FDBK RESISTOR NOISE V/HZ**.5	0.6690E-08
VPA= PREAMP NOISE V/HZ**.5	0.2770E-07
VT = TOTAL NOISE V/HZ**.5	0.6641E-07
NEP= NOISE EQUIVALENT POWER W/HZ**.5	0.2765E-12
DSTAR = PEAK DSTAR CM*HZ**.5/W	0.7195E+11

PC HGCDTE DETECTOR PERFORMANCE CHANNEL 9 75/160/MAX 8 V/CM

CH = CHANNEL NUMBER	0.9000E+01
T = DET. TEMP	0.7500E+02
HD = DET. HEIGHT CM	0.1360E-01
WD = DET. WIDTH CM	0.2910E-01
TD = DETECTOR THICKNESS CM	0.1000E-02
VB = DETECTOR BIAS VOLTAGE V	0.2328E+00
CD = DETECTOR CAPACITANCE F	0.1500E-10
RD = DETECTOR DARK RESISTANCE OHM	0.4965E+03
ZD = DETECTOR IMPEDANCE OHM	0.4965E+03
PD = DETECTOR PHASE ANGLE RAD	0.8353E-10
X = HOLE FRACTION	0.1838E+00
PO = HOLE CONC. N-TYPE DOPING CM**-3	0.1000E+15
ND = DONAR CARRIER CONC. CM**-3	0.1305E+16
NI = INTRINSIC CARRIER CONC. CM**-3	0.3612E+15
TAU= CARRIER LIFETIME S	0.1000E-05
ETA= QUANTUM EFFICIENCY	0.7000E+00
NUP= PEAK WAVENUMBER 1/CM	0.6068E+03
EG = BAND GAP ENERGY EV	0.6847E-01
SIGMA = CONDUCTIVITY 1/OHM/CM	0.4310E+01
MU = ELECTRON MOBILITY CM**2/V/S	0.2060E+05
MUH= HOLE MOBILITY CM**2/V/S	0.2958E+03
QBG= BKGD PHOTON FLUX DENSITY P/CM**2/S	0.7420E+15
QS = SGNL PHOTON FLUX DENSITY P/CM**2/S	0.4970E+14
TR1= FEEDBACK RESISTOR TEMP. K	0.1600E+03
C1 = FDBK RESISTOR CAPACITANCE F	0.3000E-12
R1 = FEEDBACK RESISTANCE OHM	0.4965E+04
P1 = FDBK RESISTOR PHASE ANGLE RAD	0.1671E-12
Z1 = FDBK RESISTOR IMPEDANCE OHM	0.4965E+04
VS = SUPPLY VOLTAGE TO R1/DET. V	0.2561E+01
AO = OPEN LOOP GAIN	0.1000E+04
VP = PREAMP NOISE (INPUT) V/HZ**.5	0.2000E-08
FC = CHOPPING FREQUENCY HZ	0.4400E+03
PW = DETECTOR BIAS POWER W	0.1092E-03
PR1= FEEDBACK RESISTOR BIAS POWER W	0.1092E-02
SIGV = SIGNAL VOLTAGE V	0.3271E-03
RE = DET. RESPONSIVITY V/W	0.2378E+05
AZ = TRANSIMPEDANCE OHM	0.5015E+04
R = DET./PREAMP RESPONSIVITY V/W	0.2402E+06
VBG= BACKGROUND NOISE V/HZ**.5	0.4185E-08
VJN= JOHNSON NOISE V/HZ**.5	0.1446E-07
VGR= GR NOISE V/HZ**.5	0.5806E-07
VNR= FDBK RESISTOR NOISE V/HZ**.5	0.6690E-08
VPA= PREAMP NOISE V/HZ**.5	0.2770E-07
VT = TOTAL NOISE V/HZ**.5	0.6641E-07
NEP= NOISE EQUIVALENT POWER W/HZ**.5	0.2765E-12
DSTAR = PEAK DSTAR CM*HZ**.5/W	0.7195E+11

Table F-4 (CH 10)

PC HGCDTE DETECTOR PERFORMANCE CHANNEL 10 75/160/MIN 8 V/CM

CH = CHANNEL NUMBER	0.1000E+02
T = DET. TEMP	0.7500E+02
HD = DET. HEIGHT CM	0.1360E-01
WD = DET. WIDTH CM	0.2920E-01
TD = DETECTOR THICKNESS CM	0.1000E-02
VB = DETECTOR BIAS VOLTAGE V	0.2336E+00
CD = DETECTOR CAPACITANCE F	0.1500E-10
RD = DETECTOR DARK RESISTANCE OHM	0.4982E+03
ZD = DETECTOR IMPEDANCE OHM	0.4982E+03
PD = DETECTOR PHASE ANGLE RAD	0.8324E-10
X = MOLE FRACTION	0.1830E+00
PO = HOLE CONC. N-TYPE DOPING CM**-3	0.1000E+15
ND = DONAR CARRIER CONC. CM**-3	0.1305E+16
NI = INTRINSIC CARRIER CONC. CM**-3	0.3612E+15
TAU= CARRIER LIFETIME S	0.1000E-05
ETA= QUANTUM EFFICIENCY	0.7000E+00
NUP= PEAK WAVENUMBER 1/CM	0.6068E+03
EG = BAND GAP ENERGY EV	0.6847E-01
SIGMA = CONDUCTIVITY 1/OHM/CM	0.4310E+01
MU = ELECTRON MOBILITY CM**2/V/S	0.2060E+05
MUH= HOLE MOBILITY CM**2/V/S	0.2950E+03
QBG= BKGD PHOTON FLUX DENSITY P/CM**2/S	0.7000E+15
QS = SGNL PHOTON FLUX DENSITY P/CM**2/S	0.9270E+13
TR1= FEEDBACK RESISTOR TEMP. K	0.1600E+03
C1 = FDBK RESISTOR CAPACITANCE F	0.3000E-12
R1 = FEEDBACK RESISTANCE OHM	0.4982E+04
P1 = FDBK RESISTOR PHASE ANGLE RAD	0.1665E-12
Z1 = FDBK RESISTOR IMPEDANCE OHM	0.4982E+04
VS = SUPPLY VOLTAGE TO R1/DET. V	0.2570E+01
AO = OPEN LOOP GAIN	0.1000E+04
VP = PREAMP NOISE (INPUT) V/HZ**.5	0.2000E-08
FC = CHOPPING FREQUENCY HZ	0.4400E+03
PW = DETECTOR BIAS POWER W	0.1095E-03
PR1= FEEDBACK RESISTOR BIAS POWER W	0.1095E-02
SIGV = SIGNAL VOLTAGE V	0.6102E-04
RE = DET. RESPONSIVITY V/W	0.2378E+05
AZ = TRANSIMPEDANCE OHM	0.5032E+04
R = DET./PREAMP RESPONSIVITY V/W	0.2402E+06
VBG= BACKGROUND NOISE V/HZ**.5	0.4071E-08
VJN= JOHNSON NOISE V/HZ**.5	0.1451E-07
VGR= GR NOISE V/HZ**.5	0.5816E-07
VNR= FDBK RESISTOR NOISE V/HZ**.5	0.6702E-08
VPA= PREAMP NOISE V/HZ**.5	0.2770E-07
VT = TOTAL NOISE V/HZ**.5	0.6650E-07
NEP= NOISE EQUIVALENT POWER W/HZ**.5	0.2769E-12
DSTAR = PEAK DSTAR CM*HZ**.5/W	0.7198E+11

PC HGCDTE DETECTOR PERFORMANCE CHANNEL 10 75/160/STD 8 V/CM

CH = CHANNEL NUMBER	0.1000E+02
T = DET. TEMP	0.7500E+02
HD = DET. HEIGHT CM	0.1360E-01
WD = DET. WIDTH CM	0.2920E-01
TD = DETECTOR THICKNESS CM	0.1000E-02
VB = DETECTOR BIAS VOLTAGE V	0.2336E+00
CD = DETECTOR CAPACITANCE F	0.1500E-10
RD = DETECTOR DARK RESISTANCE OHM	0.4982E+03
ZD = DETECTOR IMPEDANCE OHM	0.4982E+03
PD = DETECTOR PHASE ANGLE RAD	0.8324E-10
X = MOLE FRACTION	0.1830E+00
PO = HOLE CONC. N-TYPE DOPING CM**-3	0.1000E+15
ND = DONAR CARRIER CONC. CM**-3	0.1305E+16
NI = INTRINSIC CARRIER CONC. CM**-3	0.3612E+15
TAU= CARRIER LIFETIME S	0.1000E-05
ETA= QUANTUM EFFICIENCY	0.7000E+00
NUP= PEAK WAVENUMBER 1/CM	0.6068E+03
EG = BAND GAP ENERGY EV	0.6847E-01
SIGMA = CONDUCTIVITY 1/OHM/CM	0.4310E+01
MU = ELECTRON MOBILITY CM**2/V/S	0.2060E+05
MUH= HOLE MOBILITY CM**2/V/S	0.2950E+03
QBG= BKGD PHOTON FLUX DENSITY P/CM**2/S	0.7120E+15
QS = SGNL PHOTON FLUX DENSITY P/CM**2/S	0.1900E+14
TR1= FEEDBACK RESISTOR TEMP. K	0.1600E+03
C1 = FDBK RESISTOR CAPACITANCE F	0.3000E-12
R1 = FEEDBACK RESISTANCE OHM	0.4982E+04
P1 = FDBK RESISTOR PHASE ANGLE RAD	0.1665E-12
Z1 = FDBK RESISTOR IMPEDANCE OHM	0.4982E+04
VS = SUPPLY VOLTAGE TO R1/DET. V	0.2570E+01
AO = OPEN LOOP GAIN	0.1000E+04
VP = PREAMP NOISE (INPUT) V/HZ**.5	0.2000E-08
FC = CHOPPING FREQUENCY HZ	0.4400E+03
PW = DETECTOR BIAS POWER W	0.1095E-03
PR1= FEEDBACK RESISTOR BIAS POWER W	0.1095E-02
SIGV = SIGNAL VOLTAGE V	0.1251E-03
RE = DET. RESPONSIVITY V/W	0.2378E+05
AZ = TRANSIMPEDANCE OHM	0.5032E+04
R = DET./PREAMP RESPONSIVITY V/W	0.2402E+06
VBG= BACKGROUND NOISE V/HZ**.5	0.4106E-08
VJN= JOHNSON NOISE V/HZ**.5	0.1451E-07
VGR= GR NOISE V/HZ**.5	0.5816E-07
VNR= FDBK RESISTOR NOISE V/HZ**.5	0.6702E-08
VPA= PREAMP NOISE V/HZ**.5	0.2770E-07
VT = TOTAL NOISE V/HZ**.5	0.6650E-07
NEP= NOISE EQUIVALENT POWER W/HZ**.5	0.2769E-12
DSTAR = PEAK DSTAR CM*HZ**.5/W	0.7198E+11

PC HGCDTE DETECTOR PERFORMANCE CHANNEL 10 75/160/MAX 8 V/CM

CH = CHANNEL NUMBER	0.1000E+02
T = DET. TEMP	0.7500E+02
HD = DET. HEIGHT CM	0.1360E-01
WD = DET. WIDTH CM	0.2920E-01
TD = DETECTOR THICKNESS CM	0.1090E-02
VB = DETECTOR BIAS VOLTAGE V	0.2336E+00
CD = DETECTOR CAPACITANCE F	0.1500E-10
RD = DETECTOR DARK RESISTANCE OHM	0.4982E+03
ZD = DETECTOR IMPEDANCE OHM	0.4982E+03
PD = DETECTOR PHASE ANGLE RAD	0.8324E-10
X = MOLE FRACTION	0.1830E+00
PO = HOLE CONC. N-TYPE DOPING CM**-3	0.1000E+15
ND = DONAR CARRIER CONC. CM**-3	0.1305E+16
NI = INTRINSIC CARRIER CONC. CM**-3	0.3612E+15
TAU= CARRIER LIFETIME S	0.1000E-05
ETA= QUANTUM EFFICIENCY	0.7000E+00
NUP= PEAK WAVENUMBER 1/CM	0.6068E+03
EG = BAND GAP ENERGY EV	0.6847E-01
SIGMA = CONDUCTIVITY 1/OHM/CM	0.4310E+01
MU = ELECTRON MOBILITY CM**2/V/S	0.2060E+05
MUH= HOLE MOBILITY CM**2/V/S	0.2950E+03
QBG= BKGD PHOTON FLUX DENSITY P/CM**2/S	0.7300E+15
QS = SGNL PHOTON FLUX DENSITY P/CM**2/S	0.4130E+14
TR1= FEEDBACK RESISTOR TEMP. K	0.1600E+03
C1 = FDBK RESISTOR CAPACITANCE F	0.3000E-12
R1 = FEEDBACK RESISTANCE OHM	0.4982E+04
P1 = FDBK RESISTOR PHASE ANGLE RAD	0.1665E-12
Z1 = FDBK RESISTOR IMPEDANCE OHM	0.4982E+04
VS = SUPPLY VOLTAGE TO R1/DET. V	0.2570E+01
AO = OPEN LOOP GAIN	0.1000E+04
VP = PREAMP NOISE (INPUT) V/HZ**.5	0.2000E-08
FC = CHOPPING FREQUENCY HZ	0.4400E+03
PW = DETECTOR BIAS POWER W	0.1095E-03
PR1= FEEDBACK RESISTOR BIAS POWER W	0.1095E-02
SIGV = SIGNAL VOLTAGE V	0.2710E-03
RE = DET. RESPONSIVITY V/W	0.2378E+05
AZ = TRANSIMPEDANCE OHM	0.5032E+04
R = DET./PREAMP RESPONSIVITY V/W	0.2402E+06
VBG= BACKGROUND NOISE V/HZ**.5	0.4158E-08
VJN= JOHNSON NOISE V/HZ**.5	0.1451E-07
VGR= GR NOISE V/HZ**.5	0.5816E-07
VNR= FDBK RESISTOR NOISE V/HZ**.5	0.6702E-08
VPA= PREAMP NOISE V/HZ**.5	0.2770E-07
VT = TOTAL NOISE V/HZ**.5	0.6650E-07
NEP= NOISE EQUIVALENT POWER W/HZ**.5	0.2769E-12
DSTAR = PEAK DSTAR CM*HZ**.5/W	0.7197E+11

Table F-4 (CH 11)

PC HGCDTE DETECTOR PERFORMANCE CHANNEL 11 75/160/MIN 8 V/CM

CH = CHANNEL NUMBER	0.1100E+02
T = DET. TEMP	0.7500E+02
HD = DET. HEIGHT CM	0.1360E-01
WD = DET. WIDTH CM	0.3190E-01
TD = DETECTOR THICKNESS CM	0.1000E-02
VB = DETECTOR BIAS VOLTAGE V	0.2552E+00
CD = DETECTOR CAPACITANCE F	0.5000E-10
RD = DETECTOR DARK RESISTANCE OHM	0.7215E+03
ZD = DETECTOR IMPEDANCE OHM	0.7215E+03
PD = DETECTOR PHASE ANGLE RAD	0.1916E-09
X = MOLE FRACTION	0.2035E+00
PO = HOLE CONC. N-TYPE DOPING CM**-3	0.2000E+13
ND = DONAR CARRIER CONC. CM**-3	0.1010E+16
NI = INTRINSIC CARRIER CONC. CM**-3	0.4493E+14
TAU= CARRIER LIFETIME S	0.1000E-05
ETA= QUANTUM EFFICIENCY	0.7000E+00
NUP= PEAK WAVENUMBER 1/CM	0.8745E+03
EG = BAND GAP ENERGY EV	0.9891E-01
SIGMA = CONDUCTIVITY 1/OHM/CM	0.3251E+01
MU = ELECTRON MOBILITY CM**2/V/S	0.2810E+05
MUH= HOLE MOBILITY CM**2/V/S	0.2920E+03
QBG= BKGD PHOTON FLUX DENSITY P/CM**2/S	0.2670E+16
QS = SGNL PHOTON FLUX DENSITY P/CM**2/S	0.5680E+14
TR1= FEEDBACK RESISTOR TEMP. K	0.1600E+03
C1 = FDBK RESISTOR CAPACITANCE F	0.3000E-12
R1 = FEEDBACK RESISTANCE OHM	0.7215E+04
P1 = FDBK RESISTOR PHASE ANGLE RAD	0.1149E-12
Z1 = FDBK RESISTOR IMPEDANCE OHM	0.7215E+04
VS = SUPPLY VOLTAGE TO R1/DET. V	0.2807E+01
AO = OPEN LOOP GAIN	0.1000E+04
VP = PREAMP NOISE (INPUT) V/HZ**.5	0.2800E-08
FC = CHOPPING FREQUENCY HZ	0.4400E+03
PW = DETECTOR BIAS POWER W	0.9026E-04
PR1= FEEDBACK RESISTOR BIAS POWER W	0.9026E-03
SIGV = SIGNAL VOLTAGE V	0.4720E-03
RE = DET. RESPONSIVITY V/W	0.2134E+05
AZ = TRANSIMPEDANCE OHM	0.7288E+04
R = DET./PREAMP RESPONSIVITY V/W	0.2156E+06
VBG= BACKGROUND NOISE V/HZ**.5	0.1075E-07
VJN= JOHNSON NOISE V/HZ**.5	0.1746E-07
VGR= GR NOISE V/HZ**.5	0.1112E-07
VNR= FDBK RESISTOR NOISE V/HZ**.5	0.8065E-08
VPA= PREAMP NOISE V/HZ**.5	0.2770E-07
VT = TOTAL NOISE V/HZ**.5	0.3710E-07
NEP= NOISE EQUIVALENT POWER W/HZ**.5	0.1721E-12
DSTAR = PEAK DSTAR CM*HZ**.5/W	0.1210E+12

PC HGCDTE DETECTOR PERFORMANCE CHANNEL 11 75/160/STD 8 V/CM

CH = CHANNEL NUMBER	0.1100E+02
T = DET. TEMP	0.7500E+02
HD = DET. HEIGHT CM	0.1360E-01
WD = DET. WIDTH CM	0.3190E-01
TD = DETECTOR THICKNESS CM	0.1000E-02
VB = DETECTOR BIAS VOLTAGE V	0.2552E+00
CD = DETECTOR CAPACITANCE F	0.5000E-10
RD = DETECTOR DARK RESISTANCE OHM	0.7215E+03
ZD = DETECTOR IMPEDANCE OHM	0.7215E+03
PD = DETECTOR PHASE ANGLE RAD	0.1916E-09
X = MOLE FRACTION	0.2035E+00
PO = HOLE CONC. N-TYPE DOPING CM**-3	0.2000E+13
ND = DONAR CARRIER CONC. CM**-3	0.1010E+16
NI = INTRINSIC CARRIER CONC. CM**-3	0.4493E+14
TAU= CARRIER LIFETIME S	0.1000E-05
ETA= QUANTUM EFFICIENCY	0.7000E+00
NUP= PEAK WAVENUMBER 1/CM	0.8745E+03
EG = BAND GAP ENERGY EV	0.9891E-01
SIGMA = CONDUCTIVITY 1/OHM/CM	0.3251E+01
MU = ELECTRON MOBILITY CM**2/V/S	0.2810E+05
MUH= HOLE MOBILITY CM**2/V/S	0.2920E+03
QBG= BKGD PHOTON FLUX DENSITY P/CM**2/S	0.2810E+16
QS = SGNL PHOTON FLUX DENSITY P/CM**2/S	0.1817E+15
TR1= FEEDBACK RESISTOR TEMP. K	0.1600E+03
C1 = FDBK RESISTOR CAPACITANCE F	0.3000E-12
R1 = FEEDBACK RESISTANCE OHM	0.7215E+04
P1 = FDBK RESISTOR PHASE ANGLE RAD	0.1149E-12
Z1 = FDBK RESISTOR IMPEDANCE OHM	0.7215E+04
VS = SUPPLY VOLTAGE TO R1/DET. V	0.2807E+01
AO = OPEN LOOP GAIN	0.1000E+04
VP = PREAMP NOISE (INPUT) V/HZ**.5	0.2800E-08
FC = CHOPPING FREQUENCY HZ	0.4400E+03
PW = DETECTOR BIAS POWER W	0.9026E-04
PR1= FEEDBACK RESISTOR BIAS POWER W	0.9026E-03
SIGV = SIGNAL VOLTAGE V	0.1504E-02
RE = DET. RESPONSIVITY V/W	0.2134E+05
AZ = TRANSIMPEDANCE OHM	0.7288E+04
R = DET./PREAMP RESPONSIVITY V/W	0.2156E+06
VBG= BACKGROUND NOISE V/HZ**.5	0.1103E-07
VJN= JOHNSON NOISE V/HZ**.5	0.1746E-07
VGR= GR NOISE V/HZ**.5	0.1112E-07
VNR= FDBK RESISTOR NOISE V/HZ**.5	0.8065E-08
VPA= PREAMP NOISE V/HZ**.5	0.2770E-07
VT = TOTAL NOISE V/HZ**.5	0.3718E-07
NEP= NOISE EQUIVALENT POWER W/HZ**.5	0.1725E-12
DSTAR = PEAK DSTAR CM*HZ**.5/W	0.1208E+12

PC HGCDTE DETECTOR PERFORMANCE CHANNEL 11 75/160/MAX 8 V/CM

CH = CHANNEL NUMBER	0.1100E+02
T = DET. TEMP	0.7500E+02
HD = DET. HEIGHT CM	0.1360E-01
WD = DET. WIDTH CM	0.3190E-01
TD = DETECTOR THICKNESS CM	0.1000E-02
VB = DETECTOR BIAS VOLTAGE V	0.2552E+00
CD = DETECTOR CAPACITANCE F	0.5000E-10
RD = DETECTOR DARK RESISTANCE OHM	0.7215E+03
ZD = DETECTOR IMPEDANCE OHM	0.7215E+03
PD = DETECTOR PHASE ANGLE RAD	0.1916E-09
X = MOLE FRACTION	0.2035E+00
PO = HOLE CONC. N-TYPE DOPING CM**-3	0.2000E+13
ND = DONAR CARRIER CONC. CM**-3	0.1010E+16
NI = INTRINSIC CARRIER CONC. CM**-3	0.4493E+14
TAU= CARRIER LIFETIME S	0.1000E-05
ETA= QUANTUM EFFICIENCY	0.7000E+00
NUP= PEAK WAVENUMBER 1/CM	0.8745E+03
EG = BAND GAP ENERGY EV	0.9891E-01
SIGMA = CONDUCTIVITY 1/OHM-CM	0.3251E+01
MU = ELECTRON MOBILITY CM**2/V/S	0.2810E+05
MUH= HOLE MOBILITY CM**2/V/S	0.2920E+03
QBG= BKGD PHOTON FLUX DENSITY P/CM**2/S	0.2958E+16
QS = SGNL PHOTON FLUX DENSITY P/CM**2/S	0.3170E+15
TR1= FEEDBACK RESISTOR TEMP. K	0.1600E+03
C1 = FDBK RESISTOR CAPACITANCE F	0.3000E-12
R1 = FEEDBACK RESISTANCE OHM	0.7215E+04
P1 = FDBK RESISTOR PHASE ANGLE RAD	0.1149E-12
Z1 = FDBK RESISTOR IMPEDANCE OHM	0.7215E+04
VS = SUPPLY VOLTAGE TO R1/DET. V	0.2807E+01
AO = OPEN LOOP GAIN	0.1000E+04
VP = PREAMP NOISE (INPUT) V/HZ**.5	0.2800E-08
FC = CHOPPING FREQUENCY HZ	0.4400E+03
PW = DETECTOR BIAS POWER W	0.9026E-04
PR1= FEEDBACK RESISTOR BIAS POWER W	0.9026E-03
SIGV = SIGNAL VOLTAGE V	0.2634E-02
RE = DET. RESPONSIVITY V/W	0.2134E+05
AZ = TRANSIMPEDANCE OHM	0.7288E+04
R = DET./PREAMP RESPONSIVITY V/W	0.2156E+06
VBG= BACKGROUND NOISE V/HZ**.5	0.1[illegible]E-07
VJN= JOHNSON NOISE V/HZ**.5	0.1746E-07
VGR= GR NOISE V/HZ**.5	0.1112E-07
VNR= FDBK RESISTOR NOISE V/HZ**.5	0.8065E-08
VPA= PREAMP NOISE V/HZ**.5	0.2770E-07
VT = TOTAL NOISE V/HZ**.5	0.3726E-07
NEP= NOISE EQUIVALENT POWER W/HZ**.5	0.1728E-12
DSTAR = PEAK DSTAR CM*HZ**.5/W	0.1205E+12

Table F-4 (CH 12)

PV HGCDTE DETECTOR PERFORMANCE CHANNEL 12 75/160/MIN		PV HGCDTE DETECTOR PERFORMANCE CHANNEL 12 75/.60/STD		PV HGCDTE DETECTOR PERFORMANCE CHANNEL 12 75/160/MAX	
CH = CHANNEL NUMBER	0.1200E+02	CH = CHANNEL NUMBER	0.1200E+02	CH = CHANNEL NUMBER	0.1200E+02
HD = DETECTOR HEIGHT CM	0.5300E-01	HD = DETECTOR HEIGHT CM	0.5300E-01	HD = DETECTOR HEIGHT CM	0.5300E-01
WD = DETECTOR WIDTH CM	0.9450E-01	WD = DETECTOR WIDTH CM	0.9450E-01	WD = DETECTOR WIDTH CM	0.9450E-01
T = DET. TEMP. K	0.7500E+02	T = DET. TEMP. K	0.7500E+02	T = DET. TEMP. K	0.7500E+02
CS = DET. STRAY CAPACITANCE F	0.6000E-11	CS = DET. STRAY CAPACITANCE F	0.6000E-11	CS = DET. STRAY CAPACITANCE F	0.6000E-11
RS = DET. SHUNT RESISTANCE OHM	0.1050E+07	RS = DET. SHUNT RESISTANCE OHM	0.1050E+07	RS = DET. SHUNT RESISTANCE OHM	0.1050E+07
X = MOLE FRACTION	0.2143E+00	X = MOLE FRACTION	0.2143E+00	X = MOLE FRACTION	0.2143E+00
VB = BIAS VOLTAGE V	0.0000E+00	VB = BIAS VOLTAGE V	0.0000E+00	VB = BIAS VOLTAGE V	0.0000E+00
EG = BAND GAP ENERGY EV	0.1156E+00	EG = BAND GAP ENERGY EV	0.1156E+00	EG = BAND GAP ENERGY EV	0.1156E+00
NI = INTRINSIC CONC. CM**-3	0.1798E+10	NI = INTRINSIC CONC. CM**-3	0.1798E+10	NI = INTRINSIC CONC. CM**-3	0.1798E+10
NA = ACCEPTOR CONC. CM**-3	0.2000E+15	NA = ACCEPTOR CONC. CM**-3	0.2000E+15	NA = ACCEPTOR CONC. CM**-3	0.2000E+15
ND = DONOR CARRIER CONC. CM**-3	0.1000E+16	ND = DONOR CARRIER CONC. CM**-3	0.1000E+16	ND = DONOR CARRIER CONC. CM**-3	0.1000E+16
MU = ELECTRON MOBILITY CM**2/V/S	0.1900E+05	MU = ELECTRON MOBILITY CM**2/V/S	0.1900E+05	MU = ELECTRON MOBILITY CM**2/V/S	0.1900E+05
MUH= HOLE MOBILITY CM**2/V/S	0.2890E+03	MUH= HOLE MOBILITY CM**2/V/S	0.2890E+03	MUH= HOLE MOBILITY CM**2/V/S	0.2890E+03
ETA= QUANTUM EFFICIENCY	0.7500E+00	ETA= QUANTUM EFFICIENCY	0.7500E+00	ETA= QUANTUM EFFICIENCY	0.7500E+00
TAU= CARRIER LIFETIME S	0.5000E-06	TAU= CARRIER LIFETIME S	0.5000E-06	TAU= CARRIER LIFETIME S	0.5000E-06
NUP= PEAK WAVENUMBER 1/CM	0.1036E+04	NUP= PEAK WAVENUMBER 1/CM	0.1036E+04	NUP= PEAK WAVENUMBER 1/CM	0.1036E+04
QBG= BKGD PHOTON FLUX DENSITY P/CM**2/S	0.3020E+14	QBG= BKGD PHOTON FLUX DENSITY P/CM**2/S	0.3550E+14	QBG= BKGD PHOTON FLUX DENSITY P/CM**2/S	0.4150E+14
QS = SGNL PHOTON FLUX DENSITY P/CM**2/S	0.1120E+13	QS = SGNL PHOTON FLUX DENSITY P/CM**2/S	0.6320E+13	QS = SGNL PHOTON FLUX DENSITY P/CM**2/S	0.1250E+14
KAPPA = DIELECTRIC CONSTANT	0.1384E+02	KAPPA = DIELECTRIC CONSTANT	0.1384E+02	KAPPA = DIELECTRIC CONSTANT	0.1384E+02
RF = FEEDBACK RESISTANCE OHM	0.1000E+10	RF = FEEDBACK RESISTANCE OHM	0.1000E+10	RF = FEEDBACK RESISTANCE OHM	0.1000E+10
CF = FEEDBACK CAPACITACE F	0.3000E-12	CF = FEEDBACK CAPACITACE F	0.3000E-12	CF = FEEDBACK CAPACITACE F	0.3000E-12
VP = PREAMP NOISE (INPUT) V/HZ**.5	0.2800E-08	VP = PREAMP NOISE (INPUT) V/HZ**.5	0.2800E-08	VP = PREAMP NOISE (INPUT) V/HZ**.5	0.2800E-08
AO = OPEN LOOP GAIN OF PREAMP	0.1000E+04	AO = OPEN LOOP GAIN OF PREAMP	0.1000E+04	AO = OPEN LOOP GAIN OF PREAMP	0.1000E+04
TRF= FEEDBACK RESISTOR TEMP K	0.1600E+03	TRF= FEEDBACK RESISTOR TEMP K	0.1600E+03	TRF= FEEDBACK RESISTOR TEMP K	0.1600E+03
FC = CHOPPING FREQUENCY HZ	0.4400E+03	FC = CHOPPING FREQUENCY HZ	0.4400E+03	FC = CHOPPING FREQUENCY HZ	0.4400E+03
RO = DIODE DARK RESISTANCE BIAS=0 OHM	0.2096E+09	RO = DIODE DARK RESISTANCE BIAS=0 OHM	0.2096E+09	RO = DIODE DARK RESISTANCE BIAS=0 OHM	0.2096E+09
RA = R(0)*A PRODUCT OHM*CM**2	0.1050E+07	RA = R(0)*A PRODUCT OHM*CM**2	0.1050E+07	RA = R(0)*A PRODUCT OHM*CM**2	0.1050E+07
VJ = JUNCTION POTENTIAL V	0.1606E+00	VJ = JUNCTION POTENTIAL V	0.1606E+00	VJ = JUNCTION POTENTIAL V	0.1606E+00
CJ = JUNCTION CAPACITANCE F	0.1238E-09	CJ = JUNCTION CAPACITANCE F	0.1238E-09	CJ = JUNCTION CAPACITANCE F	0.1238E-09
WJ = JUNCTION WIDTH CM	0.4958E-04	WJ = JUNCTION WIDTH CM	0.4958E-04	WJ = JUNCTION WIDTH CM	0.4958E-04
VC = CONTACT POTENTIAL V	0.1606E+00	VC = CONTACT POTENTIAL V	0.1606E+00	VC = CONTACT POTENTIAL V	0.1606E+00
ZD = DETECTOR IMPEDANCE OHM	0.2749E+07	ZD = DETECTOR IMPEDANCE OHM	0.2749E+07	ZD = DETECTOR IMPEDANCE OHM	0.2749E+07
ZF = FEEDBACK RESISTOR IMPEDANCE OHM	0.5466E+09	ZF = FEEDBACK RESISTOR IMPEDANCE OHM	0.5466E+09	ZF = FEEDBACK RESISTOR IMPEDANCE OHM	0.5466E+09
PD = DET. PHASE ANGLE RAD	0.1633E-14	PD = DET. PHASE ANGLE RAD	0.1633E-14	PD = DET. PHASE ANGLE RAD	0.1633E-14
PF = FDBK RESISTOR PHASE ANGLE RAD	0.8294E-18	PF = FDBK RESISTOR PHASE ANGLE RAD	0.8294E-18	PF = FDBK RESISTOR PHASE ANGLE RAD	0.8294E-18
AZ = TRANSIMPEDANCE OHM	0.6823E+09	AZ = TRANSIMPEDANCE OHM	0.6823E+09	AZ = TRANSIMPEDANCE OHM	0.6823E+09
IS = SIGNAL PHOTOCURRENT A	0.6740E-09	IS = SIGNAL PHOTOCURRENT A	0.3803E-08	IS = SIGNAL PHOTOCURRENT A	0.7522E-08
IT = TOTAL BKGD PHOTOCURRENT A	0.1817E-07	IT = TOTAL BKGD PHOTOCURRENT A	0.2136E-07	IT = TOTAL BKGD PHOTOCURRENT A	0.2497E-07
VRF= FDBK RESISTOR NOISE V/HZ**.5	0.2028E-05	VRF= FDBK RESISTOR NOISE V/HZ**.5	0.2028E-05	VRF= FDBK RESISTOR NOISE V/HZ**.5	0.2028E-05
VBG= BACKGROUND NOISE V/HZ**.5	0.5206E-04	VBG= BACKGROUND NOISE V/HZ**.5	0.5645E-04	VBG= BACKGROUND NOISE V/HZ**.5	0.6183E-04
VJN= JOHNSON NOISE V/HZ**.5	0.3033E-05	VJN= JOHNSON NOISE V/HZ**.5	0.3033E-05	VJN= JOHNSON NOISE V/HZ**.5	0.3033E-05
VPA= PREAMP NOISE V/HZ**.5	0.4640E-06	VPA= PREAMP NOISE V/HZ**.5	0.4640E-06	VPA= PREAMP NOISE V/HZ**.5	0.4640E-06
VT = TOTAL NOISE V/HZ**.5	0.5219E-04	VT = TOTAL NOISE V/HZ**.5	0.5657E-04	VT = TOTAL NOISE V/HZ**.5	0.6114E-04
R = RESPONSIVITY V/W	0.3982E+10	R = RESPONSIVITY V/W	0.3982E+10	R = RESPONSIVITY V/W	0.3982E+10
NEP= NOISE EQUIVALENT POWER W/HZ**.5	0.1311E-13	NEP= NOISE EQUIVALENT POWER W/HZ**.5	0.1420E-13	NEP= NOISE EQUIVALENT POWER W/HZ**.5	0.1535E-13
DSTAR = CM*HZ**.5/W	0.5400E+13	DSTAR = CM*HZ**.5/W	0.4982E+13	DSTAR = CM*HZ**.5/W	0.4609E+13

Table F-4 (CH 13)

PV HGCDTE DETECTOR PERFORMANCE CHANNEL 13 75/160/MIN		PV HGCDTE DETECTOR PERFORMANCE CHANNEL 13 75/160/STD		PV HGCDTE DETECTOR PERFORMANCE CHANNEL 13 75/160/MAX	
CH = CHANNEL NUMBER	0.1300E+02	CH = CHANNEL NUMBER	0.1300E+02	CH = CHANNEL NUMBER	0.1300E+02
HD = DETECTOR HEIGHT CM	0.5300E-01	HD = DETECTOR HEIGHT CM	0.5300E-01	HD = DETECTOR HEIGHT CM	0.5300E-01
WD = DETECTOR WIDTH CM	0.8820E-01	WD = DETECTOR WIDTH CM	0.8820E-01	WD = DETECTOR WIDTH CM	0.8820E-01
T = DET. TEMP. K	0.7500E+02	T = DET. TEMP. K	0.7500E+02	T = DET. TEMP. K	0.7500E+02
CS = DET. STRAY CAPACITANCE F	0.6000E-11	CS = DET. STRAY CAPACITANCE F	0.6000E-11	CS = DET. STRAY CAPACITANCE F	0.6000E-11
RS = DET. SHUNT RESISTANCE OHM	0.1050E+07	RS = DET. SHUNT RESISTANCE OHM	0.1050E+07	RS = DET. SHUNT RESISTANCE OHM	0.1050E+07
X = MOLE FRACTION	0.2143E+00	X = MOLE FRACTION	0.2143E+00	X = MOLE FRACTION	0.2143E+00
VB = BIAS VOLTAGE V	0.0000E+00	VB = BIAS VOLTAGE V	0.0000E+00	VB = BIAS VOLTAGE V	0.0000E+00
EG = BAND GAP ENERGY EV	0.1156E+00	EG = BAND GAP ENERGY EV	0.1156E+00	EG = BAND GAP ENERGY EV	0.1156E+00
NI = INTRINSIC CONC. CM**-3	0.1798E+10	NI = INTRINSIC CONC. CM**-3	0.1798E+10	NI = INTRINSIC CONC. CM**-3	0.1798E+10
NA = ACCEPTOR CONC. CM**-3	0.2000E+15	NA = ACCEPTOR CONC. CM**-3	0.2000E+15	NA = ACCEPTOR CONC. CM**-3	0.2000E+15
ND = DONOR CARRIER CONC. CM**-3	0.1000E+16	ND = DONOR CARRIER CONC. CM**-3	0.1000E+16	ND = DONOR CARRIER CONC. CM**-3	0.1000E+16
MU = ELECTRON MOBILITY CM**2/V/S	0.1900E+05	MU = ELECTRON MOBILITY CM**2/V/S	0.1900E+05	MU = ELECTRON MOBILITY CM**2/V/S	0.1900E+05
MUH= HOLE MOBILITY CM**2/V/S	0.2890E+03	MUH= HOLE MOBILITY CM**2/V/S	0.2890E+03	MUH= HOLE MOBILITY CM**2/V/S	0.2890E+03
ETA= QUANTUM EFFICIENCY	0.7500E+00	ETA= QUANTUM EFFICIENCY	0.7500E+00	ETA= QUANTUM EFFICIENCY	0.7500E+00
TAU= CARRIER LIFETIME S	0.5000E-06	TAU= CARRIER LIFETIME S	0.5000E-06	TAU= CARRIER LIFETIME S	0.5000E-06
NUP= PEAK WAVENUMBER 1/CM	0.1036E+04	NUP= PEAK WAVENUMBER 1/CM	0.1036E+04	NUP= PEAK WAVENUMBER 1/CM	0.1036E+04
QBG= BKGD PHOTON FLUX DENSITY P/CM**2/S	0.9670E+13	QBG= BKGD PHOTON FLUX DENSITY P/CM**2/S	0.1620E+14	QBG= BKGD PHOTON FLUX DENSITY P/CM**2/S	0.2300E+14
QS = SGNL PHOTON FLUX DENSITY P/CM**2/S	0.1550E+13	QS = SGNL PHOTON FLUX DENSITY P/CM**2/S	0.6700E+13	QS = SGNL PHOTON FLUX DENSITY P/CM**2/S	0.1400E+14
KAPPA = DIELECTRIC CONSTANT	0.1384E+02	KAPPA = DIELECTRIC CONSTANT	0.1384E+02	KAPPA = DIELECTRIC CONSTANT	0.1384E+02
RF = FEEDBACK RESISTANCE OHM	0.1000E+10	RF = FEEDBACK RESISTANCE OHM	0.1000E+10	RF = FEEDBACK RESISTANCE OHM	0.1000E+10
CF = FEEDBACK CAPACITACE F	0.3000E-12	CF = FEEDBACK CAPACITACE F	0.3000E-12	CF = FEEDBACK CAPACITACE F	0.3000E-12
VP = PREAMP NOISE (INPUT) V/HZ**.5	0.2800E-08	VP = PREAMP NOISE (INPUT) V/HZ**.5	0.2800E-08	VP = PREAMP NOISE (INPUT) V/HZ**.5	0.2800E-08
AO = OPEN LOOP GAIN OF PREAMP	0.1000E+04	AO = OPEN LOOP GAIN OF PREAMP	0.1000E+04	AO = OPEN LOOP GAIN OF PREAMP	0.1000E+04
TRF= FEEDBACK RESISTOR TEMP K	0.1600E+03	TRF= FEEDBACK RESISTOR TEMP K	0.1600E+03	TRF= FEEDBACK RESISTOR TEMP K	0.1600E+03
FC = CHOPPING FREQUENCY HZ	0.4400E+03	FC = CHOPPING FREQUENCY HZ	0.4400E+03	FC = CHOPPING FREQUENCY HZ	0.4400E+03
RO = DIODE DARK RESISTANCE BIAS=0 OHM	0.2246E+09	RO = DIODE DARK RESISTANCE BIAS=0 OHM	0.2246E+09	RO = DIODE DARK RESISTANCE BIAS=0 OHM	0.2246E+09
RA = R(0)*A PRODUCT OHM*CM**2	0.1050E+07	RA = R(0)*A PRODUCT OHM*CM**2	0.1050E+07	RA = R(0)*A PRODUCT OHM*CM**2	0.1050E+07
VJ = JUNCTION POTENTIAL V	0.1606E+00	VJ = JUNCTION POTENTIAL V	0.1606E+00	VJ = JUNCTION POTENTIAL V	0.1606E+00
CJ = JUNCTION CAPACITANCE F	0.1156E-09	CJ = JUNCTION CAPACITANCE F	0.1156E-09	CJ = JUNCTION CAPACITANCE F	0.1156E-09
WJ = JUNCTION WIDTH CM	0.4958E-04	WJ = JUNCTION WIDTH CM	0.4958E-04	WJ = JUNCTION WIDTH CM	0.4958E-04
VC = CONTACT POTENTIAL V	0.1606E+00	VC = CONTACT POTENTIAL V	0.1606E+00	VC = CONTACT POTENTIAL V	0.1606E+00
ZD = DETECTOR IMPEDANCE OHM	0.2936E+07	ZD = DETECTOR IMPEDANCE OHM	0.2936E+07	ZD = DETECTOR IMPEDANCE OHM	0.2936E+07
ZF = FEEDBACK RESISTOR IMPEDANCE OHM	0.5466E+09	ZF = FEEDBACK RESISTOR IMPEDANCE OHM	0.5466E+09	ZF = FEEDBACK RESISTOR IMPEDANCE OHM	0.5466E+09
PD = DET. PHASE ANGLE RAD	0.1423E-14	PD = DET. PHASE ANGLE RAD	0.1423E-14	PD = DET. PHASE ANGLE RAD	0.1423E-14
PF = FDBK RESISTOR PHASE ANGLE RAD	0.8294E-18	PF = FDBK RESISTOR PHASE ANGLE RAD	0.8294E-18	PF = FDBK RESISTOR PHASE ANGLE RAD	0.8294E-18
AZ = TRANSIMPEDANCE OHM	0.6717E+09	AZ = TRANSIMPEDANCE OHM	0.6717E+09	AZ = TRANSIMPEDANCE OHM	0.6717E+09
IS = SIGNAL PHOTOCURRENT A	0.8706E-09	IS = SIGNAL PHOTOCURRENT A	0.3763E-08	IS = SIGNAL PHOTOCURRENT A	0.8312E-08
IT = TOTAL BKGD PHOTOCURRENT A	0.5544E-08	IT = TOTAL BKGD PHOTOCURRENT A	0.9099E-08	IT = TOTAL BKGD PHOTOCURRENT A	0.1292E-07
VRF= FDBK RESISTOR NOISE V/HZ**.5	0.1997E-05	VRF= FDBK RESISTOR NOISE V/HZ**.5	0.1997E-05	VRF= FDBK RESISTOR NOISE V/HZ**.5	0.1997E-05
VBG= BACKGROUND NOISE V/HZ**.5	0.2831E-04	VBG= BACKGROUND NOISE V/HZ**.5	0.3627E-04	VBG= BACKGROUND NOISE V/HZ**.5	0.4321E-04
VJN= JOHNSON NOISE V/HZ**.5	0.2884E-05	VJN= JOHNSON NOISE V/HZ**.5	0.2884E-05	VJN= JOHNSON NOISE V/HZ**.5	0.2884E-05
VPA= PREAMP NOISE V/HZ**.5	0.4391E-06	VPA= PREAMP NOISE V/HZ**.5	0.4391E-06	VPA= PREAMP NOISE V/HZ**.5	0.4391E-06
VT = TOTAL NOISE V/HZ**.5	0.2853E-04	VT = TOTAL NOISE V/HZ**.5	0.3644E-04	VT = TOTAL NOISE V/HZ**.5	0.4336E-04
R = RESPONSIVITY V/W	0.3920E+10	R = RESPONSIVITY V/W	0.3920E+10	R = RESPONSIVITY V/W	0.3920E+10
NEP= NOISE EQUIVALENT POWER W/HZ**.5	0.7277E-14	NEP= NOISE EQUIVALENT POWER W/HZ**.5	0.9294E-14	NEP= NOISE EQUIVALENT POWER W/HZ**.5	0.1106E-13
DSTAR = CM*HZ**.5/W	0.9396E+13	DSTAR = CM*HZ**.5/W	0.7356E+13	DSTAR = CM*HZ**.5/W	0.6182E+13

Table F-4 (CH 14)

PV HGCDTE DETECTOR PERFORMANCE CHANNEL 14	75/160/MIN	PV HGCDTE DETECTOR PERFORMANCE CHANNEL 14	75/150/STD	PV HGCDTE DETECTOR PERFORMANCE CHANNEL 14	75/160/MAX
CH = CHANNEL NUMBER	0.1400E+02	CH = CHANNEL NUMBER	0.1400E+02	CH = CHANNEL NUMBER	0.1400E+02
HD = DETECTOR HEIGHT CM	0.5300E-01	HD = DETECTOR HEIGHT CM	0.5300E-01	HD = DETECTOR HEIGHT CM	0.5300E-01
WD = DETECTOR WIDTH CM	0.9040E-01	WD = DETECTOR WIDTH CM	0.9040E-01	WD = DETECTOR WIDTH CM	0.9040E-01
T = DET. TEMP. K	0.7500E+02	T = DET. TEMP. K	0.7500E+02	T = DET. TEMP. K	0.7500E+02
CS = DET. STRAY CAPACITANCE F	0.6000E-11	CS = DET. STRAY CAPACITANCE F	0.6000E-11	CS = DET. STRAY CAPACITANCE F	0.6000E-11
RS = DET. SHUNT RESISTANCE OHM	0.1050E+07	RS = DET. SHUNT RESISTANCE OHM	0.1050E+07	RS = DET. SHUNT RESISTANCE OHM	0.1050E+07
X = MOLE FRACTION	0.2573E+00	X = MOLE FRACTION	0.2573E+00	X = MOLE FRACTION	0.2573E+00
VB = BIAS VOLTAGE V	0.0000E+00	VB = BIAS VOLTAGE V	0.0000E+00	VB = BIAS VOLTAGE V	0.0000E+00
EG = BAND GAP ENERGY EV	0.1829E+00	EG = BAND GAP ENERGY EV	0.1829E+00	EG = BAND GAP ENERGY EV	0.1829E+00
NI = INTRINSIC CONC. CM**-3	0.7530E+05	NI = INTRINSIC CONC. CM**-3	0.7530E+05	NI = INTRINSIC CONC. CM**-3	0.7530E+05
NA = ACCEPTOR CONC. CM**-3	0.7000E+15	NA = ACCEPTOR CONC. CM**-3	0.7000E+15	NA = ACCEPTOR CONC. CM**-3	0.7000E+15
ND = DONOR CARRIER CONC. CM**-3	0.1000E+17	ND = DONOR CARRIER CONC. CM**-3	0.1000E+17	ND = DONOR CARRIER CONC. CM**-3	0.1000E+17
MU = ELECTRON MOBILITY CM**2/V/S	0.1870E+05	MU = ELECTRON MOBILITY CM**2/V/S	0.1870E+05	MU = ELECTRON MOBILITY CM**2/V/S	0.1870E+05
MUH= HOLE MOBILITY CM**2/V/S	0.2770E+03	MUH= HOLE MOBILITY CM**2/V/S	0.2770E+03	MUH= HOLE MOBILITY CM**2/V/S	0.2770E+03
ETA= QUANTUM EFFICIENCY	0.7500E+00	ETA= QUANTUM EFFICIENCY	0.7500E+00	ETA= QUANTUM EFFICIENCY	0.7500E+00
TAU= CARRIER LIFETIME S	0.5000E-06	TAU= CARRIER LIFETIME S	0.5000E-06	TAU= CARRIER LIFETIME S	0.5000E-06
NUP= PEAK WAVENUMBER 1/CM	0.1639E+04	NUP= PEAK WAVENUMBER 1/CM	0.1639E+04	NUP= PEAK WAVENUMBER 1/CM	0.1639E+04
QBG= BKGD PHOTON FLUX DENSITY P/CM**2/S	0.9470E+12	QBG= BKGD PHOTON FLUX DENSITY P/CM**2/S	0.1140E+13	QBG= BKGD PHOTON FLUX DENSITY P/CM**2/S	0.1560E+13
QS = SGNL PHOTON FLUX DENSITY P/CM**2/S	0.1300E+12	QS = SGNL PHOTON FLUX DENSITY P/CM**2/S	0.3310E+12	QS = SGNL PHOTON FLUX DENSITY P/CM**2/S	0.7540E+12
KAPPA = DIELECTRIC CONSTANT	0.1361E+02	KAPPA = DIELECTRIC CONSTANT	0.1361E+02	KAPPA = DIELECTRIC CONSTANT	0.1361E+02
RF = FEEDBACK RESISTANCE OHM	0.1000E+10	RF = FEEDBACK RESISTANCE OHM	0.1000E+10	RF = FEEDBACK RESISTANCE OHM	0.1000E+10
CF = FEEDBACK CAPACITACE F	0.3000E-12	CF = FEEDBACK CAPACITACE F	0.3000E-12	CF = FEEDBACK CAPACITACE F	0.3000E-12
VP = PREAMP NOISE (INPUT) V/HZ**.5	0.2800E-08	VP = PREAMP NOISE (INPUT) V/HZ**.5	0.2800E-08	VP = PREAMP NOISE (INPUT) V/HZ**.5	0.2800E-08
AO = OPEN LOOP GAIN OF PREAMP	0.1000E+04	AO = OPEN LOOP GAIN OF PREAMP	0.1000E+04	AO = OPEN LOOP GAIN OF PREAMP	0.1000E+04
TRF= FEEDBACK RESISTOR TEMP K	0.1600E+03	TRF= FEEDBACK RESISTOR TEMP K	0.1600E+03	TRF= FEEDBACK RESISTOR TEMP K	0.1600E+03
FC = CHOPPING FREQUENCY HZ	0.4400E+03	FC = CHOPPING FREQUENCY HZ	0.4400E+03	FC = CHOPPING FREQUENCY HZ	0.4400E+03
RO = DIODE DARK RESISTANCE BIAS=0 OHM	0.2192E+09	RO = DIODE DARK RESISTANCE BIAS=0 OHM	0.2192E+09	RO = DIODE DARK RESISTANCE BIAS=0 OHM	0.2192E+09
RA = R(0)*A PRODUCT OHM*CM**2	0.1050E+07	RA = R(0)*A PRODUCT OHM*CM**2	0.1050E+07	RA = R(0)*A PRODUCT OHM*CM**2	0.1050E+07
VJ = JUNCTION POTENTIAL V	0.3139E+00	VJ = JUNCTION POTENTIAL V	0.3139E+00	VJ = JUNCTION POTENTIAL V	0.3139E+00
CJ = JUNCTION CAPACITANCE F	0.2657E-09	CJ = JUNCTION CAPACITANCE F	0.2657E-09	CJ = JUNCTION CAPACITANCE F	0.2657E-09
WJ = JUNCTION WIDTH CM	0.2173E-04	WJ = JUNCTION WIDTH CM	0.2173E-04	WJ = JUNCTION WIDTH CM	0.2173E-04
VC = CONTACT POTENTIAL V	0.3139E+00	VC = CONTACT POTENTIAL V	0.3139E+00	VC = CONTACT POTENTIAL V	0.3139E+00
ZD = DETECTOR IMPEDANCE OHM	0.1323E+07	ZD = DETECTOR IMPEDANCE OHM	0.1323E+07	ZD = DETECTOR IMPEDANCE OHM	0.1323E+07
ZF = FEEDBACK RESISTOR IMPEDANCE OHM	0.5466E+09	ZF = FEEDBACK RESISTOR IMPEDANCE OHM	0.5466E+09	ZF = FEEDBACK RESISTOR IMPEDANCE OHM	0.5466E+09
PD = DET. PHASE ANGLE RAD	0.3352E-14	PD = DET. PHASE ANGLE RAD	0.3352E-14	PD = DET. PHASE ANGLE RAD	0.3352E-14
PF = FDBK RESISTOR PHASE ANGLE RAD	0.8294E-18	PF = FDBK RESISTOR PHASE ANGLE RAD	0.8294E-18	PF = FDBK RESISTOR PHASE ANGLE RAD	0.8294E-18
AZ = TRANSIMPEDANCE OHM	0.9314E+09	AZ = TRANSIMPEDANCE OHM	0.9314E+09	AZ = TRANSIMPEDANCE OHM	0.9314E+09
IS = SIGNAL PHOTOCURRENT A	0.7944E-10	IS = SIGNAL PHOTOCURRENT A	0.1905E-09	IS = SIGNAL PHOTOCURRENT A	0.4348E-09
IT = TOTAL BKGD PHOTOCURRENT A	0.5452E-09	IT = TOTAL BKGD PHOTOCURRENT A	0.6563E-09	IT = TOTAL BKGD PHOTOCURRENT A	0.8980E-09
VRF= FDBK RESISTOR NOISE V/HZ**.5	0.2769E-05	VRF= FDBK RESISTOR NOISE V/HZ**.5	0.2769E-05	VRF= FDBK RESISTOR NOISE V/HZ**.5	0.2769E-05
VBG= BACKGROUND NOISE V/HZ**.5	0.1231E-04	VBG= BACKGROUND NOISE V/HZ**.5	0.1351E-04	VBG= BACKGROUND NOISE V/HZ**.5	0.1580E-04
VJN= JOHNSON NOISE V/HZ**.5	0.4049E-05	VJN= JOHNSON NOISE V/HZ**.5	0.4049E-05	VJN= JOHNSON NOISE V/HZ**.5	0.4049E-05
VPA= PREAMP NOISE V/HZ**.5	0.8180E-06	VPA= PREAMP NOISE V/HZ**.5	0.8180E-06	VPA= PREAMP NOISE V/HZ**.5	0.8180E-06
VT = TOTAL NOISE V/HZ**.5	0.1328E-04	VT = TOTAL NOISE V/HZ**.5	0.1439E-04	VT = TOTAL NOISE V/HZ**.5	0.1656E-04
R = RESPONSIVITY V/W	0.3436E+10	R = RESPONSIVITY V/W	0.3436E+10	R = RESPONSIVITY V/W	0.3436E+10
NEP= NOISE EQUIVALENT POWER W/HZ**.5	0.3863E-14	NEP= NOISE EQUIVALENT POWER W/HZ**.5	0.4188E-14	NEP= NOISE EQUIVALENT POWER W/HZ**.5	0.4820E-14
DSTAR = CM*HZ**.5/W	0.1792E+14	DSTAR = CM*HZ**.5/W	0.1653E+14	DSTAR = CM*HZ**.5/W	0.1436E+14

Table F-4 (CH 15)

PV HGCDTE DETECTOR PERFORMANCE CHANNEL 15 75/160/MIN		PV HGCDTE DETECTOR PERFORMANCE CHANNEL 15 75/160/STD		PV HGCDTE DETECTOR PERFORMANCE CHANNEL 15 75/160/MAX	
CH = CHANNEL NUMBER	0.1500E+02	CH = CHANNEL NUMBER	0.1500E+02	CH = CHANNEL NUMBER	0.1500E+02
HD = DETECTOR HEIGHT CM	0.5300E-01	HD = DETECTOR HEIGHT CM	0.5300E-01	HD = DETECTOR HEIGHT CM	0.5300E-01
WD = DETECTOR WIDTH CM	0.1020E+00	WD = DETECTOR WIDTH CM	0.1020E+00	WD = DETECTOR WIDTH CM	0.1020E+00
T = DET. TEMP. K	0.7500E+02	T = DET. TEMP. K	0.7500E+02	T = DET. TEMP. K	0.7500E+02
CS = DET. STRAY CAPACITANCE F	0.6000E-11	CS = DET. STRAY CAPACITANCE F	0.6000E-11	CS = DET. STRAY CAPACITANCE F	0.6000E-11
RS = DET. SHUNT RESISTANCE OHM	0.1050E+07	RS = DET. SHUNT RESISTANCE OHM	0.1050E+07	RS = DET. SHUNT RESISTANCE OHM	0.1050E+07
X = MOLE FRACTION	0.2573E+00	X = MOLE FRACTION	0.2573E+00	X = MOLE FRACTION	0.2573E+00
VB = BIAS VOLTAGE V	0.0000E+00	VB = BIAS VOLTAGE V	0.0000E+00	VB = BIAS VOLTAGE V	0.0000E+00
EG = BAND GAP ENERGY EV	0.1829E+00	EG = BAND GAP ENERGY EV	0.1829E+00	EG = BAND GAP ENERGY EV	0.1829E+00
NI = INTRINSIC CONC. CM**-3	0.7530E+05	NI = INTRINSIC CONC. CM**-3	0.7530E+05	NI = INTRINSIC CONC. CM**-3	0.7530E+05
NA = ACCEPTOR CONC. CM**-3	0.7000E+15	NA = ACCEPTOR CONC. CM**-3	0.7000E+15	NA = ACCEPTOR CONC. CM**-3	0.7000E+15
ND = DONOR CARRIER CONC. CM**-3	0.1000E+17	ND = DONOR CARRIER CONC. CM**-3	0.1000E+17	ND = DONOR CARRIER CONC. CM**-3	0.1000E+17
MU = ELECTRON MOBILITY CM**2/V/S	0.1870E+05	MU = ELECTRON MOBILITY CM**2/V/S	0.1870E+05	MU = ELECTRON MOBILITY CM**2/V/S	0.1870E+05
MUH= HOLE MOBILITY CM**2/V/S	0.2770E+03	MUH= HOLE MOBILITY CM**2/V/S	0.2770E+03	MUH= HOLE MOBILITY CM**2/V/S	0.2770E+03
ETA= QUANTUM EFFICIENCY	0.7500E+00	ETA= QUANTUM EFFICIENCY	0.7500E+00	ETA= QUANTUM EFFICIENCY	0.7500E+00
TAU= CARRIER LIFETIME S	0.5000E-06	TAU= CARRIER LIFETIME S	0.5000E-06	TAU= CARRIER LIFETIME S	0.5000E-06
NUP= PEAK WAVENUMBER 1/CM	0.1639E+04	NUP= PEAK WAVENUMBER 1/CM	0.1639E+04	NUP= PEAK WAVENUMBER 1/CM	0.1639E+04
QBG= BKGD PHOTON FLUX DENSITY P/CM**2/S	0.5790E+12	QBG= BKGD PHOTON FLUX DENSITY P/CM**2/S	0.5930E+12	QBG= BKGD PHOTON FLUX DENSITY P/CM**2/S	0.9320E+12
QS = SGNL PHOTON FLUX DENSITY P/CM**2/S	0.7600E+11	QS = SGNL PHOTON FLUX DENSITY P/CM**2/S	0.9010E+11	QS = SGNL PHOTON FLUX DENSITY P/CM**2/S	0.4290E+12
KAPPA = DIELECTRIC CONSTANT	0.1361E+02	KAPPA = DIELECTRIC CONSTANT	0.1361E+02	KAPPA = DIELECTRIC CONSTANT	0.1361E+02
RF = FEEDBACK RESISTANCE OHM	0.1000E+10	RF = FEEDBACK RESISTANCE OHM	0.1000E+10	RF = FEEDBACK RESISTANCE OHM	0.1000E+10
CF = FEEDBACK CAPACITACE F	0.3000E-12	CF = FEEDBACK CAPACITACE F	0.3000E-12	CF = FEEDBACK CAPACITACE F	0.3000E-12
VP = PREAMP NOISE (INPUT) V/HZ**.5	0.2800E-08	VP = PREAMP NOISE (INPUT) V/HZ**.5	0.2800E-08	VP = PREAMP NOISE (INPUT) V/HZ**.5	0.2800E-08
AO = OPEN LOOP GAIN OF PREAMP	0.1000E+04	AO = OPEN LOOP GAIN OF PREAMP	0.1000E+04	AO = OPEN LOOP GAIN OF PREAMP	0.1000E+04
TRF= FEEDBACK RESISTOR TEMP K	0.1600E+03	TRF= FEEDBACK RESISTOR TEMP K	0.1600E+03	TRF= FEEDBACK RESISTOR TEMP K	0.1600E+03
FC = CHOPPING FREQUENCY HZ	0.4400E+03	FC = CHOPPING FREQUENCY HZ	0.4400E+03	FC = CHOPPING FREQUENCY HZ	0.4400E+03
RO = DIODE DARK RESISTANCE BIAS=0 OHM	0.1927E+09	RO = DIODE DARK RESISTANCE BIAS=0 OHM	0.1927E+09	RO = DIODE DARK RESISTANCE BIAS=0 OHM	0.1927E+09
RA = R(0)*A PRODUCT OHM*CM**2	0.1050E+07	RA = R(0)*A PRODUCT OHM*CM**2	0.1050E+07	RA = R(0)*A PRODUCT OHM*CM**2	0.1050E+07
VJ = JUNCTION POTENTIAL V	0.3139E+00	VJ = JUNCTION POTENTIAL V	0.3139E+00	VJ = JUNCTION POTENTIAL V	0.3139E+00
CJ = JUNCTION CAPACITANCE F	0.3022E-09	CJ = JUNCTION CAPACITANCE F	0.3022E-09	CJ = JUNCTION CAPACITANCE F	0.3022E-09
WJ = JUNCTION WIDTH CM	0.2173E-04	WJ = JUNCTION WIDTH CM	0.2173E-04	WJ = JUNCTION WIDTH CM	0.2173E-04
VC = CONTACT POTENTIAL V	0.3139E+00	VC = CONTACT POTENTIAL V	0.3139E+00	VC = CONTACT POTENTIAL V	0.3139E+00
ZD = DETECTOR IMPEDANCE OHM	0.1167E+07	ZD = DETECTOR IMPEDANCE OHM	0.1167E+07	ZD = DETECTOR IMPEDANCE OHM	0.1167E+07
ZF = FEEDBACK RESISTOR IMPEDANCE OHM	0.5466E+09	ZF = FEEDBACK RESISTOR IMPEDANCE OHM	0.5466E+09	ZF = FEEDBACK RESISTOR IMPEDANCE OHM	0.5466E+09
PD = DET. PHASE ANGLE RAD	0.4335E-14	PD = DET. PHASE ANGLE RAD	0.4335E-14	PD = DET. PHASE ANGLE RAD	0.4335E-14
PF = FDBK RESISTOR PHASE ANGLE RAD	0.8294E-18	PF = FDBK RESISTOR PHASE ANGLE RAD	0.8294E-18	PF = FDBK RESISTOR PHASE ANGLE RAD	0.8294E-18
AZ = TRANSIMPEDANCE OHM	0.1029E+10	AZ = TRANSIMPEDANCE OHM	0.1629E+10	AZ = TRANSIMPEDANCE OHM	0.1029E+10
IS = SIGNAL PHOTOCURRENT A	0.4975E-10	IS = SIGNAL PHOTOCURRENT A	0.5898E-10	IS = SIGNAL PHOTOCURRENT A	0.2908E-09
IT = TOTAL BKGD PHOTOCURRENT A	0.3790E-09	IT = TOTAL BKGD PHOTOCURRENT A	0.3882E-09	IT = TOTAL BKGD PHOTOCURRENT A	0.6101E-09
VRF= FDBK RESISTOR NOISE V/HZ**.5	0.3057E-05	VRF= FDBK RESISTOR NOISE V/HZ**.5	0.3057E-05	VRF= FDBK RESISTOR NOISE V/HZ**.5	0.3057E-05
VBG= BACKGROUND NOISE V/HZ**>5	0.1133E-04	VBG= BACKGROUND NOISE V/HZ**>5	0.1147E-04	VBG= BACKGROUND NOISE V/HZ**>5	0.1438E-04
VJN= JOHNSON NOISE V/HZ**.5	0.4768E-05	VJN= JOHNSON NOISE V/HZ**.5	0.4768E-05	VJN= JOHNSON NOISE V/HZ**.5	0.4768E-05
VPA= PREAMP NOISE V/HZ**.5	0.8927E-06	VPA= PREAMP NOISE V/HZ**.5	0.8927E-06	VPA= PREAMP NOISE V/HZ**.5	0.8927E-06
VT = TOTAL NOISE V/HZ**.5	0.1270E-04	VT = TOTAL NOISE V/HZ**.5	0.1282E-04	VT = TOTAL NOISE V/HZ**.5	0.1548E-04
R = RESPONSIVITY V/W	0.3795E+10	R = RESPONSIVITY V/W	0.3795E+10	R = RESPONSIVITY V/W	0.3795E+10
NEP= NOISE EQUIVALENT POWER W/HZ**.5	0.3347E-14	NEP= NOISE EQUIVALENT POWER W/HZ**.5	0.3379E-14	NEP= NOISE EQUIVALENT POWER W/HZ**.5	0.4080E-14
DSTAR = CM*HZ**.5/W	0.2205E+14	DSTAR = CM*HZ**.5/W	0.2184E+14	DSTAR = CM*HZ**.5/W	0.1809E+14

Table F-4 (CH 16)

PV HGCDTE DETECTOR PERFORMANCE CHANNEL 16 75/160/MIN

CH = CHANNEL NUMBER	0.1600E+02
HD = DETECTOR HEIGHT CM	0.5300E-01
WD = DETECTOR WIDTH CM	0.8600E-01
T = DET. TEMP. K	0.7500E+02
CS = DET. STRAY CAPACITANCE F	0.6000E-11
RS = DET. SHUNT RESISTANCE OHM	0.1050E+07
X = MOLE FRACTION	0.2707E+00
VB = BIAS VOLTAGE V	0.0000E+00
EG = BAND GAP ENERGY EV	0.2040E+00
NI = INTRINSIC CONC. CM**-3	0.3125E+04
NA = ACCEPTOR CONC. CM**-3	0.2000E+16
ND = DONOR CARRIER CONC. CM**-3	0.5000E+17
MU = ELECTRON MOBILITY CM**2/V/S	0.1840E+05
MUH= HOLE MOBILITY CM**2/V/S	0.2730E+03
ETA= QUANTUM EFFICIENCY	0.7500E+00
TAU= CARRIER LIFETIME S	0.5000E-06
NUP= PEAK WAVENUMBER 1/CM	0.1828E+04
QBG= BKGD PHOTON FLUX DENSITY P/CM**2/S	0.2590E+12
QS = SGNL PHOTON FLUX DENSITY P/CM**2/S	0.1170E+12
KAPPA = DIELECTRIC CONSTANT	0.1354E+02
RF = FEEDBACK RESISTANCE OHM	0.1000E+10
CF = FEEDBACK CAPACITACE F	0.3000E-12
VP = PREAMP NOISE (INPUT) V/HZ**.5	0.2800E-08
AO = OPEN LOOP GAIN OF PREAMP	0.1000E+04
TRF= FEEDBACK RESISTOR TEMP K	0.1600E+03
FC = CHOPPING FREQUENCY HZ	0.4400E+03
RO = DIODE DARK RESISTANCE BIAS=0 OHM	0.2304E+09
RA = R(0)*A PRODUCT OHM*CM**2	0.1050E+07
VJ = JUNCTION POTENTIAL V	0.3722E+00
CJ = JUNCTION CAPACITANCE F	0.5177E-09
WJ = JUNCTION WIDTH CM	0.1056E-04
VC = CONTACT POTENTIAL V	0.3722E+00
ZD = DETECTOR IMPEDANCE OHM	0.6886E+06
ZF = FEEDBACK RESISTOR IMPEDANCE OHM	0.5466E+09
PD = DET. PHASE ANGLE RAD	0.6213E-14
PF = FDBK RESISTOR PHASE ANGLE RAD	0.8294E-18
AZ = TRANSIMPEDANCE OHM	0.2651E+10
IS = SIGNAL PHOTOCURRENT A	0.6407E-10
IT = TOTAL BKGD PHOTOCURRENT A	0.1418E-09
VRF= FDBK RESISTOR NOISE V/HZ**.5	0.7880E-05
VBG= BACKGROUND NOISE V/HZ**.5	0.1787E-04
VJN= JOHNSON NOISE V/HZ**.5	0.1124E-04
VPA= PREAMP NOISE V/HZ**.5	0.1238E-05
VT = TOTAL NOISE V/HZ**.5	0.2257E-04
R = RESPONSIVITY V/W	0.8778E+10
NEP= NOISE EQUIVALENT POWER W/HZ**.5	0.2573E-14
DSTAR = CM*HZ**.5/W	0.2624E+14

PV HGCDTE DETECTOR PERFORMANCE CHANNEL 16 75/160/STD

CH = CHANNEL NUMBER	0.1600E+02
HD = DETECTOR HEIGHT CM	0.5300E-01
WD = DETECTOR WIDTH CM	0.8600E-01
T = DET. TEMP. K	0.7500E+02
CS = DET. STRAY CAPACITANCE F	0.6000E-11
RS = DET. SHUNT RESISTANCE OHM	0.1050E+07
X = MOLE FRACTION	0.2707E+00
VB = BIAS VOLTAGE V	0.0000E+00
EG = BAND GAP ENERGY EV	0.2040E+00
NI = INTRINSIC CONC. CM**-3	0.3125E+04
NA = ACCEPTOR CONC. CM**-3	0.2000E+16
ND = DONOR CARRIER CONC. CM**-3	0.5000E+17
MU = ELECTRON MOBILITY CM**2/V/S	0.1840E+05
MUH= HOLE MOBILITY CM**2/V/S	0.2730E+03
ETA= QUANTUM EFFICIENCY	0.7500E+00
TAU= CARRIER LIFETIME S	0.5000E-06
NUP= PEAK WAVENUMBER 1/CM	0.1828E+04
QBG= BKGD PHOTON FLUX DENSITY P/CM**2/S	0.5330E+12
QS = SGNL PHOTON FLUX DENSITY P/CM**2/S	0.3910E+12
KAPPA = DIELECTRIC CONSTANT	0.1354E+02
RF = FEEDBACK RESISTANCE OHM	0.1000E+10
CF = FEEDBACK CAPACITACE F	0.3000E-12
VP = PREAMP NOISE (INPUT) V/HZ**.5	0.2800E-08
AO = OPEN LOOP GAIN OF PREAMP	0.1000E+04
TRF= FEEDBACK RESISTOR TEMP K	0.1600E+03
FC = CHOPPING FREQUENCY HZ	0.4400E+03
RO = DIODE DARK RESISTANCE BIAS=0 OHM	0.2304E+09
RA = R(0)*A PRODUCT OHM*CM**2	0.1050E+07
VJ = JUNCTION POTENTIAL V	0.3722E+00
CJ = JUNCTION CAPACITANCE F	0.5177E-09
WJ = JUNCTION WIDTH CM	0.1056E-04
VC = CONTACT POTENTIAL V	0.3722E+00
ZD = DETECTOR IMPEDANCE OHM	0.6886E+06
ZF = FEEDBACK RESISTOR IMPEDANCE OHM	0.5466E+09
PD = DET. PHASE ANGLE RAD	0.6213E-14
PF = FDBK RESISTOR PHASE ANGLE RAD	0.8294E-18
AZ = TRANSIMPEDANCE OHM	0.2651E+10
IS = SIGNAL PHOTOCURRENT A	0.2141E-09
IT = TOTAL BKGD PHOTOCURRENT A	0.2919E-09
VRF= FDBK RESISTOR NOISE V/HZ**.5	0.7880E-05
VBG= BACKGROUND NOISE V/HZ**.5	0.2564E-04
VJN= JOHNSON NOISE V/HZ**.5	0.1124E-04
VPA= PREAMP NOISE V/HZ**.5	0.1238E-05
VT = TOTAL NOISE V/HZ**.5	0.2911E-04
R = RESPONSIVITY V/W	0.8778E+10
NEP= NOISE EQUIVALENT POWER W/HZ**.5	0.3319E-14
DSTAR = CM*HZ**.5/W	0.2034E+14

PV HGCDTE DETECTOR PERFORMANCE CHANNEL 16 75/160/MAX

CH = CHANNEL NUMBER	0.1600E+02
HD = DETECTOR HEIGHT CM	0.5300E-01
WD = DETECTOR WIDTH CM	0.8600E-01
T = DET. TEMP. K	0.7500E+02
CS = DET. STRAY CAPACITANCE F	0.6000E-11
RS = DET. SHUNT RESISTANCE OHM	0.1050E+07
X = MOLE FRACTION	0.2707E+00
VB = BIAS VOLTAGE V	0.0000E+00
EG = BAND GAP ENERGY EV	0.2040E+00
NI = INTRINSIC CONC. CM**-3	0.3125E+04
NA = ACCEPTOR CONC. CM**-3	0.2000E+16
ND = DONOR CARRIER CONC. CM**-3	0.5000E+17
MU = ELECTRON MOBILITY CM**2/V/S	0.1840E+05
MUH= HOLE MOBILITY CM**2/V/S	0.2730E+03
ETA= QUANTUM EFFICIENCY	0.7500E+00
TAU= CARRIER LIFETIME S	0.5000E-06
NUP= PEAK WAVENUMBER 1/CM	0.1828E+04
QBG= BKGD PHOTON FLUX DENSITY P/CM**2/S	0.1030E+13
QS = SGNL PHOTON FLUX DENSITY P/CM**2/S	0.8840E+12
KAPPA = DIELECTRIC CONSTANT	0.1354E+02
RF = FEEDBACK RESISTANCE OHM	0.1600E+10
CF = FEEDBACK CAPACITACE F	0.3000E-12
VP = PREAMP NOISE (INPUT) V/HZ**.5	0.2800E-08
AO = OPEN LOOP GAIN OF PREAMP	0.1000E+04
TRF= FEEDBACK RESISTOR TEMP K	0.1600E+03
FC = CHOPPING FREQUENCY HZ	0.4400E+03
RO = DIODE DARK RESISTANCE BIAS=0 OHM	0.2304E+09
RA = R(0)*A PRODUCT OHM*CM**2	0.1050E+07
VJ = JUNCTION POTENTIAL V	0.3722E+00
CJ = JUNCTION CAPACITANCE F	0.5177E-09
WJ = JUNCTION WIDTH CM	0.1056E-04
VC = CONTACT POTENTIAL V	0.3722E+00
ZD = DETECTOR IMPEDANCE OHM	0.6886E+06
ZF = FEEDBACK RESISTOR IMPEDANCE OHM	0.5466E+09
PD = DET. PHASE ANGLE RAD	0.6213E-14
PF = FDBK RESISTOR PHASE ANGLE RAD	0.8294E-18
AZ = TRANSIMPEDANCE OHM	0.2651E+10
IS = SIGNAL PHOTOCURRENT A	0.4841E-09
IT = TOTAL BKGD PHOTOCURRENT A	0.5641E-09
VRF= FDBK RESISTOR NOISE V/HZ**.5	0.7880E-05
VBG= BACKGROUND NOISE V/HZ**.5	0.3564E-04
VJN= JOHNSON NOISE V/HZ**.5	0.1124E-04
VPA= PREAMP NOISE V/HZ**.5	0.1238E-05
VT = TOTAL NOISE V/HZ**.5	0.3821E-04
R = RESPONSIVITY V/W	0.8778E+10
NEP= NOISE EQUIVALENT POWER W/HZ**.5	0.4357E-14
DSTAR = CM*HZ**.5/W	0.1558E+14

Table F-4 (CH 17)

PV HGCDTE DETECTOR PERFORMANCE CHANNEL 17 75/160/MIN		PV HGCDTE DETECTOR PERFORMANCE CHANNEL 17 75/160/STD		PV HGCDTE DETECTOR PERFORMANCE CHANNEL 17 75/160/MAX	
CH = CHANNEL NUMBER	0.1700E+02	CH = CHANNEL NUMBER	0.1700E+02	CH = CHANNEL NUMBER	0.1700E+02
HD = DETECTOR HEIGHT CM	0.5300E-01	HD = DETECTOR HEIGHT CM	0.5300E-01	HD = DETECTOR HEIGHT CM	0.5300E-01
WD = DETECTOR WIDTH CM	0.8900E-01	WD = DETECTOR WIDTH CM	0.8900E-01	WD = DETECTOR WIDTH CM	0.8900E-01
T = DET. TEMP. K	0.7500E+02	T = DET. TEMP. K	0.7500E+02	T = DET. TEMP. K	0.7500E+02
CS = DET. STRAY CAPACITANCE F	0.6000E-11	CS = DET. STRAY CAPACITANCE F	0.6000E-11	CS = DET. STRAY CAPACITANCE F	0.6000E-11
RS = DET. SHUNT RESISTANCE OHM	0.1050E+07	RS = DET. SHUNT RESISTANCE OHM	0.1050E+07	RS = DET. SHUNT RESISTANCE OHM	0.1050E+07
X = MOLE FRACTION	0.2707E+00	X = MOLE FRACTION	0.2707E+00	X = MOLE FRACTION	0.2707E+00
VB = BIAS VOLTAGE V	0.0000E+00	VB = BIAS VOLTAGE V	0.0000E+00	VB = BIAS VOLTAGE V	0.0000E+00
EG = BAND GAP ENERGY EV	0.2040E+00	EG = BAND GAP ENERGY EV	0.2040E+00	EG = BAND GAP ENERGY EV	0.2040E+00
NI = INTRINSIC CONC. CM**-3	0.3125E+04	NI = INTRINSIC CONC. CM**-3	0.3125E+04	NI = INTRINSIC CONC. CM**-3	0.3125E+04
NA = ACCEPTOR CONC. CM**-3	0.2000E+16	NA = ACCEPTOR CONC. CM**-3	0.2000E+16	NA = ACCEPTOR CONC. CM**-3	0.2000E+16
ND = DONOR CARRIER CONC. CM**-3	0.5000E+17	ND = DONOR CARRIER CONC. CM**-3	0.5000E+17	ND = DONOR CARRIER CONC. CM**-3	0.5000E+17
MU = ELECTRON MOBILITY CM**2/V/S	0.1840E+05	MU = ELECTRON MOBILITY CM**2/V/S	0.1840E+05	MU = ELECTRON MOBILITY CM**2/V/S	0.1840E+05
MUH= HOLE MOBILITY CM**2/V/S	0.2730E+03	MUH= HOLE MOBILITY CM**2/V/S	0.2730E+03	MUH= HOLE MOBILITY CM**2/V/S	0.2730E+03
ETA= QUANTUM EFFICIENCY	0.7500E+00	ETA= QUANTUM EFFICIENCY	0.7500E+00	ETA= QUANTUM EFFICIENCY	0.7500E+00
TAU= CARRIER LIFETIME S	0.5000E-06	TAU= CARRIER LIFETIME S	0.5000E-06	TAU= CARRIER LIFETIME S	0.5000E-06
NUP= PEAK WAVENUMBER 1/CM	0.1829E+04	NUP= PEAK WAVENUMBER 1/CM	0.1829E+04	NUP= PEAK WAVENUMBER 1/CM	0.1829E+04
QBG= BKGD PHOTON FLUX DENSITY P/CM**2/S	0.2480E+12	QBG= BKGD PHOTON FLUX DENSITY P/CM**2/S	0.6270E+12	QBG= BKGD PHOTON FLUX DENSITY P/CM**2/S	0.1200E+13
QS = SGNL PHOTON FLUX DENSITY P/CM**2/S	0.1170E+12	QS = SGNL PHOTON FLUX DENSITY P/CM**2/S	0.4990E+12	QS = SGNL PHOTON FLUX DENSITY P/CM**2/S	0.1070E+13
KAPPA = DIELECTRIC CONSTANT	0.1354E+02	KAPPA = DIELECTRIC CONSTANT	0.1354E+02	KAPPA = DIELECTRIC CONSTANT	0.1354E+02
RF = FEEDBACK RESISTANCE OHM	0.1000E+10	RF = FEEDBACK RESISTANCE OHM	0.1000E+10	RF = FEEDBACK RESISTANCE OHM	0.1000E+10
CF = FEEDBACK CAPACITACE F	0.3000E-12	CF = FEEDBACK CAPACITACE F	0.3000E-12	CF = FEEDBACK CAPACITACE F	0.3000E-12
VP = PREAMP NOISE (INPUT) V/HZ**.5	0.2800E-08	VP = PREAMP NOISE (INPUT) V/HZ**.5	0.2800E-08	VP = PREAMP NOISE (INPUT) V/HZ**.5	0.2800E-08
AO = OPEN LOOP GAIN OF PREAMP	0.1000E+04	AO = OPEN LOOP GAIN OF PREAMP	0.1000E+04	AO = OPEN LOOP GAIN OF PREAMP	0.1000E+04
TRF= FEEDBACK RESISTOR TEMP K	0.1600E+03	TRF= FEEDBACK RESISTOR TEMP K	0.1600E+03	TRF= FEEDBACK RESISTOR TEMP K	0.1600E+03
FC = CHOPPING FREQUENCY HZ	0.4400E+03	FC = CHOPPING FREQUENCY HZ	0.4400E+03	FC = CHOPPING FREQUENCY HZ	0.4400E+03
RO = DIODE DARK RESISTANCE BIAS=0 OHM	0.2226E+09	RO = DIODE DARK RESISTANCE BIAS=0 OHM	0.2226E+09	RO = DIODE DARK RESISTANCE BIAS=0 OHM	0.2226E+09
RA = R(0)*A PRODUCT OHM*CM**2	0.1050E+07	RA = R(0)*A PRODUCT OHM*CM**2	0.1050E+07	RA = R(0)*A PRODUCT OHM*CM**2	0.1050E+07
VJ = JUNCTION POTENTIAL V	0.3722E+00	VJ = JUNCTION POTENTIAL V	0.3722E+00	VJ = JUNCTION POTENTIAL V	0.3722E+00
CJ = JUNCTION CAPACITANCE F	0.5358E-09	CJ = JUNCTION CAPACITANCE F	0.5358E-09	CJ = JUNCTION CAPACITANCE F	0.5358E-09
WJ = JUNCTION WIDTH CM	0.1056E-04	WJ = JUNCTION WIDTH CM	0.1056E-04	WJ = JUNCTION WIDTH CM	0.1056E-04
VC = CONTACT POTENTIAL V	0.3722E+00	VC = CONTACT POTENTIAL V	0.3722E+00	VC = CONTACT POTENTIAL V	0.3722E+00
ZD = DETECTOR IMPEDANCE OHM	0.6657E+06	ZD = DETECTOR IMPEDANCE OHM	0.6657E+06	ZD = DETECTOR IMPEDANCE OHM	0.6657E+06
ZF = FEEDBACK RESISTOR IMPEDANCE OHM	0.5466E+09	ZF = FEEDBACK RESISTOR IMPEDANCE OHM	0.5466E+09	ZF = FEEDBACK RESISTOR IMPEDANCE OHM	0.5466E+09
PD = DET. PHASE ANGLE RAD	0.6654E-14	PD = DET. PHASE ANGLE RAD	0.6654E-14	PD = DET. PHASE ANGLE RAD	0.6654E-14
PF = FDBK RESISTOR PHASE ANGLE RAD	0.8294E-18	PF = FDBK RESISTOR PHASE ANGLE RAD	0.8294E-18	PF = FDBK RESISTOR PHASE ANGLE RAD	0.8294E-18
AZ = TRANSIMPEDANCE OHM	0.3057E+10	AZ = TRANSIMPEDANCE OHM	0.3057E+10	AZ = TRANSIMPEDANCE OHM	0.3057E+10
IS = SIGNAL PHOTOCURRENT A	0.6631E-10	IS = SIGNAL PHOTOCURRENT A	0.2828E-09	IS = SIGNAL PHOTOCURRENT A	0.6064E-09
IT = TOTAL BKGD PHOTOCURRENT A	0.1406E-09	IT = TOTAL BKGD PHOTOCURRENT A	0.3554E-09	IT = TOTAL BKGD PHOTOCURRENT A	0.6981E-09
VRF= FDBK RESISTOR NOISE V/HZ**.5	0.9086E-05	VRF= FDBK RESISTOR NOISE V/HZ**.5	0.9086E-05	VRF= FDBK RESISTOR NOISE V/HZ**.5	0.9086E-05
VBG= BACKGROUND NOISE V/HZ**.5	0.2851E-04	VBG= BACKGROUND NOISE V/HZ**.5	0.3261E-04	VBG= BACKGROUND NOISE V/HZ**.5	0.4512E-04
VJN= JOHNSON NOISE V/HZ**.5	0.1318E-04	VJN= JOHNSON NOISE V/HZ**.5	0.1318E-04	VJN= JOHNSON NOISE V/HZ**.5	0.1318E-04
VPA= PREAMP NOISE V/HZ**.5	0.1262E-05	VPA= PREAMP NOISE V/HZ**.5	0.1262E-05	VPA= PREAMP NOISE V/HZ**.5	0.1262E-05
VT = TOTAL NOISE V/HZ**.5	0.2605E-04	VT = TOTAL NOISE V/HZ**.5	0.3636E-04	VT = TOTAL NOISE V/HZ**.5	0.4789E-04
R = RESPONSIVITY V/W	0.1011E+11	R = RESPONSIVITY V/W	0.1011E+11	R = RESPONSIVITY V/W	0.1011E+11
NEP= NOISE EQUIVALENT POWER W/HZ**.5	0.2576E-14	NEP= NOISE EQUIVALENT POWER W/HZ**.5	0.3595E-14	NEP= NOISE EQUIVALENT POWER W/HZ**.5	0.4736E-14
DSTAR = CM*HZ**.5/W	0.2666E+14	DSTAR = CM*HZ**.5/W	0.1918E+14	DSTAR = CM*HZ**.5/W	0.1450E+14

Table F-4 (CH 18)

PV INSB DETECTOR PERFORMANCE CHANNEL 18 75/160/MIN		PV INSB DETECTOR PERFORMANCE CHANNEL 18 75/160/STD		PV INSB DETECTOR PERFORMANCE CHANNEL 18 75/160/MAX	
CH = CHANNEL NUMBER	0.1800E+02	CH = CHANNEL NUMBER	0.1800E+02	CH = CHANNEL NUMBER	0.1800E+02
HD = DETECTOR HEIGHT CM	0.5300E-01	HD = DETECTOR HEIGHT CM	0.5300E-01	HD = DETECTOR HEIGHT CM	0.5300E-01
WD = DETECTOR WIDTH CM	0.1061E+00	WD = DETECTOR WIDTH CM	0.1061E+00	WD = DETECTOR WIDTH CM	0.1061E+00
T = DET. TEMP. K	0.7500E+02	T = DET. TEMP. K	0.7500E+02	T = DET. TEMP. K	0.7500E+02
CS = DET. STRAY CAPACITANCE F	0.6000E-11	CS = DET. STRAY CAPACITANCE F	0.6000E-11	CS = DET. STRAY CAPACITANCE F	0.6000E-11
RS = DET. SHUNT RESISTANCE OHM	0.1050E+07	RS = DET. SHUNT RESISTANCE OHM	0.1050E+07	RS = DET. SHUNT RESISTANCE OHM	0.1050E+07
VB = BIAS VOLTAGE V	0.0000E+00	VB = BIAS VOLTAGE V	0.0000E+00	VB = BIAS VOLTAGE V	0.0000E+00
EG = BAND GAP ENERGY EV	0.2267E+00	EG = BAND GAP ENERGY EV	0.2267E+00	EG = BAND GAP ENERGY EV	0.2267E+00
NI = INTRINSIC CONC. CM**-3	0.1602E+10	NI = INTRINSIC CONC. CM**-3	0.1602E+10	NI = INTRINSIC CONC. CM**-3	0.1602E+10
NA = ACCEPTOR CONC. CM**-3	0.1000E+18	NA = ACCEPTOR CONC. CM**-3	0.1000E+18	NA = ACCEPTOR CONC. CM**-3	0.1000E+18
ND = DONOR CARRIER CONC. CM**-3	0.5000E+15	ND = DONOR CARRIER CONC. CM**-3	9.5000E+15	ND = DONOR CARRIER CONC. CM**-3	0.5000E+15
MU = ELECTRON MOBILITY CM**2/V/S	0.8000E+05	MU = ELECTRON MOBILITY CM**2/V/S	0.8630E+05	MU = ELECTRON MOBILITY CM**2/V/S	0.8000E+05
MUH= HOLE MOBILITY CM**2/V/S	0.5000E+04	MUH= HOLE MOBILITY CM**2/V/S	0.5000E+04	MUH= HOLE MOBILITY CM**2/V/S	0.5000E+04
ETA= QUANTUM EFFICIENCY	0.8000E+00	ETA= QUANTUM EFFICIENCY	0.8000E+00	ETA= QUANTUM EFFICIENCY	0.8000E+00
TAU= CARRIER LIFETIME S	0.5000E-06	TAU= CARRIER LIFETIME S	0.5000E-06	TAU= CARRIER LIFETIME S	0.5000E-06
NUP= PEAK WAVENUMBER 1/CM	0.2032E+04	NUP= PEAK WAVENUMBER 1/CM	0.2032E+04	NUP= PEAK WAVENUMBER 1/CM	0.2032E+04
QBG= BKGD PHOTON FLUX DENSITY P/CM**2/S	0.9810E+11	QBG= BKGD PHOTON FLUX DENSITY P/CM**2/S	0.4860E+12	QBG= BKGD PHOTON FLUX DENSITY P/CM**2/S	0.1120E+13
QS = SGNL PHOTON FLUX DENSITY P/CM**2/S	0.4500E+11	QS = SGNL PHOTON FLUX DENSITY P/CM**2/S	0.3618E+12	QS = SGNL PHOTON FLUX DENSITY P/CM**2/S	0.1000E+13
KAPPA = DIELECTRIC CONSTANT	0.1720E+02	KAPPA = DIELECTRIC CONSTANT	0.1720E+02	KAPPA = DIELECTRIC CONSTANT	0.1720E+02
RF = FEEDBACK RESISTANCE OHM	0.1000E+09	RF = FEEDBACK RESISTANCE OHM	0.1000E+09	RF = FEEDBACK RESISTANCE OHM	0.1000E+09
CF = FEEDBACK CAPACITACE F	0.3000E-12	CF = FEEDBACK CAPACITACE F	0.3000E-12	CF = FEEDBACK CAPACITACE F	0.3000E-12
VP = PREAMP NOISE (INPUT) V/HZ**.5	0.2800E-08	VP = PREAMP NOISE (INPUT) V/HZ**.5	0.2800E-08	VP = PREAMP NOISE (INPUT) V/HZ**.5	0.2800E-08
AO = OPEN LOOP GAIN OF PREAMP	0.1000E+04	AO = OPEN LOOP GAIN OF PREAMP	0.1000E+04	AO = OPEN LOOP GAIN OF PREAMP	0.1000E+04
TRF= FEEDBACK RESISTOR TEMP K	0.1600E+03	TRF= FEEDBACK RESISTOR TEMP K	0.1600E+03	TRF= FEEDBACK RESISTOR TEMP K	0.1600E+03
FC = CHOPPING FREQUENCY HZ	0.4400E+03	FC = CHOPPING FREQUENCY HZ	0.4400E+03	FC = CHOPPING FREQUENCY HZ	9.4400E+03
RO= DIODE DARK RESISTANCE BIAS=0 OHM	0.1865E+09	RO = DIODE DARK RESISTANCE BIAS=0 OHM	0.1865E+09	RO = DIODE DARK RESISTANCE BIAS=0 OHM	0.1865E+09
RA = R(0)*A PRODUCT OHM*CM**2	0.1849E+07	RA = R(0)*A PRODUCT OHM*CM**2	0.1849E+07	RA = R(0)*A PRODUCT OHM*CM**2	0.1849E+07
VJ = JUNCTION POTENTIAL V	0.1978E+00	VJ = JUNCTION POTENTIAL V	0.1978E+00	VJ = JUNCTION POTENTIAL V	0.1978E+00
CJ = JUNCTION CAPACITANCE F	0.9876E-10	CJ = JUNCTION CAPACITANCE F	0.9876E-10	CJ = JUNCTION CAPACITANCE F	0.9876E-10
WJ = JUNCTION WIDTH CM	0.8673E-04	WJ = JUNCTION WIDTH CM	0.8673E-04	WJ = JUNCTION WIDTH CM	0.8673E-04
VC = CONTACT POTENTIAL V	0.1978E+00	VC = CONTACT POTENTIAL V	0.1978E+00	VC = CONTACT POTENTIAL V	0.1978E+00
ZD = DETECTOR IMPEDANCE OHM	0.3390E+07	ZD = DETECTOR IMPEDANCE OHM	0.3390E+07	ZD = DETECTOR IMPEDANCE OHM	0.3390E+07
ZF = FEEDBACK RESISTOR IMPEDANCE OHM	0.9234E+08	ZF = FEEDBACK RESISTOR IMPEDANCE OHM	0.9234E+08	ZF = FEEDBACK RESISTOR IMPEDANCE OHM	0.9234E+08
PD = DET. PHASE ANGLE RAD	0.1464E-14	PD = DET. PHASE ANGLE RAD	0.1464E-14	PD = DET. PHASE ANGLE RAD	0.1464E-14
PF = FDBK RESISTOR PHASE ANGLE RAD	0.8294E-17	PF = FDBK RESISTOR PHASE ANGLE RAD	0.8294E-17	PF = FDBK RESISTOR PHASE ANGLE RAD	0.8294E-17
AZ = TRANSIMPEDANCE OHM	0.9493E+08	AZ = TRANSIMPEDANCE OHM	0.9493E+08	AZ = TRANSIMPEDANCE OHM	0.9493E+08
IS = SIGNAL PHOTOCURRENT A	0.3315E-10	IS = SIGNAL PHOTOCURRENT A	0.2602E-09	IS = SIGNAL PHOTOCURRENT A	0.7783E-09
IT = TOTAL BKGD PHOTOCURRENT A	0.6493E-10	IT = TOTAL BKGD PHOTOCURRENT A	0.2926E-09	IT = TOTAL BKGD PHOTOCURRENT A	0.8072E-09
VRF= FDBK RESISTOR NOISE V/HZ**.5	0.8923E-06	VRF= FDBK RESISTOR NOISE V/HZ**.5	0.8923E-06	VRF= FDBK RESISTOR NOISE V/HZ**.5	0.8923E-06
VBG= BACKGROUND NOISE V/HZ**.5	0.4330E-06	VBG= BACKGROUND NOISE V/HZ**.5	0.9191E-06	VBG= BACKGROUND NOISE V/HZ**.5	0.1577E-05
VJN= JOHNSON NOISE V/HZ**.5	0.3163E-06	VJN= JOHNSON NOISE V/HZ**.5	0.3163E-06	VJN= JOHNSON NOISE V/HZ**.5	0.3163E-06
VGR= GEN-RECOMB NOISE V/HZ**.5	0.3163E-06	VGR= GEN-RECOMB NOISE V/HZ**.5	0.3163E-06	VGR= GEN-RECOMB NOISE V/HZ**.5	0.3163E-06
VPA= PREAMP NOISE V/HZ**.5	0.7417E-07	VPA= PREAMP NOISE V/HZ**.5	0.7417E-07	VPA= PREAMP NOISE V/HZ**.5	0.7417E-07
VT = TOTAL NOISE V/HZ**.5	0.1091E-05	VT = TOTAL NOISE V/HZ**.5	0.1359E-05	VT = TOTAL NOISE V/HZ**.5	0.1825E-05
R = RESPONSIVITY V/W	0.3015E+09	R = RESPONSIVITY V/W	0.3015E+09	R = RESPONSIVITY V/W	0.3015E+09
NEP= NOISE EQUIVALENT POWER W/HZ**.5	0.3618E-14	NEP= NOISE EQUIVALENT POWER W/HZ**.5	0.4508E-14	NEP= NOISE EQUIVALENT POWER W/HZ**.5	0.6055E-14
DSTAR = CM*HZ**.5/W	0.2073E+14	DSTAR = CM*HZ**.5/W	0.1664E+14	DSTAR = CM*HZ**.5/W	0.1238E+14

Table F-4 (CH 19)

PV INSB DETECTOR PERFORMANCE CHANNEL 19 75/160/MIN		PV INSB DETECTOR PERFORMANCE CHANNEL 19 75/160/STD		PV INSB DETECTOR PERFORMANCE CHANNEL 19 75/160/MAX	
CH = CHANNEL NUMBER	0.1900E+02	CH = CHANNEL NUMBER	0.1900E+02	CH = CHANNEL NUMBER	0.1900E+02
HD = DETECTOR HEIGHT CM	0.5300E-01	HD = DETECTOR HEIGHT CM	0.5300E-01	HD = DETECTOR HEIGHT CM	0.5300E-01
WD = DETECTOR WIDTH CM	0.1096E+00	WD = DETECTOR WIDTH CM	0.1096E+00	WD = DETECTOR WIDTH CM	0.1096E+00
T = DET. TEMP. K	0.7500E+02	T = DET. TEMP. K	0.7500E+02	T = DET. TEMP. K	0.7500E+02
CS = DET. STRAY CAPACITANCE F	0.5000E-11	CS = DET. STRAY CAPACITANCE F	0.6000E-11	CS = DET. STRAY CAPACITANCE F	0.6[illegible]E-11
RS = DET. SHUNT RESISTANCE OHM	0.1050E+07	RS = DET. SHUNT RESISTANCE OHM	0.1050E+07	RS = DET. SHUNT RESISTANCE OHM	0.1050E+07
VB = BIAS VOLTAGE V	0.9000E+00	VB = BIAS VOLTAGE V	0.8000E+00	VB = BIAS VOLTAGE V	0.0000E+00
EG = BAND GAP ENERGY EV	0.2267E+00	EG = BAND GAP ENERGY EV	0.2267E+00	EG = BAND GAP ENERGY EV	0.2267E+00
NI = INTRINSIC CONC. CM**-3	0.1602E+10	NI = INTRINSIC CONC. CM**-3	0.1602E+10	NI = INTRINSIC CONC. CM**-3	0.1602E+10
NA = ACCEPTOR CONC. CM**-3	0.1000E+18	NA = ACCEPTOR CONC. CM**-3	0.1000E+18	NA = ACCEPTOR CONC. CM**-3	0.1000E+18
ND = DONOR CARRIER CONC. CM**-3	0.5000E+15	ND = DONOR CARRIER CONC. CM**-3	0.5000E+15	ND = DONOR CARRIER CONC. CM**-3	0.5000E+15
MU = ELECTRON MOBILITY CM**2/V/S	0.8000E+05	MU = ELECTRON MOBILITY CM**2/V/S	0.8000E+05	MU = ELECTRON MOBILITY CM**2/V/S	0.8000E+05
MUH= HOLE MOBILITY CM**2/V/S	0.5000E+04	MUH= HOLE MOBILITY CM**2/V/S	0.5000E+04	MUH= HOLE MOBILITY CM**2/V/S	0.5000E+04
ETA= QUANTUM EFFICIENCY	0.8000E+00	ETA= QUANTUM EFFICIENCY	0.8000E+00	ETA= QUANTUM EFFICIENCY	0.8000E+00
TAU= CARRIER LIFETIME S	0.5000E-06	TAU= CARRIER LIFETIME S	0.5000E-06	TAU= CARRIER LIFETIME S	0.5000E-06
NUP= PEAK WAVENUMBER 1/CM	0.2032E+04	NUP= PEAK WAVENUMBER 1/CM	0.2032E+04	NUP= PEAK WAVENUMBER 1/CM	0.2032E+04
QBG= BKGD PHOTON FLUX DENSITY P/CM**2/S	0.4850E+10	QBG= BKGD PHOTON FLUX DENSITY P/CM**2/S	0.7480E+10	QBG= BKGD PHOTON FLUX DENSITY P/CM**2/S	0.4790E+11
QS = SGNL PHOTON FLUX DENSITY P/CM**2/S	0.1330E+10	QS = SGNL PHOTON FLUX DENSITY P/CM**2/S	0.3540E+10	QS = SGNL PHOTON FLUX DENSITY P/CM**2/S	0.4440E+11
KAPPA = DIELECTRIC CONSTANT	0.1720E+02	KAPPA = DIELECTRIC CONSTANT	0.1720E+02	KAPPA = DIELECTRIC CONSTANT	0.1720E+02
RF = FEEDBACK RESISTANCE OHM	0.1000E+10	RF = FEEDBACK RESISTANCE OHM	0.1000E+10	RF = FEEDBACK RESISTANCE OHM	0.1000E+10
CF = FEEDBACK CAPACITACE F	0.3000E-12	CF = FEEDBACK CAPACITACE F	0.3000E-12	CF = FEEDBACK CAPACITACE F	0.3000E-12
VP = PREAMP NOISE (INPUT) V/HZ**.5	0.2800E-08	VP = PREAMP NOISE (INPUT) V/HZ**.5	0.2800E-08	VP = PREAMP NOISE (INPUT) V/HZ**.5	0.2800E-08
AO = OPEN LOOP GAIN OF PREAMP	0.1000E+04	AO = OPEN LOOP GAIN OF PREAMP	0.1000E+04	AO = OPEN LOOP GAIN OF PREAMP	0.1000E+04
TRF= FEEDBACK RESISTOR TEMP K	0.1600E+03	TRF= FEEDBACK RESISTOR TEMP K	0.1600E+03	TRF= FEEDBACK RESISTOR TEMP K	0.1600E+03
FC = CHOPPING FREQUENCY HZ	0.4400E+03	FC = CHOPPING FREQUENCY HZ	0.4400E+03	FC = CHOPPING FREQUENCY HZ	0.4400E+03
RO = DIODE DARK RESISTANCE BIAS=0 OHM	0.1806E+09	RO = DIODE DARK RESISTANCE BIAS=0 OHM	0.1806E+09	RO = DIODE DARK RESISTANCE BIAS=0 OHM	0.1806E+09
RA = R(0)*A PRODUCT OHM*CM**2	0.1849E+07	RA = R(0)*A PRODUCT OHM*CM**2	0.1849E+07	RA = R(0)*A PRODUCT OHM*CM**2	0.1849E+07
VJ = JUNCTION POTENTIAL V	0.1978E+00	VJ = JUNCTION POTENTIAL V	0.1978E+00	VJ = JUNCTION POTENTIAL V	0.1978E+00
CJ = JUNCTION CAPACITANCE F	0.1020E-09	CJ = JUNCTION CAPACITANCE F	0.1020E-09	CJ = JUNCTION CAPACITANCE F	0.1020E-09
WJ = JUNCTION WIDTH CM	0.8673E-04	WJ = JUNCTION WIDTH CM	0.8673E-04	WJ = JUNCTION WIDTH CM	0.8673E-04
VC = CONTACT POTENTIAL V	0.1978E+00	VC = CONTACT POTENTIAL V	0.1978E+00	VC = CONTACT POTENTIAL V	0.1978E+00
ZD = DETECTOR IMPEDANCE OHM	0.3288E+07	ZD = DETECTOR IMPEDANCE OHM	0.3288E+07	ZD = DETECTOR IMPEDANCE OHM	0.3288E+07
ZF = FEEDBACK RESISTOR IMPEDANCE OHM	0.5466E+09	ZF = FEEDBACK RESISTOR IMPEDANCE OHM	0.5466E+09	ZF = FEEDBACK RESISTOR IMPEDANCE OHM	0.5466E+09
PD = DET. PHASE ANGLE RAD	0.1562E-14	PD = DET. PHASE ANGLE RAD	0.1562E-14	PD = DET. PHASE ANGLE RAD	0.1562E-14
PF = FDBK RESISTOR PHASE ANGLE RAD	0.8294E-18	PF = FDBK RESISTOR PHASE ANGLE RAD	0.8294E-18	PF = FDBK RESISTOR PHASE ANGLE RAD	0.8294E-18
AZ = TRANSIMPEDANCE OHM	0.6556E+09	AZ = TRANSIMPEDANCE OHM	0.6556E+09	AZ = TRANSIMPEDANCE OHM	0.6556E+09
IS = SIGNAL PHOTOCURRENT A	0.9901E-12	IS = SIGNAL PHOTOCURRENT A	0.2933E-11	IS = SIGNAL PHOTOCURRENT A	0.3305E-10
IT = TOTAL BKGD PHOTOCURRENT A	0.3611E-11	IT = TOTAL BKGD PHOTOCURRENT A	0.5569E-11	IT = TOTAL BKGD PHOTOCURRENT A	0.3566E-10
VRF= FDBK RESISTOR NOISE V/HZ**.5	0.1943E-05	VRF= FDBK RESISTOR NOISE V/HZ**.5	0.1949E-05	VRF= FDBK RESISTOR NOISE V/HZ**.5	0.1949E-05
VBG= BACKGROUND NOISE V/HZ**.5	0.7052E-06	VBG= BACKGROUND NOISE V/HZ**.5	0.8758E-06	VBG= BACKGROUND NOISE V/HZ**.5	0.2216E-05
VJN= JOHNSON NOISE V/HZ**.5	0.2220E-05	VJN= JOHNSON NOISE V/HZ**.5	0.2220E-05	VJN= JOHNSON NOISE V/HZ**.5	0.2220E-05
VGR= GEN-RECOMB NOISE V/HZ**.5	0.2220E-05	VGR= GEN-RECOMB NOISE V/HZ**.5	0.2220E-05	VGR= GEN-RECOMB NOISE V/HZ**.5	0.2220E-05
VPA= PREAMP NOISE V/HZ**.5	0.3988E-06	VPA= PREAMP NOISE V/HZ**.5	0.3988E-06	VPA= PREAMP NOISE V/HZ**.5	0.3988E-06
VT = TOTAL NOISE V/HZ**.5	0.3784E-05	VT = TOTAL NOISE V/HZ**.5	0.3819E-05	VT = TOTAL NOISE V/HZ**.5	0.4328E-05
R = RESPONSIVITY V/W	0.2082E+10	R = RESPONSIVITY V/W	0.2082E+10	R = RESPONSIVITY V/W	0.2082E+10
NEP= NOISE EQUIVALENT POWER W/HZ**.5	0.1817E-14	NEP= NOISE EQUIVALENT POWER W/HZ**.5	0.1834E-14	NEP= NOISE EQUIVALENT POWER W/HZ**.5	0.2079E-14
DSTAR = CM*HZ**.5/W	0.4194E+14	DSTAR = CM*HZ**.5/W	0.4155E+14	DSTAR = CM*HZ**.5/W	0.3667E+14

Table F-4 (CH 20)

PV INSB DETECTOR PERFORMANCE CHANNEL 20 75/160/MIN

CH = CHANNEL NUMBER	0.2000E+02
HD = DETECTOR HEIGHT CM	0.5300E-01
WD = DETECTOR WIDTH CM	0.7010E-01
T = DET. TEMP. K	0.7500E+02
CS = DET. STRAY CAPACITANCE F	0.6000E-11
RS = DET. SHUNT RESISTANCE OHM	0.1050E+07
VB = BIAS VOLTAGE V	0.0000E.00
EG = BAND GAP ENERGY EV	0.2267E+00
NI = INTRINSIC CONC. CM**-3	0.1602E+10
NA = ACCEPTOR CONC. CM**-3	0.1000E+18
ND = DONOR CARRIER CONC. CM**-3	0.5000E+15
MU = ELECTRON MOBILITY CM**2/V/S	0.8000E+05
MUH= HOLE MOBILITY CM**2/V/S	0.5000E+04
ETA= QUANTUM EFFICIENCY	0.8000E+00
TAU= CARRIER LIFETIME S	0.5000E-06
NUP= PEAK WAVENUMBER 1/CM	0.2032E+04
QBG= BKGD PHOTON FLUX DENSITY P/CM**2/S	0.8640E+10
QS = SGNL PHOTON FLUX DENSITY P/CM**2/S	0.3440E+10
KAPPA = DIELECTRIC CONSTANT	0.1720E+02
RF = FEEDBACK RESISTANCE OHM	0.1000E+10
CF = FEEDBACK CAPACITACE F	0.3000E-12
VP = PREAMP NOISE (INPUT) V/HZ**.5	0.2800E-08
AO = OPEN LOOP GAIN OF PREAMP	0.1000E+04
TRF= FEEDBACK RESISTOR TEMP K	0.1600E+03
FC = CHOPPING FREQUENCY HZ	0.4400E+03
RO = DIODE DARK RESISTANCE BIAS=0 OHM	0.2823E+09
RA = R(0)*A PRODUCT OHM*CM**2	0.1049E+07
VJ = JUNCTION POTENTIAL V	0.1978E+00
CJ = JUNCTION CAPACITANCE F	0.6525E-10
WJ = JUNCTION WIDTH CM	0.8673E-04
VC = CONTACT POTENTIAL V	0.1978E+00
ZD = DETECTOR IMPEDANCE OHM	0.4987E+07
ZF = FEEDBACK RESISTOR IMPEDANCE OHM	0.5466E+09
PD = DET. PHASE ANGLE RAD	0.6390E-15
PF = FDBK RESISTOR PHASE ANGLE RAD	0.8294E-18
AZ = TRANSIMPEDANCE OHM	0.6139E+09
IS = SIGNAL PHOTOCURRENT A	0.1638E-11
IT = TOTAL BKGD PHOTOCURRENT A	0.4209E-11
VRF= FDBK RESISTOR NOISE V/HZ**.5	0.1825E-05
VBG= BACKGROUND NOISE V/HZ**>5	0.7130E-06
VJN= JOHNSON NOISE V/HZ**.5	0.1663E-05
VGR= GEN-RECOMB NOISE V/HZ**.5	0.1663E-05
VPA= PREAMP NOISE V/HZ**.5	0.2763E-06
VT = TOTAL NOISE V/HZ**.5	0.3073E-05
R = RESPONSIVITY V/W	0.1950E+10
NEP= NOISE EQUIVALENT POWER W/HZ**.5	0.1576E-14
DSTAR = CM*HZ**.5/W	0.3867E+14

PV INSB DETECTOR PERFORMANCE CHANNEL 20 75/160/STD

CH = CHANNEL NUMBER	0.2000E+02
HD = DETECTOR HEIGHT CM	0.5300E-01
WD = DETECTOR WIDTH CM	0.7010E-01
T = DET. TEMP. K	0.7500E+02
CS = DET. STRAY CAPACITANCE F	0.6000E-11
RS = DET. SHUNT RESISTANCE OHM	0.1050E+07
VB = BIAS VOLTAGE V	0.0000E+00
EG = BAND GAP ENERGY EV	0.2267E+00
NI = INTRINSIC CONC. CM**-3	0.1602E+10
NA = ACCEPTOR CONC. CM**-3	0.1000E+18
ND = DONOR CARRIER CONC. CM**-3	0.5000E+15
MU = ELECTRON MOBILITY CM**2/V/S	0.8000E+05
MUH= HOLE MOBILITY CM**2/V/S	0.5000E+04
ETA= QUANTUM EFFICIENCY	0.8000E+00
TAU= CARRIER LIFETIME S	0.5000E-06
NUP= PEAK WAVENUMBER 1/CM	0.2032E+04
QBG= BKGD PHOTON FLUX DENSITY P/CM**2/S	0.1700E+11
QS = SGNL PHOTON FLUX DENSITY P/CM**2/S	0.1150E+11
KAPPA = DIELECTRIC CONSTANT	0.1720E+02
RF = FEEDBACK RESISTANCE OHM	0.1000E+10
CF = FEEDBACK CAPACITACE F	0.3000E-12
VP = PREAMP NOISE (INPUT) V/HZ**.5	0.2800E-08
AO = OPEN LOOP GAIN OF PREAMP	0.1000E+04
TRF= FEEDBACK RESISTOR TEMP K	0.1600E+03
FC = CHOPPING FREQUENCY HZ	0.4400E+03
RO = DIODE DARK RESISTANCE BIAS=0 OHM	0.2823E+09
RA = R(0)*A PRODUCT OHM*CM**2	0.1049E+07
VJ = JUNCTION POTENTIAL V	0.1978E+00
CJ = JUNCTION CAPACITANCE F	0.6525E-10
WJ = JUNCTION WIDTH CM	0.8673E-04
VC = CONTACT POTENTIAL V	0.1978E+00
ZD = DETECTOR IMPEDANCE OHM	0.4987E+07
ZF = FEEDBACK RESISTOR IMPEDANCE OHM	0.5466E+09
PD = DET. PHASE ANGLE RAD	0.6390E-15
PF = FDBK RESISTOR PHASE ANGLE RAD	0.8294E-18
AZ = TRANSIMPEDANCE OHM	0.6139E+09
IS = SIGNAL PHOTOCURRENT A	0.5476E-11
IT = TOTAL BKGD PHOTOCURRENT A	0.8095E-11
VRF= FDBK RESISTOR NOISE V/HZ**.5	0.1825E-05
VBG= BACKGROUND NOISE V/HZ**>5	0.9887E-06
VJN= JOHNSON NOISE V/HZ**.5	0.1663E-05
VGR= GEN-RECOMB NOISE V/HZ**.5	0.1663E-05
VPA= PREAMP NOISE V/HZ**.5	0.2763E-06
VT = TOTAL NOISE V/HZ**.5	0.3149E-05
R = RESPONSIVITY V/W	0.1950E+10
NEP= NOISE EQUIVALENT POWER W/HZ**.5	0.1615E-14
DSTAR = CM*HZ**.5/W	0.3774E+14

PV INSB DETECTOR PERFORMANCE CHANNEL 20 75/160/MAX

CH = CHANNEL NUMBER	0.2000E+02
HD = DETECTOR HEIGHT CM	0.5300E-01
WD = DETECTOR WIDTH CM	0.7010E-01
T = DET. TEMP. K	0.7500E+02
CS = DET. STRAY CAPACITANCE F	0.6000E-11
RS = DET. SHUNT RESISTANCE OHM	0.1050E+07
VB = BIAS VOLTAGE V	0.0000E+00
EG = BAND GAP ENERGY EV	0.2267E+00
NI = INTRINSIC CONC. CM**-3	0.1602E+10
NA = ACCEPTOR CONC. CM**-3	0.1000E+18
ND = DONOR CARRIER CONC. CM**-3	0.5000E+15
MU = ELECTRON MOBILITY CM**2/V/S	0.8000E+05
MUH= HOLE MOBILITY CM**2/V/S	0.5000E+04
ETA= QUANTUM EFFICIENCY	0.8000E+00
TAU= CARRIER LIFETIME S	0.5000E-06
NUP= PEAK WAVENUMBER 1/CM	0.2032E+04
QBG= BKGD PHOTON FLUX DENSITY P/CM**2/S	0.1090E+12
QS = SGNL PHOTON FLUX DENSITY P/CM**2/S	0.1050E+12
KAPPA = DIELECTRIC CONSTANT	0.1720E+02
RF = FEEDBACK RESISTANCE OHM	0.1000E+10
CF = FEEDBACK CAPACITACE F	0.3000E-12
VP = PREAMP NOISE (INPUT) V/HZ**.5	0.2800E-08
AO = OPEN LOOP GAIN OF PREAMP	0.1000E+04
TRF= FEEDBACK RESISTOR TEMP K	0.1600E+03
FC = CHOPPING FREQUENCY HZ	0.4400E+03
RO = DIODE DARK RESISTANCE BIAS=0 OHM	0.2823E+09
RA = R(0)*A PRODUCT OHM*CM**2	0.1049E+07
VJ = JUNCTION POTENTIAL V	0.1978E+00
CJ = JUNCTION CAPACITANCE F	0.6525E-10
WJ = JUNCTION WIDTH CM	0.8673E-04
VC = CONTACT POTENTIAL V	0.1978E+00
ZD = DETECTOR IMPEDANCE OHM	0.4987E+07
ZF = FEEDBACK RESISTOR IMPEDANCE OHM	0.5466E+09
PD = DET. PHASE ANGLE RAD	0.6390E-15
PF = FDBK RESISTOR PHASE ANGLE RAD	0.8294E-18
AZ = TRANSIMPEDANCE OHM	0.6139E+09
IS = SIGNAL PHOTOCURRENT A	0.8809E-10
IT = TOTAL BKGD PHOTOCURRENT A	0.8999E-10
VRF= FDBK RESISTOR NOISE V/HZ**.5	0.1825E-05
VBG= BACKGROUND NOISE V/HZ**>5	0.3297E-05
VJN= JOHNSON NOISE V/HZ**.5	0.1663E-05
VGR= GEN-RECOMB NOISE V/HZ**.5	0.1663E-05
VPA= PREAMP NOISE V/HZ**.5	0.2763E-06
VT = TOTAL NOISE V/HZ**.5	0.4450E-05
R = RESPONSIVITY V/W	0.1950E+10
NEP= NOISE EQUIVALENT POWER W/HZ**.5	0.2283E-14
DSTAR = CM*HZ**.5/W	0.2670E+14

Table F-4 (CH 21)

PV INSB DETECTOR PERFORMANCE CHANNEL 21 75/160/MIN

CH = CHANNEL NUMBER	0.2100E+02
HD = DETECTOR HEIGHT CM	0.5300E-01
WD = DETECTOR WIDTH CM	0.1102E+00
T = DET. TEMP. K	0.7500E+02
CS = DET. STRAY CAPACITANCE F	0.6000E-11
RS = DET. SHUNT RESISTANCE OHM	0.1050E+07
VB = BIAS VOLTAGE V	0.0000E+00
EG = BAND GAP ENERGY EV	0.2267E+00
NI = INTRINSIC CONC. CM**-3	0.1602E+10
NA = ACCEPTOR CONC. CM**-3	0.1000E+18
ND = DONOR CARRIER CONC. CM**-3	0.5000E+15
MU = ELECTRON MOBILITY CM**2/V/S	0.8000E+05
MUH= HOLE MOBILITY CM**2/V/S	0.5000E+04
ETA= QUANTUM EFFICIENCY	0.8000E+00
TAU= CARRIER LIFETIME S	0.5000E-06
NUP= PEAK WAVENUMBER 1/CM	0.2032E+04
QBG= BKGD PHOTON FLUX DENSITY P/CM**2/S	0.6880E+16
QS = SGNL PHOTON FLUX DENSITY P/CM**2/S	0.3590E+16
KAPPA = DIELECTRIC CONSTANT	0.1720E+02
RF = FEEDBACK RESISTANCE OHM	0.1000E+10
CF = FEEDBACK CAPACITACE F	0.3000E-12
VP = PREAMP NOISE (INPUT) V/HZ**.5	0.2800E-08
AO = OPEN LOOP GAIN OF PREAMP	0.1000E+04
TRF= FEEDBACK RESISTOR TEMP K	0.1600E+03
FC = CHOPPING FREQUENCY HZ	0.4400E+03
RO = DIODE DARK RESISTANCE BIAS=0 OHM	0.1796E+09
RA = R(0)*A PRODUCT OHM*CM**2	0.1049E+07
VJ = JUNCTION POTENTIAL V	0.1978E+00
CJ = JUNCTION CAPACITANCE F	0.1026E-09
WJ = JUNCTION WIDTH CM	0.8673E-04
VC = CONTACT POTENTIAL V	0.1978E+00
ZD = DETECTOR IMPEDANCE OHM	0.3271E+07
ZF = FEEDBACK RESISTOR IMPEDANCE OHM	0.5466E+09
PD = DET. PHASE ANGLE RAD	0.1579E-14
PF = FDBK RESISTOR PHASE ANGLE RAD	0.8294E-18
AZ = TRANSIMPEDANCE OHM	0.6563E+09
IS = SIGNAL PHOTOCURRENT A	0.2687E-11
IT = TOTAL BKGD PHOTOCURRENT A	0.5158E-11
VRF= FDBK RESISTOR NOISE V/HZ**.5	0.1951E-05
VBG= BACKGROUND NOISE V/HZ**.5	0.8431E-06
VJN= JOHNSON NOISE V/HZ**.5	0.2229E-05
VGR= GEN-RECOMB NOISE V/HZ**.5	0.2229E-05
VPA= PREAMP NOISE V/HZ**.5	0.4006E-06
VT = TOTAL NOISE V/HZ**.5	0.3823E-05
R = RESPONSIVITY V/W	0.2084E+10
NEP= NOISE EQUIVALENT POWER W/HZ**.5	0.1834E-14
DSTAR = CM*HZ**.5/W	0.4167E+14

PV INSB DETECTOR PERFORMANCE CHANNEL 21 75/160/STD

CH = CHANNEL NUMBER	0.2100E+02
HD = DETECTOR HEIGHT CM	0.5300E-01
WD = DETECTOR WIDTH CM	0.1102E+00
T = DET. TEMP. K	0.7500E+02
CS = DET. STRAY CAPACITANCE F	0.6000E-11
RS = DET. SHUNT RESISTANCE OHM	0.1050E+07
VB = BIAS VOLTAGE V	0.0000E+00
EG = BAND GAP ENERGY EV	0.2267E+00
NI = INTRINSIC CONC. CM**-3	0.1602E+10
NA = ACCEPTOR CONC. CM**-3	0.1000E+18
ND = DONOR CARRIER CONC. CM**-3	0.5000E+15
MU = ELECTRON MOBILITY CM**2/V/S	0.8000E+05
MUH= HOLE MOBILITY CM**2/V/S	0.5000E+04
ETA= QUANTUM EFFICIENCY	0.8000E+00
TAU= CARRIER LIFETIME S	0.5000E-06
NUP= PEAK WAVENUMBER 1/CM	0.2032E+04
QBG= BKGD PHOTON FLUX DENSITY P/CM**2/S	0.1958E+11
QS = SGNL PHOTON FLUX DENSITY P/CM**2/S	0.1630E+11
KAPPA = DIELECTRIC CONSTANT	0.1720E+02
RF = FEEDBACK RESISTANCE OHM	0.1000E+10
CF = FEEDBACK CAPACITACE F	0.3000E-12
VP = PREAMP NOISE (INPUT) V/HZ**.5	0.2800E-08
AO = OPEN LOOP GAIN OF PREAMP	0.1000E+04
TRF= FEEDBACK RESISTOR TEMP K	0.1600E+03
FC = CHOPPING FREQUENCY HZ	0.4400E+03
RO = DIODE DARK RESISTANCE BIAS=0 OHM	0.1796E+09
RA = R(0)*A PRODUCT OHM*CM**2	0.1049E+07
VJ = JUNCTION POTENTIAL V	0.1978E+00
CJ = JUNCTION CAPACITANCE F	0.1026E-09
WJ = JUNCTION WIDTH CM	0.8673E-04
VC = CONTACT POTENTIAL V	0.1978E+00
ZD = DETECTOR IMPEDANCE OHM	0.3271E+07
ZF = FEEDBACK RESISTOR IMPEDANCE OHM	0.5466E+09
PD = DET. PHASE ANGLE RAD	0.1579E-14
PF = FDBK RESISTOR PHASE ANGLE RAD	0.8294E-18
AZ = TRANSIMPEDANCE OHM	0.6563E+09
IS = SIGNAL PHOTOCURRENT A	0.1220E-10
IT = TOTAL BKGD PHOTOCURRENT A	0.1460E-10
VRF= FDBK RESISTOR NOISE V/HZ**.5	0.1951E-05
VBG= BACKGROUND NOISE V/HZ**.5	0.1419E-05
VJN= JOHNSON NOISE V/HZ**.5	0.2229E-05
VGR= GEN-RECOMB NOISE V/HZ**.5	0.2229E-05
VPA= PREAMP NOISE V/HZ**.5	0.4006E-06
VT = TOTAL NOISE V/HZ**.5	0.3993E-05
R = RESPONSIVITY V/W	0.2084E+10
NEP= NOISE EQUIVALENT POWER W/HZ**.5	0.1914E-14
DSTAR = CM*HZ**.5/W	0.3993E+14

PV INSB DETECTOR PERFORMANCE CHANNEL 21 75/160/MAX

CH = CHANNEL NUMBER	0.2100E+02
HD = DETECTOR HEIGHT CM	0.5300E-01
WD = DETECTOR WIDTH CM	0.1102E+00
T = DET. TEMP. K	0.7500E+02
CS = DET. STRAY CAPACITANCE F	0.6000E-11
RS = DET. SHUNT RESISTANCE OHM	0.1050E+07
VB = BIAS VOLTAGE V	0.0000E+00
EG = BAND GAP ENERGY EV	0.2267E+00
NI = INTRINSIC CONC. CM**-3	0.1602E+10
NA = ACCEPTOR CONC. CM**-3	0.1000E+18
ND = DONOR CARRIER CONC. CM**-3	0.5000E+15
MU = ELECTRON MOBILITY CM**2/V/S	0.8000E+05
MUH= HOLE MOBILITY CM**2/V/S	0.5000E+04
ETA= QUANTUM EFFICIENCY	0.8000E+00
TAU= CARRIER LIFETIME S	0.5000E-06
NUP= PEAK WAVENUMBER 1/CM	0.2032E+04
QBG= BKGD PHOTON FLUX DENSITY P/CM**2/S	0.2044E+12
QS = SGNL PHOTON FLUX DENSITY P/CM**2/S	0.2818E+12
KAPPA = DIELECTRIC CONSTANT	0.1720E+02
RF = FEEDBACK RESISTANCE OHM	0.1000E+10
CF = FEEDBACK CAPACITACE F	0.3000E-12
VP = PREAMP NOISE (INPUT) V/HZ**.5	0.2800E-08
AO = OPEN LOOP GAIN OF PREAMP	0.1000E+04
TRF= FEEDBACK RESISTOR TEMP K	0.1600E+03
FC = CHOPPING FREQUENCY HZ	0.4400E+03
RO = DIODE DARK RESISTANCE BIAS=0 OHM	0.1796E+09
RA = R(0)*A PRODUCT OHM*CM**2	0.1049E+07
VJ = JUNCTION POTENTIAL V	0.1978E+00
CJ = JUNCTION CAPACITANCE F	0.1026E-09
WJ = JUNCTION WIDTH CM	0.8673E-04
VC = CONTACT POTENTIAL V	0.1978E+00
ZD = DETECTOR IMPEDANCE OHM	0.3271E+07
ZF = FEEDBACK RESISTOR IMPEDANCE OHM	0.5466E+09
PD = DET. PHASE ANGLE RAD	0.1579E-14
PF = FDBK RESISTOR PHASE ANGLE RAD	0.8294E-18
AZ = TRANSIMPEDANCE OHM	0.6563E+09
IS = SIGNAL PHOTOCURRENT A	0.1585E-09
IT = TOTAL BKGD PHOTOCURRENT A	0.1527E-09
VRF= FDBK RESISTOR NOISE V/HZ**.5	0.1951E-05
VBG= BACKGROUND NOISE V/HZ**.5	0.4591E-05
VJN= JOHNSON NOISE V/HZ**.5	0.2229E-05
VGR= GEN-RECOMB NOISE V/HZ**.5	0.2229E-05
VPA= PREAMP NOISE V/HZ**.5	0.4006E-06
VT = TOTAL NOISE V/HZ**.5	0.5914E-05
R = RESPONSIVITY V/W	0.2084E+10
NEP= NOISE EQUIVALENT POWER W/HZ**.5	0.2838E-14
DSTAR = CM*HZ**.5/W	0.2693E+14

Table F-4 (CH 22)

PV INSB DETECTOR PERFORMANCE CHANNEL 22 75/168/MIN

CH = CHANNEL NUMBER	2.2200E+02
HD = DETECTOR HEIGHT CM	0.5300E-01
WD = DETECTOR WIDTH CM	0.7120E-01
T = DET. TEMP. K	0.7500E+02
CS = DET. STRAY CAPACITANCE F	0.6000E-11
RS = DET. SHUNT RESISTANCE OHM	0.1050E+07
VB = BIAS VOLTAGE V	0.0000E+00
EG = BAND GAP ENERGY EV	0.2267E+00
NI = INTRINSIC CONC. CM**-3	0.1682E+10
NA = ACCEPTOR CONC. CM**-3	0.1000E+18
ND = DONOR CARRIER CONC. CM**-3	0.5000E+15
MU = ELECTRON MOBILITY CM**2/V/S	0.8000E+05
MUH= HOLE MOBILITY CM**2/V/S	0.5000E+04
ETA= QUANTUM EFFICIENCY	0.8000E+00
TAU= CARRIER LIFETIME S	0.5000E-06
NUP= PEAK WAVENUMBER 1/CM	0.2833E+04
QBG= BKGD PHOTON FLUX DENSITY P/CM**2/S	0.1150E+11
QS = SGNL PHOTON FLUX DENSITY P/CM**2/S	0.6210E+10
KAPPA = DIELECTRIC CONSTANT	0.1720E+02
RF = FEEDBACK RESISTANCE OHM	0.1000E+10
CF = FEEDBACK CAPACITANCE F	0.3000E-12
VP = PREAMP NOISE (INPUT) V/HZ**.5	0.2800E-08
AO = OPEN LOOP GAIN OF PREAMP	0.1000E+04
TRF= FEEDBACK RESISTOR TEMP K	0.1600E+03
FC = CHOPPING FREQUENCY HZ	0.4400E+03
RO = DIODE DARK RESISTANCE BIAS=0 OHM	0.2779E+09
RA = R(0)*A PRODUCT OHM*CM**2	0.1049E+07
VJ = JUNCTION POTENTIAL V	0.1978E+00
CJ = JUNCTION CAPACITANCE F	0.6627E-10
WJ = JUNCTION WIDTH CM	0.8673E-04
VC = CONTACT POTENTIAL V	0.1978E+00
ZD = DETECTOR IMPEDANCE OHM	0.4916E+07
ZF = FEEDBACK RESISTOR IMPEDANCE OHM	0.5466E+09
PD = DET. PHASE ANGLE RAD	0.6592E-15
PF = FDBK RESISTOR PHASE ANGLE RAD	0.8294E-18
AZ = TRANSIMPEDANCE OHM	0.6150E+09
IS = SIGNAL PHOTOCURRENT A	0.3003E-11
IT = TOTAL BKGD PHOTOCURRENT A	0.5618E-11
VRF= FDBK RESISTOR NOISE V/HZ**.5	0.1828E-05
VBG= BACKGROUND NOISE V/HZ**.5	0.8245E-06
VJN= JOHNSON NOISE V/HZ**.5	0.1679E-05
VGR= GEN-RECOMB NOISE V/HZ**.5	0.1579E-05
VPA= PREAMP NOISE V/HZ**.5	0.2799E-06
VT = TOTAL NOISE V/HZ**.5	0.3129E-05
R = RESPONSIVITY V/W	0.1953E+10
NEP= NOISE EQUIVALENT POWER W/HZ**.5	0.1598E-14
DSTAR = CM*HZ**.5/W	0.3845E+14

PV INSB DETECTOR PERFORMANCE CHANNEL 22 75/168/STD

CH = CHANNEL NUMBER	0.2200E+02
HD = DETECTOR HEIGHT CM	0.5300E-01
WD = DETECTOR WIDTH CM	0.7120E-01
T = DET. TEMP. K	0.7500E+02
CS = DET. STRAY CAPACITANCE F	0.6000E-11
RS = DET. SHUNT RESISTANCE OHM	0.1050E+07
VB = BIAS VOLTAGE V	0.0000E+00
EG = BAND GAP ENERGY EV	0.2267E+00
NI = INTRINSIC CONC. CM**-3	0.1682E+10
NA = ACCEPTOR CONC. CM**-3	0.1000E+18
ND = DONOR CARRIER CONC. CM**-3	0.5000E+15
MU = ELECTRON MOBILITY CM**2/V/S	0.8000E+05
MUH= HOLE MOBILITY CM**2/V/S	0.5000E+04
ETA= QUANTUM EFFICIENCY	0.8000E+00
TAU= CARRIER LIFETIME S	0.5000E-06
NUP= PEAK WAVENUMBER 1/CM	0.2832E+04
QBG= BKGD PHOTON FLUX DENSITY P/CM**2/S	0.4930E+11
QS = SGNL PHOTON FLUX DENSITY P/CM**2/S	0.4400E+11
KAPPA = DIELECTRIC CONSTANT	0.1720E+02
RF = FEEDBACK RESISTANCE OHM	0.1000E+10
CF = FEEDBACK CAPACITANCE F	0.3000E-12
VP = PREAMP NOISE (INPUT) V/HZ**.5	0.2800E-08
AO = OPEN LOOP GAIN OF PREAMP	0.1000E+04
TRF= FEEDBACK RESISTOR TEMP K	0.1600E+03
FC = CHOPPING FREQUENCY HZ	0.4400E+03
RO = DIODE DARK RESISTANCE BIAS=0 OHM	0.2779E+09
RA = R(0)*A PRODUCT OHM*CM**2	0.1049E+07
VJ = JUNCTION POTENTIAL V	0.1978E+00
CJ = JUNCTION CAPACITANCE F	0.6627E-10
WJ = JUNCTION WIDTH CM	0.8673E-04
VC = CONTACT POTENTIAL V	0.1978E+00
ZD = DETECTOR IMPEDANCE OHM	0.4916E+07
ZF = FEEDBACK RESISTOR IMPEDANCE OHM	0.5466E+09
PD = DET. PHASE ANGLE RAD	0.6592E-15
PF = FDBK RESISTOR PHASE ANGLE RAD	0.8294E-18
AZ = TRANSIMPEDANCE OHM	0.6150E+09
IS = SIGNAL PHOTOCURRENT A	0.2128E-10
IT = TOTAL BKGD PHOTOCURRENT A	0.2384E-10
VRF= FDBK RESISTOR NOISE V/HZ**.5	0.1828E-05
VBG= BACKGROUND NOISE V/HZ**.5	0.1700E-05
VJN= JOHNSON NOISE V/HZ**.5	0.1679E-05
VGR= GEN-RECOMB NOISE V/HZ**.5	0.1679E-05
VPA= PREAMP NOISE V/HZ**.5	0.2799E-06
VT = TOTAL NOISE V/HZ**.5	0.3456E-05
R = RESPONSIVITY V/W	0.1953E+10
NEP= NOISE EQUIVALENT POWER W/HZ**.5	0.1770E-14
DSTAR = CM*HZ**.5/W	0.3471E+14

PV INSB DETECTOR PERFORMANCE CHANNEL 22 75/168/MAX

CH = CHANNEL NUMBER	0.2200E+02
HD = DETECTOR HEIGHT CM	0.5300E-01
WD = DETECTOR WIDTH CM	0.7120E-01
T = DET. TEMP. K	0.7500E+02
CS = DET. STRAY CAPACITANCE F	0.6000E-11
RS = DET. SHUNT RESISTANCE OHM	0.1050E+07
VB = BIAS VOLTAGE V	0.0000E+00
EG = BAND GAP ENERGY EV	0.2267E+00
NI = INTRINSIC CONC. CM**-3	0.1682E+10
NA = ACCEPTOR CONC. CM**-3	0.1000E+18
ND = DONOR CARRIER CONC. CM**-3	0.5000E+15
MU = ELECTRON MOBILITY CM**2/V/S	0.8000E+05
MUH= HOLE MOBILITY CM**2/V/S	0.5000E+04
ETA= QUANTUM EFFICIENCY	0.8000E+00
TAU= CARRIER LIFETIME S	0.5000E-06
NUP= PEAK WAVENUMBER 1/CM	0.2832E+04
QBG= BKGD PHOTON FLUX DENSITY P/CM**2/S	0.4110E+12
QS = SGNL PHOTON FLUX DENSITY P/CM**2/S	0.4050E+12
KAPPA = DIELECTRIC CONSTANT	0.1720E+02
RF = FEEDBACK RESISTANCE OHM	0.1000E+10
CF = FEEDBACK CAPACITANCE F	0.3000E-12
VP = PREAMP NOISE (INPUT) V/HZ**.5	0.2800E-08
AO = OPEN LOOP GAIN OF PREAMP	0.1000E+04
TRF= FEEDBACK RESISTOR TEMP K	0.1600E+03
FC = CHOPPING FREQUENCY HZ	0.4400E+03
RO = DIODE DARK RESISTANCE BIAS=0 OHM	0.2779E+09
RA = R(0)*A PRODUCT OHM*CM**2	0.1049E+07
VJ = JUNCTION POTENTIAL V	0.1978E+00
CJ = JUNCTION CAPACITANCE F	0.6627E-10
WJ = JUNCTION WIDTH CM	0.8673E-04
VC = CONTACT POTENTIAL V	0.1978E+00
ZD = DETECTOR IMPEDANCE OHM	0.4916E+07
ZF = FEEDBACK RESISTOR IMPEDANCE OHM	0.5466E+09
PD = DET. PHASE ANGLE RAD	0.6592E-15
PF = FDBK RESISTOR PHASE ANGLE RAD	0.8294E-18
AZ = TRANSIMPEDANCE OHM	0.6150E+09
IS = SIGNAL PHOTOCURRENT A	0.1959E-09
IT = TOTAL BKGD PHOTOCURRENT A	0.1980E-09
VRF= FDBK RESISTOR NOISE V/HZ**.5	0.1828E-05
VBG= BACKGROUND NOISE V/HZ**.5	0.4900E-05
VJN= JOHNSON NOISE V/HZ**.5	0.1679E-05
VGR= GEN-RECOMB NOISE V/HZ**.5	0.1679E-05
VPA= PREAMP NOISE V/HZ**.5	0.2799E-06
VT = TOTAL NOISE V/HZ**.5	0.5757E-05
R = RESPONSIVITY V/W	0.1953E+10
NEP= NOISE EQUIVALENT POWER W/HZ**.5	0.2948E-14
DSTAR = CM*HZ**.5/W	0.2034E+14

Table F-4 (CH 23)

PV INSB DETECTOR PERFORMANCE CHANNEL 23 75/160/MIN		PV INSB DETECTOR PERFORMANCE CHANNEL 23 75/160/STD		PV INSB DETECTOR PERFORMANCE CHANNEL 23 75/160/MAX	
CH = CHANNEL NUMBER	0.2300E+02	CH = CHANNEL NUMBER	0.2300E+02	CH = CHANNEL NUMBER	0.2300E+02
HD = DETECTOR HEIGHT CM	0.5300E-01	HD = DETECTOR HEIGHT CM	0.5300E-01	HD = DETECTOR HEIGHT CM	0.5300E-01
WD = DETECTOR WIDTH CM	0.1100E+00	WD = DETECTOR WIDTH CM	0.1100E+00	WD = DETECTOR WIDTH CM	0.1100E+00
T = DET. TEMP. K	0.7500E+02	T = DET. TEMP. K	0.7500E+02	T = DET. TEMP. K	0.7500E+02
CS = DET. STRAY CAPACITANCE F	0.6000E-11	CS = DET. STRAY CAPACITANCE F	0.6000E-11	CS = DET. STRAY CAPACITANCE F	0.6000E-11
RS = DET. SHUNT RESISTANCE OHM	0.1050E+07	RS = DET. SHUNT RESISTANCE OHM	0.1050E+07	RS = DET. SHUNT RESISTANCE OHM	0.1050E+07
VB = BIAS VOLTAGE V	0.0000E+00	VB = BIAS VOLTAGE V	0.0000E+00	VB = BIAS VOLTAGE V	0.0000E+00
EG = BAND GAP ENERGY EV	0.2267E+00	EG = BAND GAP ENERGY EV	0.2267E+00	EG = BAND GAP ENERGY EV	0.2267E+00
NI = INTRINSIC CONC. CM**-3	0.1602E+10	NI = INTRINSIC CONC. CM**-3	0.1602E+10	NI = INTRINSIC CONC. CM**-3	0.1602E+10
NA = ACCEPTOR CONC. CM**-3	0.1800E+18	NA = ACCEPTOR CONC. CM**-3	0.1800E+18	NA = ACCEPTOR CONC. CM**-3	0.1800E+18
ND = DONOR CARRIER CONC. CM**-3	0.5000E+15	ND = DONOR CARRIER CONC. CM**-3	0.5000E+15	ND = DONOR CARRIER CONC. CM**-3	0.5000E+15
MU = ELECTRON MOBILITY CM**2/V/S	0.8000E+05	MU = ELECTRON MOBILITY CM**2/V/S	0.8000E+05	MU = ELECTRON MOBILITY CM**2/V/S	0.8000E+05
MUH= HOLE MOBILITY CM**2/V/S	0.5000E+04	MUH= HOLE MOBILITY CM**2/V/S	0.5000E+04	MUH= HOLE MOBILITY CM**2/V/S	0.5000E+04
ETA= QUANTUM EFFICIENCY	0.8000E+00	ETA= QUANTUM EFFICIENCY	0.8000E+00	ETA= QUANTUM EFFICIENCY	0.8000E+00
TAU= CARRIER LIFETIME S	0.5000E-06	TAU= CARRIER LIFETIME S	0.5000E-06	TAU= CARRIER LIFETIME S	0.5000E-06
NUP= PEAK WAVENUMBER 1/CM	0.2032E+04	NUP= PEAK WAVENUMBER 1/CM	0.2032E+04	NUP= PEAK WAVENUMBER 1/CM	0.2032E+04
QBG= BKGD PHOTON FLUX DENSITY P/CM**2/S	0.7240E+10	QBG= BKGD PHOTON FLUX DENSITY P/CM**2/S	0.4170E+11	QBG= BKGD PHOTON FLUX DENSITY P/CM**2/S	0.2900E+12
QS = SGNL PHOTON FLUX DENSITY P/CM**2/S	0.4100E+10	QS = SGNL PHOTON FLUX DENSITY P/CM**2/S	0.3060E+11	QS = SGNL PHOTON FLUX DENSITY P/CM**2/S	0.2860E+12
KAPPA = DIELECTRIC CONSTANT	0.1720E+02	KAPPA = DIELECTRIC CONSTANT	0.1720E+02	KAPPA = DIELECTRIC CONSTANT	0.1720E+02
RF = FEEDBACK RESISTANCE OHM	0.1000E+10	RF = FEEDBACK RESISTANCE OHM	0.1000E+10	RF = FEEDBACK RESISTANCE OHM	0.1000E+10
CF = FEEDBACK CAPACITACE F	0.3000E-12	CF = FEEDBACK CAPACITACE F	0.3000E-12	CF = FEEDBACK CAPACITACE F	0.3000E-12
VP = PREAMP NOISE (INPUT) V/HZ**.5	0.2000E-08	VP = PREAMP NOISE (INPUT) V/HZ**.5	0.2000E-08	VP = PREAMP NOISE (INPUT) V/HZ**.5	0.2000E-08
AO = OPEN LOOP GAIN OF PREAMP	0.1000E+04	AO = OPEN LOOP GAIN OF PREAMP	0.1000E+04	AO = OPEN LOOP GAIN OF PREAMP	0.1000E+04
TRF= FEEDBACK RESISTOR TEMP K	0.1600E+03	TRF= FEEDBACK RESISTOR TEMP K	0.1600E+03	TRF= FEEDBACK RESISTOR TEMP K	0.1600E+03
FC = CHOPPING FREQUENCY HZ	0.4400E+03	FC = CHOPPING FREQUENCY HZ	0.4400E+03	FC = CHOPPING FREQUENCY HZ	0.4400E+03
RO = DIODE DARK RESISTANCE BIAS=0 OHM	0.1786E+09	RO = DIODE DARK RESISTANCE BIAS=0 OHM	0.1786E+09	RO = DIODE DARK RESISTANCE BIAS=0 OHM	0.1786E+09
RA = R(0)*A PRODUCT OHM*CM**2	0.1049E+07	RA = R(0)*A PRODUCT OHM*CM**2	0.1049E+07	RA = R(0)*A PRODUCT OHM*CM**2	0.1049E+07
VJ = JUNCTION POTENTIAL V	0.1978E+00	VJ = JUNCTION POTENTIAL V	0.1978E+00	VJ = JUNCTION POTENTIAL V	0.1978E+00
CJ = JUNCTION CAPACITANCE F	0.1031E-09	CJ = JUNCTION CAPACITANCE F	0.1031E-09	CJ = JUNCTION CAPACITANCE F	0.1031E-09
WJ = JUNCTION WIDTH CM	0.8673E-04	WJ = JUNCTION WIDTH CM	0.8673E-04	WJ = JUNCTION WIDTH CM	0.8673E-04
VC = CONTACT POTENTIAL V	0.1978E+00	VC = CONTACT POTENTIAL V	0.1978E+00	VC = CONTACT POTENTIAL V	0.1978E+00
ZD = DETECTOR IMPEDANCE OHM	0.3254E+07	ZD = DETECTOR IMPEDANCE OHM	0.3254E+07	ZD = DETECTOR IMPEDANCE OHM	0.3254E+07
ZF = FEEDBACK RESISTOR IMPEDANCE OHM	0.5466E+09	ZF = FEEDBACK RESISTOR IMPEDANCE OHM	0.5466E+09	ZF = FEEDBACK RESISTOR IMPEDANCE OHM	0.5466E+09
PD = DET. PHASE ANGLE RAD	0.1596E-14	PD = DET. PHASE ANGLE RAD	0.1596E-14	PD = DET. PHASE ANGLE RAD	0.1596E-14
PF = FDBK RESISTOR PHASE ANGLE RAD	0.8294E-18	PF = FDBK RESISTOR PHASE ANGLE RAD	0.8294E-18	PF = FDBK RESISTOR PHASE ANGLE RAD	0.8294E-18
AZ = TRANSIMPEDANCE OHM	0.6570E+09	AZ = TRANSIMPEDANCE OHM	0.6573E+09	AZ = TRANSIMPEDANCE OHM	0.6570E+09
IS = SIGNAL PHOTOCURRENT A	0.3086E-11	IS = SIGNAL PHOTOCURRENT A	0.2905E-10	IS = SIGNAL PHOTOCURRENT A	0.2152E-09
IT = TOTAL BKGD PHOTOCURRENT A	0.5449E-11	IT = TOTAL BKGD PHOTOCURRENT A	0.3133E-10	IT = TOTAL BKGD PHOTOCURRENT A	0.2183E-09
VRF= FDBK RESISTOR NOISE V/HZ**.5	0.1953E-05	VRF= FDBK RESISTOR NOISE V/HZ**.5	0.1953E-05	VRF= FDBK RESISTOR NOISE V/HZ**.5	0.1953E-05
VBG= BACKGROUND NOISE V/HZ**)5	0.8681E-06	VBG= BACKGROUND NOISE V/HZ**)5	0.2033E-05	VBG= BACKGROUND NOISE V/HZ**)5	0.5494E-05
VJN= JOHNSON NOISE V/HZ**.5	0.2237E-05	VJN= JOHNSON NOISE V/HZ**.5	0.2237E-05	VJN= JOHNSON NOISE V/HZ**.5	0.2237E-05
VGR= GEN-RECOMB NOISE V/HZ**.5	0.2237E-05	VGR= GEN-RECOMB NOISE V/HZ**.5	0.2237E-05	VGR= GEN-RECOMB NOISE V/HZ**.5	0.2237E-05
VPA= PREAMP NOISE V/HZ**.5	0.4024E-06	VPA= PREAMP NOISE V/HZ**.5	0.4024E-06	VPA= PREAMP NOISE V/HZ**.5	0.4024E-06
VT = TOTAL NOISE V/HZ**.5	0.3839E-05	VT = TOTAL NOISE V/HZ**.5	0.4281E-05	VT = TOTAL NOISE V/HZ**.5	0.6646E-05
R = RESPONSIVITY V/W	0.2086E+10	R = RESPONSIVITY V/W	0.2086E+10	R = RESPONSIVITY V/W	0.2086E+10
NEP= NOISE EQUIVALENT POWER W/HZ**.5	0.1840E-14	NEP= NOISE EQUIVALENT POWER W/HZ**.5	0.2052E-14	NEP= NOISE EQUIVALENT POWER W/HZ**.5	0.3185E-14
DSTAR = CM*HZ**.5/W	0.4165E+14	DSTAR = CM*HZ**.5/W	0.3735E+14	DSTAR = CM*HZ**.5/W	0.2408E+14

Table F-4 (CH 24)

PV INSB DETECTOR PERFORMANCE CHANNEL 24 75/160/MIN		PV INSB DETECTOR PERFORMANCE CHANNEL 24 75/160/STD		PV INSB DETECTOR PERFORMANCE CHANNEL 24 75/160/MAX	
CH = CHANNEL NUMBER	0.2400E+02	CH = CHANNEL NUMBER	0.2400E+02	CH = CHANNEL NUMBER	0.2400E+02
HD = DETECTOR HEIGHT CM	0.5300E-01	HD = DETECTOR HEIGHT CM	0.5300E-01	HD = DETECTOR HEIGHT CM	0.5300E-01
WD = DETECTOR WIDTH CM	0.7240E-01	WD = DETECTOR WIDTH CM	0.7240E-01	WD = DETECTOR WIDTH CM	0.7240E-01
T = DET. TEMP. K	0.7500E+02	T = DET. TEMP. K	0.7500E+02	T = DET. TEMP. K	0.7500E+02
CS = DET. STRAY CAPACITANCE F	0.6000E-11	CS = DET. STRAY CAPACITANCE F	0.6000E-11	CS = DET. STRAY CAPACITANCE F	0.6000E-11
RS = DET. SHUNT RESISTANCE OHM	0.1050E+07	RS = DET. SHUNT RESISTANCE OHM	0.1050E+07	RS = DET. SHUNT RESISTANCE OHM	0.1050E+07
VB = BIAS VOLTAGE V	0.0000E+00	VB = BIAS VOLTAGE V	0.0000E+00	VB = BIAS VOLTAGE V	0.0000E+00
EG = BAND GAP ENERGY EV	0.2267E+00	EG = BAND GAP ENERGY EV	0.2267E+00	EG = BAND GAP ENERGY EV	0.2267E+00
NI = INTRINSIC CONC. CM**-3	0.1683E+10	NI = INTRINSIC CONC. CM**-3	0.1602E+10	NI = INTRINSIC CONC. CM**-3	0.1602E+10
NA = ACCEPTOR CONC. CM**-3	0.1000E+18	NA = ACCEPTOR CONC. CM**-3	0.1000E+18	NA = ACCEPTOR CONC. CM**-3	0.1000E+18
ND = DONOR CARRIER CONC. CM**-3	0.5000E+15	ND = DONOR CARRIER CONC. CM**-3	0.5000E+15	ND = DONOR CARRIER CONC. CM**-3	0.5000E+15
MU = ELECTRON MOBILITY CM**2/V/S	0.8000E+05	MU = ELECTRON MOBILITY CM**2/V/S	0.8000E+05	MU = ELECTRON MOBILITY CM**2/V/S	0.8000E+05
MUH= HOLE MOBILITY CM**2/V/S	0.5000E+04	MUH= HOLE MOBILITY CM**2/V/S	0.5000E+04	MUH= HOLE MOBILITY CM**2/V/S	0.5000E+04
ETA= QUANTUM EFFICIENCY	0.8000E+00	ETA= QUANTUM EFFICIENCY	0.8000E+00	ETA= QUANTUM EFFICIENCY	0.8000E+00
TAU= CARRIER LIFETIME S	0.5000E-06	TAU= CARRIER LIFETIME S	0.5000E-06	TAU= CARRIER LIFETIME S	0.5000E-06
NUP= PEAK WAVENUMBER 1/CM	0.2032E+04	NUP= PEAK WAVENUMBER 1/CM	0.2032E+04	NUP= PEAK WAVENUMBER 1/CM	0.2032E+04
QBG= BKGD PHOTON FLUX DENSITY P/CM**2/S	0.1260E+11	QBG= BKGD PHOTON FLUX DENSITY P/CM**2/S	0.7900E+11	QBG= BKGD PHOTON FLUX DENSITY P/CM**2/S	0.4970E+12
QS = SGNL PHOTON FLUX DENSITY P/CM**2/S	0.6750E+10	QS = SGNL PHOTON FLUX DENSITY P/CM**2/S	0.7300E+11	QS = SGNL PHOTON FLUX DENSITY P/CM**2/S	0.4910E+12
KAPPA = DIELECTRIC CONSTANT	0.1720E+02	KAPPA = DIELECTRIC CONSTANT	0.1720E+02	KAPPA = DIELECTRIC CONSTANT	0.1720E+02
RF = FEEDBACK RESISTANCE OHM	0.1000E+10	RF = FEEDBACK RESISTANCE OHM	0.1000E+10	RF = FEEDBACK RESISTANCE OHM	0.1000E+10
CF = FEEDBACK CAPACITACE F	0.3000E-12	CF = FEEDBACK CAPACITACE F	0.3000E-12	CF = FEEDBACK CAPACITACE F	0.3000E-12
VP = PREAMP NOISE (INPUT) V/HZ**.5	0.2800E-08	VP = PREAMP NOISE (INPUT) V/HZ**.5	0.2800E-08	VP = PREAMP NOISE (INPUT) V/HZ**.5	0.2800E-08
AO = OPEN LOOP GAIN OF PREAMP	0.1000E+04	AO = OPEN LOOP GAIN OF PREAMP	0.1000E+04	AO = OPEN LOOP GAIN OF PREAMP	0.1000E+04
TRF= FEEDBACK RESISTOR TEMP K	0.1600E+03	TRF= FEEDBACK RESISTOR TEMP K	0.1600E+03	TRF= FEEDBACK RESISTOR TEMP K	0.1600E+03
FC = CHOPPING FREQUENCY HZ	0.4400E+03	FC = CHOPPING FREQUENCY HZ	0.4400E+03	FC = CHOPPING FREQUENCY HZ	0.4400E+03
RO = DIODE DARK RESISTANCE BIAS=0 OHM	0.2733E+09	RO = DIODE DARK RESISTANCE BIAS=0 OHM	0.2733E+09	RO = DIODE DARK RESISTANCE BIAS=0 OHM	0.2733E+09
RA = R(0)=A PRODUCT OHM*CM**2	0.1049E+07	RA = R(0)=A PRODUCT OHM*CM**2	0.1049E+07	RA = R(0)=A PRODUCT OHM*CM**2	0.1049E+07
VJ = JUNCTION POTENTIAL V	0.1978E+00	VJ = JUNCTION POTENTIAL V	0.1978E+00	VJ = JUNCTION POTENTIAL V	0.1978E+00
CJ = JUNCTION CAPACITANCE F	0.6739E-10	CJ = JUNCTION CAPACITANCE F	0.6739E-10	CJ = JUNCTION CAPACITANCE F	0.6739E-10
WJ = JUNCTION WIDTH CM	0.8673E-04	WJ = JUNCTION WIDTH CM	0.8673E-04	WJ = JUNCTION WIDTH CM	0.8673E-04
VC = CONTACT POTENTIAL V	0.1978E+00	VC = CONTACT POTENTIAL V	0.1978E+00	VC = CONTACT POTENTIAL V	0.1978E+00
ZD = DETECTOR IMPEDANCE OHM	0.4841E+07	ZD = DETECTOR IMPEDANCE OHM	0.4841E+07	ZD = DETECTOR IMPEDANCE OHM	0.4841E+07
ZF = FEEDBACK RESISTOR IMPEDANCE OHM	0.5466E+09	ZF = FEEDBACK RESISTOR IMPEDANCE OHM	0.5466E+09	ZF = FEEDBACK RESISTOR IMPEDANCE OHM	0.5466E+09
PD = DET. PHASE ANGLE RAD	0.6816E-15	PD = DET. PHASE ANGLE RAD	0.6816E-15	PD = DET. PHASE ANGLE RAD	0.6816E-15
PF = FDBK RESISTOR PHASE ANGLE RAD	0.8294E-18	PF = FDBK RESISTOR PHASE ANGLE RAD	0.8294E-18	PF = FDBK RESISTOR PHASE ANGLE RAD	0.8294E-18
AZ = TRANSIMPEDANCE OHM	0.6162E+09	AZ = TRANSIMPEDANCE OHM	0.6162E+09	AZ = TRANSIMPEDANCE OHM	0.6162E+09
IS = SIGNAL PHOTOCURRENT A	0.3319E-11	IS = SIGNAL PHOTOCURRENT A	0.3590E-10	IS = SIGNAL PHOTOCURRENT A	0.2415E-09
IT = TOTAL BKGD PHOTOCURRENT A	0.6196E-11	IT = TOTAL BKGD PHOTOCURRENT A	0.3885E-10	IT = TOTAL BKGD PHOTOCURRENT A	0.2444E-09
VRF= FDBK RESISTOR NOISE V/HZ**.5	0.1832E-05	VRF= FDBK RESISTOR NOISE V/HZ**.5	0.1832E-05	VRF= FDBK RESISTOR NOISE V/HZ**.5	0.1832E-05
VBG= BACKGROUND NOISE V/HZ**.5	0.8682E-06	VBG= BACKGROUND NOISE V/HZ**.5	0.2174E-05	VBG= BACKGROUND NOISE V/HZ**.5	0.5453E-05
VJN= JOHNSON NOISE V/HZ**.5	0.1696E-05	VJN= JOHNSON NOISE V/HZ**.5	0.1696E-05	VJN= JOHNSON NOISE V/HZ**.5	0.1696E-05
VGR= GEN-RECOMB NOISE V/HZ**.5	0.1696E-05	VGR= GEN-RECOMB NOISE V/HZ**.5	0.1696E-05	VGR= GEN-RECOMB NOISE V/HZ**.5	0.1696E-05
VPA= PREAMP NOISE V/HZ**.5	0.2838E-06	VPA= PREAMP NOISE V/HZ**.5	0.2838E-06	VPA= PREAMP NOISE V/HZ**.5	0.2838E-06
VT = TOTAL NOISE V/HZ**.5	0.3153E-05	VT = TOTAL NOISE V/HZ**.5	0.3730E-05	VT = TOTAL NOISE V/HZ**.5	0.6239E-05
R = RESPONSIVITY V/W	0.1957E+10	R = RESPONSIVITY V/W	0.1957E+10	R = RESPONSIVITY V/W	0.1957E+10
NEP= NOISE EQUIVALENT POWER W/HZ**.5	0.1611E-14	NEP= NOISE EQUIVALENT POWER W/HZ**.5	0.1906E-14	NEP= NOISE EQUIVALENT POWER W/HZ**.5	0.3188E-14
DSTAR = CM*HZ**.5/W	0.3844E+14	DSTAR = CM*HZ**.5/W	0.3249E+14	DSTAR = CM*HZ**.5/W	0.1943E+14

Table F-4 (CH 25)

PV INSB DETECTOR PERFORMANCE CHANNEL 25 75/160/MIN

CH = CHANNEL NUMBER	0.2500E+02
HD = DETECTOR HEIGHT CM	0.5300E-01
WD = DETECTOR WIDTH CM	0.7980E-01
T = DET. TEMP. K	0.7500E+02
CS = DET. STRAY CAPACITANCE F	0.6000E-11
RS = DET. SHUNT RESISTANCE OHM	0.1050E+07
VB = BIAS VOLTAGE V	0.0000E+00
EG = BAND GAP ENERGY EV	0.2267E+00
NI = INTRINSIC CONC. CM**-3	0.1602E+10
NA = ACCEPTOR CONC. CM**-3	0.1000E+18
ND = DONOR CARRIER CONC. CM**-3	0.5000E+15
MU = ELECTRON MOBILITY CM**2/V/S	0.8000E+05
MUH= HOLE MOBILITY CM**2/V/S	0.5000E+04
ETA= QUANTUM EFFICIENCY	0.8000E+00
TAU= CARRIER LIFETIME S	0.5000E-06
NUP= PEAK WAVENUMBER 1/CM	0.2032E+04
QBG= BKGD PHOTON FLUX DENSITY P/CM**2/S	0.1430E+11
QS = SGNL PHOTON FLUX DENSITY P/CM**2/S	0.7900E+10
KAPPA = DIELECTRIC CONSTANT	0.1720E+02
RF = FEEDBACK RESISTANCE OHM	0.1000E+10
CF = FEEDBACK CAPACITACE F	0.3000E-12
VP = PREAMP NOISE (INPUT) V/HZ**.5	0.2800E-08
AO = OPEN LOOP GAIN OF PREAMP	0.1000E+04
TRF= FEEDBACK RESISTOR TEMP K	0.1600E+03
FC = CHOPPING FREQUENCY HZ	0.4400E+03
RO = DIODE DARK RESISTANCE BIAS=0 OHM	0.2480E+09
RA = R(0)*A PRODUCT OHM*CM**2	0.1049E+07
VJ = JUNCTION POTENTIAL V	0.1978E+00
CJ = JUNCTION CAPACITANCE F	0.7428E-10
WJ = JUNCTION WIDTH CM	0.8673E-04
VC = CONTACT POTENTIAL V	0.1978E+00
ZD = DETECTOR IMPEDANCE OHM	0.4425E+07
ZF = FEEDBACK RESISTOR IMPEDANCE OHM	0.5466E+09
PD = DET. PHASE ANGLE RAD	0.8281E-15
PF = FDBK RESISTOR PHASE ANGLE RAD	0.8294E-18
AZ = TRANSIMPEDANCE OHM	0.6237E+09
IS = SIGNAL PHOTOCURRENT A	0.4282E-11
IT = TOTAL BKGD PHOTOCURRENT A	0.7751E-11
VRF= FDBK RESISTOR NOISE V/HZ**.5	0.1854E-05
VBG= BACKGROUND NOISE V/HZ**.5	0.9828E-06
VJN= JOHNSON NOISE V/HZ**.5	0.1802E-05
VGR= GEN-RECOMB NOISE V/HZ**.5	0.1802E-05
VPA= PREAMP NOISE V/HZ**.5	0.3076E-06
VT = TOTAL NOISE V/HZ**.5	0.3316E-05
R = RESPONSIVITY V/W	0.1981E+10
NEP= NOISE EQUIVALENT POWER W/HZ**.5	0.1674E-14
DSTAR = CM*HZ**.5/W	0.3085E+14

PV INSB DETECTOR PERFORMANCE CHANNEL 25 75/160/STD

CH = CHANNEL NUMBER	0.2500E+02
HD = DETECTOR HEIGHT CM	0.5300E-01
WD = DETECTOR WIDTH CM	0.7980E-01
T = DET. TEMP. K	0.7500E+02
CS = DET. STRAY CAPACITANCE F	0.6000E-11
RS = DET. SHUNT RESISTANCE OHM	0.1050E+07
VB = BIAS VOLTAGE V	0.0000E+00
EG = BAND GAP ENERGY EV	0.2267E+00
NI = INTRINSIC CONC. CM**-3	0.1602E+10
NA = ACCEPTOR CONC. CM**-3	0.1000E+18
ND = DONOR CARRIER CONC. CM**-3	0.5000E+15
MU = ELECTRON MOBILITY CM**2/V/S	0.8000E+05
MUH= HOLE MOBILITY CM**2/V/S	0.5000E+04
ETA= QUANTUM EFFICIENCY	0.8000E+00
TAU= CARRIER LIFETIME S	0.5000E-06
NUP= PEAK WAVENUMBER 1/CM	0.2032E+04
QBG= BKGD PHOTON FLUX DENSITY P/CM**2/S	0.1170E+12
QS = SGNL PHOTON FLUX DENSITY P/CM**2/S	0.1100E+12
KAPPA = DIELECTRIC CONSTANT	0.1720E+02
RF = FEEDBACK RESISTANCE OHM	0.1000E+10
CF = FEEDBACK CAPACITACE F	0.3000E-12
VP = PREAMP NOISE (INPUT) V/HZ**.5	0.2800E-08
AO = OPEN LOOP GAIN OF PREAMP	0.1000E+04
TRF= FEEDBACK RESISTOR TEMP K	0.1600E+03
FC = CHOPPING FREQUENCY HZ	0.4400E+03
RO = DIODE DARK RESISTANCE BIAS=0 OHM	0.2480E+09
RA = R(0)*A PRODUCT OHM*CM**2	0.1049E+07
VJ = JUNCTION POTENTIAL V	0.1978E+00
CJ = JUNCTION CAPACITANCE F	0.7428E-10
WJ = JUNCTION WIDTH CM	0.8673E-04
VC = CONTACT POTENTIAL V	0.1978E+00
ZD = DETECTOR IMPEDANCE OHM	0.4425E+07
ZF = FEEDBACK RESISTOR IMPEDANCE OHM	0.5466E+09
PD = DET. PHASE ANGLE RAD	0.8281E-15
PF = FDBK RESISTOR PHASE ANGLE RAD	0.8294E-18
AZ = TRANSIMPEDANCE OHM	0.6237E+09
IS = SIGNAL PHOTOCURRENT A	0.5962E-10
IT = TOTAL BKGD PHOTOCURRENT A	0.6342E-10
VRF= FDBK RESISTOR NOISE V/HZ**.5	0.1854E-05
VBG= BACKGROUND NOISE V/HZ**.5	0.2811E-05
VJN= JOHNSON NOISE V/HZ**.5	0.1802E-05
VGR= GEN-RECOMB NOISE V/HZ**.5	0.1802E-05
VPA= PREAMP NOISE V/HZ**.5	0.3076E-06
VT = TOTAL NOISE V/HZ**.5	0.4235E-05
R = RESPONSIVITY V/W	0.1981E+10
NEP= NOISE EQUIVALENT POWER W/HZ**.5	0.2139E-14
DSTAR = CM*HZ**.5/W	0.3042E+14

PV INSB DETECTOR PERFORMANCE CHANNEL 25 75/160/MAX

CH = CHANNEL NUMBER	0.2500E+02
HD = DETECTOR HEIGHT CM	0.5300E-01
WD = DETECTOR WIDTH CM	0.7980E-01
T = DET. TEMP. K	0.7500E+02
CS = DET. STRAY CAPACITANCE F	0.6000E-11
RS = DET. SHUNT RESISTANCE OHM	0.1050E+07
VB = BIAS VOLTAGE V	0.0000E+00
EG = BAND GAP ENERGY EV	0.2267E+00
NI = INTRINSIC CONC. CM**-3	0.1602E+10
NA = ACCEPTOR CONC. CM**-3	0.1000E+18
ND = DONOR CARRIER CONC. CM**-3	0.5000E+15
MU = ELECTRON MOBILITY CM**2/V/S	0.8000E+05
MUH= HOLE MOBILITY CM**2/V/S	0.5000E+04
ETA= QUANTUM EFFICIENCY	0.8000E+00
TAU= CARRIER LIFETIME S	0.5000E-06
NUP= PEAK WAVENUMBER 1/CM	0.2032E+04
QBG= BKGD PHOTON FLUX DENSITY P/CM**2/S	0.7120E+12
QS = SGNL PHOTON FLUX DENSITY P/CM**2/S	0.7060E+12
KAPPA = DIELECTRIC CONSTANT	0.1720E+02
RF = FEEDBACK RESISTANCE OHM	0.1000E+10
CF = FEEDBACK CAPACITACE F	0.3000E-12
VP = PREAMP NOISE (INPUT) V/HZ**.5	0.2800E-08
AO = OPEN LOOP GAIN OF PREAMP	0.1000E+04
TRF= FEEDBACK RESISTOR TEMP K	0.1600E+03
FC = CHOPPING FREQUENCY HZ	0.4400E+03
RO = DIODE DARK RESISTANCE BIAS=0 OHM	0.2480E+09
RA = R(0)*A PRODUCT OHM*CM**2	0.1049E+07
VJ = JUNCTION POTENTIAL V	0.1978E+00
CJ = JUNCTION CAPACITANCE F	0.7428E-10
WJ = JUNCTION WIDTH CM	0.8673E-04
VC = CONTACT POTENTIAL V	0.1978E+00
ZD = DETECTOR IMPEDANCE OHM	0.4425E+07
ZF = FEEDBACK RESISTOR IMPEDANCE OHM	0.5466E+09
PD = DET. PHASE ANGLE RAD	0.8281E-15
PF = FDBK RESISTOR PHASE ANGLE RAD	0.8294E-18
AZ = TRANSIMPEDANCE OHM	0.6237E+09
IS = SIGNAL PHOTOCURRENT A	0.3827E-09
IT = TOTAL BKGD PHOTOCURRENT A	0.3859E-09
VRF= FDBK RESISTOR NOISE V/HZ**.5	0.1854E-05
VBG= BACKGROUND NOISE V/HZ**.5	0.6935E-05
VJN= JOHNSON NOISE V/HZ**.5	0.1802E-05
VGR= GEN-RECOMB NOISE V/HZ**.5	0.1802E-05
VPA= PREAMP NOISE V/HZ**.5	0.3076E-06
VT = TOTAL NOISE V/HZ**.5	0.7624E-05
R = RESPONSIVITY V/W	0.1981E+10
NEP= NOISE EQUIVALENT POWER W/HZ**.5	0.3849E-14
DSTAR = CM*HZ**.5/W	0.1689E+14

Table F-4 (CH 26)

PV INSB DETECTOR PERFORMANCE CHANNEL 26 75/160/MIN		PV INSB DETECTOR PERFORMANCE CHANNEL 26 75/160/STD		PV INSB DETECTOR PERFORMANCE CHANNEL 26 75/160/MAX	
CH = CHANNEL NUMBER	0.2600E+02	CH = CHANNEL NUMBER	0.2600E+02	CH = CHANNEL NUMBER	0.2600E+02
HD = DETECTOR HEIGHT CM	0.5300E-01	HD = DETECTOR HEIGHT CM	0.5300E-01	HD = DETECTOR HEIGHT CM	0.5300E-01
WD = DETECTOR WIDTH CM	0.9570E-01	WD = DETECTOR WIDTH CM	0.9570E-01	WD = DETECTOR WIDTH CM	0.9570E-01
T = DET. TEMP. K	0.7500E+02	T = DET. TEMP. K	0.7500E+02	T = DET. TEMP. K	0.7500E+02
CS = DET. STRAY CAPACITANCE F	0.6000E-11	CS = DET. STRAY CAPACITANCE F	0.6000E-11	CS = DET. STRAY CAPACITANCE F	0.6000E-11
RS = DET. SHUNT RESISTANCE OHM	0.1050E+07	RS = DET. SHUNT RESISTANCE OHM	0.1050E+07	RS = DET. SHUNT RESISTANCE OHM	0.1050E+07
VB = BIAS VOLTAGE V	0.0000E+00	VB = BIAS VOLTAGE V	0.0000E+00	VB = BIAS VOLTAGE V	0.0000E+00
EG = BAND GAP ENERGY EV	0.2267E+00	EG = BAND GAP ENERGY EV	0.2267E+00	EG = BAND GAP ENERGY EV	0.2267E+00
NI = INTRINSIC CONC. CM**-3	0.1602E+10	NI = INTRINSIC CONC. CM**-3	0.1602E+10	NI = INTRINSIC CONC. CM**-3	0.1602E+10
NA = ACCEPTOR CONC. CM**-3	0.1000E+18	NA = ACCEPTOR CONC. CM**-3	0.1000E+18	NA = ACCEPTOR CONC. CM**-3	0.1000E+18
ND = DONOR CARRIER CONC. CM**-3	0.5000E+15	ND = DONOR CARRIER CONC. CM**-3	0.5600E+15	ND = DONOR CARRIER CONC. CM**-3	0.5000E+15
MU = ELECTRON MOBILITY CM**2/V/S	0.8000E+05	MU = ELECTRON MOBILITY CM**2/V/S	0.8000E+05	MU = ELECTRON MOBILITY CM**2/V/S	0.8000E+05
MUH= HOLE MOBILITY CM**2/V/S	0.5000E+04	MUH= HOLE MOBILITY CM**2/V/S	0.5000E+04	MUH= HOLE MOBILITY CM**2/V/S	0.5000E+04
ETA= QUANTUM EFFICIENCY	0.8000E+00	ETA= QUANTUM EFFICIENCY	0.8000E+00	ETA= QUANTUM EFFICIENCY	0.8000E+00
TAU= CARRIER LIFETIME S	0.5000E-06	TAU= CARRIER LIFETIME S	0.5000E-06	TAU= CARRIER LIFETIME S	0.5000E-06
NUP= PEAK WAVENUMBER 1/CM	0.2032E+04	NUP= PEAK WAVENUMBER 1/CM	0.2032E+04	NUP= PEAK WAVENUMBER 1/CM	0.2032E+04
QBG= BKGD PHOTON FLUX DENSITY P/CM**2/S	0.9800E+10	QBG= BKGD PHOTON FLUX DENSITY P/CM**2/S	0.1010E+12	QBG= BKGD PHOTON FLUX DENSITY P/CM**2/S	0.7960E+12
QS = SGNL PHOTON FLUX DENSITY P/CM**2/S	0.5360E+10	QS = SGNL PHOTON FLUX DENSITY P/CM**2/S	0.9710E+11	QS = SGNL PHOTON FLUX DENSITY P/CM**2/S	0.7960E+12
KAPPA = DIELECTRIC CONSTANT	0.1720E+02	KAPPA = DIELECTRIC CONSTANT	0.1720E+02	KAPPA = DIELECTRIC CONSTANT	0.1720E+02
RF = FEEDBACK RESISTANCE OHM	0.1000E+10	RF = FEEDBACK RESISTANCE OHM	0.1000E+10	RF = FEEDBACK RESISTANCE OHM	0.1000E+10
CF = FEEDBACK CAPACITACE F	0.3000E-12	CF = FEEDBACK CAPACITACE F	0.3000E-12	CF = FEEDBACK CAPACITACE F	0.3000E-12
VP = PREAMP NOISE (INPUT) V/HZ**.5	0.2800E-08	VP = PREAMP NOISE (INPUT) V/HZ**.5	0.2800E-08	VP = PREAMP NOISE (INPUT) V/HZ**.5	0.2800E-08
AO = OPEN LOOP GAIN OF PREAMP	0.1000E+04	AO = OPEN LOOP GAIN OF PREAMP	0.1000E+04	AO = OPEN LOOP GAIN OF PREAMP	0.1000E+04
TRF= FEEDBACK RESISTOR TEMP K	0.1600E+03	TRF= FEEDBACK RESISTOR TEMP K	0.1600E+03	TRF= FEEDBACK RESISTOR TEMP K	0.1600E+03
FC = CHOPPING FREQUENCY HZ	0.4400E+03	FC = CHOPPING FREQUENCY HZ	0.4400E+03	FC = CHOPPING FREQUENCY HZ	0.4400E+03
RO = DIODE DARK RESISTANCE BIAS=0 OHM	0.2068E+09	RO = DIODE DARK RESISTANCE BIAS=0 OHM	0.2068E+09	RO = DIODE DARK RESISTANCE BIAS=0 OHM	0.2068E+09
RA = R(0)*A PRODUCT OHM*CM**2	0.1049E+07	RA = R(0)*A PRODUCT OHM*CM**2	0.1049E+07	RA = R(0)*A PRODUCT OHM*CM**2	0.1049E+07
VJ = JUNCTION POTENTIAL V	0.1978E+00	VJ = JUNCTION POTENTIAL V	0.1978E+00	VJ = JUNCTION POTENTIAL V	0.1978E+00
CJ = JUNCTION CAPACITANCE F	0.8908E-10	CJ = JUNCTION CAPACITANCE F	0.8908E-10	CJ = JUNCTION CAPACITANCE F	0.8908E-10
WJ = JUNCTION WIDTH CM	0.8673E-04	WJ = JUNCTION WIDTH CM	0.8673E-04	WJ = JUNCTION WIDTH CM	0.8673E-04
VC = CONTACT POTENTIAL V	0.1978E+00	VC = CONTACT POTENTIAL V	0.1978E+00	VC = CONTACT POTENTIAL V	0.1978E+00
ZD = DETECTOR IMPEDANCE OHM	0.3736E+07	ZD = DETECTOR IMPEDANCE OHM	0.3736E+07	ZD = DETECTOR IMPEDANCE OHM	0.3736E+07
ZF = FEEDBACK RESISTOR IMPEDANCE OHM	0.5466E+09	ZF = FEEDBACK RESISTOR IMPEDANCE OHM	0.5466E+09	ZF = FEEDBACK RESISTOR IMPEDANCE OHM	0.5466E+09
PD = DET. PHASE ANGLE RAD	0.1191E-14	PD = DET. PHASE ANGLE RAD	0.1191E-14	PD = DET. PHASE ANGLE RAD	0.1191E-14
PF = FDBK RESISTOR PHASE ANGLE RAD	0.8294E-18	PF = FDBK RESISTOR PHASE ANGLE RAD	0.8294E-18	PF = FDBK RESISTOR PHASE ANGLE RAD	0.8294E-18
AZ = TRANSIMPEDANCE OHM	0.6403E+09	AZ = TRANSIMPEDANCE OHM	0.6403E+09	AZ = TRANSIMPEDANCE OHM	0.6403E+09
IS = SIGNAL PHOTOCURRENT A	0.3484E-11	IS = SIGNAL PHOTOCURRENT A	0.6312E-10	IS = SIGNAL PHOTOCURRENT A	0.5174E-09
IT = TOTAL BKGD PHOTOCURRENT A	0.6378E-11	IT = TOTAL BKGD PHOTOCURRENT A	0.6565E-10	IT = TOTAL BKGD PHOTOCURRENT A	0.5174E-09
VRF= FDBK RESISTOR NOISE V/HZ**.5	0.1903E-35	VRF= FDBK RESISTOR NOISE V/HZ**.5	0.1903E-05	VRF= FDBK RESISTOR NOISE V/HZ**.5	0.1903E-05
VBG= BACKGROUND NOISE V/HZ**)5	0.9148E-06	VBG= BACKGROUND NOISE V/HZ**)5	0.2937E-05	VBG= BACKGROUND NOISE V/HZ**)5	0.8245E-05
VJN= JOHNSON NOISE V/HZ**.5	0.2026E-05	VJN= JOHNSON NOISE V/HZ**.5	0.2026E-05	VJN= JOHNSON NOISE V/HZ**.5	0.2026E-05
VGR= GEN-RECOMB NOISE V/HZ**.5	0.2026E-05	VGR= GEN-RECOMB NOISE V/HZ**.5	0.2026E-05	VGR= GEN-RECOMB NOISE V/HZ**.5	0.2026E-05
VPA= PREAMP NOISE V/HZ**.5	0.3571E-06	VPA= PREAMP NOISE V/HZ**.5	0.3571E-06	VPA= PREAMP NOISE V/HZ**.5	0.3571E-06
VT = TOTAL NOISE V/HZ**.5	0.3578E-05	VT = TOTAL NOISE V/HZ**.5	0.4537E-05	VT = TOTAL NOISE V/HZ**.5	0.8941E-05
R = RESPONSIVITY V/W	0.2033E+10	R = RESPONSIVITY V/W	0.2033E+10	R = RESPONSIVITY V/W	0.2033E+10
NEP= NOISE EQUIVALENT POWER W/HZ**.5	0.1759E-14	NEP= NOISE EQUIVALENT POWER W/HZ**.5	0.2231E-14	NEP= NOISE EQUIVALENT POWER W/HZ**.5	0.4397E-14
DSTAR = CM*HZ**.5/W	0.4048E+14	DSTAR = CM*HZ**.5/W	0.3192E+14	DSTAR = CM*HZ**.5/W	0.1620E+14

Table F-4 (CH 27)

PV INSB DETECTOR PERFORMANCE CHANNEL 27 75/160/MIN		PV INSB DETECTOR PERFORMANCE CHANNEL 27 75/160/STD		PV INSB DETECTOR PERFORMANCE CHANNEL 27 75/160/MAX	
CH = CHANNEL NUMBER	0.2700E+02	CH = CHANNEL NUMBER	0.2700E+02	CH = CHANNEL NUMBER	0.2700E+02
HD = DETECTOR HEIGHT CM	0.5300E-01	HD = DETECTOR HEIGHT CM	0.5300E-01	HD = DETECTOR HEIGHT CM	0.5300E-01
WD = DETECTOR WIDTH CM	0.7760E-01	WD = DETECTOR WIDTH CM	0.7760E-01	WD = DETECTOR WIDTH CM	0.7760E-01
T = DET. TEMP. K	0.7500E+02	T = DET. TEMP. K	0.7500E+02	T = DET. TEMP. K	0.7500E+02
CS = DET. STRAY CAPACITANCE F	0.6000E-11	CS = DET. STRAY CAPACITANCE F	0.6000E-11	CS = DET. STRAY CAPACITANCE F	0.6000E-11
RS = DET. SHUNT RESISTANCE OHM	0.1050E+07	RS = DET. SHUNT RESISTANCE OHM	0.1050E+07	RS = DET. SHUNT RESISTANCE OHM	0. 950E+07
VB = BIAS VOLTAGE V	0.0000E+00	VB = BIAS VOLTAGE V	0.0000E+00	VB = BIAS VOLTAGE V	0.0000E+00
EG = BAND GAP ENERGY EV	0.2267E+00	EG = BAND GAP ENERGY EV	0.2267E+00	EG = BAND GAP ENERGY EV	0.2267E+00
NI = INTRINSIC CONC. CM**-3	0.1602E+10	NI = INTRINSIC CONC. CM**-3	0.1602E+10	NI = INTRINSIC CONC. CM**-3	0.1602E+10
NA = ACCEPTOR CONC. CM**-3	0.1000E+18	NA = ACCEPTOR CONC. CM**-3	0.1000E+18	NA = ACCEPTOR CONC. CM**-3	0.1000E+18
ND = DONOR CARRIER CONC. CM**-3	0.5000E+15	ND = DONOR CARRIER CONC. CM**-3	0.5000E+15	ND = DONOR CARRIER CONC. CM**-3	0.5000E+15
MU = ELECTRON MOBILITY CM**2/V/S	0.8000E+05	MU = ELECTRON MOBILITY CM**2/V/S	0.6000E+05	MU = ELECTRON MOBILITY CM**2/V/S	0.8000E+05
MUH= HOLE MOBILITY CM**2/V/S	0.5000E+04	MUH= HOLE MOBILITY CM**2/V/S	0.5000E+04	MUH= HOLE MOBILITY CM**2/V/S	0.5000E+04
ETA= QUANTUM EFFICIENCY	0.8000E+00	ETA= QUANTUM EFFICIENCY	0.8000E+00	ETA= QUANTUM EFFICIENCY	0.8000E+00
TAU= CARRIER LIFETIME S	0.5000E-06	TAU= CARRIER LIFETIME S	0.5000E-06	TAU= CARRIER LIFETIME S	0.5000E-06
NUP= PEAK WAVENUMBER 1/CM	0.2032E+04	NUP= PEAK WAVENUMBER 1/CM	0.2032E+04	NUP= PEAK WAVENUMBER 1/CM	0.2032E+04
QBG= BKGD PHOTON FLUX DENSITY P/CM**2/S	0.4948E+10	QBG= BKGD PHOTON FLUX DENSITY P/CM**2/S	0.5920E+11	QBG= BKGD PHOTON FLUX DENSITY P/CM**2/S	0.7000E+12
QS = SGNL PHOTON FLUX DENSITY P/CM**2/S	0.2590E+10	QS = SGNL PHOTON FLUX DENSITY P/CM**2/S	0.5690E+11	QS = SGNL PHOTON FLUX DENSITY P/CM**2/S	0.6940E+12
KAPPA = DIELECTRIC CONSTANT	0.1720E+02	KAPPA = DIELECTRIC CONSTANT	0.1720E+02	KAPPA = DIELECTRIC CONSTANT	0.1720E+02
RF = FEEDBACK RESISTANCE OHM	0.1000E+10	RF = FEEDBACK RESISTANCE OHM	0.1000E+10	RF = FEEDBACK RESISTANCE OHM	0.1000E+10
CF = FEEDBACK CAPACITACE F	0.3000E-12	CF = FEEDBACK CAPACITACE F	0.3000E-12	CF = FEEDBACK CAPACITACE F	0.3000E-12
VP = PREAMP NOISE (INPUT) V/HZ**.5	0.2800E-08	VP = PREAMP NOISE (INPUT) V/HZ**.5	0.2800E-08	VP = PREAMP NOISE (INPUT) V/HZ**.5	0.2900E-08
AO = OPEN LOOP GAIN OF PREAMP	0.1000E+04	AO = OPEN LOOP GAIN OF PREAMP	0.1000E+04	AO = OPEN LOOP GAIN OF PREAMP	0.1000E+04
TRF= FEEDBACK RESISTOR TEMP K	0.1600E+03	TRF= FEEDBACK RESISTOR TEMP K	0.1600E+03	TRF= FEEDBACK RESISTOR TEMP K	0.1600E+03
FC = CHOPPING FREQUENCY HZ	0.4400E+03	FC = CHOPPING FREQUENCY HZ	0.4400E+03	FC = CHOPPING FREQUENCY HZ	0.4400E+03
RO = DIODE DARK RESISTANCE BIAS=0 OHM	0.2550E+09	RO = DIODE DARK RESISTANCE BIAS=0 OHM	0.2550E+09	RO = DIODE DARK RESISTANCE BIAS=0 OHM	0.255JE+09
RA = R(0)*A PRODUCT OHM*CM**2	0.1049E+07	RA = R(0)*A PRODUCT OHM*CM**2	0.1049E+07	RA = R(0)*A PRODUCT OHM*CM**2	0.1849E+07
VJ = JUNCTION POTENTIAL V	0.1978E+00	VJ = JUNCTION POTENTIAL V	0.1978E+00	VJ = JUNCTION POTENTIAL V	0.1978E+00
CJ = JUNCTION CAPACITANCE F	0.7223E-10	CJ = JUNCTION CAPACITANCE F	0.7223E-10	CJ = JUNCTION CAPACITANCE F	0.7223E-10
WJ = JUNCTION WIDTH CM	0.8673E-04	WJ = JUNCTION WIDTH CM	0.8673E-04	WJ = JUNCTION WIDTH CM	0.8673E-04
VC = CONTACT POTENTIAL V	0.1978E+00	VC = CONTACT POTENTIAL V	0.1978E+00	VC = CONTACT POTENTIAL V	0.1978E+00
ZD = DETECTOR IMPEDANCE OHM	0.4541E+07	ZD = DETECTOR IMPEDANCE OHM	0.4541E+07	ZD = DETECTOR IMPEDANCE OHM	0.4541E+07
ZF = FEEDBACK RESISTOR IMPEDANCE OHM	0.5466E+09	ZF = FEEDBACK RESISTOR IMPEDANCE OHM	0.5466E+09	ZF = FEEDBACK RESISTOR IMPEDANCE OHM	0.5466E+09
PD = DET. PHASE ANGLE RAD	0.7830E-15	PD = DET. PHASE ANGLE RAD	0.7830E-15	PD = DET. PHASE ANGLE RAD	0.7830E-15
PF = FDBK RESISTOR PHASE ANGLE RAD	0.8294E-18	PF = FDBK RESISTOR PHASE ANGLE RAD	0.8294E-18	PF = FDBK RESISTOR PHASE ANGLE RAD	0.8294E-18
AZ = TRANSIMPEDANCE OHM	0.6214E+09	AZ = TRANSIMPEDANCE OHM	0.6214E+09	AZ = TRANSIMPEDANCE OHM	0.6214E+09
IS = SIGNAL PHOTOCURRENT A	0.1365E-11	IS = SIGNAL PHOTOCURRENT A	0.2999E-10	IS = SIGNAL PHOTOCURRENT A	0.3658E-09
IT = TOTAL BKGD PHOTOCURRENT A	0.2684E-11	IT = TOTAL BKGD PHOTOCURRENT A	0.3120E-10	IT = TOTAL BKGD PHOTOCURRENT A	0.3690E-09
VRF= FDBK RESISTOR NOISE V/HZ**.5	0.1847E-05	VRF= FDBK RESISTOR NOISE V/HZ**.5	0.1847E-05	VRF= FDBK RESISTOR NOISE V/HZ**.5	0.1847E-05
VBG= BACKGROUND NOISE V/HZ**)5	0.5676E-06	VBG= BACKGROUND NOISE V/HZ**)5	0.1965E-05	VBG= BACKGROUND NOISE V/HZ**)5	0.6757E-05
VJN= JOHNSON NOISE V/HZ**.5	0.1771E-05	VJN= JOHNSON NOISE V/HZ**.5	0.1771E-05	VJN= JOHNSON NOISE V/HZ**.5	0.1771E-05
VGR= GEN-RECOMB NOISE V/HZ**.5	0.1771E-05	VGR= GEN-RECOMB NOISE V/HZ**.5	0.1771E-05	VGR= GEN-RECOMB NOISE V/HZ**.5	0.1771E-05
VPA= PREAMP NOISE V/HZ**.5	0.3006E-06	VPA= PREAMP NOISE V/HZ**.5	0.3006E-06	VPA= PREAMP NOISE V/HZ**.5	0.3006E-06
VT = TOTAL NOISE V/HZ**.5	0.3178E-05	VT = TOTAL NOISE V/HZ**.5	0.3693E-05	VT = TOTAL NOISE V/HZ**.5	0.7445E-05
R = RESPONSIVITY V/W	0.1973E+10	R = RESPONSIVITY V/W	0.1973E+10	R = RESPONSIVITY V/W	0.1973E+10
NEP= NOISE EQUIVALENT POWER W/HZ**.5	0.1610E-14	NEP= NOISE EQUIVALENT POWER W/HZ**.5	0.1871E-14	NEP= NOISE EQUIVALENT POWER W/HZ**.5	0.3773E-14
DSTAR = CM*HZ**.5/W	0.3983E+14	DSTAR = CM*HZ**.5/W	0.3427E+14	DSTAR = CM*HZ**.5/W	0.1700E+14

Table F-4 (CH 28)

PV INSB DETECTOR PERFORMANCE CHANNEL 28 75/168/MIN		PV INSB DETECTOR PERFORMANCE CHANNEL 28 75/168/STD		PV INSB DETECTOR PERFORMANCE CHANNEL 28 75/168/MAX	
CH = CHANNEL NUMBER	0.2800E+02	CH = CHANNEL NUMBER	0.2800E+02	CH = CHANNEL NUMBER	0.2800E+02
HD = DETECTOR HEIGHT CM	0.5300E-01	HD = DETECTOR HEIGHT CM	0.5300E-01	HD = DETECTOR HEIGHT CM	0.5300E-01
WD = DETECTOR WIDTH CM	0.9120E-01	WD = DETECTOR WIDTH CM	0.9120E-01	WD = DETECTOR WIDTH CM	0.9120E-01
T = DET. TEMP. K	0.7500E+02	T = DET. TEMP. K	0.7500E+02	T = DET. TEMP. K	0.7500E+02
CS = DET. STRAY CAPACITANCE F	0.6000E-11	CS = DET. STRAY CAPACITANCE F	0.6000E-11	CS = DET. STRAY CAPACITANCE F	0.6000E-11
RS = DET. SHUNT RESISTANCE OHM	0.1050E+07	RS = DET. SHUNT RESISTANCE OHM	0.1050E+07	RS = DET. SHUNT RESISTANCE OHM	0.1050E+07
VB = BIAS VOLTAGE V	0.0000E+00	VB = BIAS VOLTAGE V	0.0000E+00	VB = BIAS VOLTAGE V	0.0000E+00
EG = BAND GAP ENERGY EV	0.2267E+00	EG = BAND GAP ENERGY EV	0.2267E+00	EG = BAND GAP ENERGY EV	0.2267E+00
NI = INTRINSIC CONC. CM**-3	0.1602E+10	NI = INTRINSIC CONC. CM**-3	0.1602E+10	NI = INTRINSIC CONC. CM**-3	0.1602E+10
NA = ACCEPTOR CONC. CM**-3	0.1000E+18	NA = ACCEPTOR CONC. CM**-3	0.1000E+18	NA = ACCEPTOR CONC. CM**-3	0.1000E+18
ND = DONOR CARRIER CONC. CM**-3	0.5000E+15	ND = DONOR CARRIER CONC. CM**-3	0.5000E+15	ND = DONOR CARRIER CONC. CM**-3	0.5000E+15
MU = ELECTRON MOBILITY CM**2/V/S	0.8000E+05	MU = ELECTRON MOBILITY CM**2/V/S	0.8000E+05	MU = ELECTRON MOBILITY CM**2/V/S	0.8000E+05
MUH= HOLE MOBILITY CM**2/V/S	0.5000E+04	MUH= HOLE MOBILITY CM**2/V/S	0.5000E+04	MUH= HOLE MOBILITY CM**2/V/S	0.5000E+04
ETA= QUANTUM EFFICIENCY	0.8000E+00	ETA= QUANTUM EFFICIENCY	0.8000E+00	ETA= QUANTUM EFFICIENCY	0.8000E+00
TAU= CARRIER LIFETIME S	0.5000E-06	TAU= CARRIER LIFETIME S	0.5000E-06	TAU= CARRIER LIFETIME S	0.5000E-06
NUP= PEAK WAVENUMBER 1/CM	0.2032E+04	NUP= PEAK WAVENUMBER 1/CM	0.2032E+04	NUP= PEAK WAVENUMBER 1/CM	0.2032E+04
QBG= BKGD PHOTON FLUX DENSITY P/CM**2/S	0.4158E+10	QBG= BKGD PHOTON FLUX DENSITY P/CM**2/S	0.5218E+11	QBG= BKGD PHOTON FLUX DENSITY P/CM**2/S	0.8840E+12
QS = SGNL PHOTON FLUX DENSITY P/CM**2/S	0.2110E+10	QS = SGNL PHOTON FLUX DENSITY P/CM**2/S	0.5000E+11	QS = SGNL PHOTON FLUX DENSITY P/CM**2/S	0.8840E+12
KAPPA = DIELECTRIC CONSTANT	0.1720E+02	KAPPA = DIELECTRIC CONSTANT	0.1720E+02	KAPPA = DIELECTRIC CONSTANT	0.1720E+02
RF = FEEDBACK RESISTANCE OHM	0.1000E+10	RF = FEEDBACK RESISTANCE OHM	0.1000E+10	RF = FEEDBACK RESISTANCE OHM	0.1000E+10
CF = FEEDBACK CAPACITACE F	0.3000E-12	CF = FEEDBACK CAPACITACE F	0.3000E-12	CF = FEEDBACK CAPACITACE F	0.3000E-12
VP = PREAMP NOISE (INPUT) V/HZ**.5	0.2000E-08	VP = PREAMP NOISE (INPUT) V/HZ**.5	0.2000E-08	VP = PREAMP NOISE (INPUT) V/HZ**.5	0.2000E-08
AO = OPEN LOOP GAIN OF PREAMP	0.1000E+04	AO = OPEN LOOP GAIN OF PREAMP	0.1000E+04	AO = OPEN LOOP GAIN OF PREAMP	0.1000E+04
TRF= FEEDBACK RESISTOR TEMP K	0.1600E+03	TRF= FEEDBACK RESISTOR TEMP K	0.1600E+03	TRF= FEEDBACK RESISTOR TEMP K	0.1600E+03
FC = CHOPPING FREQUENCY HZ	0.4400E+03	FC = CHOPPING FREQUENCY HZ	0.4400E+03	FC = CHOPPING FREQUENCY HZ	0.4400E+03
RO = DIODE DARK RESISTANCE BIAS=0 OHM	0.2170E+09	RO = DIODE DARK RESISTANCE BIAS=0 OHM	0.2170E+09	RO = DIODE DARK RESISTANCE BIAS=0 OHM	0.2170E+09
RA = R(0)*A PRODUCT OHM*CM**2	0.1845E+07	RA = R(0)*A PRODUCT OHM*CM**2	0.1845E+07	RA = R(0)*A PRODUCT OHM*CM**2	0.1845E+07
VJ = JUNCTION POTENTIAL V	0.1978E+00	VJ = JUNCTION POTENTIAL V	3.1978E+00	VJ = JUNCTION POTENTIAL V	0.1978E+00
CJ = JUNCTION CAPACITANCE F	0.8489E-10	CJ = JUNCTION CAPACITANCE F	0.8489E-10	CJ = JUNCTION CAPACITANCE F	0.8489E-10
WJ = JUNCTION WIDTH CM	0.8673E-04	WJ = JUNCTION WIDTH CM	0.8673E-04	WJ = JUNCTION WIDTH CM	0.8673E-04
VC = CONTACT POTENTIAL V	0.1978E+00	VC = CONTACT POTENTIAL V	0.1978E+00	VC = CONTACT POTENTIAL V	0.1978E+00
ZD = DETECTOR IMPEDANCE OHM	0.3908E+07	ZD = DETECTOR IMPEDANCE OHM	0.3908E+07	ZD = DETECTOR IMPEDANCE OHM	0.3908E+07
ZF = FEEDBACK RESISTOR IMPEDANCE OHM	0.5466E+09	ZF = FEEDBACK RESISTOR IMPEDANCE OHM	0.5466E+09	ZF = FEEDBACK RESISTOR IMPEDANCE OHM	0.5466E+09
PD = DET. PHASE ANGLE RAD	0.1082E-14	PD = DET. PHASE ANGLE RAD	0.1082E-14	PD = DET. PHASE ANGLE RAD	0.1082E-14
PF = FDBK RESISTOR PHASE ANGLE RAD	0.8294E-18	PF = FDBK RESISTOR PHASE ANGLE RAD	0.8294E-18	PF = FDBK RESISTOR PHASE ANGLE RAD	0.8294E-18
AZ = TRANSIMPEDANCE OHM	0.6355E+09	AZ = TRANSIMPEDANCE OHM	0.6355E+09	AZ = TRANSIMPEDANCE OHM	0.6355E+09
IS = SIGNAL PHOTOCURRENT A	0.1307E-11	IS = SIGNAL PHOTOCURRENT A	0.3097E-10	IS = SIGNAL PHOTOCURRENT A	0.5476E-09
IT = TOTAL BKGD PHOTOCURRENT A	0.2571E-11	IT = TOTAL BKGD PHOTOCURRENT A	0.3227E-10	IT = TOTAL BKGD PHOTOCURRENT A	0.5476E-09
VRF= FDBK RESISTOR NOISE V/HZ**.5	0.1889E-05	VRF= FDBK RESISTOR NOISE V/HZ**.5	0.1889E-05	VRF= FDBK RESISTOR NOISE V/HZ**.5	0.1889E-05
VBG= BACKGROUND NOISE V/HZ**.5	0.5768E-06	VBG= BACKGROUND NOISE V/HZ**.5	0.2044E-05	VBG= BACKGROUND NOISE V/HZ**.5	0.8418E-05
VJN= JOHNSON NOISE V/HZ**.5	0.1963E-05	VJN= JOHNSON NOISE V/HZ**.5	0.1963E-05	VJN= JOHNSON NOISE V/HZ**.5	0.1963E-05
VGR= GEN-RECOMB NOISE V/HZ**.5	0.1963E-05	VGR= GEN-RECOMB NOISE V/HZ**.5	0.1963E-05	VGR= GEN-RECOMB NOISE V/HZ**.5	0.1963E-05
VPA= PREAMP NOISE V/HZ**.5	0.3433E-06	VPA= PREAMP NOISE V/HZ**.5	0.3433E-06	VPA= PREAMP NOISE V/HZ**.5	0.3433E-06
VT = TOTAL NOISE V/HZ**.5	0.3425E-05	VT = TOTAL NOISE V/HZ**.5	0.3946E-05	VT = TOTAL NOISE V/HZ**.5	0.9070E-05
R = RESPONSIVITY V/W	0.2018E+10	R = RESPONSIVITY V/W	0.2018E+10	R = RESPONSIVITY V/W	0.2018E+10
NEP= NOISE EQUIVALENT POWER W/HZ**.5	0.1697E-14	NEP= NOISE EQUIVALENT POWER W/HZ**.5	0.1955E-14	NEP= NOISE EQUIVALENT POWER W/HZ**.5	0.4494E-14
DSTAR = CM*HZ**.5/W	0.4097E+14	DSTAR = CM*HZ**.5/W	0.3556E+14	DSTAR = CM*HZ**.5/W	0.1547E+14

Table F-5. PC HgCdTe detector performance for channels 1, 10, and 11 as a function of bias potential

Table F-5 (CH 1)a

ORIGINAL PAGE IS OF POOR QUALITY

PC HGCDTE DETECTOR PERFORMANCE CHANNEL 1 75/160/STD 2 V/CM

CH = CHANNEL NUMBER	0.1000E+01
T = DET. TEMP	0.7500E+02
HD = DET. HEIGHT CM	0.1360E-01
WD = DET. WIDTH CM	0.1990E-01
TD = DETECTOR THICKNESS CM	0.1000E-02
VB = DETECTOR BIAS VOLTAGE V	0.3980E-01
CD = DETECTOR CAPACITANCE F	0.1500E-10
RD = DETECTOR DARK RESISTANCE OHM	0.3395E+03
ZD = DETECTOR IMPEDANCE OHM	0.3395E+03
PD = DETECTOR PHASE ANGLE RAD	0.1221E-09
X = MOLE FRACTION	0.1838E+00
PO = HOLE CONC. N-TYPE DOPING CM**-3	0.1000E+15
ND = DONAR CARRIER CONC. CM**-3	0.1305E+16
NI = INTRINSIC CARRIER CONC. CM**-3	0.3612E+15
TAU= CARRIER LIFETIME S	0.1000E-05
ETA= QUANTUM EFFICIENCY	0.7000E+00
NUP= PEAK WAVENUMBER 1/CM	0.6066E+03
EG = BAND GAP ENERGY EV	0.6847E-01
SIGMA = CONDUCTIVITY 1/OHM/CM	0.4310E+01
MU = ELECTRON MOBILITY CM**2/V/S	0.2060E+05
MUH= HOLE MOBILITY CM**2/V/S	0.2950E+03
QBG= BKGD PHOTON FLUX DENSITY P/CM**2/S	0.1340E+16
QS = SGNL PHOTON FLUX DENSITY P/CM**2/S	0.5300E+14
TRF= FEEDBACK RESISTOR TEMP. K	0.1600E+03
CF = FDBK RESISTOR CAPACITANCE F	0.3000E-12
RF = FEEDBACK RESISTANCE OHM	0.3395E+04
PF = FDBK RESISTOR PHASE ANGLE RAD	0.2443E-12
ZF = FDBK RESISTOR IMPEDANCE OHM	0.3395E+04
VS = SUPPLY VOLTAGE TO RF/DET. V	0.4370E+00
AO = OPEN LOOP GAIN	0.1000E+04
VP = PREAMP NOISE (INPUT) V/HZ**.5	0.2000E-08
FC = CHOPPING FREQUENCY HZ	0.4400E+03
PW = DETECTOR BIAS POWER W	0.4666E-05
PRF= FEEDBACK RESISTOR BIAS POWER W	0.4666E-04
SIGV = SIGNAL VOLTAGE V	0.2180E-04
RE = DET. RESPONSIVITY V/W	0.5945E+04
AZ = TRANSIMPEDANCE OHM	0.3429E+04
R = DET./PREAMP RESPONSIVITY V/W	0.6005E+05
VBG= BACKGROUND NOISE V/HZ**.5	0.1163E-08
VJN= JOHNSON NOISE V/HZ**.5	0.1198E-07
VGR= GR NOISE V/HZ**.5	0.1200E-07
VRF= FDBK RESISTOR JOHNSON NOISE V/HZ**.5	0.5532E-08
VPA= PREAMP NOISE V/HZ**.5	0.2770E-07
VT = TOTAL NOISE V/HZ**.5	0.3296E-07
NEP= NOISE EQUIVALENT POWER W/HZ**.5	0.5489E-12
DSTAR = PEAK DSTAR CM*HZ**.5/W	0.2997E+11

PC HGCDTE DETECTOR PERFORMANCE CHANNEL 1 75/160/STD 4 V/CM

CH = CHANNEL NUMBER	0.1000E+01
T = DET. TEMP	0.7500E+02
HD = DET. HEIGHT CM	0.1360E-01
WD = DET. WIDTH CM	0.1990E-01
TD = DETECTOR THICKNESS CM	0.1000E-02
VB = DETECTOR BIAS VOLTAGE V	0.7960E-01
CD = DETECTOR CAPACITANCE F	0.1500E-10
RD = DETECTOR DARK RESISTANCE OHM	0.3395E+03
ZD = DETECTOR IMPEDANCE OHM	0.3395E+03
PD = DETECTOR PHASE ANGLE RAD	0.1221E-09
X = MOLE FRACTION	0.1838E+00
PO = HOLE CONC. N-TYPE DOPING CM**-3	0.1000E+15
ND = DONAR CARRIER CONC. CM**-3	0.1305E+16
NI = INTRINSIC CARRIER CONC. CM**-3	0.3612E+15
TAU= CARRIER LIFETIME S	0.1000E-05
ETA= QUANTUM EFFICIENCY	0.7000E+00
NUP= PEAK WAVENUMBER 1/CM	0.6066E+03
EG = BAND GAP ENERGY EV	0.6847E-01
SIGMA = CONDUCTIVITY 1/OHM/CM	0.4310E+01
MU = ELECTRON MOBILITY CM**2/V/S	0.2060E+05
MUH= HOLE MOBILITY CM**2/V/S	0.2950E+03
QBG= BKGD PHOTON FLUX DENSITY P/CM**2/S	0.1340E+16
QS = SGNL PHOTON FLUX DENSITY P/CM**2/S	0.5300E+14
TRF= FEEDBACK RESISTOR TEMP. K	0.1600E+03
CF = FDBK RESISTOR CAPACITANCE F	0.3000E-12
RF = FEEDBACK RESISTANCE OHM	0.3395E+04
PF = FDBK RESISTOR PHASE ANGLE RAD	0.2443E-12
ZF = FDBK RESISTOR IMPEDANCE OHM	0.3395E+04
VS = SUPPLY VOLTAGE TO RF/DET. V	0.8756E+00
AO = OPEN LOOP GAIN	0.1000E+04
VP = PREAMP NOISE (INPUT) V/HZ**.5	0.2000E-08
FC = CHOPPING FREQUENCY HZ	0.4400E+03
PW = DETECTOR BIAS POWER W	0.1866E-04
PRF= FEEDBACK RESISTOR BIAS POWER W	0.1866E-03
SIGV = SIGNAL VOLTAGE V	0.8721E-04
RE = DET. RESPONSIVITY V/W	0.1189E+05
AZ = TRANSIMPEDANCE OHM	0.3429E+04
R = DET./PREAMP RESPONSIVITY V/W	0.1201E+06
VBG= BACKGROUND NOISE V/HZ**.5	0.2325E-08
VJN= JOHNSON NOISE V/HZ**.5	0.1198E-07
VGR= GR NOISE V/HZ**.5	0.2401E-07
VRF= FDBK RESISTOR JOHNSON NOISE V/HZ**.5	0.5532E-08
VPA= PREAMP NOISE V/HZ**.5	0.2770E-07
VT = TOTAL NOISE V/HZ**.5	0.3902E-07
NEP= NOISE EQUIVALENT POWER W/HZ**.5	0.3249E-12
DSTAR = PEAK DSTAR CM*HZ**.5/W	0.5063E+11

PC HGCDTE DETECTOR PERFORMANCE CHANNEL 1 75/160/STD 6 V/CM

CH = CHANNEL NUMBER	0.1000E+01
T = DET. TEMP	0.7500E+02
HD = DET. HEIGHT CM	0.1360E-01
WD = DET. WIDTH CM	0.1990E-01
TD = DETECTOR THICKNESS CM	0.1000E-02
VB = DETECTOR BIAS VOLTAGE V	0.1194E+00
CD = DETECTOR CAPACITANCE F	0.1500E-10
RD = DETECTOR DARK RESISTANCE OHM	0.3395E+03
ZD = DETECTOR IMPEDANCE OHM	0.3395E+03
PD = DETECTOR PHASE ANGLE RAD	0.1221E-09
X = MOLE FRACTION	0.1838E+00
PO = HOLE CONC. N-TYPE DOPING CM**-3	0.1000E+15
ND = DONAR CARRIER CONC. CM**-3	0.1305E+16
NI = INTRINSIC CARRIER CONC. CM**-3	0.3612E+15
TAU= CARRIER LIFETIME S	0.1000E-05
ETA= QUANTUM EFFICIENCY	0.7000E+00
NUP= PEAK WAVENUMBER 1/CM	0.6066E+03
EG = BAND GAP ENERGY EV	0.6847E-01
SIGMA = CONDUCTIVITY 1/OHM/CM	0.4310E+01
MU = ELECTRON MOBILITY CM**2/V/S	0.2060E+05
MUH= HOLE MOBILITY CM**2/V/S	0.2950E+03
QBG= BKGD PHOTON FLUX DENSITY P/CM**2/S	0.1340E+16
QS = SGNL PHOTON FLUX DENSITY P/CM**2/S	0.5300E+14
TRF= FEEDBACK RESISTOR TEMP. K	0.1600E+03
CF = FDBK RESISTOR CAPACITANCE F	0.3000E-12
RF = FEEDBACK RESISTANCE OHM	0.3395E+04
PF = FDBK RESISTOR PHASE ANGLE RAD	0.2443E-12
ZF = FDBK RESISTOR IMPEDANCE OHM	0.3395E+04
VS = SUPPLY VOLTAGE TO RF/DET. V	0.1313E+01
AO = OPEN LOOP GAIN	0.1000E+04
VP = PREAMP NOISE (INPUT) V/HZ**.5	0.2000E-08
FC = CHOPPING FREQUENCY HZ	0.4400E+03
PW = DETECTOR BIAS POWER W	0.4199E-04
PRF= FEEDBACK RESISTOR BIAS POWER W	0.4199E-03
SIGV = SIGNAL VOLTAGE V	0.1962E-03
RE = DET. RESPONSIVITY V/W	0.1783E+05
AZ = TRANSIMPEDANCE OHM	0.3429E+04
R = DET./PREAMP RESPONSIVITY V/W	0.1801E+06
VBG= BACKGROUND NOISE V/HZ**.5	0.3488E-08
VJN= JOHNSON NOISE V/HZ**.5	0.1198E-07
VGR= GR NOISE V/HZ**.5	0.3601E-07
VRF= FDBK RESISTOR JOHNSON NOISE V/HZ**.5	0.5532E-08
VPA= PREAMP NOISE V/HZ**.5	0.2770E-07
VT = TOTAL NOISE V/HZ**.5	0.4744E-07
NEP= NOISE EQUIVALENT POWER W/HZ**.5	0.2633E-12
DSTAR = PEAK DSTAR CM*HZ**.5/W	0.6248E+11

PC HGCDTE DETECTOR PERFORMANCE CHANNEL 1 75/160/STD 8 V/CM

CH = CHANNEL NUMBER	0.1000E+01
T = DET. TEMP	0.7500E+02
HD = DET. HEIGHT CM	0.1360E-01
WD = DET. WIDTH CM	0.1990E-01
TD = DETECTOR THICKNESS CM	0.1000E-02
VB = DETECTOR BIAS VOLTAGE V	0.1592E+00
CD = DETECTOR CAPACITANCE F	0.1500E-10
RD = DETECTOR DARK RESISTANCE OHM	0.3395E+03
ZD = DETECTOR IMPEDANCE OHM	0.3395E+03
PD = DETECTOR PHASE ANGLE RAD	0.1221E-09
X = MOLE FRACTION	0.1838E+00
PO = HOLE CONC. N-TYPE DOPING CM**-3	0.1000E+15
ND = DONAR CARRIER CONC. CM**-3	0.1305E+16
NI = INTRINSIC CARRIER CONC. CM**-3	0.3612E+15
TAU= CARRIER LIFETIME S	0.1000E-05
ETA= QUANTUM EFFICIENCY	0.7000E+00
NUP= PEAK WAVENUMBER 1/CM	0.6066E+03
EG = BAND GAP ENERGY EV	0.6847E-01
SIGMA = CONDUCTIVITY 1/OHM/CM	0.4310E+01
MU = ELECTRON MOBILITY CM**2/V/S	0.2060E+05
MUH= HOLE MOBILITY CM**2/V/S	0.2950E+03
QBG= BKGD PHOTON FLUX DENSITY P/CM**2/S	0.1340E+16
QS = SGNL PHOTON FLUX DENSITY P/CM**2/S	0.5300E+14
TRF= FEEDBACK RESISTOR TEMP. K	0.1600E+03
CF = FDBK RESISTOR CAPACITANCE F	0.3000E-12
RF = FEEDBACK RESISTANCE OHM	0.3395E+04
PF = FDBK RESISTOR PHASE ANGLE RAD	0.2443E-12
ZF = FDBK RESISTOR IMPEDANCE OHM	0.3395E+04
VS = SUPPLY VOLTAGE TO RF/DET. V	0.1751E+01
AO = OPEN LOOP GAIN	0.1000E+04
VP = PREAMP NOISE (INPUT) V/HZ**.5	0.2000E-08
FC = CHOPPING FREQUENCY HZ	0.4400E+03
PW = DETECTOR BIAS POWER W	0.7465E-04
PRF= FEEDBACK RESISTOR BIAS POWER W	0.7465E-03
SIGV = SIGNAL VOLTAGE V	0.3488E-03
RE = DET. RESPONSIVITY V/W	0.2378E+05
AZ = TRANSIMPEDANCE OHM	0.3429E+04
R = DET./PREAMP RESPONSIVITY V/W	0.2402E+06
VBG= BACKGROUND NOISE V/HZ**.5	0.4650E-08
VJN= JOHNSON NOISE V/HZ**.5	0.1198E-07
VGR= GR NOISE V/HZ**.5	0.4802E-07
VRF= FDBK RESISTOR JOHNSON NOISE V/HZ**.5	0.5532E-08
VPA= PREAMP NOISE V/HZ**.5	0.2770E-07
VT = TOTAL NOISE V/HZ**.5	0.5717E-07
NEP= NOISE EQUIVALENT POWER W/HZ**.5	0.2360E-12
DSTAR = PEAK DSTAR CM*HZ**.5/W	0.6912E+11

Table F-5 (CH 1)b

PC HGCDTE DETECTOR PERFORMANCE CHANNEL 1 75/160/STD 10 V/CM

CH = CHANNEL NUMBER	0.1000E+01
T = DET. TEMP	0.7500E+02
HD = DET. HEIGHT CM	0.1360E-01
WD = DET. WIDTH CM	0.1990E-01
TD = DETECTOR THICKNESS CM	0.1000E-02
VB = DETECTOR BIAS VOLTAGE V	0.1990E+00
CD = DETECTOR CAPACITANCE F	0.1500E-10
RD = DETECTOR DARK RESISTANCE OHM	0.3395E+03
ZD = DETECTOR IMPEDANCE OHM	0.3395E+03
PD = DETECTOR PHASE ANGLE RAD	0.1221E-09
X = MOLE FRACTION	0.1838E+00
PO = HOLE CONC, N-TYPE DOPING CM**-3	0.1000E+15
ND = DONAR CARRIER CONC. CM**-3	0.1305E+16
NI = INTRINSIC CARRIER CONC. CM**-3	0.3612E+15
TAU= CARRIER LIFETIME S	0.1000E-05
ETA= QUANTUM EFFICIENCY	0.7000E+00
NUP= PEAK WAVENUMBER 1/CM	0.6068E+03
EG = BAND GAP ENERGY EV	0.6847E-01
SIGMA = CONDUCTIVITY 1/OHM/CM	0.4310E+01
MU = ELECTRON MOBILITY CM**2/V/S	0.2060E+05
MUH= HOLE MOBILITY CM**2/V/S	0.2950E+03
QBG= BKGD PHOTON FLUX DENSITY P/CM**2/S	0.1340E+16
QS = SGNL PHOTON FLUX DENSITY P/CM**2/S	0.5300E+14
TRF= FEEDBACK RESISTOR TEMP. K	0.1600E+03
CF = FDBK RESISTOR CAPACITANCE F	0.3000E-12
RF = FEEDBACK RESISTANCE OHM	0.3395E+04
PF = FDBK RESISTOR PHASE ANGLE RAD	0.2443E-12
ZF = FDBK RESISTOR IMPEDANCE OHM	0.3395E+04
VS = SUPPLY VOLTAGE TO RF/DET. V	0.2189E+01
AO = OPEN LOOP GAIN	0.1000E+04
VP = PREAMP NOISE (INPUT) V/HZ**.5	0.2800E-08
FC = CHOPPING FREQUENCY HZ	0.4400E+03
PW = DETECTOR BIAS POWER W	0.1166E-03
PRF= FEEDBACK RESISTOR BIAS POWER W	0.1166E-02
SIGV = SIGNAL VOLTAGE V	0.5451E-03
RE = DET. RESPONSIVITY V/W	0.2972E+05
AZ = TRANSIMPEDANCE OHM	0.3429E+04
R = DET./PREAMP RESPONSIVITY V/W	0.3032E+06
VBG= BACKGROUND NOISE V/HZ**.5	0.5813E-08
VJN= JOHNSON NOISE V/HZ**.5	0.1198E-07
VGR= GR NOISE V/HZ**.5	0.6002E-07
VRF= FDBK RESISTOR JOHNSON NOISE V/HZ**.5	0.5532E-08
VPA= PREAMP NOISE V/HZ**.5	0.2770E-07
VT = TOTAL NOISE V/HZ**.5	0.6766E-07
NEP= NOISE EQUIVALENT POWER W/HZ**.5	0.2253E-12
DSTAR = PEAK DSTAR CM*HZ**.5/W	0.7301E+11

PC HGCDTE DETECTOR PERFORMANCE CHANNEL 1 75/160/STD 12 V/CM

CH = CHANNEL NUMBER	0.1000E+01
T = DET. TEMP	0.7500E+02
HD = DET. HEIGHT CM	0.1360E-01
WD = DET. WIDTH CM	0.1990E-01
TD = DETECTOR THICKNESS CM	0.1000E-02
VB = DETECTOR BIAS VOLTAGE V	0.2300E+00
CD = DETECTOR CAPACITANCE F	0.1500E-10
RD = DETECTOR DARK RESISTANCE OHM	0.3395E+03
ZD = DETECTOR IMPEDANCE OHM	0.3395E+03
PD = DETECTOR PHASE ANGLE RAD	0.1221E-09
X = MOLE FRACTION	0.1838E+00
PO = HOLE CONC, N-TYPE DOPING CM**-3	0.1000E+15
ND = DONAR CARRIER CONC. CM**-3	0.1305E+16
NI = INTRINSIC CARRIER CONC. CM**-3	0.3612E+15
TAU= CARRIER LIFETIME S	0.1000E-05
ETA= QUANTUM EFFICIENCY	0.7000E+00
NUP= PEAK WAVENUMBER 1/CM	0.6068E+03
EG = BAND GAP ENERGY EV	0.6847E-01
SIGMA = CONDUCTIVITY 1/OHM/CM	0.4310E+01
MU = ELECTRON MOBILITY CM**2/V/S	0.2060E+05
MUH= HOLE MOBILITY CM**2/V/S	0.2950E+03
QBG= BKGD PHOTON FLUX DENSITY P/CM**2/S	0.1340E+16
QS = SGNL PHOTON FLUX DENSITY P/CM**2/S	0.5300E+14
TRF= FEEDBACK RESISTOR TEMP. K	0.1600E+03
CF = FDBK RESISTOR CAPACITANCE F	0.3000E-12
RF = FEEDBACK RESISTANCE OHM	0.3395E+04
PF = FDBK RESISTOR PHASE ANGLE RAD	0.2443E-12
ZF = FDBK RESISTOR IMPEDANCE OHM	0.3395E+04
VS = SUPPLY VOLTAGE TO RF/DET. V	0.2627E+01
AO = OPEN LOOP GAIN	0.1000E+04
VP = PREAMP NOISE (INPUT) V/HZ**.5	0.2800E-08
FC = CHOPPING FREQUENCY HZ	0.4400E+03
PW = DETECTOR BIAS POWER W	0.1600E-03
PRF= FEEDBACK RESISTOR BIAS POWER W	0.1600E-02
SIGV = SIGNAL VOLTAGE V	0.7845E-03
RE = DET. RESPONSIVITY V/W	0.3567E+05
AZ = TRANSIMPEDANCE OHM	0.3429E+04
R = DET./PREAMP RESPONSIVITY V/W	0.3603E+06
VBG= BACKGROUND NOISE V/HZ**.5	0.6975E-08
VJN= JOHNSON NOISE V/HZ**.5	0.1198E-07
VGR= GR NOISE V/HZ**.5	0.7202E-07
VRF= FDBK RESISTOR JOHNSON NOISE V/HZ**.5	0.5532E-08
VPA= PREAMP NOISE V/HZ**.5	0.2770E-07
VT = TOTAL NOISE V/HZ**.5	0.7859E-07
NEP= NOISE EQUIVALENT POWER W/HZ**.5	0.2181E-12
DSTAR = PEAK DSTAR CM*HZ**.5/W	0.7541E+11

PC HGCDTE DETECTOR PERFORMANCE CHANNEL 1 75/160/STD 14 V/CM

CH = CHANNEL NUMBER	0.1000E+01
T = DET. TEMP	0.7500E+02
HD = DET. HEIGHT CM	0.1360E-01
WD = DET. WIDTH CM	0.1990E-01
TD = DETECTOR THICKNESS CM	0.1000E-02
VB = DETECTOR BIAS VOLTAGE V	0.2786E+00
CD = DETECTOR CAPACITANCE F	0.1500E-10
RD = DETECTOR DARK RESISTANCE OHM	0.3395E+03
ZD = DETECTOR IMPEDANCE OHM	0.3395E+03
PD = DETECTOR PHASE ANGLE RAD	0.1221E-09
X = MOLE FRACTION	0.1838E+00
PO = HOLE CONC, N-TYPE DOPING CM**-3	0.1000E+15
ND = DONAR CARRIER CONC. CM**-3	0.1305E+16
NI = INTRINSIC CARRIER CONC. CM**-3	0.3612E+15
TAU= CARRIER LIFETIME S	0.1000E-05
ETA= QUANTUM EFFICIENCY	0.7000E+00
NUP= PEAK WAVENUMBER 1/CM	0.6068E+03
EG = BAND GAP ENERGY EV	0.6847E-01
SIGMA = CONDUCTIVITY 1/OHM/CM	0.4310E+01
MU = ELECTRON MOBILITY CM**2/V/S	0.2060E+05
MUH= HOLE MOBILITY CM**2/V/S	0.2950E+03
QBG= BKGD PHOTON FLUX DENSITY P/CM**2/S	0.1340E+16
QS = SGNL PHOTON FLUX DENSITY P/CM**2/S	0.5300E+14
TRF= FEEDBACK RESISTOR TEMP. K	0.1600E+03
CF = FDBK RESISTOR CAPACITANCE F	0.3000E-12
RF = FEEDBACK RESISTANCE OHM	0.3395E+04
PF = FDBK RESISTOR PHASE ANGLE RAD	0.2443E-12
ZF = FDBK RESISTOR IMPEDANCE OHM	0.3395E+04
VS = SUPPLY VOLTAGE TO RF/DET. V	0.3065E+01
AO = OPEN LOOP GAIN	0.1000E+04
VP = PREAMP NOISE (INPUT) V/HZ**.5	0.2800E-08
FC = CHOPPING FREQUENCY HZ	0.4400E+03
PW = DETECTOR BIAS POWER W	0.2286E-03
PRF= FEEDBACK RESISTOR BIAS POWER W	0.2286E-02
SIGV = SIGNAL VOLTAGE V	0.1068E-02
RE = DET. RESPONSIVITY V/W	0.4161E+05
AZ = TRANSIMPEDANCE OHM	0.3429E+04
R = DET./PREAMP RESPONSIVITY V/W	0.4203E+06
VBG= BACKGROUND NOISE V/HZ**.5	0.8138E-08
VJN= JOHNSON NOISE V/HZ**.5	0.1198E-07
VGR= GR NOISE V/HZ**.5	0.8403E-07
VRF= FDBK RESISTOR JOHNSON NOISE V/HZ**.5	0.5532E-08
VPA= PREAMP NOISE V/HZ**.5	0.2770E-07
VT = TOTAL NOISE V/HZ**.5	0.8982E-07
NEP= NOISE EQUIVALENT POWER W/HZ**.5	0.2137E-12
DSTAR = PEAK DSTAR CM*HZ**.5/W	0.7699E+11

PC HGCDTE DETECTOR PERFORMANCE CHANNEL 1 75/160/STD 16 V/CM

CH = CHANNEL NUMBER	0.1000E+01
T = DET. TEMP	0.7500E+02
HD = DET. HEIGHT CM	0.1360E-01
WD = DET. WIDTH CM	0.1990E-01
TD = DETECTOR THICKNESS CM	0.1000E-02
VB = DETECTOR BIAS VOLTAGE V	0.3184E+00
CD = DETECTOR CAPACITANCE F	0.1500E-10
RD = DETECTOR DARK RESISTANCE OHM	0.3395E+03
ZD = DETECTOR IMPEDANCE OHM	0.3395E+03
PD = DETECTOR PHASE ANGLE RAD	0.1221E-09
X = MOLE FRACTION	0.1838E+00
PO = HOLE CONC, N-TYPE DOPING CM**-3	0.1000E+15
ND = DONAR CARRIER CONC. CM**-3	0.1305E+16
NI = INTRINSIC CARRIER CONC. CM**-3	0.3612E+15
TAU= CARRIER LIFETIME S	0.1000E-05
ETA= QUANTUM EFFICIENCY	0.7000E+00
NUP= PEAK WAVENUMBER 1/CM	0.6068E+03
EG = BAND GAP ENERGY EV	0.6847E-01
SIGMA = CONDUCTIVITY 1/OHM/CM	0.4310E+01
MU = ELECTRON MOBILITY CM**2/V/S	0.2060E+05
MUH= HOLE MOBILITY CM**2/V/S	0.2950E+03
QBG= BKGD PHOTON FLUX DENSITY P/CM**2/S	0.1340E+16
QS = SGNL PHOTON FLUX DENSITY P/CM**2/S	0.5300E+14
TRF= FEEDBACK RESISTOR TEMP. K	0.1600E+03
CF = FDBK RESISTOR CAPACITANCE F	0.3000E-12
RF = FEEDBACK RESISTANCE OHM	0.3395E+04
PF = FDBK RESISTOR PHASE ANGLE RAD	0.2443E-12
ZF = FDBK RESISTOR IMPEDANCE OHM	0.3395E+04
VS = SUPPLY VOLTAGE TO RF/DET. V	0.3502E+01
AO = OPEN LOOP GAIN	0.1000E+04
VP = PREAMP NOISE (INPUT) V/HZ**.5	0.2800E-08
FC = CHOPPING FREQUENCY HZ	0.4400E+03
PW = DETECTOR BIAS POWER W	0.2986E-03
PRF= FEEDBACK RESISTOR BIAS POWER W	0.2986E-02
SIGV = SIGNAL VOLTAGE V	0.1395E-02
RE = DET. RESPONSIVITY V/W	0.4756E+05
AZ = TRANSIMPEDANCE OHM	0.3429E+04
R = DET./PREAMP RESPONSIVITY V/W	0.4804E+06
VBG= BACKGROUND NOISE V/HZ**.5	0.9301E-08
VJN= JOHNSON NOISE V/HZ**.5	0.1198E-07
VGR= GR NOISE V/HZ**.5	0.9603E-07
VRF= FDBK RESISTOR JOHNSON NOISE V/HZ**.5	0.5532E-08
VPA= PREAMP NOISE V/HZ**.5	0.2770E-07
VT = TOTAL NOISE V/HZ**.5	0.1012E-06
NEP= NOISE EQUIVALENT POWER W/HZ**.5	0.2107E-12
DSTAR = PEAK DSTAR CM*HZ**.5/W	0.7806E+11

Table F-5 (CH 10)a

PC HGCDTE DETECTOR PERFORMANCE CHANNEL 10 75/160/STD 2 V/CM

CH = CHANNEL NUMBER	0.1000E+02
T = DET. TEMP	0.7500E+02
HD = DET. HEIGHT CM	0.1360E-01
WD = DET. WIDTH CM	0.2920E-01
TD = DETECTOR THICKNESS CM	0.1000E-02
VB = DETECTOR BIAS VOLTAGE V	0.5840E-01
CD = DETECTOR CAPACITANCE F	0.1500E-10
RD = DETECTOR DARK RESISTANCE OHM	0.4982E+03
ZD = DETECTOR IMPEDANCE OHM	0.4982E+03
PD = DETECTOR PHASE ANGLE RAD	0.8324E-10
X = MOLE FRACTION	0.1838E+00
PO = HOLE CONC. N-TYPE DOPING CM**-3	0.1000E+15
ND = DONAR CARRIER CONC. CM**-3	0.1305E+16
NI = INTRINSIC CARRIER CONC. CM**-3	0.3612E+15
TAU= CARRIER LIFETIME S	0.1000E-05
ETA= QUANTUM EFFICIENCY	0.7000E+00
NUP= PEAK WAVENUMBER 1/CM	0.6068E+03
EG = BAND GAP ENERGY EV	0.6847E-01
SIGMA = CONDUCTIVITY 1/OHM/CM	0.4310E+01
MU = ELECTRON MOBILITY CM**2/V/S	0.2060E+05
MUH= HOLE MOBILITY CM**2/V/S	0.2954E+03
QBG= BKGD PHOTON FLUX DENSITY P/CM**2/S	0.7120E+15
QS = SGNL PHOTON FLUX DENSITY P/CM**2/S	0.1900E+14
TRF= FEEDBACK RESISTOR TEMP. K	0.1600E+03
CF = FDBK RESISTOR CAPACITANCE F	0.3000E-12
RF = FEEDBACK RESISTANCE OHM	0.4982E+04
PF = FDBK RESISTOR PHASE ANGLE RAD	0.1665E-12
ZF = FDBK RESISTOR IMPEDANCE OHM	0.4982E+04
VS = SUPPLY VOLTAGE TO RF/DET. V	0.6424E+00
AO = OPEN LOOP GAIN	0.1000E+04
VP = PREAMP NOISE (INPUT) V/HZ**.5	0.2800E-08
FC = CHOPPING FREQUENCY HZ	0.4400E+03
PW = DETECTOR BIAS POWER W	0.6846E-05
PRF= FEEDBACK RESISTOR BIAS POWER W	0.6846E-04
SIGV = SIGNAL VOLTAGE V	0.7816E-05
RE = DET. RESPONSIVITY V/W	0.5945E+04
AZ = TRANSIMPEDANCE OHM	0.5032E+04
R = DET./PREAMP RESPONSIVITY V/W	0.6005E+05
VBG= BACKGROUND NOISE V/HZ**.5	0.1027E-08
VJN= JOHNSON NOISE V/HZ**.5	0.1451E-07
VGR= GR NOISE V/HZ**.5	0.1454E-07
VRF= FDBK RESISTOR JOHNSON NOISE V/HZ**.5	0.6702E-08
VPA= PREAMP NOISE V/HZ**.5	0.2770E-07
VT = TOTAL NOISE V/HZ**.5	0.3514E-07
NEP= NOISE EQUIVALENT POWER W/HZ**.5	0.5852E-12
DSTAR = PEAK DSTAR CM*HZ**.5/W	0.3405E+11

PC HGCDTE DETECTOR PERFORMANCE CHANNEL 10 75/160/STD 4 V/CM

CH = CHANNEL NUMBER	0.1000E+02
T = DET. TEMP	0.7500E+02
HD = DET. HEIGHT CM	0.1360E-01
WD = DET. WIDTH CM	0.2920E-01
TD = DETECTOR THICKNESS CM	0.1000E-02
VB = DETECTOR BIAS VOLTAGE V	0.1168E+00
CD = DETECTOR CAPACITANCE F	0.1500E-10
RD = DETECTOR DARK RESISTANCE OHM	0.4982E+03
ZD = DETECTOR IMPEDANCE OHM	0.4982E+03
PD = DETECTOR PHASE ANGLE RAD	0.8324E-10
X = MOLE FRACTION	0.1838E+00
PO = HOLE CONC. N-TYPE DOPING CM**-3	0.1000E+15
ND = DONAR CARRIER CONC. CM**-3	0.1305E+16
NI = INTRINSIC CARRIER CONC. CM**-3	0.3612E+15
TAU= CARRIER LIFETIME S	0.1000E-05
ETA= QUANTUM EFFICIENCY	0.7000E+00
NUP= PEAK WAVENUMBER 1/CM	0.6068E+03
EG = BAND GAP ENERGY EV	0.6847E-01
SIGMA = CONDUCTIVITY 1/OHM/CM	0.4310E+01
MU = ELECTRON MOBILITY CM**2/V/S	0.2060E+05
MUH= HOLE MOBILITY CM**2/V/S	0.2950E+03
QBG= BKGD PHOTON FLUX DENSITY P/CM**2/S	0.7120E+15
QS = SGNL PHOTON FLUX DENSITY P/CM**2/S	0.1900E+14
TRF= FEEDBACK RESISTOR TEMP. K	0.1600E+03
CF = FDBK RESISTOR CAPACITANCE F	0.3000E-12
RF = FEEDBACK RESISTANCE OHM	0.4982E+04
PF = FDBK RESISTOR PHASE ANGLE RAD	0.1665E-12
ZF = FDBK RESISTOR IMPEDANCE OHM	0.4982E+04
VS = SUPPLY VOLTAGE TO RF/DET. V	0.1285E+01
AO = OPEN LOOP GAIN	0.1000E+04
VP = PREAMP NOISE (INPUT) V/HZ**.5	0.2800E-08
FC = CHOPPING FREQUENCY HZ	0.4400E+03
PW = DETECTOR BIAS POWER W	0.2738E-04
PRF= FEEDBACK RESISTOR BIAS POWER W	0.2738E-03
SIGV = SIGNAL VOLTAGE V	0.3126E-04
RE = DET. RESPONSIVITY V/W	0.1189E+05
AZ = TRANSIMPEDANCE OHM	0.5032E+04
R = DET./PREAMP RESPONSIVITY V/W	0.1201E+06
VBG= BACKGROUND NOISE V/HZ**.5	0.2053E-08
VJN= JOHNSON NOISE V/HZ**.5	0.1451E-07
VGR= GR NOISE V/HZ**.5	0.2908E-07
VRF= FDBK RESISTOR JOHNSON NOISE V/HZ**.5	0.6702E-08
VPA= PREAMP NOISE V/HZ**.5	0.2770E-07
VT = TOTAL NOISE V/HZ**.5	0.4327E-07
NEP= NOISE EQUIVALENT POWER W/HZ**.5	0.3603E-12
DSTAR = PEAK DSTAR CM*HZ**.5/W	0.5531E+11

PC HGCDTE DETECTOR PERFORMANCE CHANNEL 10 75/160/STD 6 V/CM

CH = CHANNEL NUMBER	0.1000E+02
T = DET. TEMP	0.7500E+02
HD = DET. HEIGHT CM	0.1360E-01
WD = DET. WIDTH CM	0.2920E-01
TD = DETECTOR THICKNESS CM	0.1000E-02
VB = DETECTOR BIAS VOLTAGE V	0.1752E+00
CD = DETECTOR CAPACITANCE F	0.1500E-10
RD = DETECTOR DARK RESISTANCE OHM	0.4982E+03
ZD = DETECTOR IMPEDANCE OHM	0.4982E+03
PD = DETECTOR PHASE ANGLE RAD	0.8324E-10
X = MOLE FRACTION	0.1838E+00
PO = HOLE CONC. N-TYPE DOPING CM**-3	0.1000E+15
ND = DONAR CARRIER CONC. CM**-3	0.1305E+16
NI = INTRINSIC CARRIER CONC. CM**-3	0.3612E+15
TAU= CARRIER LIFETIME S	0.1000E-05
ETA= QUANTUM EFFICIENCY	0.7000E+00
NUP= PEAK WAVENUMBER 1/CM	0.6068E+03
EG = BAND GAP ENERGY EV	0.6847E-01
SIGMA = CONDUCTIVITY 1/OHM/CM	0.4310E+01
MU = ELECTRON MOBILITY CM**2/V/S	0.2060E+05
MUH= HOLE MOBILITY CM**2/V/S	0.2950E+03
QBG= BKGD PHOTON FLUX DENSITY P/CM**2/S	0.7120E+15
QS = SGNL PHOTON FLUX DENSITY P/CM**2/S	0.1900E+14
TRF= FEEDBACK RESISTOR TEMP. K	0.1600E+03
CF = FDBK RESISTOR CAPACITANCE F	0.3000E-12
RF = FEEDBACK RESISTANCE OHM	0.4982E+04
PF = FDBK RESISTOR PHASE ANGLE RAD	0.1665E-12
ZF = FDBK RESISTOR IMPEDANCE OHM	0.4982E+04
VS = SUPPLY VOLTAGE TO RF/DET. V	0.1927E+01
AO = OPEN LOOP GAIN	0.1000E+04
VP = PREAMP NOISE (INPUT) V/HZ**.5	0.2800E-08
FC = CHOPPING FREQUENCY HZ	0.4400E+03
PW = DETECTOR BIAS POWER W	0.6162E-04
PRF= FEEDBACK RESISTOR BIAS POWER W	0.6162E-03
SIGV = SIGNAL VOLTAGE V	0.7035E-04
RE = DET. RESPONSIVITY V/W	0.1783E+05
AZ = TRANSIMPEDANCE OHM	0.5032E+04
R = DET./PREAMP RESPONSIVITY V/W	0.1801E+06
VBG= BACKGROUND NOISE V/HZ**.5	0.3080E-08
VJN= JOHNSON NOISE V/HZ**.5	0.1451E-07
VGR= GR NOISE V/HZ**.5	0.4362E-07
VRF= FDBK RESISTOR JOHNSON NOISE V/HZ**.5	0.6702E-08
VPA= PREAMP NOISE V/HZ**.5	0.2770E-07
VT = TOTAL NOISE V/HZ**.5	0.5417E-07
NEP= NOISE EQUIVALENT POWER W/HZ**.5	0.3007E-12
DSTAR = PEAK DSTAR CM*HZ**.5/W	0.6627E+11

PC HGCDTE DETECTOR PERFORMANCE CHANNEL 10 75/160/STD 8 V/CM

CH = CHANNEL NUMBER	0.1000E+02
T = DET. TEMP	0.7500E+02
HD = DET. HEIGHT CM	0.1360E-01
WD = DET. WIDTH CM	0.2920E-01
TD = DETECTOR THICKNESS CM	0.1000E-02
VB = DETECTOR BIAS VOLTAGE V	0.2336E+00
CD = DETECTOR CAPACITANCE F	0.1500E-10
RD = DETECTOR DARK RESISTANCE OHM	0.4982E+03
ZD = DETECTOR IMPEDANCE OHM	0.4982E+03
PD = DETECTOR PHASE ANGLE RAD	0.8324E-10
X = MOLE FRACTION	0.1838E+00
PO = HOLE CONC. N-TYPE DOPING CM**-3	0.1000E+15
ND = DONAR CARRIER CONC. CM**-3	0.1305E+16
NI = INTRINSIC CARRIER CONC. CM**-3	0.3612E+15
TAU= CARRIER LIFETIME S	0.1000E-05
ETA= QUANTUM EFFICIENCY	0.7000E+00
NUP= PEAK WAVENUMBER 1/CM	0.6068E+03
EG = BAND GAP ENERGY EV	0.6847E-01
SIGMA = CONDUCTIVITY 1/OHM/CM	0.4310E+01
MU = ELECTRON MOBILITY CM**2/V/S	0.2060E+05
MUH= HOLE MOBILITY CM**2/V/S	0.2950E+03
QBG= BKGD PHOTON FLUX DENSITY P/CM**2/S	0.7120E+15
QS = SGNL PHOTON FLUX DENSITY P/CM**2/S	0.1900E+14
TR1= FEEDBACK RESISTOR TEMP. K	0.1600E+03
C1 = FDBK RESISTOR CAPACITANCE F	0.3000E-12
R1 = FEEDBACK RESISTANCE OHM	0.4982E+04
P1 = FDBK RESISTOR PHASE ANGLE RAD	0.1665E-12
Z1 = FDBK RESISTOR IMPEDANCE OHM	0.4982E+04
VS = SUPPLY VOLTAGE TO R1/DET. V	0.2570E+01
AO = OPEN LOOP GAIN	0.1000E+04
VP = PREAMP NOISE (INPUT) V/HZ**.5	0.2800E-08
FC = CHOPPING FREQUENCY HZ	0.4400E+03
PW = DETECTOR BIAS POWER W	0.1095E-03
PR1= FEEDBACK RESISTOR BIAS POWER W	0.1095E-02
SIGV = SIGNAL VOLTAGE V	0.1251E-03
RE = DET. RESPONSIVITY V/W	0.2378E+05
AZ = TRANSIMPEDANCE OHM	0.5032E+04
R = DET./PREAMP RESPONSIVITY V/W	0.2402E+06
VBG= BACKGROUND NOISE V/HZ**.5	0.4106E-08
VJN= JOHNSON NOISE V/HZ**.5	0.1451E-07
VGR= GR NOISE V/HZ**.5	0.5816E-07
VNR= FDBK RESISTOR NOISE V/HZ**.5	0.6702E-08
VPA= PREAMP NOISE V/HZ**.5	0.2770E-07
VT = TOTAL NOISE V/HZ**.5	0.6650E-07
NEP= NOISE EQUIVALENT POWER W/HZ**.5	0.2769E-12
DSTAR = PEAK DSTAR CM*HZ**.5/W	0.7198E+11

Table F-5 (CH 10)b

PC HGCDTE DETECTOR PERFORMANCE CHANNEL 10 75/160/STD 10 V/CM

CH = CHANNEL NUMBER	0.1000E+02
T = DET. TEMP	0.7500E+02
HD = DET. HEIGHT CM	0.1360E-01
WD = DET. WIDTH CM	0.2920E-01
TD = DETECTOR THICKNESS CM	0.1000E-02
VB = DETECTOR BIAS VOLTAGE V	0.2920E+00
CD = DETECTOR CAPACITANCE F	0.1500E-10
RD = DETECTOR DARK RESISTANCE OHM	0.4982E+03
ZD = DETECTOR IMPEDANCE OHM	0.4982E+03
PD = DETECTOR PHASE ANGLE RAD	0.8324E-10
X = MOLE FRACTION	0.1830E+00
PO = HOLE CONC. N-TYPE DOPING CM**-3	0.1000E+15
ND = DONAR CARRIER CONC. CM**-3	0.1305E+16
NI = INTRINSIC CARRIER CONC. CM**-3	0.3612E+15
TAU= CARRIER LIFETIME S	0.1000E-05
ETA= QUANTUM EFFICIENCY	0.7000E+00
NUP= PEAK WAVENUMBER 1/CM	0.6068E+03
EG = BAND GAP ENERGY EV	0.6847E-01
SIGMA = CONDUCTIVITY 1/OHM/CM	0.4310E+01
MU = ELECTRON MOBILITY CM**2/V/S	0.2060E+05
MUH= HOLE MOBILITY CM**2/V/S	0.2950E+03
QBG= BKGD PHOTON FLUX DENSITY P/CM**2/S	0.7120E+15
QS = SGNL PHOTON FLUX DENSITY P/CM**2/S	0.1900E+14
TRF= FEEDBACK RESISTOR TEMP, K	0.1600E+03
CF = FDBK RESISTOR CAPACITANCE F	0.3000E-12
RF = FEEDBACK RESISTANCE OHM	0.4982E+04
PF = FDBK RESISTOR PHASE ANGLE RAD	0.1665E-12
ZF = FDBK RESISTOR IMPEDANCE OHM	0.4982E+04
VS = SUPPLY VOLTAGE TO RF/DET. V	0.3212E+01
AO = OPEN LOOP GAIN	0.1000E+04
VP = PREAMP NOISE (INPUT) V/HZ**.5	0.2000E-08
FC = CHOPPING FREQUENCY HZ	0.4400E+03
PW = DETECTOR BIAS POWER W	0.1712E-03
PRF= FEEDBACK RESISTOR BIAS POWER W	0.1712E-02
SIGV = SIGNAL VOLTAGE V	0.1954E-03
RE = DET. RESPONSIVITY V/W	0.2972E+05
AZ = TRANSIMPEDANCE OHM	0.5032E+04
R = DET./PREAMP RESPONSIVITY V/W	0.3003E+06
VBG= BACKGROUND NOISE V/HZ**.5	0.5133E-08
VJN= JOHNSON NOISE V/HZ**.5	0.1451E-07
VGR= GR NOISE V/HZ** 5	0.7270E-07
VRF= FDBK RESISTOR JOHNSON NOISE V/HZ**.5	0.6702E-08
VPA= PREAMP NOISE V/HZ**.5	0.2770E-07
VT = TOTAL NOISE V/HZ**.5	0.7959E-07
NEP= NOISE EQUIVALENT POWER W/HZ**.5	0.2651E-12
DSTAR = PEAK DSTAR CM*HZ**.5/W	0.7517E+11

PC HGCDTE DETECTOR PERFORMANCE CHANNEL 10 75/160/STD 12 V/CM

CH = CHANNEL NUMBER	0.1000E+02
T = DET. TEMP	0.7500E+02
HD = DET. HEIGHT CM	0.1360E-01
WD = DET. WIDTH CM	0.2920E-01
TD = DETECTOR THICKNESS CM	0.1000E-02
VB = DETECTOR BIAS VOLTAGE V	0.3504E+00
CD = DETECTOR CAPACITANCE F	0.1500E-10
RD = DETECTOR DARK RESISTANCE OHM	0.4982E+03
ZD = DETECTOR IMPEDANCE OHM	0.4982E+03
PD = DETECTOR PHASE ANGLE RAD	0.8324E-10
X = MOLE FRACTION	0.1830E+00
PO = HOLE CONC. N-TYPE DOPING CM**-3	0.1000E+15
ND = DONAR CARRIER CONC. CM**-3	0.1305E+16
NI = INTRINSIC CARRIER CONC. CM**-3	0.3612E+15
TAU= CARRIER LIFETIME S	0.1000E-05
ETA= QUANTUM EFFICIENCY	0.7000E+00
NUP= PEAK WAVENUMBER 1/CM	0.6068E+03
EG = BAND GAP ENERGY EV	0.6847E-01
SIGMA = CONDUCTIVITY 1/OHM/CM	0.4310E+01
MU = ELECTRON MOBILITY CM**2/V/S	0.2060E+05
MUH= HOLE MOBILITY CM**2/V/S	0.2950E+03
QBG= BKGD PHOTON FLUX DENSITY P/CM**2/S	0.7120E+15
QS = SGNL PHOTON FLUX DENSITY P/CM**2/S	0.1900E+14
TRF= FEEDBACK RESISTOR TEMP, K	0.1600E+03
CF = FDBK RESISTOR CAPACITANCE F	0.3000E-12
RF = FEEDBACK RESISTANCE OHM	0.4982E+04
PF = FDBK RESISTOR PHASE ANGLE RAD	0.1665E-12
ZF = FDBK RESISTOR IMPEDANCE OHM	0.4982E+04
VS = SUPPLY VOLTAGE TO RF/DET. V	0.3654E+01
AO = OPEN LOOP GAIN	0.1000E+04
VP = PREAMP NOISE (INPUT) V/HZ**.5	0.2000E-08
FC = CHOPPING FREQUENCY HZ	0.4400E+03
PW = DETECTOR BIAS POWER W	0.2465E-03
PRF= FEEDBACK RESISTOR BIAS POWER W	0.2465E-02
SIGV = SIGNAL VOLTAGE V	0.2814E-03
RE = DET. RESPONSIVITY V/W	0.3567E+05
AZ = TRANSIMPEDANCE OHM	0.5032E+04
R = DET./PREAMP RESPONSIVITY V/W	0.3603E+06
VBG= BACKGROUND NOISE V/HZ**.5	0.6159E-08
VJN= JOHNSON NOISE V/HZ**.5	0.1451E-07
VGR= GR NOISE V/HZ**.5	0.8724E-07
VRF= FDBK RESISTOR JOHNSON NOISE V/HZ**.5	0.6702E-08
VPA= PREAMP NOISE V/HZ**.5	0.2770E-07
VT = TOTAL NOISE V/HZ**.5	0.9312E-07
NEP= NOISE EQUIVALENT POWER W/HZ**.5	0.2585E-12
DSTAR = PEAK DSTAR CM*HZ**.5/W	0.7710E+11

PC HGCDTE DETECTOR PERFORMANCE CHANNEL 10 75/160/STD 14 V/CM

CH = CHANNEL NUMBER	0.1000E+02
T = DET. TEMP	0.7500E+02
HD = DET. HEIGHT CM	0.1360E-01
WD = DET. WIDTH CM	0.2920E-01
TD = DETECTOR THICKNESS CM	0.1000E-02
VB = DETECTOR BIAS VOLTAGE V	0.4088E+00
CD = DETECTOR CAPACITANCE F	0.1500E-10
RD = DETECTOR DARK RESISTANCE OHM	0.4982E+03
ZD = DETECTOR IMPEDANCE OHM	0.4982E+03
PD = DETECTOR PHASE ANGLE RAD	0.8324E-10
X = MOLE FRACTION	0.1830E+00
PO = HOLE CONC. N-TYPE DOPING CM**-3	0.1000E+15
ND = DONAR CARRIER CONC. CM**-3	0.1305E+16
NI = INTRINSIC CARRIER CONC. CM**-3	0.3612E+15
TAU= CARRIER LIFETIME S	0.1000E-05
ETA= QUANTUM EFFICIENCY	0.7000E+00
NUP= PEAK WAVENUMBER 1/CM	0.6068E+03
EG = BAND GAP ENERGY EV	0.6847E-01
SIGMA = CONDUCTIVITY 1/OHM/CM	0.4310E+01
MU = ELECTRON MOBILITY CM**2/V/S	0.2060E+05
MUH= HOLE MOBILITY CM**2/V/S	0.2950E+03
QBG= BKGD PHOTON FLUX DENSITY P/CM**2/S	0.7120E+15
QS = SGNL PHOTON FLUX DENSITY P/CM**2/S	0.1900E+14
TRF= FEEDBACK RESISTOR TEMP, K	0.1600E+03
CF = FDBK RESISTOR CAPACITANCE F	0.3000E-12
RF = FEEDBACK RESISTANCE OHM	0.4982E+04
PF = FDBK RESISTOR PHASE ANGLE RAD	0.1665E-12
ZF = FDBK RESISTOR IMPEDANCE OHM	0.4982E+04
VS = SUPPLY VOLTAGE TO RF/DET. V	0.4497E+01
AO = OPEN LOOP GAIN	0.1000E+04
VP = PREAMP NOISE (INPUT) V/HZ**.5	0.2000E-08
FC = CHOPPING FREQUENCY HZ	0.4400E+03
PW = DETECTOR BIAS POWER W	0.3355E-03
PRF= FEEDBACK RESISTOR BIAS POWER W	0.3355E-02
SIGV = SIGNAL VOLTAGE V	0.3830E-03
RE = DET. RESPONSIVITY V/W	0.4161E+05
AZ = TRANSIMPEDANCE OHM	0.5032E+04
R = DET./PREAMP RESPONSIVITY V/W	0.4203E+06
VBG= BACKGROUND NOISE V/HZ**.5	0.7186E-08
VJN= JOHNSON NOISE V/HZ**.5	0.1451E-07
VGR= GR NOISE V/HZ**.5	0.1018E-06
VRF= FDBK RESISTOR JOHNSON NOISE V/HZ**.5	0.6702E-08
VPA= PREAMP NOISE V/HZ**.5	0.2770E-07
VT = TOTAL NOISE V/HZ**.5	0.1069E-06
NEP= NOISE EQUIVALENT POWER W/HZ**.5	0.2544E-12
DSTAR = PEAK DSTAR CM*HZ**.5/W	0.7833E+11

PC HGCDTE DETECTOR PERFORMANCE CHANNEL 10 75/160/STD 16 V/CM

CH = CHANNEL NUMBER	0.1000E+02
T = DET. TEMP	0.7500E+02
HD = DET. HEIGHT CM	0.1360E-01
WD = DET. WIDTH CM	0.2920E-01
TD = DETECTOR THICKNESS CM	0.1000E-02
VB = DETECTOR BIAS VOLTAGE V	0.4672E+00
CD = DETECTOR CAPACITANCE F	0.1500E-10
RD = DETECTOR DARK RESISTANCE OHM	0.4982E+03
ZD = DETECTOR IMPEDANCE OHM	0.4982E+03
PD = DETECTOR PHASE ANGLE RAD	0.8324E-10
X = MOLE FRACTION	0.1830E+00
PO = HOLE CONC. N-TYPE DOPING CM**-3	0.1000E+15
ND = DONAR CARRIER CONC. CM**-3	0.1305E+16
NI = INTRINSIC CARRIER CONC. CM**-3	0.3612E+15
TAU= CARRIER LIFETIME S	0.1000E-05
ETA= QUANTUM EFFICIENCY	0.7000E+00
NUP= PEAK WAVENUMBER 1/CM	0.6068E+03
EG = BAND GAP ENERGY EV	0.6847E-01
SIGMA = CONDUCTIVITY 1/OHM/CM	0.4310E+01
MU = ELECTRON MOBILITY CM**2/V/S	0.2060E+05
MUH= HOLE MOBILITY CM**2/V/S	0.2950E+03
QBG= BKGD PHOTON FLUX DENSITY P/CM**2/S	0.7120E+15
QS = SGNL PHOTON FLUX DENSITY P/CM**2/S	0.1900E+14
TRF= FEEDBACK RESISTOR TEMP, K	0.1600E+03
CF = FDBK RESISTOR CAPACITANCE F	0.3000E-12
RF = FEEDBACK RESISTANCE OHM	0.4982E+04
PF = FDBK RESISTOR PHASE ANGLE RAD	0.1665E-12
ZF = FDBK RESISTOR IMPEDANCE OHM	0.4982E+04
VS = SUPPLY VOLTAGE TO RF/DET. V	0.5139E+01
AO = OPEN LOOP GAIN	0.1000E+04
VP = PREAMP NOISE (INPUT) V/HZ**.5	0.2000E-08
FC = CHOPPING FREQUENCY HZ	0.4400E+03
PW = DETECTOR BIAS POWER W	0.4382E-03
PRF= FEEDBACK RESISTOR BIAS POWER W	0.4382E-02
SIGV = SIGNAL VOLTAGE V	0.5002E-03
RE = DET. RESPONSIVITY V/W	0.4756E+05
AZ = TRANSIMPEDANCE OHM	0.5032E+04
R = DET./PREAMP RESPONSIVITY V/W	0.4804E+06
VBG= BACKGROUND NOISE V/HZ**.5	0.8212E-08
VJN= JOHNSON NOISE V/HZ**.5	0.1451E-07
VGR= GR NOISE V/HZ**.5	0.1163E-06
VRF= FDBK RESISTOR JOHNSON NOISE V/HZ**.5	0.6702E-08
VPA= PREAMP NOISE V/HZ**.5	0.2770E-07
VT = TOTAL NOISE V/HZ**.5	0.1209E-06
NEP= NOISE EQUIVALENT POWER W/HZ**.5	0.2517E-12
DSTAR = PEAK DSTAR CM*HZ**.5/W	0.7917E+11

Table F-5 (CH 11)a

PC HGCDTE DETECTOR PERFORMANCE CHANNEL 11 75/160/STD 2 V/CM

CH = CHANNEL NUMBER	0.1100E+02
T = DET. TEMP	0.7500E+02
HD = DET. HEIGHT CM	0.1360E-01
WD = DET. WIDTH CM	0.3190E-01
TD = DETECTOR THICKNESS CM	0.1000E-02
VB = DETECTOR BIAS VOLTAGE V	0.6300E-01
CD = DETECTOR CAPACITANCE F	0.1500E-10
RD = DETECTOR DARK RESISTANCE OHM	0.7215E+03
ZD = DETECTOR IMPEDANCE OHM	0.7215E+03
PD = DETECTOR PHASE ANGLE RAD	0.5747E-10
X = MOLE FRACTION	0.2835E+00
PO = HOLE CONC. N-TYPE DOPING CM**-3	0.2000E+13
ND = DONAR CARRIER CONC. CM**-3	0.1010E+16
NI = INTRINSIC CARRIER CONC. CM**-3	0.4493E+14
TAU= CARRIER LIFETIME S	0.1000E-05
ETA= QUANTUM EFFICIENCY	0.7000E+00
NUP= PEAK WAVENUMBER 1/CM	0.8745E+03
EG = BAND GAP ENERGY EV	0.9091E-01
SIGMA = CONDUCTIVITY 1/OHM/CM	0.3251E+01
MU = ELECTRON MOBILITY CM**2/V/S	0.2010E+05
MUH= HOLE MOBILITY CM**2/V/S	0.2920E+03
QBG= BKGD PHOTON FLUX DENSITY P/CM**2/S	0.2810E+16
QS = SGNL PHOTON FLUX DENSITY P/CM**2/S	0.1810E+15
TRF= FEEDBACK RESISTOR TEMP. K	0.1600E+03
CF = FDBK RESISTOR CAPACITANCE F	0.3000E-12
RF = FEEDBACK RESISTANCE OHM	0.7215E+04
PF = FDBK RESISTOR PHASE ANGLE RAD	0.1149E-12
ZF = FDBK RESISTOR IMPEDANCE OHM	0.7215E+04
VS = SUPPLY VOLTAGE TO RF/DET. V	0.7018E+00
AO = OPEN LOOP GAIN	0.1000E+04
VP = PREAMP NOISE (INPUT) V/HZ**.5	0.2800E-08
FC = CHOPPING FREQUENCY HZ	0.4400E+03
PW = DETECTOR BIAS POWER W	0.5641E-05
PRF= FEEDBACK RESISTOR BIAS POWER W	0.5641E-04
SIGV = SIGNAL VOLTAGE V	0.9400E-04
RE = DET. RESPONSIVITY V/W	0.5336E+04
AZ = TRANSIMPEDANCE OHM	0.7208E+04
R = DET./PREAMP RESPONSIVITY V/W	0.5390E+05
VBG= BACKGROUND NOISE V/HZ**.5	0.2759E-08
VJN= JOHNSON NOISE V/HZ**.5	0.1746E-07
VGR= GR NOISE V/HZ**.5	0.2781E-08
VRF= FDBK RESISTOR JOHNSON NOISE V/HZ**.5	0.8065E-08
VPA= PREAMP NOISE V/HZ**.5	0.2770E-07
VT = TOTAL NOISE V/HZ**.5	0.3395E-07
NEP= NOISE EQUIVALENT POWER W/HZ**.5	0.6290E-12
DSTAR = PEAK DSTAR CM*HZ**.5/W	0.3307E+11

PC HGCDTE DETECTOR PERFORMANCE CHANNEL 11 75/160/STD 4 V/CM

CH = CHANNEL NUMBER	0.1100E+02
T = DET. TEMP	0.7500E+02
HD = DET. HEIGHT CM	0.1360E-01
WD = DET. WIDTH CM	0.3190E-01
TD = DETECTOR THICKNESS CM	0.1000E-02
VB = DETECTOR BIAS VOLTAGE V	0.1260E+00
CD = DETECTOR CAPACITANCE F	0.1500E-10
RD = DETECTOR DARK RESISTANCE OHM	0.7215E+03
ZD = DETECTOR IMPEDANCE OHM	0.7215E+03
PD = DETECTOR PHASE ANGLE RAD	0.5747E-10
X = MOLE FRACTION	0.2835E+00
PO = HOLE CONC. N-TYPE DOPING CM**-3	0.2000E+13
ND = DONAR CARRIER CONC. CM**-3	0.1010E+16
NI = INTRINSIC CARRIER CONC. CM**-3	0.4493E+14
TAU= CARRIER LIFETIME S	0.1000E-05
ETA= QUANTUM EFFICIENCY	0.7000E+00
NUP= PEAK WAVENUMBER 1/CM	0.8745E+03
EG = BAND GAP ENERGY EV	0.9091E-01
SIGMA = CONDUCTIVITY 1/OHM/CM	0.3251E+01
MU = ELECTRON MOBILITY CM**2/V/S	0.2010E+05
MUH= HOLE MOBILITY CM**2/V/S	0.2920E+03
QBG= BKGD PHOTON FLUX DENSITY P/CM**2/S	0.2810E+16
QS = SGNL PHOTON FLUX DENSITY P/CM**2/S	0.1810E+15
TRF= FEEDBACK RESISTOR TEMP. K	0.1600E+03
CF = FDBK RESISTOR CAPACITANCE F	0.3000E-12
RF = FEEDBACK RESISTANCE OHM	0.7215E+04
PF = FDBK RESISTOR PHASE ANGLE RAD	0.1149E-12
ZF = FDBK RESISTOR IMPEDANCE OHM	0.7215E+04
VS = SUPPLY VOLTAGE TO RF/DET. V	0.1404E+01
AO = OPEN LOOP GAIN	0.1000E+04
VP = PREAMP NOISE (INPUT) V/HZ**.5	0.2800E-08
FC = CHOPPING FREQUENCY HZ	0.4400E+03
PW = DETECTOR BIAS POWER W	0.2257E-04
PRF= FEEDBACK RESISTOR BIAS POWER W	0.2257E-03
SIGV = SIGNAL VOLTAGE V	0.3760E-03
RE = DET. RESPONSIVITY V/W	0.1067E+05
AZ = TRANSIMPEDANCE OHM	0.7208E+04
R = DET./PREAMP RESPONSIVITY V/W	0.1078E+05
VBG= BACKGROUND NOISE V/HZ**.5	0.5516E-08
VJN= JOHNSON NOISE V/HZ**.5	0.1746E-07
VGR= GR NOISE V/HZ**.5	0.5562E-08
VRF= FDBK RESISTOR JOHNSON NOISE V/HZ**.5	0.8065E-08
VPA= PREAMP NOISE V/HZ**.5	0.2770E-07
VT = TOTAL NOISE V/HZ**.5	0.3462E-07
NEP= NOISE EQUIVALENT POWER W/HZ**.5	0.3211E-12
DSTAR = PEAK DSTAR CM*HZ**.5/W	0.6486E+11

PC HGCDTE DETECTOR PERFORMANCE CHANNEL 11 75/160/STD 6 V/CM

CH = CHANNEL NUMBER	0.1100E+02
T = DET. TEMP	0.7500E+02
HD = DET. HEIGHT CM	0.1360E-01
WD = DET. WIDTH CM	0.3190E-01
TD = DETECTOR THICKNESS CM	0.1000E-02
VB = DETECTOR BIAS VOLTAGE V	0.1914E+00
CD = DETECTOR CAPACITANCE F	0.1500E-10
RD = DETECTOR DARK RESISTANCE OHM	0.7215E+03
ZD = DETECTOR IMPEDANCE OHM	0.7215E+03
PD = DETECTOR PHASE ANGLE RAD	0.5747E-10
X = MOLE FRACTION	0.2835E+00
PO = HOLE CONC. N-TYPE DOPING CM**-3	0.2000E+13
ND = DONAR CARRIER CONC. CM**-3	0.1010E+16
NI = INTRINSIC CARRIER CONC. CM**-3	0.4493E+14
TAU= CARRIER LIFETIME S	0.1000E-05
ETA= QUANTUM EFFICIENCY	0.7000E+00
NUP= PEAK WAVENUMBER 1/CM	0.8745E+03
EG = BAND GAP ENERGY EV	0.9091E-01
SIGMA = CONDUCTIVITY 1/OHM/CM	0.3251E+01
MU = ELECTRON MOBILITY CM**2/V/S	0.2010E+05
MUH= HOLE MOBILITY CM**2/V/S	0.2920E+03
QBG= BKGD PHOTON FLUX DENSITY P/CM**2/S	0.2810E+16
QS = SGNL PHOTON FLUX DENSITY P/CM**2/S	0.1810E+15
TRF= FEEDBACK RESISTOR TEMP. K	0.1600E+03
CF = FDBK RESISTOR CAPACITANCE F	0.3000E-12
RF = FEEDBACK RESISTANCE OHM	0.7215E+04
PF = FDBK RESISTOR PHASE ANGLE RAD	0.1149E-12
ZF = FDBK RESISTOR IMPEDANCE OHM	0.7215E+04
VS = SUPPLY VOLTAGE TO RF/DET. V	0.2105E+01
AO = OPEN LOOP GAIN	0.1000E+04
VP = PREAMP NOISE (INPUT) V/HZ**.5	0.2800E-08
FC = CHOPPING FREQUENCY HZ	0.4400E+03
PW = DETECTOR BIAS POWER W	0.5077E-04
PRF= FEEDBACK RESISTOR BIAS POWER W	0.5077E-03
SIGV = SIGNAL VOLTAGE V	0.8460E-03
RE = DET. RESPONSIVITY V/W	0.1601E+05
AZ = TRANSIMPEDANCE OHM	0.7208E+04
R = DET./PREAMP RESPONSIVITY V/W	0.1617E+06
VBG= BACKGROUND NOISE V/HZ**.5	0.8274E-08
VJN= JOHNSON NOISE V/HZ**.5	0.1746E-07
VGR= GR NOISE V/HZ**.5	0.8343E-08
VRF= FDBK RESISTOR JOHNSON NOISE V/HZ**.5	0.8065E-08
VPA= PREAMP NOISE V/HZ**.5	0.2770E-07
VT = TOTAL NOISE V/HZ**.5	0.3571E-07
NEP= NOISE EQUIVALENT POWER W/HZ**.5	0.2208E-12
DSTAR = PEAK DSTAR CM*HZ**.5/W	0.9432E+11

PC HGCDTE DETECTOR PERFORMANCE CHANNEL 11 75/160/STD 8 V/CM

CH = CHANNEL NUMBER	0.1100E+02
T = DET. TEMP	0.7500E+02
HD = DET. HEIGHT CM	0.1360E-01
WD = DET. WIDTH CM	0.3190E-01
TD = DETECTOR THICKNESS CM	0.1000E-02
VB = DETECTOR BIAS VOLTAGE V	0.2552E+00
CD = DETECTOR CAPACITANCE F	0.5000E-10
RD = DETECTOR DARK RESISTANCE OHM	0.7215E+03
ZD = DETECTOR IMPEDANCE OHM	0.7215E+03
PD = DETECTOR PHASE ANGLE RAD	0.1916E-09
X = MOLE FRACTION	0.2835E+00
PO = HOLE CONC. N-TYPE DOPING CM**-3	0.2000E+13
ND = DONAR CARRIER CONC. CM**-3	0.1010E+16
NI = INTRINSIC CARRIER CONC. CM**-3	0.4493E+14
TAU= CARRIER LIFETIME S	0.1000E-05
ETA= QUANTUM EFFICIENCY	0.7000E+00
NUP= PEAK WAVENUMBER 1/CM	0.8745E+03
EG = BAND GAP ENERGY EV	0.9091E-01
SIGMA = CONDUCTIVITY 1/OHM/CM	0.3251E+01
MU = ELECTRON MOBILITY CM**2/V/S	0.2010E+05
MUH= HOLE MOBILITY CM**2/V/S	0.2920E+03
QBG= BKGD PHOTON FLUX DENSITY P/CM**2/S	0.2810E+16
QS = SGNL PHOTON FLUX DENSITY P/CM**2/S	0.1810E+15
TR1= FEEDBACK RESISTOR TEMP. K	0.1600E+03
C1 = FDBK RESISTOR CAPACITANCE F	0.3000E-12
R1 = FEEDBACK RESISTANCE OHM	0.7215E+04
P1 = FDBK RESISTOR PHASE ANGLE RAD	0.1149E-12
Z1 = FDBK RESISTOR IMPEDANCE OHM	0.7215E+04
VS = SUPPLY VOLTAGE TO R1/DET. V	0.2807E+01
AO = OPEN LOOP GAIN	0.1000E+04
VP = PREAMP NOISE (INPUT) V/HZ**.5	0.2800E-08
FC = CHOPPING FREQUENCY HZ	0.4400E+03
PW = DETECTOR BIAS POWER W	0.9026E-04
PR1= FEEDBACK RESISTOR BIAS POWER W	0.9026E-03
SIGV = SIGNAL VOLTAGE V	0.1504E-02
RE = DET. RESPONSIVITY V/W	0.2134E+05
AZ = TRANSIMPEDANCE OHM	0.7208E+04
R = DET./PREAMP RESPONSIVITY V/W	0.2156E+06
VBG= BACKGROUND NOISE V/HZ**.5	0.1103E-07
VJN= JOHNSON NOISE V/HZ**.5	0.1746E-07
VNR= GR NOISE V/HZ**.5	0.1112E-07
VNR= FDBK RESISTOR NOISE V/HZ**.5	0.8065E-08
VPA= PREAMP NOISE V/HZ**.5	0.2770E-07
VT = TOTAL NOISE V/HZ**.5	0.3718E-07
NEP= NOISE EQUIVALENT POWER W/HZ**.5	0.1725E-12
DSTAR = PEAK DSTAR CM*HZ**.5/W	0.1208E+12

Table F-5 (CH 11)b

PC HGCDTE DETECTOR PERFORMANCE CHANNEL 11 75/160/STD 10 V/CM

CH = CHANNEL NUMBER	0.1100E+02
T = DET. TEMP	0.7500E+02
HD = DET. HEIGHT CM	0.1360E-01
WD = DET. WIDTH CM	0.3190E-01
TD = DETECTOR THICKNESS CM	0.1000E-02
VB = DETECTOR BIAS VOLTAGE V	0.3190E+00
CD = DETECTOR CAPACITANCE F	0.1500E-10
RD = DETECTOR DARK RESISTANCE OHM	0.7215E+03
ZD = DETECTOR IMPEDANCE OHM	0.7215E+03
PD = DETECTOR PHASE ANGLE RAD	0.5747E-10
X = MOLE FRACTION	0.2035E+00
PO = HOLE CONC. N-TYPE DOPING CM**-3	0.2000E+13
ND = DONAR CARRIER CONC. CM**-3	0.1010E+16
NI = INTRINSIC CARRIER CONC. CM**-3	0.4493E+14
TAU= CARRIER LIFETIME S	0.1000E-05
ETA= QUANTUM EFFICIENCY	0.7000E+00
NUP= PEAK WAVENUMBER 1/CM	0.8745E+03
EG = BAND GAP ENERGY EV	0.9891E-01
SIGMA = CONDUCTIVITY 1/OHM/CM	0.3251E+01
MU = ELECTRON MOBILITY CM**2/V/S	0.2010E+05
MUH= HOLE MOBILITY CM**2/V/S	0.2920E+03
QBG= BKGD PHOTON FLUX DENSITY P/CM**2/S	0.2810E+16
QS = SGNL PHOTON FLUX DENSITY P/CM**2/S	0.1810E+15
TRF= FEEDBACK RESISTOR TEMP. K	0.1600E+03
CF = FDBK RESISTOR CAPACITANCE F	0.3000E-12
RF = FEEDBACK RESISTANCE OHM	0.7215E+04
PF = FDBK RESISTOR PHASE ANGLE RAD	0.1149E-12
ZF = FDBK RESISTOR IMPEDANCE OHM	0.7215E+04
VS = SUPPLY VOLTAGE TO RF/DET. V	0.3589E+01
AO = OPEN LOOP GAIN	0.1000E+04
VP = PREAMP NOISE (INPUT) V/HZ**.5	0.2800E-08
FC = CHOPPING FREQUENCY HZ	0.4400E+03
PW = DETECTOR BIAS POWER W	0.1418E-03
PRF= FEEDBACK RESISTOR BIAS POWER W	0.1418E-02
SIGV = SIGNAL VOLTAGE V	0.2350E-02
RE = DET. RESPONSIVITY V/W	0.2660E+05
AZ = TRANSIMPEDANCE OHM	0.7208E+04
R = DET./PREAMP RESPONSIVITY V/W	0.2695E+06
VBG= BACKGROUND NOISE V/HZ**.5	0.1379E-07
VJN= JOHNSON NOISE V/HZ**.5	0.1746E-07
VGR= GR NOISE V/HZ**.5	0.1398E-07
VRF= FDBK RESISTOR JOHNSON NOISE V/HZ**.5	0.8065E-08
VPA= PREAMP NOISE V/HZ**.5	0.2770E-07
VT = TOTAL NOISE V/HZ**.5	0.3899E-07
NEP= NOISE EQUIVALENT POWER W/HZ**.5	0.1447E-12
D STAR = PEAK DSTAR CM*HZ**.5/W	0.1440E+12

PC HGCDTE DETECTOR PERFORMANCE CHANNEL 11 75/160/STD 12 V/CM

CH = CHANNEL NUMBER	0.1100E+02
T = DET. TEMP	0.7500E+02
HD = DET. HEIGHT CM	0.1360E-01
WD = DET. WIDTH CM	0.3190E-01
TD = DETECTOR THICKNESS CM	0.1000E-02
VB = DETECTOR BIAS VOLTAGE V	0.3828E+00
CD = DETECTOR CAPACITANCE F	0.1500E-10
RD = DETECTOR DARK RESISTANCE OHM	0.7215E+03
ZD = DETECTOR IMPEDANCE OHM	0.7215E+03
PD = DETECTOR PHASE ANGLE RAD	0.5747E-10
X = MOLE FRACTION	0.2035E+00
PO = HOLE CONC. N-TYPE DOPING CM**-3	0.2000E+13
ND = DONAR CARRIER CONC. CM**-3	0.1010E+16
NI = INTRINSIC CARRIER CONC. CM**-3	0.4493E+14
TAU= CARRIER LIFETIME S	0.1000E-05
ETA= QUANTUM EFFICIENCY	0.7000E+00
NUP= PEAK WAVENUMBER 1/CM	0.8745E+03
EG = BAND GAP ENERGY EV	0.9891E-01
SIGMA = CONDUCTIVITY 1/OHM/CM	0.3251E+01
MU = ELECTRON MOBILITY CM**2/V/S	0.2010E+05
MUH= HOLE MOBILITY CM**2/V/S	0.2920E+03
QBG= BKGD PHOTON FLUX DENSITY P/CM**2/S	0.2810E+16
QS = SGNL PHOTON FLUX DENSITY P/CM**2/S	0.1810E+15
TRF= FEEDBACK RESISTOR TEMP. K	0.1600E+03
CF = FDBK RESISTOR CAPACITANCE F	0.3000E-12
RF = FEEDBACK RESISTANCE OHM	0.7215E+04
PF = FDBK RESISTOR PHASE ANGLE RAD	0.1149E-12
ZF = FDBK RESISTOR IMPEDANCE OHM	0.7215E+04
VS = SUPPLY VOLTAGE TO RF/DET. V	0.4211E+01
AO = OPEN LOOP GAIN	0.1000E+04
VP = PREAMP NOISE (INPUT) V/HZ**.5	0.2800E-08
FC = CHOPPING FREQUENCY HZ	0.4400E+03
PW = DETECTOR BIAS POWER W	0.2031E-03
PRF= FEEDBACK RESISTOR BIAS POWER W	0.2031E-02
SIGV = SIGNAL VOLTAGE V	0.3304E-02
RE = DET. RESPONSIVITY V/W	0.3202E+05
AZ = TRANSIMPEDANCE OHM	0.7208E+04
R = DET./PREAMP RESPONSIVITY V/W	0.3234E+06
VBG= BACKGROUND NOISE V/HZ**.5	0.1655E-07
VJN= JOHNSON NOISE V/HZ**.5	0.1746E-07
VGR= GR NOISE V/HZ**.5	0.1669E-07
VRF= FDBK RESISTOR JOHNSON NOISE V/HZ**.5	0.8065E-08
VPA= PREAMP NOISE V/HZ**.5	0.2770E-07
VT = TOTAL NOISE V/HZ**.5	0.4118E-07
NEP= NOISE EQUIVALENT POWER W/HZ**.5	0.1271E-12
DSTAR = PEAK DSTAR CM*HZ**.5/W	0.1639E+12

PC HGCDTE DETECTOR PERFORMANCE CHANNEL 11 75/160/STD 14 V/CM

CH = CHANNEL NUMBER	0.1100E+02
T = DET. TEMP	0.7500E+02
HD = DET. HEIGHT CM	0.1360E-01
WD = DET. WIDTH CM	0.3190E-01
TD = DETECTOR THICKNESS CM	0.1000E-02
VB = DETECTOR BIAS VOLTAGE V	0.4466E+00
CD = DETECTOR CAPACITANCE F	0.1500E-10
RD = DETECTOR DARK RESISTANCE OHM	0.7215E+03
ZD = DETECTOR IMPEDANCE OHM	0.7215E+03
PD = DETECTOR PHASE ANGLE RAD	0.5747E-10
X = MOLE FRACTION	0.2035E+00
PO = HOLE CONC. N-TYPE DOPING CM**-3	0.2000E+13
ND = DONAR CARRIER CONC. CM**-3	0.1010E+16
NI = INTRINSIC CARRIER CONC. CM**-3	0.4493E+14
TAU= CARRIER LIFETIME S	0.1000E-05
ETA= QUANTUM EFFICIENCY	0.7000E+00
NUP= PEAK WAVENUMBER 1/CM	0.8745E+03
EG = BAND GAP ENERGY EV	0.9891E-01
SIGMA = CONDUCTIVITY 1/OHM/CM	0.3251E+01
MU = ELECTRON MOBILITY CM**2/V/S	0.2010E+05
MUH= HOLE MOBILITY CM**2/V/S	0.2920E+03
QBG= BKGD PHOTON FLUX DENSITY P/CM**2/S	0.2810E+16
QS = SGNL PHOTON FLUX DENSITY P/CM**2/S	0.1810E+15
TRF= FEEDBACK RESISTOR TEMP. K	0.1600E+03
CF = FDBK RESISTOR CAPACITANCE F	0.3000E-12
RF = FEEDBACK RESISTANCE OHM	0.7215E+04
PF = FDBK RESISTOR PHASE ANGLE RAD	0.1149E-12
ZF = FDBK RESISTOR IMPEDANCE OHM	0.7215E+04
VS = SUPPLY VOLTAGE TO RF/DET. V	0.4913E+01
AO = OPEN LOOP GAIN	0.1000E+04
VP = PREAMP NOISE (INPUT) V/HZ**.5	0.2800E-08
FC = CHOPPING FREQUENCY HZ	0.4400E+03
PW = DETECTOR BIAS POWER W	0.2764E-03
PRF= FEEDBACK RESISTOR BIAS POWER W	0.2764E-02
SIGV = SIGNAL VOLTAGE V	0.4606E-02
RE = DET. RESPONSIVITY V/W	0.3735E+05
AZ = TRANSIMPEDANCE OHM	0.7208E+04
R = DET./PREAMP RESPONSIVITY V/W	0.3773E+06
VBG= BACKGROUND NOISE V/HZ**.5	0.1931E-07
VJN= JOHNSON NOISE V/HZ**.5	0.1746E-07
VGR= GR NOISE V/HZ**.5	0.1947E-07
VRF= FDBK RESISTOR JOHNSON NOISE V/HZ**.5	0.8065E-08
VPA= PREAMP NOISE V/HZ**.5	0.2770E-07
VT = TOTAL NOISE V/HZ**.5	0.4346E-07
NEP= NOISE EQUIVALENT POWER W/HZ**.5	0.1152E-12
DSTAR = PEAK DSTAR CM*HZ**.5/W	0.1808E+12

PC HGCDTE DETECTOR PERFORMANCE CHANNEL 11 75/160/STD 16 V/CM

CH = CHANNEL NUMBER	0.1100E+02
T = DET. TEMP	0.7500E+02
HD = DET. HEIGHT CM	0.1360E-01
WD = DET. WIDTH CM	0.3190E-01
TD = DETECTOR THICKNESS CM	0.1000E-02
VB = DETECTOR BIAS VOLTAGE V	0.5104E+00
CD = DETECTOR CAPACITANCE F	0.1500E-10
RD = DETECTOR DARK RESISTANCE OHM	0.7215E+03
ZD = DETECTOR IMPEDANCE OHM	0.7215E+03
PD = DETECTOR PHASE ANGLE RAD	0.5747E-10
X = MOLE FRACTION	0.2035E+00
PO = HOLE CONC. N-TYPE DOPING CM**-3	0.2000E+13
ND = DONAR CARRIER CONC. CM**-3	0.1010E+16
NI = INTRINSIC CARRIER CONC. CM**-3	0.4493E+14
TAU= CARRIER LIFETIME S	0.1000E-05
ETA= QUANTUM EFFICIENCY	0.7000E+00
NUP= PEAK WAVENUMBER 1/CM	0.8745E+03
EG = BAND GAP ENERGY EV	0.9891E-01
SIGMA = CONDUCTIVITY 1/OHM/CM	0.3251E+01
MU = ELECTRON MOBILITY CM**2/V/S	0.2010E+05
MUH= HOLE MOBILITY CM**2/V/S	0.2920E+03
QBG= BKGD PHOTON FLUX DENSITY P/CM**2/S	0.2810E+16
QS = SGNL PHOTON FLUX DENSITY P/CM**2/S	0.1810E+15
TRF= FEEDBACK RESISTOR TEMP. K	0.1600E+03
CF = FDBK RESISTOR CAPACITANCE F	0.3000E-12
RF = FEEDBACK RESISTANCE OHM	0.7215E+04
PF = FDBK RESISTOR PHASE ANGLE RAD	0.1149E-12
ZF = FDBK RESISTOR IMPEDANCE OHM	0.7215E+04
VS = SUPPLY VOLTAGE TO RF/DET. V	0.5614E+01
AO = OPEN LOOP GAIN	0.1000E+04
VP = PREAMP NOISE (INPUT) V/HZ**.5	0.2800E-08
FC = CHOPPING FREQUENCY HZ	0.4400E+03
PW = DETECTOR BIAS POWER W	0.3611E-03
PRF= FEEDBACK RESISTOR BIAS POWER W	0.3611E-02
SIGV = SIGNAL VOLTAGE V	0.6016E-02
RE = DET. RESPONSIVITY V/W	0.4269E+05
AZ = TRANSIMPEDANCE OHM	0.7208E+04
R = DET./PREAMP RESPONSIVITY V/W	0.4312E+06
VBG= BACKGROUND NOISE V/HZ**.5	0.2206E-07
VJN= JOHNSON NOISE V/HZ**.5	0.1746E-07
VGR= GR NOISE V/HZ**.5	0.2225E-07
VRF= FDBK RESISTOR JOHNSON NOISE V/HZ**.5	0.8065E-08
VPA= PREAMP NOISE V/HZ**.5	0.2770E-07
VT = TOTAL NOISE V/HZ**.5	0.4603E-07
NEP= NOISE EQUIVALENT POWER W/HZ**.5	0.1068E-12
DSTAR = PEAK DSTAR CM*HZ**.5/W	0.1951E+12

Table F-6. Detector performance as a function of detector and case temperature for a selected set of AMTS channels

PRECEDING PAGE BLANK NOT FILMED

Table F-6 (CH 1)

PC HGCDTE DETECTOR PERFORMANCE CHANNEL 1 75/160/STD 8 V/CM

CH = CHANNEL NUMBER	0.1000E+01
T = DET. TEMP	0.7500E+02
HD = DET. HEIGHT CM	0.1360E-01
WD = DET. WIDTH CM	0.1990E-01
TD = DETECTOR THICKNESS CM	0.1000E-02
VB = DETECTOR BIAS VOLTAGE V	0.1592E+00
CD = DETECTOR CAPACITANCE F	0.1500E-10
RD = DETECTOR DARK RESISTANCE OHM	0.3395E+03
ZD = DETECTOR IMPEDANCE OHM	0.3395E+03
PD = DETECTOR PHASE ANGLE RAD	0.1221E-09
X = MOLE FRACTION	0.1838E+00
PO = HOLE CONC, N-TYPE DOPING CM**-3	0.1000E+15
ND = DONAR CARRIER CONC, CM**-3	0.1305E+16
NI = INTRINSIC CARRIER CONC. CM**-3	0.3612E+15
TAU= CARRIER LIFETIME S	0.1000E-05
ETA= QUANTUM EFFICIENCY	0.7000E+00
NUP= PEAK WAVENUMBER 1/CM	0.6066E+03
EG = BAND GAP ENERGY EV	0.6847E-01
SIGMA = CONDUCTIVITY 1/OHM/CM	0.4310E+01
MU = ELECTRON MOBILITY CM**2/V/S	0.2060E+05
MUH= HOLE MOBILITY CM**2/V/S	0.2950E+03
QBG= BKGD PHOTON FLUX DENSITY P/CM**2/S	0.1340E+16
QS = SGNL PHOTON FLUX DENSITY P/CM**2/S	0.5300E+14
TRF= FEEDBACK RESISTOR TEMP, K	0.1600E+03
CF = FDBK RESISTOR CAPACITANCE F	0.3000E-12
RF = FEEDBACK RESISTANCE OHM	0.3395E+04
PF = FDBK RESISTOR PHASE ANGLE RAD	0.2443E-12
ZF = FDBK RESISTOR IMPEDANCE OHM	0.3395E+04
VS = SUPPLY VOLTAGE TO RF/DET. V	0.1751E+01
AO = OPEN LOOP GAIN	0.1000E+04
VP = PREAMP NOISE (INPUT) V/HZ**.5	0.2800E-08
FC = CHOPPING FREQUENCY HZ	0.4400E+03
PW = DETECTOR BIAS POWER W	0.7465E-04
PRF= FEEDBACK RESISTOR BIAS POWER W	0.7465E-03
SIGV = SIGNAL VOLTAGE V	0.3488E-03
RE = DET. RESPONSIVITY V/W	0.2378E+05
AZ = TRANSIMPEDANCE OHM	0.3429E+04
R = DET./PREAMP RESPONSIVITY V/W	0.2402E+06
VBG= BACKGROUND NOISE V/HZ**.5	0.4650E-08
VJN= JOHNSON NOISE V/HZ**.5	0.1198E-07
VGR= GR NOISE V/HZ**.5	0.4802E-07
VRF= FDBK RESISTOR JOHNSON NOISE V/HZ**.5	0.5532E-08
VPA= PREAMP NOISE V/HZ**.5	0.2770E-07
VT = TOTAL NOISE V/HZ**.5	0.5717E-07
NEP= NOISE EQUIVALENT POWER W/HZ**.5	0.2380E-12
DSTAR = PEAK DSTAR CM*HZ**.5/W	0.6912E+11

PC HGCDTE DETECTOR PERFORMANCE CHANNEL 1 75/180/STD 8 V/CM

CH = CHANNEL NUMBER	0.1000E+01
T = DET. TEMP	0.7500E+02
HD = DET. HEIGHT CM	0.1360E-01
WD = DET. WIDTH CM	0.1990E-01
TD = DETECTOR THICKNESS CM	0.1000E-02
VB = DETECTOR BIAS VOLTAGE V	0.1592E+00
CD = DETECTOR CAPACITANCE F	0.1500E-10
RD = DETECTOR DARK RESISTANCE OHM	0.3395E+03
ZD = DETECTOR IMPEDANCE OHM	0.3395E+03
PD = DETECTOR PHASE ANGLE RAD	0.1221E-09
X = MOLE FRACTION	0.1838E+00
PO = HOLE CONC, N-TYPE DOPING CM**-3	0.1000E+15
ND = DONAR CARRIER CONC, CM**-3	0.1305E+16
NI = INTRINSIC CARRIER CONC. CM**-3	0.3612E+15
TAU= CARRIER LIFETIME S	0.1000E-05
ETA= QUANTUM EFFICIENCY	0.7000E+00
NUP= PEAK WAVENUMBER 1/CM	0.6066E+03
EG = BAND GAP ENERGY EV	0.6847E-01
SIGMA = CONDUCTIVITY 1/OHM/CM	0.4310E+01
MU = ELECTRON MOBILITY CM**2/V/S	0.2060E+05
MUH= HOLE MOBILITY CM**2/V/S	0.2950E+03
QBG= BKGD PHOTON FLUX DENSITY P/CM**2/S	0.2180E+16
QS = SGNL PHOTON FLUX DENSITY P/CM**2/S	0.5300E+14
TRF= FEEDBACK RESISTOR TEMP, K	0.1600E+03
CF = FDBK RESISTOR CAPACITANCE F	0.3000E-12
RF = FEEDBACK RESISTANCE OHM	0.3395E+04
PF = FDBK RESISTOR PHASE ANGLE RAD	0.2443E-12
ZF = FDBK RESISTOR IMPEDANCE OHM	0.3395E+04
VS = SUPPLY VOLTAGE TO RF/DET. V	0.1751E+01
AO = OPEN LOOP GAIN	0.1000E+04
VP = PREAMP NOISE (INPUT) V/HZ**.5	0.2800E-08
FC = CHOPPING FREQUENCY HZ	0.4400E+03
PW = DETECTOR BIAS POWER W	0.7465E-04
PRF= FEEDBACK RESISTOR BIAS POWER W	0.7465E-03
SIGV = SIGNAL VOLTAGE V	0.3488E-03
RE = DET. RESPONSIVITY V/W	0.2378E+05
AZ = TRANSIMPEDANCE OHM	0.3429E+04
R = DET./PREAMP RESPONSIVITY V/W	0.2402E+06
VBG= BACKGROUND NOISE V/HZ**.5	0.5931E-08
VJN= JOHNSON NOISE V/HZ**.5	0.1198E-07
VGR= GR NOISE V/HZ**.5	0.4802E-07
VRF= FDBK RESISTOR JOHNSON NOISE V/HZ**.5	0.5868E-08
VPA= PREAMP NOISE V/HZ**.5	0.2770E-07
VT = TOTAL NOISE V/HZ**.5	0.5732E-07
NEP= NOISE EQUIVALENT POWER W/HZ**.5	0.2386E-12
DSTAR = PEAK DSTAR CM*HZ**.5/W	0.6894E+11

PC HGCDTE DETECTOR PERFORMANCE CHANNEL 1 80/160/STD 8 V/CM

CH = CHANNEL NUMBER	0.1000E+01
T = DET. TEMP	0.8000E+02
HD = DET. HEIGHT CM	0.1360E-01
WD = DET. WIDTH CM	0.1990E-01
TD = DETECTOR THICKNESS CM	0.1000E-02
VB = DETECTOR BIAS VOLTAGE V	0.1592E+00
CD = DETECTOR CAPACITANCE F	0.1500E-10
RD = DETECTOR DARK RESISTANCE OHM	0.1754E+03
ZD = DETECTOR IMPEDANCE OHM	0.1754E+03
PD = DETECTOR PHASE ANGLE RAD	0.2364E-09
X = MOLE FRACTION	0.1838E+00
PO = HOLE CONC, N-TYPE DOPING CM**-3	0.1000E+15
ND = DONAR CARRIER CONC, CM**-3	0.2526E+16
NI = INTRINSIC CARRIER CONC. CM**-3	0.5026E+15
TAU= CARRIER LIFETIME S	0.1000E-05
ETA= QUANTUM EFFICIENCY	0.7000E+00
NUP= PEAK WAVENUMBER 1/CM	0.6066E+03
EG = BAND GAP ENERGY EV	0.7009E-01
SIGMA = CONDUCTIVITY 1/OHM/CM	0.8341E+01
MU = ELECTRON MOBILITY CM**2/V/S	0.2060E+05
MUH= HOLE MOBILITY CM**2/V/S	0.2950E+03
QBG= BKGD PHOTON FLUX DENSITY P/CM**2/S	0.1700E+16
QS = SGNL PHOTON FLUX DENSITY P/CM**2/S	0.5300E+14
TRF= FEEDBACK RESISTOR TEMP, K	0.1600E+03
CF = FDBK RESISTOR CAPACITANCE F	0.3000E-12
RF = FEEDBACK RESISTANCE OHM	0.1754E+04
PF = FDBK RESISTOR PHASE ANGLE RAD	0.4728E-12
ZF = FDBK RESISTOR IMPEDANCE OHM	0.1754E+04
VS = SUPPLY VOLTAGE TO RF/DET. V	0.1751E+01
AO = OPEN LOOP GAIN	0.1000E+04
VP = PREAMP NOISE (INPUT) V/HZ**.5	0.2800E-08
FC = CHOPPING FREQUENCY HZ	0.4400E+03
PW = DETECTOR BIAS POWER W	0.1445E-03
PRF= FEEDBACK RESISTOR BIAS POWER W	0.1445E-02
SIGV = SIGNAL VOLTAGE V	0.1803E-03
RE = DET. RESPONSIVITY V/W	0.1229E+05
AZ = TRANSIMPEDANCE OHM	0.1772E+04
R = DET./PREAMP RESPONSIVITY V/W	0.1241E+06
VBG= BACKGROUND NOISE V/HZ**.5	0.2707E-08
VJN= JOHNSON NOISE V/HZ**.5	0.8093E-08
VGR= GR NOISE V/HZ**.5	0.2481E-07
VRF= FDBK RESISTOR JOHNSON NOISE V/HZ**.5	0.3977E-08
VPA= PREAMP NOISE V/HZ**.5	0.2770E-07
VT = TOTAL NOISE V/HZ**.5	0.3653E-07
NEP= NOISE EQUIVALENT POWER W/HZ**.5	0.3105E-12
DSTAR = PEAK DSTAR CM*HZ**.5/W	0.5299E+11

PC HGCDTE DETECTOR PERFORMANCE CHANNEL 1 80/180/STD 8 V/CM

CH = CHANNEL NUMBER	0.1000E+01
T = DET. TEMP	0.8000E+02
HD = DET. HEIGHT CM	0.1360E-01
WD = DET. WIDTH CM	0.1990E-01
TD = DETECTOR THICKNESS CM	0.1000E-02
VB = DETECTOR BIAS VOLTAGE V	0.1592E+00
CD = DETECTOR CAPACITANCE F	0.1500E-10
RD = DETECTOR DARK RESISTANCE OHM	0.1754E+03
ZD = DETECTOR IMPEDANCE OHM	0.1754E+03
PD = DETECTOR PHASE ANGLE RAD	0.2364E-09
X = MOLE FRACTION	0.1838E+00
PO = HOLE CONC, N-TYPE DOPING CM**-3	0.1000E+15
ND = DONAR CARRIER CONC, CM**-3	0.2526E+16
NI = INTRINSIC CARRIER CONC. CM**-3	0.5026E+15
TAU= CARRIER LIFETIME S	0.1000E-05
ETA= QUANTUM EFFICIENCY	0.7000E+00
NUP= PEAK WAVENUMBER 1/CM	0.6066E+03
EG = BAND GAP ENERGY EV	0.7009E-01
SIGMA = CONDUCTIVITY 1/OHM/CM	0.8341E+01
MU = ELECTRON MOBILITY CM**2/V/S	0.2060E+05
MUH= HOLE MOBILITY CM**2/V/S	0.2950E+03
QBG= BKGD PHOTON FLUX DENSITY P/CM**2/S	0.2700E+16
QS = SGNL PHOTON FLUX DENSITY P/CM**2/S	0.5300E+14
TRF= FEEDBACK RESISTOR TEMP, K	0.1600E+03
CF = FDBK RESISTOR CAPACITANCE F	0.3000E-12
RF = FEEDBACK RESISTANCE OHM	0.1754E+04
PF = FDBK RESISTOR PHASE ANGLE RAD	0.4728E-12
ZF = FDBK RESISTOR IMPEDANCE OHM	0.1754E+04
VS = SUPPLY VOLTAGE TO RF/DET. V	0.1751E+01
AO = OPEN LOOP GAIN	0.1000E+04
VP = PREAMP NOISE (INPUT) V/HZ**.5	0.2800E-08
FC = CHOPPING FREQUENCY HZ	0.4400E+03
PW = DETECTOR BIAS POWER W	0.1445E-03
PRF= FEEDBACK RESISTOR BIAS POWER W	0.1445E-02
SIGV = SIGNAL VOLTAGE V	0.1803E-03
RE = DET. RESPONSIVITY V/W	0.1229E+05
AZ = TRANSIMPEDANCE OHM	0.1772E+04
R = DET./PREAMP RESPONSIVITY V/W	0.1241E+06
VBG= BACKGROUND NOISE V/HZ**.5	0.3302E-08
VJN= JOHNSON NOISE V/HZ**.5	0.8093E-08
VGR= GR NOISE V/HZ**.5	0.2481E-07
VRF= FDBK RESISTOR JOHNSON NOISE V/HZ**.5	0.4218E-08
VPA= PREAMP NOISE V/HZ**.5	0.2770E-07
VT = TOTAL NOISE V/HZ**.5	0.3061E-07
NEP= NOISE EQUIVALENT POWER W/HZ**.5	0.3110E-12
DSTAR = PEAK DSTAR CM*HZ**.5/W	0.5289E+11

Table F-6 (CH 11)

PC HGCDTE DETECTOR PERFORMANCE CHANNEL 11 75/160/STD 8 V/CM

CH = CHANNEL NUMBER	0.1100E+02
T = DET. TEMP	0.7500E+02
HD = DET. HEIGHT CM	0.1360E-01
WD = DET. WIDTH CM	0.3190E-01
TD = DETECTOR THICKNESS CM	0.1000E-02
VB = DETECTOR BIAS VOLTAGE V	0.2552E+00
CD = DETECTOR CAPACITANCE F	0.5000E-10
RD = DETECTOR DARK RESISTANCE OHM	0.7215E+03
ZD = DETECTOR IMPEDANCE OHM	0.7215E+03
PD = DETECTOR PHASE ANGLE RAD	0.1916E-09
X = MOLE FRACTION	0.2035E+00
PO = HOLE CONC, N-TYPE DOPING CM**-3	0.2000E+13
ND = DONAR CARRIER CONC. CM**-3	0.1010E+16
NI = INTRINSIC CARRIER CONC. CM**-3	0.4493E+14
TAU= CARRIER LIFETIME S	0.1000E-05
ETA= QUANTUM EFFICIENCY	0.7000E+00
NUP= PEAK WAVENUMBER 1/CM	0.8745E+03
EG = BAND GAP ENERGY EV	0.9091E-01
SIGMA = CONDUCTIVITY 1/OHM/CM	0.3251E+01
MU = ELECTRON MOBILITY CM**2/V/S	0.2010E+05
MUH= HOLE MOBILITY CM**2/V/S	0.2920E+03
QBG= BKGD PHOTON FLUX DENSITY P/CM**2/S	0.2810E+16
QS = SGNL PHOTON FLUX DENSITY P/CM**2/S	0.1810E+15
TR1= FEEDBACK RESISTOR TEMP. K	0.1600E+03
C1 = FDBK RESISTOR CAPACITANCE F	0.3000E-12
R1 = FEEDBACK RESISTANCE OHM	0.7215E+04
P1 = FDBK RESISTOR PHASE ANGLE RAD	0.1149E-12
Z1 = FDBK RESISTOR IMPEDANCE OHM	0.7215E+04
VS = SUPPLY VOLTAGE TO R1/DET. V	0.2807E+01
AO = OPEN LOOP GAIN	0.1000E+04
VP = PREAMP NOISE (INPUT) V/HZ**.5	0.2800E-08
FC = CHOPPING FREQUENCY HZ	0.4400E+03
PW = DETECTOR BIAS POWER W	0.9026E-04
PR1= FEEDBACK RESISTOR BIAS POWER W	0.9026E-03
SIGV = SIGNAL VOLTAGE V	0.1504E-02
RE = DET. RESPONSIVITY V/W	0.2134E+05
AZ = TRANSIMPEDANCE OHM	0.7200E+04
R = DET./PREAMP RESPONSIVITY V/W	0.2156E+06
VBG= BACKGROUND NOISE V/HZ**.5	0.1103E-07
VJN= JOHNSON NOISE V/HZ**.5	0.1746E-07
VGR= GR NOISE V/HZ**.5	0.1112E-07
VNR= FDBK RESISTOR NOISE V/HZ**.5	0.8065E-08
VPA= PREAMP NOISE V/HZ**.5	0.2770E-07
VT = TOTAL NOISE V/HZ**.5	0.3718E-07
NEP= NOISE EQUIVALENT POWER W/HZ**.5	0.1725E-12
DSTAR = PEAK DSTAR CM*HZ**.5/W	0.1208E+12

PC HGCDTE DETECTOR PERFORMANCE CHANNEL 11 75/180/STD 8 V/CM

CH = CHANNEL NUMBER	0.1100E+02
T = DET. TEMP	0.7500E+02
HD = DET. HEIGHT CM	0.1360E-01
WD = DET. WIDTH CM	0.3190E-01
TD = DETECTOR THICKNESS CM	0.1000E-02
VB = DETECTOR BIAS VOLTAGE V	0.2552E+00
CD = DETECTOR CAPACITANCE F	0.1500E-10
RD = DETECTOR DARK RESISTANCE OHM	0.7215E+03
ZD = DETECTOR IMPEDANCE OHM	0.7215E+03
PD = DETECTOR PHASE ANGLE RAD	0.5747E-10
X = MOLE FRACTION	0.2035E+00
PO = HOLE CONC, N-TYPE DOPING CM**-3	0.2000E+13
ND = DONAR CARRIER CONC. CM**-3	0.1010E+16
NI = INTRINSIC CARRIER CONC, CM**-3	0.4493E+14
TAU= CARRIER LIFETIME S	0.1000E-05
ETA= QUANTUM EFFICIENCY	0.7000E+00
NUP= PEAK WAVENUMBER 1/CM	0.8745E+03
EG = BAND GAP ENERGY EV	0.9091E-01
SIGMA = CONDUCTIVITY 1/OHM/CM	0.3251E+01
MU = ELECTRON MOBILITY CM**2/V/S	0.2010E+05
MUH= HOLE MOBILITY CM**2/V/S	0.2920E+03
QBG= BKGD PHOTON FLUX DENSITY P/CM**2/S	0.4730E+16
QS = SGNL PHOTON FLUX DENSITY P/CM**2/S	0.1810E+15
TRF= FEEDBACK RESISTOR TEMP. K	0.1800E+03
CF = FDBK RESISTOR CAPACITANCE F	0.3000E-12
RF = FEEDBACK RESISTANCE OHM	0.7215E+04
PF = FDBK RESISTOR PHASE ANGLE RAD	0.1149E-12
ZF = FDBK RESISTOR IMPEDANCE OHM	0.7215E+04
VS = SUPPLY VOLTAGE TO RF/DET. V	0.2807E+01
AO = OPEN LOOP GAIN	0.1000E+04
VP = PREAMP NOISE (INPUT) V/HZ**.5	0.2800E-08
FC = CHOPPING FREQUENCY HZ	0.4400E+03
PW = DETECTOR BIAS POWER W	0.9026E-04
PRF= FEEDBACK RESISTOR BIAS POWER W	0.9026E-03
SIGV = SIGNAL VOLTAGE V	0.1504E-02
RE = DET. RESPONSIVITY V/W	0.2134E+05
AZ = TRANSIMPEDANCE OHM	0.7200E+04
R = DET./PREAMP RESPONSIVITY V/W	0.2156E+06
VBG= BACKGROUND NOISE V/HZ**.5	0.1431E-07
VJN= JOHNSON NOISE V/HZ**.5	0.1746E-07
VGR= GR NOISE V/HZ**.5	0.1112E-07
VRF= FDBK RESISTOR JOHNSON NOISE V/HZ**.5	0.6554E-08
VPA= PREAMP NOISE V/HZ**.5	0.2770E-07
VT = TOTAL NOISE V/HZ**.5	0.3839E-07
NEP= NOISE EQUIVALENT POWER W/HZ**.5	0.1781E-12
DSTAR = PEAK DSTAR CM*HZ**.5/W	0.1170E+12

PC HGCDTE DETECTOR PERFORMANCE CHANNEL 11 80/160/STD 8 V/CM

CH = CHANNEL NUMBER	0.1100E+02
T = DET. TEMP	0.8000E+02
HD = DET. HEIGHT CM	0.1360E-01
WD = DET. WIDTH CM	0.3190E-01
TD = DETECTOR THICKNESS CM	0.1000E-02
VB = DETECTOR BIAS VOLTAGE V	0.2552E+00
CD = DETECTOR CAPACITANCE F	0.1500E-10
RD = DETECTOR DARK RESISTANCE OHM	0.2767E+03
ZD = DETECTOR IMPEDANCE OHM	0.2767E+03
PD = DETECTOR PHASE ANGLE RAD	0.1499E-09
X = MOLE FRACTION	0.2035E+00
PO = HOLE CONC, N-TYPE DOPING CM**-3	0.2000E+13
ND = DONAR CARRIER CONC. CM**-3	0.2632E+16
NI = INTRINSIC CARRIER CONC. CM**-3	0.7256E+14
TAU= CARRIER LIFETIME S	0.1000E-05
ETA= QUANTUM EFFICIENCY	0.7000E+00
NUP= PEAK WAVENUMBER 1/CM	0.8745E+03
EG = BAND GAP ENERGY EV	0.1004E+00
SIGMA = CONDUCTIVITY 1/OHM/CM	0.8477E+01
MU = ELECTRON MOBILITY CM**2/V/S	0.2010E+05
MUH= HOLE MOBILITY CM**2/V/S	0.2920E+03
QBG= BKGD PHOTON FLUX DENSITY P/CM**2/S	0.3620E+16
QS = SGNL PHOTON FLUX DENSITY P/CM**2/S	0.1810E+15
TRF= FEEDBACK RESISTOR TEMP. K	0.1600E+03
CF = FDBK RESISTOR CAPACITANCE F	0.3000E-12
RF = FEEDBACK RESISTANCE OHM	0.2767E+04
PF = FDBK RESISTOR PHASE ANGLE RAD	0.2997E-12
ZF = FDBK RESISTOR IMPEDANCE OHM	0.2767E+04
VS = SUPPLY VOLTAGE TO RF/DET. V	0.2807E+01
AO = OPEN LOOP GAIN	0.1000E+04
VP = PREAMP NOISE (INPUT) V/HZ**.5	0.2800E-08
FC = CHOPPING FREQUENCY HZ	0.4400E+03
PW = DETECTOR BIAS POWER W	0.2354E-03
PRF= FEEDBACK RESISTOR BIAS POWER W	0.2354E-02
SIGV = SIGNAL VOLTAGE V	0.5768E-03
RE = DET. RESPONSIVITY V/W	0.8186E+04
AZ = TRANSIMPEDANCE OHM	0.2795E+04
R = DET./PREAMP RESPONSIVITY V/W	0.8268E+05
VBG= BACKGROUND NOISE V/HZ**.5	0.4802E-08
VJN= JOHNSON NOISE V/HZ**.5	0.1117E-07
VGR= GR NOISE V/HZ**.5	0.4266E-08
VRF= FDBK RESISTOR JOHNSON NOISE V/HZ**.5	0.4995E-08
VPA= PREAMP NOISE V/HZ**.5	0.2770E-07
VT = TOTAL NOISE V/HZ**.5	0.3095E-07
NEP= NOISE EQUIVALENT POWER W/HZ**.5	0.3743E-12
DSTAR = PEAK DSTAR CM*HZ**.5/W	0.5564E+11

PC HGCDTE DETECTOR PERFORMANCE CHANNEL 11 80/180/STD 8 V/CM

CH = CHANNEL NUMBER	0.1100E+02
T = DET. TEMP	0.8000E+02
HD = DET. HEIGHT CM	0.1360E-01
WD = DET. WIDTH CM	0.3190E-01
TD = DETECTOR THICKNESS CM	0.1000E-02
VB = DETECTOR BIAS VOLTAGE V	0.2552E+00
CD = DETECTOR CAPACITANCE F	0.1500E-10
RD = DETECTOR DARK RESISTANCE OHM	0.2767E+03
ZD = DETECTOR IMPEDANCE OHM	0.2767E+03
PD = DETECTOR PHASE ANGLE RAD	0.1499E-09
X = MOLE FRACTION	0.2035E+00
PO = HOLE CONC, N-TYPE DOPING CM**-3	0.2000E+13
ND = DONAR CARRIER CONC. CM**-3	0.2632E+16
NI = INTRINSIC CARRIER CONC. CM**-3	0.7256E+14
TAU= CARRIER LIFETIME S	0.1000E-05
ETA= QUANTUM EFFICIENCY	0.7000E+00
NUP= PEAK WAVENUMBER 1/CM	0.8745E+03
EG = BAND GAP ENERGY EV	0.1004E+00
SIGMA = CONDUCTIVITY 1/OHM/CM	0.8477E+01
MU = ELECTRON MOBILITY CM**2/V/S	0.2010E+05
MUH= HOLE MOBILITY CM**2/V/S	0.2920E+03
QBG= BKGD PHOTON FLUX DENSITY P/CM**2/S	0.5930E+16
QS = SGNL PHOTON FLUX DENSITY P/CM**2/S	0.1810E+15
TRF= FEEDBACK RESISTOR TEMP. K	0.1800E+03
CF = FDBK RESISTOR CAPACITANCE F	0.3000E-12
RF = FEEDBACK RESISTANCE OHM	0.2767E+04
PF = FDBK RESISTOR PHASE ANGLE RAD	0.2997E-12
ZF = FDBK RESISTOR IMPEDANCE OHM	0.2767E+04
VS = SUPPLY VOLTAGE TO RF/DET. V	0.2807E+01
AO = OPEN LOOP GAIN	0.1000E+04
VP = PREAMP NOISE (INPUT) V/HZ**.5	0.2800E-08
FC = CHOPPING FREQUENCY HZ	0.4400E+03
PW = DETECTOR BIAS POWER W	0.2354E-03
PRF= FEEDBACK RESISTOR BIAS POWER W	0.2354E-02
SIGV = SIGNAL VOLTAGE V	0.5768E-03
RE = DET. RESPONSIVITY V/W	0.8186E+04
AZ = TRANSIMPEDANCE OHM	0.2795E+04
R = DET./PREAMP RESPONSIVITY V/W	0.8268E+05
VBG= BACKGROUND NOISE V/HZ**.5	0.6146E-08
VJN= JOHNSON NOISE V/HZ**.5	0.1117E-07
VGR= GR NOISE V/HZ**.5	0.4266E-08
VRF= FDBK RESISTOR JOHNSON NOISE V/HZ**.5	0.5298E-08
VPA= PREAMP NOISE V/HZ**.5	0.2770E-07
VT = TOTAL NOISE V/HZ**.5	0.3124E-07
NEP= NOISE EQUIVALENT POWER W/HZ**.5	0.3778E-12
DSTAR = PEAK DSTAR CM*HZ**.5/W	0.5513E+11

Table F-6 (CH 12)

PV HGCDTE DETECTOR PERFORMANCE CHANNEL 12 75/160/STD

CH = CHANNEL NUMBER	0.1200E+02
HD = DETECTOR HEIGHT CM	0.5300E-01
WD = DETECTOR WIDTH CM	0.9450E-01
T = DET. TEMP. K	0.7500E+02
CS = DET. STRAY CAPACITANCE F	0.6000E-11
RS = DET. SHUNT RESISTANCE OHM	0.1050E+07
X = MOLE FRACTION	0.2143E+00
VB = BIAS VOLTAGE V	0.0000E+00
EG = BAND GAP ENERGY EV	0.1156E+00
NI = INTRINSIC CONC. CM**-3	0.1790E+10
NA = ACCEPTOR CONC. CM**-3	0.2000E+15
ND = DONOR CARRIER CONC. CM**-3	0.1000E+16
MU = ELECTRON MOBILITY CM**2/V/S	0.1900E+05
MUH= HOLE MOBILITY CM**2/V/S	0.2090E+03
ETA= QUANTUM EFFICIENCY	0.7500E+00
TAU= CARRIER LIFETIME S	0.5000E-06
NUP= PEAK WAVENUMBER 1/CM	0.1036E+04
QBG= BKGD PHOTON FLUX DENSITY P/CM**2/S	0.3550E+14
QS = SGNL PHOTON FLUX DENSITY P/CM**2/S	0.6320E+13
KAPPA = DIELECTRIC CONSTANT	0.1384E+02
RF = FEEDBACK RESISTANCE OHM	0.1000E+10
CF = FEEDBACK CAPACITACE F	0.3000E-12
VP = PREAMP NOISE (INPUT) V/HZ**.5	0.2000E-08
AO = OPEN LOOP GAIN OF PREAMP	0.1000E+04
TRF= FEEDBACK RESISTOR TEMP K	0.1600E+03
FC = CHOPPING FREQUENCY HZ	0.4400E+03
RO = DIODE DARK RESISTANCE BIAS=0 OHM	0.2096E+09
RA = R(0)*A PRODUCT OHM*CM**2	0.1050E+07
VJ = JUNCTION POTENTIAL V	0.1606E+00
CJ = JUNCTION CAPACITANCE F	0.1230E-09
WJ = JUNCTION WIDTH CM	0.4958E-04
VC = CONTACT POTENTIAL V	0.1606E+00
ZD = DETECTOR IMPEDANCE OHM	0.2749E+07
ZF = FEEDBACK RESISTOR IMPEDANCE OHM	0.5466E+09
PD = DET. PHASE ANGLE RAD	0.1633E-14
PF = FDBK RESISTOR PHASE ANGLE RAD	0.8294E-18
AZ = TRANSIMPEDANCE OHM	0.6823E+09
IS = SIGNAL PHOTOCURRENT A	0.3003E-08
IT = TOTAL BKGD PHOTOCURRENT A	0.2136E-07
VRF= FDBK RESISTOR NOISE V/HZ**.5	0.2028E-05
VBG= BACKGRD IND NOISE V/HZ**.5	0.5645E-04
VJN= JOHNSON NOISE V/HZ**.5	0.3033E-05
VPA= PREAMP NOISE V/HZ**.5	0.4640E-06
VT = TOTAL NOISE V/HZ**.5	0.5657E-04
R = RESPONSIVITY V/W	0.3982E+10
NEP= NOISE EQUIVALENT POWER W/HZ**.5	0.1420E-13
DSTAR = CM*HZ**.5/W	0.4982E+13

PV HGCDTE DETECTOR PERFORMANCE CHANNEL 12 75/180/STD

CH = CHANNEL NUMBER	0.1200E+02
HD = DETECTOR HEIGHT CM	0.5300E-01
WD = DETECTOR WIDTH CM	0.9450E-01
T = DET. TEMP. K	0.7500E+02
CS = DET. STRAY CAPACITANCE F	0.6000E-11
RS = DET. SHUNT RESISTANCE OHM	0.1050E+07
X = MOLE FRACTION	0.2143E+00
VB = BIAS VOLTAGE V	0.0000E+00
EG = BAND GAP ENERGY EV	0.1156E+00
NI = INTRINSIC CONC. CM**-3	0.1790E+10
NA = ACCEPTOR CONC. CM**-3	0.2000E+15
ND = DONOR CARRIER CONC. CM**-3	0.1000E+16
MU = ELECTRON MOBILITY CM**2/V/S	0.1900E+05
MUH= HOLE MOBILITY CM**2/V/S	0.2090E+03
ETA= QUANTUM EFFICIENCY	0.7500E+00
TAU= CARRIER LIFETIME S	0.5000E-06
NUP= PEAK WAVENUMBER 1/CM	0.1036E+04
QBG= BKGD PHOTON FLUX DENSITY P/CM**2/S	0.8740E+14
QS = SGNL PHOTON FLUX DENSITY P/CM**2/S	0.6320E+13
KAPPA = DIELECTRIC CONSTANT	0.1384E+02
RF = FEEDBACK RESISTANCE OHM	0.1000E+10
CF = FEEDBACK CAPACITACE F	0.3000E-12
VP = PREAMP NOISE (INPUT) V/HZ**.5	0.2000E-08
AO = OPEN LOOP GAIN OF PREAMP	0.1000E+04
TRF= FEEDBACK RESISTOR TEMP K	0.1800E+03
FC = CHOPPING FREQUENCY HZ	0.4400E+03
RO = DIODE DARK RESISTANCE BIAS=0 OHM	0.2096E+09
RA = R(0)*A PRODUCT OHM*CM**2	0.1050E+07
VJ = JUNCTION POTENTIAL V	0.1606E+00
CJ = JUNCTION CAPACITANCE F	0.1230E-09
WJ = JUNCTION WIDTH CM	0.4958E-04
VC = CONTACT POTENTIAL V	0.1606E+00
ZD = DETECTOR IMPEDANCE OHM	0.2749E+07
ZF = FEEDBACK RESISTOR IMPEDANCE OHM	0.5466E+09
PD = DET. PHASE ANGLE RAD	0.1633E-14
PF = FDBK RESISTOR PHASE ANGLE RAD	0.8294E-18
AZ = TRANSIMPEDANCE OHM	0.6823E+09
IS = SIGNAL PHOTOCURRENT A	0.3003E-08
IT = TOTAL BKGD PHOTOCURRENT A	0.5259E-07
VRF= FDBK RESISTOR NOISE V/HZ**.5	0.2151E-05
VBG= BACKGROUND NOISE V/HZ**.5	0.8857E-04
VJN= JOHNSON NOISE V/HZ**.5	0.3033E-05
VPA= PREAMP NOISE V/HZ**.5	0.4640E-06
VT = TOTAL NOISE V/HZ**.5	0.8865E-04
R = RESPONSIVITY V/W	0.3982E+10
NEP= NOISE EQUIVALENT POWER W/HZ**.5	0.2226E-13
DSTAR = CM*HZ**.5/W	0.3179E+13

PV HGCDTE DETECTOR PERFORMANCE CHANNEL 12 80/160/STD

CH = CHANNEL NUMBER	0.1200E+02
HD = DETECTOR HEIGHT CM	0.5300E-01
WD = DETECTOR WIDTH CM	0.9450E-01
T = DET. TEMP. K	0.8000E+02
CS = DET. STRAY CAPACITANCE F	0.6000E-11
RS = DET. SHUNT RESISTANCE OHM	0.1050E+07
X = MOLE FRACTION	0.2143E+00
VB = BIAS VOLTAGE V	0.0000E+00
EG = BAND GAP ENERGY EV	0.1156E+00
NI = INTRINSIC CONC. CM**-3	0.6072E+10
NA = ACCEPTOR CONC. CM**-3	0.2000E+15
ND = DONOR CARRIER CONC. CM**-3	0.1000E+16
MU = ELECTRON MOBILITY CM**2/V/S	0.1900E+05
MUH= HOLE MOBILITY CM**2/V/S	0.2890E+03
ETA= QUANTUM EFFICIENCY	0.7500E+00
TAU= CARRIER LIFETIME S	0.5000E-06
NUP= PEAK WAVENUMBER 1/CM	0.1036E+04
QBG= BKGD PHOTON FLUX DENSITY P/CM**2/S	0.5230E+14
QS = SGNL PHOTON FLUX DENSITY P/CM**2/S	0.6320E+13
KAPPA = DIELECTRIC CONSTANT	0.1384E+02
RF = FEEDBACK RESISTANCE OHM	0.1000E+10
CF = FEEDBACK CAPACITACE F	0.3000E-12
VP = PREAMP NOISE (INPUT) V/HZ**.5	0.2000E-08
AO = OPEN LOOP GAIN OF PREAMP	0.1000E+04
TRF= FEEDBACK RESISTOR TEMP K	0.1600E+03
FC = CHOPPING FREQUENCY HZ	0.4400E+03
RO = DIODE DARK RESISTANCE BIAS=0 OHM	0.2096E+09
RA = R(0)*A PRODUCT OHM*CM**2	0.1050E+07
VJ = JUNCTION POTENTIAL V	0.1545E+00
CJ = JUNCTION CAPACITANCE F	0.1263E-09
WJ = JUNCTION WIDTH CM	0.4863E-04
VC = CONTACT POTENTIAL V	0.1545E+00
ZD = DETECTOR IMPEDANCE OHM	0.2700E+07
ZF = FEEDBACK RESISTOR IMPEDANCE OHM	0.5466E+09
PD = DET. PHASE ANGLE RAD	0.1665E-14
PF = FDBK RESISTOR PHASE ANGLE RAD	0.8294E-18
AZ = TRANSIMPEDANCE OHM	0.6854E+09
IS = SIGNAL PHOTOCURRENT A	0.3003E-08
IT = TOTAL BKGD PHOTOCURRENT A	0.3147E-07
VRF= FDBK RESISTOR NOISE V/HZ**.5	0.2037E-05
VBG= BACKGROUND NOISE V/HZ**.5	0.6883E-04
VJN= JOHNSON NOISE V/HZ**.5	0.3146E-05
VPA= PREAMP NOISE V/HZ**.5	0.4711E-06
VT = TOTAL NOISE V/HZ**.5	0.6893E-04
R = RESPONSIVITY V/W	0.4001E+10
NEP= NOISE EQUIVALENT POWER W/HZ**.5	0.1723E-13
DSTAR = CM*HZ**.5/W	0.4107E+13

PV HGCDTE DETECTOR PERFORMANCE CHANNEL 12 80/180/STD

CH = CHANNEL NUMBER	0.1200E+02
HD = DETECTOR HEIGHT CM	0.5300E-01
WD = DETECTOR WIDTH CM	0.9450E-01
T = DET. TEMP. K	0.8000E+02
CS = DET. STRAY CAPACITANCE F	0.6000E-11
RS = DET. SHUNT RESISTANCE OHM	0.1050E+07
X = MOLE FRACTION	0.2143E+00
VB = BIAS VOLTAGE V	0.0000E+00
EG = BAND GAP ENERGY EV	0.1156E+00
NI = INTRINSIC CONC. CM**-3	0.6072E+10
NA = ACCEPTOR CONC. CM**-3	0.2000E+15
ND = DONOR CARRIER CONC. CM**-3	0.1000E+16
MU = ELECTRON MOBILITY CM**2/V/S	0.1900E+05
MUH= HOLE MOBILITY CM**2/V/S	0.2890E+03
ETA= QUANTUM EFFICIENCY	0.7500E+00
TAU= CARRIER LIFETIME S	0.5000E-06
NUP= PEAK WAVENUMBER 1/CM	0.1036E+04
QBG= BKGD PHOTON FLUX DENSITY P/CM**2/S	0.1040E+15
QS = SGNL PHOTON FLUX DENSITY P/CM**2/S	0.6320E+13
KAPPA = DIELECTRIC CONSTANT	0.1384E+02
RF = FEEDBACK RESISTANCE OHM	0.1000E+10
CF = FEEDBACK CAPACITACE F	0.3000E-12
VP = PREAMP NOISE (INPUT) V/HZ**.5	0.2000E-08
AO = OPEN LOOP GAIN OF PREAMP	0.1000E+04
TRF= FEEDBACK RESISTOR TEMP K	0.1800E+03
FC = CHOPPING FREQUENCY HZ	0.4400E+03
RO = DIODE DARK RESISTANCE BIAS=0 OHM	0.2096E+09
RA = R(0)*A PRODUCT OHM*CM**2	0.1050E+07
VJ = JUNCTION POTENTIAL V	0.1545E+00
CJ = JUNCTION CAPACITANCE F	0.1263E-09
WJ = JUNCTION WIDTH CM	0.4863E-04
VC = CONTACT POTENTIAL V	0.1545E+00
ZD = DETECTOR IMPEDANCE OHM	0.2700E+07
ZF = FEEDBACK RESISTOR IMPEDANCE OHM	0.5466E+09
PD = DET. PHASE ANGLE RAD	0.1665E-14
PF = FDBK RESISTOR PHASE ANGLE RAD	0.8294E-18
AZ = TRANSIMPEDANCE OHM	0.6854E+09
IS = SIGNAL PHOTOCURRENT A	0.3003E-08
IT = TOTAL BKGD PHOTOCURRENT A	0.6258E-07
VRF= FDBK RESISTOR NOISE V/HZ**.5	0.2161E-05
VBG= BACKGROUND NOISE V/HZ**.5	0.9706E-04
VJN= JOHNSON NOISE V/HZ**.5	0.3146E-05
VPA= PREAMP NOISE V/HZ**.5	0.4711E-06
VT = TOTAL NOISE V/HZ**.5	0.9713E-04
R = RESPONSIVITY V/W	0.4001E+10
NEP= NOISE EQUIVALENT POWER W/HZ**.5	0.2428E-13
DSTAR = CM*HZ**.5/W	0.2915E+13

Table F-6 (CH 14)

ORIGINAL PAGE IS OF POOR QUALITY

PV HGCDTE DETECTOR PERFORMANCE CHANNEL 14 75/160/STD		PV HGCDTE DETECTOR PERFORMANCE CHANNEL 14 75/180/STD	
CH = CHANNEL NUMBER	0.1400E+02	CH = CHANNEL NUMBER	0.1400E+02
HD = DETECTOR HEIGHT CM	0.5300E-01	HD = DETECTOR HEIGHT CM	0.5300E-01
WD = DETECTOR WIDTH CM	0.9040E-01	WD = DETECTOR WIDTH CM	0.9040E-01
T = DET. TEMP, K	0.7500E+02	T = DET. TEMP, K	0.7500E+02
CS = DET. STRAY CAPACITANCE F	0.6000E-11	CS = DET. STRAY CAPACITANCE F	0.6000E-11
RS = DET. SHUNT RESISTANCE OHM	0.1050E+07	RS = DET. SHUNT RESISTANCE OHM	0.1050E+07
X = MOLE FRACTION	0.2573E+00	X = MOLE FRACTION	0.2573E+00
VB = BIAS VOLTAGE V	0.0000E+00	VB = BIAS VOLTAGE V	0.0000E+00
EG = BAND GAP ENERGY EV	0.1829E+00	EG = BAND GAP ENERGY EV	0.1829E+00
NI = INTRINSIC CONC. CM**-3	0.7530E+05	NI = INTRINSIC CONC. CM**-3	0.7530E+05
NA = ACCEPTOR CONC. CM**-3	0.7000E+15	NA = ACCEPTOR CONC. CM**-3	0.7000E+15
ND = DONOR CARRIER CONC. CM**-3	0.1000E+17	ND = DONOR CARRIER CONC. CM**-3	0.1000E+17
MU = ELECTRON MOBILITY CM**2/V/S	0.1870E+05	MU = ELECTRON MOBILITY CM**2/V/S	0.1870E+05
MUH= HOLE MOBILITY CM**2/V/S	0.2770E+03	MUH= HOLE MOBILITY CM**2/V/S	0.2770E+03
ETA= QUANTUM EFFICIENCY	0.7500E+00	ETA= QUANTUM EFFICIENCY	0.7500E+00
TAU= CARRIER LIFETIME S	0.5000E-06	TAU= CARRIER LIFETIME S	0.5000E-06
NUP= PEAK WAVENUMBER 1/CM	0.1639E+04	NUP= PEAK WAVENUMBER 1/CM	0.1639E+04
QBG= BKGD PHOTON FLUX DENSITY P/CM**2/S	0.1140E+13	QBG= BKGD PHOTON FLUX DENSITY P/CM**2/S	0.4270E+13
QS = SGNL PHOTON FLUX DENSITY P/CM**2/S	0.3310E+12	QS = SGNL PHOTON FLUX DENSITY P/CM**2/S	0.3310E+12
KAPPA = DIELECTRIC CONSTANT	0.1361E+02	KAPPA = DIELECTRIC CONSTANT	0.1361E+02
RF = FEEDBACK RESISTANCE OHM	0.1000E+10	RF = FEEDBACK RESISTANCE OHM	0.1000E+10
CF = FEEDBACK CAPACITACE F	0.3000E-12	CF = FEEDBACK CAPACITACE F	0.3000E-12
VP = PREAMP NOISE (INPUT) V/HZ**.5	0.2000E-08	VP = PREAMP NOISE (INPUT) V/HZ**.5	0.2000E-08
AO = OPEN LOOP GAIN OF PREAMP	0.1000E+04	AO = OPEN LOOP GAIN OF PREAMP	0.1000E+04
TRF= FEEDBACK RESISTOR TEMP K	0.1600E+03	TRF= FEEDBACK RESISTOR TEMP K	0.1600E+03
FC = CHOPPING FREQUENCY HZ	0.4400E+03	FC = CHOPPING FREQUENCY HZ	0.4400E+03
RO = DIODE DARK RESISTANCE BIAS=0 OHM	0.2192E+09	RO = DIODE DARK RESISTANCE BIAS=0 OHM	0.2192E+09
RA = R(0)*A PRODUCT OHM*CM**2	0.1050E+07	RA = R(0)*A PRODUCT OHM*CM**2	0.1050E+07
VJ = JUNCTION POTENTIAL V	0.3139E+00	VJ = JUNCTION POTENTIAL V	0.3139E+00
CJ = JUNCTION CAPACITANCE F	0.2657E-09	CJ = JUNCTION CAPACITANCE F	0.2657E-09
WJ = JUNCTION WIDTH CM	0.2173E-04	WJ = JUNCTION WIDTH CM	0.2173E-04
VC = CONTACT POTENTIAL V	0.3139E+00	VC = CONTACT POTENTIAL V	0.3139E+00
ZD = DETECTOR IMPEDANCE OHM	0.1323E+07	ZD = DETECTOR IMPEDANCE OHM	0.1323E+07
ZF = FEEDBACK RESISTOR IMPEDANCE OHM	0.5466E+09	ZF = FEEDBACK RESISTOR IMPEDANCE OHM	0.5466E+09
PD = DET. PHASE ANGLE RAD	0.3352E-14	PD = DET. PHASE ANGLE RAD	0.3352E-14
PF = FDBK RESISTOR PHASE ANGLE RAD	0.8294E-18	PF = FDBK RESISTOR PHASE ANGLE RAD	0.8294E-18
AZ = TRANSIMPEDANCE OHM	0.9314E+09	AZ = TRANSIMPEDANCE OHM	0.9314E+09
IS = SIGNAL PHOTOCURRENT A	0.1905E-09	IS = SIGNAL PHOTOCURRENT A	0.1905E-09
IT = TOTAL BKGD PHOTOCURRENT A	0.6563E-09	IT = TOTAL BKGD PHOTOCURRENT A	0.2458E-08
VRF= FDBK RESISTOR NOISE V/HZ**.5	0.2769E-05	VRF= FDBK RESISTOR NOISE V/HZ**.5	0.2937E-05
VBG= BACKGROUND NOISE V/HZ**.5	0.1351E-04	VBG= BACKGROUND NOISE V/HZ**.5	0.2614E-04
VJN= JOHNSON NOISE V/HZ**.5	0.4049E-05	VJN= JOHNSON NOISE V/HZ**.5	0.4049E-05
VPA= PREAMP NOISE V/HZ**.5	0.8180E-06	VPA= PREAMP NOISE V/HZ**.5	0.8180E-06
VT = TOTAL NOISE V/HZ**.5	0.1439E-04	VT = TOTAL NOISE V/HZ**.5	0.2663E-04
R = RESPONSIVITY V/W	0.3436E+10	R = RESPONSIVITY V/W	0.3437E+10
NEP= NOISE EQUIVALENT POWER W/HZ**.5	0.4188E-14	NEP= NOISE EQUIVALENT POWER W/HZ**.5	0.7748E-14
DSTAR = CM*HZ**.5/W	0.1653E+14	DSTAR = CM*HZ**.5/W	0.8934E+13

PV HGCDTE DETECTOR PERFORMANCE CHANNEL 14 80/160/STD		PV HGCDTE DETECTOR PERFORMANCE CHANNEL 14 80/180/STD	
CH = CHANNEL NUMBER	0.1400E+02	CH = CHANNEL NUMBER	0.1400E+02
HD = DETECTOR HEIGHT CM	0.5300E-01	HD = DETECTOR HEIGHT CM	0.5300E-01
WD = DETECTOR WIDTH CM	0.9040E-01	WD = DETECTOR WIDTH CM	0.9040E-01
T = DET. TEMP, K	0.8000E+02	T = DET. TEMP, K	0.8000E+02
CS = DET. STRAY CAPACITANCE F	0.6000E-11	CS = DET. STRAY CAPACITANCE F	0.6000E-11
RS = DET. SHUNT RESISTANCE OHM	0.1050E+07	RS = DET. SHUNT RESISTANCE OHM	0.1050E+07
X = MOLE FRACTION	0.2573E+00	X = MOLE FRACTION	0.2573E+00
VB = BIAS VOLTAGE V	0.0000E+00	VB = BIAS VOLTAGE V	0.0000E+00
EG = BAND GAP ENERGY EV	0.1829E+00	EG = BAND GAP ENERGY EV	0.1829E+00
NI = INTRINSIC CONC. CM**-3	0.4876E+06	NI = INTRINSIC CONC. CM**-3	0.4876E+06
NA = ACCEPTOR CONC. CM**-3	0.7000E+15	NA = ACCEPTOR CONC. CM**-3	0.7000E+15
ND = DONOR CARRIER CONC. CM**-3	0.1000E+17	ND = DONOR CARRIER CONC. CM**-3	0.1000E+17
MU = ELECTRON MOBILITY CM**2/V/S	0.1870E+05	MU = ELECTRON MOBILITY CM**2/V/S	0.1870E+05
MUH= HOLE MOBILITY CM**2/V/S	0.2770E+03	MUH= HOLE MOBILITY CM**2/V/S	0.2770E+03
ETA= QUANTUM EFFICIENCY	0.7500E+00	ETA= QUANTUM EFFICIENCY	0.7500E+00
TAU= CARRIER LIFETIME S	0.5000E-06	TAU= CARRIER LIFETIME S	0.5000E-06
NUP= PEAK WAVENUMBER 1/CM	0.1639E+04	NUP= PEAK WAVENUMBER 1/CM	0.1639E+04
QBG= BKGD PHOTON FLUX DENSITY P/CM**2/S	0.1140E+13	QBG= BKGD PHOTON FLUX DENSITY P/CM**2/S	0.4270E+13
QS = SGNL PHOTON FLUX DENSITY P/CM**2/S	0.3310E+12	QS = SGNL PHOTON FLUX DENSITY P/CM**2/S	0.3310E+12
KAPPA = DIELECTRIC CONSTANT	0.1361E+02	KAPPA = DIELECTRIC CONSTANT	0.1361E+02
RF = FEEDBACK RESISTANCE OHM	0.1000E+10	RF = FEEDBACK RESISTANCE OHM	0.1000E+10
CF = FEEDBACK CAPACITACE F	0.3000E-12	CF = FEEDBACK CAPACITACE F	0.3000E-12
VP = PREAMP NOISE (INPUT) V/HZ**.5	0.2000E-08	VP = PREAMP NOISE (INPUT) V/HZ**.5	0.2000E-08
AO = OPEN LOOP GAIN OF PREAMP	0.1000E+04	AO = OPEN LOOP GAIN OF PREAMP	0.1000E+04
TRF= FEEDBACK RESISTOR TEMP K	0.1600E+03	TRF= FEEDBACK RESISTOR TEMP K	0.1600E+03
FC = CHOPPING FREQUENCY HZ	0.4400E+03	FC = CHOPPING FREQUENCY HZ	0.4400E+03
RO = DIODE DARK RESISTANCE BIAS=0 OHM	0.2192E+09	RO = DIODE DARK RESISTANCE BIAS=0 OHM	0.2192E+09
RA = R(0)*A PRODUCT OHM*CM**2	0.1050E+07	RA = R(0)*A PRODUCT OHM*CM**2	0.1050E+07
VJ = JUNCTION POTENTIAL V	0.3091E+00	VJ = JUNCTION POTENTIAL V	0.3091E+00
CJ = JUNCTION CAPACITANCE F	0.2678E-09	CJ = JUNCTION CAPACITANCE F	0.2678E-09
WJ = JUNCTION WIDTH CM	0.2157E-04	WJ = JUNCTION WIDTH CM	0.2157E-04
VC = CONTACT POTENTIAL V	0.3091E+00	VC = CONTACT POTENTIAL V	0.3091E+00
ZD = DETECTOR IMPEDANCE OHM	0.1313E+07	ZD = DETECTOR IMPEDANCE OHM	0.1313E+07
ZF = FEEDBACK RESISTOR IMPEDANCE OHM	0.5466E+09	ZF = FEEDBACK RESISTOR IMPEDANCE OHM	0.5466E+09
PD = DET. PHASE ANGLE RAD	0.3370E-14	PD = DET. PHASE ANGLE RAD	0.3378E-14
PF = FDBK RESISTOR PHASE ANGLE RAD	0.8294E-18	PF = FDBK RESISTOR PHASE ANGLE RAD	0.8294E-18
AZ = TRANSIMPEDANCE OHM	0.9364E+09	AZ = TRANSIMPEDANCE OHM	0.9364E+09
IS = SIGNAL PHOTOCURRENT A	0.1905E-09	IS = SIGNAL PHOTOCURRENT A	0.1905E-09
IT = TOTAL BKGD PHOTOCURRENT A	0.6563E-09	IT = TOTAL BKGD PHOTOCURRENT A	0.2458E-08
VRF= FDBK RESISTOR NOISE V/HZ**.5	0.2784E-05	VRF= FDBK RESISTOR NOISE V/HZ**.5	0.2952E-05
VBG= BACKGROUND NOISE V/HZ**.5	0.1358E-04	VBG= BACKGROUND NOISE V/HZ**.5	0.2628E-04
VJN= JOHNSON NOISE V/HZ**.5	0.4204E-05	VJN= JOHNSON NOISE V/HZ**.5	0.4204E-05
VPA= PREAMP NOISE V/HZ**.5	0.8224E-06	VPA= PREAMP NOISE V/HZ**.5	0.8224E-06
VT = TOTAL NOISE V/HZ**.5	0.1451E-04	VT = TOTAL NOISE V/HZ**.5	0.2679E-04
R = RESPONSIVITY V/W	0.3455E+10	R = RESPONSIVITY V/W	0.3455E+10
NEP= NOISE EQUIVALENT POWER W/HZ**.5	0.4199E-14	NEP= NOISE EQUIVALENT POWER W/HZ**.5	0.7754E-14
DSTAR = CM*HZ**.5/W	0.1648E+14	DSTAR = CM*HZ**.5/W	0.8927E+13

Table F-6 (CH 16)

PV HGCDTE DETECTOR PERFORMANCE CHANNEL 16 75/160/STD

CH = CHANNEL NUMBER	0.1600E+02
HD = DETECTOR HEIGHT CM	0.5300E-01
WD = DETECTOR WIDTH CM	0.8600E-01
T = DET. TEMP, K	0.7500E+02
CS = DET. STRAY CAPACITANCE F	0.6000E-11
RS = DET. SHUNT RESISTANCE OHM	0.1050E+07
X = MOLE FRACTION	0.2707E+00
VB = BIAS VOLTAGE V	0.0000E+00
EG = BAND GAP ENERGY EV	0.2040E+00
NI = INTRINSIC CONC. CM**-3	0.3125E+04
NA = ACCEPTOR CONC. CM**-3	0.2000E+16
ND = DONOR CARRIER CONC. CM**-3	0.5000E+17
MU = ELECTRON MOBILITY CM**2/V/S	0.1040E+05
MUH= HOLE MOBILITY CM**2/V/S	0.2730E+03
ETA= QUANTUM EFFICIENCY	0.7500E+00
TAU= CARRIER LIFETIME S	0.5000E-06
NUP= PEAK WAVENUMBER 1/CM	0.1828E+04
QBG= BKGD PHOTON FLUX DENSITY P/CM**2/S	0.5330E+12
QS = SGNL PHOTON FLUX DENSITY P/CM**2/S	0.3910E+12
KAPPA = DIELECTRIC CONSTANT	0.1354E+02
RF = FEEDBACK RESISTANCE OHM	0.1000E+10
CF = FEEDBACK CAPACITACE F	0.3000E-12
VP = PREAMP NOISE (INPUT) V/HZ**.5	0.2800E-08
AO = OPEN LOOP GAIN OF PREAMP	0.1000E+04
TRF= FEEDBACK RESISTOR TEMP K	0.1600E+03
FC = CHOPPING FREQUENCY HZ	0.4400E+03
RO = DIODE DARK RESISTANCE BIAS=0 OHM	0.2304E+09
RA = R(0)*A PRODUCT OHM*CM**2	0.1050E+07
VJ = JUNCTION POTENTIAL V	0.3722E+00
CJ = JUNCTION CAPACITANCE F	0.5177E-09
WJ = JUNCTION WIDTH CM	0.1056E-04
VC = CONTACT POTENTIAL V	0.3722E+00
ZD = DETECTOR IMPEDANCE OHM	0.6886E+06
ZF = FEEDBACK RESISTOR IMPEDANCE OHM	0.5466E+09
PD = DET. PHASE ANGLE RAD	0.6213E-14
PF = FDBK RESISTOR PHASE ANGLE RAD	0.8294E-18
AZ = TRANSIMPEDANCE OHM	0.2651E+10
IS = SIGNAL PHOTOCURRENT A	0.2141E-09
IT = TOTAL BKGD PHOTOCURRENT A	0.2919E-09
VRF= FDBK RESISTOR NOISE V/HZ**.5	0.7888E-05
VBG= BACKGROUND NOISE V/HZ**.5	0.2564E-04
VJN= JOHNSON NOISE V/HZ**.5	0.1124E-04
VPA= PREAMP NOISE V/HZ**.5	0.1238E-05
VT = TOTAL NOISE V/HZ**.5	0.2911E-04
R = RESPONSIVITY V/W	0.8770E+10
NEP= NOISE EQUIVALENT POWER W/HZ**.5	0.3319E-14
DSTAR = CM*HZ**.5/W	0.2034E+14

PV HGCDTE DETECTOR PERFORMANCE CHANNEL 16 75/180/STD

CH = CHANNEL NUMBER	0.1600E+02
HD = DETECTOR HEIGHT CM	0.5300E-01
WD = DETECTOR WIDTH CM	0.8600E-01
T = DET. TEMP, K	0.7500E+02
CS = DET. STRAY CAPACITANCE F	0.6000E-11
RS = DET. SHUNT RESISTANCE OHM	0.1050E+07
X = MOLE FRACTION	0.2707E+00
VB = BIAS VOLTAGE V	0.0000E+00
EG = BAND GAP ENERGY EV	0.2040E+00
NI = INTRINSIC CONC. CM**-3	0.3125E+04
NA = ACCEPTOR CONC. CM**-3	0.2000E+16
ND = DONOR CARRIER CONC. CM**-3	0.5000E+17
MU = ELECTRON MOBILITY CM**2/V/S	0.1040E+05
MUH= HOLE MOBILITY CM**2/V/S	0.2730E+03
ETA= QUANTUM EFFICIENCY	0.7500E+00
TAU= CARRIER LIFETIME S	0.5000E-06
NUP= PEAK WAVENUMBER 1/CM	0.1828E+04
QBG= BKGD PHOTON FLUX DENSITY P/CM**2/S	0.1120E+13
QS = SGNL PHOTON FLUX DENSITY P/CM**2/S	0.3910E+12
KAPPA = DIELECTRIC CONSTANT	0.1354E+02
RF = FEEDBACK RESISTANCE OHM	0.1000E+10
CF = FEEDBACK CAPACITACE F	0.3000E-12
VP = PREAMP NOISE (INPUT) V/HZ**.5	0.2800E-08
AO = OPEN LOOP GAIN OF PREAMP	0.1000E+04
TRF= FEEDBACK RESISTOR TEMP K	0.1800E+03
FC = CHOPPING FREQUENCY HZ	0.4400E+03
RO = DIODE DARK RESISTANCE BIAS=0 OHM	0.2304E+09
RA = R(0)*A PRODUCT OHM*CM**2	0.1050E+07
VJ = JUNCTION POTENTIAL V	0.3722E+00
CJ = JUNCTION CAPACITANCE F	0.5177E-09
WJ = JUNCTION WIDTH CM	0.1056E-04
VC = CONTACT POTENTIAL V	0.3722E+00
ZD = DETECTOR IMPEDANCE OHM	0.6886E+06
ZF = FEEDBACK RESISTOR IMPEDANCE OHM	0.5466E+09
PD = DET. PHASE ANGLE RAD	0.6213E-14
PF = FDBK RESISTOR PHASE ANGLE RAD	0.8294E-18
AZ = TRANSIMPEDANCE OHM	0.2651E+10
IS = SIGNAL PHOTOCURRENT A	0.2141E-09
IT = TOTAL BKGD PHOTOCURRENT A	0.6134E-09
VRF= FDBK RESISTOR NOISE V/HZ**.5	0.8358E-05
VBG= BACKGROUND NOISE V/HZ**.5	0.3716E-04
VJN= JOHNSON NOISE V/HZ**.5	0.1124E-04
VPA= PREAMP NOISE V/HZ**.5	0.1238E-05
VT = TOTAL NOISE V/HZ**.5	0.3973E-04
R = RESPONSIVITY V/W	0.8770E+10
NEP= NOISE EQUIVALENT POWER W/HZ**.5	0.4530E-14
DSTAR = CM*HZ**.5/W	0.1490E+14

PV HGCDTE DETECTOR PERFORMANCE CHANNEL 16 80/160/STD

CH = CHANNEL NUMBER	0.1600E+02
HD = DETECTOR HEIGHT CM	0.5300E-01
WD = DETECTOR WIDTH CM	0.8600E-01
T = DET. TEMP, K	0.8000E+02
CS = DET. STRAY CAPACITANCE F	0.6000E-11
RS = DET. SHUNT RESISTANCE OHM	0.1050E+07
X = MOLE FRACTION	0.2707E+00
VB = BIAS VOLTAGE V	0.0000E+00
EG = BAND GAP ENERGY EV	0.2040E+00
NI = INTRINSIC CONC. CM**-3	0.2481E+05
NA = ACCEPTOR CONC. CM**-3	0.2000E+16
ND = DONOR CARRIER CONC. CM**-3	0.5000E+17
MU = ELECTRON MOBILITY CM**2/V/S	0.1040E+05
MUH= HOLE MOBILITY CM**2/V/S	0.2730E+03
ETA= QUANTUM EFFICIENCY	0.7500E+00
TAU= CARRIER LIFETIME S	0.5000E-06
NUP= PEAK WAVENUMBER 1/CM	0.1828E+04
QBG= BKGD PHOTON FLUX DENSITY P/CM**2/S	0.5340E+12
QS = SGNL PHOTON FLUX DENSITY P/CM**2/S	0.3910E+12
KAPPA = DIELECTRIC CONSTANT	0.1354E+02
RF = FEEDBACK RESISTANCE OHM	0.1000E+10
CF = FEEDBACK CAPACITACE F	0.3000E-12
VP = PREAMP NOISE (INPUT) V/HZ**.5	0.2800E-08
AO = OPEN LOOP GAIN OF PREAMP	0.1000E+04
TRF= FEEDBACK RESISTOR TEMP K	0.1600E+03
FC = CHOPPING FREQUENCY HZ	0.4400E+03
RO = DIODE DARK RESISTANCE BIAS=0 OHM	0.2304E+09
RA = R(0)*A PRODUCT OHM*CM**2	0.1050E+07
VJ = JUNCTION POTENTIAL V	0.3685E+00
CJ = JUNCTION CAPACITANCE F	0.5203E-09
WJ = JUNCTION WIDTH CM	0.1050E-04
VC = CONTACT POTENTIAL V	0.3685E+00
ZD = DETECTOR IMPEDANCE OHM	0.6852E+06
ZF = FEEDBACK RESISTOR IMPEDANCE OHM	0.5466E+09
PD = DET. PHASE ANGLE RAD	0.6244E-14
PF = FDBK RESISTOR PHASE ANGLE RAD	0.8294E-18
AZ = TRANSIMPEDANCE OHM	0.2703E+10
IS = SIGNAL PHOTOCURRENT A	0.2141E-09
IT = TOTAL BKGD PHOTOCURRENT A	0.2924E-09
VRF= FDBK RESISTOR NOISE V/HZ**.5	0.8034E-05
VBG= BACKGROUND NOISE V/HZ**.5	0.2616E-04
VJN= JOHNSON NOISE V/HZ**.5	0.1184E-04
VPA= PREAMP NOISE V/HZ**.5	0.1242E-05
VT = TOTAL NOISE V/HZ**.5	0.2985E-04
R = RESPONSIVITY V/W	0.8943E+10
NEP= NOISE EQUIVALENT POWER W/HZ**.5	0.3387E-14
DSTAR = CM*HZ**.5/W	0.2023E+14

PV HGCDTE DETECTOR PERFORMANCE CHANNEL 16 80/180/STD

CH = CHANNEL NUMBER	0.1600E+02
HD = DETECTOR HEIGHT CM	0.5300E-01
WD = DETECTOR WIDTH CM	0.8600E-01
T = DET. TEMP, K	0.8000E+02
CS = DET. STRAY CAPACITANCE F	0.6000E-11
RS = DET. SHUNT RESISTANCE OHM	0.1050E+07
X = MOLE FRACTION	0.2707E+00
VB = BIAS VOLTAGE V	0.0000E+00
EG = BAND GAP ENERGY EV	0.2040E+00
NI = INTRINSIC CONC. CM**-3	0.2481E+05
NA = ACCEPTOR CONC. CM**-3	0.2000E+16
ND = DONOR CARRIER CONC. CM**-3	0.5000E+17
MU = ELECTRON MOBILITY CM**2/V/S	0.1840E+05
MUH= HOLE MOBILITY CM**2/V/S	0.2730E+03
ETA= QUANTUM EFFICIENCY	0.7500E+00
TAU= CARRIER LIFETIME S	0.5000E-06
NUP= PEAK WAVENUMBER 1/CM	0.1828E+04
QBG= BKGD PHOTON FLUX DENSITY P/CM**2/S	0.1120E+13
QS = SGNL PHOTON FLUX DENSITY P/CM**2/S	0.3910E+12
KAPPA = DIELECTRIC CONSTANT	0.1354E+02
RF = FEEDBACK RESISTANCE OHM	0.1000E+10
CF = FEEDBACK CAPACITACE F	0.3000E-12
VP = PREAMP NOISE (INPUT) V/HZ**.5	0.2800E-08
AO = OPEN LOOP GAIN OF PREAMP	0.1000E+04
TRF= FEEDBACK RESISTOR TEMP K	0.1800E+03
FC = CHOPPING FREQUENCY HZ	0.4400E+03
RO = DIODE DARK RESISTANCE BIAS=0 OHM	0.2304E+09
RA = R(0)*A PRODUCT OHM*CM**2	0.1050E+07
VJ = JUNCTION POTENTIAL V	0.3685E+00
CJ = JUNCTION CAPACITANCE F	0.5203E-09
WJ = JUNCTION WIDTH CM	0.1050E-04
VC = CONTACT POTENTIAL V	0.3685E+00
ZD = DETECTOR IMPEDANCE OHM	0.6852E+06
ZF = FEEDBACK RESISTOR IMPEDANCE OHM	0.5466E+09
PD = DET. PHASE ANGLE RAD	0.6244E-14
PF = FDBK RESISTOR PHASE ANGLE RAD	0.8294E-18
AZ = TRANSIMPEDANCE OHM	0.2703E+10
IS = SIGNAL PHOTOCURRENT A	0.2141E-09
IT = TOTAL BKGD PHOTOCURRENT A	0.6134E-09
VRF= FDBK RESISTOR NOISE V/HZ**.5	0.8522E-05
VBG= BACKGROUND NOISE V/HZ**.5	0.3789E-04
VJN= JOHNSON NOISE V/HZ**.5	0.1184E-04
VPA= PREAMP NOISE V/HZ**.5	0.1242E-05
VT = TOTAL NOISE V/HZ**.5	0.4062E-04
R = RESPONSIVITY V/W	0.8943E+10
NEP= NOISE EQUIVALENT POWER W/HZ**.5	0.4542E-14
DSTAR = CM*HZ**.5/W	0.1486E+14

Table F-6 (CH 19)

ORIGINAL PAGE IS OF POOR QUALITY

PV INSB DETECTOR PERFORMANCE CHANNEL 19 75/160/STD

CH = CHANNEL NUMBER	0.1900E+02
HD = DETECTOR HEIGHT CM	0.5300E-01
WD = DETECTOR WIDTH CM	0.1096E+00
T = DET. TEMP. K	0.7500E+02
CS = DET. STRAY CAPACITANCE F	0.6000E-11
RS = DET. SHUNT RESISTANCE OHM	0.1050E+07
VB = BIAS VOLTAGE V	0.0000E+00
EG = BAND GAP ENERGY EV	0.2267E+00
NI = INTRINSIC CONC. CM**-3	0.1602E+10
NA = ACCEPTOR CONC. CM**-3	0.1000E+18
ND = DONOR CARRIER CONC. CM**-3	0.5000E+15
MU = ELECTRON MOBILITY CM**2/V/S	0.8000E+05
MUH= HOLE MOBILITY CM**2/V/S	0.5000E+04
ETA= QUANTUM EFFICIENCY	0.8000E+00
TAU= CARRIER LIFETIME S	0.5000E-06
NUP= PEAK WAVENUMBER 1/CM	0.2032E+04
QBG= BKGD PHOTON FLUX DENSITY P/CM**2/S	0.7480E+18
QS = SGNL PHOTON FLUX DENSITY P/CM**2/S	0.3940E+10
KAPPA = DIELECTRIC CONSTANT	0.1720E+02
RF = FEEDBACK RESISTANCE OHM	0.1000E+10
CF = FEEDBACK CAPACITACE F	0.3000E-12
VP = PREAMP NOISE (INPUT) V/HZ**.5	0.2000E-08
AO = OPEN LOOP GAIN OF PREAMP	0.1000E+04
TRF= FEEDBACK RESISTOR TEMP K	0.1600E+03
FC = CHOPPING FREQUENCY HZ	0.4400E+03
RO = DIODE DARK RESISTANCE BIAS=0 OHM	0.1806E+09
RA = R(0)*A PRODUCT OHM*CM**2	0.1049E+07
VJ = JUNCTION POTENTIAL V	0.1978E+00
CJ = JUNCTION CAPACITANCE F	0.1020E-09
WJ = JUNCTION WIDTH CM	0.8673E-04
VC = CONTACT POTENTIAL V	0.1978E+00
ZD = DETECTOR IMPEDANCE OHM	0.3288E+07
ZF = FEEDBACK RESISTOR IMPEDANCE OHM	0.5466E+09
PD = DET. PHASE ANGLE RAD	0.1562E-14
PF = FDBK RESISTOR PHASE ANGLE RAD	0.8294E-18
AZ = TRANSIMPEDANCE OHM	0.6556E+09
IS = SIGNAL PHOTOCURRENT A	0.2933E-11
IT = TOTAL BKGD PHOTOCURRENT A	0.5569E-11
VRF= FDBK RESISTOR NOISE V/HZ**.5	0.1949E-05
VBG= BACKGROUND NOISE V/HZ**)5	0.8758E-06
VJN= JOHNSON NOISE V/HZ**.5	0.2220E-05
VGR= GEN-RECOMB NOISE V/HZ**.5	0.2220E-05
VPA= PREAMP NOISE V/HZ**.5	0.3988E-06
VT = TOTAL NOISE V/HZ**.5	0.3819E-05
R = RESPONSIVITY V/W	0.2082E+10
NEP= NOISE EQUIVALENT POWER W/HZ**.5	0.1834E-14
DSTAR = CM*HZ**.5/W	0.4155E+14

PV INSB DETECTOR PERFORMANCE CHANNEL 19 75/180/STD

CH = CHANNEL NUMBER	0.1900E+02
HD = DETECTOR HEIGHT CM	0.5300E-01
WD = DETECTOR WIDTH CM	0.1096E+00
T = DET. TEMP. K	0.7500E+02
CS = DET. STRAY CAPACITANCE F	0.6000E-11
RS = DET. SHUNT RESISTANCE OHM	0.1050E+07
VB = BIAS VOLTAGE V	0.0000E+00
EG = BAND GAP ENERGY EV	0.2267E+00
NI = INTRINSIC CONC. CM**-3	0.1602E+10
NA = ACCEPTOR CONC. CM**-3	0.1000E+18
ND = DONOR CARRIER CONC. CM**-3	0.5000E+15
MU = ELECTRON MOBILITY CM**2/V/S	0.8000E+05
MUH= HOLE MOBILITY CM**2/V/S	0.5000E+04
ETA= QUANTUM EFFICIENCY	0.8000E+00
TAU= CARRIER LIFETIME S	0.5000E-06
NUP= PEAK WAVENUMBER 1/CM	0.2032E+04
QBG= BKGD PHOTON FLUX DENSITY P/CM**2/S	0.1570E+11
QS = SGNL PHOTON FLUX DENSITY P/CM**2/S	0.3940E+10
KAPPA = DIELECTRIC CONSTANT	0.1720E+02
RF = FEEDBACK RESISTANCE OHM	0.1000E+10
CF = FEEDBACK CAPACITACE F	0.3000E-12
VP = PREAMP NOISE (INPUT) V/HZ**.5	0.2000E-08
AO = OPEN LOOP GAIN OF PREAMP	0.1000E+04
TRF= FEEDBACK RESISTOR TEMP K	0.1800E+03
FC = CHOPPING FREQUENCY HZ	0.4400E+03
RO = DIODE DARK RESISTANCE BIAS=0 OHM	0.1808E+09
RA = R(0)*A PRODUCT OHM*CM**2	0.1050E+07
VJ = JUNCTION POTENTIAL V	0.1978E+00
CJ = JUNCTION CAPACITANCE F	0.1020E-09
WJ = JUNCTION WIDTH CM	0.8673E-04
VC = CONTACT POTENTIAL V	0.1978E+00
ZD = DETECTOR IMPEDANCE OHM	0.3288E+07
ZF = FEEDBACK RESISTOR IMPEDANCE OHM	0.5466E+09
PD = DET. PHASE ANGLE RAD	0.1560E-14
PF = FDBK RESISTOR PHASE ANGLE RAD	0.8294E-18
AZ = TRANSIMPEDANCE OHM	0.6556E+09
IS = SIGNAL PHOTOCURRENT A	0.2933E-11
IT = TOTAL BKGD PHOTOCURRENT A	0.1169E-10
VRF= FDBK RESISTOR NOISE V/HZ**.5	0.2067E-05
VBG= BACKGROUND NOISE V/HZ**)5	0.1269E-05
VJN= JOHNSON NOISE V/HZ**.5	0.2219E-05
VGR= GEN-RECOMB NOISE V/HZ**.5	0.2219E-05
VPA= PREAMP NOISE V/HZ**.5	0.3988E-06
VT = TOTAL NOISE V/HZ**.5	0.3986E-05
R = RESPONSIVITY V/W	0.2082E+10
NEP= NOISE EQUIVALENT POWER W/HZ**.5	0.1915E-14
DSTAR = CM*HZ**.5/W	0.3981E+14

PV INSB DETECTOR PERFORMANCE CHANNEL 19 80/160/STD

CH = CHANNEL NUMBER	0.1900E+02
HD = DETECTOR HEIGHT CM	0.5300E-01
WD = DETECTOR WIDTH CM	0.1096E+00
T = DET. TEMP. K	0.8000E+02
CS = DET. STRAY CAPACITANCE F	0.6000E-11
RS = DET. SHUNT RESISTANCE OHM	0.1050E+07
VB = BIAS VOLTAGE V	0.0000E+00
EG = BAND GAP ENERGY EV	0.2267E+00
NI = INTRINSIC CONC. CM**-3	0.5281E+10
NA = ACCEPTOR CONC. CM**-3	0.1000E+18
ND = DONOR CARRIER CONC. CM**-3	0.5000E+15
MU = ELECTRON MOBILITY CM**2/V/S	0.8000E+05
MUH= HOLE MOBILITY CM**2/V/S	0.5000E+04
ETA= QUANTUM EFFICIENC	0.8000E+00
TAU= CARRIER LIFETIME S	0.5000E-06
NUP= PEAK WAVENUMBER 1/CM	0.2032E+04
QBG= BKGD PHOTON FLUX DENSITY P/CM**2/S	0.7470E+10
QS = SGNL PHOTON FLUX DENSITY P/CM**2/S	0.3940E+10
KAPPA = DIELECTRIC CONSTANT	0.1720E+02
RF = FEEDBACK RESISTANCE OHM	0.1000E+10
CF = FEEDBACK CAPACITACE F	0.3000E-12
VP = PREAMP NOISE (INPUT) V/HZ**.5	0.2000E-08
AO = OPEN LOOP GAIN OF PREAMP	0.1000E+04
TRF= FEEDBACK RESISTOR TEMP K	0.1600E+03
FC = CHOPPING FREQUENCY HZ	0.4400E+03
RO = DIODE DARK RESISTANCE BIAS=0 OHM	0.1808E+09
RA = R(0)*A PRODUCT OHM*CM**2	0.1050E+07
VJ = JUNCTION POTENTIAL V	0.1945E+00
CJ = JUNCTION CAPACITANCE F	0.1029E-09
WJ = JUNCTION WIDTH CM	0.8681E-04
VC = CONTACT POTENTIAL V	0.1945E+00
ZD = DETECTOR IMPEDANCE OHM	0.3263E+07
ZF = FEEDBACK RESISTOR IMPEDANCE OHM	0.5466E+09
PD = DET. PHASE ANGLE RAD	0.1573E-14
PF = FDBK RESISTOR PHASE ANGLE RAD	0.8294E-18
AZ = TRANSIMPEDANCE OHM	0.6567E+09
IS = SIGNAL PHOTOCURRENT A	0.2933E-11
IT = TOTAL BKGD PHOTOCURRENT A	0.5561E-11
VRF= FDBK RESISTOR NOISE V/HZ**.5	0.1952E-05
VBG= BACKGROUND NOISE V/HZ**)5	0.8765E-06
VJN= JOHNSON NOISE V/HZ**.5	0.2296E-05
VGR= GEN-RECOMB NOISE V/HZ**.5	0.2296E-05
VPA= PREAMP NOISE V/HZ**.5	0.4015E-06
VT = TOTAL NOISE V/HZ**.5	0.3909E-05
R = RESPONSIVITY V/W	0.2085E+10
NEP= NOISE EQUIVALENT POWER W/HZ**.5	0.1874E-14
DSTAR = CM*HZ**.5/W	0.4066E+14

PV INSB DETECTOR PERFORMANCE CHANNEL 19 80/180/STD

CH = CHANNEL NUMBER	0.1900E+02
HD = DETECTOR HEIGHT CM	0.5300E-01
WD = DETECTOR WIDTH CM	0.1096E+00
T = DET. TEMP. K	0.8000E+02
CS = DET. STRAY CAPACITANCE F	0.6000E-11
RS = DET. SHUNT RESISTANCE OHM	0.1050E+07
VB = BIAS VOLTAGE V	0.0000E+00
EG = BAND GAP ENERGY EV	0.2267E+00
NI = INTRINSIC CONC. CM**-3	0.5281E+10
NA = ACCEPTOR CONC. CM**-3	0.1000E+18
ND = DONOR CARRIER CONC. CM**-3	0.5000E+15
MU = ELECTRON MOBILITY CM**2/V/S	0.8000E+05
MUH= HOLE MOBILITY CM**2/V/S	0.5000E+04
ETA= QUANTUM EFFICIENCY	0.8000E+00
TAU= CARRIER LIFETIME S	0.5000E-06
NUP= PEAK WAVENUMBER 1/CM	0.2032E+04
QBG= BKGD PHOTON FLUX DENSITY P/CM**2/S	0.1570E+11
QS = SGNL PHOTON FLUX DENSITY P/CM**2/S	0.3940E+10
KAPPA = DIELECTRIC CONSTANT	0.1720E+02
RF = FEEDBACK RESISTANCE OHM	0.1000E+10
CF = FEEDBACK CAPACITACE F	0.3000E-12
VP = PREAMP NOISE (INPUT) V/HZ**.5	0.2000E-08
AO = OPEN LOOP GAIN OF PREAMP	0.1000E+04
TRF= FEEDBACK RESISTOR TEMP K	0.1800E+03
FC = CHOPPING FREQUENCY HZ	0.4400E+03
RO = DIODE DARK RESISTANCE BIAS=0 OHM	0.1808E+09
RA = R(0)*A PRODUCT OHM*CM**2	0.1050E+07
VJ = JUNCTION POTENTIAL V	0.1945E+00
CJ = JUNCTION CAPACITANCE F	0.1029E-09
WJ = JUNCTION WIDTH CM	0.8681E-04
VC = CONTACT POTENTIAL V	0.1945E+00
ZD = DETECTOR IMPEDANCE OHM	0.3263E+07
ZF = FEEDBACK RESISTOR IMPEDANCE OHM	0.5466E+09
PD = DET. PHASE ANGLE RAD	0.1573E-14
PF = FDBK RESISTOR PHASE ANGLE RAD	0.8294E-18
AZ = TRANSIMPEDANCE OHM	0.6567E+09
IS = SIGNAL PHOTOCURRENT A	0.2933E-11
IT = TOTAL BKGD PHOTOCURRENT A	0.1169E-10
VRF= FDBK RESISTOR NOISE V/HZ**.5	0.2070E-05
VBG= BACKGROUND NOISE V/HZ**)5	0.1271E-05
VJN= JOHNSON NOISE V/HZ**.5	0.2296E-05
VGR= GEN-RECOMB NOISE V/HZ**.5	0.2296E-05
VPA= PREAMP NOISE V/HZ**.5	0.4015E-06
VT = TOTAL NOISE V/HZ**.5	0.4074E-05
R = RESPONSIVITY V/W	0.2085E+10
NEP= NOISE EQUIVALENT POWER W/HZ**.5	0.1954E-14
DSTAR = CM*HZ**.5/W	0.3981E+14

Table F-6 (CH 25)

PV INSB DETECTOR PERFORMANCE CHANNEL 25 75/160/STD

CH = CHANNEL NUMBER	0.2500E+02
HD = DETECTOR HEIGHT CM	0.5300E-01
WD = DETECTOR WIDTH CM	0.7900E-01
T = DET. TEMP, K	0.7500E+02
CS = DET. STRAY CAPACITANCE F	0.6000E-11
RS = DET. SHUNT RESISTANCE OHM	0.1050E+07
VB = BIAS VOLTAGE V	0.0000E+00
EG = BAND GAP ENERGY EV	0.2267E+00
NI = INTRINSIC CONC. CM**-3	0.1602E+10
NA = ACCEPTOR CONC. CM**-3	0.1000E+18
ND = DONOR CARRIER CONC. CM**-3	0.5000E+15
MU = ELECTRON MOBILITY CM**2/V/S	0.8000E+05
MUH= HOLE MOBILITY CM**2/V/S	0.5000E+04
ETA= QUANTUM EFFICIENCY	0.8000E+00
TAU= CARRIER LIFETIME S	0.5000E-06
NUP= PEAK WAVENUMBER 1/CM	0.2032E+04
QBG= BKGD PHOTON FLUX DENSITY P/CM**2/S	0.1170E+12
QS = SGNL PHOTON FLUX DENSITY P/CM**2/S	0.1100E+12
KAPPA = DIELECTRIC CONSTANT	0.1720E+02
RF = FEEDBACK RESISTANCE OHM	0.1000E+10
CF = FEEDBACK CAPACITACE F	0.3000E-12
VP = PREAMP NOISE (INPUT) V/HZ**.5	0.2800E-08
AO = OPEN LOOP GAIN OF PREAMP	0.1000E+04
TRF= FEEDBACK RESISTOR TEMP K	0.1600E+03
FC = CHOPPING FREQUENCY HZ	0.4400E+03
RO = DIODE DARK RESISTANCE BIAS=0 OHM	0.2480E+09
RA = R(0)*A PRODUCT OHM*CM**2	0.1049E+07
VJ = JUNCTION POTENTIAL V	0.1978E+00
CJ = JUNCTION CAPACITANCE F	0.7428E-10
WJ = JUNCTION WIDTH CM	0.8673E-04
VC = CONTACT POTENTIAL V	0.1978E+00
ZD = DETECTOR IMPEDANCE OHM	0.4425E+07
ZF = FEEDBACK RESISTOR IMPEDANCE OHM	0.5466E+09
PD = DET. PHASE ANGLE RAD	0.8281E-15
PF = FDBK RESISTOR PHASE ANGLE RAD	0.8294E-18
AZ = TRANSIMPEDANCE OHM	0.6237E+09
IS = SIGNAL PHOTOCURRENT A	0.5962E-10
IT = TOTAL BKGD PHOTOCURRENT A	0.6342E-10
VRF= FDBK RESISTOR NOISE V/HZ**.5	0.1854E-05
VBG= BACKGROUND NOISE V/HZ**)5	0.2811E-05
VJN= JOHNSON NOISE V/HZ**.5	0.1802E-05
VGR= GEN-RECOMB NOISE V/HZ**.5	0.1802E-05
VPA= PREAMP NOISE V/HZ**.5	0.3076E-06
VT = TOTAL NOISE V/HZ**.5	0.4235E-05
R = RESPONSIVITY V/W	0.1981E+10
NEP= NOISE EQUIVALENT POWER W/HZ**.5	0.2138E-14
DSTAR = CM*HZ**.5/W	0.3042E+14

PV INSB DETECTOR PERFORMANCE CHANNEL 25 75/180/STD

CH = CHANNEL NUMBER	0.2500E+02
HD = DETECTOR HEIGHT CM	0.5300E-01
WD = DETECTOR WIDTH CM	0.7900E-01
T = DET. TEMP, K	0.7500E+02
CS = DET. STRAY CAPACITANCE F	0.6000E-11
RS = DET. SHUNT RESISTANCE OHM	0.1050E+07
VB = BIAS VOLTAGE V	0.0000E+00
EG = BAND GAP ENERGY EV	0.2267E+00
NI = INTRINSIC CONC. CM**-3	0.1602E+10
NA = ACCEPTOR CONC. CM**-3	0.1000E+18
ND = DONOR CARRIER CONC. CM**-3	0.5000E+15
MU = ELECTRON MOBILITY CM**2/V/S	0.8000E+05
MUH= HOLE MOBILITY CM**2/V/S	0.5000E+04
ETA= QUANTUM EFFICIENCY	0.8000E+00
TAU= CARRIER LIFETIME S	0.5000E-06
NUP= PEAK WAVENUMBER 1/CM	0.2032E+04
QBG= BKGD PHOTON FLUX DENSITY P/CM**2/S	0.1320E+12
QS = SGNL PHOTON FLUX DENSITY P/CM**2/S	0.1100E+12
KAPPA = DIELECTRIC CONSTANT	0.1720E+02
RF = FEEDBACK RESISTANCE OHM	0.1000E+10
CF = FEEDBACK CAPACITACE F	0.3000E-12
VP = PREAMP NOISE (INPUT) V/HZ**.5	0.2800E-08
AO = OPEN LOOP GAIN OF PREAMP	0.1000E+04
TRF= FEEDBACK RESISTOR TEMP K	0.1800E+03
FC = CHOPPING FREQUENCY HZ	0.4400E+03
RO = DIODE DARK RESISTANCE BIAS=0 OHM	0.2483E+09
RA = R(0)*A PRODUCT OHM*CM**2	0.1050E+07
VJ = JUNCTION POTENTIAL V	0.1978E+00
CJ = JUNCTION CAPACITANCE F	0.7428E-10
WJ = JUNCTION WIDTH CM	0.8673E-04
VC = CONTACT POTENTIAL V	0.1978E+00
ZD = DETECTOR IMPEDANCE OHM	0.4425E+07
ZF = FEEDBACK RESISTOR IMPEDANCE OHM	0.5466E+09
PD = DET. PHASE ANGLE RAD	0.8271E-15
PF = FDBK RESISTOR PHASE ANGLE RAD	0.8294E-18
AZ = TRANSIMPEDANCE OHM	0.6237E+09
IS = SIGNAL PHOTOCURRENT A	0.5962E-10
IT = TOTAL BKGD PHOTOCURRENT A	0.7155E-10
VRF= FDBK RESISTOR NOISE V/HZ**.5	0.1966E-05
VBG= BACKGROUND NOISE V/HZ**)5	0.2980E-05
VJN= JOHNSON NOISE V/HZ**.5	0.1801E-05
VGR= GEN-RECOMB NOISE V/HZ**.5	0.1801E-05
VPA= PREAMP NOISE V/HZ**.5	0.3076E-06
VT = TOTAL NOISE V/HZ**.5	0.4401E-05
R = RESPONSIVITY V/W	0.1981E+10
NEP= NOISE EQUIVALENT POWER W/HZ**.5	0.2222E-14
DSTAR = CM*HZ**.5/W	0.2927E+14

PV INSB DETECTOR PERFORMANCE CHANNEL 25 80/160/STD

CH = CHANNEL NUMBER	0.2500E+02
HD = DETECTOR HEIGHT CM	0.5300E-01
WD = DETECTOR WIDTH CM	0.7900E-01
T = DET. TEMP, K	0.8000E+02
CS = DET. STRAY CAPACITANCE F	0.6000E-11
RS = DET. SHUNT RESISTANCE OHM	0.1050E+07
VB = BIAS VOLTAGE V	0.0000E+00
EG = BAND GAP ENERGY EV	0.2267E+00
NI = INTRINSIC CONC. CM**-3	0.5281E+10
NA = ACCEPTOR CONC. CM**-3	0.1000E+18
ND = DONOR CARRIER CONC. CM**-3	0.5000E+15
MU = ELECTRON MOBILITY CM**2/V/S	0.8000E+05
MUH= HOLE MOBILITY CM**2/V/S	0.5000E+04
ETA= QUANTUM EFFICIENCY	0.8000E+00
TAU= CARRIER LIFETIME S	0.5000E-06
NUP= PEAK WAVENUMBER 1/CM	0.2032E+04
QBG= BKGD PHOTON FLUX DENSITY P/CM**2/S	0.1170E+12
QS = SGNL PHOTON FLUX DENSITY P/CM**2/S	0.1100E+12
KAPPA = DIELECTRIC CONSTANT	0.1720E+02
RF = FEEDBACK RESISTANCE OHM	0.1000E+10
CF = FEEDBACK CAPACITACE F	0.3000E-12
VP = PREAMP NOISE (INPUT) V/HZ**.5	0.2800E-08
AO = OPEN LOOP GAIN OF PREAMP	0.1000E+04
TRF= FEEDBACK RESISTOR TEMP K	0.1600E+03
FC = CHOPPING FREQUENCY HZ	0.4400E+03
RO = DIODE DARK RESISTANCE BIAS=0 OHM	0.2483E+09
RA = R(0)*A PRODUCT OHM*CM**2	0.1050E+07
VJ = JUNCTION POTENTIAL V	0.1945E+00
CJ = JUNCTION CAPACITANCE F	0.7490E-10
WJ = JUNCTION WIDTH CM	0.8601E-04
VC = CONTACT POTENTIAL V	0.1945E+00
ZD = DETECTOR IMPEDANCE OHM	0.4392E+07
ZF = FEEDBACK RESISTOR IMPEDANCE OHM	0.5466E+09
PD = DET. PHASE ANGLE RAD	0.8341E-15
PF = FDBK RESISTOR PHASE ANGLE RAD	0.8294E-18
AZ = TRANSIMPEDANCE OHM	0.6243E+09
IS = SIGNAL PHOTOCURRENT A	0.5962E-10
IT = TOTAL BKGD PHOTOCURRENT A	0.6342E-10
VRF= FDBK RESISTOR NOISE V/HZ**.5	0.1856E-05
VBG= BACKGROUND NOISE V/HZ**)5	0.2814E-05
VJN= JOHNSON NOISE V/HZ**.5	0.1862E-05
VGR= GEN-RECOMB NOISE V/HZ**.5	0.1862E-05
VPA= PREAMP NOISE V/HZ**.5	0.3096E-06
VT = TOTAL NOISE V/HZ**.5	0.4289E-05
R = RESPONSIVITY V/W	0.1983E+10
NEP= NOISE EQUIVALENT POWER W/HZ**.5	0.2163E-14
DSTAR = CM*HZ**.5/W	0.3006E+14

PV INSB DETECTOR PERFORMANCE CHANNEL 25 80/180/STD

CH = CHANNEL NUMBER	0.2500E+02
HD = DETECTOR HEIGHT CM	0.5300E-01
WD = DETECTOR WIDTH CM	0.7900E-01
T = DET. TEMP, K	0.8000E+02
CS = DET. STRAY CAPACITANCE F	0.6000E-11
RS = DET. SHUNT RESISTANCE OHM	0.1050E+07
VB = BIAS VOLTAGE V	0.0000E+00
EG = BAND GAP ENERGY EV	0.2267E+00
NI = INTRINSIC CONC. CM**-3	0.5281E+10
NA = ACCEPTOR CONC. CM**-3	0.1000E+18
ND = DONOR CARRIER CONC. CM**-3	0.5000E+15
MU = ELECTRON MOBILITY CM**2/V/S	0.8000E+05
MUH= HOLE MOBILITY CM**2/V/S	0.5000E+04
ETA= QUANTUM EFFICIENCY	0.8000E+00
TAU= CARRIER LIFETIME S	0.5000E-06
NUP= PEAK WAVENUMBER 1/CM	0.2032E+04
QBG= BKGD PHOTON FLUX DENSITY P/CM**2/S	0.1320E+12
QS = SGNL PHOTON FLUX DENSITY P/CM**2/S	0.1100E+12
KAPPA = DIELECTRIC CONSTANT	0.1720E+02
RF = FEEDBACK RESISTANCE OHM	0.1000E+10
CF = FEEDBACK CAPACITACE F	0.3000E-12
VP = PREAMP NOISE (INPUT) V/HZ**.5	0.2800E-08
AO = OPEN LOOP GAIN OF PREAMP	0.1000E+04
TRF= FEEDBACK RESISTOR TEMP K	0.1800E+03
FC = CHOPPING FREQUENCY HZ	0.4400E+03
RO = DIODE DARK RESISTANCE BIAS=0 OHM	0.2483E+09
RA = R(0)*A PRODUCT OHM*CM**2	0.1050E+07
VJ = JUNCTION POTENTIAL V	0.1945E+00
CJ = JUNCTION CAPACITANCE F	0.7490E-10
WJ = JUNCTION WIDTH CM	0.8601E-04
VC = CONTACT POTENTIAL V	0.1945E+00
ZD = DETECTOR IMPEDANCE OHM	0.4392E+07
ZF = FEEDBACK RESISTOR IMPEDANCE OHM	0.5466E+09
PD = DET. PHASE ANGLE RAD	0.8341E-15
PF = FDBK RESISTOR PHASE ANGLE RAD	0.8294E-18
AZ = TRANSIMPEDANCE OHM	0.6243E+09
IS = SIGNAL PHOTOCURRENT A	0.5962E-10
IT = TOTAL BKGD PHOTOCURRENT A	0.7155E-10
VRF= FDBK RESISTOR NOISE V/HZ**.5	0.1968E-05
VBG= BACKGROUND NOISE V/HZ**)5	0.2989E-05
VJN= JOHNSON NOISE V/HZ**.5	0.1862E-05
VGR= GEN-RECOMB NOISE V/HZ**.5	0.1862E-05
VPA= PREAMP NOISE V/HZ**.5	0.3096E-06
VT = TOTAL NOISE V/HZ**.5	0.4455E-05
R = RESPONSIVITY V/W	0.1983E+10
NEP= NOISE EQUIVALENT POWER W/HZ**.5	0.2247E-14
DSTAR = CM*HZ**.5/W	0.2895E+14

Table F-6 (CH 28)

PV INSB DETECTOR PERFORMANCE CHANNEL 28 75/160/STD

CH = CHANNEL NUMBER	0.2800E+02
HD = DETECTOR HEIGHT CM	0.5300E-01
WD = DETECTOR WIDTH CM	0.9120E-01
T = DET. TEMP, K	0.7500E+02
CS = DET. STRAY CAPACITANCE F	0.6000E-11
RS = DET. SHUNT RESISTANCE OHM	0.1050E+07
VB = BIAS VOLTAGE V	0.0000E+00
EG = BAND GAP ENERGY EV	0.2267E+00
NI = INTRINSIC CONC. CM**-3	0.1602E+10
NA = ACCEPTOR CONC. CM**-3	0.1000E+18
ND = DONOR CARRIER CONC. CM**-3	0.5000E+15
MU = ELECTRON MOBILITY CM**2/V/S	0.8000E+05
MUH= HOLE MOBILITY CM**2/V/S	0.5000E+04
ETA= QUANTUM EFFICIENCY	0.8000E+00
TAU= CARRIER LIFETIME S	0.5000E-06
NUP= PEAK WAVENUMBER 1/CM	0.2032E+04
QBG= BKGD PHOTON FLUX DENSITY P/CM**2/S	0.5210E+11
QS = SGNL PHOTON FLUX DENSITY P/CM**2/S	0.5000E+11
KAPPA = DIELECTRIC CONSTANT	0.1720E+02
RF = FEEDBACK RESISTANCE OHM	0.1000E+10
CF = FEEDBACK CAPACITACE F	0.3000E-12
VP = PREAMP NOISE (INPUT) V/HZ**.5	0.2800E-08
AO = OPEN LOOP GAIN OF PREAMP	0.1000E+04
TRF= FEEDBACK RESISTOR TEMP K	0.1600E+03
FC = CHOPPING FREQUENCY HZ	0.4400E+03
RO = DIODE DARK RESISTANCE BIAS=0 OHM	0.2170E+09
RA = R(0)*A PRODUCT OHM*CM**2	0.1049E+07
VJ = JUNCTION POTENTIAL V	0.1978E+00
CJ = JUNCTION CAPACITANCE F	0.8489E-10
WJ = JUNCTION WIDTH CM	0.8673E-04
VC = CONTACT POTENTIAL V	0.1978E+00
ZD = DETECTOR IMPEDANCE OHM	0.3908E+07
ZF = FEEDBACK RESISTOR IMPEDANCE OHM	0.5466E+09
PD = DET. PHASE ANGLE RAD	0.1002E-14
PF = FDBK RESISTOR PHASE ANGLE RAD	0.8294E-18
AZ = TRANSIMPEDANCE OHM	0.6355E+09
IS = SIGNAL PHOTOCURRENT A	0.3097E-10
IT = TOTAL BKGD PHOTOCURRENT A	0.3227E-10
VRF= FDBK RESISTOR NOISE V/HZ**.5	0.1869E-05
VBG= BACKGROUND NOISE V/HZ**)5	0.2044E-05
VJN= JOHNSON NOISE V/HZ**.5	0.1963E-05
VGR= GEN-RECOMB NOISE V/HZ**.5	0.1963E-05
VPA= PREAMP NOISE V/HZ**.5	0.3433E-06
VT = TOTAL NOISE V/HZ**.5	0.3946E-05
R = RESPONSIVITY V/W	0.2018E+10
NEP= NOISE EQUIVALENT POWER W/HZ**.5	0.1955E-14
DSTAR = CM*HZ**.5/W	0.3556E+14

PV INSB DETECTOR PERFORMANCE CHANNEL 28 75/160/STD

CH = CHANNEL NUMBER	0.2800E+02
HD = DETECTOR HEIGHT CM	0.5300E-01
WD = DETECTOR WIDTH CM	0.9120E-01
T = DET. TEMP, K	0.7500E+02
CS = DET. STRAY CAPACITANCE F	0.6000E-11
RS = DET. SHUNT RESISTANCE OHM	0.1050E+07
VB = BIAS VOLTAGE V	0.0000E+00
EG = BAND GAP ENERGY EV	0.2267E+00
NI = INTRINSIC CONC. CM**-3	0.1602E+10
NA = ACCEPTOR CONC. CM**-3	0.1000E+18
ND = DONOR CARRIER CONC. CM**-3	0.5000E+15
MU = ELECTRON MOBILITY CM**2/V/S	0.8000E+05
MUH= HOLE MOBILITY CM**2/V/S	0.5000E+04
ETA= QUANTUM EFFICIENCY	0.8000E+00
TAU= CARRIER LIFETIME S	0.5000E-06
NUP= PEAK WAVENUMBER 1/CM	0.2032E+04
QBG= BKGD PHOTON FLUX DENSITY P/CM**2/S	0.5400E+11
QS = SGNL PHOTON FLUX DENSITY P/CM**2/S	0.5000E+11
KAPPA = DIELECTRIC CONSTANT	0.1720E+02
RF = FEEDBACK RESISTANCE OHM	0.1000E+10
CF = FEEDBACK CAPACITACE F	0.3000E-12
VP = PREAMP NOISE (INPUT) V/HZ**.5	0.2800E-08
AO = OPEN LOOP GAIN OF PREAMP	0.1000E+04
TRF= FEEDBACK RESISTOR TEMP K	0.1800E+03
FC = CHOPPING FREQUENCY HZ	0.4400E+03
RO = DIODE DARK RESISTANCE BIAS=0 OHM	0.2172E+09
RA = R(0)*A PRODUCT OHM*CM**2	0.1050E+07
VJ = JUNCTION POTENTIAL V	0.1978E+00
CJ = JUNCTION CAPACITANCE F	0.8489E-10
WJ = JUNCTION WIDTH CM	0.8673E-04
VC = CONTACT POTENTIAL V	0.1978E+00
ZD = DETECTOR IMPEDANCE OHM	0.3908E+07
ZF = FEEDBACK RESISTOR IMPEDANCE OHM	0.5466E+09
PD = DET. PHASE ANGLE RAD	0.1000E-14
PF = FDBK RESISTOR PHASE ANGLE RAD	0.8294E-18
AZ = TRANSIMPEDANCE OHM	0.6355E+09
IS = SIGNAL PHOTOCURRENT A	0.3097E-10
IT = TOTAL BKGD PHOTOCURRENT A	0.3395E-10
VRF= FDBK RESISTOR NOISE V/HZ**.5	0.2004E-05
VBG= BACKGROUND NOISE V/HZ**)5	0.2096E-05
VJN= JOHNSON NOISE V/HZ**.5	0.1962E-05
VGR= GEN-RECOMB NOISE V/HZ**.5	0.1962E-05
VPA= PREAMP NOISE V/HZ**.5	0.3433E-06
VT = TOTAL NOISE V/HZ**.5	0.4028E-05
R = RESPONSIVITY V/W	0.2018E+10
NEP= NOISE EQUIVALENT POWER W/HZ**.5	0.1996E-14
DSTAR = CM*HZ**.5/W	0.3483E+14

PV INSB DETECTOR PERFORMANCE CHANNEL 28 80/160/STD

CH = CHANNEL NUMBER	0.2800E+02
HD = DETECTOR HEIGHT CM	0.5300E-01
WD = DETECTOR WIDTH CM	0.9120E-01
T = DET. TEMP, K	0.8000E+02
CS = DET. STRAY CAPACITANCE F	0.6000E-11
RS = DET. SHUNT RESISTANCE OHM	0.1050E+07
VB = BIAS VOLTAGE V	0.0000E+00
EG = BAND GAP ENERGY EV	0.2267E+00
NI = INTRINSIC CONC. CM**-3	0.5281E+10
NA = ACCEPTOR CONC. CM**-3	0.1000E+18
ND = DONOR CARRIER CONC, CM**-3	0.5000E+15
MU = ELECTRON MOBILITY CM**2/V/S	0.8000E+05
MUH= HOLE MOBILITY CM**2/V/S	0.5000E+04
ETA= QUANTUM EFFICIENCY	0.8000E+00
TAU= CARRIER LIFETIME S	0.5000E-06
NUP= PEAK WAVENUMBER 1/CM	0.2032E+04
QBG= BKGD PHOTON FLUX DENSITY P/CM**2/S	0.5230E+11
QS = SGNL PHOTON FLUX DENSITY P/CM**2/S	0.5000E+11
KAPPA = DIELECTRIC CONSTANT	0.1720E+02
RF = FEEDBACK RESISTANCE OHM	0.1000E+10
CF = FEEDBACK CAPACITACE F	0.3000E-12
VP = PREAMP NOISE (INPUT) V/HZ**.5	0.2800E-08
AO = OPEN LOOP GAIN OF PREAMP	0.1000E+04
TRF= FEEDBACK RESISTOR TEMP K	0.1600E+03
FC = CHOPPING FREQUENCY HZ	0.4400E+03
RO = DIODE DARK RESISTANCE BIAS=0 OHM	0.2172E+09
RA = R(0)*A PRODUCT OHM*CM**2	0.1050E+07
VJ = JUNCTION POTENTIAL V	0.1945E+00
CJ = JUNCTION CAPACITANCE F	0.8560E-10
WJ = JUNCTION WIDTH CM	0.8601E-04
VC = CONTACT POTENTIAL V	0.1945E+00
ZD = DETECTOR IMPEDANCE OHM	0.3870E+07
ZF = FEEDBACK RESISTOR IMPEDANCE OHM	0.5466E+09
PD = DET. PHASE ANGLE RAD	0.1089E-14
PF = FDBK RESISTOR PHASE ANGLE RAD	0.8294E-18
AZ = TRANSIMPEDANCE OHM	0.6363E+09
IS = SIGNAL PHOTOCURRENT A	0.3097E-10
IT = TOTAL BKGD PHOTOCURRENT A	0.3240E-10
VRF= FDBK RESISTOR NOISE V/HZ**.5	0.1891E-05
VBG= BACKGROUND NOISE V/HZ**)5	0.2059E-05
VJN= JOHNSON NOISE V/HZ**.5	0.2029E-05
VGR= GEN-RECOMB NOISE V/HZ**.5	0.2029E-05
VPA= PREAMP NOISE V/HZ**.5	0.3456E-06
VT = TOTAL NOISE V/HZ**.5	0.4017E-05
R = RESPONSIVITY V/W	0.2021E+10
NEP= NOISE EQUIVALENT POWER W/HZ**.5	0.1988E-14
DSTAR = CM*HZ**.5/W	0.3497E+14

PV INSB DETECTOR PERFORMANCE CHANNEL 28 80/180/STD

CH = CHANNEL NUMBER	0.2800E+02
HD = DETECTOR HEIGHT CM	0.5300E-01
WD = DETECTOR WIDTH CM	0.9120E-01
T = DET. TEMP, K	0.8000E+02
CS = DET. STRAY CAPACITANCE F	0.6000E-11
RS = DET. SHUNT RESISTANCE OHM	0.1050E+07
VB = BIAS VOLTAGE V	0.0000E+00
EG = BAND GAP ENERGY EV	0.2267E+00
NI = INTRINSIC CONC. CM**-3	0.5281E+10
NA = ACCEPTOR CONC. CM**-3	0.1000E+18
ND = DONOR CARRIER CONC. CM**-3	0.5000E+15
MU = ELECTRON MOBILITY CM**2/V/S	0.8000E+05
MUH= HOLE MOBILITY CM**2/V/S	0.5000E+04
ETA= QUANTUM EFFICIENCY	0.8000E+00
TAU= CARRIER LIFETIME S	0.5000E-06
NUP= PEAK WAVENUMBER 1/CM	0.2032E+04
QBG= BKGD PHOTON FLUX DENSITY P/CM**2/S	0.5400E+11
QS = SGNL PHOTON FLUX DENSITY P/CM**2/S	0.5000E+11
KAPPA = DIELECTRIC CONSTANT	0.1720E+02
RF = FEEDBACK RESISTANCE OHM	0.1000E+10
CF = FEEDBACK CAPACITACE F	0.3000E-12
VP = PREAMP NOISE (INPUT) V/HZ**.5	0.2800E-08
AO = OPEN LOOP GAIN OF PREAMP	0.1000E+04
TRF= FEEDBACK RESISTOR TEMP K	0.1800E+03
FC = CHOPPING FREQUENCY HZ	0.4400E+03
RO = DIODE DARK RESISTANCE BIAS=0 OHM	0.2172E+09
RA = R(0)*A PRODUCT OHM*CM**2	0.1050E+07
VJ = JUNCTION POTENTIAL V	0.1945E+00
CJ = JUNCTION CAPACITANCE F	0.8560E-10
WJ = JUNCTION WIDTH CM	0.8601E-04
VC = CONTACT POTENTIAL V	0.1945E+00
ZD = DETECTOR IMPEDANCE OHM	0.3870E+07
ZF = FEEDBACK RESISTOR IMPEDANCE OHM	0.5466E+09
PD = DET. PHASE ANGLE RAD	0.1089E-14
PF = FDBK RESISTOR PHASE ANGLE RAD	0.8294E-18
AZ = TRANSIMPEDANCE OHM	0.6363E+09
IS = SIGNAL PHOTOCURRENT A	0.3097E-10
IT = TOTAL BKGD PHOTOCURRENT A	0.3395E-10
VRF= FDBK RESISTOR NOISE V/HZ**.5	0.2006E-05
VBG= BACKGROUND NOISE V/HZ**)5	0.2099E-05
VJN= JOHNSON NOISE V/HZ**.5	0.2029E-05
VGR= GEN-RECOMB NOISE V/HZ**.5	0.2029E-05
VPA= PREAMP NOISE V/HZ**.5	0.3456E-06
VT = TOTAL NOISE V/HZ**.5	0.4097E-05
R = RESPONSIVITY V/W	0.2021E+10
NEP= NOISE EQUIVALENT POWER W/HZ**.5	0.2027E-14
DSTAR = CM*HZ**.5/W	0.3429E+14